Deep Water Massive Sands: Grain to Depositional Element Scale Analysis of their Internal Character.

Urval Satish Patel

Submitted for the degree of Doctor of Philosophy

Heriot-Watt University

School of Energy, Geoscience, Infrastructure and Society

January 2018

Supervisors:

Professor Dorrik A. V. Stow

Dr Andy R. Gardiner

ABSTRACT

Deep Water Massive Sands (DWMS) are ubiquitous in the modern and ancient sedimentary rock record, where they form important hydrocarbon reservoirs. Despite their economic importance and decades of research concerning their origin and internal character, they remain relatively enigmatic. This study, therefore, aims to shed light on their internal character and the processes responsible for their formation, and the implications this may have on hydrocarbon exploration and production. The study utilises outcrop (Grès de Peïra Cava and Numidian Flysch) and subsurface (East Brae Field) data to investigate the sedimentary character of DWMS at the grain, bed and element scale, by employing digital image analysis, vertical and lateral facies analysis, geostatistics (Markov chain and Entropy analysis) and static heterogeneity coefficients. From the analysis of the data, the following contribution to the field of deep-water sedimentology can be made: (1) three varieties of massive sands have been identified: ungraded and graded massive sands, and massive sands with patchy texture; (2) massive sands are characterised by a variety of grain size trends within the different grain size percentiles; (3) oblique-to-flow and high imbrication angle is the typical fabric character; (4) massive sands form the 'core' of the deep-water deposits in proximal and medial locations, but DWMS *sensu stricto* are primarily located in the distal locations of a basin; (5) graded and ungraded massive sands are laterally extensive, but those exhibiting 'patchy' texture are spatially restricted; and (6) massive sand facies associations are characterised by low heterogeneity, but distinct layering can be defined using petrophysical properties that are not observed at the macroscopic scale. Based on these findings, new models of DWMS deposition are presented for graded and ungraded massive sands, and massive sands with 'patchy' texture. These new modes of deposition for DWMS control grain- to element-scale heterogeneity in the sedimentological characteristics, which in turn controls petrophysical trends at different scales and ultimately affect how hydrocarbons hosted in massive sands are produced.

DEDICATION

To my family who do not know what massive sands are, and to my friends (Anne, Sophie, Neil, Nina, and Alex) who do not care!

Also to anyone who reads this thesis…

ACKNOWLEDGEMENTS

The completion of this study would not have been possible without the continuous support and guidance of two amazing supervisors: **Prof. Dorrik Stow** and **Dr. Andy Gardiner**… Sorry it took so long!

Thank you **to Rachel Brackenridge**, **Jim Buckman**, **Zeyun Jiang**, **John Mills**, **Mike Watson**, and **Patrick Corbett** for their helpful discussions during the course of this study and write-up phase. Thank you to **Sami Riahi** for accompanying me in the field in northern Tunisia. A special thanks to **Ben Gardiner** for being my field partner in Peïra Cava, for collecting the samples and helping me carry them down the mountain, and for warning me when there were snakes nearby.

The write up phase of this study was particularly difficult, and would not have been completed without the input and guidance of **Looi Lee Teng** who helped me with the petrophysical analysis of the East Brae data. To **Ankesh Anupam** and **Joseph Thompson**, thank you for your help with the heterogeneity analysis. To **John Turner**, thank you for training me in creating thin sections.

However, I would like to unacknowledge all those sedimentologist on my fieldtrips who mistook the word *massive* to mean thick bedded!

DECLARATION STATEMENT

ACADEMIC REGISTRY
Research Thesis Submission

Name:			
School:			
Version: *(i.e. First, Resubmission, Final)*		Degree Sought:	

Declaration

In accordance with the appropriate regulations I hereby submit my thesis and I declare that:

1) the thesis embodies the results of my own work and has been composed by myself
2) where appropriate, I have made acknowledgement of the work of others and have made reference to work carried out in collaboration with other persons
3) the thesis is the correct version of the thesis for submission and is the same version as any electronic versions submitted*.
4) my thesis for the award referred to, deposited in the Heriot-Watt University Library, should be made available for loan or photocopying and be available via the Institutional Repository, subject to such conditions as the Librarian may require
5) I understand that as a student of the University I am required to abide by the Regulations of the University and to conform to its discipline.
6) I confirm that the thesis has been verified against plagiarism via an approved plagiarism detection application e.g. Turnitin.

* *Please note that it is the responsibility of the candidate to ensure that the correct version of the thesis is submitted.*

Signature of Candidate:		Date:	

Submission

Submitted By *(name in capitals):*	
Signature of Individual Submitting:	
Date Submitted:	

For Completion in the Student Service Centre (SSC)

Received in the SSC by *(name in capitals):*			
Method of Submission *(Handed in to SSC; posted through internal/external mail):*			
E-thesis Submitted (***mandatory for final theses)***			
Signature:		Date:	

Please note this form should be bound into the submitted thesis.
Academic Registry/Version (1) August 2016

TABLE OF CONTENTS

Chapter 1 – Introduction.

1.1 Deep-Water Massive Sands.

Deep-Water Massive Sands (DWMS) form an important constituent of many turbidite systems around the world, both modern and ancient. They are defined as structureless sand beds that are macroscopically devoid of any primary sedimentary structures and where grading is largely absent (Stow and Johansson, 2000). The term deep-water refers to water depths below the effective storm-wave base (>200 m), and the term massive has no reference to the thickness of the bed. A minimum thickness of 1 m was considered by Stow and Johansson (2000), since it was these thick beds that posed a problem in terms of interpretation. They are usually a deposit of a single depositional event, however, examples exist where a number of beds have been amalgamated into a massive sandstone unit or body (Figure 1-1). In many turbidite plays around the world, they form prolific hydrocarbon reservoir due to their simple sandbody geometry and high sand: shale ratios. Numerous example can be found in the North Sea (e.g. Captain, Maureen, East Brae, Magnus, Buzzard fields), as well as along the Atlantic passive margins (e.g. Baobab, Lion, Marlim and Albacora fields), South East Asia (e.g. Kutei, Kikeh, Tembungo fields), and Gulf of Mexico (e.g. Garden Banks 191, Tiber fields).

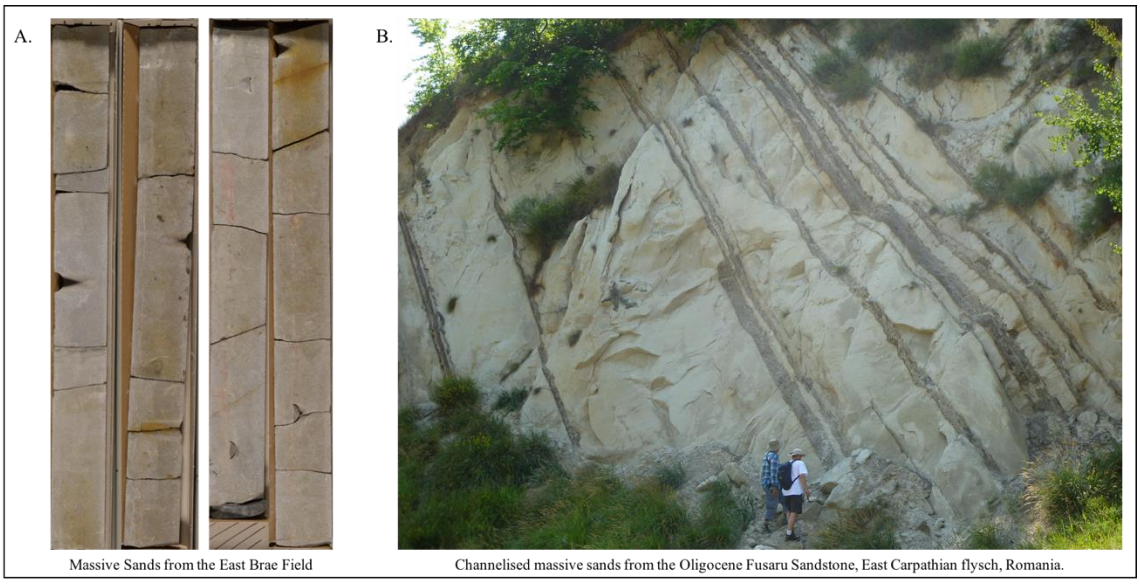

Figure 1-1: Examples of massive sand from the East Brae gas condensate field in the North Sea (A) and the East Carpathian flysch deposits in Romania (B). They have been defined as sand beds that are macroscopically devoid of primary sedimentary structures.

Stow and Johansson (2000) published a detailed synthesis of over 70 examples of massive sands of different ages and depositional environment that outlined the salient characteristics of massive sands. The main conclusion of this study was the recognition that: (1) massive sands occur in association with a closely related range of facies termed the Massive Sandstone Facies Association (MSFA); (2) the MSFA is varied in textural and compositional attributes, being

typically coarse grained, poorly to moderately sorted and compositionally immature; (3) although essentially devoid of primary sedimentary structures, massive sands can contain dewatering features and mudclasts, which can yield information on depositional processes; (4) the MSFA is typically a high net-to-gross succession (7:1 to > 9:1); (5) sand body geometries can range from small scale chutes and shallow channels (<0.25 km^2), larger lobate complexes (up to 50 km^2) to lensoid and tabular basin fill successions (up to 500 km^2); and (6) they are observed in varied depositional settings from fan deltas and muddy slope aprons, to channel-lobe complexes and distal basin settings.

While the above study shed light on the gross character of massive sands, it failed to address the age old controversy concerning their emplacement mechanism(s). Over the last 40 years, a number of mechanisms have been proposed for their formation, including: (1) continuous aggradation from a quasi-steady, but depletive flow (Kneller and Branny, 1995); (2) En-masse freezing from a fast-moving, semi-rigid sandy mass flow (Shanmugam, 1996); (3) post depositional removal of structured intervals (Baas, 2004); (4) continuous aggradation from a turbidity current displaying reversing buoyancy (Gladstone and Pritchard, 2010; Stevenson and Peakall, 2010); and (5) partially liquefied debris flows (Talling et al., 2013). Although it is plausible that massive sands are polygenetic, being able to differentiate massive sands based on their emplacement mechanism can lead to a better understanding of their distribution in the deep-water systems. This is of particularly importance for the hydrocarbon industry since sediment transport and depositional processes control reservoir architecture, fluid pathways and connectivity. This in turn will have an influence on the development strategies and the recovery factor, as well as project economics.

Furthermore, Stow and Johansson (2000) neglected to characterise the textural variation in massive sands nor quantify the degree of heterogeneity. All reservoirs are intrinsically heterogeneous and this heterogeneity varies with scale and resolution. At the grain- and bed-scale, sedimentological variations can influence porosity-permeability trends and can form local thief zones, baffles and barriers. At the element-scale, heterogeneities can affect connectivity and displacement mechanics. And lastly, at the field-scale, heterogeneities determine hydrocarbon volumes, trends of hydrocarbon production and ultimately recovery factor. It is therefore imperative that we advance our knowledge of the internal character and emplacement mechanisms of massive sands for the continued success of the hydrocarbon industry.

Recent technological advances in monitoring sensors and autonomous data recovery has allowed turbidity currents to be measured in nature (e.g. two turbidity currents in the Monterey Canyon in 2002; Xu et al., 2014). Nevertheless, the dilute and fine-grain (silt and clay) character

of these flows makes them unsuitable as analogues for studying the formation of massive sands. For massive sand depositing flow processes, the inaccessible nature of the deep-water environment, and the paucity and high destructive character of the flow, will always make direct observation technically and logistically difficult. As such, research into their hydrodynamic character has to rely upon modelling (theoretical, numerical and physical) and careful analysis of their deposit. Recent experimental and numerical modelling has shed light on the importance of turbulence dampening, grain size distribution, competence and capacity-driven deposition in influencing deposit architecture (e.g. Baas et al., 2011; Breien et al., 2010; Cantero et al., 2012; Cartigny et al., 2013, Dorrell et al., 2013 Eggenhusisen et al., 2017; Shringarpure et al., 2014; Steel et al., 2017; Talling et al., 2013b). There is a need now to investigate the implication of these processes by linking them to deposit character. Attempts have been made by e.g. Amy et al. (2006a), Fonnesu et al. (2015), Mueller et al. (2017), Patacci et al. (2014), Patacci et al. (2015) Sumner et al. (2012), Talling et al. (2007) and Talling et al. (2013a) to bridge this gap by utilising laterally extensive and correlatable beds to document changes in facies and geometries at the bed scale. These studies are a valuable source of knowledge for interpreting modern and ancient turbidite sequences, and developing static models in reservoir characterisation studies. It is against this background of recent advances in deep-water sedimentology that massive sands are evaluated in this thesis.

1.2 Thesis Aims.

The primary aim of this thesis is to elucidate the internal character of massive sands and identify the processes responsible for their formation. A better understanding of their character and origins has significant implications for the hydrocarbon industry. The definition of DWMS as proposed by Stow and Johansson (2000) is adopted here, with the exception of the 1 m minimum thickness limit. While many of the studied massive sands are > 1 m in thickness, a broader thickness definition is adopted since bed thickness is dependent on flow duration and rate of sediment fallout, and not on flow processes. A secondary aim of this thesis is to assess how the internal character introduces vertical and lateral heterogeneity in terms of reservoir quality (i.e. porosity and permeability) and the effect this may have on the development and production strategies of hydrocarbons hosted in massive sands. To fulfil these two aims, this study will:

1. Undertake a comprehensive review of massive sand depositional models.
2. Document vertical trends in grain size and grain fabric in the framework and zircon components from graded and ungraded massive sands.
3. Document the macroscopy internal bed character and external bed geometry of massive sands in laterally extensive beds.

4. Describe and quantify sedimentological and petrophysical heterogeneity in a MSFA.

1.3 Research Method.

To fulfil these aims, a detailed study using multiple outcrops (Numidian Flysch in northern Tunisia and the Grès de Peïra Cava in SE France) and subsurface (East Brae Formation) examples was undertaken. The outcrops were chosen due to their familiarity, relatively well exposed and extensive nature, and abundance of massive sands. An additional reason for selecting the Grès de Peïra Cava was due to the existence of a comprehensive correlation framework (Amy, 2000), which facilitated long distance correlation of beds containing massive sand facies. The selection of the East Brae Formation was based on the vertical and lateral coverage of core, quality of the wireline data and the degree of diagenetic alteration of the pore distribution. A hierarchical descriptive facies scheme was developed and employed to document vertical and lateral changes in facies for each locale. Orientated samples from the Numidian Flysch and Grès de Peïra Cava beds were selected at regular intervals for textural analysis. All subsequent analysis was undertaken at the Institute of Petroleum Engineering (IPE), Edinburgh.

1.4 Thesis Structure.

The thesis is separated into 6 chapters and an appendix with supplemental information and data. Original research is presented in **Chapters 3-5**, which also include substantive discussions on the character and emplacement mechanism(s) of DWMS at different scales, and a synthesis is provided in **Chapter 6**. The structure is as follows:

Chapter 1 (this chapter) introduces the study and provides context, aims and a description of the research method employed.

Chapter 2 provides a comprehensive review of DWMS depositional processes that brings together disparate studies on their vertical and lateral facies variability and geometry, which utilised outcrops, and theoretical, numerical and experimental data. This review then allows a comparison to be made to the newly collected data from the Grès de Peïra Cava outlier (**Chapter 3**).

Chapter 3 documents vertical and lateral changes in sediment facies in eight laterally extensive beds in the Grès de Peïra Cava outlier. Markov chain and Entropy analysis is used to describe the vertical arrangement and degree of randomness in the facies in a bid to describe the hydrodynamic processes responsible for massive sand formation. While Markov chain has previously been used extensively in previous studies to evaluate vertical arrangement of facies, to date, no study has made use of Entropy analysis to describe temporal evolution of flow processes. This part of the study provides the foundation to assess the validity of existing models in terms of the internal bed architecture and external geometry that is discussed in **Chapter 2**. Due to the confining nature of the Peïra Cava sub-basin, effects related to flow

reflections, deflection and transformation are also assessed, and incorporated into the development of a new model for the deposition of massive sands.

Chapter 4 details the textural characteristics of massive sands from the Numidian Flysch and the Grès de Peïra Cava. Digital image analysis was employed to automatically quantify the size, shape, and spatial arrangement of the grains. As part of this study, a new algorithm was developed to segment and separate touching grains, an issue that has troubled textural studies employing digital image analysis in the past. Following on from this, the impact on porosity and permeability trends at the bed-scale is discussed.

Chapter 5 describes and quantifies sedimentological and petrophysical heterogeneity in the MSFA of the East Brae Field at the bed and element-scale. An extensive core logging campaign was undertaken to describe approximately 4000 ft of core to study the sedimentological heterogeneity. The sedimentological heterogeneity will be investigated using Markov chain and Entropy analysis. In terms of petrophysical heterogeneity, static heterogeneity measures such as the Lorenz Coefficient (LC), Coefficient of Variation (CV), and the Dykstra-Parsons Coefficient (Vdp) were employed to quantify the variability in porosity and permeability in massive sands. For the purpose of this study, a moving window approach is used to create a curve to better visualise the changes in heterogeneity. These curves are also utilised to define internal layering in massive sands and relate them to reservoir behaviour. Such an approach has not been previously used to study massive sands.

And finally, **Chapter 6** provides a synthesis of the key findings. Since each of the preceding chapters have a substantive discussion relevant to the chapter aims, this chapter is primarily used to summarise the results, to develop and present new model(s) for DWMS, identify limitations in the present study, explore the significance of the study for the hydrocarbon industry and recommend future work in massive sands.

Supporting material, such as description of the facies scheme, correlation panels, tables, lists, algorithms and codes, which would have otherwise interrupted the flow of the thesis has been included as Appendices in **Chapter 7** and an accompanying **CD** for outsized documents.

Chapter 2 – Review: Deep-Water Massive Sands (DWMS) Depositional Models.

Following a general introduction to Deep-Water Massive Sands (DWMS), this chapter provides a critical review of the various models proposed for their formation. The review will incorporate data from field studies, physical experiments, theoretical analysis and numerical simulations in terms of textural characteristics, vertical and lateral organisation of facies, and facies and bed geometries.

2.1 Deep-Water Massive Sands (DWMS).

Stow and Johansson (2000) carried out an extensive rock-based study to characterise the nature and variability of DWMS. These authors defined DWMS as a single bed or a unit (comprising several beds) greater than 1 m in thickness. The term massive has no reference to the thickness of the bed or unit, but rather refers to the structureless nature of the deposit i.e. lacking primary sedimentary structures. The term deep-water refers to water depths greater than the storm-wave base. While isolated DWMS were observed in a variety of tectonic basins worldwide, the above authors noticed they are more commonly found in association with other coarse-grained deep-water facies they referred to as the Massive Sandstone Facies Association (MSFA; Figure 2-1). It is as part of these thick sequences that DWMS has received much attention in the geological literature due to their economic importance as hydrocarbon reservoirs (e.g. Mesozoic and Tertiary reservoirs in the North Sea, Oligo-Miocene flysch deposits in northern Africa, and Cretaceous deposits along the southern Atlantic margins).

The rock-based study of over 70 examples of massive sands of different ages and depositional settings by Stow and Johansson (2000) attempted to define the salient characteristics of these deposits, including; vertical facies association, geometries, likely depositional settings and transport and depositional processes. The main conclusions were the recognition that: (1) massive sands occur in association with a closely related range of facies which they termed the Massive Sandstone Facies Association (MSFA; Figure 2-1); (2) the MSFA is varied in textural and compositional attributes, being typically coarse grained, poorly to moderately sorted and compositionally immature; (3) although essentially devoid of primary sedimentary structures, massive sands can contain a variety of dewatering features and mudclasts, which can yield information on depositional processes; (4) the MSFA is typically a high net-to-gross succession (7:1 to > 9:1); (5) sand body geometries can range from small scale chutes and shallow channels (<0.25 km^2), larger lobate complexes (up to 50 km^2) to lensoid and tabular basin fill succession

(up to 500 km^2; Figure 2-2); (6) they are observed in varied depositional settings from fan deltas and muddy slope aprons, to channel-lobe complexes and distal basin settings; and (7) debris flows and turbidity currents are the most likely emplacement mechanisms.

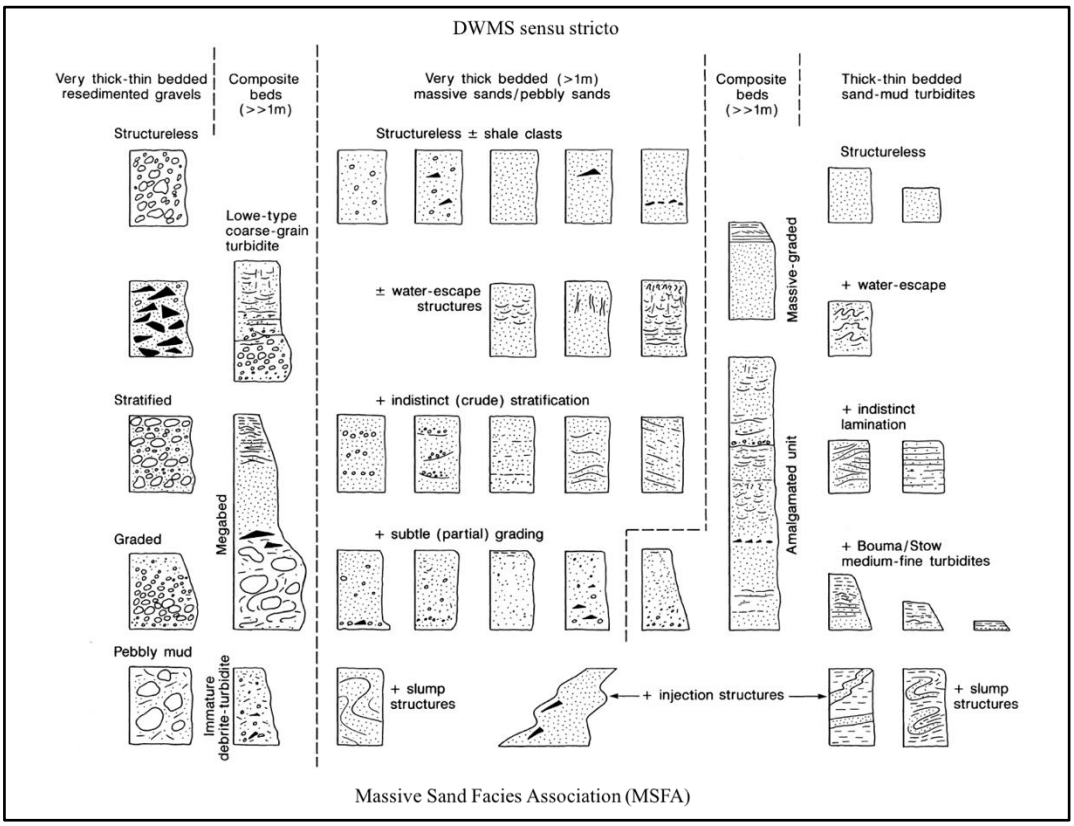

Figure 2-1: Massive Sandstone Facies Association showing DWMS (central facies panel) and the facies variability in a given deep-water resedimented succession (after Stow and Johansson, 2000).

In terms of the internal character and vertical sequence, the massive sand bodies in general mirror the larger-scale depositional element e.g. in lobe settings, individual sands are lensoid or lobate, while in channels they tend to concave-downward to erosive gully-shaped (Stow and Johansson, 2000). In each setting, bed compensation processes, where by successive flows fill-in topographic lows, can result in symmetrical cycles and micro-sequences, and along with bed amalgamation, can lead to tabular geometries (*ibid.*). This also produces a blocky vertical sequences in terms of bed thicknesses. Nevertheless, sand body can be modified by syn- and post-depositional processes, including: fluidisation and liquefaction; syn-sedimentary faulting; and, differential compaction.

However, despite this comprehensive study and in light of recent advances in deep-water flow processes, DWMS remain enigmatic in terms of their transport and depositional processes, internal variability (e.g. reservoir parameters such as porosity and permeability) and external geometry. In the following sections, a critical review of the various models of DWMS formation is outlined. This review incorporates data from field studies, physical experiments, theoretical analysis and numerical simulations in terms of textural characteristics, vertical and

lateral organisation of facies, and facies and bed geometries. These models are subsequently compared to new data collected from the Numidian Flysch (Tunisia), Grès de Peïra Cava (France) and the East Brae Formation (South Viking Graben), which aims to shed light on the validity of depositional models (Chapter 3) and the variability of DWMS (Chapters 4 and 5). While Stow and Johansson (2000) incorporated a thickness cut-off in their original definition, for the purpose of this review, as well as in subsequent chapters, this lower limit is discarded. This was based on the knowledge that bed thickness is dependent on flow duration and sediment-fallout rates, and not on flow processes.

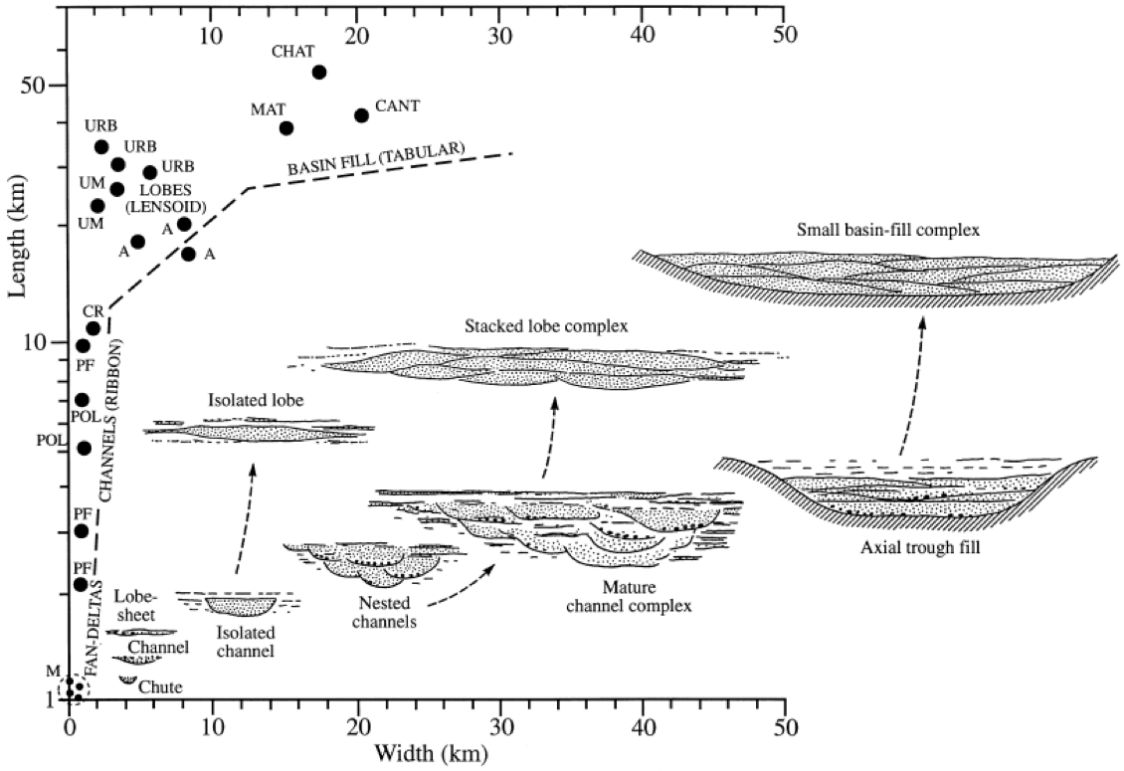

Figure 2-2: Massive sand body geometry from 21 examples (black dots) and schematic representation in two dimensions of sand body geometry for different system. Case studies: CHAT, Chatsworth formation; CANT, Canua sandstones; MAT, Matilija sandstone; URB, Urbanian sandstone; UM, Umegase formation; A, Annot sandstone; CR, Contrada di Romani; POL, Pollina; PF, Ponte Finale; M, Maesan. After Stow and Johansson (2000).

2.2 Continuous Aggradation Beneath a Quasi-Steady Turbidity Current.

Kneller (1995) and Kneller and Branney (1995) demonstrated that the vertical and spatial evolution of sediment facies in a given bed are a reflection of the temporal (steadiness) and spatial (uniform) evolution of the velocity profile and density structure of the flow (Figure 2-3). They argued that flow unsteadiness is not necessary for deposition of sediments from a turbidity current, as was suggested by Lowe (1982). Flow steadiness is defined as fluctuations in the velocity of a flow at a given point. During unsteady flow conditions, grains of particular size

will settle out of a flow as the shear velocity of the flow falls below the terminal settling velocity of the grains. In contrast, using the concept of substantive acceleration ($du/dt=\partial u/dt+u.\partial u/\partial x$, where x is the streamwise distance, u is velocity, t is time and the terms $\partial u/dt$ and $u.\partial u/\partial x$ describe temporal and spatial velocity changes respectively), Kneller (1995) and Kneller and Branney (1995) postulated that flows may deposit their sediment load when the net acceleration experienced by the grains in the flow is negative i.e. steady flow conditions (Figure 2-3).

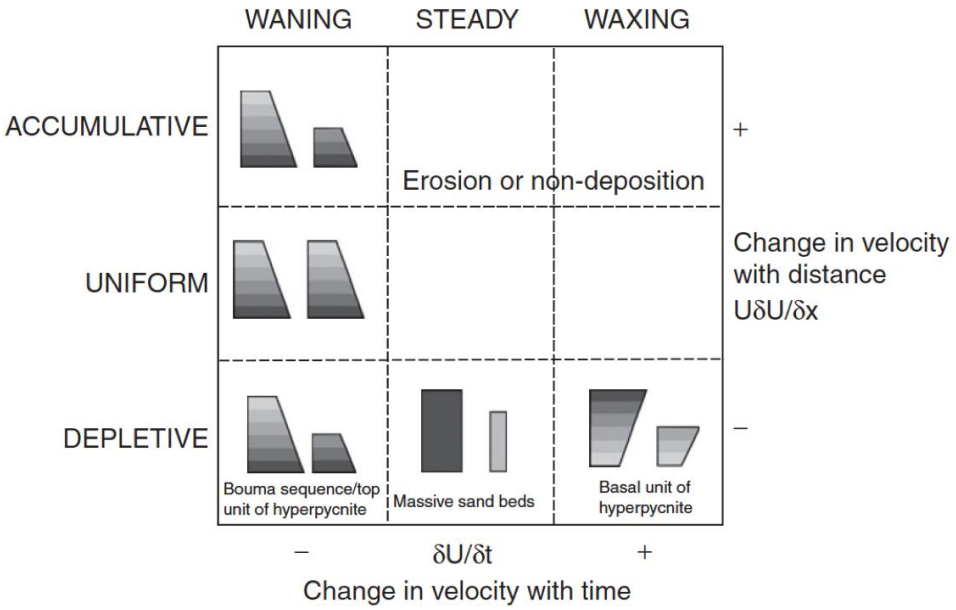

Figure 2-3: Acceleration matrix showing changes in velocity with time and distance, and illustrative bed sequences for each field. For each field, the bed sequence on the right shows downstream equivalent. Modified after Kneller (1995).

2.2.1 Depositional Model.

Applying the substantive acceleration notion to DWMS, Kneller and Branney (1995) envisioned a steady (temporally), but depletive (spatially) high-density turbidity current as a plausible mechanism for the formation of massive sands. At a given geographical location, the high downward flux of grains from a quasi-steady high-density turbidity current creates a concentrated, non-turbulent basal layer where processes other than turbulence dominate. This basal part of the current is subject to continuous deposition at its base and is replenished with sediments from above. Due to the loosely compacted and water-saturated nature of the sediments that have just been rapidly deposited, there may be negligible difference in concentration between the highly concentrated basal layer of the flow and the static substrate (especially since de-watering processes operating in the substrate create a continuous concentration gradient between the settling dispersion and the substrate; Figure 2-4A). Since viscosity is related to grain concentration, this basal zone (i.e. high concentration dispersion and

dewatering substrate; depositional boundary) is likely to behave as a liquefied zone and display non-Newtonian behaviour with finite yield strength (Bagnold, 1952; Shanmugam, 1996). The effects of dispersive pressure and other non-turbulent processes will *progressively* decrease downwards as a result of the increasing shear strength in the basal zone. Due to this lack of a sharp rheological boundary through the basal zone, no traction structures develop. As sedimentation continues through this zone, the deposit progressively aggrades, the static substrate gradually rises, and the resulting deposit is massive. Since deposition is competence driven, the final deposit should also be well sorted (Kneller and Branney, 1995; Sylvester and Lowe, 2004). Furthermore, the final deposit thickness is unrelated to flow thickness, but is dependent on the flow duration and rate of sediment fallout.

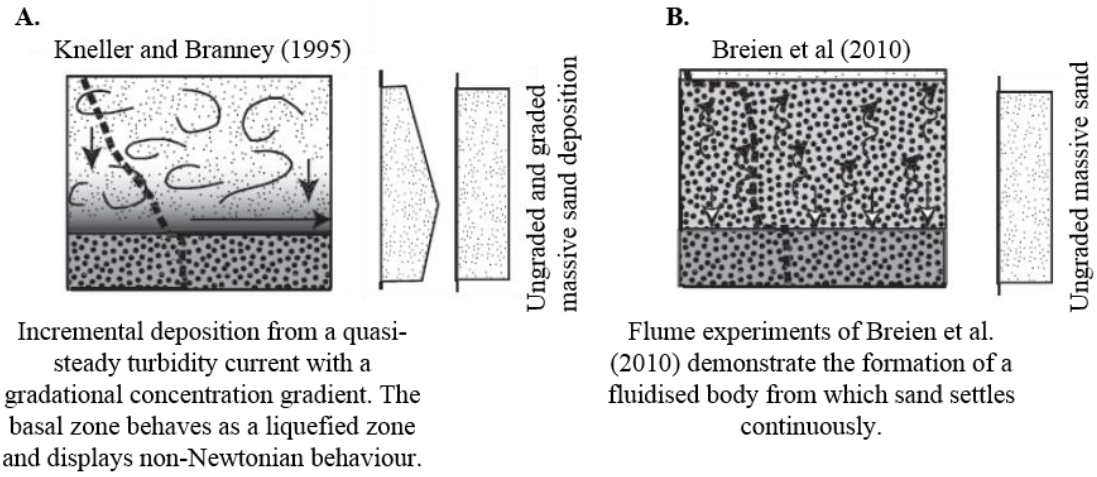

Figure 2-4: Generalised diagram showing a sustained liquefied zone in processes models for massive sands deposition. A) Continuous aggradation beneath quasi-steady high-density turbidity currents (Kneller and Branney, 1995). B) liquefied body in a concentrated flow from the experiments of Breien et al. (2010). In both cases, the flow is driven by its own weight, hindered settling is active and the deposit is aggraded progressive. Dashed line indicates concentration gradient. Modified after Talling et al. (2012).

The above rheological model has been recreated in a number of experimental studies with varying degrees of success (e.g. Amy et al., 2005; Amy et al., 2006a; Breien et al., 2010; Cartigny et al., 2013; LeClair and Arnott, 2005; Sumner et al., 2008; Vrolijk and Southard, 1997). In these experiments, the interface between the high-concentration basal layer and the deposit is generally gradational, although only Amy et al. (2006a) and Cartigny et al. (2013) were able to recreate the gradational transition to the overlying fully turbulent suspension (sensu stricto Kneller and Branney, 1995). In other studies though, a sharp, undulating interface exists between the high-concentration layer and the overlying layer due a sharp change in concentration across the boundary. The internal character of deposits produced from these experiments varied from crudely stratified to massive and from ungraded to strongly graded, depending on flow concentration, density, viscosity, sediment fallout rates, and clay content.

Similar to the theoretical model of Kneller and Branney (1995), the majority of these authors only considered the vertical flux of sediments to the high-concentration zone. Kneller and Branney (1995) did nonetheless acknowledge that massive sands may also be produced by a high-concentration zone that is fed laterally (e.g. as a high concentration liquefied dispersion) from the body and tail of the flow. Flume experiments by Breien et al. (2010) have shown clean massive sands being deposited from dense flows through fluidised layers that are fed laterally (Figure 2-4B). The experimental flows contained 10 weight % clays, and once released into the flume, decomposed vertically and longitudinally into a turbulent head, fluidised body with a turbulent top, and a laminar clay-rich tail. In the body, clay is lost through elutriation and sand continuously settles from the fluidised zone, resulting in a deposit similar to the Ta interval of Bouma (1962). The clay-rich tail of the flows injects the fluidised region with new, homogenised material, thus allowing the fluidised body to operate for longer periods and deposit laterally extensive beds (Breien et al., 2010).

2.2.2 Vertical and Lateral Facies Transition.

When considering the longitudinal velocity and density structure of turbidity currents, Kneller and McCaffrey (2003) suggested a sequence of sedimentary structures that would be produced in a vertical and downslope transect. Where flow non-uniformity is the cause for massive sand deposition (*sensu* Kneller and Branney, 1995), spatial changes in flow velocity would result in massive sand intervals being deposited along the base of the bed in a downstream direction. As the current velocity and density decreases, the massive interval is overlain by an interval of tractionally reworked sediments which increase in thickness distally at the expense of the massive sand. As long as the current continues to be steady, both intervals will be ungraded and relatively well sorted. The lateral transition of the massive sand into a tractionally reworked deposit downstream is gradual. Since turbidity currents must eventually wane, there is a progressive loss of competence and a vertical transition from weakly to strongly graded massive sand, into parallel and rippled laminated facies at the top (Baas, 2004). The deposit is also expected to be well-sorted since flow competence, and not flow capacity, is the driving mechanism for deposition. Baas et al. (2004) observed a similar sequence in flume experiments of quasi-steady, non-uniform flows, in which high sediment fallout rates suppressed bedform development in proximal locations (Figure 2-5). Vertically and laterally, the massive sands transition into laminated sands due to lower sediment fall-out rates. Vertical and lateral grain size segregation was observed to be active within the high-concentration layers developed beneath high-concentration flows. The resulting deposit is ungraded to weakly normal graded in proximal locations, becoming strongly graded in the upper parts of the beds downstream (Baas, 2004).

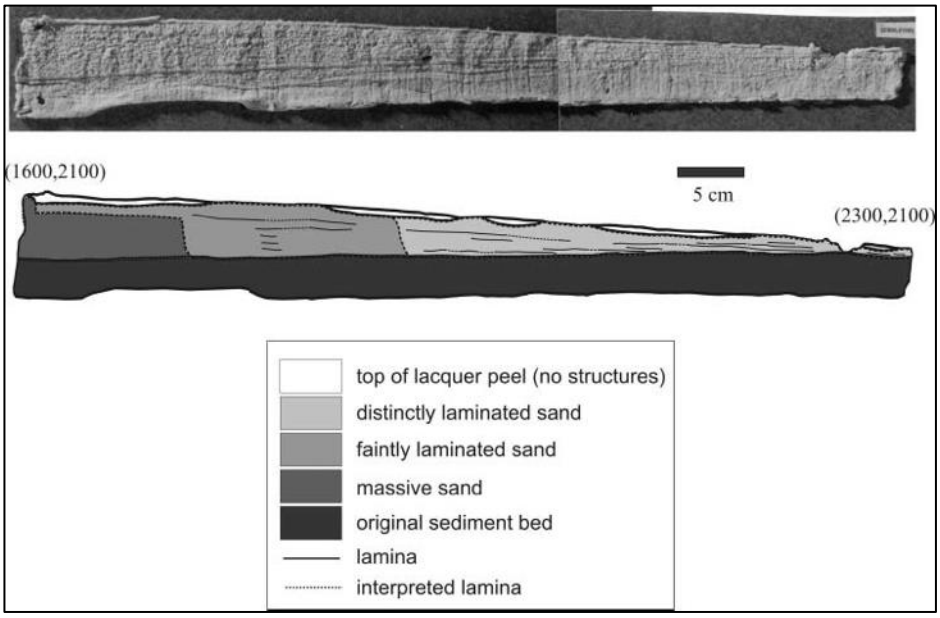

Figure 2-5: Lacquer peel (above; and its interpretive drawing below) showing a transverse section through part of the lobe (massive sand deposit) and its fringe of the fan deposit (laminated sands). After Baas et al. (2004).

2.2.3 External Bed Geometry.

For temporally steady and spatially depletive flows (Kneller, 1995; Kneller and Branney, 1995), laboratory experiments show that bed thicknesses decrease monotonically with an exponential trend, irrespective of surge or continuous input, flow volume or grain size distribution (Bursik and Woods, 2000; Dade and Huppert, 1995; Gladstone et al. 1998; Gray et al., 2005; Kubo, 2004; de Rooij and Dalzeil, 2001; Laval et al., 1988; Sequeiros et al., 2009; Spinewine et al., 2009). Similar bed geometries are also produced from depth-averaged (Kubo, 2004; Salaheldin et al., 2000) and vertically-resolved (Blanchette et al., 2005) numerical models, which produce simple concave-upward bed geometries. However, in the experiments of Dade et al. (1994) and Gladstone et al. (1998), the earliest stage of deposition in proximal locations are dominated by the flow's initial state, leading to relatively uniform deposit thickness. If the flow is sufficiently energetic to cause sediment re-entrainment, then a slight thickening of the deposit thickness downslope is to be expected. The deposit thickness decreases progressively downslope, as the initial unsteady conditions of the flow are overcome and sediment is lost through progressive settling. As a result the bed geometry decays exponentially distally. The overall shape of deposits is thus sigmoidal to linear with convex upward distal parts. Flow dynamics in these studies were characterised by decreasing sediment concentrations and sedimentation rates away from the source, since rate of deposition exceed rate of sediment re-entrainment. The decrease in sediment concentration downslope results in a progressive thinning/tapering of the deposit. This suggests that a 'wedge shaped' deposit with decreasing thickness downslope, is a salient feature of steady, but non-uniform turbidity currents. Even though, a general deposit trend has

emerged from experimental and numerical studies, studies of ancient and modern turbidite systems show little consensus.

In ancient deposits, variable bed geometries have been reported, although sigmoidal, concave-upward or linear thinning trends with abrupt convex upward distal thinning appear to be the archetypal shape. In the comprehensively studied Marnoso Arenacea Formation of the Italian Apennines, a broadly concave-upward trend is observed for small volume flows (< ~0.5 km^3; Amy et al., 2006; Amy and Talling, 2005; Malgesini et al., 2015; Talling et al., 2007b). However, Talling et al., (2007b) noted that the rate of thinning is several orders of magnitude shorter in experimental flows compared to natural flows. This discrepancy can be related to flow efficiency; deposit thickness decreases more gradually for finer grained natural flows (Gladstone et al., 1998; Baas et al., 2004), since the flow has to expend less turbulent energy to keep finer grains in suspension and thus maintain its momentum for longer. Additionally, in the basin plain, small volume natural flows possess a more tabular geometry. This characteristic also deviates from experimental (e.g. Dade and Huppert, 1995; Kubo 2004; Laval et al. 1988) and numerical studies (e.g. Blanchette et al. 2005; Kubo, 2004; Salaheldin et al. 2010), and can be correlated to tractional reworking of sediment by natural flows in distal locations (Talling et al., 2007b). In fact, experimental and outcrop studies have shown the rate of thinning may be related to the bed thickness at a given point, with thicker beds possessing higher thinning rates than thinner beds.

For larger volume natural flows (> 2.5 km^3), Talling et al. (2007a), Sumner et al. (2012), and Remacha and Fernandez (2003) reported a broad thickness maximum in proximal locations for the Marnoso Arenacea Formation, the Agadir Basin, offshore Morocco and the Hecho group, NE Spain, respectively. This thickness maximum has not been satisfactorily reproduced in experimental studies. Talling et al. (2007a) associated these trends to: flow unsteadiness and corresponding migration of deposition basinward; tractional reworking of initial suspension fallout or high concentration near bed processes; and sediment re-entrainment. In each of these examples, the thickness maximum is associated with thick intervals of ungraded to weakly graded massive sands, which thin to form gradually tapering beds characterised by parallel and ripple lamination (Remacha and Fernandez, 2003; Tinterri et al., 2003). A recent re-analysis of beds in the Marnoso Arenacea Formation by Malgesini et al. (2015) reaffirms these observations. They suggested the thickness maximum is related to hindered settling processes based on the close association with the massive sands.

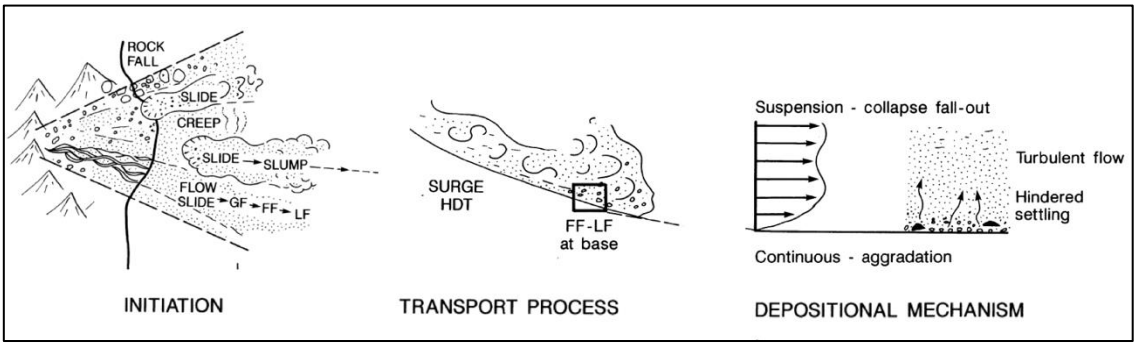

Figure 2-6: Initiation, transport processes and depositional mechanisms involved in massive sands from surge-type turbidity current. Modified after Stow and Johansson (2000).

2.3 High Sediment Fallout Beneath a Surge-Type Turbidity Current.

Bouma (1962) was one of the first authors to ascribe massive intervals in deep-water deposits to suspension fallout from surge-type turbidity currents. Surge-type turbidity currents are initiated by slumping/deformation of a finite amount of sediments that are suspended and move downslope as a turbid front. Since the deformation takes placed over a short time interval, sediments to the current are also fed over a short time, and the temporal and spatial velocity profile is characterised by unsteadiness and nonuniformity (Figure 2-6; Luthi, 1981; Kneller and McCaffrey, 1999). The longitudinal structure of surge-type turbidity currents may consist of a more-or-less clearly differentiated head, body and tail. In experimental studies, such currents have their analogues in the finite volume currents generated by the release of a lock gate. The deposit character resulting from surge-type turbidity currents is typically described in terms of the classical Bouma and Lowe sequences. In both of these sequences, the massive interval is postulated to exist by suppression of bedforms at higher sediment fallout rates from the head and body of the current. Rapid deposition of sediments also leads to unstable grain packing and excess pore-pressure build-up, which manifests itself in the deposit as de-watering structures (e.g. dish and pipe structures). The tail of the flow is characterised by lower concentrations and velocities, compared to the head and body, leading to the formation of tractive features (i.e. Tb-Td). Grading, if present, results from the unsteady nature of the current and can range from distribution to coarse-tail grading (Lowe, 1982).

2.3.1 Depositional Model.

The formation of massive sands beneath surging turbidity currents has commonly evoked high-sedimentation rates to suppress traction features (Figure 2-6). Arnott and Hand (1989) carried out flume experiments to determine the effects of sedimentation rates on the development of bedforms. At sediment fallout rates of 0.7 mm s^{-1} and higher, the authors found that bedform development was suppressed by burial of near-bed high concentration layers without tractional reworking, producing a massive bed. More recent studies, however, have found different values of sediment fallout rates and bedform suppression (Leclair and Arnott, 2005; Sumner et al.,

2008; Vrolijk and Southard, 1997). But as noted by Lowe (1988), sediment fallout rate is only one component in determining the development of bedforms. The critical value at which bedforms development is suppressed is also dependent on grain size and composition, flow concentration and deceleration speeds of the flow (Baas, 1999, Baas et al., 2004; Leclair and Arnott, 2005; Sumner et al., 2008). The latter two parameters and their influence on deposit character have recently been given extensive theoretical and experimental consideration.

Due to the unsteady and nonuniform nature of surge-type turbidity currents, Allen (1991) and Hiscott (1994) argued that it is capacity and not competence that govern depositions from turbidity currents. Capacity represents the amount of sediments a flow can carry per unit cross-sectional area, and is dependent on the size of the grains and flow intensity. During flow deceleration, the capacity of the flow progressively decreases and grains of variable size settle onto the sediment bed. Since the flow velocity has no direct influence on sediment size distribution in the flow, it is likely that capacity driven deposition coupled with high sediment fall out rates will result in massive, poorly sorted deposits (coarse-tail grading), with little or no elutriation of finer grains. This hypothesis has been recently reaffirmed by the settling tube experiments of Amy et al. (2006a), numerical sedimentation models of Dorrell et al. (2011) and annular ring experiments of Sumner et al. (2008). In all of these studies, massive, poorly sorted sediments were deposited from a near bed high-concentration layer characterised by hindered settling processes. Elutriation of finer grains was reduced under high sediment fall-out rates, but increased as the settling regime changed with lower sediment fall-out rates. Based on these experiments, it is valid to assume that the natural limit on the amount of sediments a flow can carry controls deposition. A simple example was provided by Blatt et al. (1980), who used the suspension criterion ($U_s < 0.8U^*$, where U_S is the grain settling velocity and U^* is the shear velocity) to demonstrate a flow at full capacity carrying maximum 1 mm grains and decelerating from 15 to 5.5 ms^{-s}, would deposit 85% of its sediment load even though it is competent to carry the coarsest grain size faction.

Field based studies have also used capacity-driven deposition models to explain complex grain size distribution trends observed in massive sands (e.g. Hiscott and Middleton, 1980, Sylvester and Lowe, 2004). In a detailed textural analysis of turbidite beds in the East Carpathian Flysch Belt, Sylvester and Lowe (2004) identified overloading of the flow (i.e. sediment capacity) and corresponding high-sediment fallout rates as the main cause of massive sand deposition. This was based on the observation of high degree of fines entrapment at the base of the flow. With reduced sediment fallout rates and change in sediment settling regime, elutriation removed finer grains from the deposit, but sediment fallout rates were sufficiently low to allow the flow to rework the deposit. Other authors (e.g. Kneller and McCaffrey, 2003) have proposed explanations for the ungraded and graded nature of massive sands based on the cause of loss of

capacity. Where flow unsteadiness (increasing discharge from rivers or passages of surges/pulses related to slope failures) is the cause of capacity-driven deposition, a normal graded deposit is likely to form, while nonuniformity (changes in slope angle, topographic barriers) is likely to result in ungraded massive intervals (Kneller and McCaffrey, 2003). Although deposition of massive sand from capacity driven deposition is not instantaneous, due to the lag between onset of grain settling and arrival at the depositional interface, what can be concluded from experimental, field-based and theoretical studies is that grain settling processes may be equally important as horizontal flow processes in governing deposit character in turbidity currents

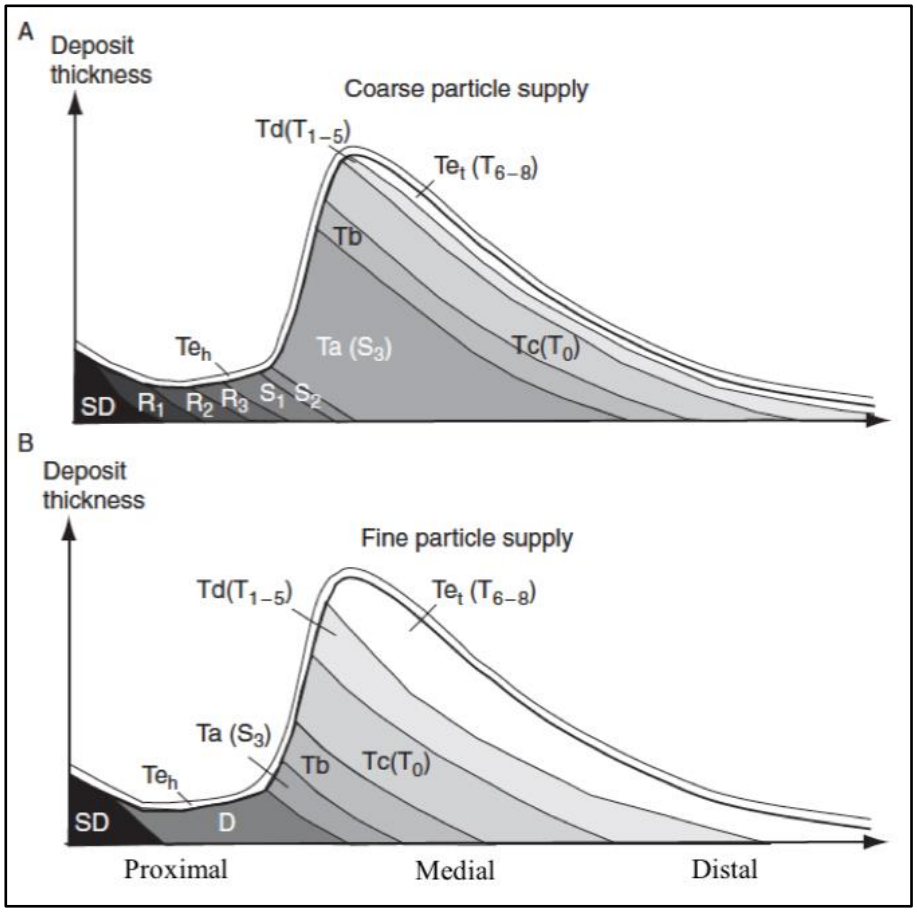

Figure 2-7: Downslope changes observed in facies character from a surge-type turbidity current comprising: A) coarse grained sediments and B) fine grained sediments. Modified after Lowe (1982) and Shanmugam (2000).

2.3.2 Vertical and Lateral Facies Transition.

Massive sand intervals deposited by surge-type flows have been incorporated in idealised vertical facies schemes of Lowe (1982; S_3) and Bouma (1962; T_a). Both of these schemes describe flow evolution that is hydrodynamically similar, and can be thought of as proximal and distal expressions of the same flow, respectively. A generalised downslope transition in facies deposited by surge-type turbidity currents is shown in Figure 2-7. In proximal locations, coarse

grained massive sands are deposited by the head of the flow. Progressive decrease in concentration, density and velocity as the flow moves downslope results in deposition of finer grain sizes that make up thin S_3/T_a divisions, capped by traction structures (T_{b-d}) from the Bouma sequence. This lateral transition in facies character is, however, speculative and based on extrapolation of flow hydrodynamics from single outcrops.

Utilising detailed field observations, facies analyses and long-distance correlation between facies, Mutti (1992) and Mutti et al. (1999; 2003) suggested unsteady and non-uniform flows undergo a series of hydrodynamic transformations as they move downstream, and produce two distinct types of massive sand facies (i.e. F5 and F8; *sensu* Mutti, 1992). The first type (F5) the authors concluded is deposited from *en-masse* sedimentation involveing significant grain support from excess fluid pore-pressure, and is common in more proximal locations. The above authors emphasised that temporal and spatial evolution of the flow resulted in two intergradational facies transitions from the F5 massive sands (Figure 2-8): 1) the massive sand is overlain by and passes laterally into crudely stratified horizontal lamination (Figure 2-8A), or 2) the massive sand is capped by and replaced downslope by finer grained stratified intervals (Figure 2-8B). In the latter case, the stratified interval is separated from the underlying massive sand by a grain size break due to a change in the sediment settling regime and short-term by-pass of sediments. This second model is similar in the vertical and lateral profile to a conceptual model proposed by Kneller and McCaffrey (2003) which associates unsteadiness as the cause of capacity-driven deposition of massive sands. Following the initial deposition of massive sand, the current may fall below capacity and re-entrain or rework deposited sediments (Figure 2-8C). The second type of massive sands (F8) in Mutti's genetic facies tract is deposited further downslope in distal locations after the flow has undergone transformation from a dense, laminar flow into a turbulent flow. This massive sand is equivalent to the Bouma Ta division, and as suggested by Middleton and Hampton (1973), is formed by high rates of sediment fallout from an overlying suspension that suppresses traction features. The final depletive and waning stages of the turbulent flow are marked by the gradual vertical and lateral transition into classic Tb through Td divisions of the Bouma model (Figure 2-7: Mutti et al., 2003). Again this is similar to the distal vertical profiles in the conceptual model of Kneller and McCaffrey (2003) (Figure 2-8C). Where the two models differ is in the degree of rheological transformations a high concentration flow may undergo from proximal to distal.

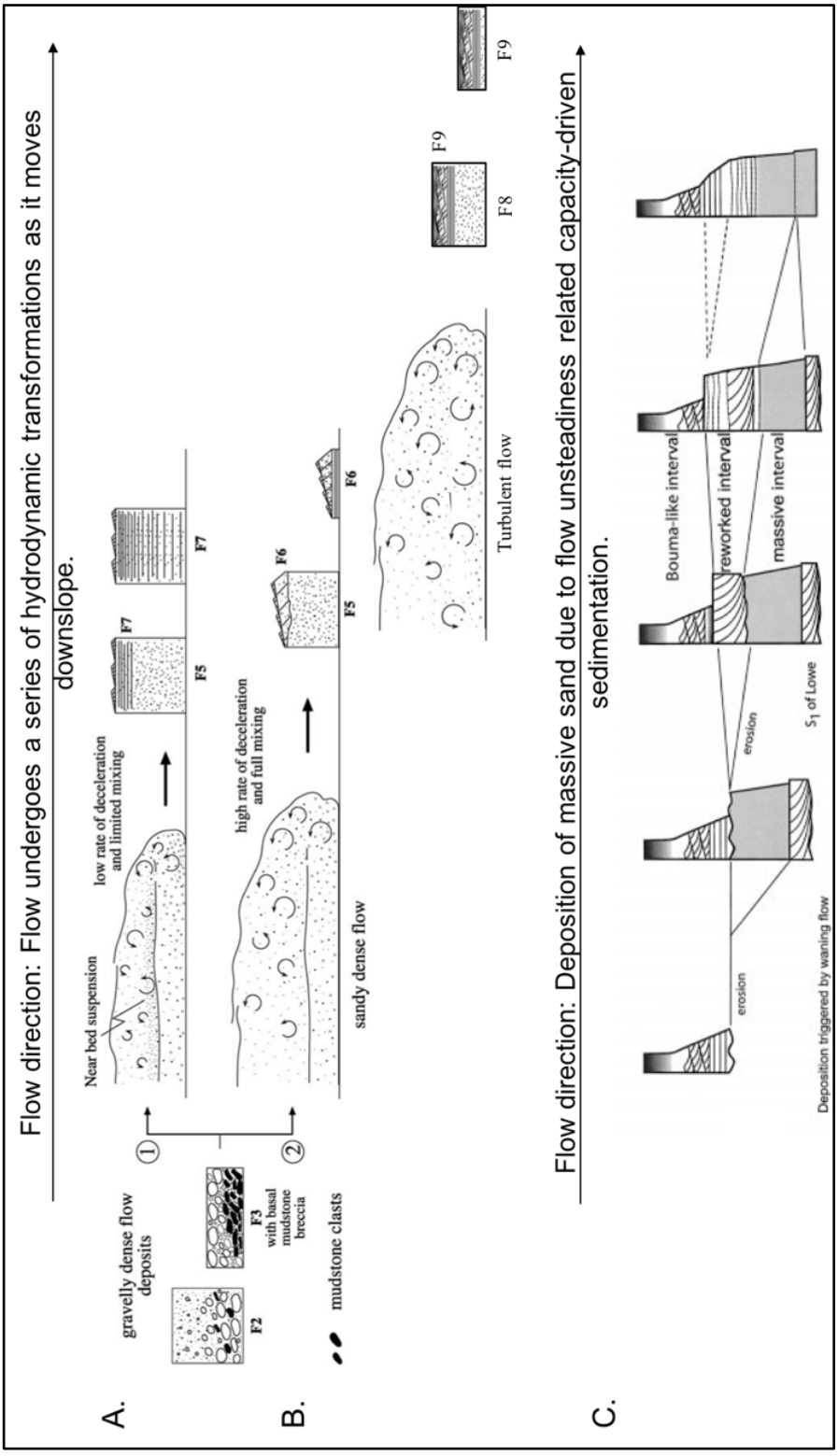

Figure 2-8: A generalised facies tract of depletive surge-type turbidity currents. A). Two massive sand (F5 and F8) facies are recognised in the genetic classification of Mutti (1992) and Mutti et al. (1999) that form in proximal and distal locations respectively, as the flow undergoes hydrodynamic transformation from a dense flow to a turbulent flow. Massive sand facies in both instances are overlain and laterally pass into various facies consisting of tractive features. B). Conceptual model showing a case where massive sand deposition is triggered by capacity-driven sedimentation due to flow unsteadiness. As the flow falls below capacity, deposited sediments may be re-entrained and/or reworked producing a grain size break and tractive features above. Modified after Mutti et al. (2003) and Kneller and McCaffrey (2003).

2.3.3 External Bed Geometry.

Similar to quasi-steady turbidity currents, external bed geometry of surge-type turbidity currents show sigmoidal to exponential decrease in bed thickness with distance. For a comprehensive analysis of bed geometries produced in unobstructed basins, please refer to Section 2.2.3. In this section, recent research on surge-type turbidity currents and their resulting deposits in confined basins is reviewed. Extensive outcrop studies in the Grès d'Annot, SE France reveal flow interaction with the confining topography influence external bed geometry (e.g. Amy, 2000; Kneller and McCaffrey, 1999; Pickering and Hiscott, 1998; Sinclair, 1994; Pattaci et al., 2014 to name a few). Bed geometry in these studies ranged from sigmoidal to concave-upwards as the beds approach the confining slope. Using the acceleration matrix of Kneller (1995), Kneller and McCaffrey (1999) related the effects of a lateral margin on bed geometry trends and associated facies transitions to an initially depletive flow (proximal to confining slope), which became accumulative as the streamlines converged due to deflection off the confining slope, and eventually uniform as the flow moved parallel to it. Flow interaction with the bounding slope is also known to produce similar bed geometries depending on the angle of the confining slope, although a variety of bed pinch-outs have been noted (see Gardiner (2006) for detail).

For experimental surge-type flows entering a confined basin, Lamb et al. (2004) found that individual surge deposits approached a drape geometry, with proximal deposits relatively thinner compared to basin plain deposits. The authors attributed this to enhanced flow competence in the head compared to the body of the turbidity current, which bypassed proximal regions and deposited their sediment load in the basin plain. With deposition of successive flows, the geometry approached that of a ponded deposit with thicker deposits in the centre of the basin. But is should be noted that the authors used a concave up basin profile which resulted in thicker beds in the centre of the flume. Relatively few experiments have studied the effects of an abrupt change in slope on deposit geometry (e.g. Amy et al., 2004; Kneller et al., 1991; Lee et al., 2004; Mulder and Alexander, 2001b). Intuitively, where a surge encounters an abrupt change in slope, an asymmetrical thickening of the deposit is to be expected towards the base of slope. This can be related to the loss of capacity (and/or competence) of the flow and associated increased sediment fallout rates (Lee et al., 2004; Mulder and Alexander, 2001b). In experiments (and basins) with a lateral confining margin, geometries that thin and thicken away from the slope have been observed (Amy et al., 2004). In this study, non-uniform flow concentration was cited to explain thinning away from the slope geometries, where lateral spreading of the flow on the side furthest away from slope controlled deposit thickness. In cases where deposit thickness increased away from slope, Amy et al. (2004) suggested flow velocity non-uniformity can explain the observed thickening, if deposit thickness is assumed to be controlled by the sediment-load fallout rate away from the slope.

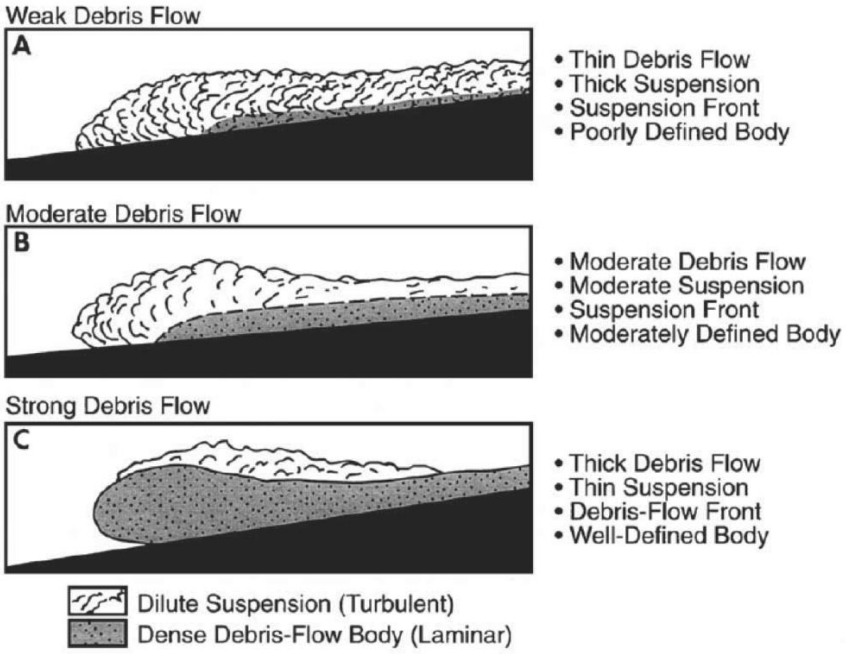

Figure 2-9: Three profiles of sandy debris flows depending on the clay and water content. After Marr et al. (2001)

2.4 En-masse Freezing from a Debris Flow.

2.4.1 Depositional Model.

Building upon the work of Hampton (1975), and dissatisfied with the prevailing interpretation of DWMS, Shanmugam (1996; 2000) proposed that 'sandy debris flows' or 'sandy mass flows' are the primary transport and depositional agents responsible for emplacing thick sequences of massive sands (Figure 2-9). The authors considered these flows as a continuum of processes between cohesive and cohesionless debris flows, and to be characterised by: 1) plastic behaviour, 2) matrix, collision and friction-dominated clast-support mechanisms, 3) >25% sand content, 4) 25-95% sediment concentration by volume, and 6) variable clay content (> 0.5% by weight; Shanmugam, 2000). These characteristics cannot be easily measured in the field, hence deposits of these flows cannot be readily differentiated from deposits of turbidity currents (especially DWMS). As such, Shanmugam (1995), Shanmugam and Moiola (1995) and Shanmugam (1996) used the following deposit-based criteria to differentiate turbidites and sandy debris flow deposits: (1) massive structure; (2) concentration of rafted mudstone clasts near the tops of sandstone beds; (3) inverse grading of clasts; (4) planar clast fabric (laminar flow); (5) floating quartz granules in fine-grained sandstones; (6) preservation of fragile shale clasts; (7) abrupt pinch out geometry, and; (8) detrital matrix. However, many of these feature can also be explained using the acceleration matrix (sensu stricto Kneller, 1995) or considering the longitudinal variation in flow concentration and near bed settling processes operating in turbidity currents (see discussion by Cartigny et al., 2013; Kneller and McCaffrey, 2003; Sumner et al., 2008).

Based on observations in the Marnoso Arenacea Formation of the Italian Apennines, additional deposit-based criteria for 'sandy' debris flow deposits were proposed by Amy and Talling (2005a) and Talling et al. (2012, 2013) that include abrupt bed termination and 'patchy' texture in the massive sands (Figure 2-10). In terms of the 'patchy' texture, Talling et al. (2012, 2013) related its formation to partial or complete liquefaction of the debris flow, and slow elutriation and dissipation of pore fluid after deposition. In order for the flow to be liquefied, transient excess pore pressure must characterise the flow during and after deposition. Transient excess pore pressure in debris flows has been observed in both subaerial and subaqueous experimental flows (Breien et al., 2010; Ilstad et al., 2004; Iverson, 1997; Major and Iverson, 1999). In subaqueous experiments, Breien et al. (2010) observed settling of grains within a laminar flow displaces pore fluid upwards, which in turn provided a support mechanism for grains higher up. Although the authors did not observe the formation of a 'patchy' texture, it is easy to envisage transient excess pore pressure existing in the mass of sediments after deposition due to low hydraulic diffusivity. As the pore pressure dissipates, upward migration of pore fluids and slow convection may juxtapose patches of finer and coarser grains in the final deposit (Figure 2-11). Since dissipation of excess pore pressure occurs gradually once the flow has stopped moving, any overriding dilute flow may deposit sediments that founder into the underlying debrite or partially rework the bed producing a grain size break (Talling et al., 2013).

Figure 2-10: Patchy texture observed in the Marnoso Areanacea Formation of the Italian Apennines. Such deposit features could be produced by partial or pervasive liquefaction caused by transient excess pore pressure in a non-cohesive debris flow. The patchy texture is composed of irregular, juxtaposed patches of fine and coarse grained material. Photos taken from Talling et al. (2013).

Despite normal grading being attributed to suspension settling beneath a turbulent flow, flume experiments of sandy debris flows have shown a basal graded layer forming through hindered settling after the flow has stopped moving (Shanmugam, 2000). More recent experiments by Baas et al. (2011) and Sumner et al. (2009) have also shown grain size segregation occurring in rapidly decelerated debris flows (laminar plugs *sensu stricto*) after the flow has stopped moving. This produced clean, ungraded to graded massive sands. However, this occurred in flows with

intermediate mud volume (11.25 – 14.25%), when the yield strength of the muddy matrix was insufficient to suspend the sand after deposition. At lower mud concentrations or slower deceleration rates (at similar mud volumes), sand aggraded progressively from high-concentration basal layers and suspension settling, to produce graded deposits typical of turbidity currents. Since debrites with normal grading can be misinterpreted as turbidites, the presence of outsize clasts may provide a more reliable means to differentiate the two deposits. In subaerial flows, inverse grading or clast accumulation at the upper boundary and the head is observed by means of preferential transport, chiefly kinetic sieving (Iverson, 1997; Middleton, 1970). Despite being less studied in subaqueous debris flows, grading or accumulation of outsized clasts can occur in debris flows depending on the matrix strength and the density difference between the matrix and outsized clast (Postma et al., 1988).

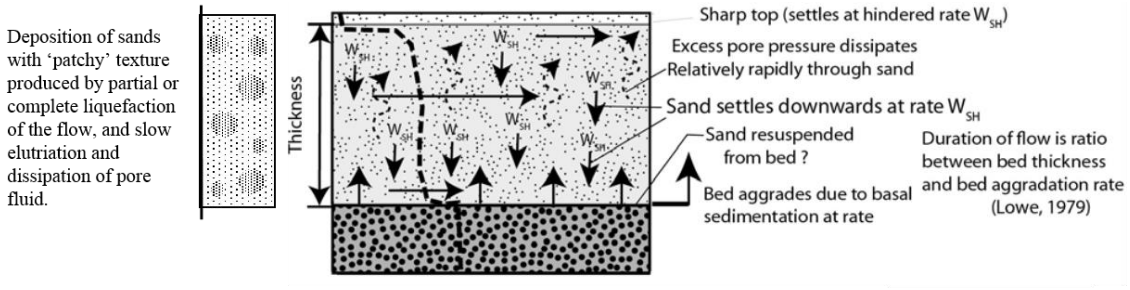

Figure 2-11: Diagram illustrating the main depositional processes responsible for producing massive sands with 'patchy' texture. Dashed lines indicated vertical sediment concentration profile. Modified after Talling et al. (2013).

2.4.2 Runout Distance and Facies Transition.

Numerous sedimentological studies of ancient and modern debrites have shown that they can be distributed from the proximal to the most distal reaches of a basin, hundreds of kilometres downslope. Debris flow deposits found in distal localities have represented a hydrodynamic paradox due to their increased viscous drag and reduced effective gravity, which was once thought to restrict their lateral distribution (Hampton, 1972). Two possible hypothesis have been proposed to account for their widespread distribution: 1) long distance run-out or 2) localised transformation from a dilute turbulent flow or disintegration from a slump or slide. Unlike subaerial flows, laboratory experiments have shown that the long-distance runout of subaqueous flows may be partly down to hydroplaning (e.g. Mohrig et al. 1998) and riding on an over-pressured underlying sand layer (e.g. Haughton et al. 2003). Hydroplaning occurs when the debris flow is sufficiently mobile to reach a critical velocity, without transforming into a turbulent suspension. However, for non-cohesive flows, similar to those that deposit massive sands, analysis by Lowe (1976) showed run out distances of less than ~ 1.2 km. These short run out distances could be a result of high hydraulic diffusivity, which promotes rapid dissipation of excess pore-pressure (Iverson, 1997; Major, 2000; Iverson, 2010). The run out distance in non-

cohesive flows may then be determined by the basal sedimentation rates, velocity of the flow, and flow thickness, as the excess pore pressure dissipates (Mesri et al., 1996). It is therefore likely that non-cohesive debris flows, that deposit massive sands, will not run out for long distances, even on steep slopes (Lowe, 1982; Talling et al. 2012). However, by introducing a small amount of cohesive mud (from ~2 wt% to ~5 wt%), the hydraulic diffusivity can be reduced by three orders of magnitude, which promotes high and persistent pore pressures and enables long run-out distances in poorly or moderately cohesive flows (Iverson, 1997; Iverson et al., 2010; Major, 2000). According to Talling et al. (2012), such a decrease in hydraulic diffusivity can delay dissipation of excess pore pressure from hours to weeks, and enable long run-out distances. Runout distance in these moderately cohesive flows will then depend on the yield strength and applied shear stresses. Regardless, the ability of non-cohesive and poorly cohesive flows to traverse long-distances into distal areas of basin remain poorly understood. Alternatively, Haughton et al. (2003) presented a model in which flows travelled on a wet and actively dewatering sand layer that was emplaced prior to the debris flow. As illustrated above, the mobility of a debris flow is controlled by the water content, and the dispelling water creates a basal low-friction and over-pressured zone that sustains debris flow runout (*ibid.*).

The second hypothesis that may explain the presence of debris flows in distal part of the basin is localised flow transformation from either a turbidity current or a slump/slide. Various studies have intimated that the key component of flow transformation from turbulent flows is the role of clay in dampening turbulence and modifying flow behaviour. Recent experimental evidence (e.g. Baas et al. 2014; Baas et al. 2016) and field studies (e.g. Ito, 2008; Lee et al., 2013; Terlaky and Arnott, 2014) has shown that ingestion of small amounts of mud near the base by an erosive flow can induce transitional to laminar flow behaviour as the flow moves downslope. Such a mechanism has also previously been used to interpret the H3 division in hybrid bed models (Haughton et al. 2009), based on the association of rafted mudclasts derived from within the basin (Fonnesu et al. 2015). Other authors have studied downslope transition in internal bed character to suggest flow transformation. In the Marnoso Arenacea Formation, 'patchy texture' observed in some distal sand beds show upstream transition to graded massive to parallel laminated sands. Such a lateral transition in facies suggests that at least some debris flows originated from localised flow transformation from a high-density turbidity current (Talling et al., 2013). However, no exact cause or mechanism for this flow transformation was provided by Talling et al. (2013). Alternatively, debris flow may originate from disintegration of a prior submarine landslide or slump. The extreme mobility of the Storegga Slide, the 1929 Grandbank Events and the 1979 Nice Event has been used as some of the examples, where disintegration of the slide and changes to the solid-fluid ratio were sufficient to provide low strength, and allow the failed mass to move as a flow (Bryn et al., 2003; De Blasio et al., 2003; Mulder et al. 1997; Piper et al., 1999).

2.4.3 External Bed Geometry.

An important characteristic of debris flow deposits is their narrow, tabular to lobate geometries with abrupt lateral pinch outs of the margins. This bed property has been observed in the field (e.g. Amy et al., 2005; Gee et al., 1999; Fonnesu et al., 2015; Talling et al. 2012b; Tripsanas et al., 2007) and experimental studies (Major, 1996; Naruse and Masuda, 2006) and is induced in non-cohesive debris flows with little or no mud content due to the frictional strength imparted by interlocking grains (Dasgupta, 2003). More cohesive debris flows from modern seafloors also show this type of bed geometry (Laberg and Vorren, 1995), which is produced by the cohesive strength of the matrix. Deposition occurs from the base upwards, with the head and lateral margins coming to rest first, while the body and tail maintain elevated pore fluid pressure and remain in a nearly liquefied state after deposition. If the body and tail have enough momentum, they may override the front of the flow and continue further downslope as another surge. Thus, en-masse deposition of debris flow may not be instantaneous, but incremental. However, unlike incremental deposition from turbidity currents, the final deposit thickness of debrites is more closely related to the flow thickness.

2.5 Post-Depositional Removal of Sedimentary Structures.

2.5.1 Depositional Model.

Baas (2004) presented a mathematical model that questioned a turbidity current's potential to form completely massive intervals without having to invoke post-depositional processes, i.e erosion, bioturbation, and/or liquefaction to remove or destroy stratification. Using a bedform stability diagram, it can be shown that turbidity currents, regardless of their character or flow history (Kneller and Branney, 1995; Kneller and McCaffrey, 2003), should pass through a final phase of waning during which tractional structures are likely to develop. The development of tractional structures is dependent on the residence time of the flow in the corresponding bedform stability field. Baas (2004) showed that even under unrealistically short residence times of seconds, tractional structures were able to form. Approximately 16 s were required to develop ripples at a height of 0.1 cm and an angle of climb of 3.8°, while parallel laminated divisions formed above all models beds regardless of accumulation times. This conclusion has been supported by various flume experiments that simulated rapidly waning flows and bedform development (Baas et al., 2004; LeClair and Arnott, 2005; Sumner et al., 2008). The rate of deceleration of natural turbidity currents is likely to be much longer, allowing for more time to develop traction structures at the top of turbidity currents. Based on these observations, Baas (2004) concluded that massive sands result from the post-depositional removal of tractional structures via a combination of erosion, liquefaction or bioturbation processes. Thick packages of amalgamated massive sands that lack evidence of bioturbation or liquefaction, could therefore potentially be explained by erosion of structured tops.

2.5.2 Vertical and Lateral Facies Transition.

A physical expression of post-depositional removal of tractive features by successive flows, or indeed by the same flow at different stages of its life, could be distinctive grain size breaks (abrupt changes in grain size vertically). This could be between 1) successive massive sand facies, 2) massive sands and overlying structured facies, or 3) massive sand and an overlying mudstone facies. Study of spatial distribution of grain size breaks suggest the former two case is more abundant in proximal locations of a basin, while the latter may occur throughout the system (Stevenson et al., 2015; Stevenson et al., 2014). In the former, thick sequences of amalgamated sands are common components of many channel axis, base of slope settings and channel lobe transition zones (CLTZ; Stow and Johansson, 2000). Amalgamated massive sands deposited in channel axis settings show a progressive lateral transition to non-amalgamated, thinner-bedded sandstones with traction structures towards channel margins, which are deposited by the more dilute, non-erosional parts of the turbidity current (Hubbard et al., 2014; Macauley and Hubbard, 2013; Mutti and Normark, 1987). In base of slope and CLTZ setting, grain size breaks and bed amalgamation are abundant in proximal localities, and become less frequent moving into the distal basin floor. In these settings, erosion of tractive features could be due to successive flows, by longitudinal or vertical variations in flow structure or a combination of these factors. For example, in considering the longitudinal structure of flows, a flow may turn to a state of sediment by-pass and or erosion, following a period of capacity-induced massive sand deposition (Kneller, 1995; Kneller and McCaffrey, 2003; Sumner et al., 2008). In such cases, a grain size break may develop above the massive sand interval. A massive and/or structured sand deposit may follow the erosive surface, depending on flow character once the flow has returned to a net depositional phase. In proximal locations, the final deposit may show multiple grain size breaks due to greater temporal fluctuation in flow sediment concentration and velocity. Moving distally, the grain size breaks reduce in frequency as the proximal causes of flow instability organises itself with distance and the flow becomes net depositional (Kneller and McCaffrey, 2003; Stevenson et al., 2015). As such, tractional structures are more likely to be preserved as the sediment fall-out rate reduces temporally and spatially, and sediments are reworked by the flow.

In cases where grain size breaks exist between sandstone and an overlying mudstone facies, Stevenson et al. (2014) suggested temporal and spatial variation in flow capacity may not adequately explain a sharp transition from sand to mud, particularly in distal parts of the basin. The authors argued that the strongest variations in capacity between the head and body of the flow occur close to the source, where a larger change in the grain size can be expected. As the flow moves downslope, it has time to equilibrate its velocity and sediment load, such that grain size breaks further downslope display a smaller variation. Since the above authors observed a consistent grain size break composed of model grain size of *ca* 70 to 100 μm, overlain by mud,

irrespective of location from the source, an argument can be made that fluctuations in capacity alone cannot generate the grain size break. Rather, these authors invoked the development of fluid layers at the rear of the turbidity current which hindered the settling of finer non-cohesive grain, and transported them to distal locations. It has been shown experimentally that increased clay concentrations modify the behaviour of a sediment flow by developing a fluid mud layer, which moves on top of a sandy layer of reduced turbulence (Baas et al., 2009; Baas et al., 2011). With increasing mud concentration, these fluid mud layers have the yield strength to partially or fully suspend non-cohesive grains within the layer and by-pass them further downslope. In natural flows, regions of high clay concentration may exist towards the rear of the flow, where sediment concentration and shear velocity are low, allowing flocculation of clay and suppression of turbulence (Talling et al., 2012). In such conditions, fluid mud layers may develop and by-pass finer non-cohesive sediments downslope.

2.6 Reversing Buoyancy Turbidity Currents.

2.6.1 Depositional Model.

A recent addition to the group of mechanisms thought to produce DWMS is the concept of turbidity currents with reversing buoyancy (Carey et al. 1988; Gladstone and Pritchard, 2010; Sparks et al. 1993; Stevenson and Peakall, 2010). The sediments carried by these types of flows are not suspended in the cold, denser fluid characterising the ocean basins, but in warmer, less dense surface sea water or river water, particularly in the case of sediment flows that form as a continuation of river discharge. These types of flows have been known to exist for over a hundred years (Gilbert, 1890), but only recently have received attention in terms of the deposits they produce and their economic importance (e.g. Mulder and Syvitski, 1995; Mulder and Alexander, 2001; Mulder et al., 2003; Mutti et al. 2003; Zavala et al., 2011). If the density of the sediment and fluid mixture is less than the ambient fluid, the flow forms a surface plume (also known as hypopycnal flows) from which sediment settles out of suspension. However, if the density of the flow is greater than the ambient (hyperpycnal flows), the flow then progresses downslope as a negatively buoyant, bottom hugging turbidity current (Figure 2-12A-B). In this case, the distribution and characteristic of the deposit depends on how the sediments and interstitial fluid contribute to the bulk density of the flow (Gladstone and Pritchard, 2010). Provided that no vigorous mixing occurs with the ambient fluid, a turbidity current may reverse its buoyancy if it reaches the ocean floor with its interstitial fluid still relatively buoyant. With progressive loss of sediments through deposition, the bulk density of the flow will reach neutral density, at which point, the forward motion of the flow will cease. With further sedimentation, all or parts of the flow will become positively buoyant (Figure 2-12C-E), such that the mixture of less dense interstitial fluid and sediment loft (detach from the sea floor) as a buoyant cloud or plume. This lofting or detachment point is associated with rapid suspension settling of coarser

sediments, as well as removal of finer grains in the rising plume (Sparks et al., 1993; Sequerios et al., 2009; Gladstone and Pritchard, 2010). If the sedimentation rate is high enough to suppress bedform development, or if the lofting flow deposits its sediment-load under no lateral motion, it is possible to postulate the formation of massive sands.

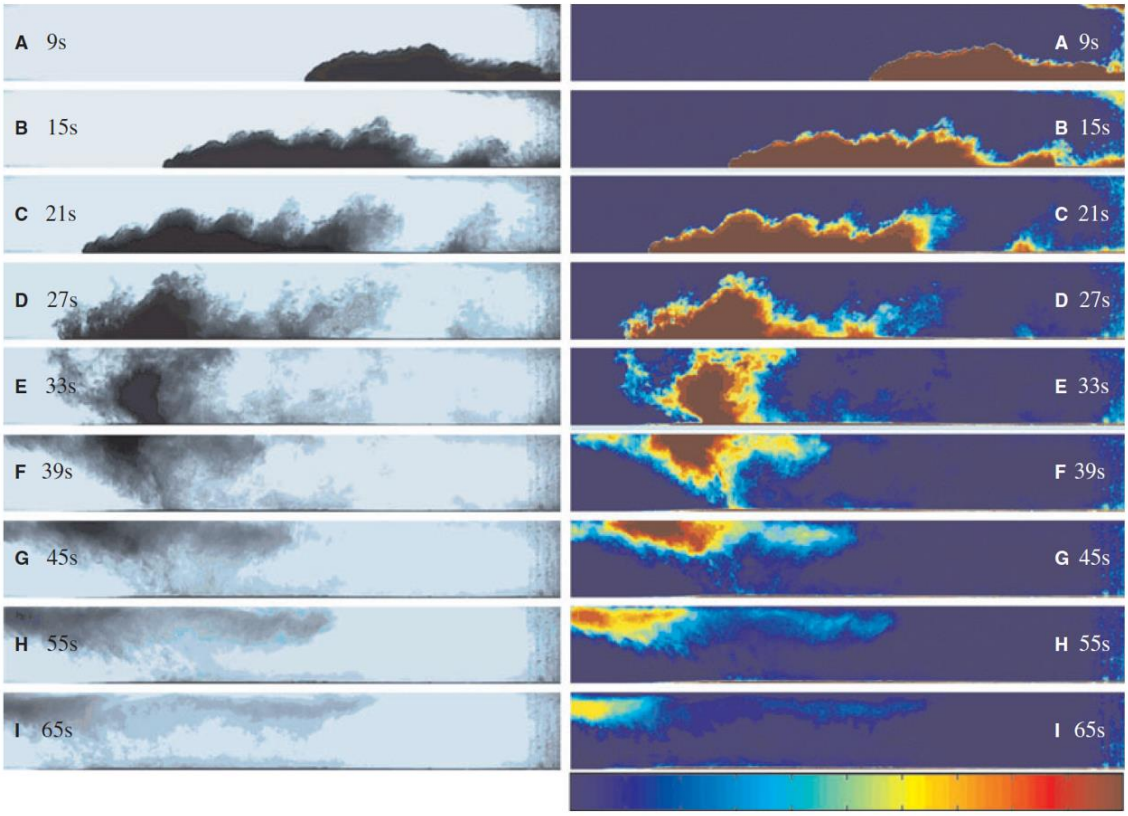

Figure 2-12: A series of photographs showing turbidity currents with reversing buoyancy in laboratory experiments after Gladstone and Pritchard (2010). Lofting occurred initially at the rear of the flow (B), prior to a series of plumes lofting along the length of the current and at the front (C-E). Sediments still held in suspension at this stage rise with the lofting fluid and propagate horizontally before falling out of suspension.

Recent experiments by Gladstone and Pritchard (2010) and Stevenson and Peakall (2010) investigated the deposition of massive sands from surge-type lofting turbidity currents. While Gladstone and Pritchard (2010) explored the influence of grain size on flow dynamics and the resulting deposit character, Stevenson and Peakall (2010) examined the interaction of seafloor topography upon lofting and sedimentation patterns. In both experiments, the flow behaved initially as a normal bottom-hugging flow. The head and the upper boundary of the flow exhibit extensive mixing with the ambient, while the body generated small scale lofting convection structures. However, at a certain distance away from the source and depending on the initial flow concentration, density of the interstitial and ambient fluid, initial sediment size distribution, rate of ambient entrainment and topographic relief, the flow would reverse in buoyancy and loft (Gladstone and Pritchard, 2010; Hürzeler et al., 1996). In both experiments, lofting was almost simultaneous along the entire length and is associated with enhanced

sediment deposition. This general flow behaviour has also been observed in the experiments of Hogg et al. (1999), Sequeiros et al. (2009) and Sparks et al. (1993). However, there is considerable debate on the final internal deposit character generated from lofting turbidity currents.

2.6.2 Vertical and Lateral Facies Transition.

Gladstone and Pritchard (2010) noted the non-uniqueness of the deposit architecture regardless of varying initial flow concentrations, grain size distribution or flow hydrodynamics (i.e. lofting or non-lofting). For both bottom hugging and lofting flows, Gladstone and Pritchard (2010) produced the same weakly to strongly graded deposits. The grading is likely to be more subtle or absent in lofting flows if the fine material is elutriated by the rising plume and transported away from the site of deposition by cross-currents in natural environments. This non-uniqueness in deposit characteristics makes differentiating lofting and non-lofting flows from their deposits difficult. In terms of DWMS deposition, the authors identified the initial grain size distribution and the fraction of sediment that remain suspended at the point of lofting as controlling factors. Since experimental studies have shown a rapid drop in velocity near the point of lofting (Hüzeler et al., 1996; Mcleod et al., 1999; Sparks et al., 1993), little horizontal motion and rapid dumping of sediments from the lofting plume would lead to DWMS deposition (Gladstone and Pritchard, 2010). The deposit is likely to be ungraded if most of the finer sediments have been lost through elutriation in the rising plume.

While the above trends in deposit characteristics are mostly the result from surge-type lofting turbidity currents, Mulder et al. (2001; 2003) considered the vertical and lateral facies trends produced by sustained hyperpycnal currents, which are directly fed by rivers during flood events. Due to the sustained injection of undiluted material towards the head of the flow, these authors suggested that the vertical bed character is a reflection of the flood hydrograph and can be predicted using the acceleration matrix of Kneller (1995). The ideal sequence consists of inverse grading representing the waxing discharge phase at the river mouth, followed by a fining upward succession representing the waning phase. Expanding on this sequence to take into account the deposits of the lofting plume, Stevenson and Peakall (2010) proposed a sequence consisting of (1) inversely graded, structured sands (waxing phase), (2) ungraded, massive sands (representing the lofting phase), (3) inversely/ungraded, structured sand (representing lateral advancement of the flow), and finally (4) normally graded structured sands (waning phase). The authors further hypothesised that as the flow moves progressively basinward, less and less undiluted material is transported to the head, resulting in lofting points remaining stationary for longer, and shorter distances between lofting points. These flow characteristics are likely to produce a laterally extensive massive sand deposit. In cases where turbidity currents are obstructed by topography, the experiments of Stevenson and Peakall

(2010) showed localised high sedimentation on the stoss side of the obstacle. The impeded lateral motion of the flow results in deposits lacking tractive features.

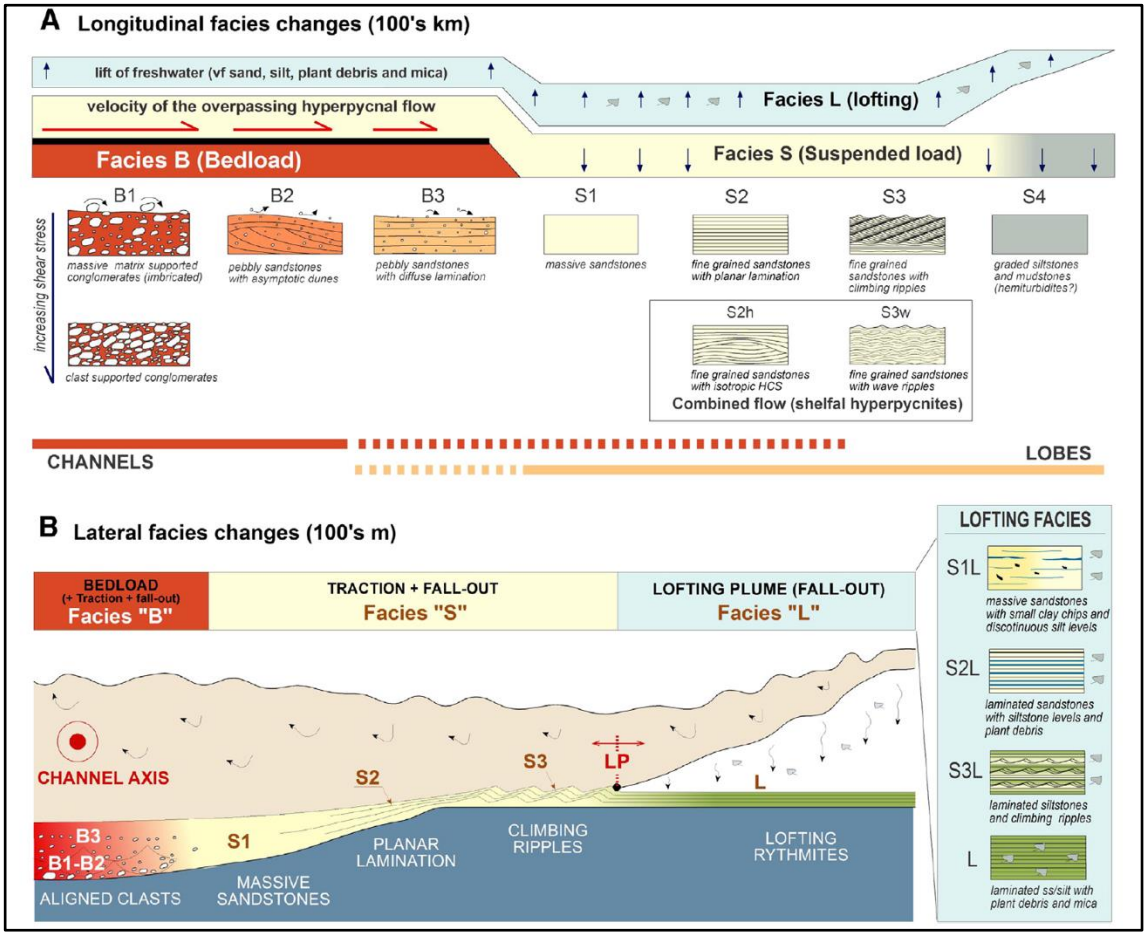

Figure 2-13: Longitudinal and lateral genetic facies tract for turbidity currents with reversing bouyancy. Type B facies relate to bedload transport and deposition, Type S from suspension sedimentation, and Type L originate from the lofting plume. The lofted facies in this model comprise thin couplets of sand and silt with complex grading patterns. After Zavala et al. (2011) and Zavala and Arcuri (2016).

Examples of ancient and modern DWMS deposits that have been attributed to reversing buoyancy turbidity currents are sparse. One of the few DWMS examples comes from the Eocene Central Basin of Spitsbergen (Plink-Björklund and Steel, 2004). While examples of other deposited facies include: (1) silty rhythmites (Nakajima, 2006); thin to thick bedded sandstone with crude stratification (Soliman and Balilah, 2015), and; mudstone layers containing ice-rafted debris (Hesse et al., 2004; Hesse and Khodabahsh, 2006). Based on analysis of seventeen lacustrine and marine basins, Zavala et al. (2011) and Zavala and Arcuri (2016) constructed a genetic facies tract to aid recognition of hyperpycnal flows (Figure 2-13), and identified three facies group deposited by bed-load transport (Facies B), gravitational collapse of suspended load transport (Facies S), and flow lofting during buoyancy reversal (Facies L). The massive sands (S1) in this facies tract are attributed to deposition from suspension under high aggradation from 'conventional' bottom hugging flows. The deposits representing the lofting plume, in contrast, consist of thin sand and silt couplets with plant debris. Locally and closer to the source, the sand layers are thicker and massive in character,

with thin discontinuous lenses of silt. Similar facies have been reported by Nakajima (2006) and Soliman and Balilah (2015), who related the cyclic recurrence of these facies, as well as the complex grading patterns (inverse, ungraded and normal graded) to the flood hydrograph and the acceleration matrix of Kneller (1995).

One of the few examples of DWMS (*sensu* Stow and Johansson, 2000) interpreted to have been deposited by hyperpycnal flows comes from the Eocene Central Basin of Spitsbergen (Plink-Björklund and Steel, 2004). In this basin, a clear physical connection can be demonstrated between a fluvial source and a turbidity system on the shelf edge. Plink-Björklund and Steel (2004) proposed that sustained turbidity currents initiated during floodwater discharge deposited large volumes of sand on the shelf and basin floor. These authors observed a systematic change in facies laterally, from graded, ungraded and inverse graded, thick bedded laminated sands in proximal locations, to alternating laminated and massive sands further downslope, and finally ungraded massive sands distally. Sandstone beds were tabular in geometry, with abrupt pinch outs of the ungraded, massive sands in distal locations. Plink-Björklund and Steel (2004) interpreted this gradual change in facies character as a result of flow evolution from an initially ground hugging, unsteady turbidity current, which became positively buoyant at a certain point from the source. The rapid dumping of coarser sediments as the flow lofted produced thick massive sands with abrupt pinch-out. These observations broadly conform to the experiments of Stevenson and Peakall (2010), in that massive sands are deposited in the distal part of the basin. However, in the absence of a direct link to a fluvial source, lofting as a mechanism for massive sand deposition could be difficult to justify from deposit character alone.

2.6.3 External Bed Geometry.

Despite the internal vertical and lateral character of reversing buoyancy turbidity currents being poorly defined in both experimental and field-studies, their geometries on the other hand may be used as a diagnostic characteristic. The surge type reversing buoyancy currents modelled by Gladstone and Pritchard (2010) produced a tabular geometry, with an abrupt pinch-out or stepped distal end due to the cessation of forward motion associated with reversal in buoyancy. These trends are broadly in agreement with the flume experiments of Hürzeler et al. (1996), Sparks et al. (1993) and Stevenson and Peakall (2010), as well as outcrop studies (Plink-Björklund and Steel, 2004). While these authors focused on the longitudinal geometry of the flow, Steel et al. (2017) also considered the lateral spreading of the flow and thus the three-dimensional geometry in flume experiments. Along with the head of the flow, Steel et al. (2017) observed lofting along the lateral margins which reduced the lateral spreading of the flow. Low pressure zones were seen to develop beneath the lofting plumes, which pulled fluid inwards, preventing lateral spreading. The geometry of deposits produced by reversing buoyancy flows are thus likely to form narrow, elongated bodies with abrupt or stepped margins. This is in

contrast to the general tapering of the deposit geometry observed in negatively buoyant turbidity currents (refer to Section 2.2.3), and may serve as a key recognition criterion for deposits of turbidity current with reversing buoyancy.

2.7 Two-Phase Hydraulic Jump.

2.7.1 Model.

Turbidity currents are known from direct observations and experimental studies to be vertically stratified in terms of their density and grain concentration. As such, the basal parts of the flow are highly concentrated where grain support mechanisms including grain interaction, turbulence and excess pore pressure operate, while grains in the overlying less concentrated and less dense part are predominantly held in suspension by fluid turbulence. Such two-phase flows travelling down a submarine canyon slope steeper than 0.001° are known to be supercritical (Froude number > 1), while in the submarine channel-fan complex region, they are subcritical (Froude number < 1; Komar, 1971; Spinewine et al., 2009). This transformation in flow regime would require the flow to pass through a hydraulic jump at the canyon-fan transition, during which the velocity of the flow would drop significantly and its thickness substantially increased (Figure 2-14). Similar changes are also experienced as the head of a turbidity current reflects and deflects off confining topography. In such cases, the flow generates a hydraulic jump that migrates upstream (Lamb et al., 2006; Sequeiros et al., 2009; Toniolo et al., 2006). These changes in flow parameters induced by the hydraulic jump results in a drop in bed shear stresses and deposition of sediments; the character of which have been subject to much speculation (Garcia and Parker, 1989; Menard, 1964; Mutti, 1977; Spinewine et al., 2009).

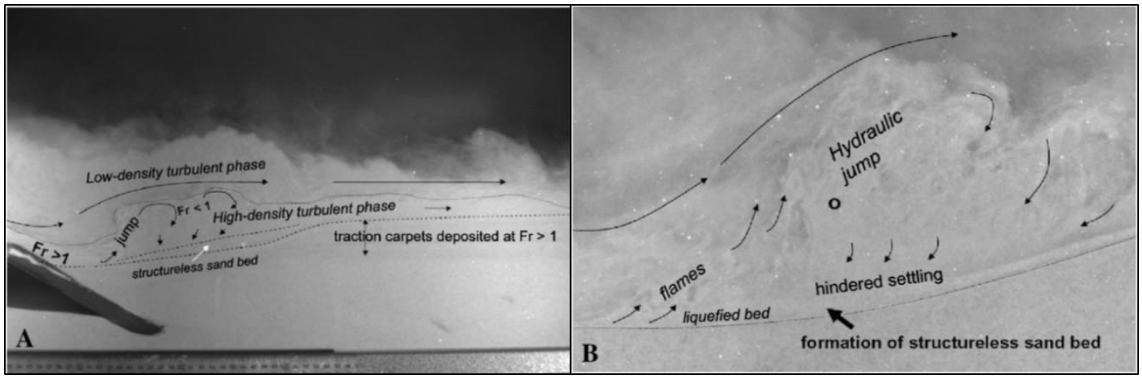

Figure 2-14: Film stills of two-phase subaqueous sediment flows modelled by Postma et al. (2009). At the base of slope, the sediment flow undergoes a hydraulic jump with strong upward expansion of the flow. At this locality, there is little lateral shear of particles and abundant hindered settling to form a massive deposit. Downstream of the hydraulic jump, the flow becomes supercritical and spaced-stratifications is produced.

2.7.2 Vertical and Lateral Facies Transitions, and External Geometry.

Leclair and Arnott (2003) and Postma et al. (2009) experimentally investigated the deposit character resulting from a two-phase super-critical flow as it experiences a hydraulic jump near

a break in slope (Figure 2-14A). In both studies, as the high concentration basal layer of the flow passed the break in slope, it expanded vigorously into the overlying less concentrated turbulent suspension. This expansion in flow thickness was also associated with substantially decreased flow velocity, resulting in high sediment fall-out under no lateral shear and the development of a massive substrate (Figure 2-14B). In the experiments of Arnott and Leclair (2004), this substrate was seen to rise at a rate of 3.6 mm/s. Since the sediments are deposited under static settling conditions, the resulting deposits were normally graded, and much of the coarser sediment would be confined to the proximal, up-dip part of the deposit (*ibid.*). However, owing to the limited dimensions of the flume, the extent and lateral facies transition of the massive substrate was not investigated in the experiments by these authors. Nevertheless, it is easy to hypothese that as the flow waxes and wanes, the location of the hydraulic jump will migrate. Based on this, it could be speculated that massive deposits produced at the hydraulic jump transition into high length-width ratio sand bodies downstream. The deposit character would vary depending on the location of the hydraulic jump and the hydrodynamics of the flow; the flow may re-establish a two-phase character downstream and deposit classical Bouma and Lowe sequences. The vertical sorting within the deposit is also expected to be good due to the dilation and expansion of the flow during the jump, with the finer material being carried away further downslope.

2.7.3 Controlling Factors.

Most field-based and experimental studies have focused on the canyon-fan or channel-lobe transition as the location of the hydraulic jump (e.g. Garcia and Parker, 1989; Komar, 1971; Lee et al., 2004; Mulder and Alexander, 2001; Mutti, 1979; Postma et al., 2009). These settings are associated with widespread cut and fill features that are characterised by deposition of thick, massive to stratified, amalgamated sands. Away from the canyon-fan or channel-lobe transition, flows may undergo internal hydraulic jumps as they encounter topographic features or other rapid changes in flow conditions. Furthermore, the location of the hydraulic jump is also dependent on flow volume; smaller volume flows are more sensitive to changes in gradient for initiation of the jump, whilst larger flows may not experience the jump until reaching the basin plain (Mutti and Normark, 1987). It is therefore important to note that massive sands deposited by flows experiencing hydraulic jumps are not only dependent on the presence of a specific depositional settings, but also specific depositional conditions, and as such are not restricted to proximal locations as suggested by Stevenson and Peakall (2010).

2.7.4 External Bed Geometry

The migration of the hydraulic jump up or downstream, due to the subtle changes in the density and velocity structure of the flow, may create sheet-like massive sands (Postma et al. 2009). However, more commonly, a wedged or lens shaped deposit that thins downstream, or a deposit

with undulating boundaries is generated as the flow is rapidly decelerated (Spinewine et al. 2009). Such deposits have been observed and described in the Tabernas basin in south-eastern Spain and in the Grés de Peïra Cava, south-east France (Lee et al. 2004; Postma and Cartigny, 2014; Postma et al. 2014). In the latter locality, the deposits are closely associated with a break-in-slope, and sit within deep erosional scours (Lee et al. 2004). The external geometry of the beds exhibits lateral pinch out over several hundred metres in a downstream direction (*ibid.*). The scour features within which these sands sit in were interpreted to have been created by the hydraulic jump and flow impact erosion.

Chapter 3 – Formation of Deep-Water Massive Sands and Related Facies in a Topographically Confined Basin: The Grès de Peïra Cava.

3.1 Introduction.

In the absence of detailed textural analysis (Chapter 4), it is difficult to determine from single outcrops with limited extent how DWMS are deposited. However, the documentation and analysis of sediment facies in laterally correlatable beds can greatly aid our understanding of the temporal and spatial evolution of flows that deposit DWMS (Amy and Talling, 2006; Fonnesu et al., 2015; Sumner et al., 2012; Talling et al., 2007a; Talling et al., 2007b). The first aim of this chapter is to test the validity of existing models of DWMS. A comprehensive review of DWMS depositional models was undertaken in Chapter 2, in which data from field, experimental, theoretical and numerical simulation studies were taken into consideration. The validity of these models is discussed in terms of the internal bed architecture and external bed geometry by examining newly collected data from the Piera Cava Outlier. However, not all the models discussed in Chapter 2 can be assessed here, due to unique geomorphic requirements (e.g. hydraulic jump) and/or initial hydrodynamics conditions of the flow (e.g. lofting of hyperpycnal flows). The second aim of this contribution is to propose a new or an updated depositional model of DWMS that integrates recent advances in deep-water sedimentology, particularly in topographically confined basins. To achieve these aims, eight beds were correlated and documented across a distance of 11 km in the Grès de Peïra Cava, SE France. For each bed, lateral and vertical changes in internal bed character and geometries are documented to infer flow processes. All the beds have a sheet-like geometry and were deposited onto a relative flat seabed but topographically confined sub-basin, in a system analogous to the modern day intra-slope basins of the Gulf of Mexico (Pickering and Hilton, 1998; Amy, 2000). Due to the confining nature of the basin, effects of flow reflection, deflection and/or flow transformation induced by local topography are also taken into consideration when developing new model(s) for DWMS.

3.2 Geological Background

The Grès de Peïra Cava forms part of the more extensive Grès d'Annot Formation of SE France and NW Italy (Figure 3-1). The formation is Eocene-Oligocene in age and records the initiation of siliciclastic sedimentation in a series of sub-basins in the deeper parts of the Alpine foreland

basin, which was located to the west of the developing Alpine thrust belt and north of the emergent Pyrenean-Provençal mountain belt (Pickering and Hilton, 1998; Sinclair, 2000). The Grès d'Annot (deeper water sandstones and mudstones) forms the top most lithostratigraphic unit in a sequence comprising the Calcaires Nummulitiques (a bioclastic nummulitic limestone) and the Marnes Bleues (hemipelagic marls; Figure 3-2), which together represents the gradual deepening and migration of the foreland basin (Apps, 1987).

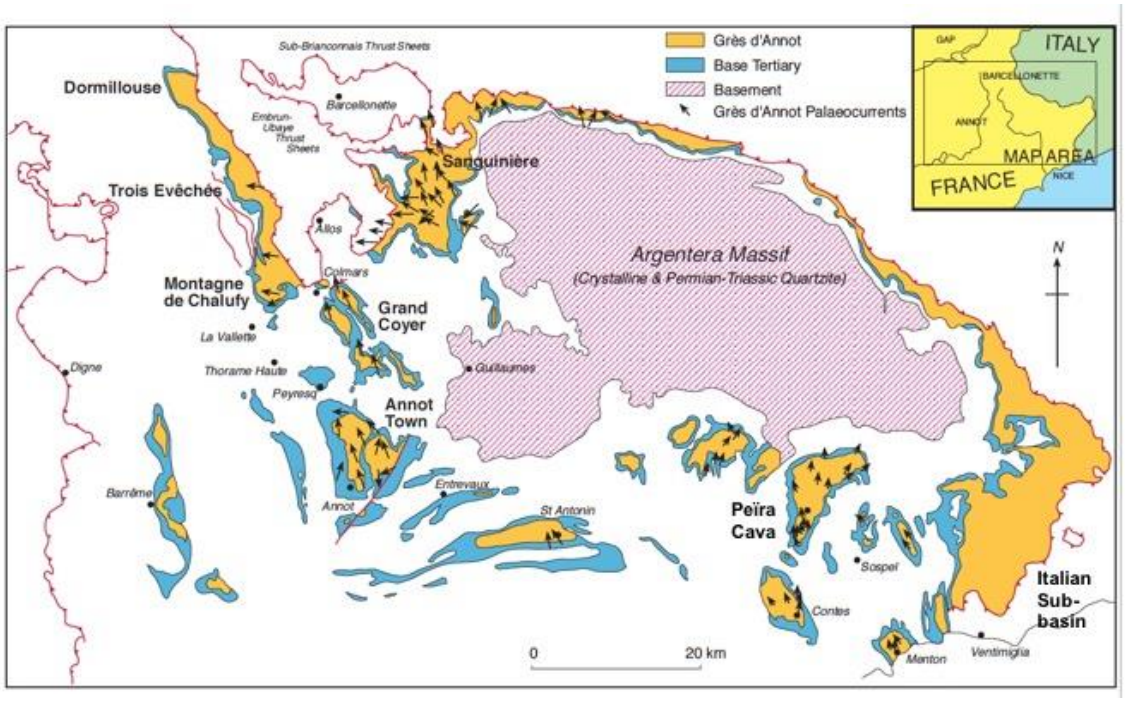

Figure 3-1: Distribution of the Grès d'Annot in SE France and NW Italy (after Apps, 1987). The main sub-basins are labelled in bold. Palaeocurrent directions have been surmmarised from Sinclair (1994) and Bouma and Coleman (1985).

The Grès d'Annot basin was characterised by several north-south trending depocentres (sub-basins) which were created by the folding of the Mesozoic strata during the Eocene regional flexure (Apps, 1987). These sub-basins were separated by topographic highs, as demonstrated by the common occurrence of an onlap relationship between the Grès d'Annot and the underling Marnes Bleues. Onlaps locally reach angles of 25° and typically have apparent slopes of 3° (Elliot et al., 1985). The palaeotopography is interpreted to be formed by shallow alpine thrusts in the underlying Cretaceous strata and was likely 100's of metres in height (Apps, 1987). Sediments were sourced from the Corsica-Sardinia and Maurès-Esterel massifs, which was originally located to the south of the Alpine foreland basin (Bouma, 1962; Ivaldi, 1971; Sinclair, 1994). They were transported northwards, parallel to the basin's axis, and deposited by a variety of subaqueous sediment flows. Due to the basin floor topography, flows were locally reflected and deflected, which significantly influenced deposit character (McCaffrey and Kneller, 2001). The widely accepted depositional model for the Grès d'Annot is that of sand-rich delta-fed ramp deep-water system (Pickering and Hilton, 1998; Joseph and Lomas, 2004). Architectural

elements consist of fan deltas in the proximal intra-slope region, transitioning to channels in the confined zones, and evolving to sheet-like elements in the less confined basin plain zones (Joseph and Lomas, 2004).

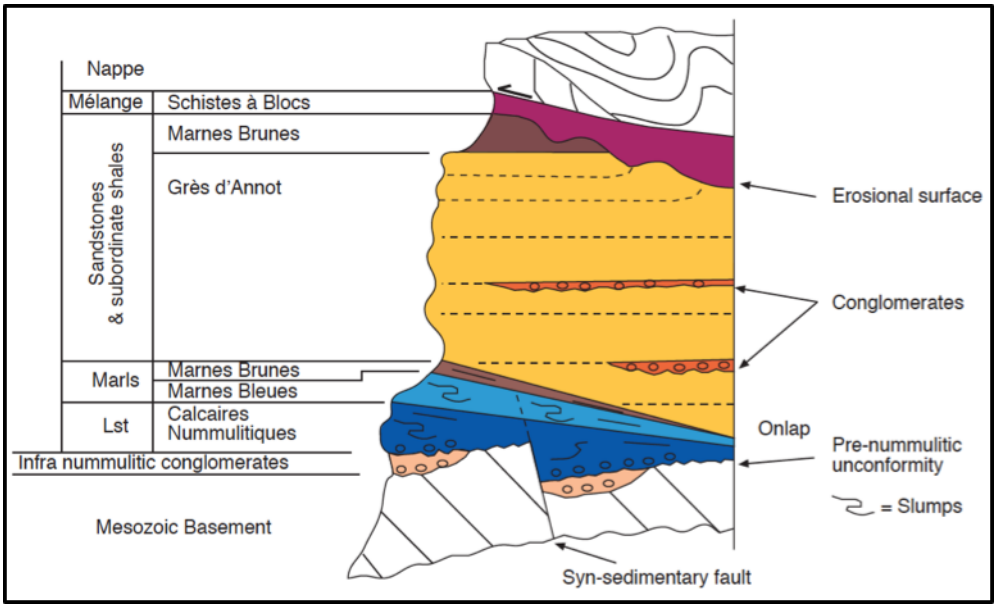

Figure 3-2: Stratigraphic column of the Tertiary sequence in the Alpine Foreland Basin (after Ravenne et al. 1987, 1995). Sequence consists of the deep-water Grès d'Annot and the Marnes Bleues formations, and the shallower water Calcaires Nummulitique. The sequence is underlain by a Mesozoic basement and overlain by the Embrun-Ubaye Nappe, which terminated siliciclastic sedimentation in the basin.

Five sub-basins have been identified within the Alpine foreland basin, and include from east to west: the Italian sub-basin, the Contes-Peïra Cava sub-basin (this study), the Mont Tournairet sub-basin, the Quatre Cantons-Sanguinière-Trois Evèchès sub-basin and the Saint Antonin-Annot-Grand Coyer-Chalufy sub-basin. The sediments in these sub-basins are today preserved mainly in synclinal outliers in the outer fold-and-thrust belt of the Alpine mountain chain (Figure 3-1 and 3-3).

3.2.1 Grès de Peïra Cava Outlier.

The Grès de Peïra outlier is a remnant of a sub-basin that formed part of the larger Alpine foreland basin. It is located approximately 25 km north of Nice, in the eastern part of the Grès d'Annot outcrop area (Figure 3-1). It covers an area of approximately 130 km^2. The outlier preserves approximately 50 m of the Calcaires Nummulitques, 150-200 m of the Marnes Bleues and 1.2 kms of deep-water sandstones and mudstones of the Grès de Peïra Cava within a NNE-SSW trending open syncline (Figure 3-2 and 3-3: Pickering and Hilton, 1998; Amy, 2000).

Figure 3-3: View of the Grès de Peïra Cava outlier looking North East from the Contes outlier. Approximate location of the onlap surfaces/contacts of the stratigraphy are shown as dashed lines. Field of view ~3.5 km.

The Grès de Peïra Cava outlier has received considerable attention in the geological literature, due in part to development of the Bouma model (Bouma, 1962). The fill of the outlier has been previously interpreted as deposits of high and low-density turbidity currents, with minor contribution from debris flows and other deep-water processes (Bouma, 1962; Stanley et al., 1978; Kneller and McCaffrey, 1998; Pickering and Hilton, 1998: Amy, 2000). Turbidite proximality trends (e.g. decreasing grain size and bed thickness) were reported by Pickering and Hilton (1998) using facies observed from a southern and northern measured section. Lee et al. (2004) interpreted sediment by-pass, large-scale scour features and the development of anomalously thick (decametres) sandstone bodies in the proximal locations of the outlier as base of slope sedimentation. More recently, Shanmugam (2002) reinterpreted the majority of the sands layers in the outlier as deposits of sandy debris flows, with the tops reworked by tidal bottom currents. The author based this interpretation on the presence of anomalous facies, such as inverse grading, large pockets of mudclasts, pebble nests, and sigmoidal cross-bedding with mud drapes which the author claimed cannot be readily interpreted according to the Bouma model or the prevailing turbidite paradigm.

Early studies on the depositional environment and architecture of the Grès de Peïra Cava suggested a submarine canyon-fan system consisting of channels and overbank deposits (Bouma, 1990; Bouma and Coleman, 1984; Stanley, 1990; Stanley et al., 1978). To the south, the Menton and Contes sub-basins were interpreted as the canyon feeder systems due to the coarse nature of the deposits and palaeocurrent trends, with the Grès de Peïra Cava area as the fan setting (Figure 3-4A). The channel-like elements were based on observations of channel-shaped erosional surfaces and discontinuous sand bodies in many southern localities (Bouma, 1990; Bouma and Coleman, 1985). However, more recent studies have emphasised the sheet-like nature of the beds; Pickering and Hilton (1998) correlated beds in a cross-stream direction for approximately 3 km, while Amy (2000) correlated beds in a down-stream direction for 10 km. The present depositional model of the Grès de Peïra Cava envisions subaqueous sediment

flows transporting northwards through the Contes (and possibly the Menton) sub-basin, before travelling sub-parallel to the strike of the western lateral slope of the Peïra Cava sub-basin and depositing their sediment load. The basin is interpreted to be confining in nature, and ponding of the flows is based on: i) onlap relationship of the Grès de Peïra Cava and the underlying Marnes Bleues, ii) thick mudstone caps, iii) anomalous orientation of palaeocurrent and erosive structures, indicative of flow reflection and deflection, iv) thick beds positioned adjacent to the base of slope, v) repeated or stepwise normal grading, and iv) grain size sorting across the topography suggesting flow stripping (Amy et al. 2004; Kneller and McCaffrey, 1999, Sinclair, 1994). As the sub-basins filled up, flows are understood to have spilled-over into adjacent sub-basins to the west. However, no correlations have been established between the sub-basins to demonstrate this relationship (Pickering and Hilton, 1998). Based on onlap relationships and palaeocurrent data, only the western and southern margins of the Peïra Cava sub-basin are known to be preserved (Figure 3-4B; Amy, 2000; Amy et al., 2004; Pickering and Hilton, 1998).

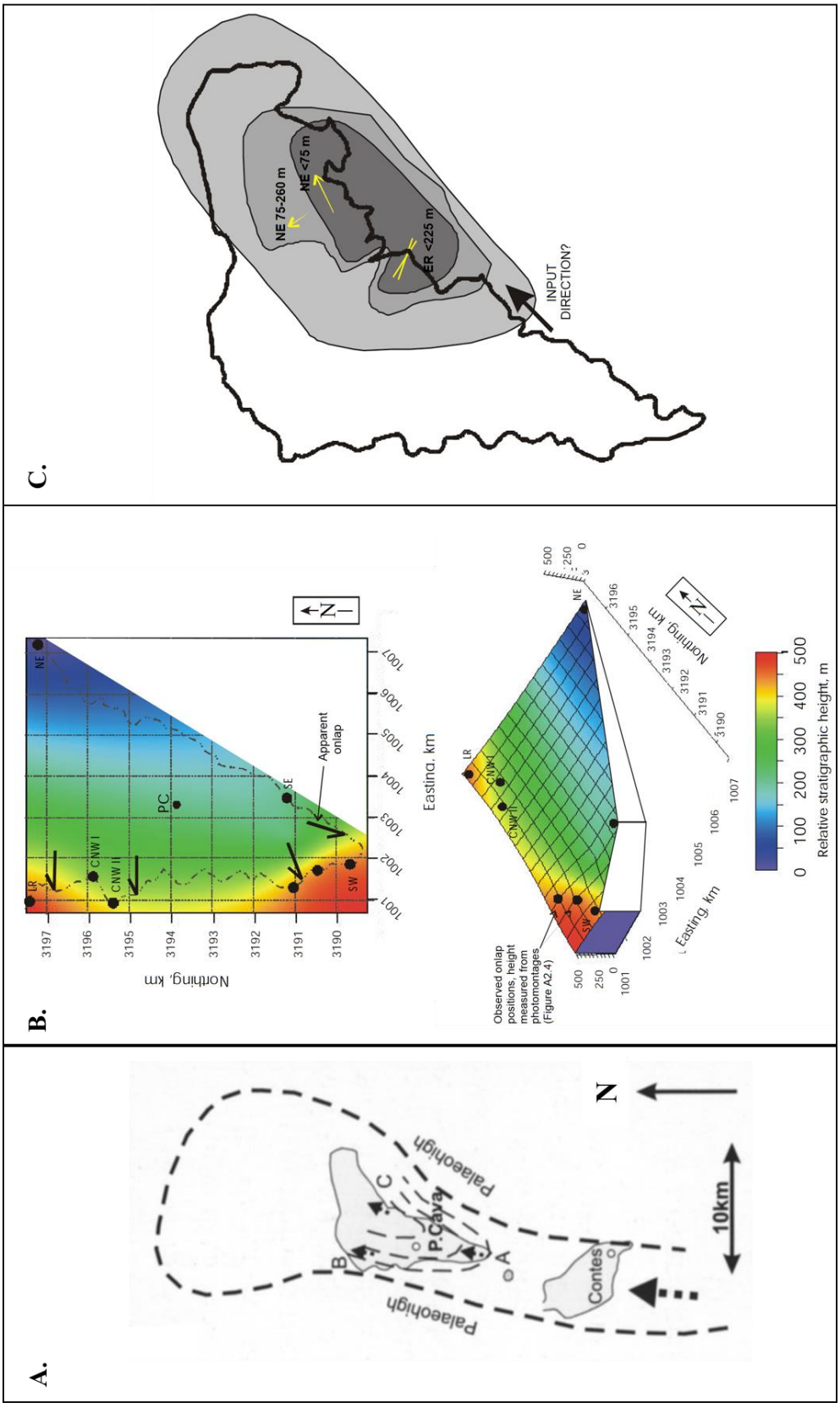

Figure 3-4: (A) Schematic map of the general sediment flow direction and palaeobathymetry in the Contes and Peïra Cava (modified after Amy (2000) and Ravenne et al. (1987)). (B) Basin palaeotopography constrained by Amy (2000) using stratigraphic height of the onlap surface. Only the southern slope and western lateral slope are preserved, while an eastern lateral slope is inferred based on palaeocurrent directions but is not shown. Top map showing a plan view and the outline of the Grès de Peïra Cava. The bottom map showing an oblique aerial view of the outlier. (C) Local changes in the strike of the eastern slope used to explain anomalous palaeoflow indicators (i.e. flow deflection) in the NE and ER sections.

3.2.2 Grès de Peïra Cava Paleotopography

To understand how the confining nature of the Grès de Peïra Cava basin influences flow processes, deposit architecture and the bed geometry, the palaeotopography of the Peïra Cava sub-basin needs to be taken into consideration.

Alpine deformation prior to the deposition of the wider Grès d'Annot resulted in the development of complex seafloor topography and separate domains of sediment accumulation. The topography was controlled primarily by shallow alpine thrusts in the underlying Cretaceous strata and was hundreds of metres in height (Apps, 1987; Pochat and Van Den Driessche, 2007). It exerted a strong control on spatial variation in flow properties, which in turn controlled sediment facies and sand distribution. Based on the onlap relationship between the Grès de Peïra Cava and the Marnes Bleues, only the western and southern margins of the Peïra Cava sub-basin are known to be preserved (Figure 3-4B; Pickerng and Hilton, 1998; Amy, 2000; Amy et al., 2004). The western basin margin was oriented in an approximately northwest to southeast direction, and rotates clockwise to north-northeast to south-southwest moving northwards. In southern areas the dip of this slope was between 4-7° towards the east, increasing to ~15° between the Baisse de Beasse and Cime de Claudine (Amy, 2000; Amy et al, 2004). The existing correlation framework (Amy, 2000) suggest approximately 510 m of the eastern section is lost towards the west due to the onlap with the Marnes Bleues. The southern basin margin, based on palaeotopographic reconstruction by Hilton (1994), is a continuation of a northward dipping (~ 8°) slope preserved in the Contes sub-basin. The eastern side of the margin is not well preserved and an onlap relationship is not observed. Nevertheless, the presence of a low angle lateral slope is inferred from highly variable palaeocurrent directions observed in beds in the eastern sections (Figure 3-4C; Amy, 2000). Based on the observed palaeoslope angles, a number of possible basin configurations have been proposed. The simplest reconstruction envisages a western lateral slope with decreasing slope angle to the east (Figure 3-4B; Amy, 2000). In the northern parts of the basins, the stratigraphy is folded and overturned, and the margin has not been preserved. This is thought to relate to basin inversion and exhumation of the Argentera-Dome de Barot massifs (Apps, 1987). The occurrence of thick mudstone caps separating sandstone beds (below <1200 m; Amy (2000)) indicates that the northern bounding slope completely ponded the sediment flows entering the Peïra Cava sub-basin (Sinclair and Tomasso, 2002).

Within the basin, bed geometry may locally vary due to erosive (metre-scale scours) and depositional relief, and the frequency of large highly efficient flows which deposited its sediment load in distal localities (e.g. CB5; Amy, 2000). Despite these controls on bed geometry, and contrary to the distal thinning of sand beds observed in this study and others (e.g. Amy et al. 2007), the system is thought to have aggraded uniformly via deposition of thicker

mudstone caps in distal locations. Based on this observation, a relatively flat floor is assumed for the Peïra Cava sub-basin. This assumption is also validated by Aas et al. (2010), who attempted to reconstruct the Peïra Cava palaeobathymetry through backstripping of overburden and removal of the synclinal structural overprint using surface-based modelling. The modelled paleo-basin floor revealed three bathymetric lows separated by topographic highs (the Rocaillion and Pourcel ridges). The degree of confinement by these obstacles was relatively high, especially for the early stages of basin fill, with complete or partial ponding of large flows in proximal locations. This is confirmed by basin-wide correlation framework constructed by Amy (2000). The degree of confinement lessens as the proximal bathymetric lows were filled, and the flows spilled over to the distal lows. The transition from local confinement to sheet-like geometry of the bed occurred just prior to the deposition of CB5, which can be correlated across the outlier (Figure 3-5; Amy, 2000).

Based on the interpreted palaeotopography and observed palaeocurrent directions across the outlier, Hilton (1994) and Amy (2000) proposed a model in which sediment flows travelled down a confining slope before encountering a break-of-slope, which is preserved in the southernmost part of the outlier. Upon entering the sub-basin, the flows were confined to the west by the lateral slope and flowed parallel to it for much of the length of the basin. In the eastern sections (SE, ET, ET), after reaching the break-of-slope, the flows were directed along the strike of the eastern margin. Individual beds (this study), as well as average vectors of each section (Amy, 2000), indicate that the flows were spreading out towards the east as they moved downslope. As the flows travelled northwards, it is likely they underwent orthogonal flow deflection (based on ~45° clockwise rotation of palaeocurrent indicators) at the very least along the western confining slope. The effect of flow deflection may be reduced as you move up-stratigraphy at a given geographical location due to the increased distance from the lateral slope. Using the base figures of Amy (2000), for a given 300 m vertical distance between 2 marker units in his study, there will be an increase in distance of ~2.4 km from the lateral slope for the top unit. Since the proximity to the lateral slopes will affect flow velocity and concentration, the retreat of the slope at a given geographical location will therefore be reflected in the sedimentological characteristics preserved at that location. Moving northwards towards the NE locality, for the stratigraphic interval studied here (~500 to 800 m), anomalous palaeocurrent trends indicative of flow reflection against an obstacle (northern margin) are not observed. This could be due to the smooth nature of the confining margin or that the confining slope was further away and did not influence the flow. Regardless, the flows are assumed to be ponded for the reasons outlined above.

3.3 Methodology.

The correlation framework of Amy (2000) is extensively used to correlate and document the proximal to distal change in sediment facies, and the geometry of the beds and sediment facies. Eight beds were chosen based on the presence of DWMS facies along the facies tract of the beds after initial reconnaissance work in the Peïra Cava outlier. These eight beds correspond to intervals CB/MU (Correlatable Bed/Marker Unit) 5, 6, 7, 10, and 11 of Amy (2000) and Amy et al. (2007), and are equivalent to first and second order correlatable beds of Remacha and Fernandez (2003). For continuity, the naming scheme is adopted from the original correlation (i.e. Amy, 2000). CB10 and 11 are packages of beds consisting of two and three beds respectively. Individual beds within CB10 and 11 will therefore have the suffix -1 or -2 to differentiate the beds.

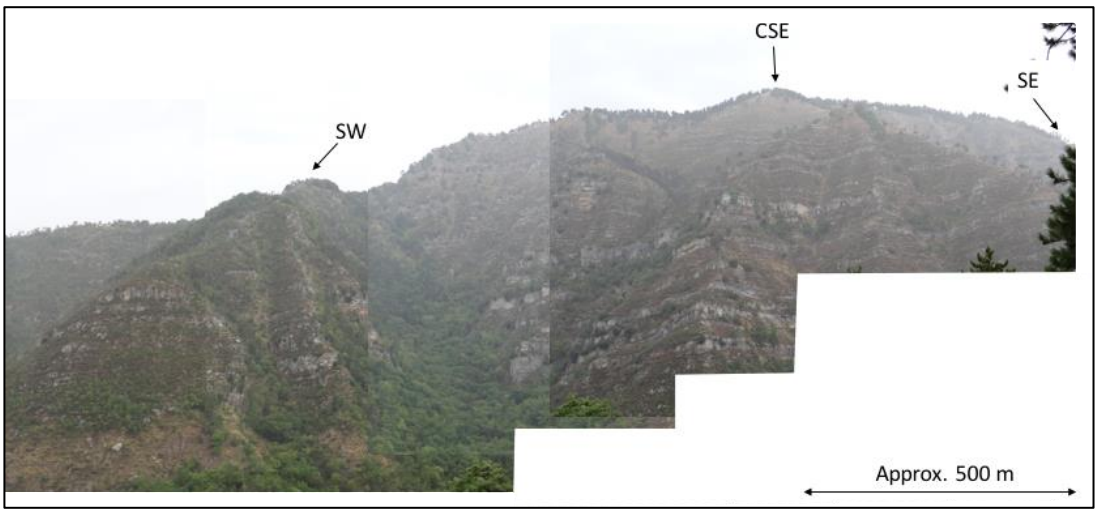

Figure 3-5: Photo taken from the proximal location of the outlier showing the CSE locality and the approximate location of SW and SE. Walk out of individual beds was only possible between localities SW and SE, where it was used more extensively for correlation due to amalgamation of beds. Photograph view towards the NW.

3.3.1 Correlation Framework of Amy (2000) and Selection of Beds.

The correlation framework for the Peïra Cava outlier was constructed by Amy (2000) through visual comparison of measured sections, photomontages, walk out of individual beds and analysis of the vertical sedimentary trends. Beds were originally logged at a scale of 1:200 by the author to gain an overview of the stratigraphic succession. The distribution and character of facies were then analysed and correlated between measured sections. Intervals that were difficult to correlate at the 1:200 scale were re-logged at 1:20 to improve the correlation, which also allowed the validation of the original correlation. The author also validated the correlation framework by using photomontages, but only after the initial correlations had been established between measured sections. These photomontages were integrated with the sedimentological sections to produce photostratigraphic correlations showing individual beds or distinct packages of beds along the mountainside. Finally, the author used the distribution of sandstone thickness,

sandstone percentage, mudstone-cap thickness and maximum grain size to further assess the validity of the correlation framework.

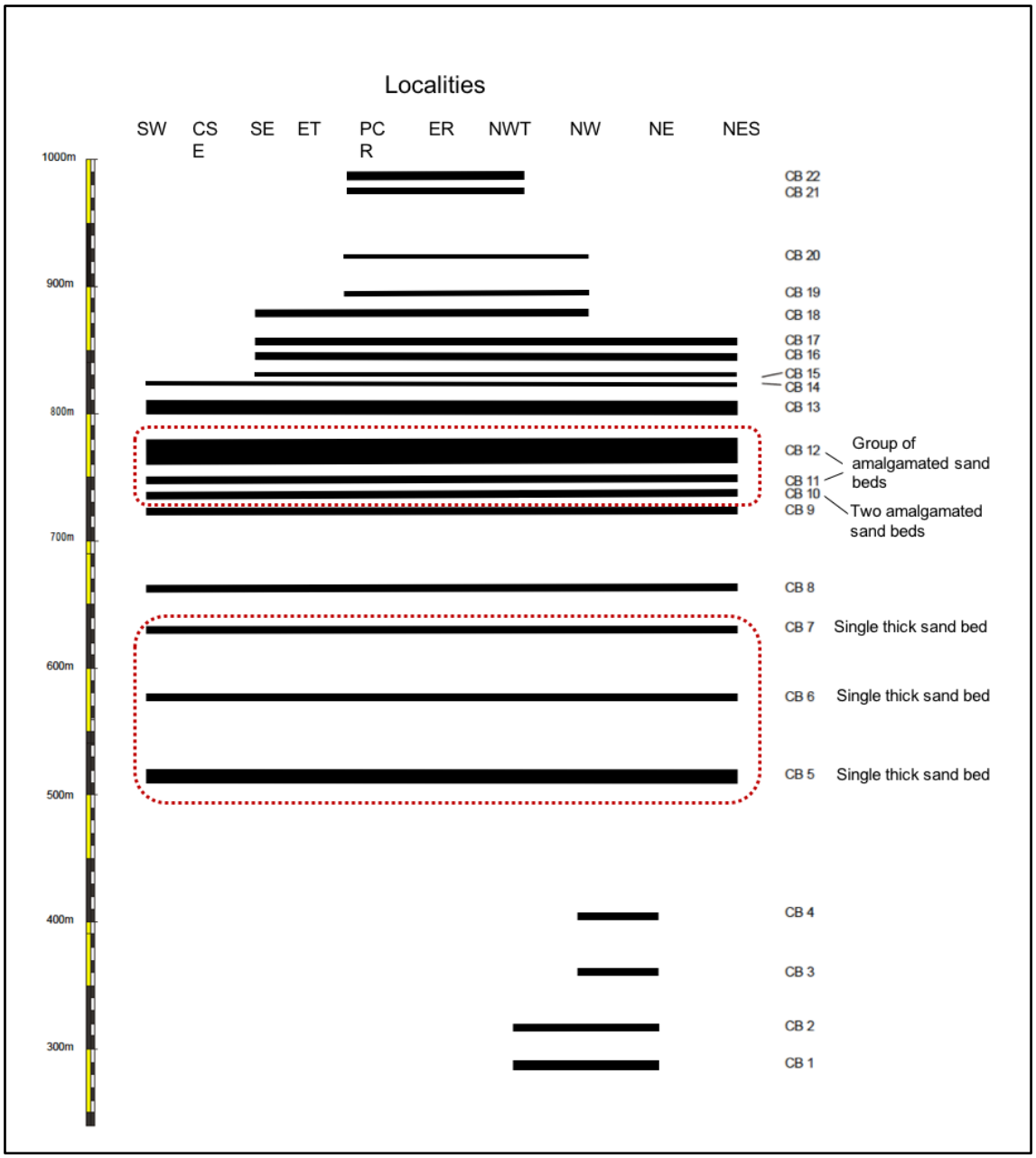

Figure 3-6: Simplified correlation of the twenty-two major units/beds in the Peïra Cava outlier. Eight beds (circled red) were chosen from this correlation framework to study the proximal to distal changes in DWMS facies. CB 5-7 consist of single very thick sand beds, while CB 10 and 11 are amalgamated units consisting of 2 and 3 thick sand beds respectively. Modified after Amy (2000).

Using the above techniques, twenty-two marker units were identified by Amy (2000), from which eight beds were chosen for this study. The marker beds were identified in the field using the 1:200 and 1:20 logs, and photostratigraphic correlations during an initial reconnaissance trip. They were chosen because they contain DWMS facies somewhere along their downslope transect. These eight beds were also the most easily accessible and widely exposed compared to the other marker units. Due to the mountainous terrane in the study area, walking out of

individual beds was not possible, except between the most proximal sections (SW to SE; Figure 3-6). Since bed amalgamation was most common in this area, walk out of beds between these sections was used more extensively. The Grès de Peïra Cava exhibits sheet-like geometry, with sandstone at most localities separated by hemipelagic layers. This characteristic, along with distinct bed thickness and grain size trends, sedimentary structures, and walkout of beds, made identification and correlation of chosen units elementary.

3.3.2 Sedimentary Logs.

Eight units were chosen for this study based on the correlation framework of Amy (2000) and Amy et al. (2007), and correspond to CB5, 6, 7, 10 and 11 (Figure 3-6). All eight units can be easily identified in the field and correlated across the Peïra Cava outlier. Figure 3-8 shows the location of the 10 measured sections. At each section, the units were logged at a scale of 1:10, with bed thickness, sedimentary structures, grain size and palaeocurrent indicators among some of the observations recorded. Grain size was typically measured every 5 cm and at smaller intervals where abrupt changes in grading occur or where grain size breaks were observed. Grain size was measured with a grain size comparator using the Wentworth scale. This method biases the measurement of the grain size to the coarsest 5% of grains within the sandstone bed (Table 3-2; Amy and Talling, 2006; Talling et al., 2004; Talling et al., 2013; Tucker, 1988), as measured from thin section analysis. However, this qualitative method allowed the dominant grain size range to be measured in the field and provided a reliable measurement of relative grain-size changes between beds. Palaeocurrent measurements were taken from grooves, flutes and obstacle scour features. No measurements were taken from current lineations. A minimum of 5 measurements were taken for each unit were possible. Bed thicknesses were measured with a standard measuring tape orientated perpendicular to the bed. Sedimentary facies were described using a hierarchical descriptive facies scheme (Table 3-1 and Appendix A) that describes the units initially on (i) lithofacies, and then on (ii) subfacies based on sedimentary structures. Outsized clasts (sand and mud) and dewatering structures were not incorporated into the facies scheme, but appear as accessory features within each facies. They have been described using the classification scheme of Johansson and Stow (1995) and Stow (2005). Thus along a facies tract, discrete units will be composed of lithofacies and subfacies arranged vertically and laterally.

3.3.3 Textural Analysis.

Field samples were collected from four DWMS (*sensu lato*) at regular intervals to provide additional information on the textural characteristics, including the vertical grading, sorting and mud content. The samples were collected from NE CB5, NES MU10-2, NWT CB10-1 and NES CB11-2. Thin sections were cut parallel to bedding plane to document changes in vertical grain size through a bed. Under most hydrodynamic flow conditions, the preferred orientation of the

a-axis of grains is parallel or at low angle to the bedding plane. The choice of bedding-parallel thin sections is thus likely to produce the most accurate results when measuring the true long axis length of the grains (Baas et al., 2007; Johnson, 1994). A total of twenty-two samples were processed to obtain SEM backscattered electron (BSE) images. Quantitative measurement on the size and sorting of the grains were generated using Scandium Digital Imaging Solution software after pre- and post-processing of the images (Figure 3-7; see Chapter 4 and Appendix B for detail). A minimum of 300 quartz, feldspar or lithic grains coarser than 8 μm were measured from each BSE image. A comparison between the field and thin section derived grain size measurements are shown in Table 3-2. The mud matrix content was estimated by thresholding the images to isolate the clay component and calculating the percentage area occupied after binarisation of the image. Grain sorting for the grain size distribution was calculating using the inclusive graphic standard deviation of Folk and Ward (1957).

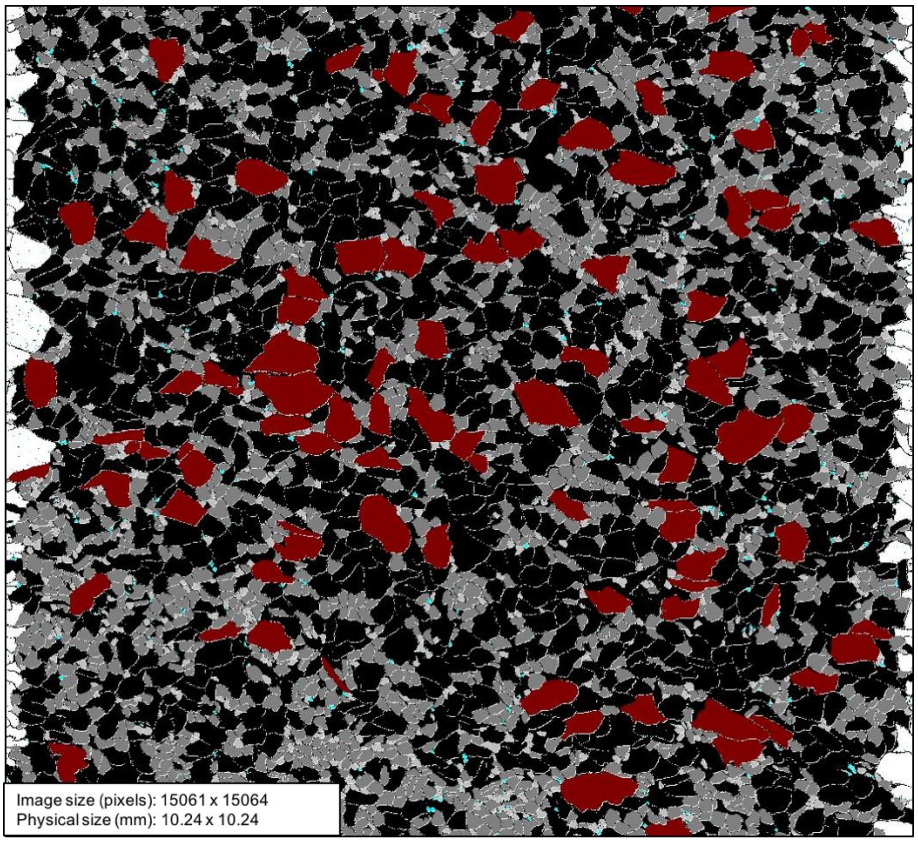

Figure 3-7: An example of a processed and segmented image used for determining the grain size distribution of the massive sands. The current image has been classified according to the Wentworth scale. The field of view is 1.02 cm horizontally and vertically.

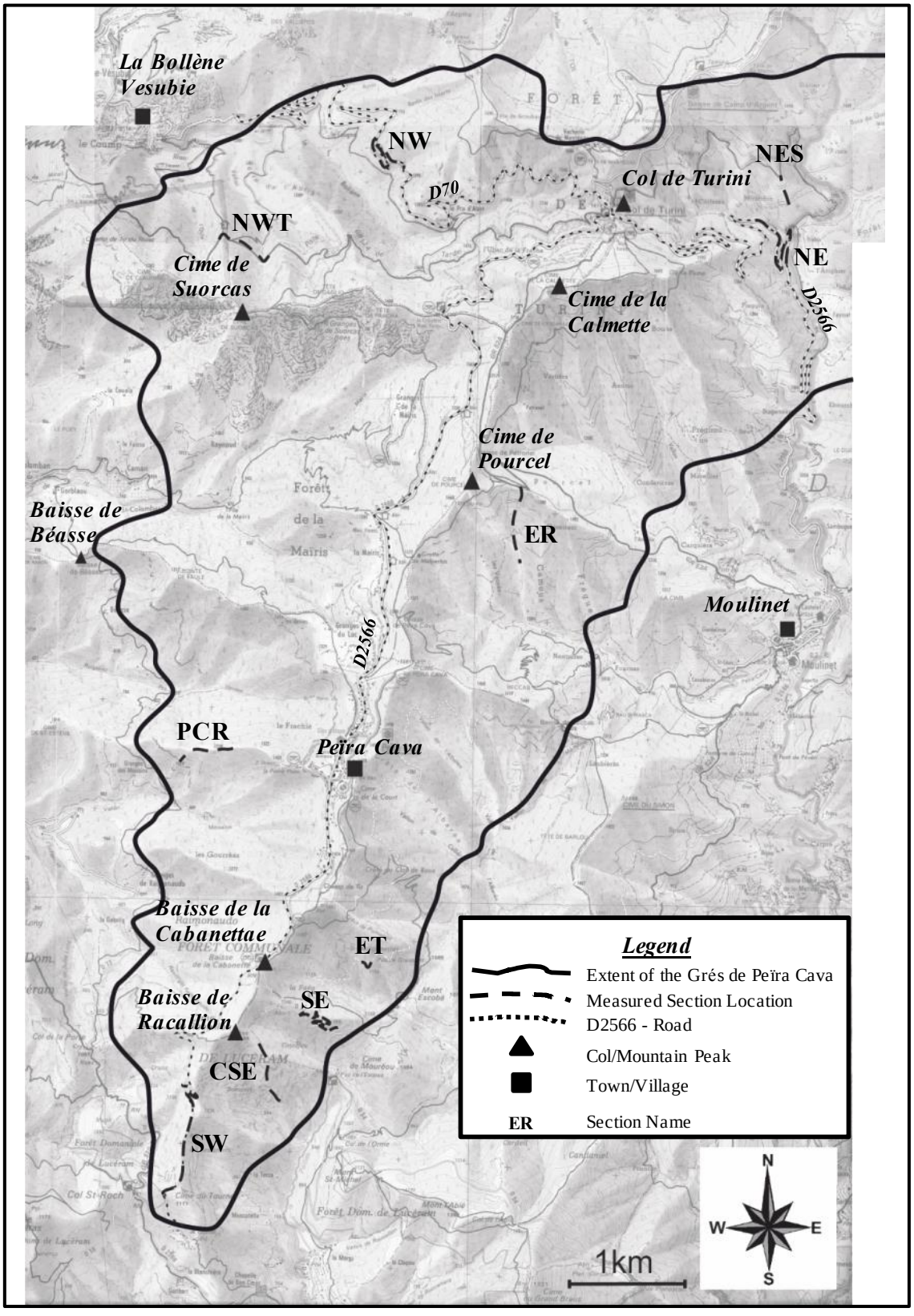

Figure 3-8: Map of the Peïra Cava outlier showing the location of the measured sections of the eight units correlated in this study. Section names scheme follows Amy (2000), Amy et al. (2004) and Amy et al. (2007) for consistency. Base topographic map is the Vallée de la Bévéra 1:25 000, 3741 ET, IGN map.

3.3.4 Markov Chain and Entropy Analysis.

Embedded Markov Chain and Entropy analysis was undertaken to describe the vertical arrangement and degree of random occurrence of facies. Such an analysis is useful not only for characterising potential vertical arrangement of facies (Gingerich, 1969; Miall, 1973; Potter and Blakey, 1968;), but also when, for example, the particular order of facies helps in describing the hydrodynamic processes. For the purpose of this study, the locations of the measured sections were allocated into one of three groups; proximal (SW, CSE, SE, and ET), medial (PCR and ER) and distal (NWT, NW, NE, and NES), based on geographic locations within the outlier. This grouping not only allow us to statistically analyse the vertical arrangement of facies, and therefore the temporal evolution of the flow, but also qualitatively characterise the downslope transitions in facies arrangement. The vertical to lateral transition in facies was not investigated as part of this study using Markov chain due to the inherent complexity of downslope transition of facies. In vertical sequences, the underlying facies must be older than subsequently overlying facies, therefore the Markov process, the occurrence of one state depending on to some extent on a previous state or states, can be applied. However, this concept breaks down when applying to downslope facies transitions where timelines may not be horizontal.

Markov Chain Analysis. The analytical procedure used in this study follows that of Power and Easterling (1982), modified by Tewari et al. (2009). Power and Easterling (1982) introduced the concept of embedded Markov Chain, in which a transition from one facies to the same facies is not recorded, even in situations where they are observed. In the present study, such a state may arise when the two facies are separated by a grain size break. Furthermore, the thickness of the facies is not considered since it does not influence the formation of massive sands, but is a product of flow duration and/or flow thickness. In addition, when constructing the initial Transition Frequency Matrix (*Fij*), only the sand and coarser facies are used for the analysis in order to reduce diffusion of transitions between certain lithofacies (i.e. structured sands transitioning into overlying silt and mudstones at the top of beds). The analytical procedure used in this study is as follows:

Let E(nij) denote the number of expected transitions from facies state i to facies state j. Then the quasi-independence model of Goodman (1968), which is used to accommodate the structural zeros in the embedded matrix (Power and Easterling, 1982; Tewari et al., 2009), is:

$$Enji = aibj,\ i \neq j$$

$$= 0,\ i = j.$$

Estimating the paramaters, ai and bj, i, j = 1, 2, 3, …, m, requires an iterative process, which is as follows. First iteration:

$$ai^{(I)} = n_{i+}/(m-1),\ i = 1, 2, 3, \ldots, m,$$

$$bj^{(I)} = n_{+j} / \sum_{i \neq j} ai,\ j = 1, 2, 3, \ldots, m,$$

*I*th iteration:

$$ai^{(i)} = n_{i+} / \sum_{j \neq i} bj^{I-1},\ i = 1, 2, 3, \ldots, m,$$

$$bj^{(I)} = n_{+j} / \sum_{i \neq j} ai^{I},\ j = 1, 2, 3, \ldots., m,$$

where n_{i+} and n_{+j} are the row *i* and column *j* totals respectively. Iterations are continued until a convergence criterion of 1% is obtained. That is:

$$a_i^{(I)} - a_i^{(I-1)} < 0.01ai^{(I)},\ \text{for } i = 1, 2, \ldots, m,$$

$$b_j^{(I)} - b_j^{(I-1)} < 0.01bj^{(I)},\ \text{for } j = 1, 2, \ldots, m,$$

Using the expected frequency (*Eij*) and the transition frequency (*Fij*) values in the expression:

$$\sum_{i=1}^{n} \sum_{j=1}^{n} = (Fij - Eij)^2/Eij$$

for $\boldsymbol{\chi}^2$ yields a statistic which is approximately chi-squared distributed with $(m-1)^2 - m$ degrees of freedom. The larger the $\boldsymbol{\chi}^2$ value for a given degree of freedom, the strong the evidence for cyclicity in the facies arrangement.

Entropy Analysis. Entropy is interpreted as the degree of disorder or randomness in a system. Hattori (1976) applied the concept to sedimentary successions which are governed by a Markov process to evaluate the degree of randomness. The author recognised two types of entropy with respect to each state; 1) entropy after the deposition (i.e. post-deposition), which refers to leaving a particular j^{th} state for any other state and is designated as E(Post), and 2) entropy before deposition (i.e. pre-deposition), which refers to entering a particular j^{th} state from any

other state. The inter-relationship between these two types of entropy is used to classify various cyclic patterns into asymmetric, symmetric and random cycles (Hattori, 1976; Sarmah, 2013). Since entropy analysis has not been widely used in the study of sedimentary successions, the analytical procedure is covered in more detail than Markov chain analysis (given above), and is as follows:

E_i(Post) with respect to lithofacies state i is:

$$E_i^{(Post)} = \sum_{j=0}^{n} P_{ij} log_2(p_{ij})$$

where P_{ij} is the upward probabilities of the transitions, calculated as fij/n_{+I}, i represents the lower bed and j represent the upper bed. If E(Post) = 0, it can be said that state i is likely to be succeeded by state j in sequence (i.e i exerts a decisive control on selection of next state). If E(Post) > 0, the memory of i is obscure and i is likely to be overlain by different states. The smaller the E(Post) value, the greater the dependence on state i.

E_j(Pre) with respect to lithofacies state i is:

$$E_i^{(Pre)} = \sum_{j=0}^{n} Q_{ij} log_2(Q_{ij})$$

where Q_{ij} represents the probability of a given transition being proceeded by any other state (i.e. downward probability transitions), and is calculated by fij/n_{+j}. If E_j(Pre) = 0, i is underlain by a specific state j in sequence. If E(Pre) > 1, i occurs independently of the preceding state j. The larger the E(Pre), the greater the independence.

Together, E_i(Post) and E_j(Pre) demonstrate the variety of lithological transitions which precede and proceed a given state, and is a useful tool alongside the transition probability matrix which can aid interpretation on the style of cyclicity (Hattori, 1976): i) if E_i(Post) = E_j(Pre) = 0, the state preceding and succeeding state i can be predicted; ii) if E_i(Post) = E_j(Pre) = > 0, state i overlies and is overlain by more than one state; iii) if E(Pre) > E(Post), state i can possibly occur after state j, and is also followed by them; however, the degree of dependency is uneven, therefore, in this case, state i can influence the succeeding state j, and finally; iv) if E(Post) > E(Pre), then state i is influenced by the preceding state j, but may not influence the succeeding state j.

Since the values of E_i(post) and E_j(pre) are affected by the number of states selected (i.e. increases with increases states), Hattori (1976) normalised the entropies with the equation:

$$R_{(pre)} = E_{(pre)}/E_{(\max)}$$

$$R_{(post)} = E_{(post)}/E_{(\max)}$$

$$E_{(\max)} = -log_2(1/(n-1)$$

where $E_{(max)}$ denotes the maximum entropy possible in a system with *n* number of states. $E_{(max)}$ allows the comparison between states in different system regardless of the number of states being studies (Hattori, 1976; Tewari et al., 2009). Using the normalised entropy sets, cyclicity in a sedimentary succession can be analysed and classified into symmetrical, asymmetrical, truncated (lower, upper or both) or disordered.

Table 3-1: Hierarchical descriptive facies scheme used in this study. See Appendix A for more detail on depositional processes for each of the facies.

Facies/Code	*Description*	*Texture*			*Thickness range*	*Position*		*Interpretation*	*Equivalent Facies*	*Photograph*
		Grading	*Grain size distribution*	*Sorting*		*Temporal*	*Spatial*			
SM1 – Sandstone, ungraded, massive	*Massive (massive), ungraded clean sands. Mudclasts, - dispersed graded to locally clustered floating and ordered stratified.*	*Ungraded to subtly coarse-tail graded*	*250μm-2mm*	*Moderate to poor*	*dm to > m*	*Base and middle*	*Proximal to distal, increasing in percentage in distal sections*	*See text*	*F5 and F8 (Mutti, 1992).*	
SM2 – Sandstone, graded, massive	*Massive (massive), graded clean sands. Mudclass – typically occur as ordered stratified and dispersed graded.*	*Normal graded – distribution and coarse-tail grading*	*187μm–2mm*	*Moderate to poor*	*dm to > m*	*Middle and top*	*Proximal to distal, greater percentage in proximal and medial sections*	*See text*	*F5 and F8 (Mutti, 1992). Ta (Bouma, 1962).*	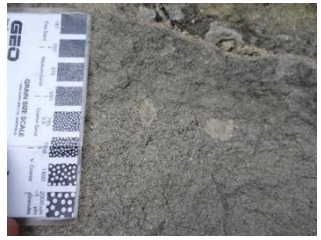

SM3 – Sandstone, massive, patchy texture	*Massive (massive), ungraded clean sand. Patchy texture consisting of irregular 'patches' of coarse grains adjacent to fine grains. Chaotic to locally stratified mudclast conglomerates/breccia.*	*Ungraded to weakly coarse-tail graded.*	*250μm-2mm*	*Poorly sorted*	*dm to > m*	*Whole bed, base and middle*	*Medial and distal sections*	*See text*	*Dcs (Talling et al. 2012).*	
SL1 – Sandstone, laminated	*Laminated sands, <3 mm thick, planar to wavy, locally convoluted. No grain size variation between laminae. Laminae typically more distinct upwards in the bed. Laminar traced for metres. Rarely contain <2-3 cm mudclast along distinct horizon.*	*Normal graded to ungraded*	*125μm-354μm*	*Moderate to moderately well*	*cm to > m*	*Top of beds*	*Proximal to medial. Rarely distal*	*Formed from low-density turbidity current in the upper stage plane-bed regime. Experimental work have shown lamination forming via migration and burial of low amplitude bedwaves under low sediment fallout rates.*	*F9 (Mutti, 1992), Tb (Bouma, 1962), Tb-1 (Talling et al. 2012).*	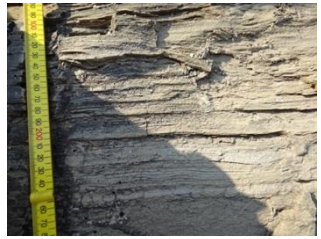

SL2 – Sandstone, thin (mm to < 1cm) spaced stratification	*Alternating coarser and finer grained laminae. 3 - <10mm thick. Laminae thickness decreases with height from base, and becomes more distinct towards the top. Planar to locally wavy/irregular, sharp contacts. Individual laminae are ungraded to normal and inverse graded. Laminae traced for cm at base, increasing towards the top.*	*Weakly normal graded.*	*354μm-1.5mm*	*Poor to moderately poor.*	*cm-dm*	*Middle and top*	*Proximal and medial sections.*	*Formed by concentrated turbidity currents from near bed high-concentration layers with sediment concentration of 10-40%. Hindered settling and frictional interlocking of grains are likely to play important roles in these layers. The layers are fed and driven by the overriding current. Shearing of the layers and partial erosion by the current produces a crude planar stratification, that become more defined at lower sediment-fallout rates.*	*F6-F7 (Mutti, 1992). Tb-2 (Talling et al. 2012)*	
SL3 – Sandstone, thick (> 1 cm.) spaced stratification	*Thick (>1cm to <15cm), alternating coarse and fine grained lamination. Thickness of individual layers decreases with height from base. Diffuse and irregular at the base, become more distinct upwards. Sharp to gradational contacts between lamination. Coarser laminae are typically ungraded, but rarely normal and inverse graded. Finer grained laminae are normal graded.*	*Normal graded*	*545μm-4mm*	*Poor*	*dm to > m*	*Base and middle*	*Exclusively proximal*	*Not reproduced in experimental studies. Thought to be produced by similar processes to above but wth coarser grain sizes, higher sediment concentrations and higher shear stresses. Traction carpets of Hiscott (1994), Sohn (1997).*	*F4 (Mutti, 1992), S2 (Lowe, 1982), Tb-3 (Talling et al. 2012)*	

SR – Sandstone, rippled	*Ripple cross lamination, planar to trough, climbing ripples Locally convoluted. Wavelength <15 cm and typically < 10 cm.*	*Normal graded*	*125μm-354μm*	*Moderate to well sorted*	*cm-dm*	*Exclusively top of beds*	*Predominantly proximal to medial*	*Unambiguous evidence of deposition from low density turbidity currents. Sand reworked as bedload into ripples in the lower flow regime. Relatively low rates of sediment fall-out.*	*F9 (Mutti, 1992), Tc (Bouma, 1962)*	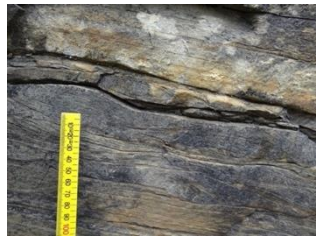
ZM – Siltstone, massive	*Massive (massive), gradational contacts to the underlying sand and overlying mud. Abundant carbonaceous fragments*	*Ungraded, to normal graded*	*n/a*	*n/a*	*mm to dm*	*Exclusively top of beds*	*Proximal sections*	*Sedimentation via settling flocs at the rare of a dilute, fine grained turbidity current.*	*F9 (Mutti, 1992), Td (Bouma, 1962). TE-2 and TE-3 (Talling et al. 2012).*	
ZL – Siltstone, laminated	*Planar laminated siltstone, fissile, gradational contact, abundant carbonaceous fragments*	*Ungraded to normal graded*	*n/a*	*n/a*	*mm to dm*	*Exclusively top of beds*	*Rarely in distal section, predominantly in proximal and medial*	*Not reproduced in experimental studies to satisfactory degree. Though to be produced by tractional reworking beneath a dilute, fine grained turbidity current.*	*F9 (Mutti, 1992), Td (Bouma, 1962), TE-1 (Talling et al. 2012).*	
MM – Mudstone, massive	*Massive (massive), minor silt fraction at the base*	*n/a*	*n/a*	*n/a*	*cm to > m*	*Mudstone cap at top of beds*	*Proximal to distal, increasing in thickness and preservation in distal sections.*	*Static settling of clay or formation of fluid mud layers from a collapsing mud cloud.*	*F9 (Mutti, 1992), Te (Bouma, 1962), TE (Talling et*	

									al. 2012).	
ML – Mudstone, laminated	*Laminated mudstone. Laminae are 0.1 to < 1mm thick. Locally the laminae are silt/ v.f grained. Fissile.*	*n/a*	*n/a*	*n/a*	*cm-dm, rarely > 1m*	*Mudstone cap at top of beds*	*Predominantly in proximal locations, decreasing in thickness distally.*	*Settling of flocs from a dilute and expanded suspension cloud. Rapid suspension of mud laminae upon dampened turbulence. Silt laminae are deposited when the mud flocs are broken up by shearing from the flow.*	*F9 (Mutti, 1992), Te (Bouma, 1962), TE (Talling et al. 2012).*	
CM1 – Conglomerate, clean, matrix supported/Pebbly sandstone	*Matrix-supported conglomerate, mixture of cobble, and pebble material floating in a matrix of poorly sorted coarse sand to granules. Massive. Mud- and sandclasts, where present, are disorganised and chaotic distributed to locally inversely/normally graded and ordered stratified. Mud and sandclast vary in size from cm to > 1m locally.*	*Dispersed graded mud and sand clasts. Coarse-tail grading in the matrix component*	*Matrix – 545µm-4mm.* *Clasts - >4mm - <3 cm.*	*Matrix – moderately to poorly sorted.* *Clasts – poorly sorted*	*dm to >1m*	*Base of beds*	*Predominantly in proximal to medial sections, rarely in distal sections.*	*Non-cohesive debris flows, hyperconcentrated flows or inflated sandflow with ~40-70% concentration by volume, characterised by excess pore pressure and grain to grain interaction upon flow deceleration. Deposition occur via en-masse freezing due to interlocking of grains. High hydraulic diffusivity and well connected pores allows flow transformation to concentrated turbidity currents downslope.*	*F2 (Mutti, 1992), R2 (Lowe, 1982), DCS and DVCS (Talling et al. 2012), A1.4, (Pickering and Hiscott, 2015)*	

CM2 – Conglomerate, clean, clast-supported	*Clast-supported conglomerate, massive (massive), locally stratified. Mud- and sandclasts, where present, occur either along distinct horizon (ordered stratified) towards the top of beds or chaotically distributed towards the base. Mud- and sandclast vary in size from cm to > 1m.*	*Dispersed graded mud and sandclasts. Coarse-tail grading in the framework component.*	*Matrix > 4mm-* *Clasts - > 6mm - < 16 cm.*	*Moderately to poorly sorted*	*dm to >1m*	*Base of beds*	*Proximal and medial locations*	*Non-cohesive debris flows, hyperconcentrated flows or inflated sandflow with ~40-70% concentration by volume, characterised by excess pore pressure and grain to grain interaction upon flow deceleration. Deposition occur via en-masse freezing due to interlocking of grains. High hydraulic diffusivity and well connected pores allow flow transformation to concentrated turbidity currents downslope.*	*F3 (Mutti, 1992), R2 (Lowe, 1982), DCS and DVCS (Talling et al. 2012), A1.1, (Pickering and Hiscott, 2015).*	
CM3 – Conglomerate, mud-rich, matrix-supported	*Chaotic/disorganised unit consisting of floating clasts in a muddy matrix. Mud- and sand clasts are disorganised and consist of marls, limestones and turbidite beds. Clasts range in size from cm to > 1m.*	*disorganised*	*Matrix – mud.* *Clasts – cm to >1 m*	*Very poorly sorted*	*dm to > 1m.*	*Base of bed*	*Exclusively in proximal sections*	*Highly to moderately cohesive debris flow characterised by matrix strength which provides the main grain support mechanism for clasts. Liquefaction and grain interaction may be locally important. Moderate to high clay content imparts low hydraulic diffusivity. The flow comes to rest en-masse.*	*F1 (Mutti, 1992), DM-2 (Talling et al. 2012), A1.3 (Pickering and Hiscott, 2015).*	

3.4 Results.

A series of correlation panels of the eight beds investigated in this study are presented in Figures 3-15 to 3-19 (the master correlation panel is in Appendix C). The correlation panels are orientated approximately parallel to the palaeoflow in a north-easterly direction (except between NW and NE section which show a cross flow transect). The eight beds include; CB5, CB6, CB7, CB10-1, CB10-2, CB11-1, CB11-2, and CB11-3. These correlations, as well individual vertical sections of beds, form the basis for evaluating the temporal and spatial changes in bed character (e.g. internal architecture, deposit geometry, grain size breaks etc.) of DWMS. From this analysis, we can assess the hydrodynamic conditions of DWMS depositing flows, validate existing depositional models, and update or develop new depositional models incorporating recent advances in deep-water sedimentology, including the influence of local topography.

Table 3-2: Comparison of grain size of ungraded (SM1) and graded massive (SM2) sands, and ungraded massive sands with patchy texture as measured in the field using a hand lens and a grain size comparator, and SEM image analysis. Grain measurements taken in the field record the coarsest 5% of the grain size distribution seen in the SEM images.

				SEM Image Analysis (μm/phi)					
Location/Bed	Facies	Field Measured Grain Size (μm)	Mud%	D10	D50	D90	D95	D99	Sorting
NES/CB11-2	Sm_3	250-375	9.5	19.2/5.61	81.8/3.61	226.9/2.14	302.9/1.72	522.4/0.94	2.05
	Sm_3	300-375	8.3	10.7/6.54	111.5/3.16	298.5/1.74	375.3/1.41	587.5/0.77	1.86
	Sm_3	250-375	10.3	55.0/4.18	141.8/2.82	294.8/1.76	345.0/1.54	465.5/1.10	1.76
	Sm_3	177-250	9.7	26.7/5.25	75.1/3.73	156.3/2.68	178/2.49	223/2.16	1.03
NES/CB10-2	Sm_1	500-750	4.5	58.8/4.09	150.4/2.73	381.0/1.39	487.8/1.04	769.1/0.38	1.24
	Sm_1	375-710	6.1	14.5/6.10	149.8/2.74	356.2/1.49	427.6/1.23	606.1/0.72	1.73
	Sm_1	375-500	3.3	11.07/6.50	147.4/2.76	355.9/1.49	455.2/1.17	671.98/0.57	1.86
	Sm_1	375-500	7.1	13/6.26	138.4/6.26	351.9/1.51	454.9/1.14	781.5/0.36	1.6
	Sm_1	375-500	4.5	12/6.37	142/2.82	376.5/1.41	476.9/1.07	689.7/0.54	2.82
	Sm_2	300-400	3.4	9.9/6.66	133.3/2.91	325.6/1.62	399.8/1.32	541.8/0.88	1.9
NE/CB5	Sm_1	710-1000	2.3	68.22/3.87	156.7/2.67	500.5/1	705.6/0.5	1174/-0.23	1.11
	Sm_1	710-1000	3.4	11.7/6.61	141.2/2.82	544.9/0.88	737.8/0.44	1414/-0.50	2.16
	Sm_1	710-1000	2.5	11/6.50	168.8/2.57	545.8/0.87	749.7/0.42	1312.5/-0.39	2.21
	Sm_1	710-1000	4.5	9.8/6.67	202.5/2.30	535.1/0.90	733.7/0.45	1261.3/-033	2.03
	Sm_2	500-750	4.7	22.6/5.47	213/2.23	502.7/0.99	732.6/0.45	735.3/0.44	1.49
	Sm_2	375-500	3.4	10.2/6.6	142/2.82	387.4/1.37	470/1.09	635.9/0.65	2.04
	Sm_2	250-375	2.6	12.7/6.30	135.8/2.88	302.7/1.72	376.4/1.41	516.3/0.95	1.39
	Sm_2	250-375	3.4	58.8/4.09	130.1/2.94	230.3/2.12	267.5/1.90	350.8/1.51	0.8
NWT/CB10-1	Sm_1	710-1000	2.1	12.3/6.34	145.3/2.78	514.1/0.96	737.2/0.44	1431.8/-0.52	2.13
	Sm_1	710-1000	3.2	12.2/6.35	171.2/2.55	513.9/0.96	717/0.48	1132.9/-018	2.08
	Sm_1	710-1000	2.6	12.5/6.32	224.5/2.15	554.6/0.85	727.5/0.46	1134.9/-0.18	1.93
	Sm_2	375-500	4.1	61.8/4.02	166.5/2.59	332.6/1.59	407.7/1.29	616/0.70	1.14
	Sl_1	177-250	3.1	27.63/5.18	105.1/3.23	190.1/2.39	218.5/2.19	281.2/1.83	1.06

3.4.1 Internal Bed Character at a Single Outcrop.

A facies scheme based initially on lithology and then on sedimentary structure (Table 3-1) was developed for this study to document temporal changes at a single outcrop. This is the 'usual' case in many outcrop based studies due to a lack of laterally extensive outcrops or poorly developed correlation frameworks. Since many of the facies in the scheme have been well documented by existing schemes, they are only briefly summarised in Table 3-1 (see Appendix A for detail). However, as the main focus of this study concerns the origin of massive sands

(SM facies), these facies are described in greater detail below. Furthermore, embedded Markov chain and entropy analysis was performed on the measured sections to investigate non-random facies arrangement, and lends additional support to the analysis on internal bed character. This analysis is discussed separately in subsequent sections.

Sandstone – Ungraded, Massive (SM1). Ungraded, massive sand facies comprise grains covering the entire spectrum of the sand size range (2 mm to 62 μm, e.g. CB5). The facies is completely devoid of any primary sedimentary and dewatering structures. Grain size measurements using a comparator in the field show no vertical grading (e.g. CB10-2; Figure 3-16; Table 3-1). This is confirmed by thin section analysis which shows no statistically significant changes in the coarsest 5% of the grain size distribution (NES CB10-2; Table 3-2). However, complex grading trends are observed in the finer grain size distribution in thin sections, and may be indicative of one or more different flow processes. Mud content is low, typically between 2.1 and 7.1% of the total thin section area. Grain sorting is poorly to very poorly sorted (between 1.1 and 2.82 phi). Mudclasts are rare, but where present, are up to 10 cm in diameter and are clustered floating (A3), occurring in a thin zone parallel to the bedding plane or at low angle. Grain size trends below and above the mudclast zone tends to be stable. Intervals of ungraded, massive sands (SM1) are commonly overlain by graded, massive sands (SM2) or thin, spaced stratification (SL2). In distal localities this typically occurs without an intervening grain size break. However, in proximal and medial locations, Type II and III grain size breaks separate ungraded massive sands and the overlying facies, which are typically thin, spaced stratification (SL2).

Sandstone – Graded, Massive (SM2). Similar to the SM1 facies, this facies is devoid of primary sedimentary structures and consists of grain size covering the entire spectrum of the sand grain size range (2 mm to 62 μm; e.g. PCR and NWT CB10-2). Vertical normal grading is observable in the field using a grain size comparator (Table 3-1), but is only recognisable in the coarsest 5% of the grain size distribution. Grain size measurements from thin sections confirm this trend, but is further characterised by complex grain size trends (i.e. fining or coarsening fine-tail distribution) with increasing height from the base of the facies (NE CB5; Table 3-2). Locally, subtle inverse grading is also visible in this facies (ibid.). Mud content is relatively low (between 2.6 and 4.7%), similar to ungraded massive sand facies, and grain sorting ranges from moderately sorted (0.8) to very poorly sorted (2.21). Similar values in the sorting parameter are also observed in other beds based on visual estimates using a grain size comparator. Mudclasts, where present, are granular to medium pebble in size (2 mm – 16 mm) and rarely greater than 5cm. They are predominantly ordered stratified (B5); aligned along the long axis and occurring within thin zones parallel or at a low angle to the bedding plane (e.g. SE CB10-2 Figure 3-16). The larger clasts are isolated and tend to be more tabular with increasing clast size. Secondary

dewatering features are present only in one location (PCR CB10-2) where they occur as widely-spaced consolidation laminae, passing into shallow dish structures and pipes towards the top. Intervals of graded, massive sands (SM2) are commonly overlain by structured intervals consisting of parallel lamination (SL1) and thin spaced stratification (SL2). This transition is progressive, but in a few cases, a Type II grain size break marks the transition between the facies. In the latter case, the transition is between graded, massive sands and parallel laminated sands (SL1).

Sandstone – Massive, Patchy Texture (SM3). Facies type SM3 is relatively rare and consists of irregular patches of poorly sorted coarser and better sorted finer material. Grain size ranges from medium to coarse as measured in the field, which is confirmed in the coarsest 5% of the grain size distribution measured from thin sections (Table 3-2). Grading is highly erratic due to the juxtaposition of coarse and finer grained sediments (Table 3-1), which also makes it difficult to observe in thin sections. However, the top 5 to 10 cm of this facies in some beds shows distribution grading. Sorting is highly variable, between 1 and 2.1 phi, possibly a result of the patchy texture. The mud content is low (between 8.3 and 10.3%), but higher compared to the two other massive facies (Table 3-2). Mudclasts are common in this facies; observable in the middle or towards the top of beds, surrounded by clean sandstone matrix. The clasts vary from small pebble (4 mm) to cobbles (<40 cm) in size and occur as nested discontinuous zones sub-parallel to bedding. They are elongated, sub-angular to rounded and are very poorly sorted. In distal locations (e.g. NES, NE), they are generally dispersed graded (Type B4) and less chaotic than proximal and medial locations. Similar to facies SM1 and SM2, the clasts where derived from within the basin. No dewatering (e.g. dishes, pipes and convoluted consolidation laminae) or burrowing features were observed in this facies. The facies typically comprises the basal and middle portion of beds and is separated by Type II grain size breaks from overlying structured facies (i.e. parallel lamination or thin, spaced stratification). This facies is similar to the swirly or patchy texture massive sandstone facies (Cs7) of Talling et al. (2012) and Talling et al. (2013). And whilst it does not adhere to the definition of DWMS as proposed by Stow and Johansson (2000), its inclusion as part of the MSFA can be justified based on the lack of primary sedimentary structures and its association with coarser-grained resedimented facies.

Table 3-3: The transition count, upward transition, upward expected probability and the difference matrices for the proximal, medial and distal grouping of the Peïra Cava Outlier. Values in bold in the difference matrix are used to construct the markov chain diagram, supplemented by data from the transition count matrix.

Proximal

Transition Count Matrix (Fij)

i, j	Sr	Sl1	Sl2	Sl3	Sm1	Sm2	Sm3	Cm1	Cm2	Cm3	Total i
Sr	-	2.00	1.00	0.00	0.00	1.00	0.00	0.00	0.00	0.00	**4.00**
Sl1	18.00	-	1.00	0.00	0.00	1.00	0.00	0.00	0.00	0.00	**20.00**
Sl2	2.00	13.00	-	0.00	2.00	3.00	0.00	0.00	0.00	0.00	**20.00**
Sl3	0.00	2.00	2.00	-	1.00	5.00	0.00	5.00	0.00	0.00	**15.00**
Sm1	0.00	2.00	4.00	0.00	-	5.00	0.00	0.00	0.00	0.00	**11.00**
Sm2	1.00	4.00	10.00	1.00	3.00	-	0.00	0.00	0.00	0.00	**19.00**
Sm3	0.00	0.00	0.00	2.00	0.00	0.00	-	0.00	0.00	0.00	**2.00**
Cm1	0.00	0.00	2.00	2.00	5.00	7.00	2.00	-	2.00	0.00	**20.00**
Cm2	0.00	0.00	0.00	0.00	1.00	0.00	0.00	1.00	-	0.00	**2.00**
Cm3	0.00	0.00	0.00	0.00	0.00	0.00	0.00	2.00	0.00	-	**2.00**
Total j	**21.00**	**23.00**	**20.00**	**5.00**	**12.00**	**22.00**	**2.00**	**8.00**	**2.00**	**0.00**	115.00

Upward Transition Probability Matrix (Ṕij)

i,j	Sr	Sl1	Sl2	Sl3	Sm1	Sm2	Sm3	Cm1	Cm2	Cm3
Sr	-	0.50	0.25	0.00	0.00	0.25	0.00	0.00	0.00	0.00
Sl1	0.90	-	0.05	0.00	0.00	0.05	0.00	0.00	0.00	0.00
Sl2	0.10	0.65	-	0.00	0.10	0.15	0.00	0.00	0.00	0.00
Sl3	0.00	0.13	0.13	-	0.07	0.33	0.00	0.33	0.00	0.00
Sm1	0.00	0.18	0.36	0.00	-	0.45	0.00	0.00	0.00	0.00
Sm2	0.05	0.21	0.53	0.05	0.16	-	0.00	0.00	0.00	0.00
Sm3	0.00	0.00	0.00	1.00	0.00	0.00	-	0.00	0.00	0.00
Cm1	0.00	0.00	0.10	0.10	0.25	0.35	0.10	-	0.10	0.00
Cm2	0.00	0.00	0.00	0.00	0.50	0.00	0.00	0.50	-	0.00
Cm3	0.00	0.00	0.00	0.00	0.00	0.00	0.00	1.00	0.00	-

Upward Expected Probability Matrix (Ṕij)

i, j	Sr	Sl1	Sl2	Sl3	Sm1	Sm2	Sm3	Cm1	Cm2	Cm3
Sr	-	0.25	0.22	0.05	0.12	0.24	0.02	0.09	0.02	0.00
Sl1	0.21	-	0.23	0.05	0.13	0.25	0.02	0.09	0.02	0.00
Sl2	0.20	0.26	-	0.05	0.12	0.24	0.02	0.09	0.02	0.00
Sl3	0.17	0.22	0.19	-	0.10	0.21	0.02	0.07	0.02	0.00
Sm1	0.18	0.24	0.20	0.05	-	0.22	0.02	0.08	0.02	0.00
Sm2	0.20	0.26	0.23	0.05	0.12	-	0.02	0.09	0.02	0.00
Sm3	0.17	0.22	0.19	0.04	0.10	0.20	-	0.07	0.02	0.00
Cm1	0.18	0.23	0.20	0.05	0.11	0.22	0.02	-	0.02	0.00
Cm2	0.17	0.22	0.19	0.04	0.10	0.20	0.02	0.07	-	0.00
Cm3	0.16	0.21	0.18	0.04	0.10	0.20	0.02	0.07	0.02	-

Difference Matrix (Dij) (Ṕij-Ṕij)

i, j	Sr	Sl1	Sl2	Sl3	Sm1	Sm2	Sm3	Cm1	Cm2	Cm3
Sr	-	**0.25**	**0.03**	-0.05	**-0.12**	0.01	-0.02	-0.09	-0.02	0.00
Sl1	**0.69**	-	-0.18	-0.05	-0.13	-0.20	-0.02	-0.09	-0.02	0.00
Sl2	-0.10	**0.39**	-	-0.05	-0.02	-0.09	-0.02	-0.09	-0.02	0.00
Sl3	-0.17	-0.09	-0.06	-	-0.04	**0.12**	-0.02	**0.26**	-0.02	0.00
Sm1	-0.18	-0.05	**0.16**	-0.05	-	**0.23**	-0.02	-0.08	-0.02	0.00
Sm2	-0.15	-0.05	**0.30**	0.00	**0.03**	-	-0.02	-0.09	-0.02	0.00
Sm3	-0.17	-0.22	-0.19	**0.96**	-0.10	-0.20	-	-0.07	-0.02	0.00
Cm1	-0.18	-0.23	-0.10	**0.05**	**0.14**	**0.13**	**0.08**	-	**0.08**	0.00
Cm2	-0.17	-0.22	-0.19	-0.04	0.40	-0.20	-0.02	**0.43**	-	0.00
Cm3	-0.16	-0.21	-0.18	-0.04	-0.10	-0.20	-0.02	**0.93**	-0.02	-

Medial

Transition Count Matrix (Fij)

i, j	Sr	Sl1	Sl2	Sl3	Sm1	Sm2	Sm3	Cm1	Cm2	Cm3	Total i
Sr	-	1.00	0.00	0.00	0.00	0.00	0.00	0.00	0.00	0.00	**1.00**
Sl1	2.00	-	1.00	0.00	0.00	0.00	0.00	0.00	0.00	0.00	**3.00**
Sl2	1.00	3.00	-	0.00	2.00	2.00	0.00	0.00	0.00	0.00	**8.00**
Sl3	0.00	0.00	0.00	-	1.00	2.00	0.00	0.00	0.00	0.00	**3.00**
Sm1	1.00	0.00	4.00	0.00	-	5.00	0.00	0.00	0.00	0.00	**10.00**
Sm2	2.00	1.00	4.00	0.00	4.00	-	0.00	0.00	0.00	0.00	**11.00**
Sm3	0.00	0.00	0.00	0.00	0.00	0.00	-	0.00	0.00	0.00	**0.00**
Cm1	0.00	0.00	0.00	1.00	3.00	2.00	0.00	-	0.00	0.00	**6.00**
Cm2	0.00	0.00	0.00	0.00	0.00	0.00	0.00	1.00	-	0.00	**1.00**
Cm3	0.00	0.00	0.00	0.00	0.00	0.00	0.00	0.00	0.00	-	**0.00**
Total j	**6.00**	**5.00**	**9.00**	**1.00**	**10.00**	**11.00**	**0.00**	**1.00**	**0.00**	**0.00**	43.00

Upward Transition Probability Matrix (Ṕij)

i,j	Sr	Sl1	Sl2	Sl3	Sm1	Sm2	Sm3	Cm1	Cm2	Cm3
Sr	-	1.00	0.00	0.00	0.00	0.00	0.00	0.00	0.00	0.00
Sl1	0.67	-	0.33	0.00	0.00	0.00	0.00	0.00	0.00	0.00
Sl2	0.13	0.38	-	0.00	0.25	0.25	0.00	0.00	0.00	0.00
Sl3	0.00	0.00	0.00	-	0.33	0.67	0.00	0.00	0.00	0.00
Sm1	0.10	0.00	0.40	0.00	-	0.50	0.00	0.00	0.00	0.00
Sm2	0.18	0.09	0.36	0.00	0.36	-	0.00	0.00	0.00	0.00
Sm3	0.00	0.00	0.00	0.00	0.00	0.00	-	0.00	0.00	0.00
Cm1	0.00	0.00	0.00	0.17	0.50	0.33	0.00	-	0.00	0.00
Cm2	0.00	0.00	0.00	0.00	0.00	0.00	0.00	1.00	-	0.00
Cm3	0.00	0.00	0.00	0.00	0.00	0.00	0.00	0.00	0.00	-

Upward Expected Probability Matrix (Ṕij)

i, j	Sr	Sl1	Sl2	Sl3	Sm1	Sm2	Sm3	Cm1	Cm2	Cm3
Sr	-	0.11	0.23	0.02	0.28	0.33	0.00	0.02	0.00	0.00
Sl1	0.13	-	0.23	0.02	0.28	0.32	0.00	0.02	0.00	0.00
Sl2	0.14	0.13	-	0.02	0.31	0.36	0.00	0.03	0.00	0.00
Sl3	0.12	0.10	0.21	-	0.25	0.29	0.00	0.02	0.00	0.00
Sm1	0.15	0.13	0.28	0.03	-	0.38	0.00	0.03	0.00	0.00
Sm2	0.16	0.14	0.29	0.03	0.35	-	0.00	0.03	0.00	0.00
Sm3	0.00	0.00	0.00	0.00	0.00	0.00	-	0.00	0.00	0.00
Cm1	0.12	0.10	0.21	0.02	0.25	0.30	0.00	-	0.00	0.00
Cm2	0.11	0.10	0.21	0.02	0.25	0.29	0.00	0.02	-	0.00
Cm3	0.00	0.00	0.00	0.00	0.00	0.00	0.00	0.00	0.00	-

Difference Matrix (Ṕij-Ṕij)

i, j	Sr	Sl1	Sl2	Sl3	Sm1	Sm2	Sm3	Cm1	Cm2	Cm3
Sr	-	**0.89**	-0.23	-0.02	-0.28	-0.33	0.00	-0.02	0.00	0.00
Sl1	**0.54**	-	0.10	-0.02	-0.28	-0.32	0.00	-0.02	0.00	0.00
Sl2	**-0.02**	**0.25**	-	-0.02	-0.06	-0.11	0.00	-0.03	0.00	0.00
Sl3	-0.12	-0.10	-0.21	-	**0.08**	**0.37**	0.00	-0.02	0.00	0.00
Sm1	-0.05	-0.13	**0.12**	-0.03	-	**0.12**	0.00	-0.03	0.00	0.00
Sm2	0.02	-0.05	**0.07**	-0.03	**0.01**	-	0.00	-0.03	0.00	0.00
Sm3	0.00	0.00	0.00	0.00	0.00	0.00	-	0.00	0.00	0.00
Cm1	-0.12	-0.10	-0.21	**0.15**	**0.25**	**0.04**	0.00	-	0.00	0.00
Cm2	-0.11	-0.10	-0.21	-0.02	-0.25	-0.29	0.00	**0.98**	-	0.00
Cm3	0.00	0.00	0.00	0.00	0.00	0.00	0.00	0.00	0.00	-

Distal

Transition Count Matrix (Fij)

i, j	Sr	Sl1	Sl2	Sl3	Sm1	Sm2	Sm3	Cm1	Cm2	Cm3	Total i
Sr	-	0.00	0.00	0.00	0.00	0.00	0.00	0.00	0.00	0.00	**0.00**
Sl1	4.00	-	0.00	0.00	0.00	0.00	0.00	0.00	0.00	0.00	**4.00**
Sl2	0.00	3.00	-	0.00	0.00	0.00	0.00	0.00	0.00	0.00	**3.00**
Sl3	0.00	0.00	0.00	-	0.00	0.00	0.00	0.00	0.00	0.00	**0.00**
Sm1	1.00	0.00	0.00	0.00	-	11.00	0.00	0.00	0.00	0.00	**12.00**
Sm2	1.00	6.00	2.00	0.00	6.00	-	0.00	0.00	0.00	0.00	**15.00**
Sm3	0.00	2.00	1.00	0.00	0.00	0.00	-	0.00	0.00	0.00	**3.00**
Cm1	0.00	0.00	0.00	0.00	0.00	0.00	1.00	-	0.00	0.00	**1.00**
Cm2	0.00	0.00	0.00	0.00	0.00	0.00	0.00	0.00	-	0.00	**0.00**
Cm3	0.00	0.00	0.00	0.00	0.00	0.00	0.00	0.00	0.00	-	**0.00**
Total j	**6.00**	**11.00**	**3.00**	**0.00**	**6.00**	**11.00**	**1.00**	**0.00**	**0.00**	**0.00**	38.00

Upward Transition Probability Matrix (Ṕij)

i,j	Sr	Sl1	Sl2	Sl3	Sm1	Sm2	Sm3	Cm1	Cm2	Cm3
Sr	-	0.00	0.00	0.00	0.00	0.00	0.00	0.00	0.00	0.00
Sl1	1.00	-	0.00	0.00	0.00	0.00	0.00	0.00	0.00	0.00
Sl2	0.00	1.00	-	0.00	0.00	0.00	0.00	0.00	0.00	0.00
Sl3	0.00	0.00	0.00	-	0.00	0.00	0.00	0.00	0.00	0.00
Sm1	0.08	0.00	0.00	0.00	-	0.92	0.00	0.00	0.00	0.00
Sm2	0.07	0.40	0.13	0.00	0.40	-	0.00	0.00	0.00	0.00
Sm3	0.00	0.67	0.33	0.00	0.00	0.00	-	0.00	0.00	0.00
Cm1	0.00	0.00	0.00	0.00	0.00	0.00	1.00	-	0.00	0.00
Cm2	0.00	0.00	0.00	0.00	0.00	0.00	0.00	0.00	-	0.00
Cm3	0.00	0.00	0.00	0.00	0.00	0.00	0.00	0.00	0.00	-

Upward Expected Probability Matrix (Ṕij)

i, j	Sr	Sl1	Sl2	Sl3	Sm1	Sm2	Sm3	Cm1	Cm2	Cm3
Sr	-	0.00	0.00	0.00	0.00	0.00	0.00	0.00	0.00	0.00
Sl1	0.15	-	0.08	0.00	0.21	0.54	0.03	0.00	0.00	0.00
Sl2	0.12	0.25	-	0.00	0.17	0.44	0.02	0.00	0.00	0.00
Sl3	0.00	0.00	0.00	-	0.00	0.00	0.00	0.00	0.00	0.00
Sm1	0.14	0.28	0.07	0.00	-	0.49	0.02	0.00	0.00	0.00
Sm2	0.20	0.40	0.10	0.00	0.27	-	0.03	0.00	0.00	0.00
Sm3	0.12	0.24	0.06	0.00	0.16	0.42	-	0.00	0.00	0.00
Cm1	0.11	0.23	0.06	0.00	0.16	0.41	0.02	-	0.00	0.00
Cm2	0.00	0.00	0.00	0.00	0.00	0.00	0.00	0.00	-	0.00
Cm3	0.00	0.00	0.00	0.00	0.00	0.00	0.00	0.00	0.00	-

Difference Matrix (Ṕij-Ṕij)

i, j	Sr	Sl1	Sl2	Sl3	Sm1	Sm2	Sm3	Cm1	Cm2	Cm3
Sr	-	**0.00**	0.00	0.00	0.00	0.00	0.00	0.00	0.00	0.00
Sl1	**0.85**	-	-0.08	0.00	-0.21	-0.54	-0.03	0.00	0.00	0.00
Sl2	-0.12	**0.75**	-	0.00	-0.17	-0.44	-0.02	0.00	0.00	0.00
Sl3	0.00	0.00	0.00	-	0.00	0.00	0.00	0.00	0.00	0.00
Sm1	-0.05	-0.28	-0.07	0.00	-	**0.43**	-0.02	0.00	0.00	0.00
Sm2	-0.13	0.00	**0.03**	0.00	**0.13**	-	-0.03	0.00	0.00	0.00
Sm3	-0.12	**0.43**	**0.27**	0.00	-0.16	-0.42	-	0.00	0.00	0.00
Cm1	-0.11	-0.23	-0.06	0.00	-0.16	-0.41	**0.98**	-	0.00	0.00
Cm2	0.00	0.00	0.00	0.00	0.00	0.00	0.00	0.00	-	0.00
Cm3	0.00	0.00	0.00	0.00	0.00	0.00	0.00	0.00	0.00	-

3.4.2 Markov Chain.

Markov Process at Proximal, Medial and Distal Locations. The transition counts (Fij), upward transition probability (Pij), upward expected probability (Ṕij) and the difference (D) matrices for the three grouped locations (proximal, medial and distal) are given in Table 3-3. For each transition pair, the row facies code represents the lower facies and the column facies code, the upper facies. The chi-squared statistics for the proximal and distal location at 71 and 29 degrees of freedom respectively, and a 99.5% confidence level, indicate that there is a strong inclination toward an ordered sequence. However, the chi-squared value for the medial section is lower than the limiting value at 41 degrees of freedom and a 99.5% confidence level, thus rejecting the null-hypothesis. This implies that deposition of facies at least in medial sections was not by Markovian process. Figures 3-9 to 3-11 shows Markov transition diagrams based on the difference matrices (Dij) for the strongest transition paths (arbitrary limit of 0.10) of the sediment facies in the three grouped localities. It is important to note at this stage that the difference matrices record the most probable facies transitions, and not the observed frequency in the studied sedimentary beds. The observed frequency of facies transitions for the three groups can be seen in the transition count matrices in Table 3-3. Therefore, in order to better understand deep-water processes, it is essential that both the statistically significant transitions and the observed facies transitions are examined when developing 'typical' trends in vertical facies arrangement.

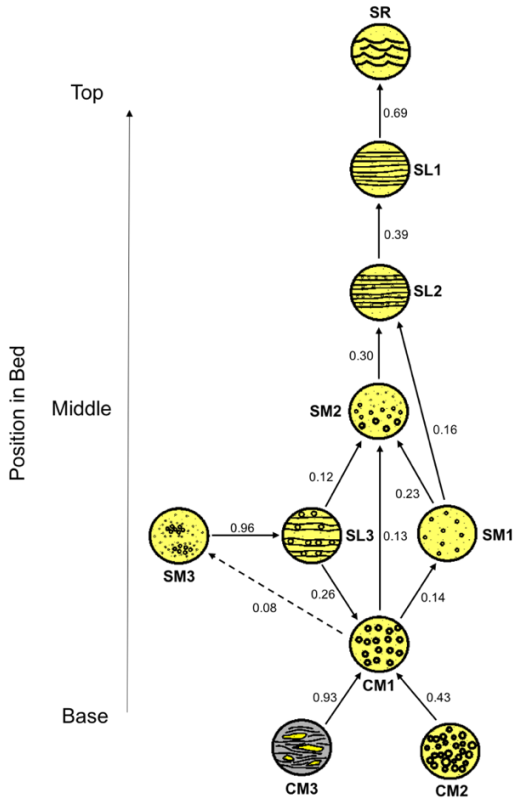

Figure 3-9: Markov chain diagram showing the probabilities of preferred upward transition (arbitrary value of 0.10) between facies states in proximal localities of the Peïra Cava Outlier. Three general trends can be

discerned based on the statistical analysis and observed facies transitions, and are discussed in more detail in the text.

Proximal Markov Chain. *Three* broad vertical facies trends can be recognised in proximal locations based on the difference and observed frequency matrices in Table 3-3. Two of the trends begin with either Facies CM3 or CM2 transitioning to CM1 with a probability of 0.93 and 0.43 respectively. The CM1 facies is in turn overlain by either graded (SM2; 0.16) or ungraded (SM1, 0.13) massive sands (Figure 3-9). Following the SM2 facies path, the *first* vertical facies trend follows a transition through thin, spaced stratified sands (SL2; 0.30), followed by parallel laminated sands (SL1; 0.39) and ripple laminated sands (SR; 0.69). The rippled sands are in turn overlain by finer grained facies (not included as part of this analysis). The *second* vertical facies trend follows a path through the ungraded massive sands (SM1), transitioning to graded massive sands (SM2; 0.23), which is in turn overlain by thin, spaced stratified sands (SL2, 0.30), parallel laminated sands (SL1, 0.39) and eventually ripple laminated sands (SR; 0.69; Figure 3-9). In a few instances, the SM1 facies transitions directly to SL1 facies (0.16). The *third* trend observed in proximal locations has the thick, spaced stratification (SL3) facies at the base of beds, transitioning to matrix-supported conglomerates (CM1; 0.30) or graded massive sands (SM2; 0.16), and then into thin, spaced stratification (SL2; 0.24), parallel laminated sands (SL1; 0.37) and finally into ripple laminated sands (SR; 0.69). Figure 3-9 also shows a strong transition from SM3 to SL3 (0.95). However, this facies is not incorporated into any of the three general trends above due to its infrequent occurrence.

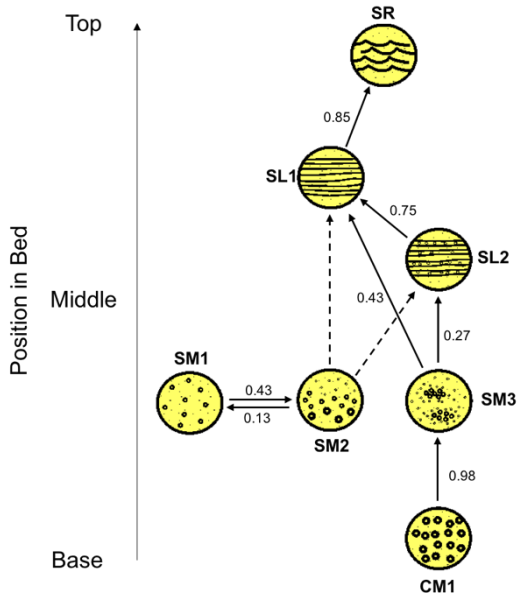

Figure 3-10:Markov chain diagram showing probabilities of preferred upward transition (arbitrary value of 0.10) between facies states in the distal localities of the Peïra Cava outlier. Sold lines with associated probabilities are based on the difference matrix calculated as part of the statistical analysis, while dashed lines are based on observed facies transitions from the transition count matrix and sedimentary logs. Two broad facies trends can be discerned in distal localities, which are discussed in more detail in the text.

Distal Markov Chain. Similar to the proximal facies trends, *two* broad vertical transition trends can be discerned in distal locations based on the difference and observed frequency matrices. The first trend starts with the graded (SM2) or ungraded massive (SM1) sands at the base. These two facies occur as repeating cycles (Figure 3-10), and are eventually overlain by finer grained facies. However, observed transitions also show thin, spaced stratification (SL2) and/or laminated sands (SL1) commonly following massive sands prior to transition to finer grained facies. These transitions are not clearly seen from the statistical analysis, but have been incorporated into the Markov chain diagram (dashed lines Figure 3-10). In the second pathway, the massive sands with patchy texture (SM3) is preferentially overlain by parallel laminated sands (SL1; 0.43), which passes vertically into ripple laminated sands (SR; 0.89). However, the SM3 facies also has relative high probability of passing into the thin, spaced stratification (SL2; 0.27) facies prior to the transition into the parallel laminated sands (SL1; 0.81). In an isolated case (NW CB10-1), the SM3 facies is underlain by matrix-supported conglomerate (CM1).

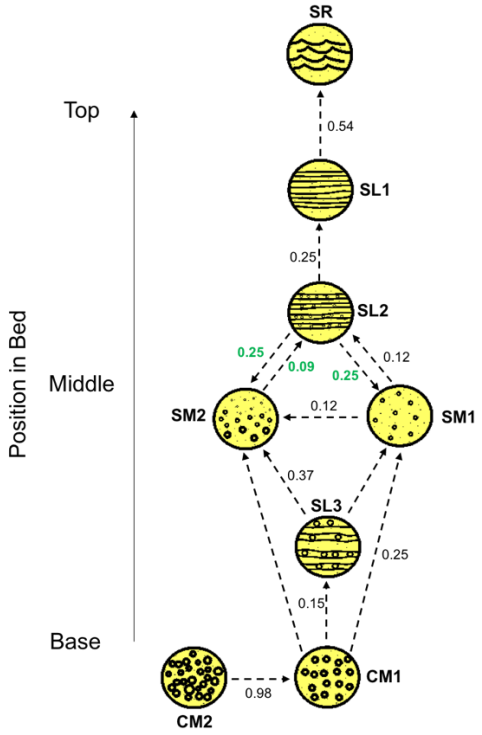

Figure 3-11: Markov chain diagram showing the probabilities of preferred transitions based partly on statistical analysis and observed facies transition for the medial localities in the Peïra Cava outlier. Transition values highlighted in green are taken from the upward transition probability matrix. The chi-squared value for the medial localities is below the limiting value at 95% confidence level, thus indicating that facies transitions were random. However, a general trend has been constructed and described in the text.

Medial Markov Chain: Chi-squared test of the observed transition frequency against equivalent random events for the medial localities group gave a value (34.54) lower than the limiting value of 56.94 at 41 degrees of freedom. Therefore, the hypothesis of quasi-independence cannot be rejected; that is, there is no evidence of predictable arrangement of

facies. However, based on observed frequencies of facies transition, a general trend can be constructed that includes coarser grained CM1 facies at the base, followed upwards by massive sands (either graded or ungraded), passing into laminated (SL1 and SL2) and ripple laminated sand facies, and terminating with finer grained facies (Figure 3-11). Similar to the trends observed in distal locations (above), a crude repetition or cyclicity can be discerned that includes vertical transitions between ungraded and graded massive sands (SM1 and SM2) and thin, spaced lamination (SL2). Furthermore, locally, thick, spaced stratification or clast-support conglomerates occur at the base of beds in the medial localities or overly the CM1 facies (Figure 3-11).

The significance of these facies transitions in terms of the formation of DWMS will be discussed in a later section of this chapter. However, the usefulness of Markov Chain analysis may be limited in this case for several reasons. Firstly, the Markov Chain analysis enables the rejection of random sedimentation with a stated degree of confidence; it does not prove cyclicity nor capture it accurately. In a number of distal beds, cyclic/repetitive transition is observed between SM1 and SM2 facies. Such cyclicity may be indicative of subtle fluctuations in flow dynamics temporally, but is not captured by the difference matrix. Secondly, the embedded matrix used in this study does not take into account transitions from one facies to another facies of the same type, even when such transitions are recorded e.g. above and below a grain size break. Such transitions are typical in proximal locations in the Peïra Cava outlier, where they may represent waxing phases characterised by erosion, and/or sediment by-pass. Thirdly, no sedimentary sequences are truly random. However, Powers (1984), noted that states with only very small contributions towards departure from randomness can give the impression of great order, both statistically and visually. Any interpretation on flow hydrodynamics based on these results thus need to be undertaken with great care.

3.4.3 Entropy Analysis.

The computed entropy E(Post) and E(Pre), and the respective normalised entropy R(Post) and R(Pre) for each state are shown in Table 3-4. E(Post) and E(Pre) relationship show that the influence of each facies on the preceding or succeeding facies is non-random, but is also non-cyclic i.e. asymmetrical. For most of the facies in the three groupings, the entropies are subequal and $E(Pre) = E(Post) \neq 0$, which indicates a level of dependency of one facies on the other. For a minority of facies $E(Post) = 0$, implying that facies i is always succeeded by facies j in the sequence. Furthermore, the majority of facies states have higher values of E(Pre) compared to E(Post) (Table 3-4), suggesting that facies states following them can be discerned with more confidence than those preceding them i.e. these facies exert a stronger influence on the following facies state, whilst being less influence by their predecessor.

Table 3-4: Table show the entropy sets for the three location groups. E(Pre) is entropy before deposition, while E(Post) is entropy after deposition. Together they serve as an indicaton of the variety of lithological transitions immediately after and before the occurrence of state i, respectively

Entropy with respect to deposition of facies in proximal localities.

State	E(Post)	E(Pre)	R(Post)	R(Pre)	Relationship
SR	1.50	0.70	0.47	0.22	E(Post)>E(Pre)
SL1	0.56	0.59	0.17	0.18	E(Pre)>E(Post)
SL2	1.47	1.61	0.46	0.50	E(Pre)>E(Post)
SL3	2.09	1.82	0.66	0.57	E(Post)>E(Pre)
SM1	1.49	1.23	0.47	0.38	E(Post)>E(Pre)
SM2	1.82	2.13	0.57	0.67	E(Pre)>E(Post)
SM3	0.00	0.52	0.00	0.16	E(Pre)>E(Post)
CM1	2.35	1.88	0.74	0.59	E(Post)>E(Pre)
CM2	1.00	0.67	0.31	0.21	E(Post)>E(Pre)
CM3	0.00	0.50	0.00	0.15	E(Pre)>E(Post)
E(Max)	3.16		E(System)	4.48	

Entropy with respect to deposition of facies in medial localities.

State	E(Post)	E(Pre)	R(Post)	R(Pre)	Relationship
SR	0.00	0.99	0.00	0.35	E(Pre)>E(Post)
SL1	0.92	1.52	0.33	0.54	E(Pre)>E(Post)
SL2	1.90	1.86	0.67	0.66	E(Post)>E(Pre)
SL3	0.38	0.52	0.13	0.18	E(Pre)>E(Post)
SM1	1.02	0.78	0.36	0.28	E(Post)>E(Pre)
SM2	1.82	1.77	0.64	0.63	E(Pre)>E(post)
CM1	1.45	1.04	0.52	0.37	E(Post)>E(Pre)
CM2	0.00	0.52	0.00	0.18	E(Pre)>E(post)
E(Max)	2.81		E(System)	3.85	

Entropy with respect to deposition of facies in distal localities.

State	E(Post)	E(Pre)	R(Post)	R(Pre)	Relationship
SR	0.00	0.00	0.00	0.00	E(Pre) = E(Post) = 0
SL1	0.00	0.39	0.00	0.15	E(Pre)>E(Post)
SL2	0.00	0.51	0.00	0.19	E(Pre)>E(Post)
SM1	0.41	0.43	0.16	0.17	E(Pre)>E(Post)
SM2	1.70	1.35	0.65	0.52	E(Post)>E(Pre)
SM3	0.92	0.76	0.35	0.29	E(Post)>E(Pre)
CM1	0.00	0.00	0.00	0.00	E(Pre) = E(Post) = 0
E(Max)	2.58		E(System)	2.99	

Entropy Analysis for Proximal Localities. For facies SL1, SL2, SM2, SM3 and CM3, E(Pre) > E(Post), indicating deposition of these facies did not depend on the precursor facies, but had a strong influence on the successor. Facies SM3 and CM3 have E(Post) = 0, demonstrating that these facies are succeeded by specific (j) facies (SL3 and CM1, respectively) in the sequence, as can be seen in the transition counts matrix (Fij) in Table 3-3. For the remaining facies, SR, SL3, SM1, CM1 and CM2, E(Post) > E(Pre), indicating that they were deposited under specific depositional conditions, with facies strongly dependent on the precursor facies. This is more so for SR facies, where there is a larger difference between E(Post) and E(Pre) values. A plot of normalised entropy sets (Figure 3-12A) for each state shows that facies SR, SL2, SL3, SM1, SM2, CM1 and CM2 fall within the distribution for A-4 asymmetrical cycle of Hattori (1976). Facies SL1, SM3 and CM3 fall outside this field and may represent lower truncated cycles.

Entropy Analysis for Medial Localities. For facies SR, SL1, SL3, SM2 and CM2, E(Pre) > E(Post), while for facies SL2, SM1 and CM1, E(Post) > E(Pre). Facies SR and CM2 have E(Post) = 0, and are succeeded by SL1 and CM1, respectively. Still, it should be noted that each of these transitions only occurs once and may not be representative of true cycles or trends. R(Pre) and R(Post) plot of the medal facies sets are shown in Figure 3-12B. The plots show that many of the facies states fall close to the X-Y reference, thus corresponding to symmetrical facies trends. Facies SL1 and CM2 deviates from this trend, with SL1 having a greater influence on the succeeding facies and CM2 on the preceding. Nonetheless, any further analysis of the entropy sets should be mindful of the fact that medial localities did not meet the Chi-squared test for Markovian property. For example, for facies SL2 and SM2, the large E(Post) and E(Pre) values suggest that a variety of facies states can be preceded and proceeded by them. That is, deposition of these facies is the most random in the medial localities.

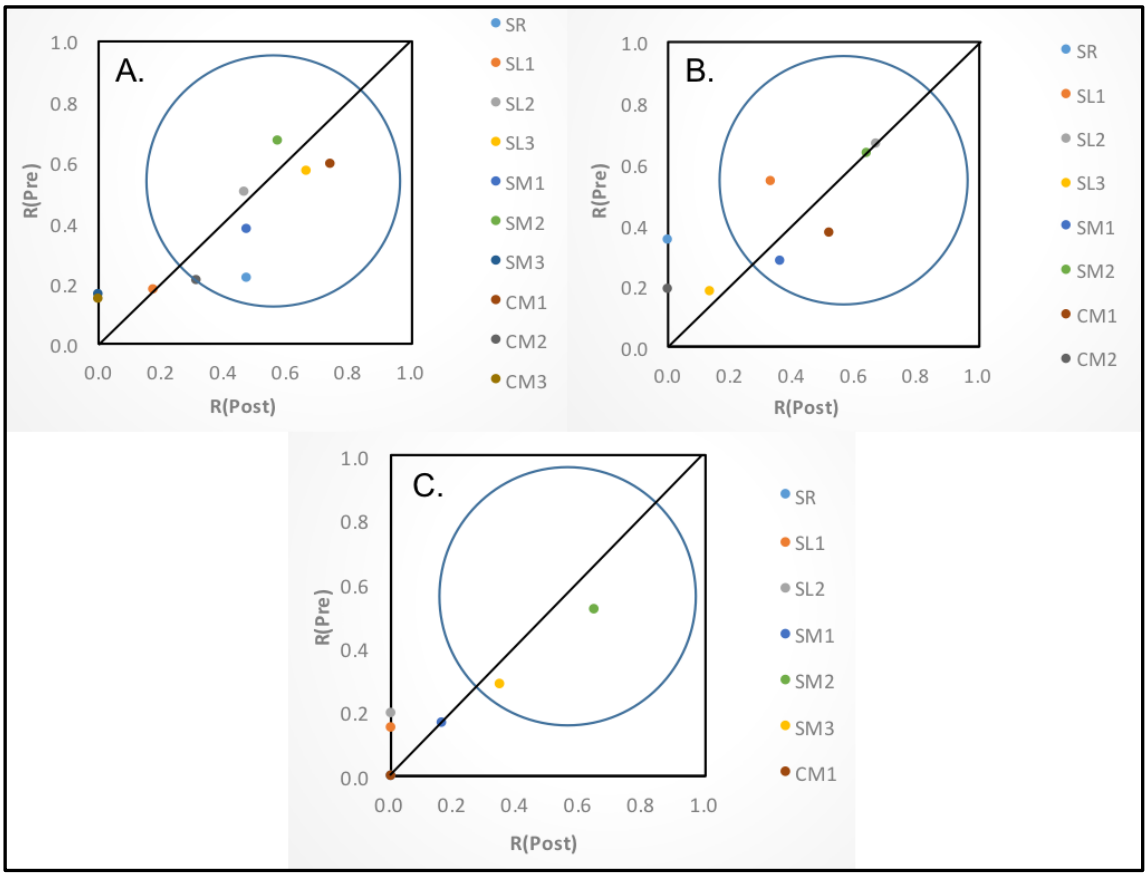

Figure 3-12: Distribution of entropy sets with respect to individual states for the three grouped locations: A. Proximal; B. Medial; and C. Distal locations. The area within the circular region represents asymmetrical Type A-4 cycles of Hattori (1976).

Entropy Analysis for Distal Localities. Values of E(Pre) compared to E(Post) are higher for facies SL1, SL2 and SM1 (these facies exerted a strong influence on the succeeding facie), while SM2 and SM3 have entropy sets of E(Post) > E(Pre) (i.e. strong dependence on the preceding state). E(Post) = E(Pre) = 0 for facies SR and CM1, implying preceding and succeeding states for facies i are predicted precisely. However, since Facies SR and CM1 form

the top and base of beds in distal localities, the entropy sets of these two facies can best be described as truncated upper and lower, respectively. E(Post) = 0 for facies SL1 and SL2, indicating these facies exhibit a decisive influence in selecting the successive facies states, in this case SR and SL1 respectively. R(Pre) and R(Post) values are shown in Figure 3-12C. Similar to medial localities, the entropy sets fall close to the X-Y reference line, indicating a symmetrical facies arrangement. Facies SL1 and SL2 fall away from this reference towards the lower truncated cycle. These truncations can be clearly seen in the correlation panels (Figure 3-15 to 3-19) and are marked by grain size breaks (Type II grain size breaks - see subsequent sections).

Figure 3-13: Examples of different types of grains size breaks found in the Peïra Cava outlier. Grain size breaks are indicated by the black arrow. A. Type II grain size break found in CB6 - PCR section; B and C. Type III grain size breaks observed in CB7 – SE section; D. Type II grain size break in CB11-1 – CSE section; E. Type III grain size break in CB10-1 – CSE section; F. Type I grain size break observed at the top of CB6 – CSE section; G. Type 4 grain size break observed at the top of most beds e.g. CB11-3 – NWT section; and H. Type II grain size break observed in the middle in CB11-3 – CSE section.

3.4.4 Grain Size Break.

The grain size distribution of the framework component in the eight beds ranges from medium pebble (< 16mm) to mud. Similar to other deep-water systems in the world, a general proximality trend exists in terms of grain size; the deposits fine vertically and laterally across the Peïra Cava outlier. However, within all of the beds examined, four types of grain size breaks (i.e. abrupt changes in grain size vertically within a single bed) have been observed (Figure 3-13): Type I separates gravel and coarser sediments, and overlying finer sediments; Type II

separates coarser sand and overlying finer sand; Type III marks the transition from finer gravel and sand and overlying coarser material; and Type IV separates sand and an overlying mudstone layer. Table 3-5 shows the summarised characteristics of the observed grain size breaks. In the following sections, the spatial and temporal distribution of the four grain size breaks are presented.

Type I Grain Size Break. Type I grain size breaks separate gravelly and pebbly intervals (16 mm to 2.5 mm) and overlying finer material (4mm to 500 μm; Figure 3-13F.). This grain size break is found and correlated primarily in proximal (SW, CSE, SE and ET) and medial (PCR) localities, and rarely in distal localities (e.g. CB10-1), towards the base and middle of beds. In proximal and medial localities, Type I grain size breaks separates graded and ungraded conglomeratic facies (CM) from overlying ungraded or graded massive sands (SM1 and SM2) in CB6, 7 and 10-1. The only exception to these trends is seen in CB11-2 and 5, where thick, stepped laminated sands (SL3) occur below the grain size break, and thick, spaced stratification (SL3) and massive sand (SM1) above, respectively. In CB6 and 7, the grains size breaks can be correlated to adjacent downslope sections for a distance of ~2-3 km. In both instances, the underlying facies is CM1, while the overlying facies is CB6 transition from thin stepped laminae (SL2) to ungraded massive sands (SM1) downslope. In CB7 the overlying facies (i.e. SM3) remains the same between sections. In distal localities, Type I grain size breaks are observed only in CB10-2 and show characteristics similar to proximal localities, i.e. CM1 separated from an overlying massive sand facies.

Type II Grain Size Break. Type II grain size breaks separate coarse sand (2 mm to 177 μm) and overlying finer grained (1 mm to 62 μm) sediments (Figure 3-13A, D and H.). These are observed in a majority of beds from proximal to distal sections. However, in CB5, 7 and 11-3 they are only observed in proximal to medial localities. These three beds belong to Facies Tract III (see section 3.4.5). Across the outlier, Type II grain size breaks are typically located towards the middle and top of beds. Those located in the middle are primarily restricted to proximal and medial localities, where they predominantly separate massive sands (SM1 and SM2) from an overlying structured (SL1 and SL2) interval. However, in beds CB7 and 11-3, the opposite facies sequence is observed. In proximal localities, these grain size breaks can be correlated between sections, becoming more infrequent and discontinuous in medial sections. Grain size breaks located towards the top of beds occur throughout the outlier. In proximal and medial locations, they typically separate thick to thin, spaced stratified stratification (SL3 and SL2) from overlying parallel laminated to ripple laminated sands (SL or SR; e.g. CB5, 6, 10-2 and 11-1). Moving distally, there is a gradual change in terms of facies above and below the break, with massive sands (SM1 and SM3) exclusively below the grain size break, and structured

sands (SL1 or SL2) above (e.g. CB6, 10-1, 10-2, 11-1 and 11-2). Type II size breaks in distal localities can be correlated in a downflow and cross-flow direction.

Table 3-5: Characteristics of the four grain size breaks observed in the Peïra Cava Outlier. An asterisk (*) above the facies code refers to the predominate facies below or above the grain size break.

Bed (CB Unit)	No of observations	Lateral Position in Basin	Position vertically in bed	Grading below G/S break	Grading above G/S break	Grain size below break	Grain size above break	Facies below break	Facies above Break
Type I - Gravel overlain by Finer grains									
CB5	3	Proximal and Medial	Base and Middle	Ungraded	Normal Graded	> 4 mm	1.5 - 1	*CM1, SL3	SM1, SM2
CB6	4	Proximal and Medial	Base to Top	Normal to Ungraded	Ungraded	6 - 2.5 mm	1.5 mm - 500 µm	CM1	*SM1, SL2
CB7	3	Proximal	Base and Middle	Inverse	Ungraded	16 - 6 mm	4 - 2mm	CM1	CM1, *SM3
CB10-1	3	Proximal and Medial	Base and Middle	Inverse, Ungraded, Normal	Ungraded	8 - 3 mm	1.5 mm - 500 µm	CM1	*SM1, SM3
CB10-2	0	-	-	-	-	-	-	-	-
CB11-1	0	-	-	-	-	-	-	-	-
CB11-2	2	Proximal	Base	Inverse to Normal	Normal Graded	4 -3 mmm	2 - 1 mm	SL3	SL3
CB11-3	0	-	-	-	-	-	-	-	-
Type II - Coarse Sand overlain by Fine Sand									
CB5	2	Proximal to Medial	Top	Normal to Ungraded	Normal Graded	250 - 177 µm	125 - 62 µm	SL2	SL1
CB6	7	Proximal to Distal	Top and Middle	Normal to Ungraded	Ungraded	375 µm - 1.5 mm	1 mm - 100 µm	*SM, SL2	SM, SL1, *SL2
CB7	4	Proximal	Top Middle	Normal to Ungraded	Normal to Ungraded	2 - 1 mm	1 mm - 125 µm	SL3	SM1, *SL1
CB10-1	3	Proximal to Distal	Predominately Top	Normal to Ungraded	Normal to Ungraded	1 mm - 375 µm	1 mm - 187 µm	SL2, *SM3	*SL1, SL2
CB10-2	3	Proximal to Distal	Top	Normal to Ungraded	Normal to Ungraded	500 - 250 µm	187-100 µm	*SL2, SM2	*SR, SL1
CB11-1	4	Proximal to Distal	Top and Middle	Normal to Ungraded	Normal to Ungraded	500 - 250 µm	250 - 125 µm	*SM, SL2	*SR, SM1
CB11-2	1	Distal	Top	Graded	Ungraded	250 µm	187 µm	SL2	SL1
CB11-3	4	Proximal to Medial	Top and Middle	Graded to Ungraded	Ungraded	1 mm	500 -187 µm	*SL2, *SM2	*SL2, SM1, SR
Type III - Fine grains overlain by Coarser grains									
CB5	-	-	-	-	-	-	-	-	-
**CB6	2	Proximal to Medial	Base to Top	Normal to Ungraded	Normal to Ungraded	> 500 µm	>750 µm	SM	SM1, SL2
CB7	5	Proximal to Medial	Base to Top	Normal to Ungraded	Normal to Ungraded	4 mm - 500 µm	6 - 1 mm	CM1, SM1	CM1, SL3, SM2
CB10-1	2	Proximal	Base	Normal to Ungraded	Normal to Ungraded	3 - 1.5 mm	8 - 3 mm	CM1	SL3, CM1
CB10-2	1	Medial	Top	Normal	Ungraded	125 µm	500 µm	SL1	SL2
CB11-1	0	-	-	-	-	-	-	-	-
CB11-2	0	-	-	-	-	-	-	-	-
CB11-3	3	Proximal to Medial	Predominately Top	Normal to Ungraded	Normal to Ungraded	750 - 125 µm	4 mm - 375 µm	SL1, *SR	SM1, SL2, SR
Type IV -Sand overlain by Mud									
CB5	5	Proximal to Distal	Top	Normal to Ungraded	-	88 µm	Mud	SR, ZL	MM, ML
CB6	6	Proximal to Distal	Top	Normal to Ungraded	-	750 - 100 µm	Mud	SL, SR	MM, ML
CB7	6	Proximal to Distal	Top	Normal	-	354 - 100 µm	Mud	SR	MM, ML
CB10-1	5	Proximal to	Top	Normal	-	187 - 88	Mud	SL2, SR	MM, ML
CB10-2	7	Proximal to Distal	Top	Normal to Ungraded	-	250 - 100 µm	Mud	SR	ML
CB11-1	5	Proximal to Distal	Top	Normal	-	250 - 125 µm	Mud	SR	ML
CB11-2	4	Proximal to Distal	Top	Ungraded	-	250 - 125 µm	Mud	SR, SL	ML
CB11-3	6	Proximal to Distal	Top	Normal	-	250 - 125 µm	Mud	SR, SL, SM2	ML

Type III Grain Size Breaks. Type III grain size breaks separate finer gravel and sand (6 mm to 125 μm) and overlying coarser material (16 mm to 375 μm; Figure 3-13B, C and E.). This grain size break is restricted to proximal (SW, CSE, and SE) and medial (PCR and ER) localities, and is observed in all beds except CB11-1 and CB11-2. In many of these beds, the grain size break is discontinuous at the outcrop scale, disappearing over a distance of 20 metres. Vertically, the grain size break can be observed at any height within the bed. In proximal and medial locations, grain size breaks located at the base of beds separate CM1 facies from an overlying coarser grained CM1 facies. The only exception to this trend is at the base of CB10-1, where the overlying facies is SL3. Moving vertically up from the base, Type III grain size breaks are observed in the middle of CB6 and CB7. In CB6, the grain size break is observed in the CSE section only, where it separates CM1 facies. Within CB7, in contrast, the grain size break separates SM3 and SL3 facies from an overlying interval of SL3. Moving downslope in CB7 to the ER section (~4 km), the facies transition to graded massive sands above and below the break. Type III grain size breaks located at the top of beds are observed in CB6, CB10-2 and CB11-3, and are more variable in character than those located at the base and middle of beds. Nevertheless, a general trend is observed in CB11-3 and CB6, where facies above the grain size break transition from tractionally reworked SR and SL2 in proximal localities, respectively, to massive, ungraded sands in medial localities. A similar trend is observed in CB11-3 for the underlying facies and consists of ripple laminated sands (SR) in proximal locations, transitioning to thin, stepped laminae (SL2) downslope. The underlying facies in CB6 is ungraded, massive sands across the outlier.

Type IV Grain Size Breaks. Type IV grain size breaks are the most common across the outlier and separate sand (750 to 88 μm) from an overlying laminated to massive mudstone (MM and ML) interval (Figure 3-13G). They occur exclusively at the top of sand beds. In proximal locations (SW and CSE), due to erosion and amalgamation of beds, Type IV grain size breaks are less common compared to more distal locations. Vertically, the grain size break occurs predominantly between graded, structured facies (i.e. SL or SR) and ungraded mudstone; the rippled sand (SR) facies being more prominent of the two in proximal locations. Distally, there is an increased occurrence of graded massive sands below the grain size break (e.g. ER CB7 and NES CB102, 11-2, 11-3).

3.4.5 Downflow Facies Tract, Internal Bed Character and External Shape.

A number of correlation panels are provided in Figures 3-15 to 3-19 to illustrate the temporal and spatial changes in internal bed character and external shape of the eight units across the Peïra Cava outlier. The key to the correlation panel is provided in Figure 3-14. The correlation panels are orientated roughly parallel to the palaeoflow direction and cover a distance of ~12 km. Although some characteristics such as progressive fining and thinning of beds distally and the low percentage mud content of sandstones is consistent between facies tracts, the internal

bed character and the geometry of individual facies along downflow transects are highly variable, especially in proximal locations. To summarise these changes and pick out trends, a number of downslope facies tracts (sensu stricto Mutti, 1992) are described below. These facies tracts are described primarily in terms of spatial and temporal evolution of the massive sand facies i.e. SM1, SM2 and SM3. Due to the limited lateral extent of the outlier, especially in the proximal and medial parts, as well as the mountainous terrane, multiple transects (e.g. downflow and cross stream) of the same beds could not be acquired. However, a distal cross-flow transect from the NWT/NW to NE/NES localities has been shown as part of the downslope transect and marked on the correlation (Figures 3-15 to 3-19). These cross-flow transects show broadly similar characteristics from NW to NE/NES.

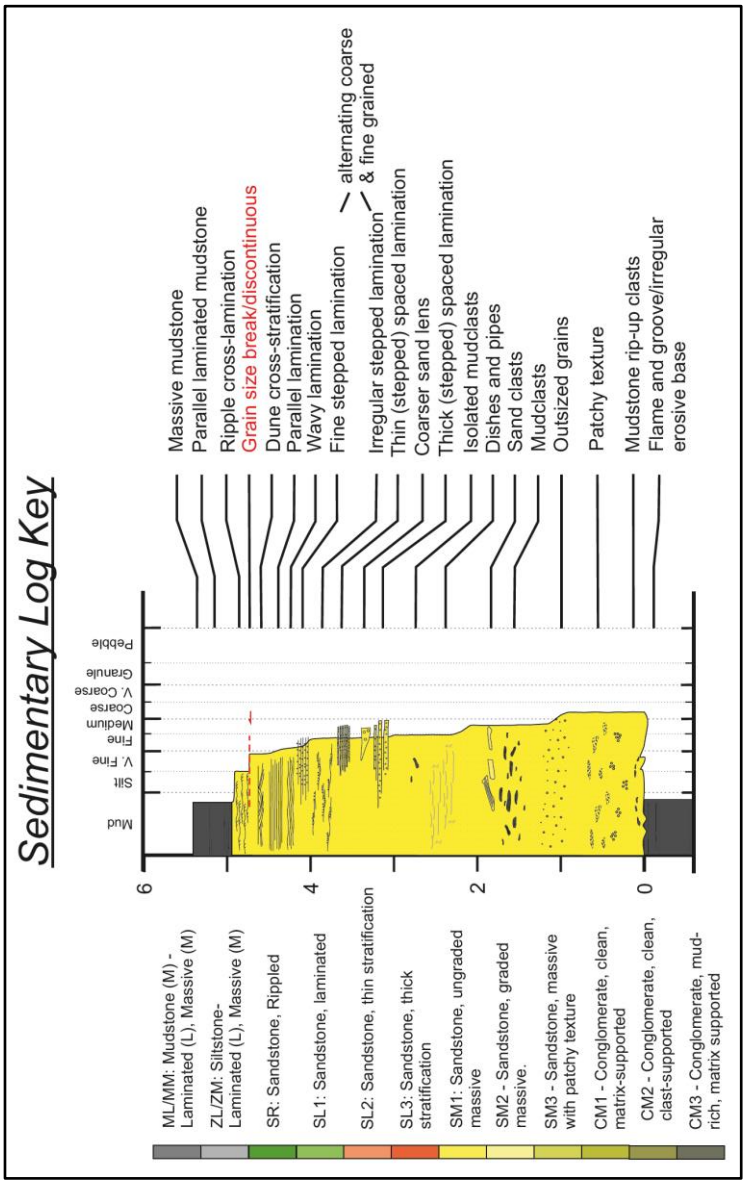

Figure 3-14: Key to the correlation panels in Figure 3-15 to 3-19

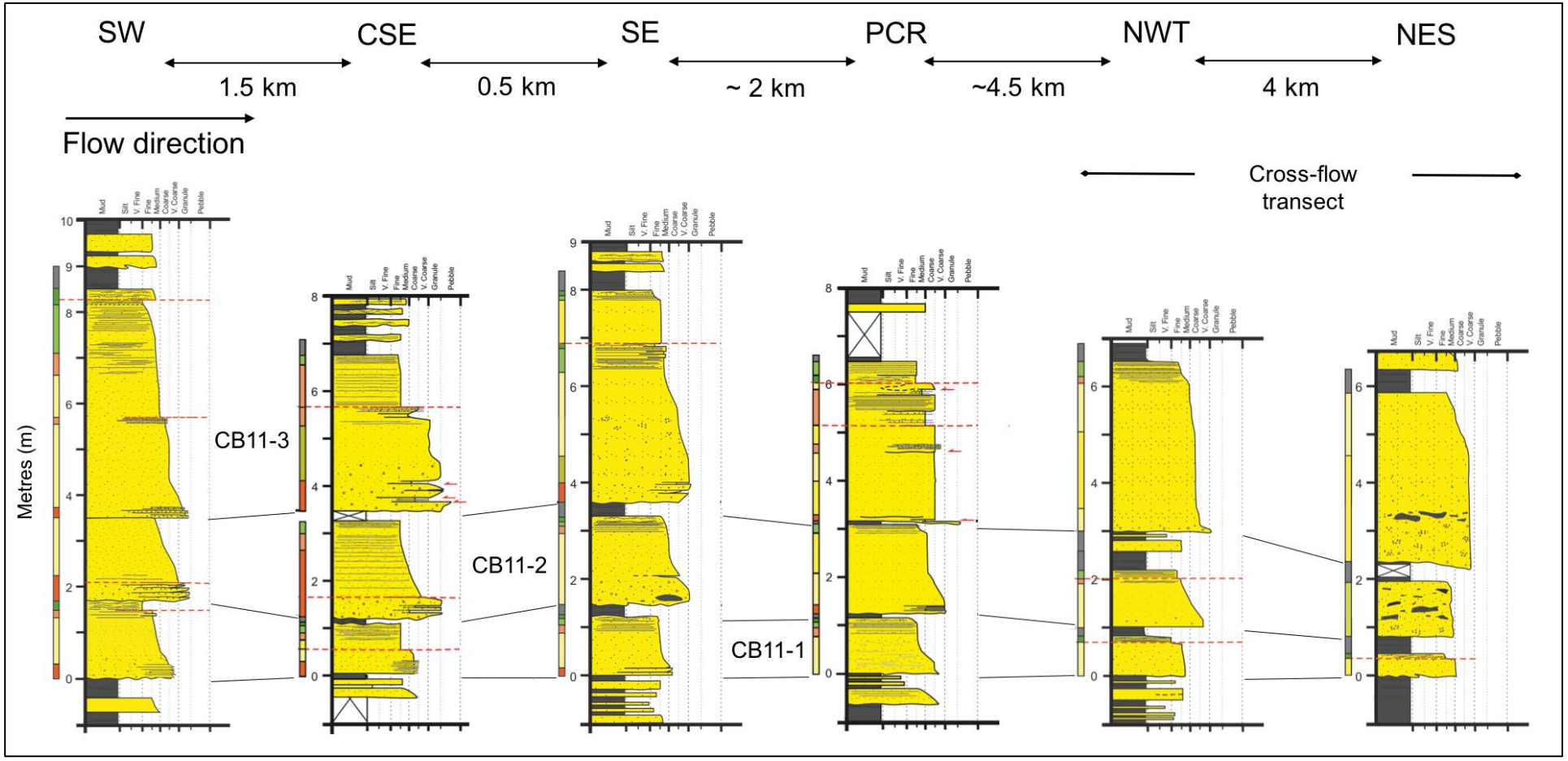

Figure 3-15: Correlation panel of the CB11 unit consisting of 3 beds, showing lateral changes in internal bed character and external geometry. The correlation panel is orientated roughly parallel to the palaeoflow direction. Key to the correlation panel is provided in Figure 3-14, while Figure 3-8 shows the section locations.

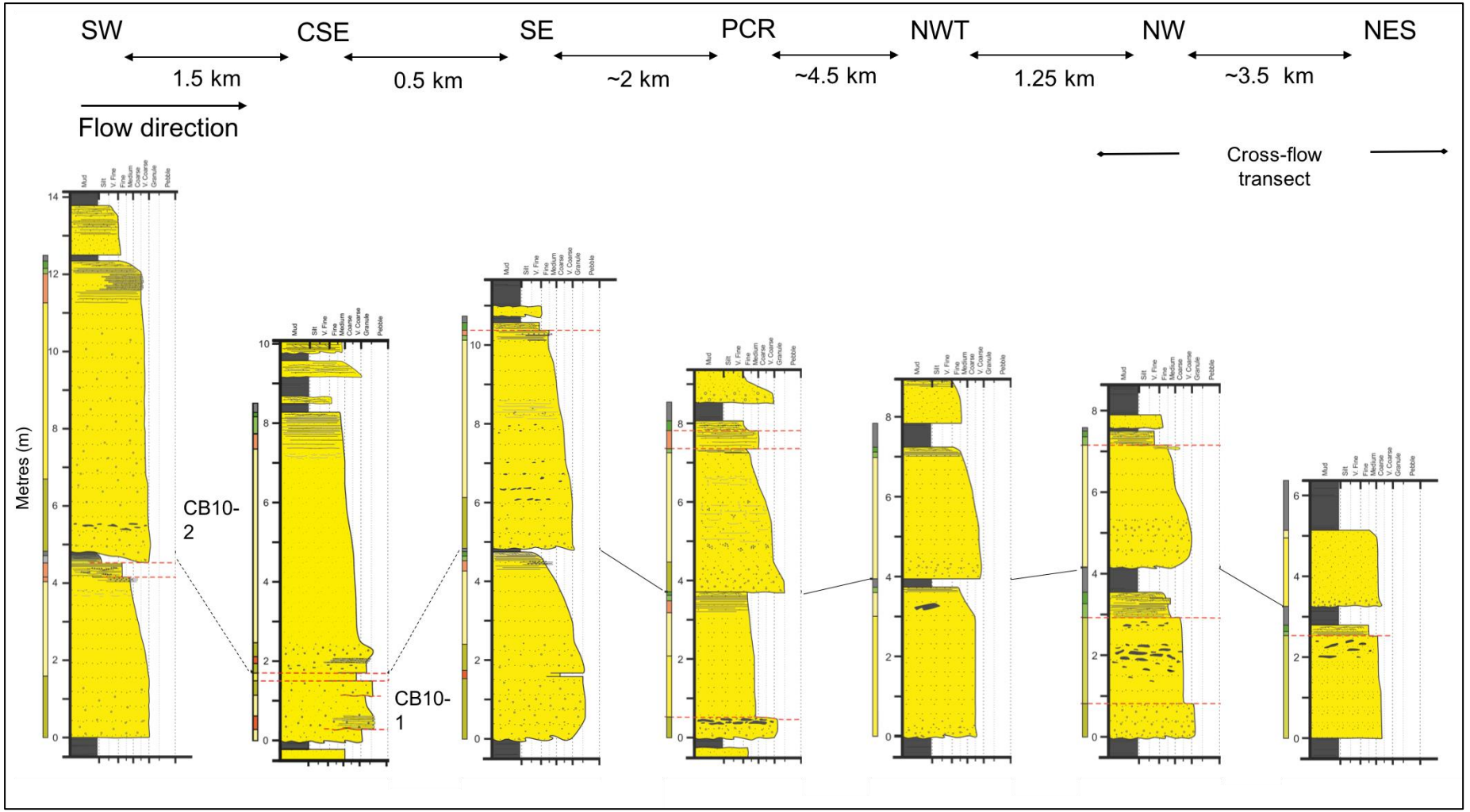

Figure 3-16: Correlation panel of the CB10 unit consisting of 2 beds, showing lateral changes in internal bed character and external geometry. The correlation panel is orientated roughly parallel to the palaeoflow direction. Key to the correlation panel is provided in Figure 3-14, while Figure 3-8 shows the section locations

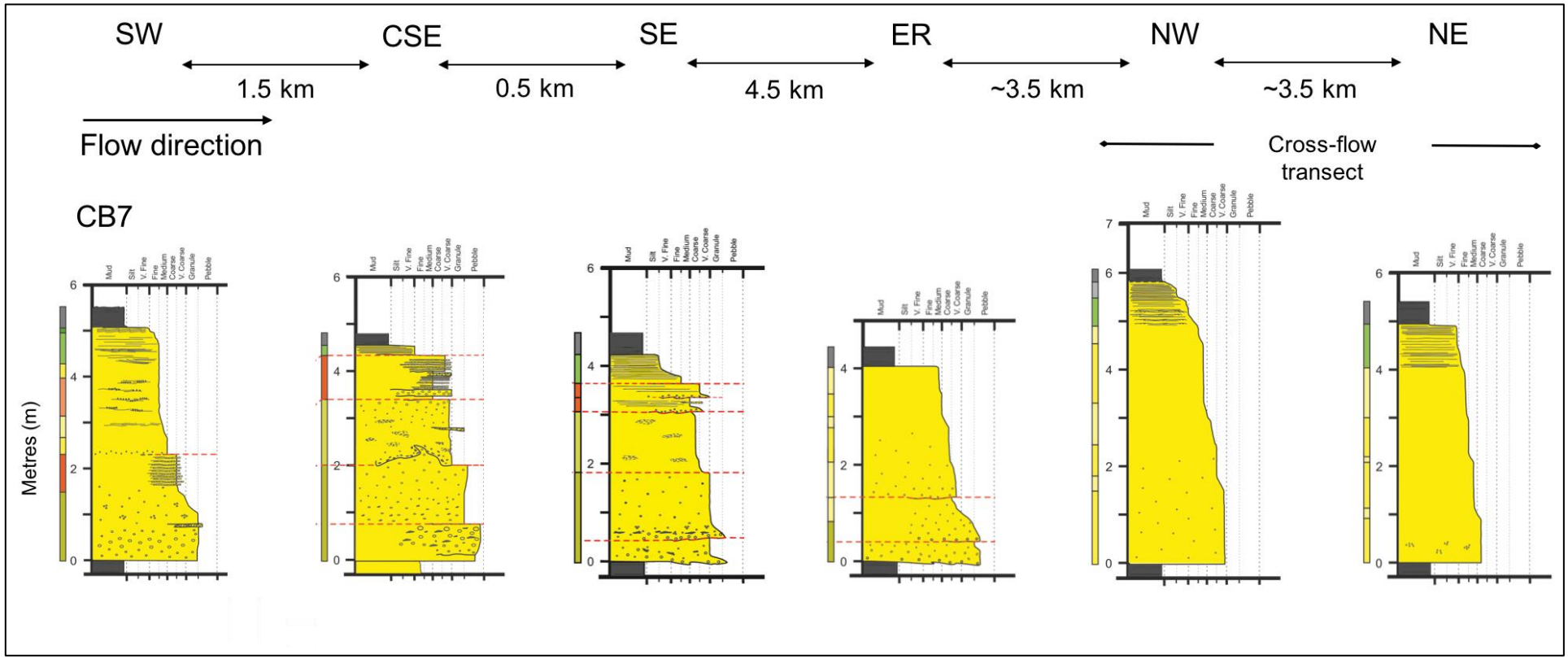

Figure 3-17: Correlation panel of the CB7 unit, showing lateral changes in internal bed character and external geometry. The correlation panel is orientated roughly parallel to the palaeoflow direction. Key to the correlation panel is provided in Figure 3-14, while Figure 3-8 shows the section locations.

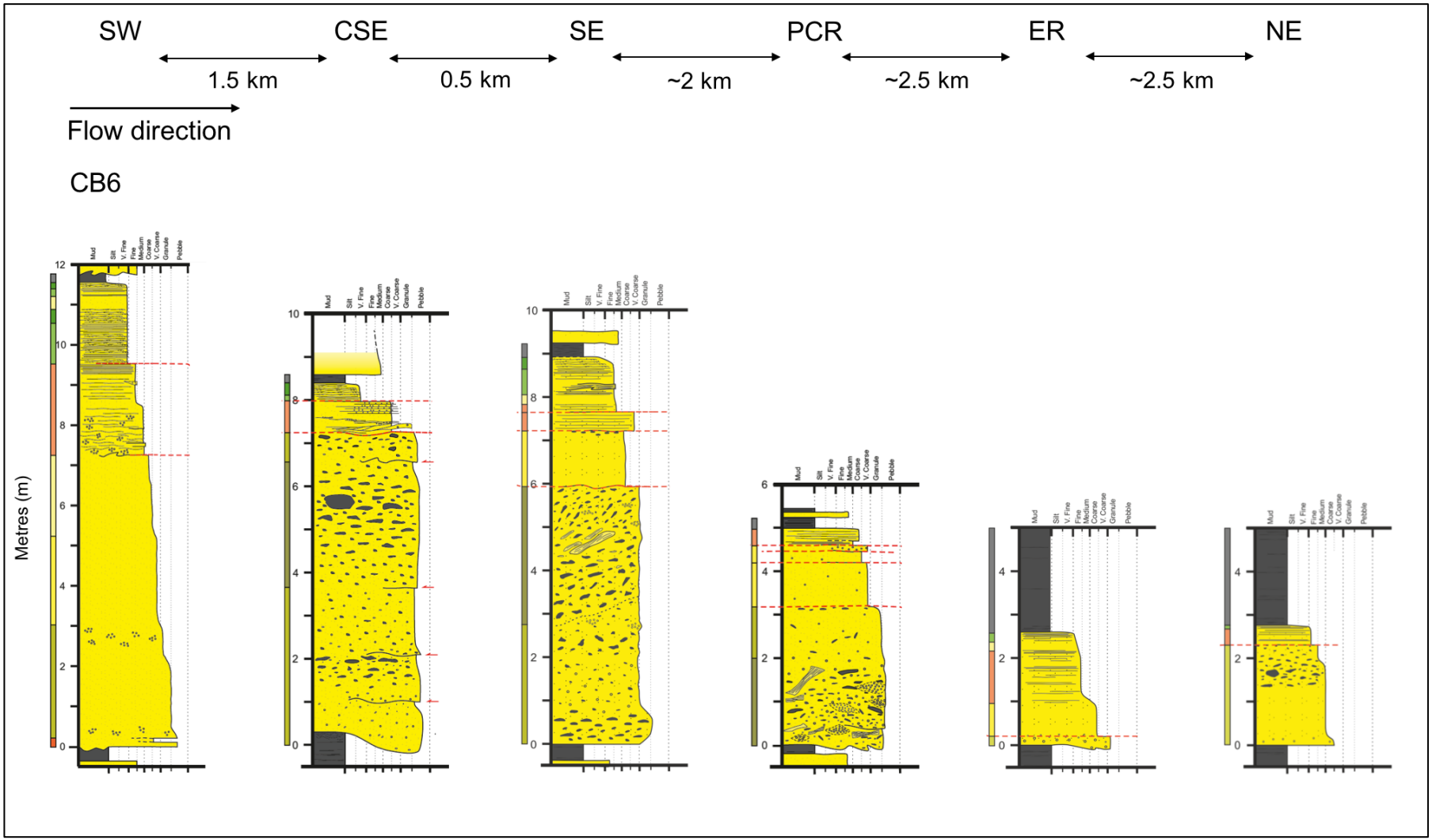

Figure 3-18: Correlation panel of the CB6 unit, showing lateral changes in internal bed character and external geometry. The correlation panel is orientated roughly parallel to the palaeoflow direction. Key to the correlation panel is provided in Figure 3-14, while Figure 3-8 shows the section locations.

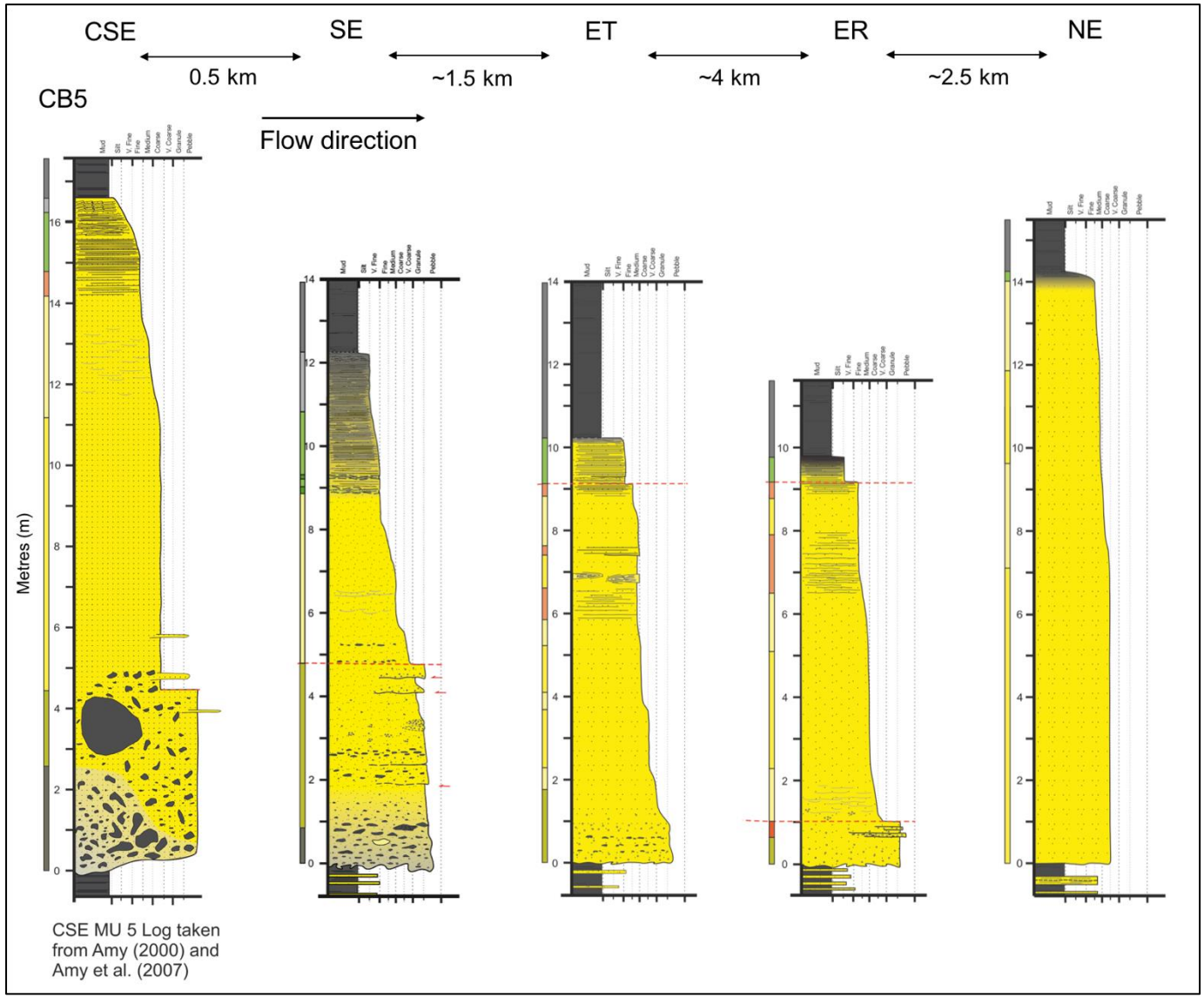

Figure 3-19: Correlation panel of the CB5 unit showing lateral changes in internal bed character and external geometry. The correlation panel is orientated roughly parallel to the palaeoflow direction. Key to the correlation panel is provided in Figure 3-14, while Figure 3-8 shows the section locations. CSE – CB5 is taken from Amy (2000) and Amy et al. (2007) due to the difficulty in accessing the bed during the field excursion

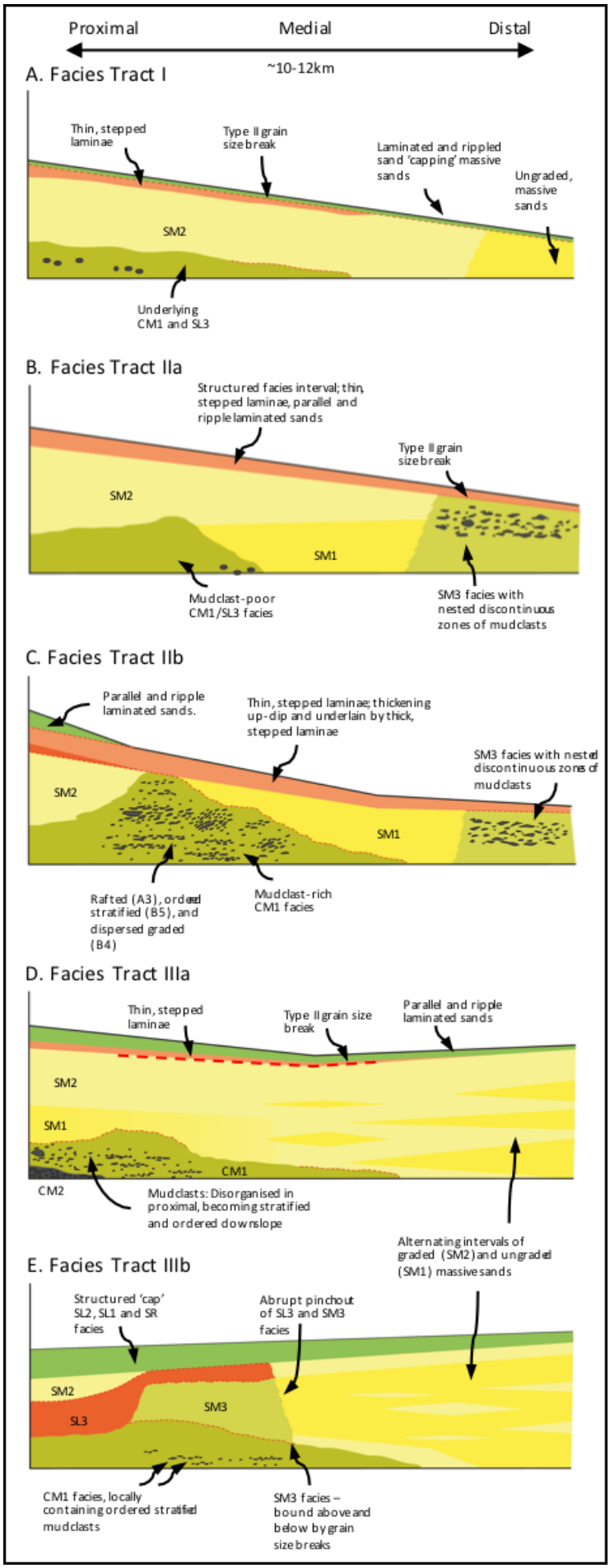

Figure 3-20: Generalised facies tract of the correlatable beds showing internal bed character. Due to high sediment facies variability between sections in proximal locations, only the most common characteristics between beds are incorporated into the corresponding facies tract. As such, certain elements of a bed character are not shown in the facie tracts. Furthermore, the overlying turbidite mudstone and siltstone have also not been incorporated into the facies tract since the main focus of this study is the formation of massive sands. Bed thickness changes are illustrative, not quantitative changes, and show overall trend in downslope variation.

Facies Tract I (Beds CB11-1 and CB10-2). Facies Tract I is characterised by a gradual transition from graded, massive sands in proximal and medial localities, to visually ungraded, massive sands (DWMS; *sensu* Stow and Johansson, 2000) in distal localities. These facies are located in the core of the bed in proximal and medial localities, progressively becoming the dominant facies moving downslope (Figure 3-20A).

In proximal localities, Facies CM1 and SL3 typically underlie the graded, massive sands. These facies reduce in thickness gradually towards medial localities, where they taper out and transition laterally into SM2 facies. The overlying facies consist of SL2 and SL1. The SM2 facies gradually transition to SM1 facies downslope. A Type II grain size break separates the SM1 facies and the overlying SL1 and SR facies. This grain size break can be correlated in a downflow direction to adjacent sections. Type II grain size breaks are also present in proximal locations, but the facies above and below the break are more variable. Typically, SL2 facies occur below and SL1 facies occur above the grain size break. The structured facies interval is thickest in proximal locations, obtaining a thickness of 1 m, before thinning progressively downflow. This thickness change is primarily related to tapering and pinch out of the SL2 facies, with the SL1 and SR facies maintaining their thicknesses (typically 10-15 cm) across the outlier (Figure 3-16 and 3-20A). Centimetre-scale mudclasts are also present in proximal locations and are characterised by Type B5 (stratified ordered) of Johansson and Stow, (1995), passing vertically and laterally into Type B4 (graded dispersed types). In distal localities, mudclasts are exclusively mm-scale Type B4.

The external bed geometry has a thickness maximum at the SW section and most closely approximates a linear (CB11-1) to sigmoidal (CB10-2) profile. For CB11-1, the proximal maximum would be the minimum preserved thickness due to the partial erosion of the bed by subsequent flows (Figure 3-15). Bed thickness decreases gradually across the outlier; by as much as ~75% over a distance of ~11 km. However, a more pronounced decrease (~40-45%) in bed thickness is seen between the NWT/NW and NES sections in both beds. In CB10-2, a local increase in bed thickness of ~9% is observed between NWT and NW section, possibly a result of flow interaction with local topography. In terms of the massive sand interval, a progressive decrease (~ 50-56%) in facies thickness is observed across the outlier, although the thickness remains consistent between medial sections (+/- 9%).

Facies Tract II (CB11-2, CB10-1 and CB6). Facies Tract II comprises ungraded, massive sands with patchy texture (SM3) in distal localities, which is exclusively bounded by Type II

grain size breaks. The upper grain size break typically separates the SM3 facies from an overlying thin interval of structured sand facies (SL2 or SR) or the overlying mudstone, while the lower grain size break separates an underlying CM1 facies. In a crossflow direction, the upper grain size break can be correlated between distal sections (e.g. CB10-1 NW and NES sections; Figure 3-16 and Appendix C). The SM3 sands always contains mudclasts in the core and top of the bed, with clast size varying from 4 mm to <40 cm. These mudclasts occur as nested discontinuous zones sub-parallel to bedding and may exhibit weak grading.

Up-dip from distal localities, SM3 sandstones typically transition abruptly to SM1 and SM2 facies. For an ~ 2 m thick SM3 interval, this transition occurs over a distance of 1.25 km (Figure 3-16; NWT to NW section). Similar to Facies Tract I, a thin (<20 cm) structured facies interval comprising SL2, SL1 and SR drapes the SM3 facies. This structured interval thickens progressively up-dip at the expense of the underlying SM1, which tapers out in proximal localities. The SM2 interval, in contrast, maintains or increases its thickness up-dip. In proximal locations, Facies Tract IIa (e.g. CB11-2 and 10-1) and IIb (CB6) can be distinguished based on the presence of large mud and sandstone clasts in the coarser (>2 mm) grained facies underlying the SM2 interval (Figure 3-20). Facies tract IIa is characterised by coarser grained (>2 mm) facies that lack mudclasts. The coarser grained facies can be massive (CM1; bed CB10-1) or structured into thick, spaced stratification (SL3; bed CB11-2). Downflow, the CM1 and SL3 facies pinch out abruptly, transitioning laterally and vertically into massive (SM1 and SM2) sands. Facies Tract IIb is characterised by very thick intervals (>3 m) of CM1 and CM2 facies with rafted (A3), ordered stratified (B5) and dispersed graded (B4) mud and sand clasts. The interval has a highly variable geometry, doubling in thickness over a distance of ~1.5 km (between SW and SE sections), before decreasing and pinching out abruptly over 2 km (Figure 3-18 and 3-20). The transition to the overlying massive sands (SM1 and SM2) and structured facies (SL2) is marked by a Type I grain size break, which can be correlated downslope for a distance of ~5-6 km. Immediately up-dip of the CSE section (~0.5 km), the clast-rich CM1 and CM2 facies transition abruptly to clast-poor CM1 and massive sands facies, similar to Facies Tract IIa.

Facies Tract II have a thickness maximum in proximal localities. Bed thicknesses for Facies Tract IIa decrease gradually; < 40% over a distance of 11 km. A significant portion of this can be related to the pinch out of the coarser grained CM1 facies, with the overlying sand grained facies maintaining a relatively uniform thickness. The downslope profile most closely resembles a linear trend, with increased rates of thinning in medial sections. In comparison, Facies Tract 11b has more abrupt thickness change in the medial localities, deceasing by as much as 71% over a distance of ~ 4.5 km. This is largely due to the highly variable thickness of clast-rich CM1 and CM2 intervals. Between the medial (ER) and distal (NE) localities (a distance of ~ 3

km), Facies Tract IIb maintains a comparatively uniform thickness (+/- 10% change). This facies tract has a pronounced sigmoidal profile.

Facies Tract III (CB11-3, CB7 and CB5). Facies Tract III consists of entire beds comprising alternating intervals of ungraded (SM1) and graded (SM2) massive sands in distal and medial localities. The ungraded, massive sand intervals are typically thicker than the graded intervals that separate them (Figure 3-20). In all beds, the proportion of massive sand facies, in particularly SM1, increases progressively downslope.

In distal localities, these massive sands are capped by thin intervals of parallel laminated (SL1) and rippled (SR) sands without an intervening grain size break. Up-dip, however, this transition is separated by a Type II grain size break, with the underlying facies typically SM2 and SL2. Moving up-dip from distal localities, the 'structured' cap progressively thickens at the expense of the massive sand interval, which is also gradually underlain by thicker intervals of CM1and/or SL3 facies. The alternating graded and ungraded massive sand intervals thus forms the 'core' of the bed in medial and proximal localities. The transition between the CM1/SL3 facies is sharp, marked either by a Type I grain size break or a short, strongly graded interval. The CM facies in proximal locations contains mm to cm, and locally to dm-scale mudclasts. They are typically disorganised Type A2 rafted clasts in the most proximal sections (e.g. SW and CSE), evolving downslope to more organised ordered stratified (B5) and/or dispersed graded (B4) types. The former type is closely associated with locations of internal grain size breaks and erosive scours (Figure 3-19). The mudclast interval pinches out abruptly over a distance of 2 km.

In proximal localities, Facies Tract IIIa and IIIb can be distinguished based on the presence of SM3 facies. Facies Tract IIIa lacks a lateral transition to SM3 facies in proximal localities, and instead shows a progressive thinning of the SM1 and SM2 facies in the core of the bed. Vertically, these two facies also become more 'organised', such that beds lack the cyclic transitions seen in distal localities, and instead show a simple transition from SM1 to SM2 or are exclusively SM2 (Figure 3-20D and E). Facies Tract IIIb is characterised by a transition from SM1 and SM2 to massive sands with patchy texture (SM3). This facies has locally foundered into the underlying CM1 facies, and is characterised by a Type I grain size break. The SM3 facies is also separated from the overlying SL3 facies by a grain size break. Both of these grain size breaks can be correlated between proximal localities. Up-dip, the SM3 facies pinches out abruptly over ~0.5 km, with the SL3 facies overlying the CM1 in the most proximal section (SW).

Similar to Facies Tract I and II, the external bed geometry of Facies Tract IIIa has a thickness maximum in proximal localities. Bed thicknesses decrease by ~40% from the SW section to the PCR/ER sections. Moving downslope, however, bed thicknesses tend to increase distally to +/-10% of the maximum thicknesses observed in proximal sections. Thus, this facies tract has accentuated highs (e.g. CB5 and CB11-3). In comparison, Facies Tract IIIb also has accentuated proximal and distal highs, with only a minor decrease (~-15%) in bed thickness in medial localities. However, distal bed thicknesses are marginally larger (+10-15%) relative to proximal locations.

3.5 Discussion.

Various models have been proposed over the years for the formation of DWMS based on studies using single outcrops, laterally correlatable beds, theoretical analysis, flume experiments and/or numerical simulations. In this section, the analysis of the results on the spatial and temporal evolution of internal bed character, grain size discontinuities, and bed and facies geometry is used to understand flow processes responsible for depositing DWMS, validate existing models and to propose a new model (if necessary).

3.5.1 Grain Size Breaks.

Four grain size breaks were recognised across the Peïra Cava outlier. They vary in terms of their vertical position within the bed and lateral distribution across the outlier. Mechanisms for their formation are now discussed and related to evolution of flow hydrodynamics that would eventually lead to the deposition of DWMS. Flow reflection or deflection due to interaction with a confining slope or a topographic obstacle have been known to produce grain size breaks in confined basins. However, evidence for grain size breaks produced in this manner, such as opposing palaeocurrent directions in individual beds (Kneller and McCaffrey, 1999a) or complex grading patterns separated by grain size breaks adjacent to confining slopes (Haughton, 1994; Remacha et al., 2005) is not seen. Furthermore, grain size breaks created by local topographic obstacles are also not likely due to the relatively flat *intra*-basin floor topography (Aas et al., 2010; Sinclair and Cowie (2003). Thus, the grains size breaks in this study are thought to be products of transport and depositional processes.

Type I Grain Size Break. Stevenson et al. (2014) discussed the origin of this type of grain size break and concluded that it represents a sharp rheological transition between a highly concentrated basal layer and an overriding lower concentration plume. This interpretation was based partly on experimental observations that show a sharp rheological transition involving flows with high-sediment concentrations (Ilstad et al., 2004; Postma et al., 1988), and partly on the poorly sorted, coarse-grained facies observed below the grain size break in their study, which they interpreted as debrites. The dominant underlying facies beneath Type I grain size

breaks in the present study is the CM facies. This is largely considered to be a deposit of a debris flow or inflated sandflow (sensu stricto Pickering and Hiscott, 2015) that was laminar in character and deposited *en-masse* due to frictional interlocking of grains. The overlying facies (SM to SL) is more indicative of incremental deposition from a flow driven by an overriding turbulent current (see below for detail). Thus, based on these field observations, it is surmised that Type I grain size breaks represent a rheological transition from a highly-concentrated basal flow that would have deposited sediments *en-masse* or via a strongly hindered late-stage settling, to a less concentrated flow with reduced hindered settling of grains (Figure 3-22A). Deposition of the lower layer is inferred to have occurred rapidly, while the overlying layer may have begun deposition soon after, or after a phase of sediment by-pass, in an incremental manner. This preserves the vertical structure of the flow in the deposit, separated by a grain size break.

For CB7, 6 and 5, Type I grain size breaks can be correlated between proximal sections (~0.5-1km); extending downslope to medial localities in the case of CB6 (~2 km further). If Type I grain size breaks record the vertical structure of a flow (Stevenson et al. 2014), the pinch out of these grain size breaks can thus provide the potential run-out distance of the basal high-concentration layer. In most cases, the pinch out or the distal most occurrence of Type I grain size breaks is in medial localities. This also coincides with the abrupt pinchout of CM1 and SL3 facies. Downslope, these two facies transition into thick sequences of ungraded and graded massive sands (SM1 and SM2). The exact cause of this transition is unclear, although rapid arrest of the basal high-concentration layer allowing the overriding turbulent flow to overtake and deposit massive sands could be a likely mechanism. An alternative mechanism could be transformation of the basal high concentration layer through ingestion of ambient fluid, at and just behind the head of the flow, into a turbulent flow. High hydraulic diffusivity and well connected pores in the lower basal layer may help facilitate this transformation. This would lead to lower sediment concentrations and corresponding decrease in hindered settling of grains.

Type II Grain Size Break. Gladstone and Sparks (2002) attributed a similar grain size discontinuity to deposition from a bipartite turbidity current consisting of a body and an overlying wake. Both layers are relatively dilute and fully turbulent in character, with the grain size break attributed to a switch in deposition from the body to the wake (*ibid.*). However, these authors failed to consider that deposition from turbidity currents is incremental. Thus, unless deposition occurred very rapidly to preserve the vertical structure of the flow, the vertical structure of a turbidite records the longitudinal structure of the flows velocity and concentration gradient (Kneller and McCaffrey, 2003). Kneller and McCaffrey (2003) provide an alternative explanation and ascribed the Type II grain size breaks to a transition from capacity- to competence-driven deposition. Such an evolution in settling regimes, the authors argued, would

be marked by sediment by-pass, reworking and/or erosion of earlier deposited sediments. Experimental studies (e.g. Sumner et al. 2008) involving temporal deceleration of the flows have been able to reproduce such a change in settling regimes, including a short phase of sediment by-pass, reworking and/or erosion. During the capacity-driven depositional phase of the experimental flows, sediments were deposited incrementally by collapsing high-concentration layers in which sediment settling was hindered. However, during the competence-driven phases, sediment fallout rates were markedly lower, with a notable decrease in hindered settling and an increase in elutriation of fines (*ibid.*).

In the present study, Type II grain size breaks observed in proximal location separate thin to thick, spaced stratified sand (SL3 and SL2) from an overlying laminated and rippled sand (SL1 and SR) interval. Moving downslope, the underlying facies transitions to massive sands, while laminated and rippled sand remain the dominant facies above the grain size break. The underlying facies is considered to have been deposited by collapsing high concentrations layers characterised by high sediment fallout rates and hindered settling (e.g. Arnott and Hand, 1989; Cartigny et al., 2013; Dorrell et al., 2011; Hiscott, 1994; LeClair and Arnott, 2005; Lowe, 1982; Sohn, 1997; Sumner et al., 2008). While the overlying facies are deposited by relatively dilute and turbulent flows, with low rates of sediment fallout and reduced hindered settling (Baas et al. 2011; Dorrell et al. 2011; Mutti, 1992; Talling et al., 2012). Thus, this study concurs with Kneller and McCaffrey (2003) that Type II grain size breaks represent a change in settling regimes (Figure 3-22B). Similar conclusions were also reached by Stevenson et al. (2014) and Sumner et al. (2012) to explain grain size breaks separating well sorted fine grained and poorly sorted coarser grained deposits in modern turbidites fans. In these instances, the changing settling regime (i.e. hindered to unhindered settling) is argued to have enhanced grain segregation processes.

The above interpretation may also explain the lack of Type II grain size breaks observed in distal locations in Facies Tract III. As will be discussed in Section 3.5.5, highly efficient flows traversing the basin floor produced a distal thickening bed profiles. Interaction with the confining topography and resulting deceleration of the flow induced capacity-driven deposition which prevented the formation of Type II grain size breaks in distal locations in Facies Tract III.

Type III Grain Size Break. Kneller and McCaffrey (2003) considered the theoretical origin of this grain size break and surmised that it forms from waxing flow conditions (Kneller, 1995; Kneller and Branney, 1995) which becomes sufficiently energetic to increase the capacity of the flow and erode the previously deposited sediment. The overlying coarser material is in turn deposited under conditions of increased turbulent energy and shear velocity. A similar

interpretation was also adopted by Sylvester and Lowe (2004); Stevenson et al. (2014) and Sumner et al. (2012), who reported the presence of inverse grading in the underlying deposit to demonstrate waxing conditions.

In the present study, no inverse grading is seen in the underlying facies, suggesting that flows were steady or waning prior to the formation of the grain size break (Kneller, 1995). However, it is likely that increased flow shear velocities and turbulence intensities completely removed the depositional record of the waxing phase.. Furthermore, the discontinuous nature of the grain size break (e.g. CB6) suggest that the flows were highly unsteady or pulsatory at a given location. In a majority of beds, attempting to trace the grain size break downslope shows a transition to ungraded to normally graded intervals without an intervening grain size break; the only exception being CB7, where a Type III grain size break can be correlated for ~4 km between the SE and ER sections. It is therefore conceivable that the flows were initially dominated by surging conditions in proximal locations, characterised by waxing and waning phases due to the passage of a surge or multiple surges (Figure 3-22C). Multiple surges would account for multiple Type III grain size breaks seen vertically in a bed e.g. CB 10-1, 6, 5. Downslope, however, such conditions were not recorded since the flows developed a simple surge structure that was depletive and waning (Figure 3-22B). The lack of Type III grain size breaks in distal sections lends further support to this longitudinal organisation of the flows, while the limited size of the Peïra Cava outlier demonstrates that such organisation occurred over a relatively short distance (~6 km).

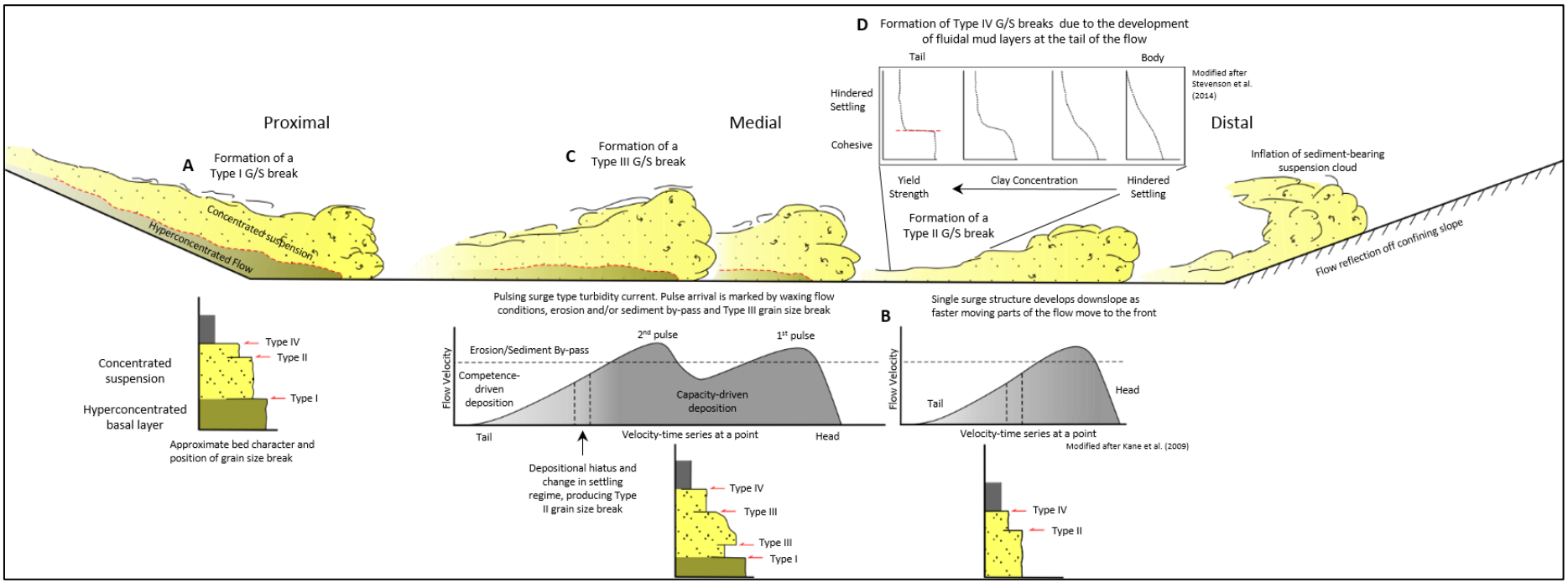

Figure 3-21: Four models showing the development of grain size breaks in the Peïra Cava Basin. A) Type I grain size break created by vertical concentration boundary that separates a hyper-concentrated lower layer and a concentrated, but turbulent upper layer. The grain size break is created by en-masse freezing of the lower layer and sediment reworking the overlying turbulent layer. This type of grain size break is restricted to proximal and medial localities. Further downslope, the hyper-concentrated basal layer transforms into a turbulent flow. B) Type II grain size break represents change in settling regime within a turbulent flow from capacity to competence driven deposition. The grain size break is a result of sediment by-pass prior to competence-driven sediment settling. Due to incremental deposition of sediments from a turbulent flow, Type II grain size break represent the longitudinal structure of the flow. C) Type III grain size break created by multiple surges within a single flow. Each surge is characterised by waxing conditions, during which earlier deposited sediments may eroded. Return to net deposition may lead to sedimentation of coarser sediments. D) Type IV grain size break created by sediment bypass within fluid mud layers. Lower non-cohesive sediment concentration, high mud content and lower velocities at the tail of the leads to clay flocculation. With sufficient yield strength, the developing mud layers hinder settling of non-cohesive grains and carry them downslope.

Type IV Grain Size Breaks. This grain size type has been observed in many locations worldwide (e.g. Amy, 2000; Bouma, 1962; Gladstone and Sparks, 2002; Fonnesu et al., 2015; Kane et al., 2007; Macdonald, 1986; Remacha et al., 2005; Sumner et al., 2012). The spatial facies distribution below the grain size break in the present study suggests that the flow was waning, relatively dilute and of low concentration in proximal locations. It possibly became concentrated downslope to deposit the graded massive sands in distal locations. Above the grain size break, the dominant facies is massive mudstones (MM). The vertical transition from sand to turbidite mud suggests the onset of cohesive settling behaviour may be responsible for formation of the grain size break. A similar mechanism has been advocated by Piper (1978) and Stevenson et al. (2014), associated with a period of sediment by-pass. Surge-type turbidity currents are not only vertically stratified in terms of density and concentration, but also longitudinally (Amy et al., 2005b; Kneller and McCaffrey, 2003). The tail of such flows may also be under-saturated with respect to sediments and mud-rich due to the low shear velocities. These conditions may allow clay to settle out, leading to the development of a high concentration near-bed layer that hinders non-cohesive grain settling (Stevenson et al., 2014 and references therein). At sufficient concentrations, experimental studies have shown such fluid mud layers supporting non-cohesive grains and suppressing turbulence (Baas and Best, 2002; Baas et al., 2009; Baas et al., 2014; Sumner et al., 2009). As the fluid layers continue to move downslope, they transport grain size factions that would have otherwise settled out of suspension to create the grain size break (Stevenson et al. 2014). The Type IV grain size breaks observed in the Peïra Cava are here considered to have formed in a similar manner (Figure 3-22D).

Implication of the Grain Size Breaks. The development of these grain size breaks demonstrates that massive sand depositing flows are not simply steady or single surge type waning flows, but in fact, highly stratified and unsteady flows. Type II to IV grain size breaks may have an active role in forming DWMS (*sensu stricto* Stow and Johansson, 2000), in which erosion and/or by-pass of sediments either removes or prevents tractive structures from forming. The present study suggests that massive intervals form in association with related coarse grained facies (i.e. MSFA *sensu stricto* Stow and Johansson, 2000) in proximal and medial locations. It is possible that amalgamated massive sands may also form in these settings, where erosion by succeeding flows is more likely to remove structured intervals. Further downslope, isolated massive sand may form due to the development of fluid mud layer which hinders settling and tractional reworking of finer grains. By-pass of finer non-cohesive grains in these layers creates the Type IV grain size break above a massive interval.

3.5.2 Depositional Processes leading to Massive Sand Facies.

To understand the formation of massive sands (SM1, SM2 and SM3 facies) intervals, observations from single outcrops are discussed first. This will include a discussion on the results of the Markov chain and entropy analysis. A discussion on lateral transition and geometrical changes in facies in each correlatable bed follows. These changes can be used to discriminate processes and interpret how a flow evolved spatially leading to the deposition of massive sands. (Amy et al., 2005a; Amy et al., 2006a; Talling et al., 2013). Interpretation of depositional processes for the remaining facies are not discussed in this section, and the reader should refer to Table 3-1 and Appendix A for their interpretation.

Graded, Massive Sand (SM2). Graded massive sands were identified in the field using a grain size comparator, which biased the measurement towards the coarsest 5% of grain (Amy and Talling, 2006; Talling et al., 2004; Talling et al., 2013). This was supplemented by thin section analysis for a number of beds (Table 3-2) and confirmed a normal graded trends, albeit with complex fine and coarse-tailing grading patterns (e.g. locally inverse grading in NE CB5; Table 3-2). Normal grading has long been considered a product of deposition from suspension settling from a turbidity current (Kuenen and Migliorini, 1950; Lowe, 1982; Middleton and Hampton, 1973; Sanders, 1965; Shanmugam, 1997), whereas, the massive character could be formed by quasi-steady or surge-type turbidity currents via static suspension settling, suspension fall out without traction, incrementally in a layer-by-layer fashion or a sustained near bed liquefied zone (Arnott and Hand, 1989; Cantero et al., 2012; Dorrell et al., 2013; Kneller and Branney, 1995; Lowe, 1982; Sumner et al., 2008; Stow and Johansson, 2000).

Grain size analysis for graded massive sand intervals (NE CB5) reveals a crude distribution grading except in the fine-tail component, which is inverse graded (Table 3-2). The sorting parameter also exhibits an irregular trend and ranges from very poorly sorted (2.04 phi) at the base to moderately sorted (0.8 phi) at the top. Similar trends are also observed in other beds based on visual estimation using a grain size comparator. These results imply that the suspension criterion (i.e. flow competence; Komar, 1985; Lowe, 1982; Middleton, 1967), may not adequately explain normal grading trends seen in the Peïra Cava outlier. Alternatively, it is argued here that loss of capacity is responsible for the normally grading, albeit poorly sorted sands observed in this study. In this scenario, even if shear velocities are higher than those needed to suspend individual grain size, a flow may deposit sediment as its capacity is exceeded. This decrease in capacity results from a sharp drop in shear velocities, which in turn reduces turbulence support (Felix 2002; Baas et al., 2000). The resulting deposit is likely to be graded and poorly sorted, due to a lack of grain size segregation caused by hindered settling and high-sediment fallout rates (Hiscott, 1994a; Dorrell et al., 2011). The initial sediment-fall out rates are high enough to prevent elutriation of fine grains, trapping them towards the base. As

sediment fall-out rates decline, grain size segregation becomes meaningful to improve the sorting towards the top of the bed, as observed in NE CB5 (Table 3-2). A similar mechanism has also been proposed by Sylvester and Lowe (2004) based on a outcrop study in the Romanian Carpathians and by Amy et al. (2006b), Dorrell et al. (2013) and Sumner et al. (2008) from experimental studies. In the latter studies, temporal deceleration of flows occurred at rates where the different suspended grain size ranges could not have readjusted to the decreased velocity prior to deposition. As such, deposition of all grain sizes (i.e. capacity-driven) commenced as soon as the flow decelerated, resulting in a poorly graded and sorted deposit. The poorly sorted nature of the graded sands in these and the current study implies that the massive character could not have developed from static suspension settling.

The vertical transition from graded massive sands to structured facies (SL2, SL1 and SR) observed in the logs and deduced from the statistical analysis demonstrates temporal decrease in flow velocity and concentration during and succeeding massive sand deposition. This, therefore, rules out massive sand deposition from a sustained near bed layer (*sensu stricto* Kneller and Branney, 1995). The statistical analysis indicate that successor states are non-random (typically thin, spaced stratified or parallel laminated sands) and there is a strong dependence on the graded massive sand. Extrapolating the hydrodynamic interpretation of the structured intervals (SL2 and SL1; Table 3-1) down to the massive sands, therefore, advocates incremental deposition by repeated collapse of high-concentration near bed layers, similar to the experiments of Arnott and Hand (1989), Cartigny et al. (2013), Leclair and Arnott (2005), Sumner et al. (2008) and Vrolijk and Southard (1997). The formation of crude stratification in these experiments is connected to lateral shearing of grains as the near-bed layers were deposited and subsequently eroded by the overlying turbulent flow (Sumner et al. 2008). However, the characteristics of these layers vary depending on the concentration of the layers (typically in the range of 10-35%), which is in turn dependent on the sediment-fallout-rate from the overlying turbulent suspension. At higher concentrations, formation of stratification is suppressed, leading to the development of a massive deposit (*ibid.*). Since the layers are fed and driven by the overriding turbulent flow (Hiscott, 1994b), deposition occurs from the base-upwards due to interlocking of grains. Generation of new layers occurs through bursts of turbulent energy and sediment flux from the turbulent layer at time of lower shear velocity. With temporal decrease in flow velocity and concentration, the sediment flux to the near bed layers decreases leading to thinner layers and the transition to crudely laminated sands (*sensu stricto* T_{B-2} of Talling et al., 2012) as observed in most beds. However, the rate at which sediment fall-out suppresses stratification has been known to vary. Arnott and hand (1989) reported rates of 4 cm^{-1}, while Sumner et al. (2008) observed rates of 2.64 cm^{1}. Presently, the only plausible explanation for this discrepancy is that the initial textural characteristics (i.e.

grain morphology and size distribution) may have a fundamental control on the rate at which bedforms are suppressed.

Ungraded, Massive Sand (SM1). Similar to the SM2 facies, ungraded massive sand intervals were identified in the field using a grain size comparator, cross-checked with thin section analysis (Table 4-2). Comparable grain size and sorting trends were also observed; coarse-tail normal grading, irregular to locally inverse graded fine-tail component and poor sorting. Previous models of ungraded massive sands have been ascribed to rapid sediment fall-out from a steady flow (Kneller and Branny, 1995). The high sediment fall-out rates may have also contributed to the development of a 'quick bed' that would disrupt the fabric and scatter imbrication angles of grains (Hiscott and Middleton, 1980; Lowe, 1982; Middleton, 1967).

In proximal and medial localities, entropy and Markov Chain analysis demonstrates a dependence of the ungraded, massive sands on the preceding facies (i.e. matrix-supported conglomerates and locally graded, massive sands; Table 3-4). While in distal localities, ungraded massive sands exert a strong influence on the succeeding graded (i.e. massive sands). The presence of a Type I grain size break between the conglomeratic and ungraded massive sand facies impedes extrapolation of hydrodynamic processes upwards. Based on the interpretation of a Type I grain size break, the flow is at the very least bipartite with a highly concentrated basal layer and a lower concentration upper layer. However, the gradual transition from ungraded to graded massive sands in the distal locations may provide evidence to its formation if the above interpretation of the *graded massive sand* is valid. This transition has been observed in laboratory and numerical experiments involving relatively high-sediment concentrations (e.g. Amy et al., 2006b; Breien et al., 2010; Dorrrell et al., 2011; Dorrell et al., 2013; Cartigny et al., 2013; Sumner et al., 2008). Though these studies reported disparate grain support mechanisms and near bed-settling processes within the flows, they all reported incremental deposition from a near bed layer where grain segregation was inhibited. In the settling tube experiments of Amy et al. (2006b), frictional interlocking of grains inhibited grain segregation at ~50% sediment concentration to produce an ungraded massive sand. Similar concentrations and settling behaviour were observed by Cartigny et al. (2013), where concentrations exceeding 45% fully suppressed turbulence in a grain friction dominated basal layer (their Type III layers). These layers are analogues to the high concentration near bed layers of Sumner et al. (2008) and Vrolijk and Southard (1997).

It is concluded that ungraded massive sands are formed in a similar manner to graded massive sands, but from higher concentration basal layers. Turbulence would be completely dampened in these layers and grains are in near continuous contact. This would prevent grain segregation

and the final deposit will be ungraded and poorly sorted. The shear stresses and velocities necessary to generate these layers would prevent deposition, unless small scale fluctuations in flow velocity are present (Cartigny et al., 2013; Sumner et al., 2008). During these velocity fluctuations, it is not difficult to envisage high and constant aggradation rates that would lead to the massive character of the deposit. Since deposition of these layers is incremental, they are here interpreted to form from turbidity currents, rather than sandy debris flows, irrespective of the concentration in the layers.

Massive Sands with Patchy Texture (SM3). With the exception of CSE CB6, intervals of massive sands with 'patchy' texture are located in distal sections of the outlier. The patchy texture (Table 3-1) was confirmed by visual observation and a grain size comparator. Despite thin section analysis to confirm these grain size trends (Table 3-2), the physical size of the slides could not accurately capture the abrupt transitions. Discontinuous zones of mudclasts are present in the middle and top of the bed. The presence of these mudclasts, along with the massive character, has been used by Shanmugam (1996; 1997; 2000; 2002; 2006) to indicate *en-masse* deposition from sandy debris flows. In light of recent field-based and experimental studies, massive sands with 'patchy' texture are here interpreted to be deposits of debris flows, but not for the reasons outlined by Shanmugam (1996). This is due to the fact that many of the criteria used by the author can be explained by deposition from turbidity currents, particularly if deposition occurred from high-concentration near bed layers (see above; Talling et al., 2012).

Instead, the 'patchy' texture is interpreted according to the mechanism of Talling et al. (2013), in which a debris flow is partly or wholly liquefied and from which sands can partially settle out. Numerous experiments on subaerial and subaqueous debris flows have shown the development of a transient excess pore pressure by gravitational loading which can support grains during transport (Breien et al., 2010; Ilstad et al., 2004; Iverson, 1997; Kaitna et al., 2016; Major, 2000; Major and Iverson, 1999). Dissipation of this pore pressure through transit and deposition of the debris flow may mobilise sediments via slow convection and elutriation. A physical expression of this could be an irregular or 'patchy' texture in the sand (Table 3-1). However, to date, no experimental work has reproduced this textural characteristic. The presence of chaotically organised mudclasts towards the middle and top of the beds may, however, lend support to *en-masse* deposition from debris flows (Figure 3-23). In the graded and ungraded massive sands (SM1 and SM2), mudclasts occur along distinct horizons that clearly indicate incremental deposition. In debris flows, by contrast, clasts are typically located at the top and may undergo size segregation depending on the relative density difference between the clast and matrix, and the matrix strength.

Crude normal grading was also identified in the 'patchy' massive sands from thin sections analysis (Table 3-2), which may allude to deposition from turbidity currents. Numerous recent experimental studies have, nevertheless, shown crude coarse-tail grading occurring in debris flows after the flow has stopped moving (e.g. Baas et al. 2009; Baas et al. 2011; Major, 2000; Sumner et al. 2009). This could be related to the hydraulic diffusivity of the debris flow, which may promote a crude normal grading. In a more permeable debris flow, fluid pore pressures and effective stresses change more rapidly due to the presence of pervasive pathways for fluid migration. As the pore pressure dissipates, the deposit undergoes consolidation from the base upwards. The simultaneous expulsion of the pore fluid elutriates finer grains, while a coarser sediments settle under hindered settling, producing a crudely graded interval. This latter explanation for normal grading goes hand-in-hand with the mechanism proposed by Talling et al. (2012; 2013) for the formation of 'patchy' texture.

Mud Clasts. In a small number of beds, the mudclasts are observed in the massive sand facies or close to the transition into a massive sand. These mud clasts are mm to cm-scale and commonly ordered stratified mudclasts (Type B5; Johansson and Stow, 1995) with their long axis aligned sub-parallel to parallel to the bedding plane (Figure 3-19 and 3-20). In CSE and SE CB5, SE CB10-2 and PCR CB10-1, these mudclasts are located close to or at the location of Type I grain size breaks. Type I grain size breaks are interpreted as a rheological interface between a high-concentrated debris flow and a less concentrated turbulent flow. It is likely the mud clasts were transported between this rheological interface prior to deposition (Postma et al. 1988). Away from this rheological boundary, stratified mudclasts were most probably deposited base upwards via incremental layer-by-layer deposition. This would mean that the mudclasts were carried by the body and tail of the flow and deposited on top of earlier deposited sediments (Kneller and McCaffrey, 2003). The vertical position therefore corresponds to the static seabed at that point in time. Isolated mudclasts (Figure 3-16 NWT section) also deposited in this manner would appear to be 'floating' in a matrix of sand.

3.5.3 Vertical Facies Transition.

Chi-squared statistics was performed to assess Markovian property in three geographically grouped areas of the Peïra Cava outlier: Proximal (SW, CSE, SW, and ET), Medial (PCR and ER) and Distal (NWT, NW, NE, and NES). The proximal and distal grouping passed the test of independence at an appropriate degree of freedom at the 99.5% confidence level. However, the medial grouping failed the test of independence, implying that deposition was not by Markovian process. These trends are broadly confirmed by entropy analysis, which show no cases where $E(Pre) \approx E(Post) \neq 0$ (Table 3-4), implying some level of dependency of one state on another. Markov and entropy analysis therefore support in a statistical manner the otherwise obvious conclusion that the deposition of the various facies depends on evolving flow conditions at that

point in time. The analysis is therefore used to discuss the validity of models outlined in Chapter 2, at least based on facies transitions in the vertical profile.

The most common vertical transitions in the three groupings is thin, spaced stratification (SL2), parallel lamination (SL1) and rippled sands (SR), which broadly resembles the T_b and T_c division of Bouma (1962) and in particular the modified Bouma sequence of Talling et al. (2012). This sequence occurs at the top of beds and was originally interpreted as deposits of depletive low density flows in the upper flow plane bed regime, followed by tractional reworking in the lower flow regime. However, due to observations of thin to thick laminae forming under high concentration experimental flows (e.g. Leclair and Arnott, 2005; Sumner et al., 2008), the boundary between high- and low-density turbidity current in the present study is placed within the Bouma T_b division, but maintaining the overall hydrodynamic nature of the flow (Talling et al. 2012). Furthermore, the vertical position of these facies implies that they were deposited by the body and tail of the flow, and from progressively lower concentration and velocities (Baas et al. 2016).

Proximal Locations. In terms of the massive sand division, a common trend can be seen in the proximal group consisting of massive sands (SM1 and SM2), overlain by laminated and rippled sand (as above) and underlain by thick, spaced stratification (SL3) or the conglomeratic facies (CM). This sequence is similar to that identified by Hiscott and Middleton (1979) and broadly conforms with the model of Lowe (1982). The sequence, however, differs from the Lowe (1982) model in terms of its position from the source i.e. the sequence is representative of medial locations along the downslope transect rather than proximal locations (Chapter 2 Figure 2-7). This discrepancy can, nevertheless, be solved if the Contes sub-basin immediately to the south is considered the proximal equivalent of the Peïra Cava succession and the SW section as the medial equivalent. Furthermore, the sequence consists of a prominent structured cap that locally makes up half the bed. This is in contrast to the Lowe model, which envisages a thin drape. The Peïra Cava beds are thus likely to have undergone significant tractional reworking from the body and tail of the flow, rather than by-pass of fine sediments. Moreover, the Lowe (1982) model does not consider the vertical position of grain size breaks that locally separate the massive sand from the underlying and overlying facies (Figure 3-15 to 3-19; SW, CSE, SE and ET sections). Although Lowe (1982) did identify internal erosive features and grain size fluctuations, grain size discontinuities were not placed in his conceptual model. In this regard, the genetic facies tract of Mutti (1992) and Mutti et al. (1999; 2003), and vertical profiles of Kneller and McCaffrey (2003) more accurately captures the temporal changes in deposit character observed in proximal sections (Chapter 2 Figure 2-8). In these models, a switch in sediment settling regime creates the grain size break above the massive sand (Type II). Where they differ is the mode of formation of the massive sands; Mutti (1992) suggested *en-masse*

deposition from a highly concentrated flow, while Kneller and McCaffrey (2003) proposed capacity-driven deposition from a concentrated flow. The overlying facies in both of the models is tractionally reworked sands. Given the interpretation of massive sand intervals above, the results from the present study are more in line with the vertical profile of Kneller and McCaffrey (2003); massive sands are initially deposited under a capacity-driven settling regime from near-bed high-concentration layer, and separated from an overlying structured interval by a grain size break denoting a change in settling regime.

Medial Locations. The medial group did not meet the requirement for Markovian property. Nevertheless, a trend has been discerned based on the transitional count matrix, and is broadly similar to that of proximal sections. The main contributing factor for the rejection of the null hypothesis is the multiple occurrences of the same facies at different stratigraphic heights in some beds, but without displaying strong cyclicity (Figure 3-19 and 3-20). This repetition in facies is used as a defining feature of Facies Tract III. In confined basins, repeating sequences of normal graded massive, laminated and rippled sands has been interpreted as deposits of reflected flows due to the proximity to the confining slope and opposing palaeocurrent dips in ripples (Felletti, 2002; Haughton, 1994; Kneller and McCaffrey, 2001; Patacci et al., 2015; Sinclair, 1994). However, this interpretation is not consistent with the observed vertical transition in this study owing to a lack of or consistent (e.g. PCR CB11-3) palaeocurrent data within the beds, as well as the inferred distance between certain localities to the paleo-slope. A couple of alternative mechanisms are thus proposed to explain the non-cyclic repetition of facies in medial locations: 1) surging behaviour of the flow, or 2) generation of internal waves due to interaction with confining topography. In the former hypothesis, longitudinal variation in flow concentration and velocity due to the passage of pulses or surges, could lead to repetitive deposits of massive (ungraded and graded) and thin, spaced stratified sands. The presence of grain size breaks locally suggests that passage of these surges eroded the previously deposited facies. As the surges progress downslope, they may cannibalise slower moving surges and the flow organises itself into a single surge.

Alternatively, passage of internal waves, created by segments of the flow deflecting and reflecting off confining topography, may have produced the repetitive sequences (Edwards et al., 1994; Kneller et al., 1991; Pantin and Leeder, 1987; Patacci et al., 2010, 2015; Sequeiros et al., 2009). In this instance, the internal waves will oscillate between the density interface between the ambient fluid and a turbidity current, or along a density interface within the flow. They are known to suppress Kelvin-Helmoholtz instability, permitting propogation with little loss of energy (Kneller et al. 1991). As these waves sweep across the body and tail of the flow, subtle fluctuations in flow velocity and concentrations related to their passage can affect the aggrading deposit (Patacci et al. 2010). These fluctuations are greatest near the confining slope,

where the internal waves have the maximum amplitude. Here, the deposit structure may be characterised by internal erosion and tractionally reworked structures (Kneller et al., 1991; Kneller and McCaffrey, 1999). With distance from the slope, the waves weaken and variations in flow velocity and concentration become subtler. This may translate into subtler facies transitions such as repeating facies of ungraded and graded massive sands, and thin spaced laminae (Figure 3-23) The proximity of the PCR section to the western confining slope suggests that this is a viable mechanism to explain the repetitive facies occurrence. Similar vertical facies sequences in the ER section could therefore suggest the presence of an eastern confining slope, which has not been preserved in the present day.

Distal Locations. The most common vertical order of facies in the distal group has many similarities to the facies sequences observed in proximal and medial localities; ungraded or graded massive sand overlain by structured facies. Locally, the massive sand is separated from the overlying facies by a Type II grain size break. Also similar to the medial grouping is the presence of repetitive occurrence of facies consisting of alternating ungraded and graded massive sands (Figures 3-11 and 3-20). These sequences are interpreted to have been deposited in a manner comparable to that of medial sections i.e. passage of multiple surges or interaction with confining topography. However, in the latter case, rather than deflection of the flow due to the lateral confining slope, these sequences are likely to have formed from flow reflection off its distal equivalent. In such cases, the backflow down the slope would have generated an upstream migrating bore that would have weakened with distance (Edwards, 1994; Patacci et al. 2015). It is proposed that the passage of internal waves, generated from this migrating bore, may have influenced the development of the repetitive ungraded and graded massive sands in the distal sections away from the slope.

A second vertical facies sequence identified by the expected and transitional matrices consists of massive sands with ‘patchy’ texture overlain by structured facies, typically parallel laminated sands. A similar sequence was observed by Talling et al. (2013), who related the structured facies to an overriding dilute and turbulent flow reworking the top of the deposit (Figure 3-23). In the present study, this transition in settling behaviour is always accompanied by a Type II grain size break.

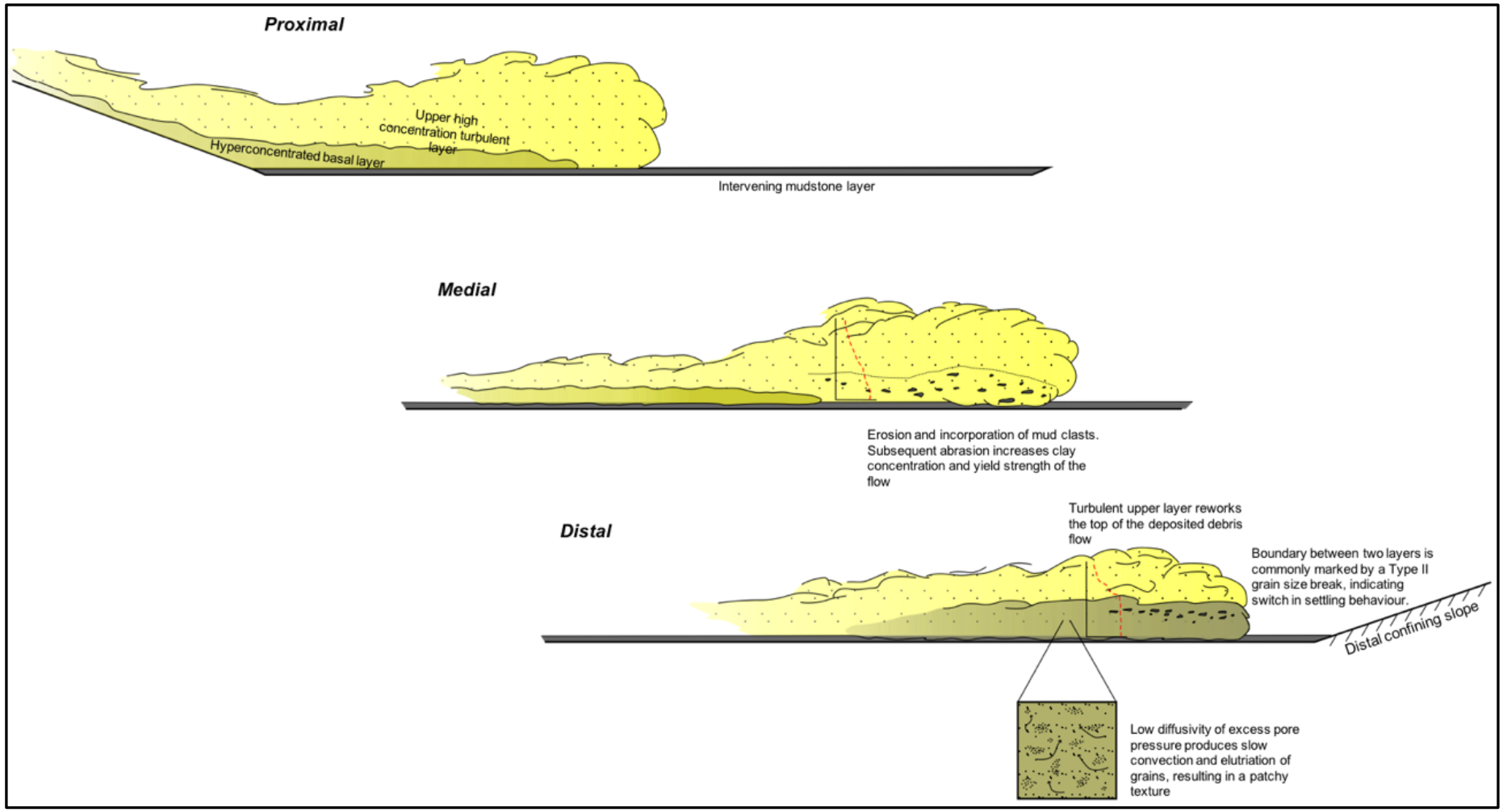

Figure 3-22: Model showing the formation of the massive sand with 'patchy' texture. An initially erosive flow entrains mud clasts which disaggregates, leading to increased clay content in the flow. The increased clay content in turn promotes the development of excess pore pressure and laminar behaviour. As the flow comes to rest, the excess pore pressure dissipates gradually leading to remobilisation of sediments to produce a 'patchy' texture.

3.5.4 Lateral Facies Transition and Geometry.

The lateral transitions to and from the massive sand facies is now discussed in each Facies Tract to infer spatial evolution of flow processes. Existing models will also be discussed in terms of their validity and applicability in the Peïra Cava sub-basin.

A consistent relationship has been observed in studies that have investigated facies architecture of turbidity current deposits; the core of the bed is composed of massive sands and thick to thin spaced stratified sands, capped by a thin and laterally extensive structured interval (Tb, Tc and Td; e.g. Amy et al., 2006; Hirayama and Nakajima, 1977; Macdonald, 1986; Malgesini et al., 2015; McIntosh, 2007; Remacha et al., 2005; Talling et al., 2013). Distally, the structured interval dominates the bed as the 'core' facies pinches out (ibid.). Grain size and bed thickness also decrease with distance. These ubiquitous trends have been incorporated numerous conceptual facies tract (e.g. Lowe, 1982; Kneller and McCaffrey, 2003; Mutti, 1992; Mutti and Ricci Lucchi, 1972; and Mulder and Alexander, 2001a), have been reproduced in flume tanks and numerical simulations (e.g. Baas et al., 2004, Tinterri et al., 2003, Dade et al., 1994), and are diagnostic of depletive and waning flows. Although grain size and bed thicknesses (except for Facies Tract III, refer to section 3.5.5.) decrease with distance in the present study, the internal character of the beds do not conform to existing conceptual facies tracts. The internal character of the beds (Figure 3-20) demonstrate opposing trends, with the structured facies (SL2, SL1 and SR) decreasing and massive sands increasing in relative proportions downslope. In Facies Tract I and III, the internal bed character gradually transitions to ungraded and graded massive sands (except for CB7) distally, while in Facies Tract II, massive sands with 'patchy' texture is the dominant facies.

Two plausible mechanisms may account for the above discrepancy; 1) flow transformation to a concentrated flow distally, and/or 2) flow interaction with the confining topography. Due to the basin configuration and spatial distribution of massive sands, these mechanisms may work in tandem rather than exclusively. Fisher (1983) identified body and gravity transformation as possible means to transform dilute flows to highly concentrated flows. Body transformation involves transformation between turbulent and laminar flows without significant addition or loss of interstitial fluid. Experimental studies have shown the ability of small volumes of clay (~ 3-4wt %) to modulate turbulence and modify the settling regime (Baas and Best, 2002; Baas et al. 2009; Baas et al. 2011; Baas et al. 2016; Sumner et al. 2009). This clay may be introduced to the flow through erosion of a muddy substrate or disintegration of mudclasts (Amy et al., 2006; Davis et al., 2009; Haughton et al. 2009; Ito, 2008; and Kane and Pontén, 2012). The abundance of mudclasts and mud content up to ~ 10%, particularly in facies SM3, indicates erosion and assimilation of the substrate, which subsequently influenced flow evolution and deposit architecture (Figure 3-23). The rate of deceleration, size of clay particles, the concentration and

size of non-cohesive grains, the turbulence structure of the flow and flow velocity will all control how the increased clay percentage will modulate flow behaviour (Baas et al. 2009; Sumner et al. 2009). In the experiments of Breien et al. (2010) and Marr et al. (2001), increasing clay concentrations produced a liquefied basal layer (their fluidised layer) behind a turbulent and erosive head, with an overriding dilute turbulent plume. These authors used sand-clay-water mixture ranging from 77-5-28 wt% to 47-25-28 wt% respectively. The sand size was ~330 μm, and the sand-clay density was 2.65 g/cm^3 and 2.75 g/cm^3. Using these parameters, the liquefied layers were characterised by transient excess pore pressure and laminar flow, with sediments 'floating' freely in the sediment-fluid mixture (Breien et al. 2010). A downslope transformation to such a flow is postulated here to explain the transition to massive sand with 'patchy' texture (SM3). Due to the distal location and/or proximity to the confining topography, the transformation was most likely triggered by change in slope gradient that induced rapid deceleration of the flow. Under such conditions, a weakly to moderately coherent debris flow (*sensu stricto* Marr et al., 2001) formed that consisted of a liquefied body with laminar flow. Excess pore pressure is maintained during deceleration of the flow and deposition of the sediments (Major and Iverson, 1999). As the sediments come to rest, excess pore pressure dissipates and may mobilise sediments via slow convection and elutriation to produce the 'patchy' texture in SM3 facies (Figure 3-23). The turbulent plume that follows this phase reworks the top of the deposit to produce the grain size break and the thin interval of tractive structures that commonly cap SM3 facies in distal locations. This evolution in flow behaviour is postulated to have produced the SM3 facies in distal localities and the overall character of Facies Tract II.

The second type of flow transformation that may lead to massive sand deposition in distal localities is gravity transformation. Gravity transformation involves gravitational segregation of the flow into a highly concentrated lower underflow and a turbulent, less concentrated upper layer (Fisher, 1983). Vertical stratification of this nature is reflected in the viscosity and density profiles of the flow and is ubiquitous in nature due to variable characteristics of the flow in terms of grain size, settling regime, entrainment of ambient fluid and erosion of the substrate. External factors that influence this vertical stratification include local topography and loss of confinement. The dimensionless parameters that govern turbulence are the shear Richardson number (Ri_τ; buoyant production or consumption of turbulence divided by the shear production of turbulence), the shear Reynold number (Re_τ; characterises turbulence in the absence of stratification) and the dimensionless fall velocity (V). Cantero et al. (2009; 2012a, and 2012b) argued numerically that Ri_τ and V modulate the degree of turbulence and thus turbulence dampening. For a given V, increasing the Ri_τ value dampens the turbulence, leading sediments to concentrate in a near-bed layer. This also holds true if V is increased with respect to Ri_τ. Critical values were observed by the above authors for both Ri_τ and V, beyond which turbulence

was dampened by stratification. These critical values are known to be influenced by subtle changes in slope, grain size and loss of confinement. Taking this into consideration, a change in slope angle due to interaction with topography may lead to increased sediment stratification and turbulence suppression. This in turn influences the development of highly concentration near bed layers (sensu stricto Sumner et al. 2008) and deposition of massive sands. This mechanism is likely to have produced the graded and ungraded massive DWMS (sensu stricto Stow and Johansson, 2000) layers in distal localities belonging to Facies Tract I.

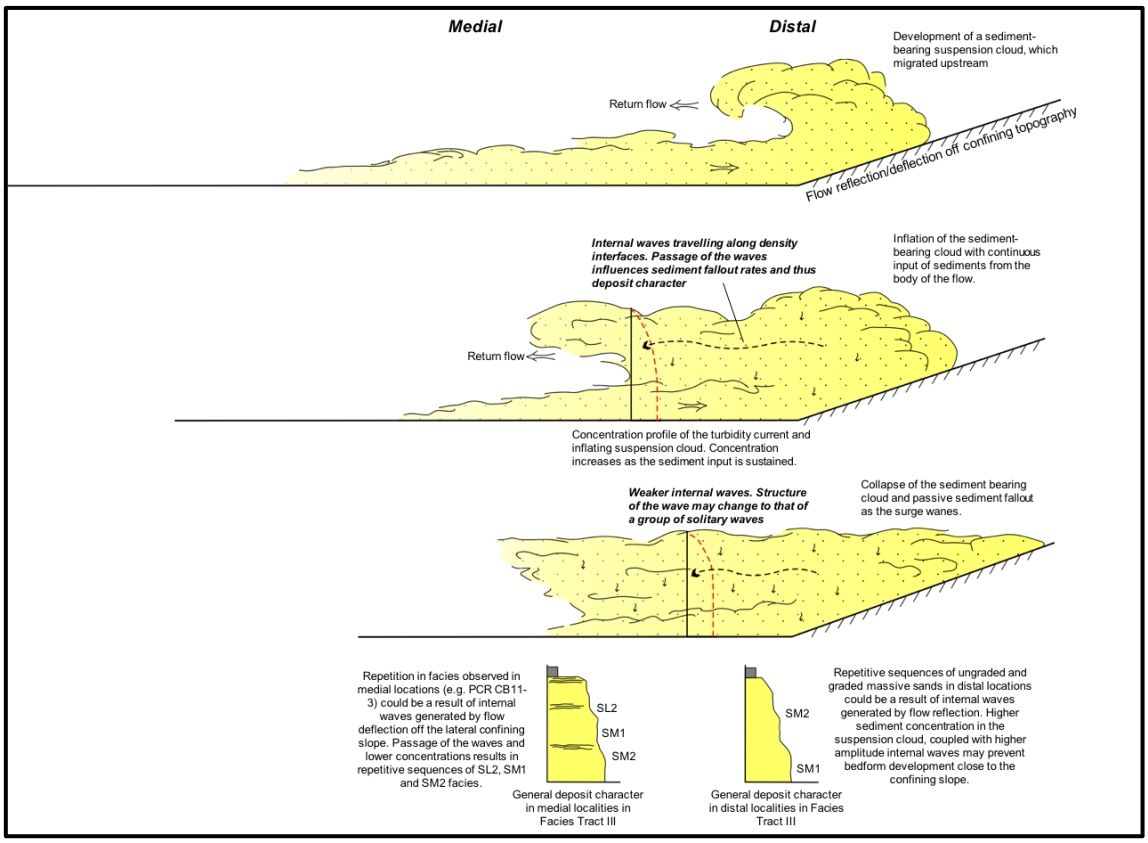

Figure 3-23: Formation of a sediment-bearing suspension cloud as a result of flow interaction with distal confining topography. As the flow approaches and travels up the confining slope, a sediment plume is generated by the continuous supply of sediments from the flow. The plume inflates and migrates upstream. The corresponding increase in sediment concentrations results in higher sediment fall out rates, hindered settling and deposition of massive sands in distal setting. The generation and passage of internal waves at density interfaces may be responsible for the repetitive facies sequences observed in Facies Tract III. Red line shows the evolution of the concentration profile of the suspension plume over time.

While the above mechanisms explain the abundance of massive sands in distal location, they do not explain the repetitive ungraded and graded massive facies in Facies Tract III. Nevertheless, the confining nature of the Peïra Cava sub-basin may provide clues to the formation of this internal character. Within confined basins, the majority of the sediments are ponded during the initial fill stage (Sinclair and Tomasso, 2002). This leads to the creation of a 'ponded' sediment-bearing suspension cloud, as witnessed in flume experiments of ponded surge-type and sustained turbidity currents (e.g. Edwarda et al., 1995; Lamb et al., 2004, 2006; Patacci et al., 2015; Toniolo et al., 2006). Such suspension clouds are turbulent in nature and result from the

interaction with confining topography, and migrate upstream as they are fed and sustained from the turbidity current (Figure 3-23). If surge-type turbidity currents are involved in their development, as is likely to be the case here, the suspension cloud is expected to move upstream before breaking into a series of internal waves (Edwards et al., 1994). The initial development of the suspension cloud corresponds to increased sediment concentrations. As the flow wanes, the cloud cannot be sustained by fresh material and begins to collapse. This consequently increases sediment fallout rates and causes the gravitational transformation of the flow. Passage of internal waves at this stage is likely to create subtle fluctuations in flow velocity and concentrations (Edwards et al. 1994; Patacci et al. 2015), which in turn lead to variations in sediment fallout rates to the static bed. As mentioned previously, these subtle fluctuations may be expressed in the deposit as repetitive intervals of thick to thin stratification and massive sands in Facies Tract III (Figure 3-23). Field evidence for this mechanism is provided by observations of parallel laminated sand vertically transitioning to massive sand in the vicinity of onlap surfaces in the Tabernas Basin of SE Spain and the Tertiary Piedmont Basin of NW Italy (Haughton 2000, Felletti, 2002). The relative small extent of these basins encourages the ponding and inflation of sediment-bearing clouds that temporally increases the flow concentration.

3.5.5 Bed Geometry.

Two general trends in external bed geometry are recognised for the correlated beds in this study: i) beds that show a gradual decrease in thickness downslope, and ii) beds that maintain their thickness or thicken downslope. These two thickness trends correspond to Facies Tract I and II, and Facies Tract III respectively.

Decreasing bed thickness distally (Facies Tract I and II). All beds in Facies Tract I and II display a general basinward decrease in bed thickness, and loosely resemble a linear to sigmoidal downslope profile. Across-slope (from NWT/NE to NE/NES section) thickness trends have only been documented in CB11-2, 11-1, 10-2 and 10-1, which show a decrease in bed thickness away from the western confining slope (except for CB11-2, which maintains its thickness between the two distal sections).

The sigmoidal to linear trend in bed thickness observed in Facies Tract I and II is comparable to experimental studies (Bursik and Woods, 2000; Dade and Huppert, 1995; Gladstone et al. 1998; Gray et al., 2005; Kubo, 2004; Lamb et al., 2006; Laval et al., 1988; de Rooij and Dalzeil, 2001; Sequeiros et al., 2009; Spinewine et al., 2009), outcrop studies utilising long-distance bed correlation (Amy and Talling, 2006; Remacha and Fernandez, 2003; Talling et al., 2007a, b; Sumner et al., 2012) and to numerical simulations (Blanchette et al; 2005; Dade et al., 1994;

Salaheldin et al., 2000). Interpreted flow character in these studies suggest a depletive, waning flow with decreasing sediment concentration and decreasing sediment fallout rates downslope. However, the pattern and rate of thinning in each of the studied beds is highly variable (Figure 3-15 to 3-19). Irregular basin floor topography may explain some or all of the local variations. Indeed, an irregular basin floor topography is likely to have affected the early basin fill as suggested by Amy (2000) and Aas et al. (2010). However, these irregularities appear to have filled-in prior to the deposition of CB5, which can be correlated across the outlier (Amy, 2000). This attests to a fairly smooth and flat basin floor for beds which are located stratigraphically higher than CB5. Systematic variations in deposit geometry for the beds analysed in this study may then be a product of depositional processes, locally influenced by the lateral confining slopes.

All or most of the beds in Facies Tract I and II have a thickness maximum in the proximal SW location (Figure 3-15 to 3-19). For beds CB11-2, CB10-2 and CB6, this thickness maximum extends downslope for ~ 2-3 km, before declining more rapidly. Owing to the relative small size of the Peïra Cava basin, a broad thickness maximum such as those seen in the Agadir Basin (north-west Moroccan Turbidite System; Wynn et al. 2002), Eocene Hecho Group (south-central Spanish Pyrenees; Remacha et al., 2003; Tinterri et al., 2003) and the Marnoso Arenacea Formation (north-east Italian Apennines), which extend for 10's of km downslope, cannot be created. The proximal broad thickness maximum in these locations has been used to depict deposition from a uniform flow over a considerable distance. Furthermore, the close association of massive and parallel laminated sands with the thickness maximum led Talling et al. (2007a) to hypotheses that hindered settling played an important role in controlling bed thicknesses (in proximal locations). This is based on the hypothesis that massive sands are generated by high-concentration near bed layers (Lowe, 1982; Talling et al., 2012; Vrolijk and Southard, 1997), dominated by grain interaction and hindered settling. The link between parallel laminated sands and hindered settling is more tentative, but is based on the observation of massive sands transitioning into parallel laminated sands without a decrease in bed thickness, and flume experiments showing the development of thin-spaced stratification from high-concentration near-bed layers (LeClair and Arnott, 2005; Cartigny et al., 2013; Sumner et al., 2008). Based on these relationships, a link between the broad thickness maximum and hindered settling inferred from sediment facies seems plausible. Although a broad thickness maximum is not seen in CB11-2, CB10-2 and CB6, the depositing flows are likely to be characterised by hindered settling and grain-to-grain interaction, especially near the base of the flow in proximal location, if not uniform flow conditions.

The presence of multiple Type I, II and III grain size breaks in the studied beds, especially in proximal locations, indicates unsteady flow conditions. At a given point this translates into

phases of waxing and waning flow velocity and sediment concentrations. Numerical analysis by Dade et al. (1994) established a relationship when considering the downslope evolution of depletive, unsteady flows and their external geometry, and showed that the surge propagation speed (dependent on the overall Froude number, slope angle, and the surge aspect ratio) and the corresponding deposit thickness are closely related. Dade et al. (1994) inferred that while a surging flow in proximal locations adjusts to a change in slope gradient, the decelerating flow generates a relatively uniform deposit thickness. It is thus surmised that proximal thickness maximums seen in CB11-2, 10-2 and CB6 are dominated by the surging head (and subsequent surges), where sediment re-entrainment or by-pass led to greater depositional lengths. Further downslope, a flow may organise itself longitudinally into a simple waning flow (Ho et al. 2018: Kneller and McCaffrey, 2003). The reduce abundance and variety of grain size breaks in the distal locations attests to this downslope flow evolution (Ho et al. 2018).

Downslope of the narrow proximal thickness maximum, all beds (except CB6) decrease in thickness gradually to crudely resemble a linear (CB11-1 and 10-1) to concave upward (CB11-2 and 10-2) bed geometry (Figure 3-18 and 3-19). A broadly similar trend was also observed in outcrops by Talling et al. (2007a), Talling et al. (2007b) and Murray et al. (2002). However, the former author did note that the rate of thinning was several orders of magnitude shorter in experimental studies; discrepancy that can be correlated to basin upscaling in experimental studies or flow efficiency and tractional reworking of sediments by natural flows in distal locations. Since the beds in this study do not show the characteristic concave upward bed profile in medial and distal localities, a simple depletive flow with decreasing sediment concentration downslope is not considered to have produced the bed profiles in Facies Tract I and II. Rather, the dominantly massive (SM facies) to laminated (SL1 and SL2) sand intervals in all the beds along their downslope profile indicates that the flows maintained their high sediment concentrations. As discussed earlier, flow transformation (Figure 3-22) and/or interaction with the confining topography (Figure 3-23) may have contributed to the observed facies, especially for Facie Tract I and II. However, regardless of the exact cause of the high sediment concentration, it is reasonable to assume that hindered settling continued to play an important role as the flow progressed downslope. With hindered sediment settling, sediment accumulation rates are reduced. It is then easy to envisage relatively uniform sediment fall-out across the medial and distal localities to produce crudely linear to concave upward bed profile (Talling et al., 2007a).

The decrease in bed thickness away from the lateral slope (i.e. from NWT/NE to NE/NES sections) was observed in CB11-2, 11-1, 10-2 and 10-1. Amy et al. (2004) also observed similar lateral thinning patterns, and surmised that a flow maintain higher concentrations, and thus

higher sediment fallout rates, to produce thicker deposits proximal to the base of slope. This study concurs with the interpretation of Amy et al. (2004).

Basinward Increase in Thickness (Facies Tract III). All beds in Facies Tract III display bed profiles with accentuated highs in proximal and distal areas, with a noticeable decrease in bed thickness in medial locations (Figure 3-15, 3-17 and 3-19). Only CB7 shows a greater thickness in distal locations relative to proximal areas. In proximal locations, the similarities, in terms of bed thickness, facies distribution and grain size breaks, to Facies Tract I and II suggest flows may have evolved in a similar fashion. Therefore, the following discussion will focus on the bed thickness patterns observed in medial and distal locations for Facies Tract III.

Deposits of CB5 were not observed along the western sections of the outlier, close to the lateral slope. Therefore, the effects the lateral slope had on bed geometry cannot be readily examined in this study. For CB11-3 and CB7, a small increase of ~7% and ~13% in bed thickness, respectively, is seen away from the western slope. Both beds also show an increase in bed thickness basinward relative to medial sections (i.e. PCR and ER section, respectively). This lateral thickening was attributed to flow velocity non-uniformity and competence driven deposition by Amy et al. (2004), where deposit thickness is assumed to be controlled by the sediment-load fallout rate away from the slope. Parts closer to the confining (western) slope maintained their relative velocity, enabling by-pass or erosion of the substrate, while away from the slope, the flow was mainly depositional, leading to thicker deposits. The well-sorted nature of the grains in the beds studied by Amy et al. (2004) was used to verify competence driven deposition. However, grain size analysis of bed CB5 as part of this study show that only the top of the bed approaches a well sorted grain size distribution (Table 3-2). For the bulk of CB5, grain sorting varies from poorly sorted (σ = 1.11) to very poorly sorted (σ = 2.23). Similar grain sorting is also observed in CB11-3 and CB7, albeit based on measurements from a grain size comparator. It therefore seems plausible that competence driven deposition may not have been the main contributor to bed thickness trends, at least for the beds studied here.

Basinward increase in bed thickness in confined basins have been reproduced experimentally (e.g. Kubo, 2004; Lamb et al. 2004; Lamb et al. 2006; Mulder et al. 2001b). In these experiments, the loss of capacity upon encountering the confining slope resulted in thicker deposits in the basin relative to proximal locations. However, accentuated highs as seen in proximal locations in the present study, were only reproduced by experiments with sustained flows (e.g. Kubo, 2004 and Lamb et al. 2006). Sustained turbidity currents may result from continuation of river discharge during flood events. Yet, surge type flows, such as those initiated by slope failure and responsible for infilling the Peïra Cava outlier (Amy, 2000), may

also be steady for periods of several hours (Kneller and McCaffrey, 2003; Piper et al. 1988; Piper et al. 1999; Talling et al., 2007a). With a relatively steady flow, uniform settling rates could be expected to generate the uniform deposits seen in CB7. However, the reduced thickness in medial sections for CB11-3 and CB5, suggests that these depositing flows were depletive.

The poorly sorted nature of the studied deposits may provide an alternative explanation for the increased bed thickness in distal locations. Flume experiments (Gladstone et al., 1998) and numerical simulations (Salaheldin et al., 2000) have demonstrated that polydispersed sediments with a high proportion of fine sediments (clays, silts and very fine sands) can substantially increase flow efficiency, with a corresponding increase flow run out distances. Beds belonging to Facies Tract III contain mud concentrations up to 4.7% (CB5 Table 3-2) and significant portion of silt and very fine sand. It is proposed that surge-type flows, highly efficient and sustained for a period of time traversed the Peïra Cava outlier. Proximal locations were dominated by the surging head, while medial localities recorded the depletive phases of the flow and generated deposits with reduced thickness (i.e. CB11-3 and CB5). However, due to the high efficiency of the flow, the flows encountered the confining slope. The resulting deceleration preferentially deposited thicker beds on the upstream side of the topography. The interaction with the confining topography is further postulated to have created an upstream migrating sediment-bearing suspension cloud and internal waves, whose passage resulted in subtle fluctuations in flow velocity and sediment concentrations, and the deposition of repetitive sequences of facies (Figure 3-23).

3.6 Summary.

The present study analysed vertical and lateral transition in bed character to understand how DWMS are deposited in a topographically confined basin. The most widely accepted models of DWMS include: 1) continuous aggradation beneath quasi-steady turbidity currents; 2) high sediment fallout beneath surge-type turbidity currents; 3) sandy debris flows; and, 4) post-depositional removal of structured intervals. Newly collected data from eight laterally correlated beds in the Peïra Cava sub-basin was analysed and compared to these models to assess their validity and to develop a new model(s). The data shows the presence of three type of massive sand facies: graded massive sands, ungraded massive sands and massive sands with ‘patchy’ texture. The graded and ungraded massive sands are interpreted as deposits of high-concentration near bed layers beneath surge-type turbidity currents. These layers are characterised by hindered settling, grain to grain interaction and frictional freezing from the base up. Deposition is capacity driven since the poorly sorted nature indicates size segregation of grains was inhibited in the near bed layers. This also accounts for the crude normal grading

observed in many massive sand intervals. The ungraded intervals are likely to be deposited where concentrations exceed a limiting value (45% based on experimental studies) in the near bed layers, which completely suppress turbulence and allow frictional interlocking of grains. In contrast, the massive sands with 'patchy' texture are here interpreted to be deposits of liquefied debris flows. Dissipation of excess pore pressure via slow convection and elutriation results in remobilisation of sediments creating the 'patchy' texture. The limited extent of the facies, as well as the presence of disorganised mud-clasts, reinforces this interpretation.

Three downslope Facies Tracts are recognised in the eight studied beds. Facies Tract I and II contain dominantly ungraded massive sand (DWMS sensu stricto) and massive sand with 'patchy' texture in distal locations, respectively. Facies Tract III contains repetitive occurrences of ungraded and graded massive sand in distal locations. When compared to vertical and lateral profiles predicted by existing models, the Facies Tracts show subtle, but significant deviation in internal bed character and sandbody geometry. This is mostly likely a consequence of interaction with the confining topography, sediment concentration, clay content, flow velocity and grain size distribution in the flow. Markov chain, supplemented by entropy analysis, demonstrates that the most consistent vertical sequences comprise the Tb-Tc divisions of Bouma (1962), which forms a downslope thinning 'cap' to the massive sands beneath it. In *proximal* Markov grouping, thick spaced stratification and conglomeratic facies underlie the massive sands, such that the vertical profiles bear similarities to the models of Lowe (1982), Mutti (1992) and Kneller and McCaffrey (2003). These models describe unsteady and spatially depletive flows. Departures from these models is reflected by the absence of the silt fraction, presence of multiple grain size breaks and repetitive occurrence of certain facies. In contrast, vertical profiles in *medial* and *distal* grouping bear little resembles to vertical profiles predicted by existing models. All vertical profiles in the present study show a relative increase in the proportion of massive sand facies compared to the structured facies (SL2, SL1 and SR). Locally, the structured 'cap' is absent in some distal sections. While Facie Tract III displays repetitive sequences of ungraded and graded massive sands, and stratified sands.

The relative increase in massive sand proportion, particularly ungraded massive sands compared to the structured interval (SL2, SL2 and SR) as you move downslope is also incompatible with existing models. Three mechanisms have been proposed to account for the dominance of the three massive sands facies distally. Body transformation may account for the distal transition from graded or ungraded massive sands to massive sand with 'patchy' texture observed in Facies Tract II. This transition, along with the presence of discontinuous, sub-parallel zones of mud clasts and elevated mud content in SM3 suggests that an initial concentrated turbidity current transformed downslope to a liquefied debris flow. *En-masse* deposition, coupled with low hydraulic diffusivity, ensures elevated pore pressures is maintained as the sediments come

to rest. Slow convection and elutriation of fines in response to dissipation of pore pressures remobilise sediments to create a 'patchy' texture. In turn, gravity transformation may account for the distal presence of ungraded massive sands in Facies Tract I. Fluctuations in the shear Richardson number and the dimensionless fall velocity with respect to each other can modulate near bed turbulence in flows, leading to flow self-stratification and deposition of massive sands (SM1 and SM2; Cantero et al. 2009, 2012a and 2012b). Both of these flow transformations can be induced by changing slope angle on approach to confining topography. Interaction with confining may also account for the repetition in facies seen in medial and distal localities of Facies Tract III. The relatively uniform to downslope thickening bed geometries in Facies Tract III suggests large, highly efficient flows traversed the basin intermittently. Internal waves, generated because of flow deflection and reflection, propagated across the body and tail of the flows. Subtle variations in flow velocity and sediment fallout rates, associated with their passages, is surmised to create the repetitive graded and ungraded massive sands. Further away from the slope, where flow transformation may not have generated a sufficiently concentrated flow, a repetitive occurrence of thin-spaced stratification may intermix with the massive sands.

Grain size breaks are also common features in the eight beds, and have until recently (e.g. Talling et al. 2012), not been included as part of a facies model. These grain size breaks demonstrate that flows were not single surge type waning flows (i.e. Type II and III) with uniform vertical sediment concentrations (Type I and IV), but rather highly stratified with multiple pulses. Locally, grain size breaks (Type II and III) separating massive sands may indicate post-depositional removal of structured intervals. Further downslope, the reduced abundance or lack of Type I to III grain break in beds suggest the flows organised themselves into simple surge structures. In these distal beds, Type IV grain size breaks typically separate the massive interval from the overlying mud, indicating bypass of finer non-cohesive grains which may have otherwise been reworked into structured intervals

External bed geometries for Facies Tract I and II thin downslope. Based on previous studies, this shape appears to be a salient feature of depletive flows. A proximal thickness maximum observed in these beds indicates hindered settling and grain-to-grain interaction was active, at least in a near bed high-concentration layer. In contrast, bed geometries in Facies Tract III maintain their thickness or thicken distally, indicating either uniform flow conditions and/or sediment by-pass due to enhanced flow efficiency. In the latter case, distal thickening of beds can be attributed to longer runout distances and preferential deposition on the upstream side of the topographic barrier.

Chapter 4– Textural Trends in Graded and Ungraded Deep Water Massive Sands (DWMS).

4.1 Introduction

The structureless nature of massive sands is the main reason why studies investigating their emplacement mechanisms have encountered difficulties, particularly in outcrops of limited extent. Therefore, in this contribution, the textural parameters (i.e. grain size, sorting and fabric) of graded and ungraded massive sands will be analysed to characterise grain and bed-scale heterogeneity and to elucidate processes responsible for their deposition. Part of this analysis includes characterising the zircon grain size distribution which may have experienced differential settling processes compared to the framework component. It is anticipated that such an analysis can be used to infer reservoir quality, since grain texture and by extension depositional processes, are the primary control on porosity and permeability. The massive sands selected for this study belong to the Grès de Peïra Cava (SE France) and the Numidian Flysch (northern Tunisia) formations. An automated image analysis method, using backscattered electron images, was employed to help fulfil this aim.

4.2 Geological Background.

Thick to very thick massive sandstone beds from the Numidian Flysch Formation outcropping in northern Tunisia and the Grès de Peïra Cava outcropping in SE France were chosen for detailed textural analysis. What follows is a brief tectonostratigraphic summary of these two basins and a description of the character of the sediments within them.

4.2.1 Tunisia.

Tectonic and Stratigraphic Setting. The Oligo-Miocene Numidian Flysch of Northern Tunisia represents the most widespread tectono-stratigraphic unit in the Western Mediterranean. It stretches some 2500km from the Betic Cordillera in southern Spain, through the Rif-Tellian domains of northern African, and eastwards into Sicily and mainland Italy (Figure 4-1; Wezel, 1970). The thickness of the formation varies from a few hundred metres to over 3000 m. It was deposited in an east-west trending foreland basin, the Mahgrebian Flysch Basin (MFB) that constituted the southern branch of the western Tethys Ocean, together with its continuation in the Lucanian Ocean (Guerrera et al., 2012; Guerrera et al., 2005). The northern margin of the MFB was an active margin that consisted of a southward verging accretionary wedge, underlain by European crustal blocks, which rode above a northward subducting oceanic crust. The

southern margin formed the passive margin to the African Craton, consisting of thick Mezosoic to Cenozoic age platform carbonates and shallow marine deposits (Dewey et al., 1989; Guerrera et al., 1993; Guerrera et al., 2005; Johansson et al., 1998a).

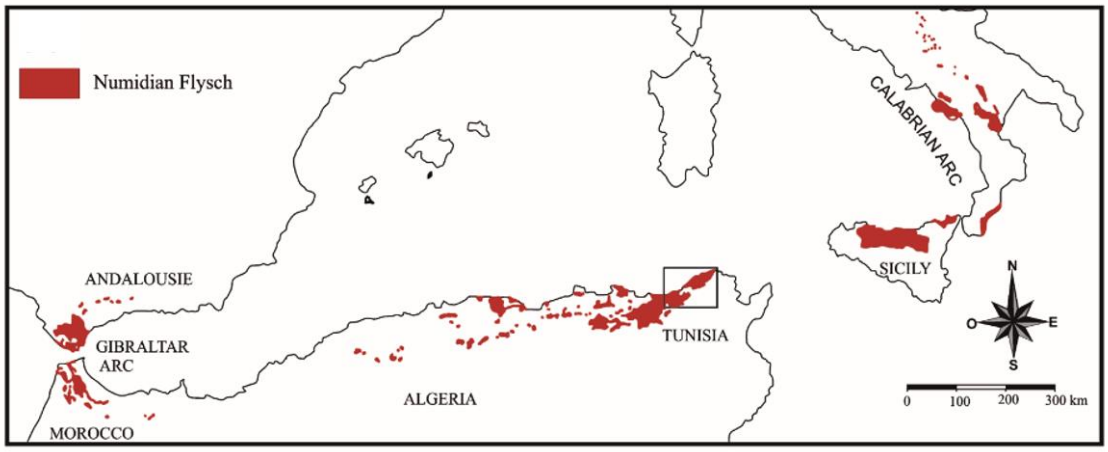

Figure 4-1: Extent of the Numidian Flysch tectono-stratigraphic unit in the Western Mediterranean (modified after Fildes et al. 2010).

The geological evolution of the MFB since its conception exhibits a complicated alternation of compressional and extensional events that are constrained within the overall convergence of the African and Eurasian plates (Dewey et al., 1989). The basin formed during the Cretaceous, and from early Eocene onwards, was progressively translated to the southeast as a result of slab roll back, fragmentation and rifting of crustal blocks (variously termed the Meso-Mediterranean Terrain) from the southern European margin and opening of new basins north of the MFB. This southeast translation caused associated compressional tectonics along the northern African margin, resulting in the formation of a peripheral bulge and the northward tilting of the shelf area towards the fronting foredeep. The main phase of Numidian deposition is likely to have occurred during the Oligocene and early Miocene, with a tentative source area towards the south from the African Craton (Figure 4-2A; Riahi, 2011; Thomas, 2011). Deposition ceased during the middle Miocene when compression along the African Margin, related to the emplacement of the Meso-Mediterranean Terrain, induced the detachment and southward displacement of the Numidian Flysch to its present day location in the Tellian domain of northern Tunisia (Figure 4-1 and 4-3A; El Euchi et al., 2004; El Maherssi., 2001).

Numidian Flysch in Northern Tunisia. In northern Tunisia, the Numidian Flysch can be seen outcropping in the Kroumirie mountain range, trending northeast, parallel to the Mediterranean coast (Figure 4-3A). Stratigraphically, the formation can be sub-divided into three members: (1) the predominantly mud-rich Zouza Member; (2) the sand- and conglomerate-rich Kroumirie Member; and (3) the siliceous mud-rich Babouche Member (Riahi et al., 2010; Rouvier, 1977; Torricelli and Biffi, 2001). The three members were originally considered vertically stacked, resulting in a formation that was greater than 2000 metres in thickness. However, in recent

studies, the Zouza and Kroumirie members are considered coeval, based on biostratigraphic and sedimentological characteristics, with the vertical superposition attributed in part due to the tectonic activity associated with the south-east translation of the MFB (Riahi et al., 2010; Torricelli and Biffi, 2001). Present sedimentological models indicate that the formation represents an upper slope environment (Figure 4-2B), with the sediments being deposited by quasi-steady and waning turbidity currents and hemipelagic processes, with a minor proportion of other downslope processes (e.g. debris flows; Fildes et al, 2010; Riahi, 2011; Thomas, 2011).

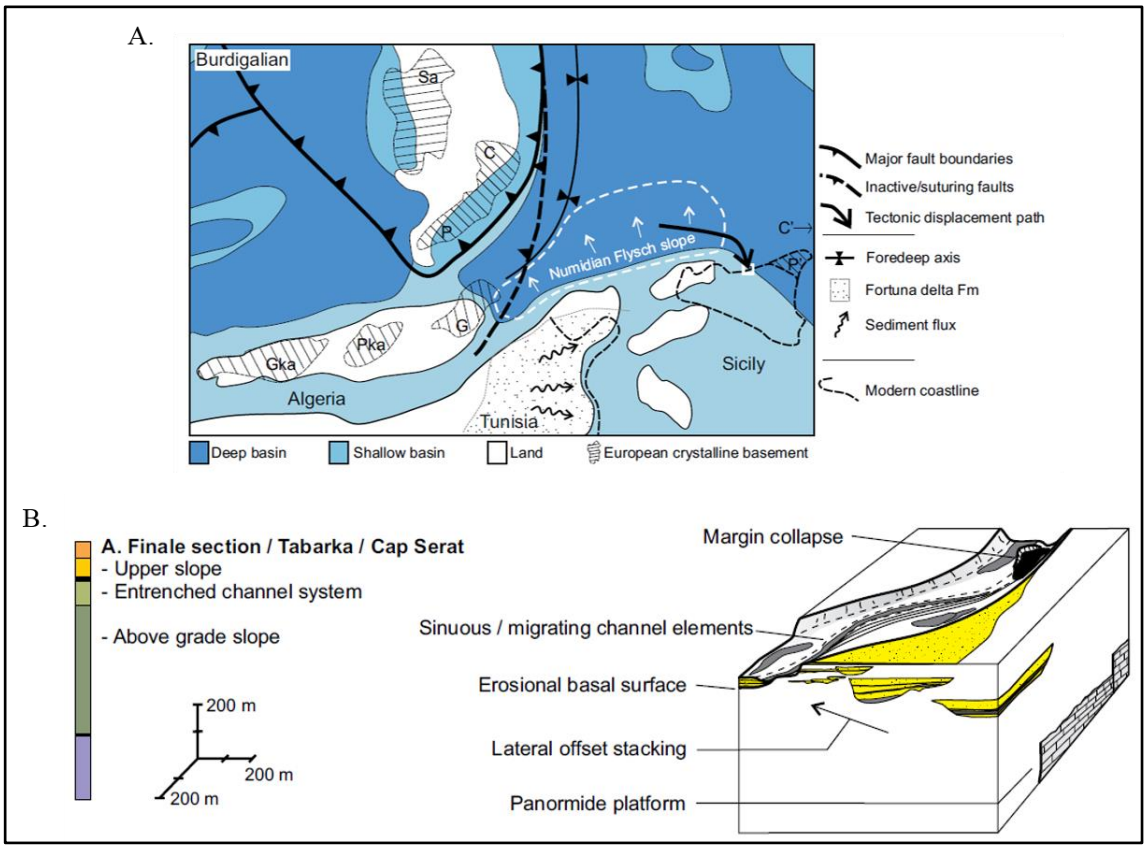

Figure 4-2: (A) Palaeographic map of the Tunisian Numidian Flysch slope along the eastern section of the Mahgrebian Flysch Basin (B) Conceptual model of the depositional system for the Numidian Flysch in the Cap Serat area. The Cap Serat area represents an upper slope environment containing multiple channel complex that are offset vertically and laterally. After Thomas (2010).

The area under investigation is located at the northeastward jutting headland Cap Serrat, along the Mediterranean coast, where ~1400 m of the stratigraphy is exposed (Figure 4-3B, C). The exposures forms part of the Kroumirie Member and have been dated as Early Miocene in age (Riahi, 2011; Torricelli and Biffi, 2001). The stratigraphy contains a high proportion of thick to very-thick massive sandstone layers that can be identified according to Stow and Johansson's (2000) massive sand facies association (MSFA). These sandstone layers are ungraded and completely devoid of any internal sedimentary structures. Bouma division Tb, Tc and Td are locally present in the upper parts of some layers, but may only represent the waning tail end of the depositing flow. A 15 m thick massive sand facies association at the northern most tip of Cap Serrat was logged and sampled (Figure 4-3C). The section can be traced for 3 km laterally,

before gradually pinching out, and when considered in terms of the overall sedimentological characteristics of the succession, has been interpreted as presenting a proximal upper slope channel environment (Fildes et al., 2010; Riahi, 2011; Thomas, 2011). Palaeoflow indicators are highly variable, ranging from 150-200° towards the SE and SSW (Riahi, 2011). Three thick to very thick massive sandstone layers (Figures 4-3 and 4-5) were selected from the 15 m interval to investigate the vertical changes in textural parameters of both the framework and zircon component to interpret flow hydrodynamics.

Petrography of the Numidian Flysch. The Numidian Flysch samples are mineralogically mature to supermature with a mean Q, F, L values of 98%, 1% and 1% respectively (Fildes et al. 2010; Riahi, 2011; Riahi et al. 2010). The mica content is less than 5% and the heavy mineral faction is between 2-6% (*ibid.)*. In terms of the framework component, monocyrstalline quartz is the dominant form with values up to 80%, while the polycrystalline quartz is more common in coarser samples, ranging up to 40%. The heavy mineral assemblage is dominated by zircon (45%) and tourmaline (40), with a lesser proportion of rutile (15%). Garnet, anatase, monazite, titanite, apatite, glauconite and chlorite are also present as accessory heavy minerals (Fildes et al. 2010). Based on these petrographic characteristics, as well as the widely published Eburnian and Pan-African ages of the zircon grains (Fildes et al., 2010; Gaudette et al., 1975; Riahi, 2011), a cratonic source region in northern Africa seems the most plausible source for the detrital sediments (Alcalá et al., 2013; Thomas, 2011).

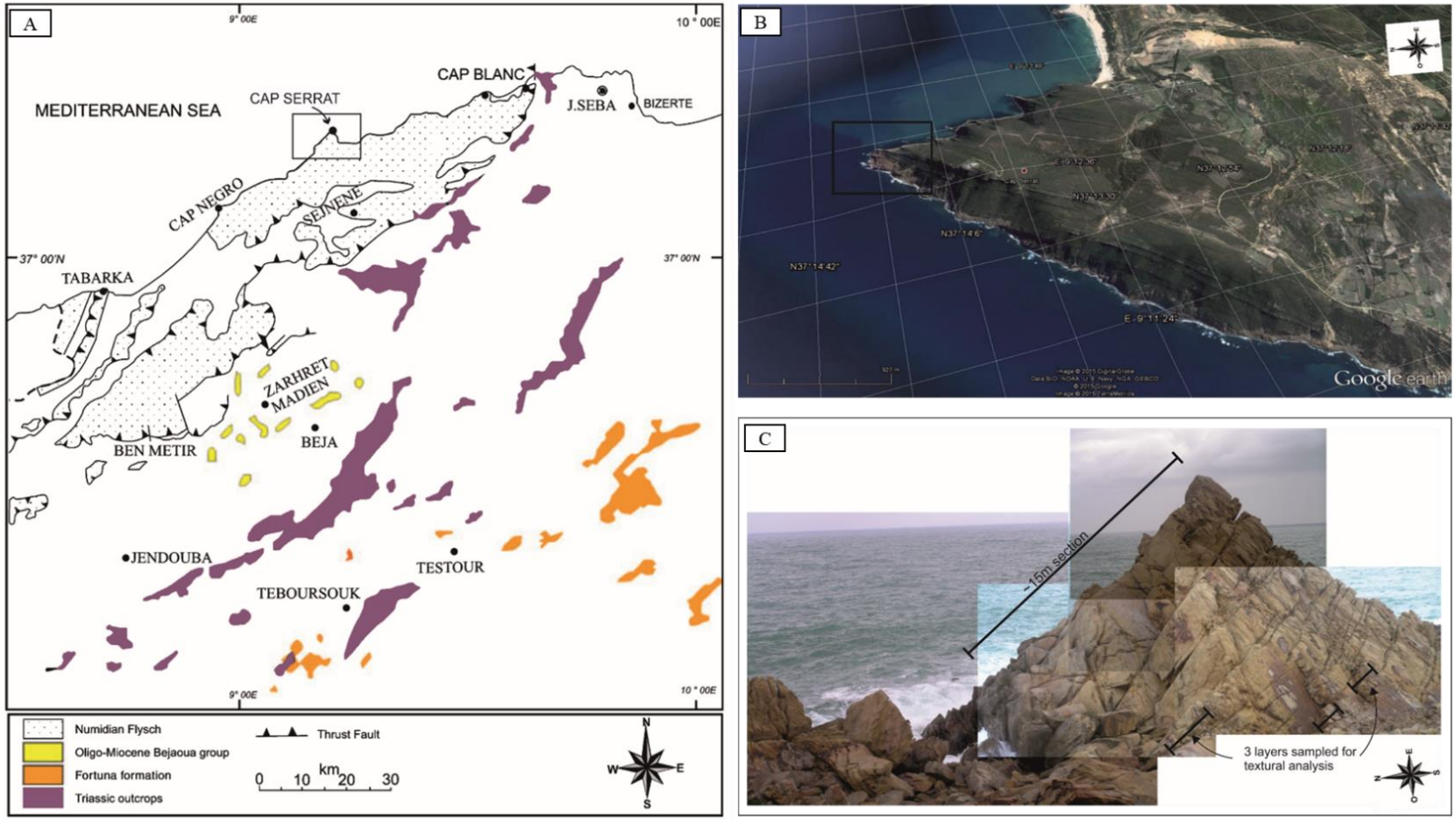

Figure 4-3: Geographic distribution of the Numidian Flysch along northern Tunisia (A; modified after Fildes et al. (2010).). (B) Satellite image of the Cap Serrat headland where approximately 1400 m of the Kroumirie member is exposed. Laterally extensive MSFA can be seen trending parallel to the coast, which have been interpreted as upper slope channel deposits. (C) Photograph of the sand-rich interval that was logged and sampled for textural analysis.

4.2.2 France.

Tectonic and Stratigraphic Setting. A detailed tectono-stratigraphic description of the Grès de Peïra Cava is provided in Chapter 3. For the purpose of this study, four thick to very thick massive sandstone beds (Figure 4-4 and 4-5) were selected to investigate the vertical changes in textural parameters of the framework component to interpret flow hydrodynamics. The beds were selected as they contain predominantly ungraded and graded massive intervals, whose origin is difficult to reconcile in terms of the current depositional models of the Peïra Cava outlier. The beds were also selected as they provide an opportunity to compare and contrast textural trends of graded and ungraded intervals within the same bed.

Petrography of the Grès de Peïra Cava. The Grès de Peïra Cava is predominantly arkosic with Q, F, L values ranging from 43-61% (av. 50%), 30-50% (av. 40%) and 5-20% (av. 10%), respectively (Jean, 1985; Mulder et al., 2010). However, no consistent mineralogical trends are observed from the base to top of the Grès de Peïra Cava succession. Stanley (1961, 1963) demonstrated that the mineralogy was closely related to the grain size distribution of the sample. In fact, the variability in a single normally graded sandstone layer is as great as that observed throughout the formation (*ibid*.). The framework component is invariably angular to rounded, being more angular in the fine-tail distribution (Apps, 1987; Jean, 1985; Mulder et al., 2010). Average percentages of monocrystalline and polycrystalline quartz are 17-57% and 3-32%, respectively (*ibid.*). Both plagioclase and alkali feldspar are present in approximately equal proportion. The plagioclase is represented by the sodium-rich albite and oligoclase variety, while alkali feldspars are represented by orthoclase (locally displaying perthitic texture), sanidine and microcline (Apps, 1987; Garcia et al. 2004). Lithic fragments are predominantly granular and larger, and comprise mainly metaquartzite, granite, gneiss with minor amounts of volcanic and sedimentary rocks (arkosic sands, shales and carbonates; Apps, 1987). The mica content is significant in fine-grained samples, reaching up to ~30%. The heavy mineral fraction consists primarily of Fe-garnet, apatite, zircon, rutile and monazite in varying proportion, possibly reflecting a complex hydrodynamic equivalence with the framework component (Garcia et al., 2004). Diagenetic features include partial to complete dissolution of feldspar grains and limited development of quartz overgrowth in most samples. Based on these petrographic characteristics, as well as quartz thermoluminescence study by Ivaldi (1987), a southern granite-dominated provenance (i.e. Corsica-Sardinian massif) is the most likely source of the Grès de Peïra Cava and the wider Grès d'Annot (Garcia et al., 2004; Jean, 1985; Stanley, 1961, 1963; Stanley and Bouma, 1964).

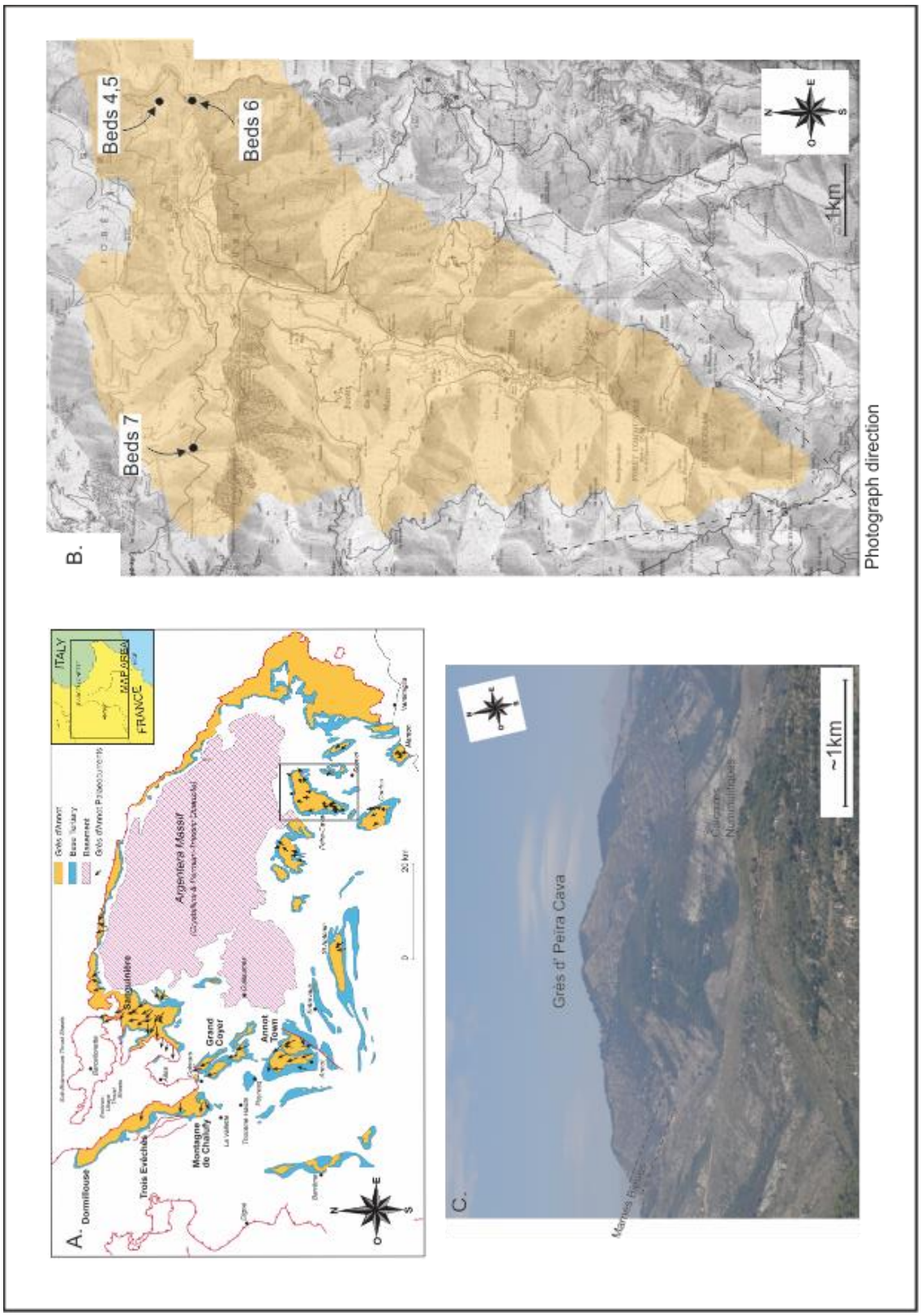

Figure 4-4: Geographic distribution of the Grès d' Annot (A) and a close-up topographic map showing the extent of the Grès de Peïra Cava in the Provence-Alpes-Côte d'Azur region and the approximate location of the logged beds analysed as part of this study (B). (C) Photograph taken looking north down the axis of the Peïra Cava syncline and the approximate position of the onlap surface with the Marnes Bleues. (A) modified after Apps (1987).

4.3 Methodology – Digital Image Analysis.

A fully automated digital image analysis method was employed to obtain quantitative information from the massive sands. Digital image analysis refers to a series of computer operations that are applied to an image to extract quantitative information (Fortey, 1995; Francus et al., 2004). The standard series of operations include; 1) image acquisition, 2) image pre- and post-processing, and 3) image measurement. While the technique is not a recent development in the field of sedimentology, it has been slow to find widespread use for textural studies using thin sections. The main reason for this is due to the heterogeneous nature of the image to be analysed. For example, it is often difficult to distinguish boundaries between grains or between grains and cement. This introduces error into the measurement; a problem that was encountered in this study and discussed in detail in section 4.3.3. The operations that are applied to the images to extract information must therefore be tailored to the characteristics of the sample and methods used to acquire the image. The following sections describe the process of logging and collecting samples from the massive sands, and the subsequent operations used to derive quantitative textural information from images produced from the collected samples.

4.3.1 Sandstone Beds and Sample Preparation.

Seven thick (>50 cm) and very thick (>1 m) sandstone beds were selected from the Grès de Peïra Cava and the Numidian Flysch formations for textural analysis (Figure 4-6). They can be roughly divided into ungraded and graded massive beds. Each bed was logged at a scale of 1:10. Grain size was measured every 2 – 5cm with a grain size comparator, which in this study has biased the measurements to the coarsest 5% of the grain size distribution (Amy and Talling, 2006; Talling et al., 2004, Tucker, 1988). The beds were sampled at pre-selected intervals along a vertical section, with each sample marked with a way up indicator, dip and strike of the bed, and the palaeo-flow directions to ensure proper orientation for textural analysis. The palaeo-flows directions were measured to allow interpretation of potential links between flow direction, grain fabric and depositional processes. Polished thin sections parallel and perpendicular to the bedding plane were prepared from thirty-nine samples (totalling 78 slides). Despite the fact that textural data obtained from thin sections is less accurate than full grain techniques (i.e. laser diffraction analysis), certain procedures can be followed to ensure the validity of the results (see section 4.3.5 for detail). Under most hydrodynamic conditions, the preferred orientation of the a-axis is parallel or at a low angle to the bedding plane, hence the choice of bedding-parallel sections is likely to produce the most accurate results (Baas et al., 2007; Johnson, 1994). The choice of sections perpendicular to the bedding plane was based on the mean grain orientation measured on the bedding parallel plane (ibid). This will provide grain inclination angles relative to the bedding plane. An estimate of angular error associated with the sampling programme, as well as with the choice of perpendicular sections, was not calculated. All textural measurements were performed on SEM images of the sample.

Figure 4-5: Photographs of the beds logged and analysed as part of this study. Beds from Tunisia are found in the Car Serrat promontory, while beds from the Grès de Peïra Cava outcrop in the northern field areas of the outlier (see Figure 4-4B for locations).

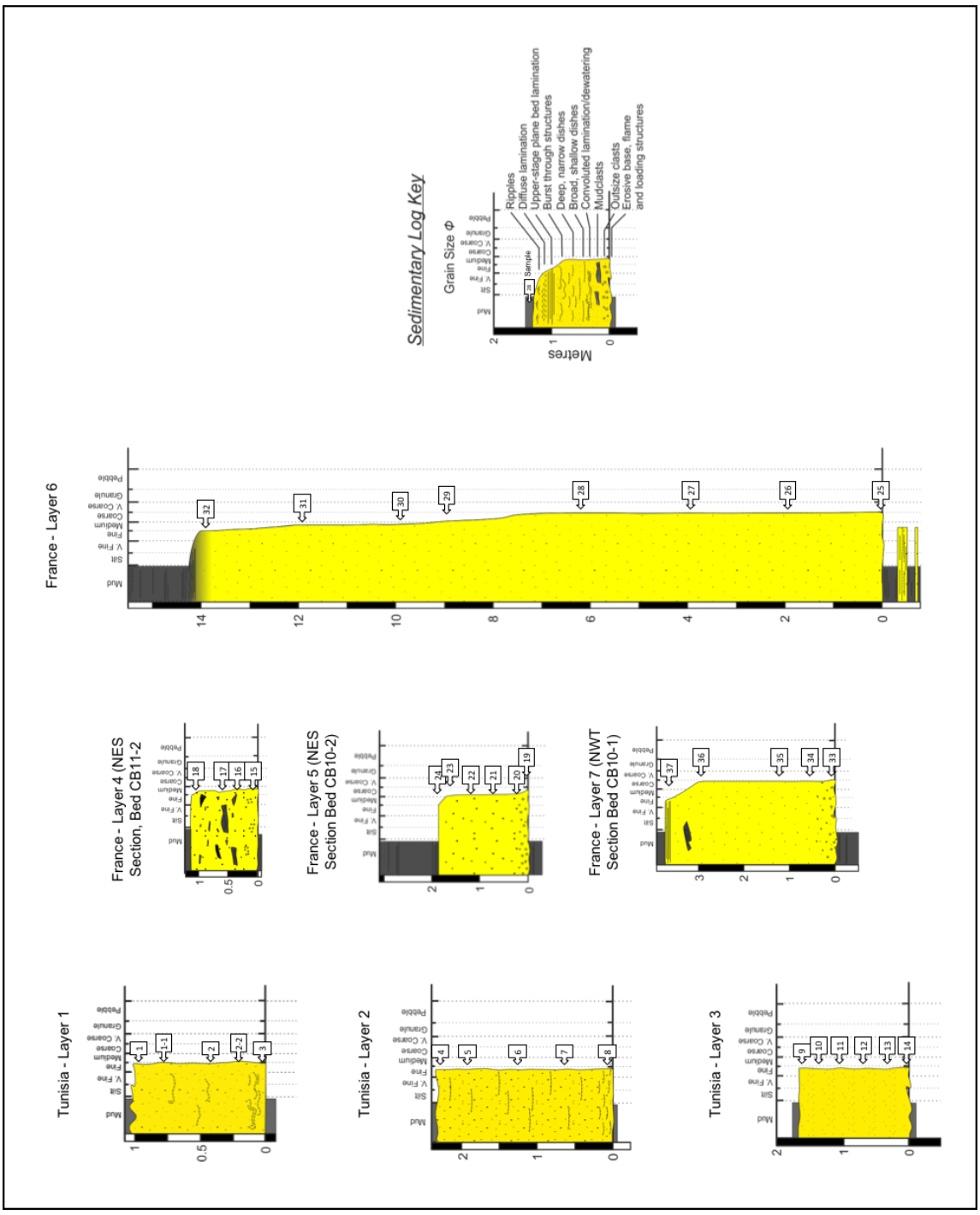

Figure 4-6: Detailed logged sections from the Numidian Flysch in Tunisian and the Grès de Peïra Cava n France. Sections were logged at a scale of 1:10 in the field and grain size measured every 2 cm with a grain size comparator. Sample were collected at regular intervals vertically and their locations marked with an arrows.

4.3.2 Image Acquisition.

SEM Images. Bedding parallel and perpendicular sections from the seventy-eight samples were prepared as carbon-coated polished thin sections for microprobe observation. The samples were analysed using a FEI Quanta 650 field-emission gun scanning electron microscope (SEM), under high vacuum, at 20 kV, with a spot size of 4.5 µm and a working distance of 10mm. High-resolution, large-format 256-level grayscale images of the samples were acquired using the Modular Automated Processing System (MAPS) software from FEI. Each image was

acquired as a series of individual tiled backscattered electron (BSE) images with a width of 259 μm and a pixel resolution of 768x512. Individual image tiles had 10% overlap, and were subsequently checked for alignment (and manually adjusted where necessary), before being automatically stitched and saved as an uncompressed RAW file to prevent data loss. The combination of MAPS and field-emission SEM provided a stable platform with zero-drift, where illumination was centred and even, facilitating the acquisition of high-quality images. Furthermore, in all samples the image plane was parallel with the object plane and the spatial resolution of the image was taken to be constant across the entire image and required no orthorectification.

Zircon Analysis. Zircon analysis was performed only on the Tunisian samples due to the homogeneous mineralogical character of the deposits, which made identification and measurement of the zircon grains straight forward. All thirty-two slides from the Tunisian beds were examined using the Quanta 650 SEM with a BSE detector in combination with an Oxford Instruments X-Max^N 150 mm elemental dispersive X-ray detector. The SEM was set at 20 kV under high vacuum, with a spot size of 3.5 and a working distance of 10mm. Images were acquired at a magnification of x400, a horizontal field of view of 518 μm, and the contrast and brightness set to 67 and 96, respectively. Oxford Instruments INCAfeature software was used to analyse zircon grains within the sandstone samples. Images were filtered and thresholded so that zircon grains were segmented. The software was used to filter out features smaller than 250 pixels (~9.25 μm equivalent circle diameter, ECD), with a guard zone set to 100 pixels (51.86 μm). Frames were acquired at a resolution of 1024 x 704, using the BSE detector, with a first pass set to 2 microseconds. In order to reduce the number of false positives, zircon detection was thresholded between 170 and 255 during the EDX set-up. A post-processing set-up of five 'close' procedures was also used to improve selection of whole grains. For elemental analysis, livetime was set to 0.10 secs with a process time of 5 s and the whole area of each detected particle was analysed. Finally, a zircon distribution map was created by selecting a representative area of the thin section as a four-point rectangle, and all fields were selected to be scanned with a 10% overlap. After acquisition, duplicate scans of the same grains, as well as images with multiple grains were manually removed so as not to bias the results. In addition, other heavy minerals (rutile, ilmenite, monazite, etc.) that had been unintentionally analysed were also removed, leaving whole zircon grains.

4.3.3 Image Pre- and Post-Processing.

The image processing procedures involved image *pre-processing, classification* (segmentation) and *post-processing* steps, and were all performed with the commercially available image analysis software Scandium Digital Imaging Solutions. The pre-processing steps involved applying various filters to the images to reduce 'noise' from uneven illumination of the polished thin section, random electronic noise, image distortion during BSE image acquisition and

inherent heterogeneity in sedimentological samples (Francus, 2004). Since the working distance, spot size, magnification, focus and spatial resolution were kept constant during image acquisition, no significant orthorectification was required. As such, only a 3 x 3 median filter was applied to the images to reduce electronic noise. The images were subsequently classified in to grains (white pixels) and matrix (black pixels) on the basis of their grey-level values. The threshold grey-level values were selected after visual inspection of the BSE image histograms and a binary image representing the classification was produced.

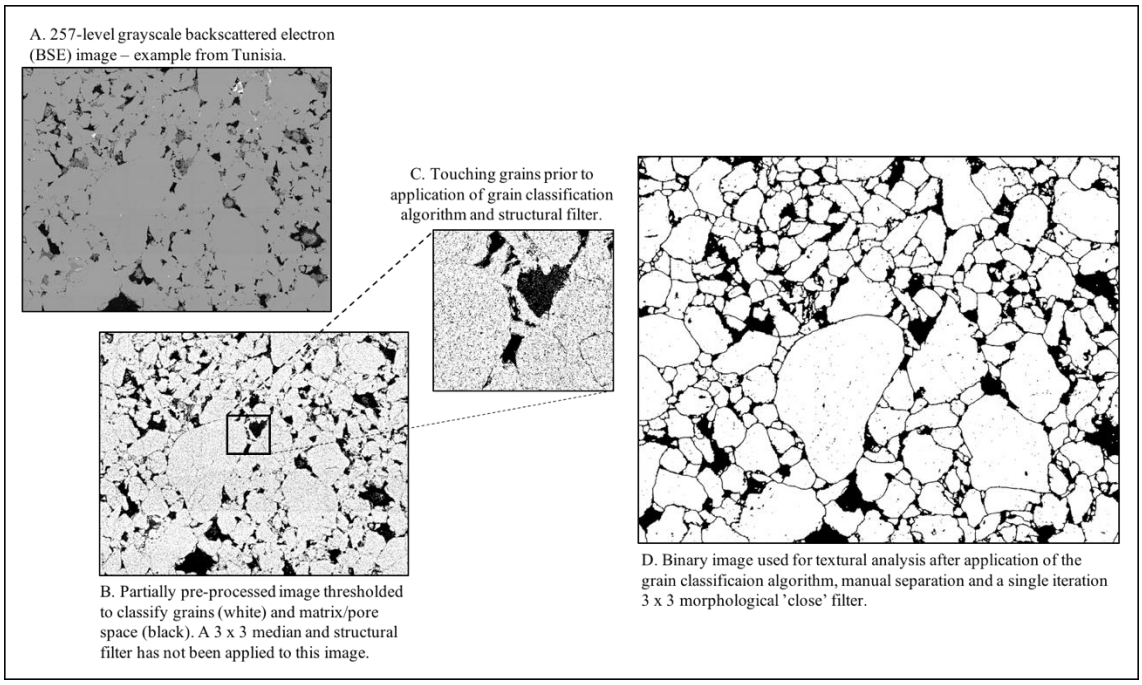

Figure 4-7: Steps involved in the image pre- and post-processing prior to textural analysis of the slides. Due to their simple mineralogy, the Numidian Flysch slides were relatively simply to process. In contrast, the Grès de Peïra samples had significant issues related to grain dissolution and fractures, and required extensive processing steps including manual separation of the grains.

However, the initial classified images were rarely complete and required additional post-processing involving noise cleaning and structural filtering to separate touching grains. This was primarily due to the pressure dissolution and quartz overgrowth, and locally calcite cementation, in all the selected samples. Furthermore, fracturing of grains and weathering of chemically unstable grains had also produced artefact 'boundaries' which required corrections before any analysis could take place. Over the years, many algorithms have been developed to separate touching grains (e.g. (Francus, 1998; Lewis et al., 2010; Seelos and Sirocko, 2005; van den Berg et al., 2002) with limited success. In this study, a simple algorithm was written to aid in separating touching grains after the classification step. Details of the algorithm are provided in Appendix B.

After application of the algorithm, the images were visually inspected to assess the success of the grain separation. Figure 4-7 shows an example of the original grey-scale image, the input binary image and the resulting classified image after structural filtering. The visual inspection

again showed a limited success in separating all the grains. As a result, significant manual modification of the images was required before image analysis. However, since manual separation of touching grains over the entire SEM image was considered impractical, an optimised sampling area was adopted for the study which allows for manual separation that is considered both time and cost effective (see section 4.3.4).

Finally, after manual separation of grains, a single iteration 3 x 3 morphological 'close' filter was applied to the images to separate any remaining grains. A morphological 'close' also has the effect of smoothing objects and filling small holes. As such, only a small kernel size and a single iteration were used so as not to significantly influence the shape of the grains which could later affect grain size and fabric analysis. After the post-processing steps, the images were visually inspected a final time.

4.3.4 Optimised Sampling Strategy.

Due to the limitations associated with the classification algorithm (see above) and because manual separation of touching grains over the entire SEM image was considered impractical, an optimised minimum sample size, whereby a much smaller yet constitutively valid area, was utilised for each SEM image (see below). The concept of representative elementary area (REA) provides an effective means to measure the smallest volume over which a measurement can be made that will yield a statistically stable value that is representative of the whole. In other words, the REA allows us to correlate the effective or macroscopic properties, by studying microscopic constituents and microscopic structures of the sample. It is generally assumed that an REA exists for any sediment aggregate and that the size of it is initially prescribed (Gitman et al., 2007). However, presently little quantitative information exists concerning the minimum REA size needed to study heterogeneous sandstone samples, though a number of attempts have been made.

For the purpose of this study, REA calculations are derived from the experiments of van den Berg et al. (2003). These authors employed a numerical approach to verify the REA of natural sands by investigating laboratory measurements of grain size distribution characteristics of uniform glass spheres (350μm in diameter) under thin section. The authors utilised the ratio of the mean grain size to the REA of the laboratory samples, evaluated by incrementally increasing the REA in the horizontal and vertical direction until a stable mean grain size value was attained to estimate the REA of natural sands. The REA of the collected samples can be estimated by assuming a constant ratio of grain size to the REA over the whole sand size distribution (Van Den Berg et al. 2003). Therefore, when the grain size increases, the REA should also increase in order to be representative of the macroscopic properties. The REA for each SEM image (REA_{Sample}) in the current study is estimated by:

$$REA_{Sample} = \frac{REA_{Ref}}{Mean\ G_{Ref}} Mean\ G_{Sample} \cdot \left[\frac{Res_{Ref}}{Res_{Sample}}\right]^2$$

where REA_{Ref} is the REA of the reference sample (1300^2), Mean G_{Ref} is the mean grain size of the glass spheres (350μm), Res_{Ref} is the pixel resolution of the reference sample in μm/pixels (5.38μm/pixel), Res_{Sample} is the pixel resolution of the samples in this study and Mean G_{Sample} is the mean grain size of the samples obtained from field logs of each bed. Since only the minimum REA was needed for each image, the use of mean grain size derived from field measurements using a grain size comparator was considered appropriate given that the approach tends to skew the measurements towards the coarsest 10% of grains (Talling, 2001; Talling et al., 2004). The term in brackets corrects for the difference in pixel resolutions between the images of the reference sample in the study of van den Berg et al. (2003) and the samples used in this study. The minimum REA for each slide is given in Appendix D. The sensitivity of the REA on the sample grain size distribution was not assessed as part of this study. Thus, uncertainty and error associated with changing the REA of the samples, and the influence this has on the statistical analysis, could not be assessed.

4.3.5 Image Measurement.

Framework Component. Quantitative measurements of the size (μm; min, max, mean diameters, equivalent-circular diameter), shape (aspect ratio, sphericity, elongation, shape factor, convexity), and spatial arrangement of the framework grains were generated automatically using Scandium Digital Imaging Solutions. For grain orientation and imbrication angles, the mathematical angle convention of anti-clockwise from east is used. However, several limitations related to measurement of textural parameters from two-dimensional images have to be addressed first.

First, in terms of measuring grain size from thin sections, since we are dealing with two-dimensional images of three-dimensional features, any measurements must be considered apparent characteristics (Russ, 2011). As noted by Johnson (1994), the long axis of a grain as measured in thin sections is on average underestimated by a factor of 0.2023 Φ. In this study, no corrections were applied to the measurements obtained in Scandium and only the 'raw' data was used for the statistical analysis. In addition, the fine- and coarse-tail of the measured distributions are affected by the resolution of the measurement technique and difficulties in obtaining representative thin section sample of poorly sorted, coarser grained sandstones, respectively. Since the SEM images used in this study provided reasonable precision to measure grains size down to 6 Φ (0.016 mm), the final fine-tail distribution was not significantly truncated. However, quantifying the coarse-tail distribution may be more problematic and coarse-tail grading that is obvious in the outcrop may not be observed in thin sections.

Secondly, and with respect to measuring the apparent grain long axis orientation, certain procedures have been adopted to ensure the accuracy of the measurement. First, only quartz and feldspar grains were measured since they were easily distinguishable from the matrix and cement. Secondly, only grains with a degree of elongation greater than 1.2:1 were chosen for fabric analysis, and then only if the grains had a max diameter greater than 2 Φ (0.25 mm). Using this lower threshold for degree of elongation and grain size has a physical justification as it reduces possible bias in the distinction between spherical and non-spherical grains, and because large elongated grains tend to be less variable in orientation than small, elongated grains from the same sample (Baas et al. 2007). And finally, at least 300 grains were measured to obtain a statistically stable value for the grain fabric of a sample. This lower limit was necessary to keep the maximum expected error in mean grain size orientation to 10° or lower for the majority of the samples (Baas et al. 2007).

Zircon Component. Quantitative measurements for the analysed zircon grains included position (x and y in mm), element composition, area (μm^2), aspect ratio, breadth (μm), orientation, aspect ratio, ECD (μm), length (μm), shape and perimeter (μm). All measurements were acquired in the software INCAfeature. Like the framework component, the quantitative measurements must be considered apparent characteristics. Grain fabric analysis was not performed on the zircon data since they did not meet the grain size criteria (see above).

4.3.6 Statistical Analysis for Grain-Size and Fabric Trends.

Grain Size Trends. Pierce and Graus (1981) argued that the mean grain size using ϕ scale more closely approximated the central tendency of a grain size distribution than the arithmetic mean. As such all grain size measurements were converted to the ϕ scale prior to the statistical treatment of the data. Thus, the mean on the ϕ scale will closely resemble the geometric mean on the metric scale, since this takes into consideration the variable ranges on the metric scale. Error bars on the mean and the standard deviation are based on the standard errors of the mean (σ_m) and the standard deviation (σ_s), respectively, and are calculated as follows.

$$\sigma_m = \sigma/\sqrt{n}$$

$$\sigma_s = \sigma/\sqrt{(2n)}$$

Where σ is the standard deviation of the population and n is sample count.

Sorting was calculated using the inclusive graphic standard deviation and associated descriptive scale (Folk and Ward, 1957). For each sample, vertical trends in the 10th, 50th, 90th and 95th percentile of the grain size distribution, as well as the sorting parameter where analysed to infer flow processes. Prior to this analysis, however, it is necessary to determine whether the grain size distribution of two adjacent samples is statistically different. Hypothesis testing was utilised

to calculate significance level for the median (50th) percentile. The Shapiro-Wilks normality test was initially employed to test for normal distribution within the sampled data (Table 4-1). Since all the samples rejected the hypothesis of normality at the 95% confidence level, the nonparametric Kruskal-Wallis Test was used to assess equal sample median between samples (H_0; the alternative hypothesis (H_1) being that the median of two or more samples is different). Significance levels (ρ-values) were calculated for specific interval ranges, recognised from visual trends in the grain size for a given bed. Simple variations of the boxplot were used to visualise changes in the coarse- and fine-tail, and relate them to sedimentological processes.

Table 4-1: Normality Test for the framework component. All samples reject the hypothesis of normality.

Sample	ρ-values	Sample	ρ-values
1	1.92E-40	19	9.76E-55
1_1	2.23E-44	20	1.65E-50
2	3.68E-46	21	1.54E-51
2_2	1.04E-48	22	4.92E-46
3	2.58E-41	23	7.68E-51
4	6.40E-50	24	1.40E-54
5	1.59E-46	25	7.81E-21
6	1.62E-44	26	4.04E-42
7	3.17E-45	27	8.67E-41
8	3.47E-56	28	5.92E-43
9	4.29E-48	29	4.20E-46
10	1.46E-47	30	5.79E-49
11	6.03E-50	31	2.82E-51
12	8.30E-56	32	9.76E-65
13	4.57E-44	33	3.68E-41
14	1.39E-49	34	1.50E-45
15	2.37E-34	35	8.16E-49
16	2.18E-48	36	1.73E-55
17	3.60E-57	37	1.00E-50
18	3.12E-31		

Grain Fabric Trends. The computer programmes EZ-ROSE and PAST were used for the statistical analysis of the grain fabric data, and their automatic processing functions for the construction of the equal-area circular rose diagrams. The use of an equal area, rather than an equal length rose diagram is preferred since this prevents bias when interpreting the raw directional data without any statistical analysis (Baas, 2000). Prior to the derivation of the descriptive statistics (i.e. mean, variance etc.), hypothesis uniformity testing was employed to test the directional data points for preferential distribution. The 'null' hypothesis tests the directional data for uniform distribution (i.e. non-preferential, chaotic), while the alternative hypothesis states that the directional data has a non-uniform distribution (i.e. preferential). The programme EZ-ROSE was used for the hypothesis testing, which performs three robust and commonly used test statistics: the non-parametric Kuiper (V) and Watson (U^2) tests, and the parametric Rayleigh test (R; please refer to Baas (2000) for the formulas of the test statistics). The Kuiper and Watson tests are non-parametric tests for uniformity in ungrouped orientation data, where no prior assumptions about the underlying distributions dispersion or shape are made (Pewsey et al. 2013). The parametric Rayleigh Test, on the other hand, assumes a von

Mises distribution, which is the circular plane equivalent of the continuous probability distribution and a close analogue to the normal (Gaussian) distribution. The von Mises distribution is characterised by two parameters: (1) the orientation of the mean vectors (*M*) and (2) the dispersion of the unit vectors around the mean. The dispersion of the unit vectors is inverse to the magnitude of the mean vector; the greater the dispersion, the smaller the magnitude of the mean vector, and hence greater the deviation from a non-uniform distribution (Baas, 2000). The Rayleigh Test thus employs the magnitude of the mean vector (*R*) to test the null hypothesis. In all three test statistics, the null hypothesis is rejected if the statistic value is larger than a critical value (significance level of 0.05 and 0.01). For the Watson Test, the critical value at the 0.05 and 0.01 significance level is 0.187 and 0.267, respectively.

The descriptive statistics for each sample, proceeding from the test statistics, is summarised by the following parameters: the mean vector orientation (*M*), the magnitude of the vector mean (*R),* the vectoral concentration (*K*; i.e. strength of the vector mean), the circular variance (S^2_B), the confidence sector for the mean vector (d°) at significance level of 0.05 and 0.01, and the bootstrapped confidence interval (0.05 significance level) using 5000 bootstrap replicates. The rose diagram uses the bootstrapped confidence intervals on the mean, which was constructed using PAST. For detailed formulation of descriptive statistics, please refer to Baas (2000) and the PAST Manual (Hammer, 2017).

4.4 Results.

4.4.1 Bed Character.

Numidian Flysch. Sandstone beds from the Numidian Flysch (Figure 4-6) are upper fine (177 μm) to medium (250 μm) grained and completely devoid of primary sedimentary structures. The beds are ungraded as measured visually with the aid of a grain size comparator and moderately to moderately well sorted. Bed bases are sharp and planar, while the bed tops are marked by a sharp grain size break into the overlying mudstone. No mudstone (or sandstone) clasts are present in all three beds. Dewatering structures are common in beds in 1 and 2. These structures typically consist of shallow and broad dishes with convoluted to concave up wings. Closely spaced convoluted consolidation laminae are present towards the base of bed 1, while bed 2 consists of widely spaced narrower and deeper dishes. No other post-depositional features were observed.

Grès de Peïra Cava. Sandstone beds in the Grès de Peïra Cava (Figure 4-6) are very fine (125 μm) to very coarse grained (2 mm), as measured from a grain size comparator, and largely devoid of primary sedimentary structures (except in bed 7, wherein a thin laminated interval is observed at the top of the bed). Bed bases commonly have dispersed granular material,

however, these are under-represented in the grain size analysis (see below). Grain sorting varies vertically from poorly to moderately sorted, but improves with height from the base of the bed. Normal grading (denoted by facies code Sm_2), where present, is restricted to the base and top of beds, which commonly exhibit coarse-tail and distribution grading, respectively. The thickness of these graded intervals is variable, but typically < 30 cm in beds 5 and 7, and > 1 m in bed 6. In bed 6, an anomalous non-cyclic repetitive sequence of ungraded and graded intervals is seen in the top six metres (see Chapter 3 section 3.4.2 for detail). Grading is not clearly recognised in bed 4 due to the presence of a patchy texture, which is discussed in more details below. Mudclasts are only present in bed 4 and 7, where they occur as tabular clasts ranging between 10 and 40 cm in diameter. They predominantly occupy a position in the middle or the top of the bed with bed parallel orientations. In the former bed, the mud clasts occur in nested discontinuous zones sub-parallel to bedding as dispersed graded clasts (Type B4; Johansson and Stow, 1995), while in the latter, they are isolated floating clasts (B2).

Figure 4-8: Outcrop image of the 'patchy' texture of bed 4. The patchy texture consists of irregular juxtaposition of better sorted finer and poorly sorted coarser material. Talling et al. (2013) interpreted this texture as a record of slow excess pore pressure dissipation from a liquefied debris flow.

Unlike beds 5, 6, and 7 where certain intervals within the bed show distinct grading patterns, grading trends in bed 4 are highly erratic. This is due to the patchy nature of the grain size (Figure 4-8 and denoted by facies code Sm_3) within the bed, which consists of irregularly juxtaposed patches (5 to 10 cm diameter) of poorly sorted coarser and better sorted finer material. This texture is most perceptible towards the base of the bed, below the nested discontinuous mud clast zone. As a result of the patchy texture, the vertical sorting trends is also visually highly erratic. The mudstone clasts vary from small pebbles (4 mm) to cobbles (< 40 cm) in size and occur sub-parallel to bedding. Overall, the bed shares many similarities to the swirly or patchy massive sandstone facies (CS 7) of Talling et al. (2012) and Talling et al. (2013). The patchy texture is unlikely to have been created by dewatering processes, since no dish, pipes and/or convoluted lamination structures were observed. The observable texture also

negates post-depositional destruction of structures/conventional grading by bioturbation. Thus it is likely that the patchy texture is a primary depositional structure of the sediment flow. While these beds do not fit the definition of DWMS *sensu stricto* Stow and Johansson (2000), their lack of primary sedimentary structures justifies their inclusion into the DWMS or MSFA.

Due to the scale difference between the irregular grain size 'patches' and standard thin section slides, it was impossible to collect representative textural data for bed 4. Even if larger thin sections (see Garton and Mcllroy (2004) for detail) were created and analysed as part of this study, the use of a single REA window in this study would have prevented a more thorough analysis of the textural parameters. As such, the quantitative textural results and subsequent analysis may not reflect the true depositional processes. Their origin is treated in a more complete manner in Chapter 3.

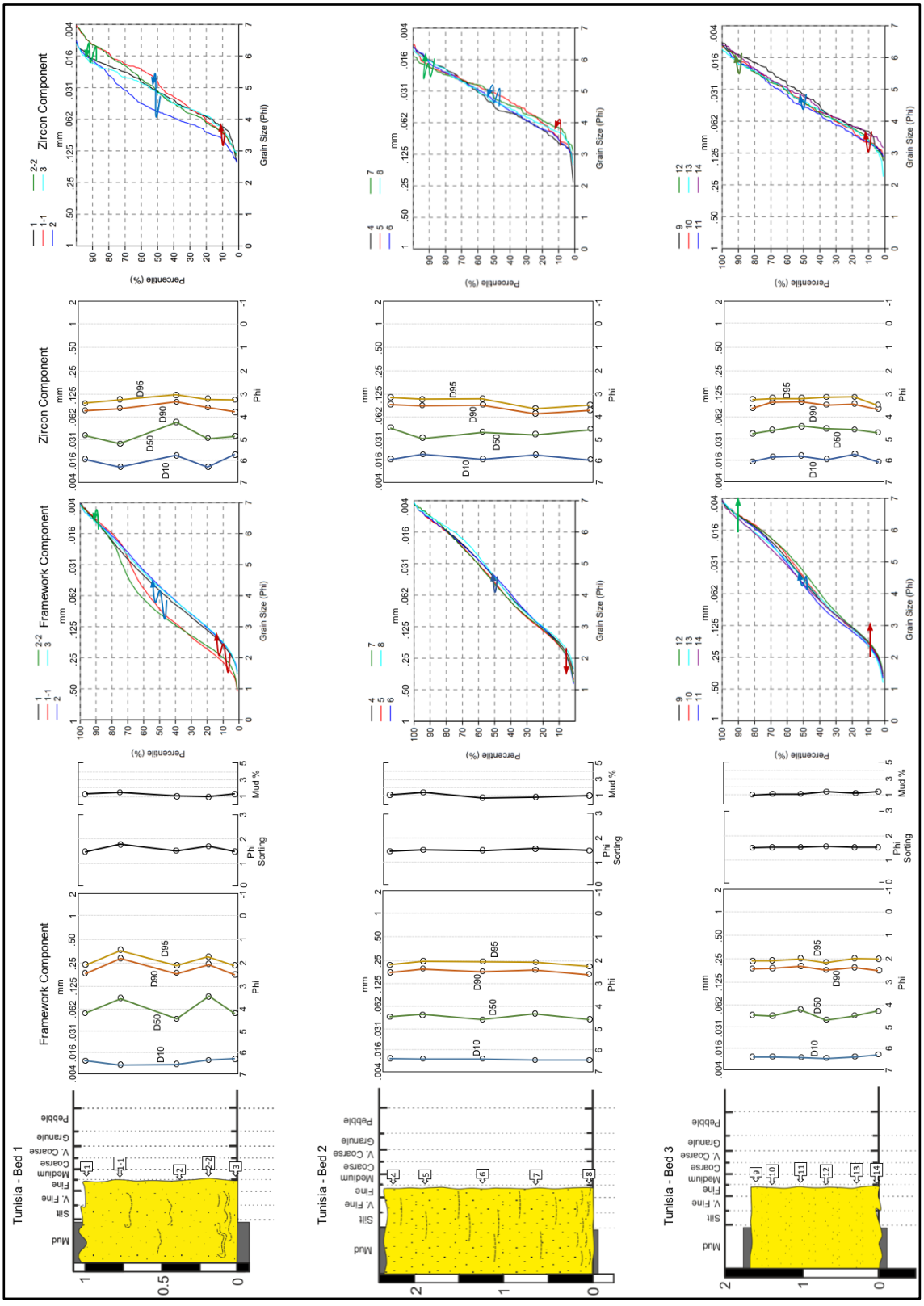

Figure 4-9: Grain size analysis of the DWMS beds from the Numidian Flysch. Data was analysed using the phi scale. Sample locations are given in the boxes on the sedimentary log. D10, D50, D90 and D95 correspond to the different percentiles of the grain size distribution in both the framework and zircon component. Coloured arrows indicate the vertical variation in the coarse-tail (red), median (blue) and fine-tail (green) components.

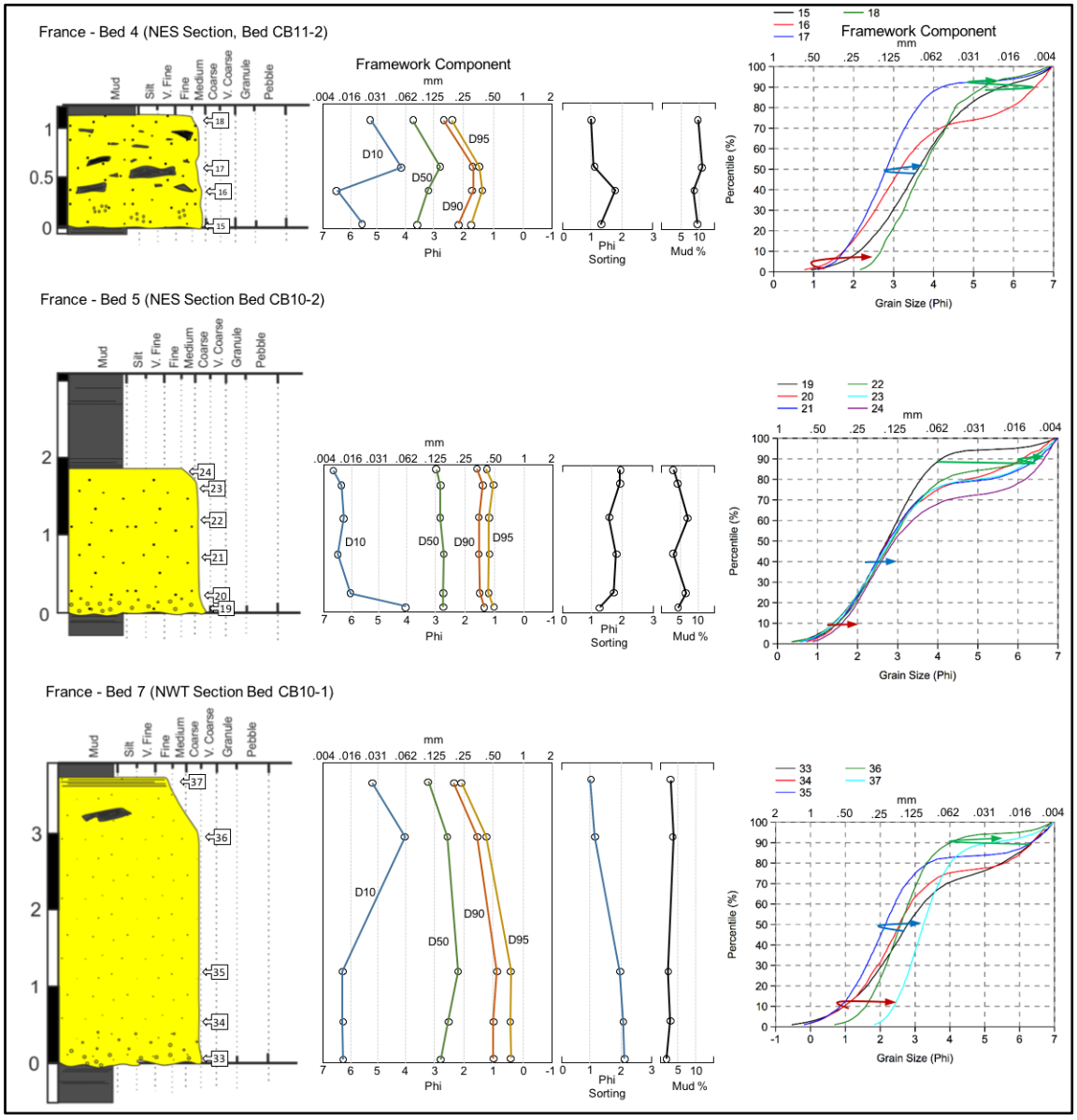

Figure 4-10: Grain size analysis of the DWMS beds from the Grés de Peïra Cava. Data was analysed using the phi scale. Sample locations are given in the boxes on the sedimentary log. D10, D50, D90 and D95 correspond to the different percentiles of the grain size distribution in the framework component. Coloured arrows indicate the vertical variation in the coarse-tail (red), median (blue) and fine-tail (green) components.

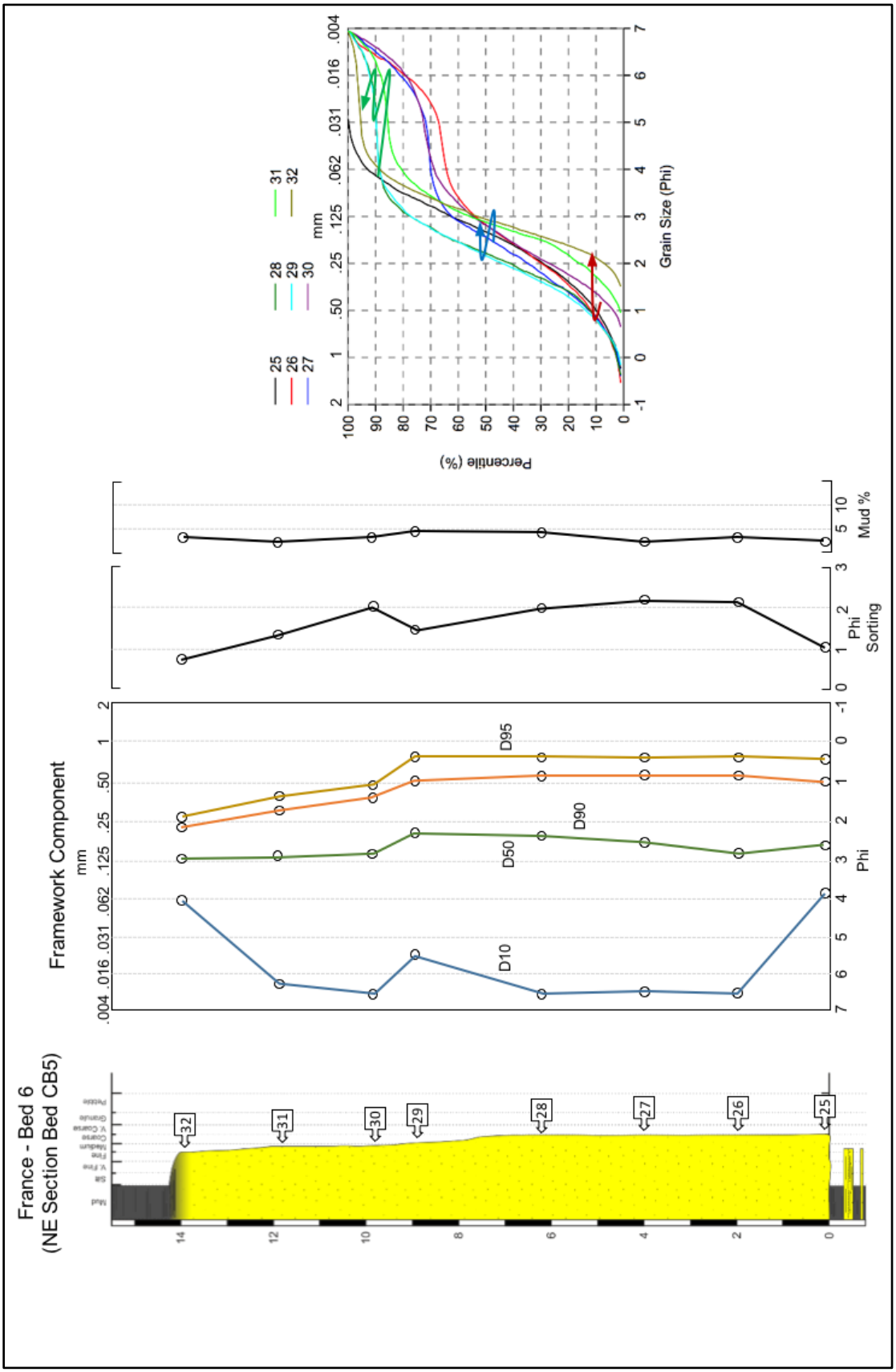

Figure 4-11: Grain size analysis of the DWMS beds from the Grés de Peïra Cava. Data was analysed using the phi scale. Sample locations are given in the boxes on the sedimentary log. D10, D50, D90 and D95 correspond to the different percentiles of the grain size distribution in the framework component. Coloured arrows indicate the vertical variation in the coarse-tail (red), median (blue) and fine-tail (green) components.

4.4.2 Grain Size and Sorting Trends.

Grain Size Trends – Framework Component. Figures 4-9 to 4-11 display the grain size trends in the framework component for the sandstone beds in the Numidian Flysch and the Grés de Peïra Cava. All the beds studied are visually massive, except for bed 7 which exhibits a thin parallel laminated cap. However, a quantitative assessment of the results suggests a variety of grading patterns are present. This includes; (1) coarse tail normal grading (beds 1, 4, 5, 6 and 7), (2) coarse tail inverse grading (beds 1, 4 and 6), (3) fine-tail grading (beds 1, 3, 5, and 6), (4) fine-tail inverse grading (bed 1, 2, 4, 5, 6, and 7), (5) ungraded (beds 2 and 3) and (6) weakly developed distribution grading (bed 4 and 7). In many of these beds, the grading is highly erratic, consisting of fine and coarse-tail fractions displaying normal to inverse to normal grading (e.g. bed 1 Figure 4-9). It should also be emphasised that no single trend is common in all the beds or the majority of beds, which makes subsequent interpretation of flow processes very difficult.

Table 4-3 summarises the results from hypothesis testing for statistically significant vertical trends in the beds. All of the samples, except for beds 2 and 3, reject the null hypothesis of equal grain size distribution (Table 4-2). For samples in bed 2 and 3, the Kruskal-Wallis test indicates that there is no significant difference between sample medians (p-values of 1) for the framework component. This also holds true for the zircon component (see below for details), and implies that the analysis fails to reject the null hypothesis. Based on this statistical analysis, a number of textural trends are clearly visible when considering the grain size distribution and their position within the beds. In beds 6 and 7, a distinct coarse-tail inverse grading is associated with fine-tail grading at the base of the beds. This can be correlated to a poorly sorted grain size distribution. In the middle of beds 5, 6 and 7, inverse grading in the fine-tail is associated with coarse-tail grading and a vertical improvement in grading. The 50^{th} percentile in bed 5 also shows subtle inverse to normal grading. In fact, with the exception of coarse-tail inverse grading at the base, bed 5 shares many similarities to beds 6 and 7. For all the Peïra Cava beds, distribution grading characterises the bed tops, except for the 10^{th} percentile of bed 6. For bed 1, a highly irregular/meandering grain size trend characterised by inverse-normal-inverse grading is visible. The same trend is also seen in the zircon component (see below for more details). And lastly, based on the statistical analysis, an ungraded trend is interpreted for beds 2 and 3. Nevertheless, a pronounced normal grading involving the 50^{th} percentile is seen in the latter bed. This trend is not seen in the other percentiles.

Field description of bed 4 reveals an anomalous ‘patchy’ grain size trend as measured by a grain size comparator. As explained previously, this texture makes it difficult to acquire a representative sample for textural analysis. Additionally, the use of a REA during the analysis may have further biased the results. Nonetheless, a crude grain size trend is observed involving

inverse grading in the 50th and coarse-tail percentiles at the base and distribution grading at the top. The fine-tail faction shows a highly erratic grading showing alternating normal and inverse grading at the base and middle of the bed.

Table 4-2:Kruskal-Wallis Hypothesis tetst for equal sample medians for both the framework component and zircon component. H is computed Kruskal-Wallis statistic, H_c is he tie correction for the test statistic. *P*-value is taken at the 1% significance level.

	Kruskal-Wallis Test for Equal Median - Framework Component			
Bed	H (Chi^2)	H_c (tie corrected	*P*-value	Result
1	983.7	983.7	1.23E-211	There is significant difference between sample medians
2	-4.30E+05	-4.30E+05	1	There is no significant difference between sample median
3	-3.33E+06	-3.33E+06	1	There is no significant difference between sample medians
4	1904	1904	6.37E-215	There is a significant difference between sample medians
5	319.1	319.1	7.65E-67	There is a significant difference between sample medians
6	2093	2093	8.59E-289	There is a significant difference between sample medians
7	3655	3655	3.54E-349	There is a significant difference between sample medians

	Kruskal-Wallis Test for Equal Median - Heavy Mineral Component			
Bed	H (Chi^2)	H_c (tie corrected	*P*-value	Result
1	65.64	65.64	1.88E-18	There is a significant difference between sample medians
2	3.41	3.41	0.491	There is no significant difference between sample median
3	7.08	7.08	0.214	There is no significant difference between sample median

Table 4-3: Table showing the different percentiles of the grain size distribution of the framework component from beds 1 to 7, and the associated summary statistics. Grain sizes were measured automatically using binary images in Scandium software after pre- and post-processing of the images.

			SEM Image Analysis (µm/phi)						Summary Statistics							
Bed/Sample/Position	Facies	Field Measured Grain Size (µm)	Mud%	D10	D50	D90	D95	D99	Sorting	Variance	Stand. Dev	Std. Error	Mean	Coeff. Var	Std. Error Std Dev.	N
Tunisia Bed 1/ 1 /Top	Sm_1	177-250	1.2	11.74/6.41	55.68/4.16	189.1/2.40	235.76/2.08	359.72/1,48	1.52	2.13	1.45	0.01	4.27	34.14	0.03	10129
Tunisia Bed 1/ 1_1	Sm_1	177-350	1.5	11.39/6.46	84.41/3.57	276.84/1.85	344.97/1.54	526.7/0.92	1.79	3.02	1.73	0.02	3.93	44.14	0.04	5885
Tunisia Bed 1/ 2	Sm_1	177-250	1	11.87/6.40	50.59/4.30	181.29/2.46	227.96/2.13	338.93/1.56	1.52	2.1	1.45	0.01	4.37	33.17	0.03	11962
Tunisia Bed 1/ 2_2	Sm_1	177-250	0.9	11.88/6.40	93.26/3.42	249.41/2.00	302.8/1.72	497.78/1.01	1.69	2.62	1.62	0.01	3.82	42.36	0.03	7540
Tunisia Bed 1/ 3 /Base	Sm_1	177-251	1.2	12.25/6.35	51.64/4.28	177.78/2.49	226.88/2.14	355.77/1.49	1.48	2.05	1.43	0.01	4.32	32.91	0.03	10391
Tunisia Bed 2/ 4 /Top	Sm_1	177-250	1.1	11.71/6.42	43.02/4.54	178.29/2.49	227.25/2.14	354.18/1.50	1.53	2.23	1.49	0.01	4.47	33.34	0.03	11330
Tunisia Bed 2/ 5	Sm_1	177-250	1.3	11.79/6.41	47.08/4.41	190.21/2.39	243.80/2.04	399.76/1.32	1.56	2.31	1.52	0.01	4.38	34.74	0.03	9773
Tunisia Bed 2/ 6	Sm_1	177-250	1.4	11.69/6.42	41.05/4.61	185.84/2.43	249.63/2.0	436.18/1.20	1.56	2.3	1.51	0.01	4.47	33.9	0.01	99447
Tunisia Bed 2/ 7	Sm_1	177-250	1.3	10.98/6.51	48.81/4.36	185.1/2.43	245.2/2.03	418.5/1.26	1.59	2.36	1.53	0.01	4.4	34.95	0.03	9565
Tunisia Bed 2/ 8 /Base	Sm_1	177-250	1.6	11.21/6.48	42.08/4.57	169.54/2.56	209.72/2.25	312.85/1.68	1.53	2.26	1.5	0.01	4.54	33.12	0.03	12320
Tunisia Bed 3/ 9 Top	Sm_1	177-250	1.1	11.46/6.45	45.48/4.46	184.07/2.44	232.67/2.10	359.85/1.47	1.56	2.34	1.53	0.01	4.44	34.43	0.03	8902
Tunisia Bed 3/ 10	Sm_1	177-250	1.2	11.14/6.49	43.60/4.52	183.09/2.45	235.17/2.09	396.05/1.34	1.58	2.43	1.55	0.01	4.48	34.75	0.04	8080
Tunisia Bed 3/ 11	Sm_1	177-250	1.1	11.53/6.44	51.63/4.28	192.88/2.37	245.47/2.03	387.40/1.37	1.59	2.42	1.55	0.01	4.35	35.78	0.03	10020
Tunisia Bed 3/ 12	Sm_1	177-250	1.4	11.29/6.47	38.38/4.70	178.48/2.49	226.11/2.14	358.40/1.48	1.55	2.31	1.52	0.01	4.54	33.46	0.03	12674
Tunisia Bed 3/ 13	Sm_1	177-250	1.3	11.79/6.41	45.95/4.44	191.85/2.38	256.75/1.96	436.21/1.20	1.55	2.31	1.52	0.01	4.39	34.67	0.03	9973
Tunisia Bed 3/ 14 /Base	Sm_1	177-250	1.5	12.41/6.33	49.51/4.32	180.18/2.47	240.26/2.06	329.66/1.60	1.51	2.15	1.46	0.01	4.34	33.72	0.03	13983
France Bed 4/ 15 /Base	Sm_3	250-375	9.5	19.2/5.61	81.8/3.61	226.9/2.14	302.9/1.72	522.4/0.94	1.38	1.83	2.35	0.01	3.74	36.15	0.03	9538
France Bed 4/ 16	Sm_3	300-375	8.3	10.7/6.54	111.5/3.16	298.5/1.74	375.3/1.41	587.5/0.77	1.86	3.05	1.74	0.02	3.66	47.74	0.04	5368
France Bed 4/ 17	Sm_3	250-375	10.3	55.0/4.18	141.8/2.82	294.8/1.76	345.0/1.54	465.5/1.10	1.76	1.47	1.21	0.01	3.05	40.4	0.03	6070
France Bed 4/ 18 /Top	Sm_3	177-250	9.7	26.7/5.25	75.1/3.73	156.3/2.68	178/2.49	223/2.16	1.03	1.06	1.03	0.01	3.86	26.69	0.05	3321
France Bed 5/ 19 /Base	Sm_1	500-750	4.5	58.8/4.09	150.4/2.73	381.0/1.39	487.8/1.04	769.1/0.38	1.24	1.61	1.27	0.01	2.82	45	0.02	9687
France Bed 5/ 20	Sm_1	375-710	6.1	14.5/6.10	149.8/2.74	356.2/1.49	427.6/1.23	606.1/0.72	1.73	2.67	1.63	0.02	3.21	50.8	0.03	5818
France Bed 5/ 21	Sm_1	375-500	3.3	11.07/6.50	147.4/2.76	355.9/1.49	455.2/1.17	671.98/0.57	1.86	3.09	1.75	0.02	3.27	53.67	0.03	4936
France Bed 5/ 22	Sm_1	375-500	7.1	13/6.26	138.4/2.85	351.9/1.51	454.9/1.14	781.5/0.36	1.6	2.63	1.62	0.02	3.19	50.82	0.03	4796
France Bed 5/ 23	Sm_1	375-500	4.5	12/6.37	142/2.82	376.5/1.41	476.9/1.07	689.7/0.54	1.89	3.01	1.73	0.02	3.25	53.31	0.03	5520
France Bed 5/ 24 /Top	Sm_2	300-400	3.4	9.9/6.66	133.3/2.91	325.6/1.62	399.8/1.32	541.8/0.88	1.9	3.55	1.88	0.02	3.59	52.42	0.03	5501
France Bed 6/ 25 /Base	Sm_1	710-1000	2.3	68.22/3.87	156.7/2.67	500.5/1	705.6/0.5	1174/-0.23	1.11	1.21	1.1	0.01	2.54	43.32	0.03	4011
France Bed 6/ 26	Sm_1	710-1000	3.4	11.7/6.61	141.2/2.82	544.9/0.88	737.8/0.44	1414/-0.50	2.16	4.55	2.12	0.03	3.42	62.17	0.04	4137
France Bed 6/ 27	Sm_1	710-1000	2.5	11/6.50	168.8/2.57	545.8/0.87	749.7/0.42	1312.5/-0.39	2.21	4.47	2.11	0.03	3.17	66.65	0.04	3156
France Bed 6/ 28	Sm_1	710-1000	4.5	9.8/6.67	202.5/2.30	535.1/0.90	733.7/0.45	1261.3/-033	2.03	2.56	1.6	0.03	2.47	64.7	0.03	2838
France Bed 6/ 29	Sm_2	500-750	4.7	22.6/5.47	213/2.23	502.7/0.99	732.6/0.45	735.3/0.44	1.49	2.56	1.6	0.02	2.44	65.34	0.03	3460
France Bed 6/ 30	Sm_2	375-500	3.4	10.2/6.6	142/2.82	387.4/1.37	470/1.09	635.9/0.65	2.04	3.78	1.94	0.02	3.46	56.17	0.04	4303
France Bed 6/ 31	Sm_2	250-375	2.6	12.7/6.30	135.8/2.88	302.7/1.72	376.4/1.41	516.3/0.95	1.39	2.25	1.5	0.02	3.26	46.08	0.04	4314
France Bed 6/ 32 /Top	Sm_2	250-375	3.4	58.8/4.09	130.1/2.94	230.3/2.12	267.5/1.90	350.8/1.51	0.8	0.95	0.97	0.01	3.1	31.47	0.02	9388
France Bed 7/ 33 /Base	Sm_1	710-1000	2.1	12.3/6.34	145.3/2.78	514.1/0.96	737.2/0.44	1431.8/-0.52	2.13	3.78	1.94	0.02	3.21	60.47	0.03	5732
France Bed 7/ 34	Sm_1	710-1000	3.2	12.2/6.35	171.2/2.55	513.9/0.96	717/0.48	1132.9/-018	2.08	3.71	1.92	0.02	3.06	62.95	0.03	4452
France Bed 7/ 35	Sm_1	710-1000	2.6	12.5/6.32	224.5/2.15	554.6/0.85	727.5/0.46	1134.9/-0.18	1.93	3.42	1.84	0.03	2.63	70.18	0.03	3408
France Bed 7/ 36	Sm_2	375-500	4.1	61.8/4.02	166.5/2.59	332.6/1.59	407.7/1.29	616/0.70	1.14	1.44	1.2	0.01	2.77	43.4	0.03	5646
France Bed 7/ 37 /Top	Sl_1	177-250	3.1	27.63/5.18	105.1/3.23	190.1/2.39	218.5/2.19	281.2/1.83	1.06	1.32	1.15	0.009	3.5	32.85	0.02	15805

Grain Size Trends – Zircon Component. Figure 4-9 displays the grain size trend in the zircon component in the Numidian Flysch beds. Grain sizes of the zircons vary from fine silt to fine sand. Kruskal-Wallis test indicates that only samples from bed 1 show significant difference in the median values, while samples from beds 2 and 3 fail to reject the null hypothesis of equal distributions. However, it should be emphasised that most of the samples have less than the recommended 300 number of grains (Johnson, 1994), which could lead to significant bias in the statistical analysis. Johnson (1994) claimed that estimation of the mean size to within 0.1 phi with 90% confidence level requires 100 grains, and only if the grain size distribution is well sorted (Stand. Dev. < 0.6). For poorly sorted grains (>1), a minimum of 270 grains is required. Many of the samples fail to meet this criterion, and thus estimates of the mean and other percentiles will have low confidence levels (Table 4-4).

In general, the temporal evolution of the zircon grain size distribution is not too dissimilar to the framework component, at least in terms of the coarse-tail percentile (i.e. 90th and 95th; Figure 4-9). For example, a subtle inverse grading is observed in beds 3 at the base, followed by normal grading. At the top of bed 2, the coarse tail appears relatively ungraded, again similar to the coarse-tail framework component. Nonetheless, a number of distinct trends not seen in the framework component are visible in the zircon data, including: (1) inverse to normal grading in the coarse tail component (90th and 95th) of bed 1; (2) inverse to normal grading in the 50th percentile of bed 3; (3) alternating inverse to normal grading in the 10th and 50th percentile that has the opposite sense of grading to the framework component; and (4) no overall trends in the sorting, which remains stable vertically (i.e. moderately to poorly sorted; Figure 4-9 and Table 4-4).

Table 4-4:Table showing the different percentiles of the grain size distribution of zircon grains from beds 1 to 3, and the associated summary statistics. Grain sizes were measured automatically from greyscale images using INCAfeature software.

		SEM Image Analysis (µm/phi)				Summary Statistics							
Bed/Sample/Position	Facies	D10	D50	D90	D95	Sorting	Variance	Stand. Dev	Std. Error	Mean	Coeff. Var	Std. Error Std Dev.	N
Tunisia Bed 1/ 1 /Top	Sm_1	5.91/16.64	4.87/34.07	3.78/72.9	3.45/91.23	0.84	0.73	0.85	0.056	4.84	17.73	0.04	228
Tunisia Bed 1/ 1_1	Sm_1	6.35/12.21	5.2/27.15	3.6/82.53	3.24/105.91	1.1	1.12	1.06	0.075	5.04	21.08	0.05	197
Tunisia Bed 1/ 2	Sm_1	5.86/17.23	4.24/52.90	3.35/97.97	3.02/122.91	0.98	0.86	0.92	0.05	4.42	20.99	0.04	343
Tunisia Bed 1/ 2_2	Sm_1	6.35/12.25	4.90/33.43	3.60/82.75	3.27/103.8	1.1	1.13	1.06	0.05	4.93	21.62	0.04	345
Tunisia Bed 1/ 3 /Base	Sm_1	5.77/16.03	4.48/34.94	3.76/73.92	3.30/101.2	0.81	0.66	0.81	0.05	4.78	17.04	0.04	248
Tunisia Bed 2/ 4 /Top	Sm_1	5.98/15.86	4.53/43.2	3.38/95.99	3.23/106.75	0.99	0.94	0.97	0.06	4.66	20.81	0.04	233
Tunisia Bed 2/ 5	Sm_1	5.77/18.34	4.95/32.26	3.51/87.26	3.34/98.68	0.86	0.72	0.85	0.062	4.8	17.73	0.04	189
Tunisia Bed 2/ 6	Sm_1	5.89/16.9	4.7/38.39	3.47/89.94	3.23/196.89	0.95	0.85	0.92	0.06	4.69	19.66	0.04	225
Tunisia Bed 2/ 7	Sm_1	5.57/18.64	4.79/36.12	3.85/69.5	3.64/80.03	0.74	0.55	0.74	0.06	4.8	15.53	0.04	148
Tunisia Bed 2/ 8 /Base	Sm_1	5.95/16.16	4.66/39.65	3.70/76.88	3.47/90	0.88	0.74	0.86	0.06	4.74	18.24	0.04	194
Tunisia Bed 3/ 9 Top	Sm_1	6.08/14.77	4.84/34.8	3.69/77.67	3.19/109.46	1	0.92	0.96	0.08	4.81	19.9	0.06	118
Tunisia Bed 3/ 10	Sm_1	5.90/18.8	4.68/38.96	3.34/98.68	3.23/106.4	0.99	0.88	0.94	0.09	4.63	20.28	0.07	99
Tunisia Bed 3/ 11	Sm_1	5.86/17.18	4.45/45.66	3.36/97.43	3.2/108.64	0.99	0.9	0.95	0.07	4.55	20.87	0.05	174
Tunisia Bed 3/ 12	Sm_1	5.92/16.47	4.61/41.04	3.47/90.3	3.13/114.33	0.96	0.85	0.92	0.07	4.63	19.98	0.05	164
Tunisia Bed 3/ 13	Sm_1	5.79/18.12	4.65/39.88	3.42/93.62	3.17/111.47	0.93	0.86	0.93	0.07	4.62	20.16	0.05	165
Tunisia Bed 3/ 14 /Base	Sm_1	6.04/15.23	4.78/36.51	3.60/82.64	3.51/87.78	0.91	0.8	0.89	0.07	4.75	18.8	0.05	155

Table 4-5: Hypothesis uniformity testing of the directional data points for preferential distribution in bedding parallel samples. n is the grain count, V_n is the Kuiper statistic, $V_{0.05}$ and $V_{0.01}$ are the critical values of the Kuiper Test for a given significance level, u^2 is the Watson statistics, $u^2_{0.05}$ and $u^2_{0.01}$ are the Watson critical values, R is the mean vector length (the Rayleigh statistic), SB is the circular standard deviation, K is the vectorial concentration and $R_{0.05}$ and $R_{0.01}$ are critical values for Rayleigh statistics. $H_{0.05}$ and $H_{0.01}$ are the parametric and non-parametric hypothesis test at the 5% and 1% significance level. d° is the confidence sector for the mean vector. a refers to the null hypothesis being accepted, while r refers to rejection of the null hypothesis. See text for description of the test statistics.

			Bedding Parallel Orientation																							
			Kuiper's Test					Watson's Test					Rayleigh's Test							Mean Vector	Confidence interval			Distribution		Fabric
Bed/Position	Sample	n	V_n	$V_{0.05}$	$V_{0.01}$	$H0_{0.05}$	$H0_{0.01}$	u^2	$u^2_{0.05}$	$u^2_{0.01}$	$H_{0\ 0.05}$	$H_{0\ 0.01}$	R	s_B	K	$R_{0.05}$	$R_{0.01}$	$H0_{0.05}$	$H0_{0.01}$	M	$d°_{0.05}$	$d°_{0.01}$	Bootstrap (95%)	Dist	Dist	
1 / Top	1a	384	0.152	0.089	0.101	r	r	0.756	0.187	0.267	r	r	0.193	36.39	0.393	0.088	0.11	r	r	89.4	10.38	13.71	79, 100.5	Von Mises	Von Mises	a(p)
1	1-1a	729	0.113	0.064	0.074	r	r	0.6494	0.187	0.267	r	r	0.123	37.93	0.248	0.064	0.08	r	r	73.34	11.86	15.68	60.58, 85.75	Von Mises	Von Mises	a(p)
1	2a	414	0.28	0.085	0.097	r	r	3.767	0.187	0.267	r	r	0.417	30.93	0.917	0.08	0.1	r	r	23.1	4.45	5.88	18.65, 27.41	Von Mises	Von Mises	a(o)
1	2-2a	724	0.25	0.065	0.074	r	r	4.913	0.187	0.267	r	r	0.362	32.37	0.775	0.064	0.08	r	r	146.2	3.93	5.19	142, 150	Von Mises	Von Mises	a(o)
1/ Base	3a	344	0.104	0.094	0.107	r	**a**	0.244	0.187	0.267	r	**a**	0.107	38.29	0.214	0.093	0.116	r	**a**	24.2	19.9	26.3	2.12, 46.93	Von Mises	**Uniform**	a(o)*
2 / Top	4a	391	0.355	0.088	0.1	r	r	5.72	0.187	0.267	r	r	0.526	27.88	1.232	0.088	0.109	r	r	28.49	3.518	4.648	25.08, 31.89	Gaussian	Gaussian	a(o)
2	5a	412	0.2	0.086	0.098	r	r	1.591	0.187	0.267	r	r	0.273	34.55	0.567	0.085	0.106	r	r	11.08	7.01	9.27	4.19, 17.95	Von Mises	Von Mises	a(t)
2	6a	431	0.138	0.084	0.096	r	r	0.782	0.187	0.267	r	r	0.178	36.72	0.363	0.083	0.103	r	r	69.3	10.6	14.01	57.71, 79.97	Von Mises	Von Mises	a(o)
2	7a	427	0.273	0.084	0.096	r	r	3.436	0.187	0.267	r	r	0.39	31.64	0.847	0.084	0.104	r	r	35.06	4.71	6.2	30.48, 39.45	Von Mises	Von Mises	a(o)
2 / Base	8a	289	0.141	0.102	0.116	r	r	0.438	0.187	0.267	r	r	0.161	37.1	0.327	0.102	0.126	r	r	137.5	14.35	18.97	122.4, 151.9	Von Mises	Von Mises	a(o)
3 / Top	9a	343	0.2	0.094	0.107	r	r	1.4	0.187	0.267	r	r	0.277	34.44	0.577	0.094	0.116	r	r	134.05	7.56	9.99	126.6, 141.6	Von Mises	Von Mises	a(o)
3	10a	313	0.182	0.098	0.112	r	r	1.07	0.187	0.267	r	r	0.255	34.96	0.528	0.098	0.121	r	r	172.3	8.62	11.4	163.6, 180.9	Von Mises	Von Mises	a(t)
3	11a	439	0.236	0.083	0.095	r	r	2.608	0.187	0.267	r	r	0.338	32.97	0.717	0.083	0.102	r	r	6.28	5.43	7.17	0.75, 11.67	Von Mises	Von Mises	a(t)
3	12a	408	0.045	0.086	0.098	**a**	**a**	0.38	0.187	0.267	**a**	**a**	0.023	40.05	0.045	0.086	0.106	**a**	**a**	86.54	**n/a**	**n/a**	8.6, 163.7	**Uniform**	**Uniform**	-
3	13a	497	0.247	0.078	0.089	r	r	3.613	0.187	0.267	r	r	0.375	32.04	0.808	0.078	0.096	r	r	172.14	4.56	6.03	167.5, 176.8	Von Mises	Von Mises	a(t)
3 / Base	14a	579	0.233	0.072	0.083	r	r	2.975	0.187	0.267	r	r	0.312	33.6	0.657	0.072	0.089	r	r	91.59	5.14	6.79	86.67, 96.59	Von Mises	Von Mises	a(p)
4 / Top	18a	698	0.507	0.066	0.075	r	r	3.21	0.187	0.267	r	r	0.297	33.96	0.622	0.066	0.081	r	r	109.88	4.93	6.51	105, 114.8	Von Mises	Von Mises	a(o)
4	17a	985	0.121	0.055	0.063	r	r	1.242	0.187	0.267	r	r	0.155	37.241	0.314	0.055	0.068	r	r	8.13	8.08	10.68	0.22, 16.39	Von Mises	Von Mises	a(t)
4	16a	795	0.031	0.062	0.071	**a**	**a**	0.025	0.187	0.267	**a**	**a**	0.01	40.312	0.02	0.061	0.076	**a**	**a**	46.03	**n/a**	**n/a**	-36.5, 129	**Uniform**	**Uniform**	-
4 / Base	15a	721	0.109	0.065	0.074	r	r	0.699	0.187	0.267	r	r	0.135	37.681	0.272	0.065	0.08	r	r	108.53	10.87	14.37	97.32, 119.4	Von Mises	Von Mises	a(t)
5 / Top	24a	1084	0.194	0.053	0.06	r	r	4.774	0.187	0.267	r	r	0.292	34.08	0.611	0.053	0.065	r	r	7.86	4.027	5.32	3.90, 11.99	Von Mises	Von Mises	a(t)
5	23a	1279	0.073	0.049	0.056	r	r	0.655	0.187	0.267	r	r	0.097	38.49	0.195	0.048	0.06	r	r	148.99	11.35	15.01	137.2, 160.9	Von Mises	Von Mises	a(o)
5	22a	996	0.072	0.055	0.063	r	r	0.412	0.187	0.267	r	r	0.081	38.84	0.162	0.055	0.068	r	r	105.46	15.48	20.45	88.96, 121.4	Von Mises	Von Mises	a(o)
5	21a	1076	0.153	0.053	0.061	r	r	2.855	0.187	0.267	r	r	0.277	35.63	0.465	0.053	0.065	r	r	63.83	5.259	6.949	58.38, 69.17	Von Mises	Von Mises	a(o)
5	20a	1293	0.142	0.048	0.055	r	r	3.067	0.187	0.267	r	r	0.214	35.91	0.438	0.048	0.06	r	r	78.84	5.083	6.716	73.82, 83.89	Von Mises	Von Mises	a(o)
5 / Base	19a	2208	0.054	0.037	0.042	r	r	0.653	0.187	0.267	r	r	0.075	38.97	0.15	0.037	0.046	r	r	145.22	11.28	14.9	133.5, 157.2	Von Mises	Von Mises	a(o)
6 / Top	32a	641	0.143	0.069	0.078	r	r	1.312	0.187	0.267	r	r	0.198	36.28	0.404	0.068	0.085	r	r	120.78	7.81	10.33	112.9, 128.5	Von Mises	Von Mises	a(o)
6	31a	670	0.074	0.067	0.077	r	**a**	0.271	0.187	0.267	r	r	0.074	38.97	0.147	0.067	0.083	r	**a**	149.07	20.52	27.12	125.9, 171.2	Von Mises	**Uniform**	a(o)*
6	30a	1085	0.148	0.053	0.06	r	r	2.631	0.187	0.267	r	r	0.217	35.84	0.446	0.053	0.065	r	r	64.86	5.462	7.21	59.27, 70.23	Von Mises	Von Mises	a(o)
6	29a	1440	0.071	0.046	0.052	r	r	0.662	0.187	0.267	r	r	0.094	38.56	0.188	0.046	0.057	r	r	20.84	11.11	14.68	9.272, 32.31	Von Mises	Von Mises	a(o)
6	28a	1098	0.071	0.053	0.06	r	r	0.497	0.187	0.267	r	r	0.088	38.68	0.177	0.052	0.065	r	r	163.12	13.53	17.89	148.5, 176.8	Von Mises	Von Mises	a(o)
6	27a	1015	0.051	0.055	0.062	**a**	**a**	0.189	0.187	0.267	r	**a**	0.056	39.36	0.112	0.054	0.067	r	**a**	26.47	22.13	29.13	0.6715, 51.26	**Uniform**	**Uniform**	-
6	26a	1149	0.088	0.051	0.059	r	r	0.929	0.187	0.267	r	r	0.123	37.93	0.249	0.051	0.063	r	r	13.25	9.42	12.45	3.604, 22.93	Von Mises	Von Mises	a(t)
6 / Base	25a	1102	0.087	0.052	0.06	r	r	0.736	0.187	0.267	r	r	0.107	38.27	0.216	0.052	0.065	r	r	20.95	11.07	14.64	9.961, 32.11	Von Mises	Von Mises	a(o)
7 / Top	37a	363	0.233	0.091	0.104	r	r	1.761	0.187	0.267	r	r	0.302	33.85	0.633	0.091	0.113	r	r	4.833	6.72	8.88	-1.547, 11.31	Von Mises	Von Mises	a(t)
7	36a	1268	0.136	0.048	0.056	r	r	2.382	0.187	0.267	r	r	0.191	36.43	0.39	0.049	0.06	r	r	63.309	5.76	7.61	57.46, 69.36	Von Mises	Von Mises	a(o)
7	35a	1438	0.078	0.046	0.053	r	r	0.786	0.187	0.267	r	r	0.1	38.42	0.202	0.046	0.057	r	r	62.87	10.36	13.69	51.89, 73.61	Von Mises	Von Mises	a(o)
7	34a	1329	0.081	0.048	0.055	r	r	0.84	0.187	0.267	r	r	0.109	38.24	0.219	0.048	0.059	r	r	126.57	9.95	13.15	116.1, 137.1	Von Mises	Von Mises	a(o)
7 / Base	33a	1579	0.06	0.044	0.05	r	r	0.349	0.187	0.267	r	r	0.063	39.21	0.127	0.044	0.054	r	r	42.06	15.73	20.79	25.3, 58.67	Von Mises	Von Mises	a(o)

Table 4-6: Hypothesis uniformity testing of the directional data points for preferential distribution in bedding parallel samples. n is the grain count, V_n is the Kuiper statistic, $V_{0.05}$ and $V_{0.01}$ are the critical values of the Kuiper Test for a given significance level, u^2 is the Watson statistics, $u^2_{0.05}$ and $u^2_{0.01}$ are the Watson critical values, R is the mean vector length (the Rayleigh statistic), SB is the circular standard deviation, K is the vectorial concentration and $R_{0.05}$ and $R_{0.01}$ are critical values for Rayleigh statistics. $H_{0.05}$ and $H_{0.01}$ are the parametric and non-parametric hypothesis test at the 5% and 1% significance level. d° is the confidence sector for the mean vector. a refers to the null hypothesis being accepted, while r refers to rejection of the null hypothesis. See text for description of the test statistics.

			Bedding Perpendicular Orientation																					
			Kuiper's Test					Watson's Test					Rayleigh's Test							Mean Vector	Confidence interval			Distribution	
Bed/Position	Sample	n	V_n	$V_{0.05}$	$V_{0.01}$	$H0_{0.05}$	$H0_{0.01}$	u^2	$u^2_{0.05}$	$u^2_{0.01}$	$H_{0\ 0.05}$	$H_{0\ 0.01}$	R	s_B	K	$R_{0.05}$	$R_{0.01}$	$H0_{0.05}$	$H0_{0.01}$	M	$d°_{0.05}$	$d°_{0.01}$	Bootstrap (95%)	Dist	Dist
1 / Top	1b	1334	0.128	0.048	0.055	r	r	2.311	0.187	0.267	r	r	0.184	36.604	0.374	0.047	0.059	r	r	30.18	5.85	7.73	24.3, 36.16	Von Mises	Von Mises
1	1-1b	1376	0.204	0.047	0.054	r	r	6.391	0.187	0.267	r	r	0.298	33.93	0.625	0.047	0.058	r	r	98.703	3.49	4.61	95.29, 102.1	Von Mises	Von Mises
1	2b	932	0.237	0.057	0.065	r	r	6.339	0.187	0.267	r	r	0.363	32.34	0.778	0.057	0.07	r	r	67.59	3.45	4.56	64.28, 70.95	Von Mises	Von Mises
1	2-2b	1277	0.177	0.049	0.056	r	r	4.115	0.187	0.267	r	r	0.249	35.107	0.515	0.048	0.06	r	r	93.4	4.37	5.78	89.14, 97.61	Von Mises	Von Mises
1/ Base	3b	898	0.244	0.057	0.066	r	r	6.507	0.187	0.267	r	r	0.374	32.059	0.806	0.058	0.072	r	r	28.2	3.4	4.49	24.82, 31.6	Von Mises	Von Mises
2 / Top	4b	967	0.091	0.056	0.064	r	r	0.755	0.187	0.267	r	r	0.122	37.97	0.245	0.056	0.069	r	r	97.95	10.44	13.79	86.8, 108.8	Von Mises	Von Mises
2	5b	1180	0.179	0.051	0.058	r	r	4.14	0.187	0.267	r	r	0.262	34.81	0.542	0.05	0.063	r	r	101.95	4.32	5.71	97.78, 106.2	Von Mises	Von Mises
2	6b	1082	0.223	0.053	0.061	r	r	6.28	0.187	0.267	r	r	0.337	32.98	0.716	0.053	0.065	r	r	138.17	3.46	4.57	134.8, 141.7	Von Mises	Von Mises
2	7b	1341	0.221	0.048	0.054	r	r	7.47	0.187	0.267	r	r	0.33	33.16	0.699	0.047	0.059	r	r	40.61	3.18	4.21	37.33, 43.82	Von Mises	Von Mises
2 / Base	8b	1108	0.114	0.052	0.06	r	r	1.41	0.187	0.267	r	r	0.154	37.25	0.313	0.052	0.065	r	r	178.48	7.65	10.11	171, 186	Von Mises	Von Mises
3 / Top	9b	1142	0.16	0.052	0.059	r	r	3.31	0.187	0.267	r	r	0.237	35.38	0.488	0.051	0.064	r	r	83.24	4.86	6.43	78.33, 88.19	Von Mises	Von Mises
3	10b	1222	0.133	0.05	0.057	r	r	2.557	0.187	0.267	r	r	0.202	36.2	0.412	0.05	0.061	r	r	126.67	5.55	7.34	121.1, 132.3	Von Mises	Von Mises
3	11b	1143	0.174	0.052	0.059	r	r	3.817	0.187	0.267	r	r	0.255	34.96	0.528	0.051	0.064	r	r	75.62	4.51	5.95	71.08, 80.08	Von Mises	Von Mises
3	12b	1188	0.085	0.051	0.058	r	r	0.867	0.187	0.267	r	r	0.118	38.04	0.238	0.05	0.062	r	r	15.26	9.7	12.82	5.31, 24.66	Von Mises	Von Mises
3	13b	1296	0.245	0.048	0.055	r	r	8.959	0.187	0.267	r	r	0.366	32.26	0.786	0.048	0.06	r	r	14.79	2.9	3.83	11.77, 17.69	Von Mises	Von Mises
3 / Base	14b	1092	0.097	0.053	0.06	r	r	1.189	0.187	0.267	r	r	0.144	37.49	0.29	0.052	0.065	r	r	118.72	8.29	10.96	110.1, 127	Von Mises	Von Mises
4 / Top	18b	710	0.172	0.065	0.075	r	r	2.309	0.187	0.267	r	r	0.25	35.09	0.517	0.065	0.081	r	r	99.53	5.84	7.71	93.54, 105.4	Von Mises	Von Mises
4	17b	881	0.186	0.059	0.067	r	r	3.45	0.187	0.267	r	r	0.273	34.54	0.567	0.058	0.072	r	r	0.82	4.79	6.33	-3.821, 5.585	Von Mises	Von Mises
4	16b	868	0.143	0.059	0.068	r	r	1.709	0.187	0.267	r	r	0.195	36.35	0.398	0.059	0.073	r	r	168.9	6.82	9.02	162, 176	Von Mises	Von Mises
4 / Base	15b	1131	0.124	0.052	0.059	r	r	1.62	0.187	0.267	r	r	0.166	37	0.336	0.052	0.064	r	r	110.16	7.05	9.31	102.7, 117.3	Von Mises	Von Mises
5 / Top	24b	870	0.107	0.059	0.067	r	r	0.841	0.187	0.267	r	r	0.134	37.71	0.27	0.059	0.073	r	r	8.59	10	13.22	-2.057, 18.37	Von Mises	Von Mises
5	23b	947	0.105	0.057	0.065	r	r	0.903	0.187	0.267	r	r	0.133	37.723	0.268	0.056	0.07	r	r	16.39	9.63	12.75	6.861, 26.3	Von Mises	Von Mises
5	22b	752	0.108	0.063	0.072	r	r	0.584	0.187	0.267	r	r	0.115	38.1	0.232	0.063	0.078	r	r	98.94	12.46	16.47	86.48, 111.4	Von Mises	Von Mises
5	21b	1005	0.137	0.055	0.063	r	r	1.852	0.187	0.267	r	r	0.188	36.5	0.383	0.055	0.068	r	r	27.19	6.58	8.69	20.48, 33.87	Von Mises	Von Mises
5	20b	1089	0.103	0.053	0.06	r	r	1.04	0.187	0.267	r	r	0.132	37.74	0.266	0.052	0.065	r	r	14.22	9.04	11.95	5.044, 23.44	Von Mises	Von Mises
5 / Base	19b	1672	0.121	0.043	0.049	r	r	2.725	0.187	0.267	r	r	0.178	36.74	0.361	0.042	0.053	r	r	75.81	5.41	7.15	70.27, 81.29	Von Mises	Von Mises
6 / Top	32b	678	0.318	0.067	0.076	r	r	7.609	0.187	0.267	r	r	0.462	29.71	1.04	0.067	0.082	r	r	1.68	3.1	4.1	-1.323, 4.79	Von Mises	Von Mises
6	31b	752	0.152	0.063	0.072	r	r	2.024	0.187	0.267	r	r	0.229	35.58	0.47	0.063	0.078	r	r	99.09	6.22	8.23	92.91, 105.2	Von Mises	Von Mises
6	30b	705	0.041	0.066	0.075	**a**	**a**	0.045	0.187	0.267	**a**	**a**	0.023	40.04	0.046	0.065	0.081	**a**	**a**	175.72	n/a	n/a	103.2, 249.8	**Uniform**	**Uniform**
6	29b	757	0.119	0.063	0.072	r	r	0.993	0.187	0.267	r	r	0.159	37.15	0.0323	0.063	0.078	r	r	6.25	8.98	11.87	-3.106, 15.27	Von Mises	Von Mises
6	28b	884	0.117	0.059	0.067	r	r	0.959	0.187	0.267	r	r	0.144	37.94	0.29	0.058	0.072	r	r	137.67	9.22	12.19	127.9, 147	Von Mises	Von Mises
6	27b	541	0.124	0.075	0.085	r	r	0.765	0.187	0.267	r	r	0.165	37.02	0.334	0.074	0.092	r	r	118.93	10.25	13.55	108.3, 129.5	Von Mises	Von Mises
6	26b	591	0.074	0.072	0.082	r	**a**	0.242	0.187	0.267	r	**a**	0.085	38.75	0.171	0.071	0.088	r	**a**	87.67	19.1	25.24	67.47, 109	Von Mises	**Uniform**
6 / Base	25b	1063	0.12	0.053	0.061	r	r	1.64	0.187	0.267	r	r	0.173	36.84	0.35	0.053	0.066	r	r	50.89	6.96	9.19	43.77, 57.79	von Mises	Von Mises
7 / Top	37b	438	0.327	0.083	0.095	r	r	5.084	0.187	0.267	r	r	0.468	29.55	1.05	0.083	0.103	r	r	9.37	3.8	5.02	5.732, 12.98	Von Mises	Von Mises
7	36b	1319	0.125	0.048	0.055	r	r	1.732	0.187	0.267	r	r	0.155	37.23	0.314	0.048	0.059	r	r	154.78	6.97	9.22	148.1, 161.7	Von Mises	Von Mises
7	35b	1074	0.132	0.053	0.061	r	r	2.08	0.187	0.267	r	r	0.192	36.4	0.392	0.053	0.066	r	r	178.57	6.22	8.21	172.4, 184.4	Von Mises	Von Mises
7	34b	945	0.106	0.057	0.065	r	r	0.907	0.187	0.267	r	r	0.133	37.71	0.269	0.056	0.07	r	r	32.622	9.62	12.71	22.93, 42.16	Von Mises	Von Mises
7 / Base	33b	1210	0.11	0.05	0.057	r	r	1.428	0.187	0.267	r	r	0.148	37.4	0.299	0.05	0.062	r	r	143.88	7.66	10.12	135.9, 151.3	Von Mises	Von Mises

4.4.3 Grain Fabric Trends.

Results of the statistical analysis are shown in Tables 4-5 and 4-6. The majority of the samples, both in the bedding parallel and perpendicular planes, exhibit an anisotropic fabric with a von Mises distribution. Only three samples in the bedding parallel plane and one in the perpendicular plane failed to reject the null hypothesis at the 0.05 significance level. This decreased to two samples in the bedding parallel plane and only one sample in the perpendicular plane at the 0.01 significance level. The corresponding equal-area rose diagrams using 36° intervals are shown in Figure 4-12 and 4-18, along with the vector magnitude to facilitate comparison between samples and to identity trends in the grain fabric.

Bedding Parallel. Visual analysis of the bedding parallel rose diagrams reveal a number of subtle trends in the grain fabric. However, the reader should be mindful of the fact that no consistent trend is observed in all the beds, which makes subsequent interpretation of flow processes more problematic. To differentiate between fabric types (i.e. flow parallel, oblique and transverse) in the bedding parallel sections, a 15° cut-off value has been employed for both sides of the flow direction (flow parallel or oblique) and perpendicular to the flow direction (flow transverse or oblique). (1) Nearly all samples have an anisotropic distribution, with the mean vector orientations aligned obliquely to the palaeocurrent direction (e.g beds 1, 2, 4 5, 6 and 7; Table 4-5). The exception to this general character is beds 3 and 4 (Figure 4-14 and 4-15), which reveal flow parallel fabric at the base, a highly variable flow- transverse to parallel fabric in the middle (locally isotropic), and flow-oblique at the top of the beds. In bed 3, these changes occur vertically within an ungraded massive interval almost identical to beds 1 and 2. In contrast, the changes in bed 4 coincide with a bedding parallel aligned mudclast-rich interval. (2) For beds 1, 2, 4 5, 6 and 7 the mean vectors are remarkably consistent vertically, but with the tops displaying an increasingly flow aligned or transverse fabric (Table 4-5). For the latter three beds, this change in vector mean coincides with a change in grading trends and/or transition to tractional structures (Figure 4-16 to 4-18). (3) Despite most beds showing a consistently oblique vector mean, there is little consistency in the mean vector rotation about the palaeocurrent direction, with most beds showing alternating patterns between clockwise and counter-clockwise rotation. However, a visual analysis of the deviation distribution does indicate a clockwise preference. Taken collectively, the mean deviation angle between the mean grain orientation and the palaeoflow direction is 47.9° ± 26.5°. (4) It is also observed that the vector magnitude for most beds are highly variable, with only beds 4 and 7 showing a progressing larger magnitudes with height (Figure 4-15 and 4-17). Furthermore, there is no perceptible link or trends between vector mean, vector magnitude, and palaeocurrent direction.

Bedding Perpendicular. All samples bar seven have an imbrication angle greater than 15° (Table 4-6). Hiscott and Middleton (1980) took the 15° threshold as being statistically

significant, and is used here as a cut-off value for imbricated and horizontal fabric. Taken collectively, the mean imbrication angle relatively to the horizontal is 80° ± 55.9° for both sets of beds. Visual analysis of Figure 4-12 to 4-18 does reveal a number of subtle patterns, although it should be noted that no single trait is common in all the beds. (1) Vertical trends within individual beds reveal highly variable imbrication angles from one sample to the next with large circular variance and frequent reversal of polarity. However, both up-current and downcurrent polarities occur in approximately equal frequency, with 56% of the sample exhibiting an up-current trend, and only bed 5 showing a predominantely up-current polarity vertically (Figure 4-16). (2) High angle imbrication is frequently observed at the base of beds. High imbrication angles are also observed at the top of all Tunisian beds, which is in contrast to the nearly flat, low angle imbrication observed in the French beds. In the latter, this could be tentatively correlated to the normal grading and/or transition to tractional structures (Figure 4-16 to 4-18). In both formations, however, the middle parts of the beds show variable imbrication angles. (3) Vector magnitudes over the massive interval in all beds are highly variable and relatively low in comparison to vector magnitudes observed for laminated intervals at the top of beds (i.e. beds 6 and 7). Furthermore, there appears to be no relationship between the vector magnitudes and imbrication angles within the massive intervals. For the two samples collected from the laminated interval, there is a strong dependence between low imbrication angles and high vector magnitudes (4) Except for bed 4 (Figure 4-15), there is no relationship between a-axis orientation in the bedding parallel sections and imbrication angles. Nevertheless, for bed 4, which shows an isotropic to flow transverse fabric with almost horizontal imbrication angles, the link between the two parameters is tentative since the samples were collected in a bed exhibiting patchy grain texture. This patchy texture could be the macroscopic equivalent of the micro-domains identified by Hiscott and Middleton (1980).

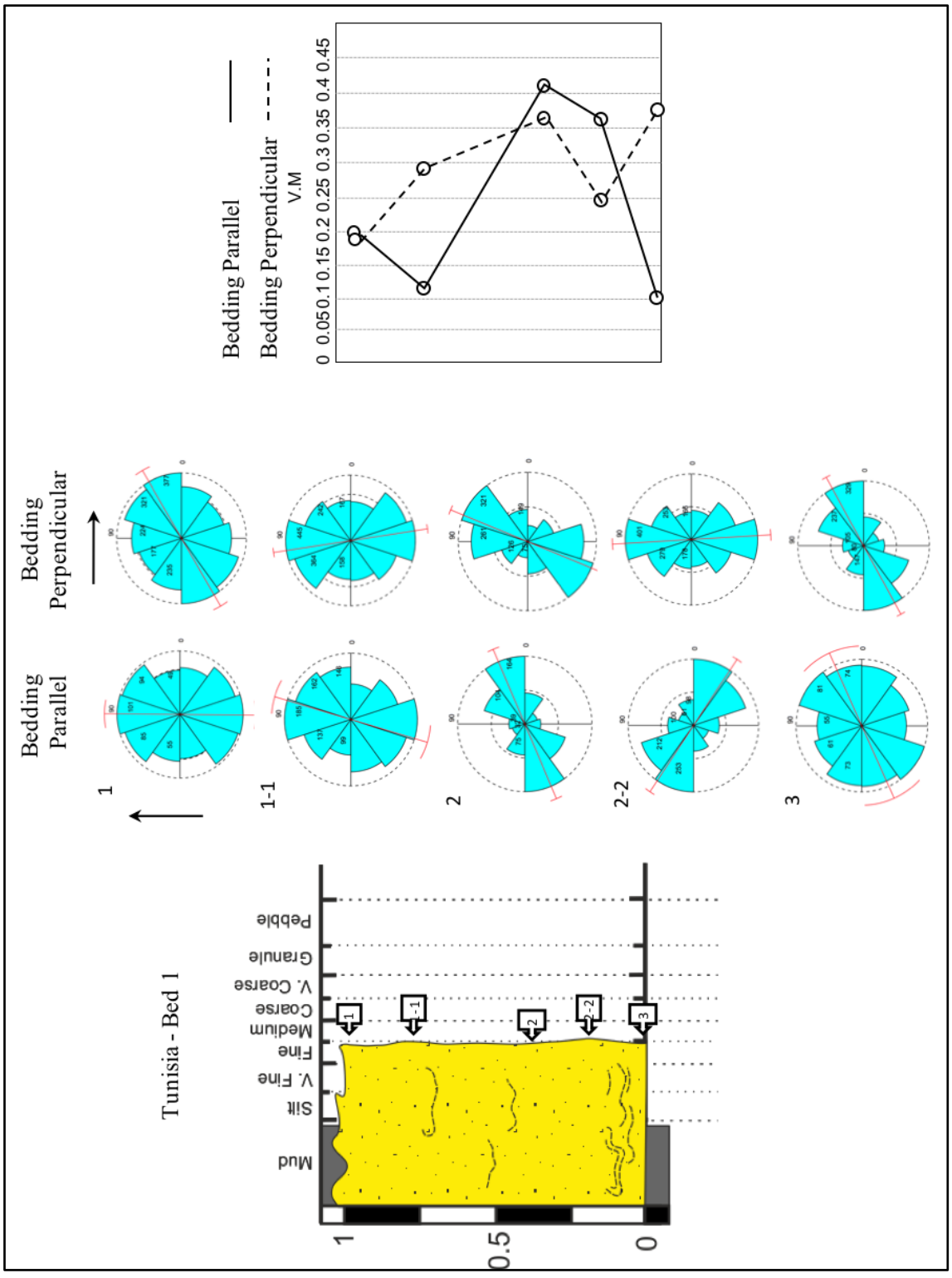

Figure 4-12: Fabric result for bed 1. Preferred grain long axis orientation in bedding parallel plane are shown relative to palaeocurrent direction derived from sole marks. The choice of sections in the vertical section was based on the mean grain orientation measure in the bedding parallel plane. This provided grain imbrication angles relative to the horizontal. Equal area rose diagram were generated in the software PAST and are shown in 36° intervals. V.M is vector magnitude, which measures the degree of alignment.

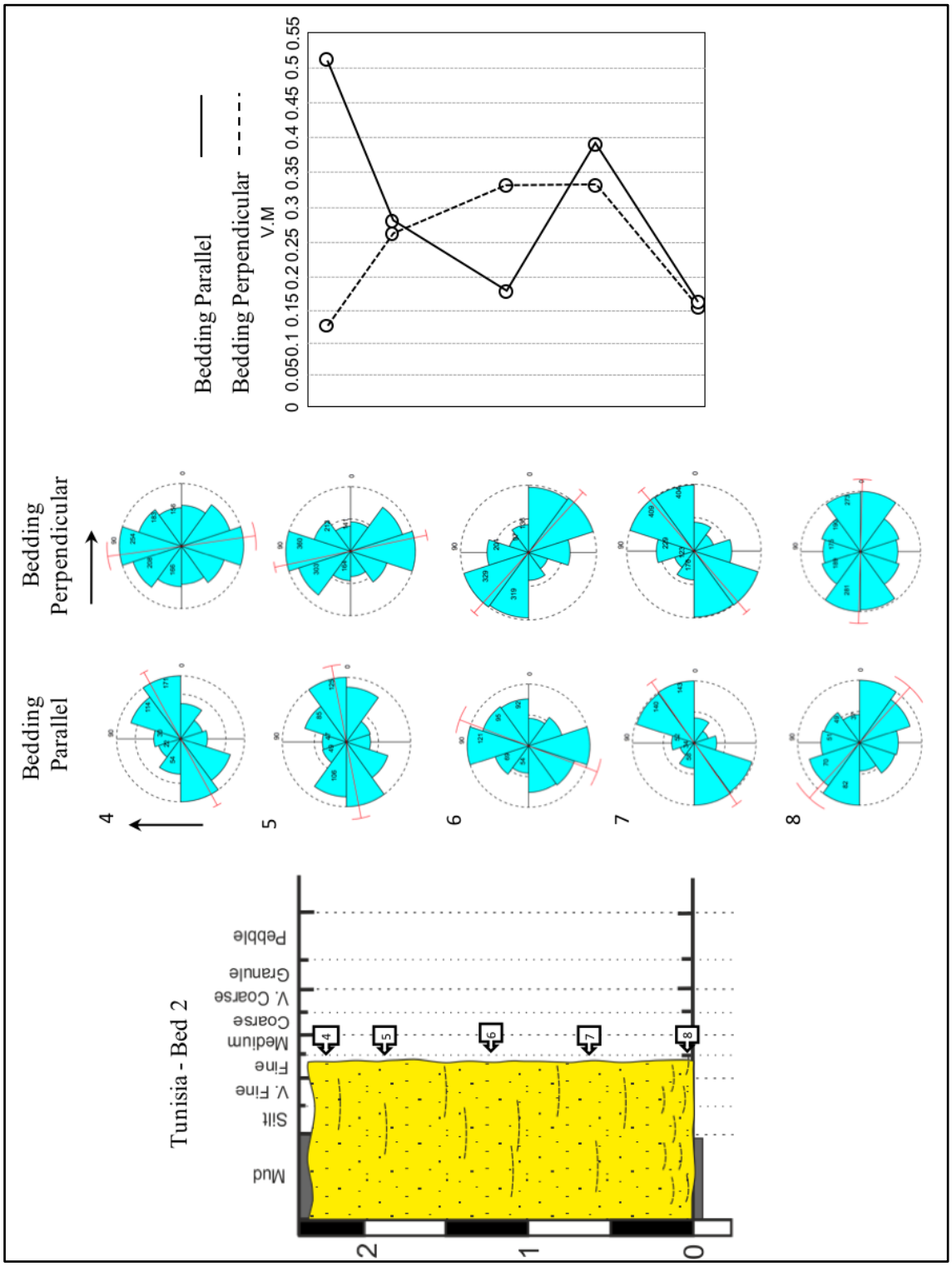

Figure 4-13: Fabric result for bed 2. For further explanation, refer to Figure 4-12.

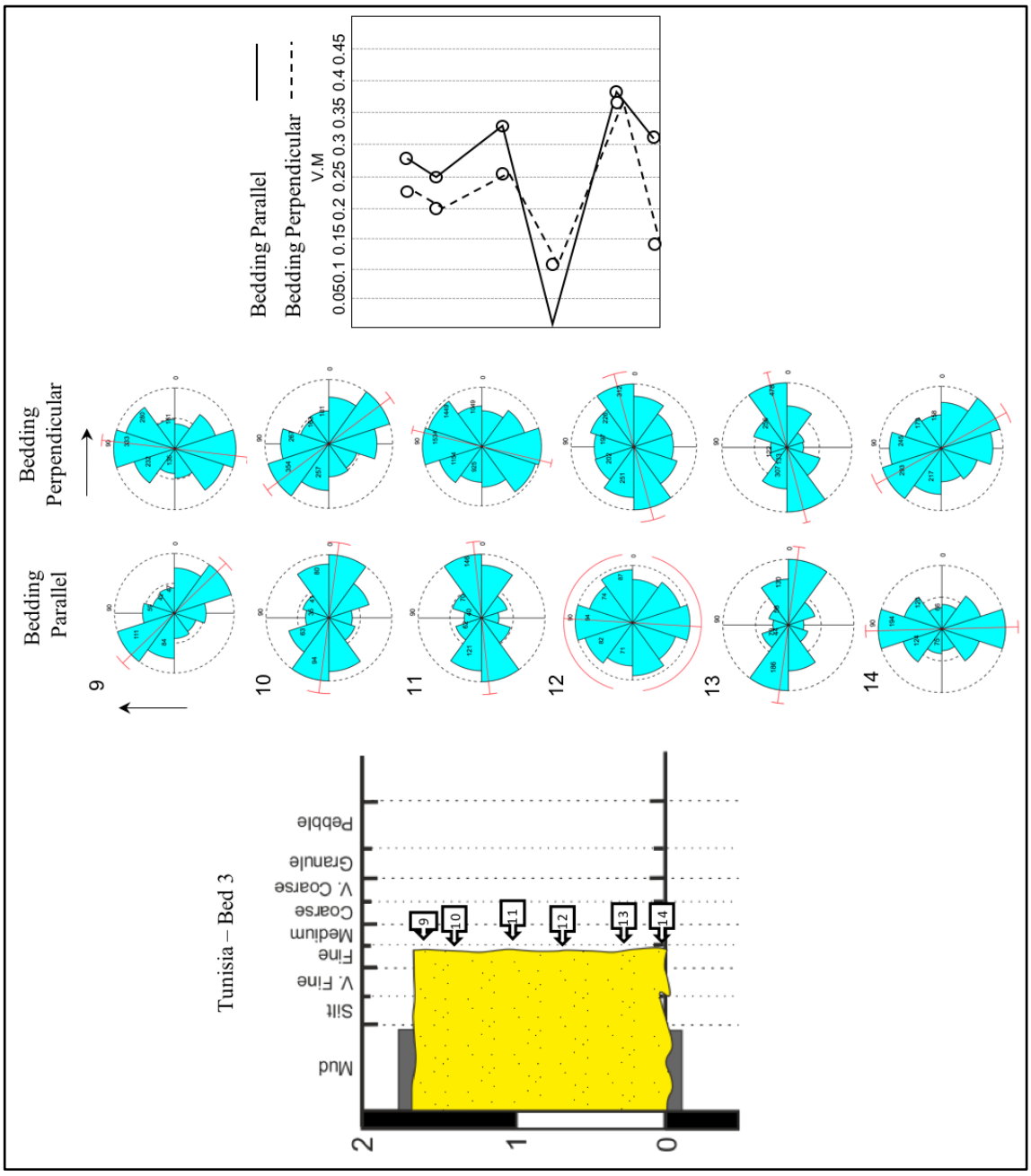

Figure 4-14: Fabric result for bed 3. For further explanation, refer to Figure 4-12.

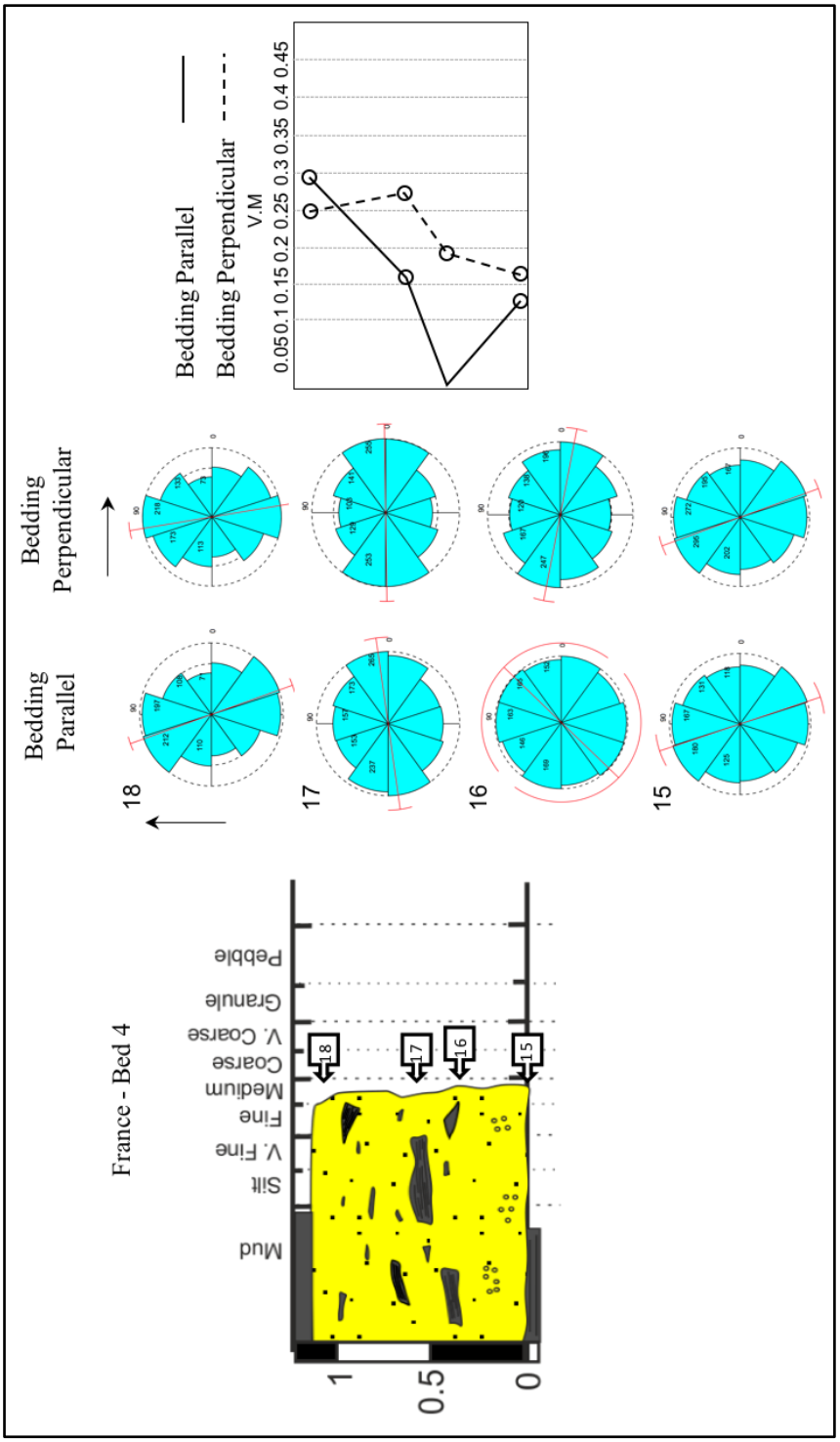

Figure 4-15: Fabric result for bed 4. For further explanation, refer to Figure 4-12. A change in fabric pattern in both planes is seen the middle and coincides with the large bedding parallel clasts.

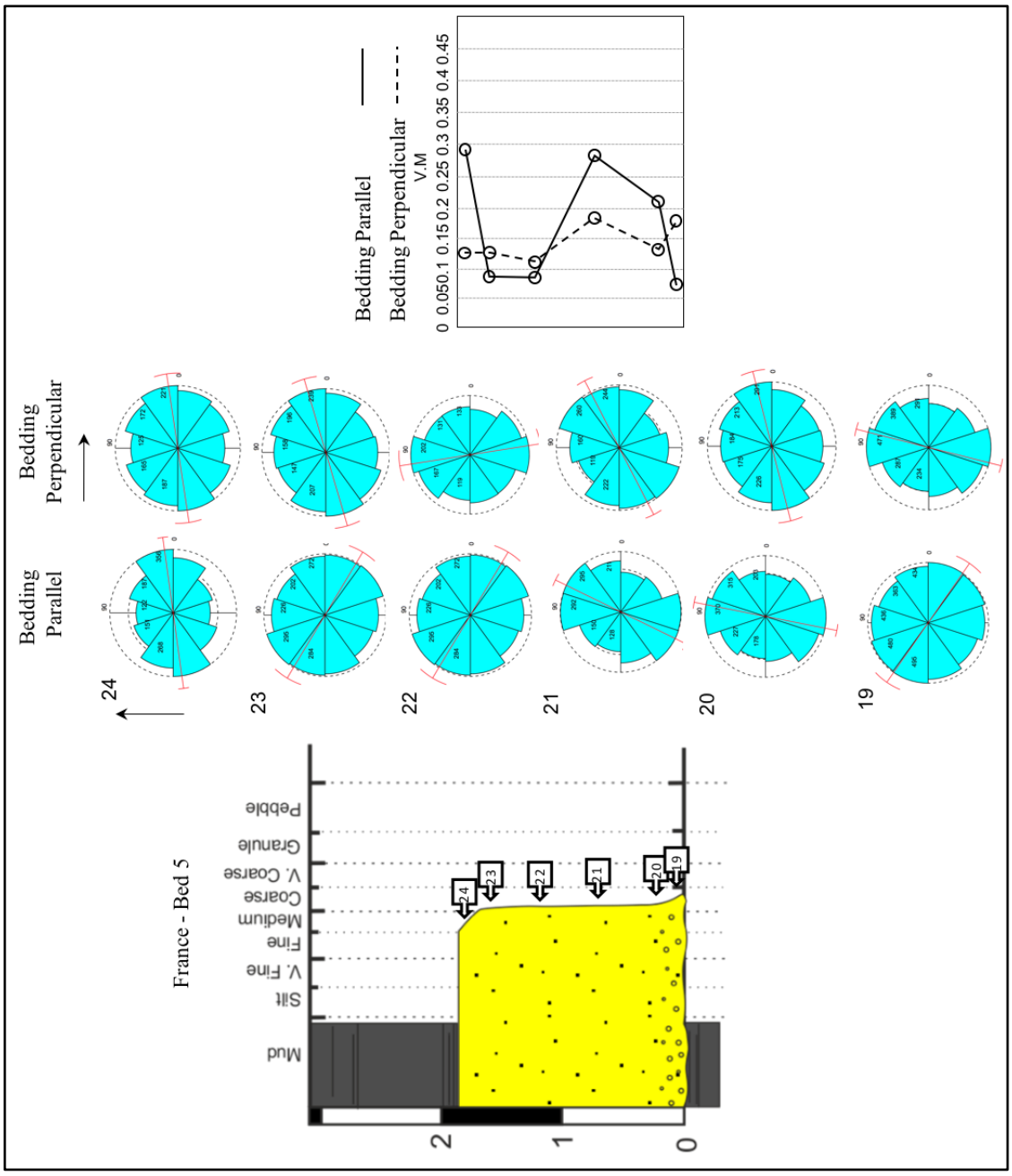

Figure 4-16: Fabric result for bed 5. For further explanation, refer to Figure 4-12.

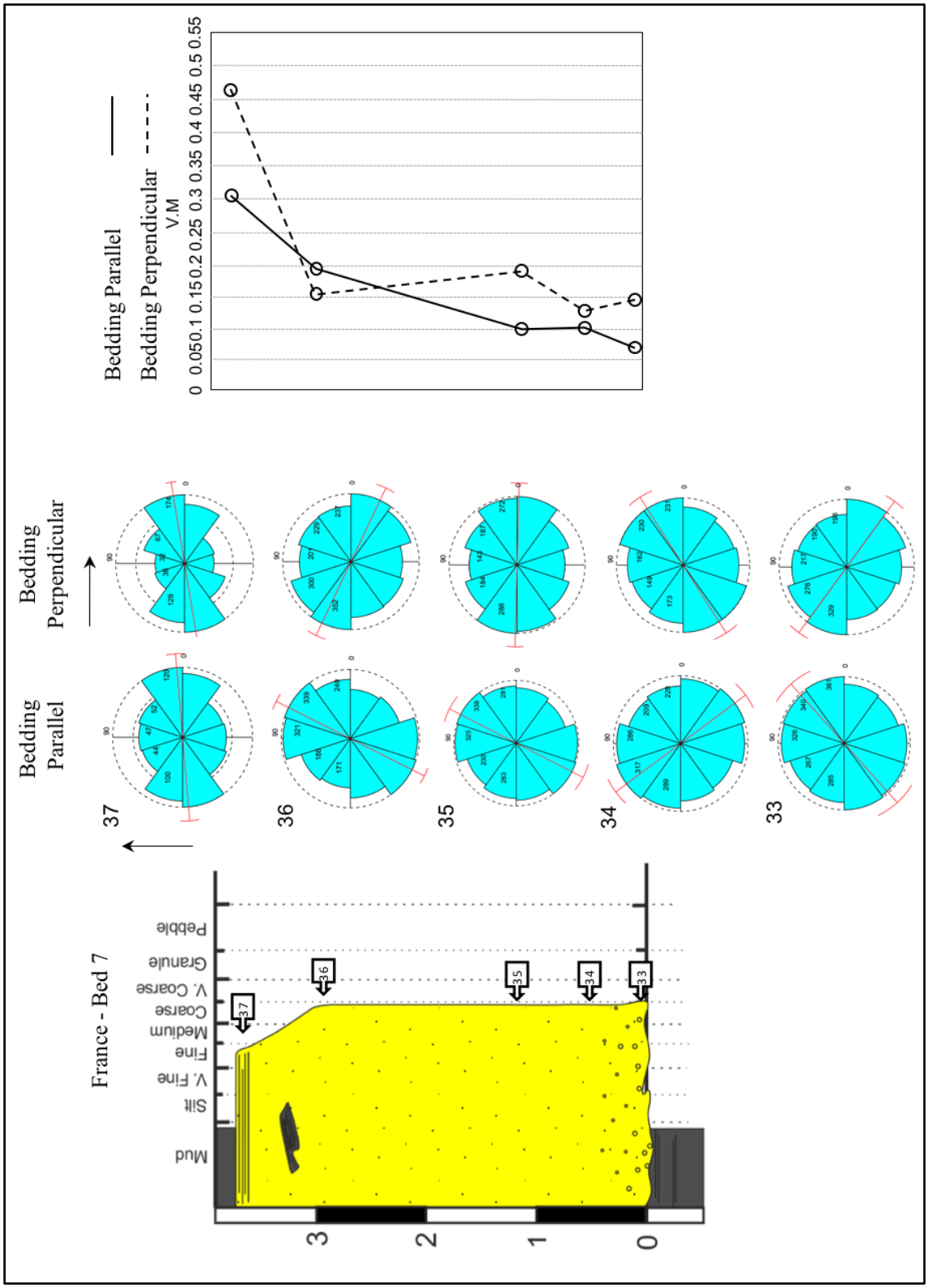

Figure 4-17: Fabric result for bed 7. For further explanation, refer to Figure 4-12.

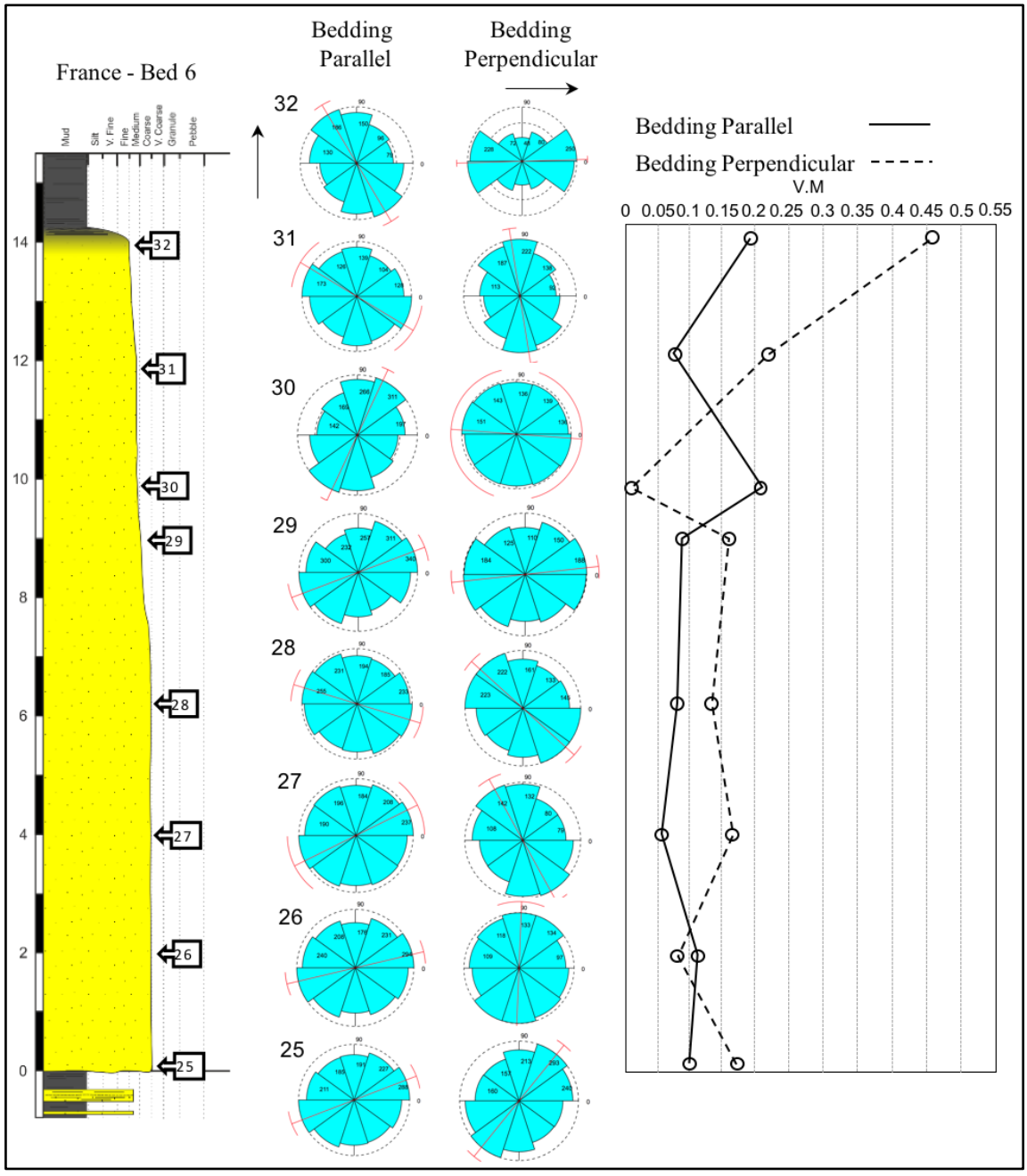

Figure 4-18: Fabric result for bed 6. For further explanation, refer to Figure 4-12. Vector magnitude in both planes is greatest in the graded and laminated cap. See text for detail.

4.5 Interpretation.

A significant body of research exists detailing textural trends in deep-water sediment flow deposits. However, research that pertains exclusively to massive sands has been rare and sporadic. In the following section, the textural trend identified in the framework and zircon components at a single outcrop will be used to understand flow processes responsible for emplacing massive sands. Since no single textural trend was common to all the massive beds, dominant trends are discussed initially, followed by isolated trends.

4.5.1 Grain Size and Sorting Trends in the Framework Component.

Coarse-Tail Inverse Grading associated with Fine-Tail Normal Grading. In beds 6, and 7, a distinct coarse-tail inverse grading is associated with fine-tail grading at the base. A general decrease in sorting is also visible over this interval, except in bed 7, where due to a comparatively small degree of inverse grading, in the 90^{th} percentile, sorting improves vertically. Previous observations and documentation of inverse grading were interpreted as deposits of traction carpets (Gonalez-Bonorino and Middleton, 1979; Hiscott and Middleton, 1979, 1980; Sallenger, 1979), wherein dispersive pressure pushed larger grains upwards towards the zone of least shear strain. In contrast, Shanmugam and Benedict (1978), Shanmugam (1996, 2000, 2012 and 2016) and Mulder and Alexander (2001) interpreted inverse grading as a product of dispersive pressure in debris flows, due to grain to grain interaction and matrix strength. However, Legros (2002) argued against dispersive pressure as a mechanism for inverse grading, theorising that dispersive pressure must equal the applied normal stress at every level within the traction carpet. If dispersive pressure increases, there is an associated upward force that results in an immediate expansion of the traction carpet, and thus a decrease in grain concentration and dispersive pressure. Since applied normal stress increase downwards within the traction carpet, the vertical gradient of dispersive pressure is also equal to the static pressure gradient. Thus only grains with lower densities than the bulk density of the flow are pushed upwards (*ibid.).*

The inverse grading cannot also be explained by waxing flow conditions (e.g. Mulder et al. 2001; Kneller, 1995; Kneller and Branney, 1995). While it is conceivable that such condition can create coarsening-upward basal units, these sequences are often associated with grain size breaks that indicate erosion of earlier deposited sediments when flow velocity become sufficiently energetic (Kneller and McCaffrey, 2003; Stevenson et al. 2014; Sumner et al 2012; Talling et al. 2007). Since no grain size breaks were observed within the studied beds (Figure 4-6), waxing flow conditions are not thought to be responsible for the inverse grading characterising the bottom of beds. Furthermore, any interpretation relating changes in grain size to changes in flow velocity has so far failed to establish a relationship between the two variables (Komar, 1985; Middleton, 1962). In fact, obverse trends have been seen in experimental flows of Sumner et al. (2008). In addition, competence driven deposition should theoretically deposit a well sorted bed (Sylvester and Lowe, 2004). However, the poorly sorted nature (σ 1 – 2) over which the inverse grading occurs in the present beds is indicative of capacity driven deposition (Allen, 1991; Hiscott, 1994).

Alternatively, inverse grading could be attributed to kinetic sieving (Middleton, 1970). Kinetic sieving describes the selective percolation of small grains through voids that open and close due to the agitation of larger grains. In engineering literature, numerous physical experiments have

established the efficiency of kinetic sieving in dry granular flows (Delannay et al. 2017; Gillemot et al. 2017; and Johnson et al. 2012 and references therein). In the subaqueous environment, Cassar et al. (2005) demonstrated similar processes within dense granular flows on a steeply inclined slope, but with translocation of smaller grains occurring over a longer time-scale due to the effects of buoyancy. Inverse grading seen in the coarse-tail faction in the present study could arguably be produced in such a manner. Kinetic sieving has been shown to operate in near bed high-concentration layers that form at the base of concentrated turbidity currents (Cartigny et al. 2013; Spinewine et al. 2013; Sumner et al. 2008; Vrolijk and Southard, 1997). These layers are characterised by turbulence damping and prolonged shearing of grains. Cartigny et al (2013) and Sumner et al (2008) argued that kinetic sieving is only active in these layers during low aggradation rates, when the low upward flux of escaping fluid would not hinder percolation of the smaller grains. Under higher aggradation rates, the higher net upward flux of escaping pore fluid would instead promote elutriation of fine grains, and prevent kinetic sieving. The internal character of a deposit produced from such a model should display inverse '*distribution'* grading. However, the fine-tail inverse grading makes this model antithetical to the current grain size trends.

The grain size trends observed in this study are not unlike those reported by Sylvester and Lowe (2004) from Carpathian turbidites, at least in terms of the median- and coarse-tail fraction. They attributed the inverse grading to rapid capacity driven deposition that trapped fine material towards the base, including the mud faction. In the context of a waning turbidity current experiencing capacity-driven deposition, inverse grading is created as a function of the declining sediment fallout rates and corresponding increasing elutriation of fines. While this model was discounted by Cartigny et al. (2013) and Sumner et al. (2008) based on the negative correlation between inverse grading and aggradation rates, elements of the model may help explain the fine-tail grading associated with coarse tail inverse grading. Especially in light of physical and numerical settling experiments undertaken by Amy et al. (2006) and Dorrell et al. (2011), in which high sedimentation rates resulted in poorly sorted deposits with little or no elutriation of finer grains.

To explain the diverging grain size trends at the base (Figure 4-10 and 4-11), the model proposed here evokes both kinetic sieving and entrapment of fines under high sediment fallout rates. This leads to increased entrapment of finer grains as the influence of grain segregation processes (i.e. elutriation) diminishes in the near bed layers. In the coarse component, due to the increasing effects of grain-to-grain interaction, kinetic sieving is activated and leads to inverse-grading and bedform suppression. As sediment-fall out rates decline gradually, elutriation by escaping pore-fluids eventually contributes to the removal of fines in the near bed layers, leading to inverse grading in the fine-tail (Figure 4-19A). At this point, grain size segregation in

the downward coarser sediment flux also becomes meaningful to produce a graded deposit (beds 6 and 7). This latter process thus explains the converging grain size trends in the extreme percentiles, which are discussed below. The poor sorting, observed at the base of bed 6 and 7 reinforces the rapid dumping of sediments. In the case of beds 6, the sorting is inversely graded, reflecting the diverging trends in the fine and coarse-tail. In bed 7, a weak normal grading is seen, possibly a reflection of the strong inverse grading observed in the 50^{th} percentile, which has the effect of narrowing the distribution. A case could be made that the effect of trapping was strong enough to influence the 50^{th} percentile (Sylvester and Lowe, 2004). Even though inverse grading was not observed at the base of bed 5, the preceding model could yet explain the initial character with minor fluctuations in sediment fallout rates and grain segregation processes operating in the near bed layer.

Coarse-Tail Normal Grading associated with Fine-Tail Inverse Grading. In the middle to top of beds 5, 6 and 7, a converging trend in the fine-tail and coarse-tail is visible (i.e. fine-tail inverse grading and coarse-tail normal grading; Figure 4-10 to 4-11 and 4-19B). Although quantitative documentation of fine-tail inverse grading is rare in downslope process literature, the cause(s) of normal grading has been well documented. It has been interpreted as evolving temporal and density structure of near bed layers at the base of a turbidity current (Bass et al. 2000; Kneller and Branny, 1995; Kneller and McCaffrey, 2003; Kuenen and Migiorini, 1950; Middleton and Hampton, 1973; Shanmugam, 1997; Sumner et al. 2008; Sylvester and Lowe, 2004) or grain segregation during suspension settling (Lowe, 1982; Shanmugam, 2010). However, the poorly sorted nature of the beds implies that normal grading could not have developed from static suspension, and capacity, not competence, is the fundamental control on deposition (Dorrell et al. 2013; Hiscott, 1994a; Pickering and Hiscott, 2015). This is reinforced by the quantitative field analysis by Komar (1985) who found inconsistencies between velocity estimated on grain size and that based on bedform stability diagrams. The author went further and concluded that agreement between grain and bedform-estimated flow velocity could only be achieved if one considers only the 95^{th} percentile of the grain size distribution; a condition that questions the presence of the finer material in the bed during competence-driven deposition.

The converging grain size trends in the middle of beds (i.e. 5, 6, and 7) is likely created under capacity-induced deposition, where sediment fallout rates were initially high, but not so high as to prevent grain segregation in the near bed layers, at least in the coarse tail component. Such flow characteristics have been observed by Marr et al. (2001), who reported coarse-tail grading in coal slag from decelerating turbulent and weakly turbulent flows. These results were corroborated by Sumner et al. (2008) and Postma et al. (2009), who observed coarse-tail grading during conditions of hindered settling under high sediment fallout rates from concentrated turbidity currents. With time, sediment concentration in the flow declines and the

downward flux of sediments to feed the near bed layers also decreases. As a result, hindered settling and elutriation by escaping pore-fluid becomes important, resulting in inverse fine-tail grading and a stronger normal coarse-tail grading (i.e. convergent trend; Figure 4-19B). Further decline in sediment fallout rates results in distribution graded caps of most beds, with or without tractional structures (beds 1, 4, 5 and 7; Figure 4-19B and C; Sumner et al. 2008). The overall grain size profile from the above model for the coarse-tail component would be convex up due to the temporal change in sediment fallout rates and influence of grain segregation processes.

Alternating inverse-normal-inverse graded. Bed 1 shows a systematic alternation between inverse and normal graded intervals in the 50^{th}, 90^{th} and 95^{th} percentiles vertically, and only normal to inverse grading trends in the fine-tail (Figure 4-9). Despite being difficult to reconcile using the above model, the trends can be explained by short-term non-steady effects that influence deposition from high-concentration near-bed layers. As witnessed in experiments that generated high-concentration near beds layers (e.g. Cartigny et al. 2013; Sumner et al. 2008; Vrolijk and Southard, 1997), expansion and deflation of the layer over time scales of a few seconds is controlled by sediment flux from the overlying turbulent flow. During periods of high sediment flux (corresponding to low velocity pulses in the experiments), the near bed layers expand, and grain-to-grain interaction and kinetic sieving become active. During periods of low sediment flux, grain segregation processes dominate and a graded deposit is likely to form. These non-steady effects were observed over timescale between 0.2 to 2 seconds by Cartigny et al. (2013). It is speculated that while the coarse-tail trend reflected the changing flow behaviour in the near bed layers in bed 1, the fine-tail component may have not had sufficient time to respond to the evolving flow conditions (i.e. trapped at the base of the flow). Alternatively, sample bias may have contributed towards the grain size trend in bed 1. A practical approach used by geologist is to sample at regular intervals, and this strategy was employed for ungraded sands, unless changes in grain size were observed. It is plausible that the grain size changes not discernible with the naked eye where not sampled. Thus, to resolve the alternating grain size changes, more samples may need to be analysed.

Ungraded. The Kruskal-Wallis test indicates no significant difference between sample medians in the framework component for beds 2 and 3. Although this does not imply wholly ungraded textural trends, visual comparison of the percentiles indicates minor/no variability vertically (except for bed 3 between sample 12 and 11 for the 50^{th}, 90^{th} and 95^{th} percentiles). Kneller and Branney (1995) attributed ungraded deposits to sustained, quasi-steady turbidity currents governed by competence driven deposition. As explained above, capacity is the determining factor in governing deposition as indicated by the poorly sorted deposits. Experimental results (e.g. Amy et al. 2006; Breien et al. 2010; Dorrell et al. 2011; Dorrell et al 2013; Cartigny et al. 2013; Sumner et al. 2008) suggest ungraded massive sands can form from incrementally

deposition of high-concentration near-bed layers that have sediment concentrations in excess of 45%. Turbulence is completely dampened in these layers and grains are in near continuous contact. This would prevent grain segregation and the final deposit will be ungraded and poorly sorted. The shear stresses and velocities necessary to generate these layers would prevent deposition, unless small scale fluctuations in flow velocity are present (Cartigny et al. 2013; Sumner et al. 2008). During these velocity fluctuations, it is not difficult to envisage high and constant aggradation rates that would lead to the massive character of the deposit.

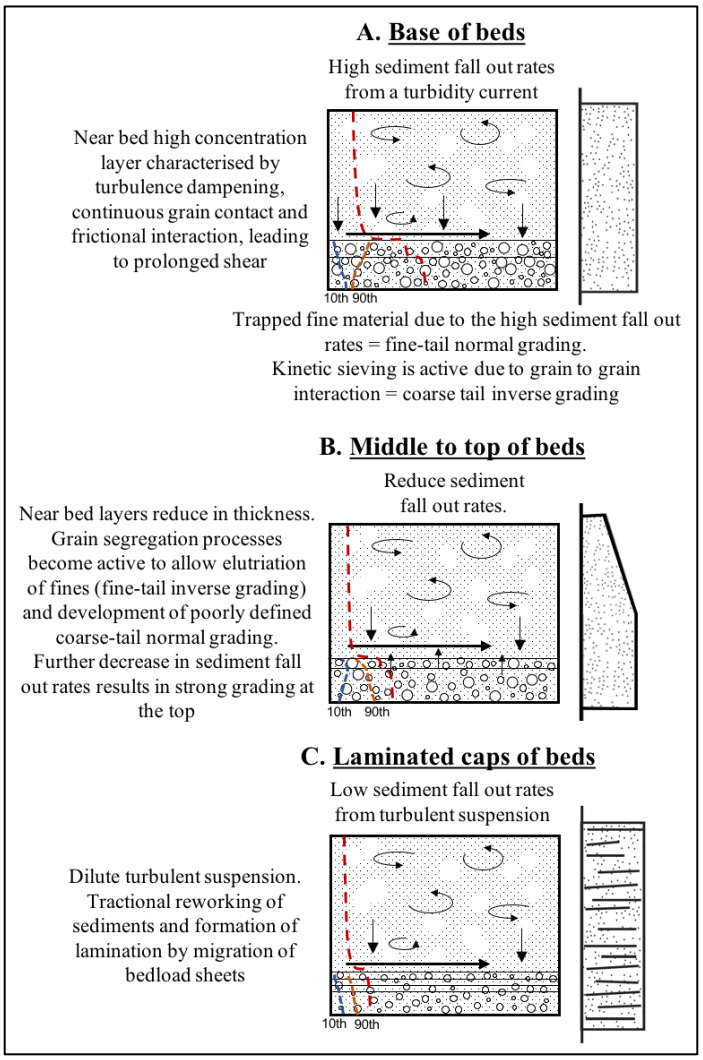

Figure 4-19: An idealised model to explain the divergent to convergent grain size trends. Dashed red, orange and blue lines are the sediment concentration, coarse-tail and fine-tail profile respectively.

Repetitive graded and ungraded massive sands. Sedimentary log of bed 6 demonstrates an anomalous repetition of facies (Figure 4-6, Appendix C) consisting of ungraded and graded intervals. This alternating trend, although observable using a grain size comparator, is not detected in the grain size analysis. Sample sufficiency is an issue in this bed due to its unusually large size, and a more appropriate strategy may have revealed a more heterogeneous grain size trend similar to the other beds. A detailed explanation of this repetition pattern is provided in

Chapter 4 when considering the longitudinal evolution of the flows. However, at a single outcrop, short-term unsteady concentration and velocity effects can explain the patterns in the sedimentary logs.

4.5.2 Grain Size and Sorting Trends in the Zircon Component.

A hydraulic equivalence exists between quartz and zircon grains, which results in comparable grain settling trends, but within a significantly finer grade for the zircon grains (Motanated, 2014; Poulsen et al. 2007; Sallenger, 1979). This is corroborated in the present study by the similar grain size patterns observed between the two components. Experiments of polydispersed sediments with varying densities, however, indicate that quartz and zircon settling behaviour converged only when sediment concentrations exceeded 25% and grain segregation processes were diminished (Dorrell et al. 2011; Motanated and Tice, 2016). This concentration threshold conforms with the model presented above for the deposition of the framework component. Sediment concentrations in excess of 20% have been observed in near bed high-concentration layers by Vrojilk and Southard (1997), LeClair and Arnott (2005), Sumner et al. (2008) and Cartigny et al. (2013). Thus, it is proposed here that the same processes influenced both grain size components.

Nevertheless, a number of distinct patterns not seen in the framework component are defined by the zircon grains. In bed 1 an inverse to normal grading trend is observed in the coarse-tail component, and a meandering trend in the fine-tail and 50^{th} percentile. While the trend in the finer grain size grade is similar to the framework component, it has the opposite sense of grading (Figure 4-9). The cause of these trends is as yet unknown. Poulsen et al. (2007) observed remobilisation by fluidisation resulted in an unpredicted distribution, giving a 'jagged' appearance to the grain size profile. Whilst this may explain the alternating grain size pattern in the 10^{th} and 50^{th} percentiles, it does not explain the patterns in the coarse-tail. Alternatively, short-scale non-steady effects could account for the 'jagged' profile, but this too fails to adequately account for the consistent inverse to normal grading in the coarse-tail, particularly since the coarse-tail component in the framework grains shows the jagged profile. In bed 3, an inverse to normal grading is observed in the 50^{th} percentile. This is more in line with the trends discussed above for the framework component in bed 5 and could be explained by stronger entrapment effect to influence the 50^{th} percentile. However, it does not correlate with the trends in the fine tail, which should also show inverse grading. Other than sedimentological causes, the most likely explanation for these ambiguous trends could be insufficient grain and/or sample numbers. As noted in Section 4.4.2, most of the samples had grain counts less than 300. It is probable that the grain size percentiles have not reached a statistically stable value, and hence may not be representative of actual deposition processes. In terms of sample sufficiency, the

sample spacing may have been too large to resolve cm-scale grain size changes in the zircon grain (and framework component).

4.5.3 Grain Fabric Trends in the Framework Component.

Analysis of the grain fabric data obtained for the 7 beds reveals statistically significant fabric patterns. This is largely a response of the complex interaction between the three main forces governing sediment transport and ultimately deposition: gravity, lift and drag forces (Allen, 1984). These forces are in turn controlled by the physical properties of the grains, flow rheology, flow direction and velocity, transport medium (temperature, density and viscosity) and the topography of the static bed (Baas et al. 2007). However, post-depositional processes such as bioturbation, fluidisation, soft-sediment deformation, compaction or tectonic deformation can also induce a statistically significant fabric pattern. Thus, for any meaningful interpretation on flow processes deduced from the fabric data, a relationship between primary processes and the grain fabric needs to be established (Dall'olio et al. 2013). A parallelism between the orientation of the observed grain fabric, sole marks and the lateral basin slopes could help corroborate this relationship (*ibid.*). The tilt-corrected grain fabrics were not analysed as part of this study, thus a comparison between the grain fabric and lateral basin slope directions cannot be made for either basin (in the case of the Numidian Flysch, the lateral slopes of the basin have not been preserved). However, many of the studied samples do exhibit parallel or sub-parallel grain orientation to the palaeoflow directions as measured from sole marks. Furthermore, there appears to be a systematic difference between grain orientations observed in massive intervals, and that observed in laminated intervals, at least for the Piera Cava beds. Both of these depositional structures form under different hydrodynamic conditions (Talling et al. 2012 and discussed in detail below). If secondary processes influenced the grain fabric, the fabric over the entire bed would have been modified, and not restricted to specific sediment facies intervals. In addition, and in terms of the tectonic and compactional controls on grain orientation, previous fabric studies have shown a layer parallel shortening such that a-axis orientations are perpendicular to the shortening direction (e.g. Parés et al. 2007; Cifelli et al. 2009). In most of the samples analysed in the bedding perpendicular section, the a-axis lies at a high angle to the bedding plane (imbricated), an orientation that is inconsistent with compactional or tectonic induced fabric (Dall'olio et al. 2013; Felletti et al. 2016). Based on this indirect evidence, it is tentatively considered that the grain fabric analysed in this study are essentially primary (i.e. syn-sedimentary) in origin.

Grain Fabric in Massive Sands. Studies detailing the grain fabric of deep water deposits have observed a variety of fabric patterns: uniform, oblique or flow aligned. More importantly, these grain fabrics are non-unique to facies and flow types (e.g. (e.g. Baas et al. 2007; Colburn, 1968; Hiscott and Middleton, 1980; Rees et al. 1968; Sakai et al. 2002; Scott, 1967). Nevertheless, the

flow-oblique fabric that is comparable to the dominant grain fabric of the studied massive sands is essentially restricted to this facies. For example, thin to thick massive beds from the Silurian Riccarton-Raeberry Castle flysch by Scott (1967) found deviations between 18° to 44° from the average palaeoflow direction. Similarly, Hiscott and Middleton (1980) observed reveal oblique grain alignment with mean deviation of 43°±28° in a predominantly-clockwise direction in the Tourelle Sandstone (Quebec, Canada). It has also been experimentally reproduced by Rees (1983), who revealed an interdependence between increasing sediment concentration and increasing grain deviation due to frequent grain interactions. More recently, Baas et al. (1999) found oblique fabric in ungraded and graded massive sand with a mean deviation of 44°±11° and 55°±16°, respectively. The similarity between the two facies types led the authors to suggest that similar processes deposited both facies. Baas et al. (2007) also reported a strong flow-oblique mode deviating 40° from the palaeoflow, as did Felletti et al. (2016), albeit with smaller deviation angles (between ~ 15 to 20°). In the present study, the dominant fabric pattern observed in the massive intervals is oblique to palaeoflow (Table 4-5), with an average deviation of 48° ± 26°, which is broadly consistent with the above results.

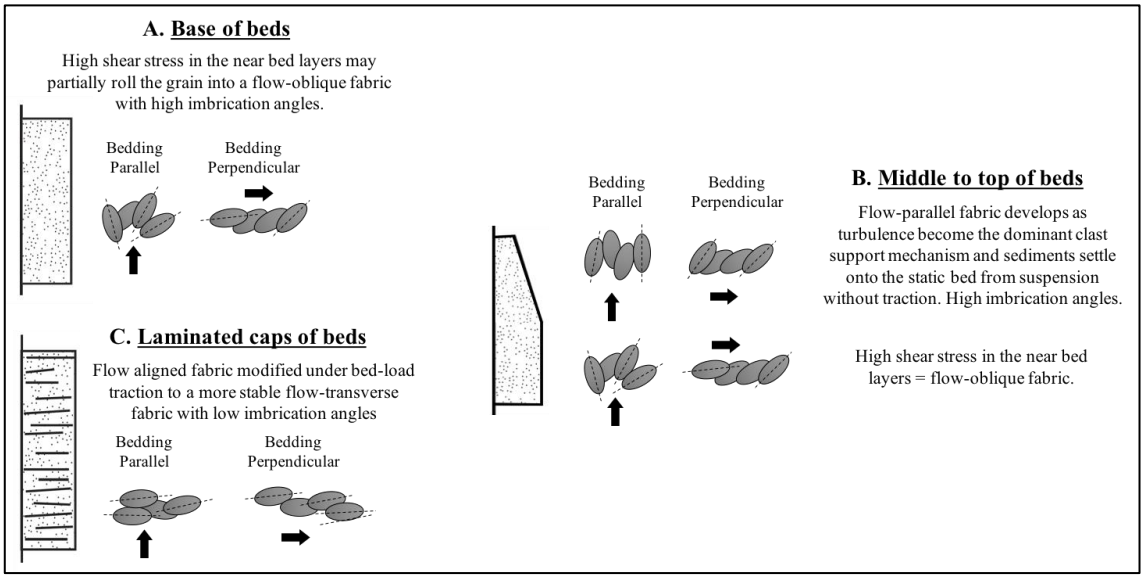

Figure 4-20: An idealised model showing the systematic change in grain fabric trends vertically within the studied beds. The base and middle of the beds show predominately flow-oblique trend created by prolonged shearing within high concentration near bed layers. As sediment fallout rates decline, grains are deposited onto the static bed from suspension without tractional working. This leads to the development of flow parallel fabric with high imbrication angles. With further reduction in sediment fallout rates and tractional working prior to deposition, grain orientations become transverse to flow with low imbrication angles. Dashed line indicate long-axis orientation.

Under controlled flume experiments, statistically significant deviation from the paleoflow direction has been observed by Sakai et al. (2002) and Arnott and Hand (1989). The cause of this deviation was attributed to local flow divergence by Sakai et al. (2002), yet the difference could also be caused by different phases of flow deposition or distinct flow mechanisms (Baas et al. 2007). The studied samples show little consistency in the mean vector rotation, with

frequent alternation between clockwise and counter-clockwise rotation about the mean. While short-term flow divergence cannot be completely ruled out, the lack of a systematic change in orientations in the studied beds may preclude flow divergence (Clark and Stanbrook, 2001; Duller et al. 2010). Alternative mechanisms for oblique grain fabric include incomplete reorientation of a rolling fabric, either into a flow-parallel or flow-transverse pattern, or post depositional modification by soft-sediment deformation and/or bioturbation. While the former is likely to be related to flow processes, the latter can be discounted in the majority of the beds (except beds 1 and 2) due to a lack of evidence of post-depositional deformation and bioturbation. Therefore, the cause of the oblique-fabric in the massive sands may have to be sought in specific hydrodynamic flow conditions.

Baas et al. (2007) intimated that there is a better correspondence between a depositional mechanism and the orientation of grains, than between grain orientations and different divisions of the Bouma sequence. Flow-parallel fabric forms when grains settling from a turbulent suspension orientate their a-axis parallel to the flow (Allen, 1984; Ruznal, 1957), while flow transverse fabric develop when bed load sediments orientate their a-axis perpendicular to flow direction when flow strength is sufficient to roll elongated grains (Schwarzacher, 1963). However, flow-oblique fabric remains largely enigmatic, though it has been speculatively attributed to deposits of sheared dispersion that inhibits "certain types of orbits though not so frequent as to prevent the orbiting mechanism dominating the production of preferred orientation" (Rees, 1979; 1983). These dispersions are characterised by turbulence damping, continuous grain contact and frictional interaction, which creates prolonged shear (Cartigny et al. 2013; Sumner et al. 2008; Vrolijk and Southard, 1997). It is proposed that such flow processes are responsible for the dominantly oblique grain fabric developed in the massive beds of the Grès de Peïra Cava and the Numidian Flysch. The dispersions can reach concentrations up to 65% (e.g. Cartigny et al. 2013) and correspond to the frictional regime of Sohn (1997). The higher shear stress may at first prevent deposition and the grains may be partially rolled along the static bed to produce the flow-oblique fabric (Figure 4-20A). This is predicated on the experimental work of Hughes (1995), who observed negligible rolling of grains in moderately concentrated flows (up to 20%) prior to deposition. With decreasing concentrations and sediment fallout rates, the sediments settle out of suspension on to the static bed with or without tractional reworking. This is likely to produce parallel fabric and eventually flow-transverse fabric with increasing tractional working (Figure 4-20B-C; Allen, 1984; Arnott and Hand, 1989; Baas et al. 2007). In the latter stages, the degree of alignment (vector magnitude) also increases as grains experience a longer residence time of tractional reworking prior to deposition. This temporal evolution in the grain support mechanism(s) not only supports the development of the dominantly oblique fabric at the base and middle of most beds in the massive sands, but can

also explain the crude transition to flow-parallel and -transverse fabric at the top where normal grading and parallel lamination is common (i.e. beds 1, 2, 4, 5, 6 and 7; Figure 4-12 to 4-18).

In bed 3, an alternating flow-parallel to transverse fabric is seen vertically from the base. Presently this trend is difficult to explain and could be a consequence of: (1) sampling error in the field, (2) measurement error in the bedding parallel section, (3) post-depositional reorientation of grain fabric, (4) incomplete reorientation of flow-parallel, -oblique or –transverse fabric, and/or (5) small scale fluctuations in flow direction. In bed 4, flow-transverse and isotropic fabric occurs over an interval that is dominated by large mudclasts and a patchy grain size texture. It could be argued that this bed, and the resulting fabric pattern, was deposited by a debris flow (Bouma and Pluenneke, 1975; Felletti et al., 2016; Naruse and Masuda, 2006; Talling et al., 2013). The patchy texture, which was interpreted by Talling et al. (2013) as a record of pervasive liquefaction in debris flows, lends support to this interpretation. The more or less parallel to flow fabric at the base and top of bed 4 could be due to intense shearing and rapid sediment fall out from an overriding turbulent suspension, respectively.

Imbrication Angles in Massive Sands. In addition to the predominantly flow-oblique fabric, the corresponding imbrication angles for the massive intervals are also relatively high, with a mean imbrication angle of 80° ± 55.96°, and only seven of the samples exhibiting angles less than 15°. This is significantly higher than imbrication angles reported by Parkash and Middleton (1970), Taira and Scholle (1979), Hiscott and Middleton (1980), Arnott and Hand (1989), Baas et al. (1999) and Baas et al. (2007) for massive sands, where angles approached up to 40°. However, Hiscott and Middleton (1980) found imbrication angles up to 71° in beds with de-watering structures. Very subtle de-watering structures are seen in beds 1 and 2 in the form of dish structures, and could explain high imbrication angles in these beds. Nevertheless, this does not explain the high angles observed in the remaining beds, which contained no de-watering structures. In fact, a comparison of mean imbrication angle for beds 1 and 2, and the remaining beds, shows similar angles (i.e. 87° and 77°) and suggests they are likely to have formed by related processes. It is plausible that syn- and post-deposition de-watering has modified all the studied beds, and the lack of de-watering structures in the sedimentary logs (Figure 4-6) is due to a failure to recognise them because of poor weathering and exposure. The high variance and frequent changes in polarity in the samples does lend support this hypothesis. Still, it is difficult to discount a primary origin to the high imbrication angles.

Numerous studies combine to show imbrication angles in massive sands are typically higher than laminated and rippled intervals (e.g. Allen, 1964; Baas et al. 2007; Hiscott and Middleton, 1980; Sestini and Pranzini, 1965, Tiara and Scholle, 1979). Grain interaction was thought by

Hiscott and Middleton (1980) to be responsible for these high angles. In the flume experiments of Arnott and Hand (1989), highest imbrication angle was linked to highest sediment fallout rates, most likely due to intense grain interactions, while Yagishita et al. (2004) related high imbrication angles to high Froude numbers and transmission forces generated by frequent grain collision. Collectively, these studies describe a process similar to the one proposed above for the generation of flow-oblique fabric. That is, high angle imbrication developed within a high concentration near-bed layer that formed due to high sediment fallout from a turbulent suspension (Figure 4-20A). As sediment fallout rates decreased, lower imbrication angles developed (Figure 4-20B and C). This is supported by the high imbrication angles at the base of most beds, which typically decrease vertically and becomes almost horizontal at the top (e.g. beds 5, 6 and 7). Such vertical trends have also been reported by Sakai et al. (2002), who analysed continuous imbrication angles in two flume generated beds. Furthermore, these experiments reveal disorganised vertical changes in polarity of the imbrications angles, similar to those reported in this study. While Hiscott and Middleton (1980) also attributed this to the high sediment fallout rates, Sakai et al (2002) related the polarity reversals to Kelvin-Helmholtz instabilities. In these instances, the vortices induced at the interface generate temporary up-current directed shear stress that could create downcurrent imbrication angles. The experimental flows of Cartigny et al. (2013) generated multiple interfaces at which these instabilities formed. However, only the lower interface separating the near bed high-concentration layer and overlying turbulent suspension, had a direct influence on the character of the deposit (*ibid*.). This interpretation is therefore also consistent with the mode of deposition that generates the flow-oblique fabric and the high imbrication angles described above.

4.6 Summary.

Macroscopically massive sands are ubiquitous in many modern and ancient turbidite systems. The massive nature and limited outcrop extent of these sands restricts any field-based analysis to their textural components. Grain size, sorting and fabric components of massive sands in the Numidian Flysch (northern Tunisia) and the Grès de Peïra Cava (SE France) have been analysed to characterise grain scale heterogeneity and to elucidate the mechanism(s) of emplacement using digital image analysis. The massive sands show statistically significant trends vertically in both grain size and fabric. Grain size can be normally or inverse graded, or ungraded in any of the percentiles. However, a common trend showing a divergent followed by a convergent profile involving the coarse- (90^{th}) and fine-tail (10^{th}) component is seen in a number of beds. Grain fabric is dominantly oblique to the palaeoflow, with grains imbricated at a high angle relative to the horizontal. There is no correlation between vector mean and vector magnitude, although a crude transition to either a flow-aligned or transverse fabric is seen at the top of most beds.

These textural trends are a fingerprint of the hydrodynamic conditions of the flow immediately prior to and during deposition of the sediments. They can be explained by active near bed sedimentation processes that are controlled by sediment fallout rates from a concentrated sediment flow. High sediment fallout rates initially prevent elutriation of fine material from the base of the flow, which is characterised by grain-to-grain interaction, kinetic sieving and prolonged shearing. The differential impact of these processes on the various distribution percentile contributes towards fine-tail normal grading and coarse-tail inverse grading. These near bed processes are also responsible for the oblique fabric trends with high imbrication angles. With declining sediment fallout rates, the influence of grain segregation processes grows, to the extent that elutriation of fines results in fine-tail inverse grading and coarse-tail normal grading. Deposition of from suspension also produces flow-parallel fabric. The latter stage of deposition is characterised by low sediment fallout rates and distribution grading with or without the development of lower plane stratification, and flow-transverse fabric.

Chapter 5– Depositional Facies and Reservoir Heterogeneity in the Massive Sand Facies Association (MSFA) of the East Brae Formation, South Viking Graben.

5.1 Introduction.

Most previous studies on massive sands have focused on flow processes responsible for their emplacement (e.g. Hiscott and Middleton, 1980; Kneller and Branney, 1995; Naruse and Masude, 2006; Stow and Johansson, 2000; Shanmugam, 1996), since this will fundamentally influence reservoir architecture and connectivity. However, studies detailing their internal heterogeneity have been scarce and limited to descriptions of sediment facies variability in a Massive Sand Facies Association (MSFA). This chapter aims to address this short-coming by describing and quantifying the vertical heterogeneity of the MSFA that constitutes the majority of succession of the East Brae Field in the South Viking Graben, North Sea (Figure 5-1).

Heterogeneity can be defined as the variability of an individual property or combination of properties within a known space and/or time, and at a specified scale (Fitch et al., 2015). This can include properties related to sedimentary architecture such as sand-body geometry, shale continuity, bed amalgamation, channelization processes etc. or petrophysical properties such as porosity, permeability and fluid saturation. Since these properties are genetically related, they have a fundamental control on reservoir performance in terms of reservoir sweep efficiency, pressure distribution, production profiles and ultimately the recovery factor (Onyeagoro et al., 2007). A poor understanding of the internal heterogeneity of MSFA can lead to unforeseen compartmentalisation, early water breakthrough and by-passed oil, necessitating infill well drilling. As such, a crucial task during reservoir description is to accurately describe and quantitatively capture heterogeneity in these properties, which can be used to model reservoir behaviour under different production scenarios.

5.2 Aims.

The overall aim of this chapter is to describe and quantify the heterogeneity within a MSFA. Heterogeneity is scale dependent and the scale of importance may change depending on the reservoir description study. As such a detailed analysis of the heterogeneity that exists at various scales in a MSFA is crucial.

The first aim of this study is to describe the facies, and vertical arrangement and degree of randomness of facies within the East Brae MSFA using core data and statistical analysis (i.e. Markov Chain and Entropy Analysis). This is the smallest scale possible for this study given the current dataset and methods. Such an analysis is useful not only for describing the vertical heterogeneity at the bed and facies scale, but also for describing the hydrodynamic processes and interpreting the depositional environment of the deposits. The lateral heterogeneity, in turn, will be described qualitatively and by inference to knowledge of sedimentary environments and flow processes.

The second aim of the study is to describe and quantify the heterogeneity in the East Brae MSFA at the element scale. This will involve detailed facies analysis of the core data and characterising the variability in the porosity and permeability within each facies association or element. In the East Brae, porosity and permeability is largely controlled by the depositional texture, with only minor modification by calcite and quartz cementation (Hussain 2012; Lieshman, 1994, Maas et al., 2011). Consequently, reservoir heterogeneity can be related and analysed in terms of sedimentary processes. To quantify the variability in porosity and permeability, static *heterogeneity coefficients*, including the Lorenz Coefficient (LC), Dkystra-Parsons Coefficient (V_{DP}) and the Coefficient of Variation (CV) are employed. These coefficients traditionally give a single value that represents the numerical variation in a given dataset (i.e. heterogeneity), and have been frequently used in recovery and reservoir management studies to assess the volumetric sweep efficiency (e.g. Sahni et al., 2005; Hongling et al., 2011). However, in this study, a continuous record of the coefficient values are generated using a moving window. This was based on the assumption that such an approach will capture subtle variations in heterogeneity as we move stratigraphically from one element to another. The output from these two aims will form the foundation for a discussion on the implications of developing and producing from massive sands and MSFA.

The third and final aim of this study is to assess the applicability of the continuous record of heterogeneity coefficients in aiding identification of layering and reservoir behaviour within the East Brae MSFA. Such dynamic-conditioning of the reservoir zonation can be a useful tool as input into a static and dynamic model in terms of identifying drains, speed zones, thief zones, baffles and barriers, and storage tanks.

5.3 East Brae Field.

The East Brae gas condensate field is located in Quadrant 16 of the United Kingdom Continental Shelf (UKCS), approximately 260 km northeast of Aberdeen (Figure 5-1). It was discovered in 1980 by Well 16/03a-1, which encountered a gross hydrocarbon column of 650ft

in Upper Jurassic deep-water deposits. Five appraisal wells, drilled between 1982 and 1986, delineated the size of the field and estimated an initial oil in-place of 447 MMSTB and wet gas initially in-place of 2303 BCF (Branter, 2003). All the wells encountered a similar gross hydrocarbon column to 16/03a-1, ranging between 650 and 770 ft and a field wide hydrocarbon-water contact at ~13735 ft TVDss. The fifth appraisal Well, 16/03b-9, was drilled in 1986 on the northern sector of the structure with the objective of providing further geological control, and encountered a similar, but water-bearing reservoir interval. Presently the field is operated by Marathon Oil UK limited on behalf of BP, Centrica, GDF Suez, Nippon Oil and TAQA.

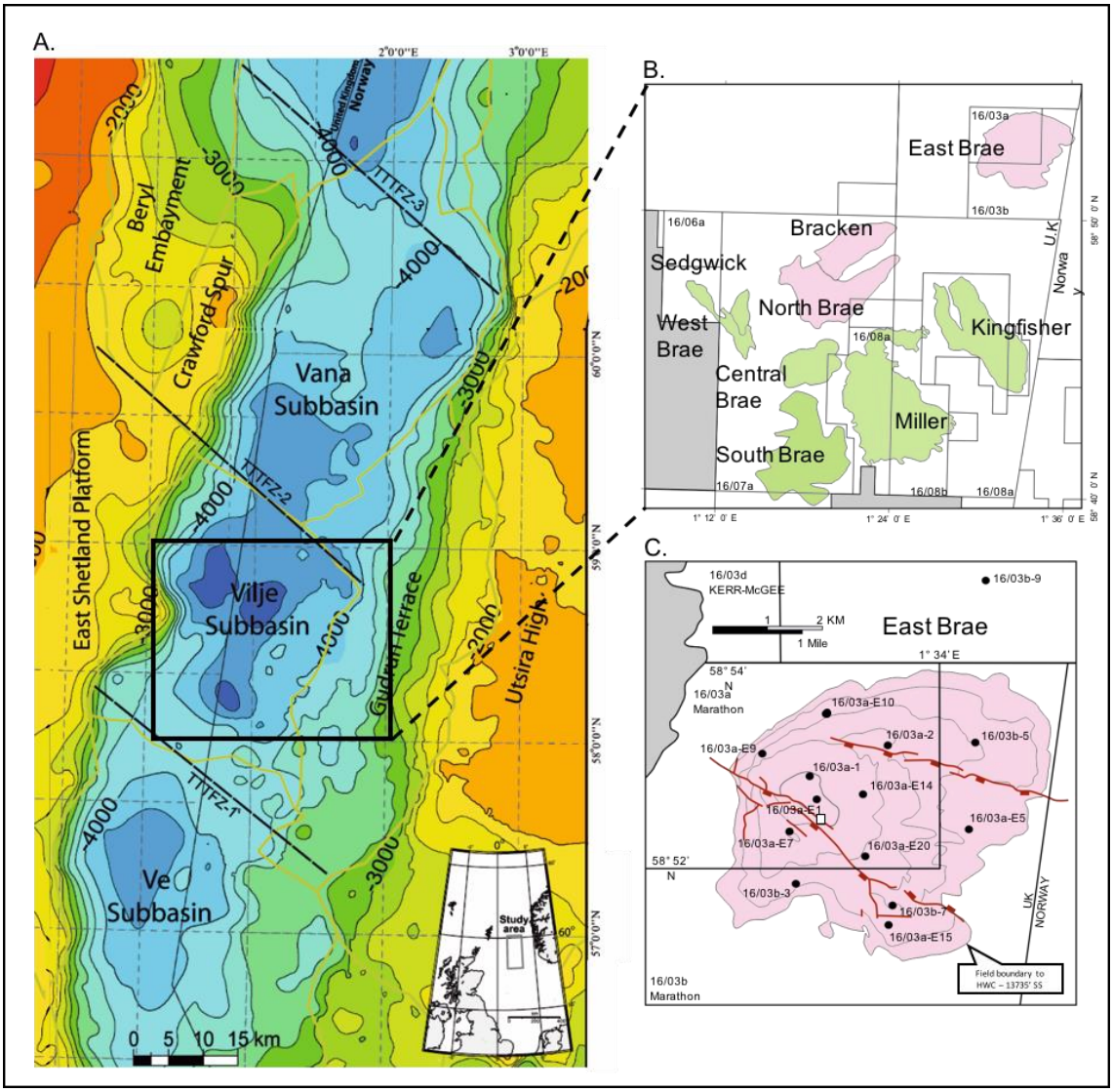

Figure 5-1: A map of the study area showing: (A) major structural elements of the South Viking Graben (after Maast et al. 2011). The transfer fault zones are identified and annotated as the Thornquist-trending transfer fault zones (TTFZ) 1 to 3. The depth map is from the base Cretaceous reflector; (B) location of the Brae, Miller and Kingfisher fields, and (C) East Brae top reservoir structure map with study well locations and major ESE-WNW faults. The wells are placed at the approximate top Brae location in the subsurface. The HWC is encountered at ~13735 ft, ss and the contour interval is every 500ft (modified after Branter, 2004).

5.3.1 East Brae Structure.

The East Brae Field forms part of the larger 'Brae Province' that consists of six large oil and gas fields within Blocks 03, 07 and 08 of the South Viking Graben, a pronounced graben structure ~20 to 40 km wide and ~120 km long, that lies at the junction with the Central and Witch Ground Grabens (Underhill, 2003). It is bound to the west by the Fladen Ground Spur (part of the East Shetland Platform) and to the east by the Utsira High (Figure 5-1). The graben initiated in the Late Permian- Early Triassic, and accelerated in the Jurassic during E-W extension that took place between the East Shetland and Horda Platform along N-S trending listric faults. This extension was asymmetrical in character, leading to half-graben development controlled by the bounding faults to the Fladen Ground Spur in the West and antithetic faults to the Utsira High in the East (Leishman, 1994). Extension was also accommodated by strike slip faults, along reactivated north-east trending pre-rift Caledonian structural features. These strike-slip structures had a significant influence on rift geometry, such that the rift depo-centre was offset to form several sub-basins, as well as controlling the position of sediment entry points into the sub-basins (Coward, 1996; Cherry, 1993).

Economically, the Upper Jurassic system is the most important within the South Viking Graben, marking the onset of source and reservoir rock deposition within the graben. The sedimentary succession is dominated by deep-marine argillaceous deposits of the Heather and Kimmeridge Clay Formations. Movement along the western margin fault system during the Middle Oxfordian led to rapid footwall uplift on the Fladen Ground Spur. As a result, prograding, deep-water gravel and sand-dominated fans systems belonging to the Brae Province accumulated adjacent to the western margin. Deposition of the clastic sediments ceased in the latest Jurassic, probably due to tectonic-induced drowning of the local sediment source area on the Fladen Ground Spur (Leishman, 1994; Turner and Connell, 1991). Following this deposition, the extensional geometry of the graben was modified by multiple phases of basin inversion during the latest Jurassic and Early Cretaceous (Cherry, 1993). The result of this inversion is the variable reactivation and back-rotation of NNE-SSE graben bounding faults, and the development of hanging wall anticlines. In the East Brae area, this manifested in the formation of a four-way dip structural trap (Figure 5-2 and 5-3). The structure is divided by two field-wide NE-SE trending extensional faults that compartmentalises the field into three main segments (Figure 5-1).

5.3.2 Field Stratigraphy.

The stratigraphy of the East Brae Field is illustrated in Figure 5-2 and 5-3 using a series of correlation panels across the field. The main reservoir consists of deep-water deposits belonging to the Upper Jurassic Brae Formation, which was interbedded with the basinal mudstones of the

Kimmeridge Clay Formation. The latter forms both the source and seal for the hydrocarbon accumulation. Biostratigraphic analysis indicates the reservoirs are Kimmeridgian (JB63) to Late Volgian (JB73) in age and are the distal equivalent of the conglomeratic facies encountered in the North Brae Field (Brehm, 2003; Leishman, 1994; Partington et al., 1993; Riley et al., 1989).

The reservoir is sub-divided into two broad units, the Upper and Lower Brae sands, separated by a field-wide mudstone layer (D1 shale) ~30-60 ft thick (Figure 5-2 and 5-3). This shale layer represents a major flooding event and acts as a field-wide barrier to flow. The layer also facilitates correlation of reservoir sub-divisions across the field. The sand-dominated intervals can be further subdivided into five intervals (A-E) locally separated by discontinuous mud layers such as the E Shale or C1 shale (Figure 5-2 and 5-3). These zonations are based on regional transgressive and regressive cycles (Rawson and Riley, 1982) and detailed palynological analysis by Riley et al. (1989). The Lower Brae consists of two units (D2 and E Sands) separated by a locally discontinuous mudstone unit (E Shale). Similarly, the upper Brae consists of up to three reservoir units (A-C) that are locally separated by discontinuous shale layers (C1 shale).

5.3.3 Reservoir Sedimentology.

Sedimentological analysis by Leishman (1994) and Turner and Connell (1991) indicate the Lower and Upper Brae reservoir intervals are dominated by amalgamated massive, medium to coarse-grained sandstone units up to 30-40 m thick. The grains are texturally and compositional mature, and well sorted. Locally, the sequences are interrupted by metre to decimetre thick intervals of thin mud and sand couplets, remobilised deposits and/or background hemipelagic deposits. Previous studies have indicated moderate to high reservoir quality with porosity up to 28% and permeability up to 8490 mD, with a mean porosity of 17% and permeability of 558 mD. Petrological studies have shown that depositional texture and detrital clay content are the primary control on reservoir quality (Branter, 2003; Leishman, 1994). However, locally, quartz cementation has a strong impact on reservoir quality, with low porosity sandstones found where the reservoir was exposed to temperatures above the regional average, and high porosity sand where grain-coating microquartz cement has inhibited the precipitation of quartz overgrowth (Leishman, 1994; Maast et al. 2011).

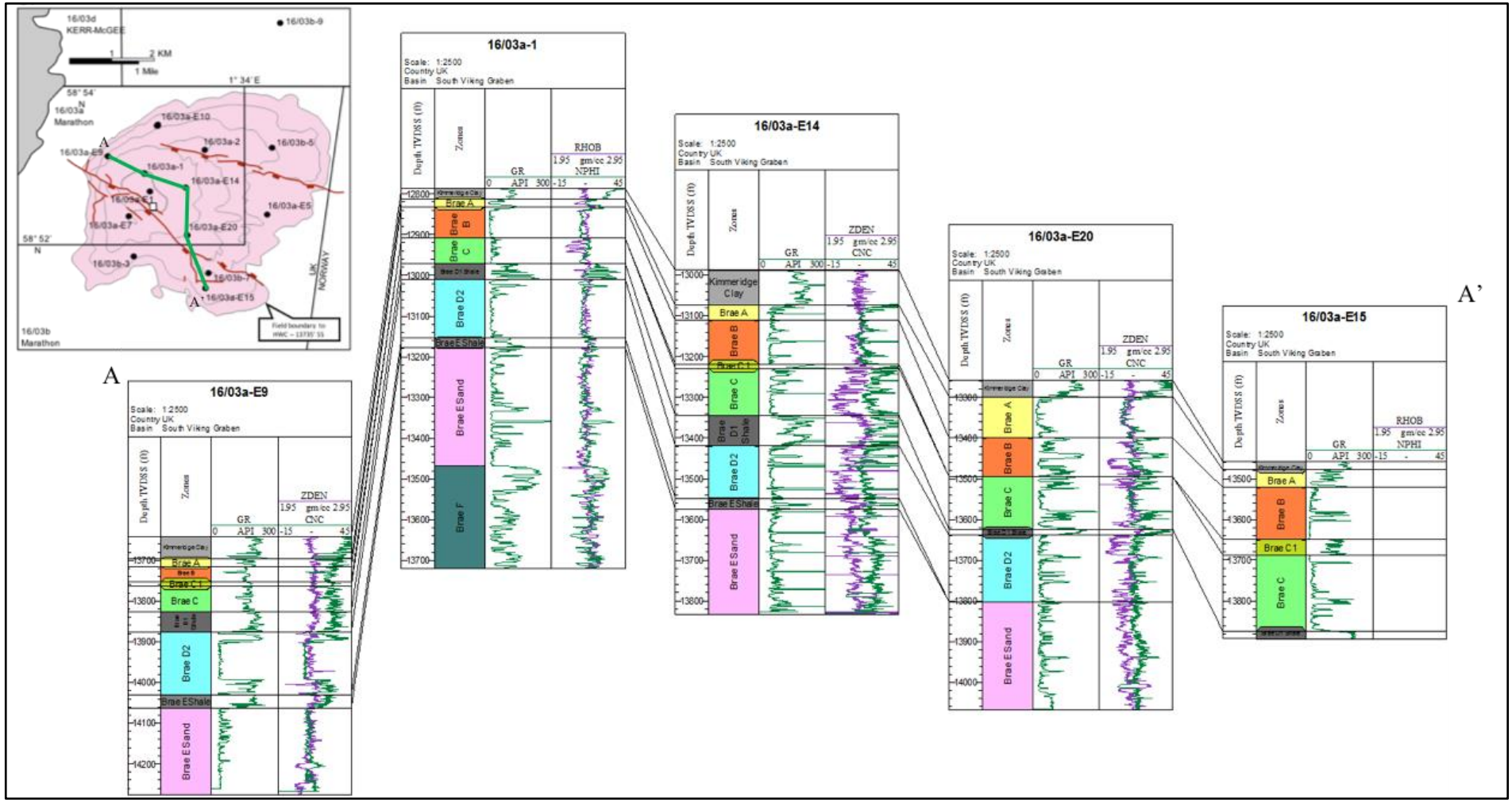

Figure 5-2: NW - SE correlation across the East Brae Field displaying the anticlinal trap and the stratigraphic zonation of the Brae Formation. HWC is at 13735 ft tvdss.

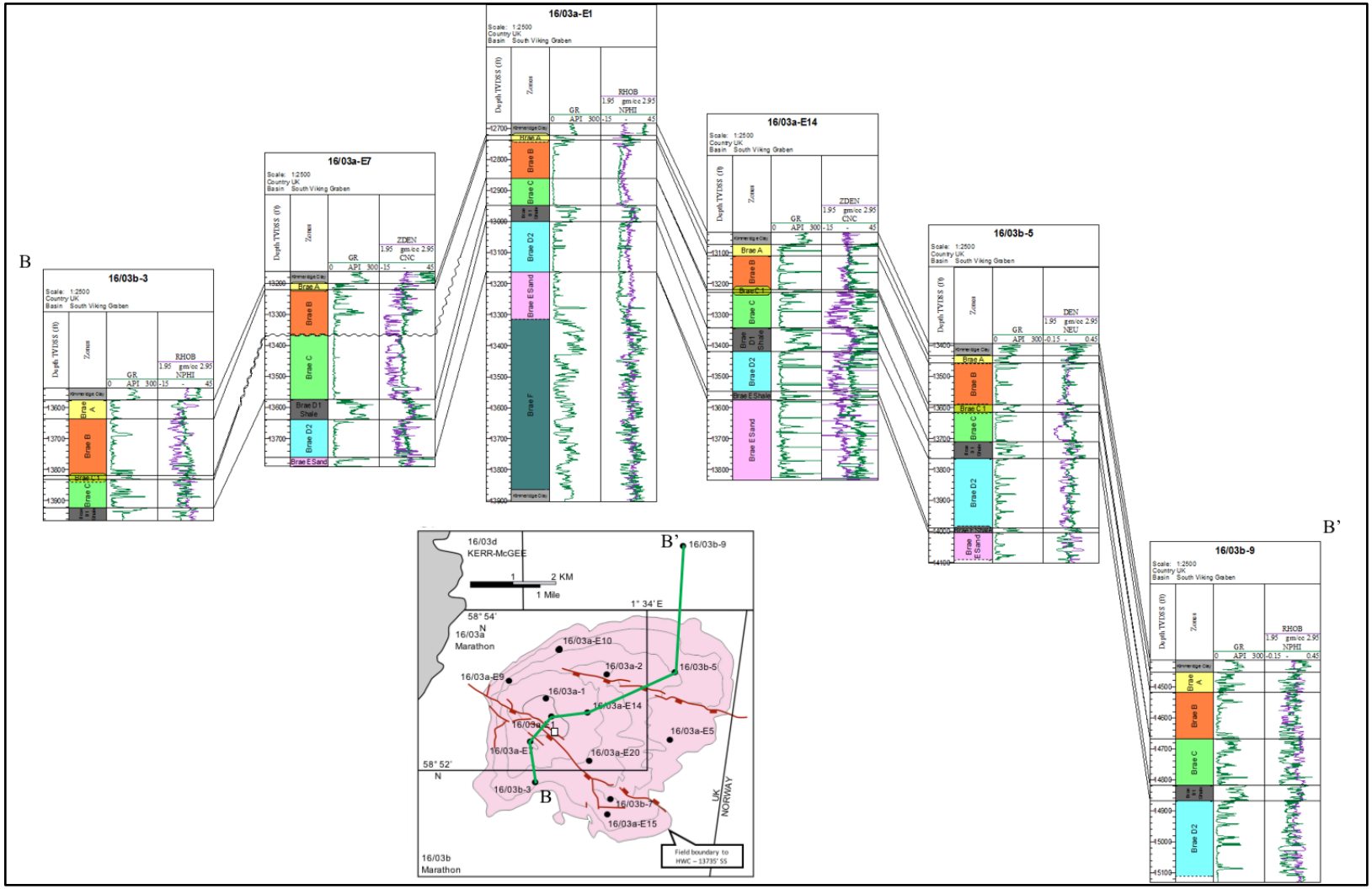

Figure 5-3: N – S correlation across the East Brae Field with wells hung at depth zero. Well 16/3b-9 was drilled on the northern most flank of the structure and encountered a water-bearing succession.

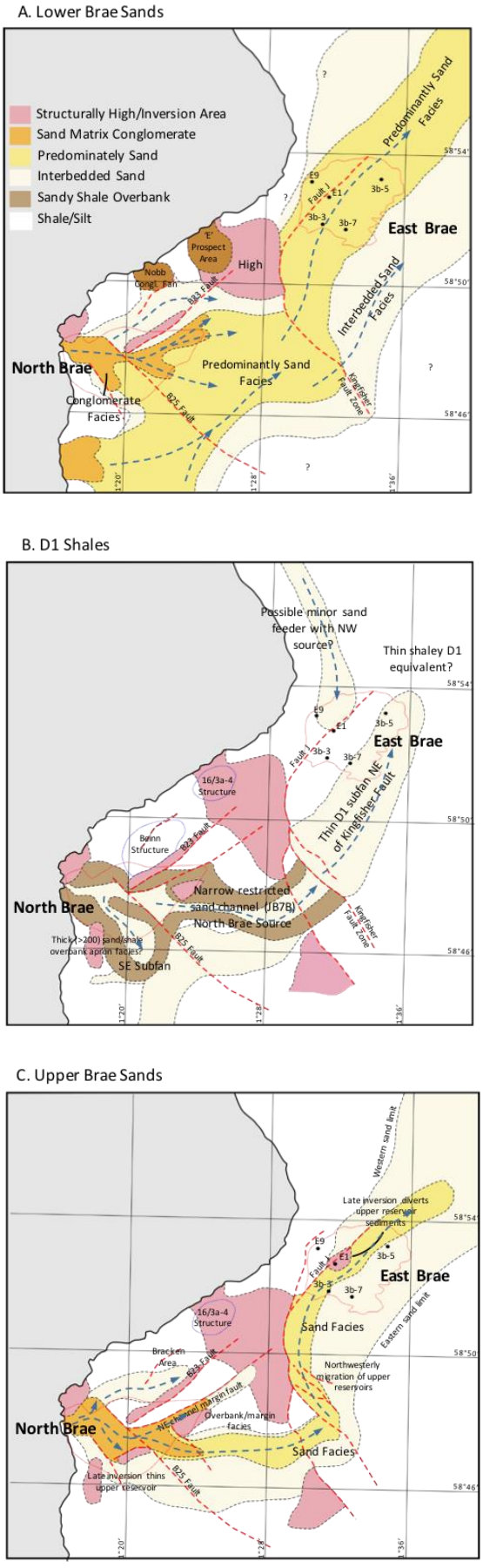

Figure 5-4: Interpreted depositional system for the Lower and Upper Brae sands and the D1 Shale of the East Brae Fields. Modified after Brehm (2003).

5.3.4 Palaeogeography.

The most recent models of the East Brae system envisage it as the distal equivalent of the North Brae system and despite their sedimentological differences, are age-equivalent and represent different portions of the same genetic facies tract (Figure 5-4; Branter, 2003; Brehm, 2003; Turner and Allen 1991; Turner and Connell, 1991). Brehm (2003) and Turner (Pers. Comm., 2016) proposed the sediments that constitute the Lower Brae sandstones were directed along sinuous E-W oriented conduits created by the effects of normal fault movement in the North Brae area (Figure 5-4). These faults had a NW-SE and NE-SW orientations. Proximal localities at the foot of the Fladen Ground Spur received conglomeratic material. As the flows travelled eastwards, they were directed north-eastwards by a bathymetric low created by the intra-Jurassic Kingfisher fault system. In the East Brae area, present well constraints and seismic data suggests that the sediments entered the sub-basin across a broad front, depositing laterally extensive sheet-like sandstones (Figure 5-4A). In this context, the Lower Brae sandstones occupies a position similar to the middle-fan setting of classical submarine fan models (Turner and Connell, 1991). The East Brae sub-basin was asymmetrical in profile with the axis of the sub-basin generally closer to the western boundary fault system (Cocking et al. 2007). In contrast, well correlation indicates that the Upper Brae sandstones are more spatially confined (Figure 5-4C). This confinement is related to weak regional compression during the early to mid Volgian, which resulted in the northwesterly migration of the upper reservoir sands closer towards the graben fault boundary (Branter, 2003). The East Brae sub-basin thus represents a topographically confined depo-centre with laterally confining margins.

5.4 Data and Method.

Fourteen wells were selected for detailed facies analysis and quantification of the heterogeneity of the MSFA that constitutes the East Brae Field reservoir (Figure 5-1). A list of the wells, as well as the available well data, is shown in Table 5-1. The wells are of mixed vintage and quality, but were chosen due to the availability of core data, spatial coverage across the field and quality of the wireline logs. A total of ~4050ft of core was logged to characterise the sedimentary facies and depositional environment. For the uncored wells, wireline logs, calibrated to the core data, is used for facies analysis and interpreting elements of the MSFA. Furthermore, core-derived porosity and permeability data is used to calibrate a continuous record of log-porosity and permeability from petrophysical analysis of wireline logs. These log-derived properties are employed in the heterogeneity coefficients to quantify the variability in the system over the whole reservoir interval.

Table 5-1: Well data summary for the wells used in this study. Wireline data was acquired through CDA (Common Data Access Limited) and is assumed to be corrected for environmental and borehole effects. Zonation data for most was acquired from literature review (incl. well reports, biostratigraphic reports, composite logs and journal articles). For wells where zonation data was not available, the stratigraphy is subdivided based on wireline log character and cross-checked with near-by wells at similar stratigraphic height. A single log-shift for each was sufficient to accurate match the core- and log-derived properties.

Well	Core/Logged	CCA	Wireline Logs	Zonation Data	Core – Log Shift
16/03a-1	Y/Y	Y	GR, NPHI, LLS, MSFL, LLD, RHOB, SP, DT	Y	- ~8ft
16/03a-2	Y/Y	N	GR, NPHI, RHOB, SP, IDL, ILM	Y	Variable: + ~ 6- 8ft
16/03a-E1	Y/Y	Y	GR, NPHI, RHOB, SP, ILD, ILM, CALI, DT, SFLU	N – Based on log character	+ ~12ft
16/03a-E10	Y/N	Y	GR, CAL, CNC, RIPD, ZDEN, PE, DT24, RERD, RERM	Y	
16/03a-E14	N	N	GR, CAL, CNC, PE, RIPD, ZDEN, DT24, REID, REIM,	Y	
16/03a-E15	Y/N	Y	GR, SP, CALI, RIPD, DEN, NEU, PE, DT, ILM, RIPD, RDEP	Y	
16/03a-E20	N	N	GR, CAL, CNC, RIPD, ZDEN, RERD, RERM, DTCM,	Y	
16/03a-E5	Y/N	N	GR, NPHI, RHOB, SP, ILD, ILM, CALI,	Y	
16/03a-E7	Y/N	Y	GR, CAL, CNC, PE, RIPD, ZDEN	Y	
16/03a-E9	Y/N	Y	GR, CAL, CNC, PE, RIPD, ZDEN, DT24, RERD, RERM	Y	
16/03b-3	Y/Y	Y	GR, NPHI, ILD, ILM, RHOB, SP, DT, SFLU, RILD, RILM, RSFL	N – Based on log character	+ ~16ft
16/03b-5	Y/Y	Y	GR, SP, CALI, DEN, NEU, PEF, RDEP, DT, ILM,	N – Based on log character	+ ~3ft
16/03a-7	Y/Y	Y	GR, NPHI, RHOB, SP, ILD, ILM, CALI, DT, SFLU, RIPD, DT24, RERD, RERM, RSFL	N – Based on log character	+ ~6ft
16/03a-9	Y/N	N	GR, NPHI, RHOB, ILD, ILM, CALI, DT, RILD, RILM, SFLA	N – Based on log character	

5.4.1 Core logging.

Core material was available for ten out of the fourteen wells, of which only six wells were logged due to time constraints (Table 5-1 and Figure 5-5). In total ~ 4050ft of core was logged, covering much of the five reservoir intervals of the Brae Formation. Thus, the core material provided an excellent opportunity to document the vertical variability in sediment facies. However, lateral variability in sediment facies across the Brae field could not be easily assessed due to the poor spatial coverage of the cored intervals (Figure 5-5). Furthermore, only minor corrections were required to the driller's depth (D.D) to derive the measured logger's depth based on the wireline logs. While depth shifting is not strictly necessary for core description, it is necessary for subsequent petrophysical analysis that incorporates the geological data.

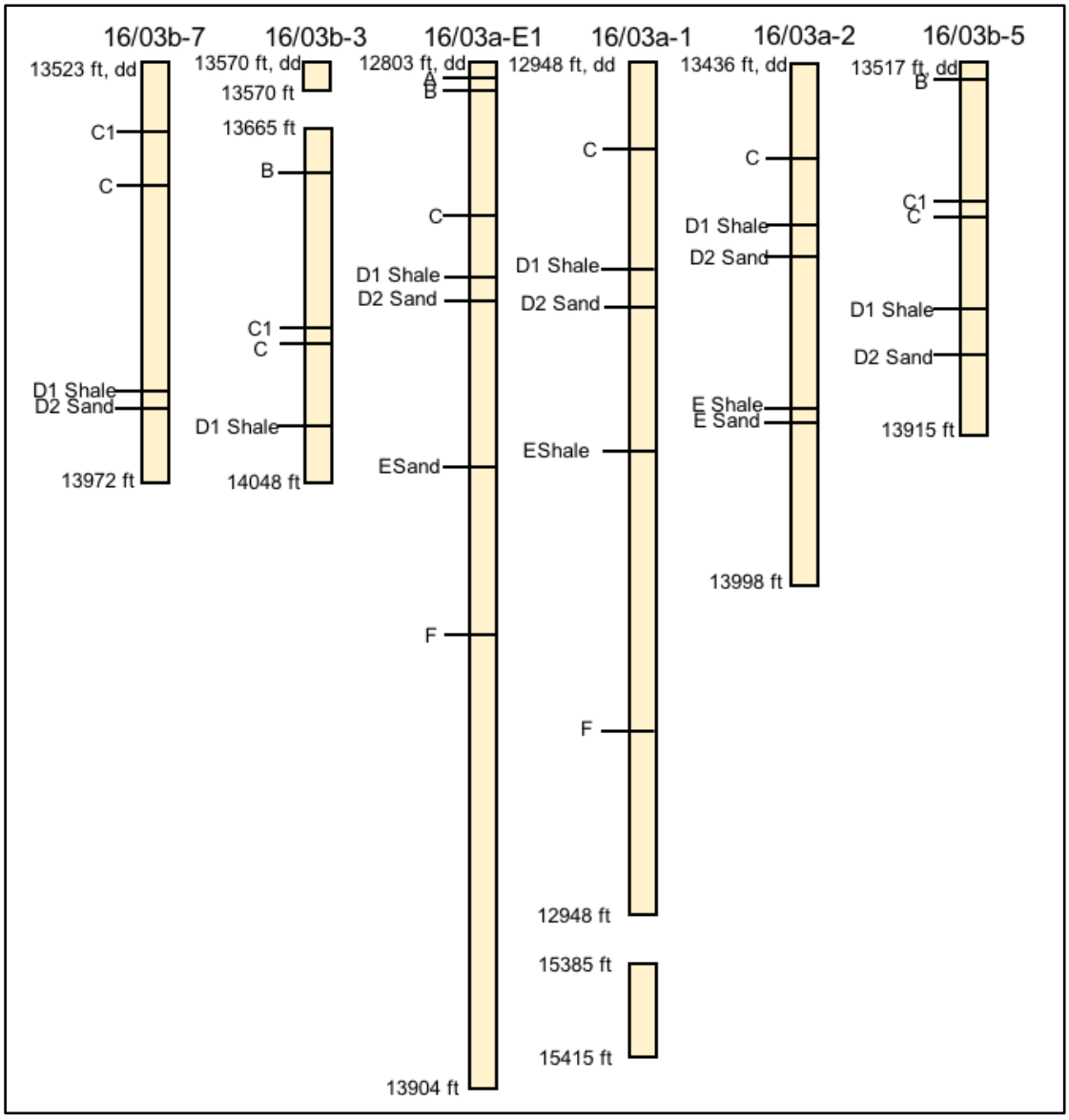

Figure 5-5: A diagram showing the cored intervals and the stratigraphy encountered in the East Brae Field. The stratigraphic zonation is based on biostratigraphic analysis by Riley et al. (1989). See Figure 5-1 for well locations.

Each core was logged at a scale of one inch to the foot (1:12), with bed thickness, sedimentary structures, grain size, cementation, sand-mud percentage etc. among some of the observations recorded. Grain size was measured every 5 cm and at smaller intervals where abrupt changes in grading occurs or where grain size breaks are observed. Grain size measurements were acquired with a grain size comparator using the Wentworth scale, which biases the measurements to the coarsest 5% of grains within beds (Amy and Talling, 2006a; Talling et al. 2004; Talling et al. 2013; Tucker, 1988). However, this qualitative method allowed the dominant grain size range to be measured in the core, and provided a robust means to measure relative grain size changes between beds. Bed thicknesses were measured with a standard measuring tape. Sediment facies were described using a hierarchal descriptive facies scheme that describes the beds on (i) lithofacies, (ii) internal organisation (i.e. interbedded sand and mud, and discordant facies), and

(iii) subfacies based on sedimentary structures (Figure 5-6 and Table 5-2). Discordant and deformed intervals where also treated as separate facies. However, outsized clasts and dewatering structures are incorporated into the facies scheme as accessory features. Both have been described according to Johansson and Stow (1995) and Stow and Johansson (2000). Diagenetic and small-scale structural features are also treated as accessories. Thus individual units consist of lithofacies and subfacies arranged vertically, and aim to capture primary depositional feature.

5.4.2 Markov Chain and Entropy Analysis

Embedded Markov Chain and Entropy analysis was undertaken to describe the vertical arrangement and degree of random occurrence of facies. For this study, the six wells have been grouped into proximal (16/03b-3 and -7), medial (16/03a-E1 and -1) and distal (16/03a-2 and -03b-5) locations based on the interpreted palaeoflow direction (Figure 5-4). This grouping not only allow us to statistically analyse the vertical arrangement of facies, and therefore the temporal evolution of the flow, but also qualitatively characterise the downslope transitions in facies arrangement. Details on the procedures of the statistical analysis is provided section 3.3.4. However, unlike previous studies, amalgamation contacts and grain size breaks are treated as a separate facies to allow for transitions between the same facies types to be analysed in the thick sand packages.

5.4.3 Combined Log-Pattern Analysis.

Multiple wireline log types, including gamma (GR), dip-meter, resistivity, bulk density, neutron and sonic logs were used for analysing and interpreting MSFA elements in uncored wells. The method involves defining the responses of the different wireline logs and their corresponding log character in the constituent parts of the MSFA penetrated in cored wells, prior to being transferred to uncored wells. The log characters are correlated across wells to infer spatial variability in sediment facies to aid interpretation of the depositional environment only. A predefined reservoir zonation scheme, based on biostratigraphic data and internal laterally extensive shale units (e.g. C1, E Shale etc.) are employed as marker horizons to guide the correlation.

Table 5-2: Description of the lithofacies used in this study.

Facies Code	Description	Texture			Thickness Range	Interpretation	Equivalent Facies	Facies Association
		Grading	Grain size	Sorting				
Sandstone, Massive (SM) SM1 – Ungraded Massive Sands SM2 – Graded Massive Sand SM3 - Massive sands with Patchy Texture	Structureless (massive) clean sands. Abundant mm-scale carbonaceous fragments (dispersed graded to locally clustered floating and ordered stratified). SM3 facies has a distinctive patchy texture consisting of irregular 'patches' of coarse grains adjacent to fine grains.	Ungraded (SM1) to distribution normal grading (SM2). coarse-tail at the base common. Ungraded to weakly coarse-tail graded (SM3).	125µm - 750µm	Moderate to very well. Poorly to moderately sorting for SM3.	cm to > m. Amalgamated sequence can reach up to 40 metres thick.	Deposits of high-concentration near bed layers beneath surge-type and quasi-steady turbidity currents (SM1 and SM2). Layers are characterised by hindered settling, grain to grain interaction and frictional freezing. Patchy texture in SM3 is liquefied debris flows from dissipation of excess pore pressure and elutriation of fines.	SM1 and SM2 - F5 and F8 (Mutti, 1992), T_a (Bouma, 1962). SM3 – Dcs (Talling et al. 2012).	Element 1 (shallow channels in an axial lobe or channel-lobe transition zone) and 2 (off-axis sedimentation).
Sandstone, Laminated (SL) SL1 – Laminated	SL1 - Laminated sands, <3 mm thick, planar to wavy, locally convoluted. No grain size variation between laminae. Laminae typically more distinct upwards in the bed. Laminar traced for metres. Rarely contain <2-3 cm mudclast along distinct horizon.	Distribution graded to ungraded	125µm - 350µm	Moderate to very well.	SL1 and Sl2 from cm to dm caps to massive sandstone beds. SL3 facies typically occur at the base and middle of beds, and rarely towards the top as caps to massive sands.	Thin to thick stratification (SL2 and SL3) formed by concentrated turbidity currents from near bed high-concentration layers with sediment concentration of 10-40%. SL1 formed from low-density turbidity current. Sand reworked as bedload.	F4, F6-F7, F9 (Mutti, 1992), S2 (Lowe, 1982), $T_{B-3,}$ T_{B-2} T_{B-1} (Talling et al. 2012), T_C (Bouma, 1962).	SL2 and SL3 are predominately associated with Elements 1, while SL1 is associated with Element 2 and 3 (peripheral to the active sand-rich system, most likely distal and lateral-margin equivalent). SL1 is also a minor facies in Element 1 (shallow channels in an axial lobe or channel lobe transition zone).
SL2 - Thin, spaced lamination	SL2 - Alternating coarser and finer grained laminae. 3 - <10mm thick. Laminae thickness decreases with height from base, and becomes more distinct towards the top. Planar to locally wavy/irregular, sharp contacts.	Individual laminae are ungraded to normal and inverse graded.						
SL3 – Thick, spaced lamination	Rarely encountered in the Brae Formation. Thick (>1cm to <15cm), alternating coarse and fine grained lamination. Thickness of individual layers decreases with height from base. Diffuse and irregular at the base, become more distinct upwards. Sharp to gradational contacts between lamination.	Coarser laminae are typically ungraded, but rarely normal and inverse graded. Finer grained laminae are normal graded						
Sandstone, Rippled (SR)	Ripple cross lamination, planar to trough, climbing ripples Locally convoluted. Wavelength <15 cm and typically < 10 cm.	Normal graded	125µm - 187µm	Moderate to well sorted.	cm to <dm caps to massive and laminated sandstone beds.	Unambiguous evidence of deposition from low density turbidity currents. Sand reworked as bedload into ripples in the lower flow regime. Relatively low rates of sediment fall-out.	F9 (Mutti, 1992), Tc (Bouma, 1962)	Predominately associated with Element 2 and 3.
Mudstone (MM)	Massive (massive), minor silt fraction at the base	n/a	n/a	n/a	Cm to > m	Static settling of clay or formation of fluid mud layers from a collapsing mud cloud	F9 (Mutti, 1992), Te (Bouma, 1962), TE (Talling et al. 2012).	Major facies in element 4 (abandonment of the sand-rich system). Minor facies in element 1, 2 and 3 were it occurs as thin intercalations.
Mudstone (ML)	Black to dark grey, silt laminated to massive mudstone. Bioturbation is rare, but locally rhizocorallium can be identified.	n/a	n/a	n/a	cm to > m. Can form sequences up to 30 metres thick.	Settling of flocs from a dilute and expanded suspension cloud. Rapid suspension of mud laminae upon dampened turbulence. Silt laminae are deposited when the mud flocs are broken up by shearing from the flow.	F9 (Mutti, 1992), Te (Bouma, 1962), T_E (Talling et al. 2012).	Major facies in element 4 (abandonment of the sand-rich system). Minor facies in element 1, 2 and 3 were it occurs as thin intercalations.
Chaotic, Disorganised Slumped (DC!1) intervals and sand injections (DC2).	Disogranised slumped intervals and discordant sand injection.	n/a	Clay - 250µm	n/a	1 – 2 m	Cyclic shock or above grade slope for slumped intervals. Fluidisation and excess pore pressure for sand injections.	n/a	Element 5.

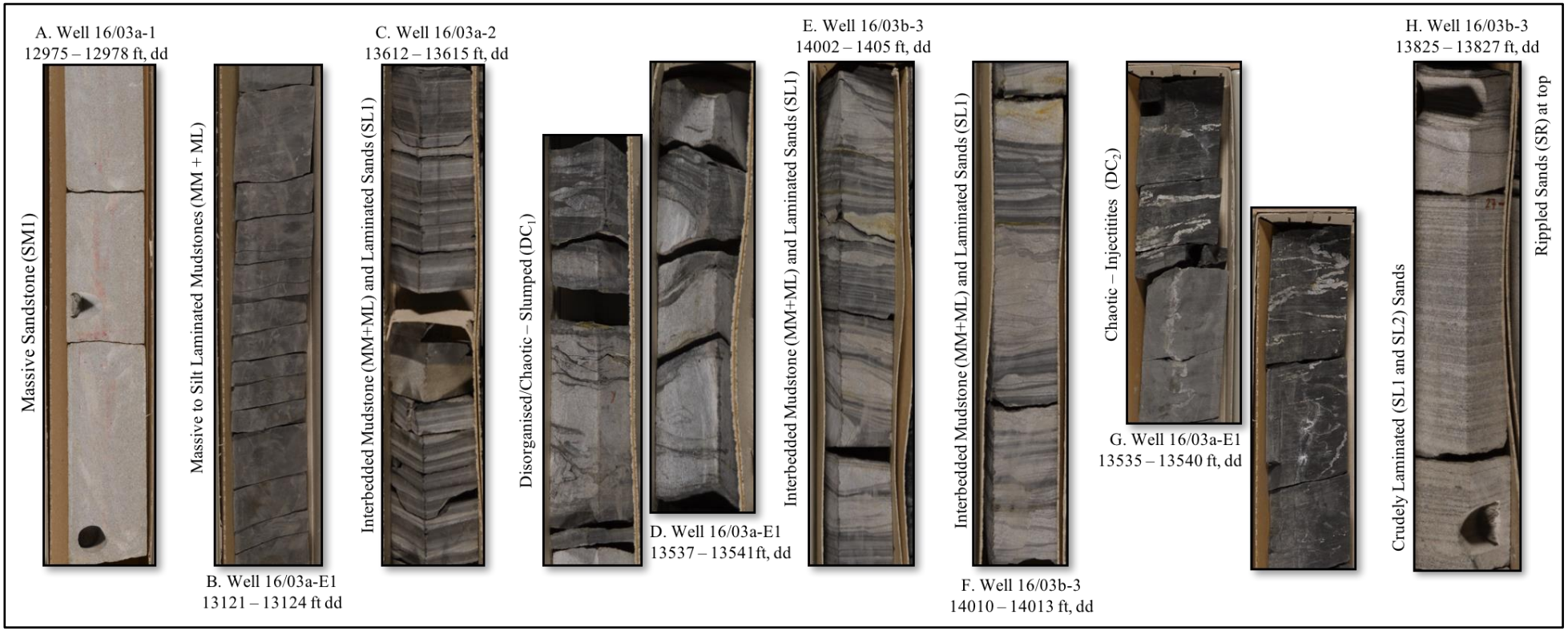

Figure 5-6: Core photos displaying the typical facies seen in the East Brae Field: A) Fine to coarse grained, massive sandstones (SM); B) Massive to silt laminated mudstones; C) Heterolithic (HM_1) consisting of interbedded thin mudstone (MM and ML) and sandstones (SL and SM) layers with a sand shale ratio of <40: 60; D) slumped and deformed intervals, which in this example consists of irregular patches of sandstone with mudstone clasts; E) thin to medium interbedded mudstone (MM and ML) and sandstone (SL1) layer with a sand shale ratio between 40:60 and 70:30; (F) sequence with increased sand shale ratio >70:30 comprising MM, ML, SL1 and SR facies; G) discordant contorted sand injection in a background of massive to silt laminated mudstone, and; H) structured sandstone showing mm to cm scale stratification through the bed and subtle ripple lamination at the top.

5.4.4 Log-derived Porosity-Permeability.

For the heterogeneity analysis, a continuous record of porosity and permeability for the reservoir interval in each well was derived using the software Techlog. The log-derived porosity and permeability were calibrated to the available core data (Figure 5-7), and then cross-checked by quantifying the difference between the core and log-derived properties to assess the uncertainty at the 90% confidence level using the method of Adams (2005a, b; Table 5-3). All core measurements were corrected for reservoir conditions. For most wells, core plugs were taken every 1ft including the mudstone-rich intervals. Calibration of log-derived porosity-permeability for uncored wells was based on proximity to the nearest cored well, taking into account the depth of the reservoir in both wells. Core to wireline log depth shift was required in a few wells and the incremental change is given in Table 5-1.

Log-Derived Porosity. Total porosity (ϕ) was calculated as a function of bulk density (ρ_b), matrix density (ρ_m) and fluid density (ρ_f). Solving for (ϕ),

$$\emptyset = \frac{\rho_b - \rho_m}{\rho_m - \rho_f}$$

where the ρ_m is adjusted between 2.65 and 2.67 g/cc and ρ_f between 0.23 – 0.58 g/cc for gas condensate. Due to the presence of residual gas, a hydrocarbon correction was applied using the resistivity logs. Mud filtrate is set to 1 g/cc and the formation temperature is taken into consideration to correct for the density variation with temperature. Good borehole conditions were encountered based on the maximum mudcake (~0.08") and lack of washout zones in the intervals of interest for all fourteen wells. Thus, little or no borehole effect corrections were applied to the bulk density measurements. Figure 5-7 shows the core and log derived porosity for Well 16/3a-E7, -E15 and 3b-05. A good match was achieved for the core-calibrated log-derived porosity based on visual observations. In locations where core and log-derived porosity do not match, observations from the core indicate the presence of minor shale laminae and or carbonate stringers that have locally affected the bulk density measurements. The uncertainty in the log-derived porosity from these shale and carbonate cemented layers is assessed quantitatively below.

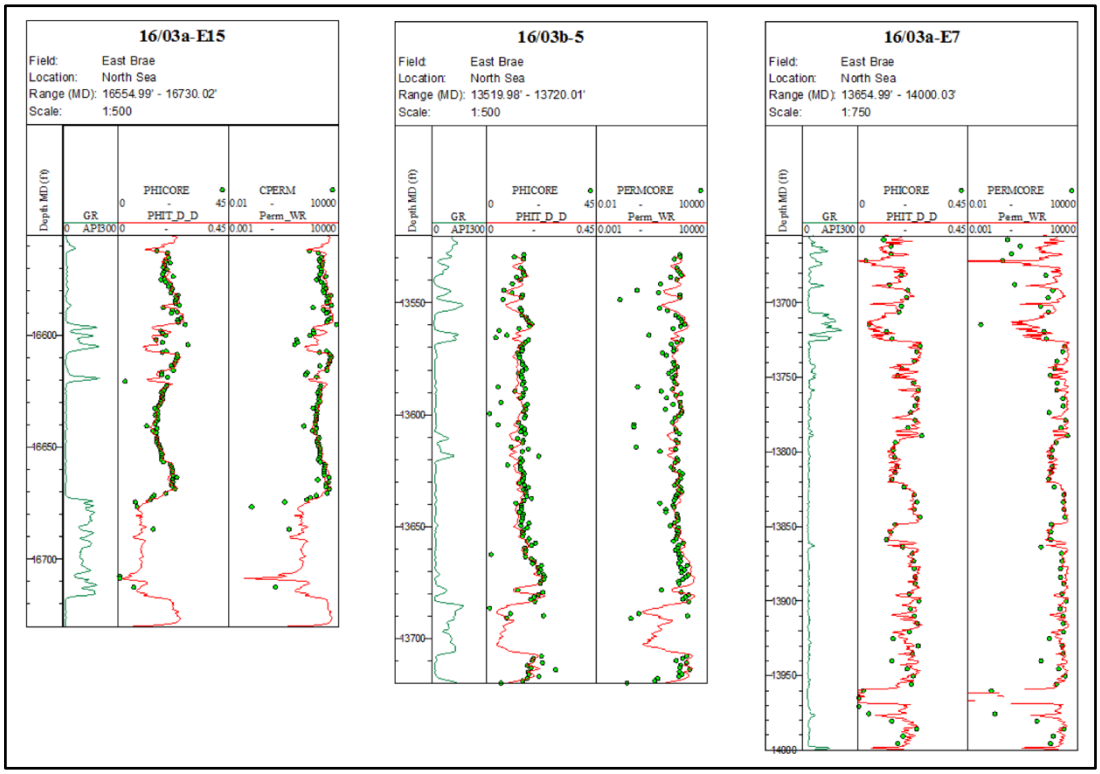

Figure 5-7: Core- (green circles) and log-derived porosity and permeability values for wells 16/03a-E15, -E7 and 03b-5. The uncertainity in the mis-match has been quantified in Table 5-2.

Log-Derived Permeability. Permeability (*k)* was calculated as a function of the log-derived porosity using the Wyllie-Rose model and calibrated to the horizontal core permeability. Solving for *k* (mD),

$$k = \left(\frac{c\emptyset^{d}}{Swi}\right)^{e}$$

where Morris-Biggs parameters are used, d = 6.0, e = 2, c = 62500 and irreducible water saturation (Swi) is 0.23v/v. Figure 5-6 shows the core and log-derived porosity for Well 16/03a-E7, -E15 and 3b-5. Similar to the log-derived porosity curve, log-permeability is also locally affected by shale laminae and irregular carbonate cemented layers. The match may also be affected by a complex pore size distribution that cannot be inferred from the resistivity, density, neutron and sonic logs.

Table 5-3: Uncertainty quantification for the core-calibrated log-derived porosity (ϕ) and permeability (k). Based on analysis of fifteen fields, Adams (2005a, b) recommended mean difference between core and log-derived porosities be less than 0.6 p.u and that for log-derived permeability be less than a factor of 1.5x at the 90% confidence level. All wells except 16/03a-1 (porosity) and 16/03b-3 (permeability) are within defined limiting values according to Adams (2005a, b).

Wells	Mean Ølog - Øcore (v/v)	Mean $\log_{10}$(Klog) - $\log_{10}$(Kcore)
16/03a-1	0.0072	0.44
16/03-E1	0.0026	0.25
16/03a-E15	0.00002	0.062
16/03b-3	0.0026	0.73
16/03b-5	0.0042	0.31
16/03b-7	0.0053	0.47
16/03a-E7	0.0047	0.48
16/03a-E10	0.0021	0.44

5.4.5 Heterogeneity Coefficients.

Static measures of heterogeneity are used to characterise reservoir variability in the fourteen wells from the East Brae Field. Such measures include the Coefficient of Variation (CV), Lorenz Coefficient (Lc) and the Dykstra-Parson Coefficient (Vdp), and utilise core or log-derived properties (i.e. ϕ, k, Sw or Vclay) to assess reservoir variability. Rather than using the conventional approach to calculate the heterogeneity (i.e. Fitch et al., 2015; Jensen and Lake, 1990; Jensen et al., 2000), in this study a user-defined moving window is used to generate a curve of the CV, LC and V_{DP} heterogeneity coefficients. Similar heterogeneity curves have been generated previously, but using predefined interval, to interpret variation in wireline log data through the reservoir interval (e.g. Fitch, 2011). However, a moving window approach is preferred over these and conventional techniques as it attempts to deal with issues related to the spatial organisation of the property (i.e. non-uniqueness of the heterogeneity measure), and identify layering within the system similar to the modified Lorenz plots (MLP; see below for detail). The moving windows have been varied to investigate heterogeneities at various scales, and involves moving the window one sample point at a time as the calculations are performed. The heterogeneity value for a given interval is plotted at the mid-point of the interval. Three different windows sizes were employed: 10, 20 and 50ft. Sample spacing is every 0.5ft, thus the sample size for each window is 21, 41 and 101. All computation was performed in MatLab (Appendix F) and the results viewed in the software IC^{TM}.

To derive a single heterogeneity value for each facies and element, an average is calculated for that facies or element using the 20ft curves. The 20ft curve (i.e. 41 sample points) was chosen since heterogeneity values are compressed when using datasets smaller than 40 samples, particularly for LC and VDP (Fitch et al., 2015; Jensen and Lake, 1988). The 20ft curve is also used to identify layering, whereby values are binned into non-overlapping intervals of heterogeneity. Although all three window sizes can be used to identify layering, the 20ft curve was chosen for the same reason mentioned above. This method of identifying layering is then

compared to the modified Lorenz plot, which is another useful indicator of stratigraphic layering within a succession, to assess its validity.

Coefficient of Variation (CV). The coefficient of variation is becoming more widely employed to define a level of reservoir heterogeneity (e.g. Hovadik and Larue, 2007; Malureanu and Batistatu, 2010; Meyer and Krause, 2006) relative to a mean value. The most widely used method for calculating CV is:

$$CV = \frac{SD}{\bar{x}}$$

where SD is the standard deviation and $\bar{x}$ is the arithmetic average. For perfectly homogeneous or isotropic reservoirs CV = 0; for homogeneous reservoir CV < 0.5; for moderately heterogeneous reservoirs CV is between 0.5 and 0.7; and for strongly heterogeneous reservoir CV > 0.7. The CV increases with increasing heterogeneity and has no upper-limit. For an infinitely heterogeneous reservoir, CV increases to infinite. Various authors (e.g. Fitch et al., 2015; Lake and Jensen, 1991) intimate that this can be a major advantage, in that it allows one to distinguish extreme variation in reservoir properties. However, it can also prove to be a disadvantage since it may not allow direct comparison across datasets from different fields or studies (Fitch et al., 2015). Despite this limitation, the CV is considered an appropriate measure of heterogeneity since dividing the standard deviation by the arithmetic mean, a measure of variation is produced that removes the influence of the original scale of measurement (*ibid.*).

Lorenz Coefficient (Lc). The Lorenz Coefficient is used in reservoir characterisation to define a relationship between cumulative flow capacity against cumulative thickness, as a function of measured porosity (storativity; C_j) and permeability (transmissivity; F_j). For a given dataset, arranging the measured porosity and permeability in decreasing order of k/ϕ, the Lorenz coefficient can be calculated from the partial sums:

$$F_j = \frac{\sum_{j=1}^{J} k_j h_j}{\sum_{i=1}^{I} k_i h_i}$$

$$C_j = \frac{\sum_{j=1}^{J} \emptyset_j h_j}{\sum_{i=1}^{I} \emptyset_i h_i}$$

where $0 \leq J \leq I$ and there are I data points. By plotting F_j versus C_j on a linear plot, the LC can be calculated as twice the area between the Lorenz curve and the line of perfect equality (Figure 5-8A). In a purely homogeneous reservoir, the cumulative properties will increase by a constant value and will follow the line of perfect equality. In such instances, the reservoir will have equal flow and storage capacity. An increase in the heterogeneity of the reservoir will result in a deviation away from this line of perfect equality (Figure 5-8A). The LC is bounded to the range 0, 1, where calculated LC = 0 in a perfectly homogeneous reservoir; LC < 0.16 indicates a homogeneous dataset; LC between 0.16 to 0.25 indicates a moderately heterogeneous dataset with linear variation (increase or decrease) in property values within the dataset; LC of 0.25 to 0.86 reflects high level heterogeneity where property values change exponentially within the dataset; and LC = 1 indicates an infinitely heterogeneous reservoir (Fitch et al., 2015). Since the LC is bounded by a range, it is easier to compare the level of heterogeneity between datasets, as well as datasets with different scales, resolutions and bounds. Conversely, Jansen and Lake (1988) noted that extreme values are compressed by the bounded range and that the LC is negatively biased giving a lower estimate than the population heterogeneity. These authors calculated that this bias is significant for sample size less than 40.

A modified version of the Lorenz Coefficient employs the natural or stratigraphic ordering of the data, in which the slope of the segments represents flow performance of the reservoir (Modified Lorenz Plots (MLP); Figure 5-8B). Segments with steep slopes indicate greater percentage of flow transmissivity relative to storativity and thus higher reservoir process speed (Rahimpour-Bonab et al., 2012). These intervals have been variously termed speed or thief zones (Corbett, 2012). In contrast, segments with gentle slopes are used to identify intervals with high storativity and low transmissivity. Such intervals can act as baffles (i.e. zones that throttle fluid flow) and/or barriers (seal to fluid flow). Intervals that have neither transmissivity and storativity plot on top of each other, and are potential seals if they are laterally extensive. By inference, any intervals with a slope angle of 45° indicates even vertical sweep of the fluid. Such an analysis is not only useful for analysing the stratigraphic architecture of the system, but also to calibrate and analysis hydraulic flow units (e.g. Gunter et al., 1997; Rahimpour-Bonab et al., 2012). In the present study, the MLP is used to validate zones identified by the heterogeneity curves, as well as identify vertical stratification not clearly manifest in core data.

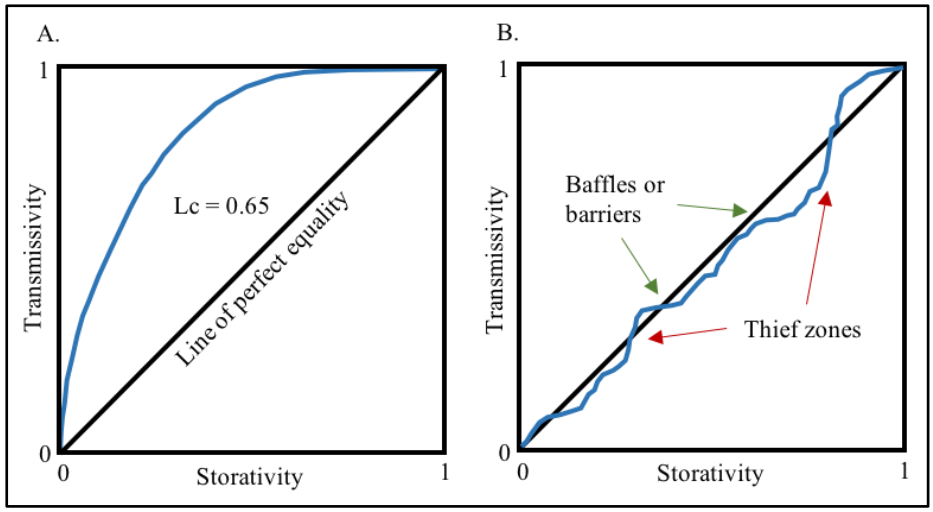

Figure 5-8: Example Lorenz Coefficient plots showing A) ordered Lorenz plot where the area between the blue line and the line of perfect equality is the calculated Lc that quantifies the degree of heterogeneity in the system, and B) the modified Lorenz plots that indicate the presence of barrier, baffles and speed or thief zones. If the MLP approaches the angle of the line of perfect equality (i.e. 45°), perhaps that is an indication of randomness or small scale variabilty that could be assessed by variogram analysis.

Dykstra-Parson Coefficient (Vdp). The Dykstra-Parsons Coefficient (Vdp) is a commonly used geostatistical descriptor of permeability heterogeneity. A method for calculating Vdp is provided by Jensen et al. (2000), where Vdp is:

$$Vdp = \frac{x_{50} - x_{84}}{x_{50}}$$

where x_{50} is the 50th and x_{84} is the 84th property percentile. These parameters are best determined by plotting a probability plot of log(k), from which the slope and intercept of a line of best fit gives you the 50th and 84th probability percentile. The Vdp ranges from 0 (pure homogeneous) to 1 (infinitely heterogeneous), with most reservoirs spanning values between 0.5 and 0.9. However, this method assumes a log-normal distribution of permeability, which is not always the case in reservoirs. Therefore, care has to be taken when using Vdp to assess the permeability heterogeneity. It is possible that for reservoirs with non-log-normal distribution, the Vdp may be unbound (greater than 1 or less than 0), and thus unrepresentative of reservoir heterogeneity (refer to section 5.7 for detail). As well as measuring the variability in permeability values in a reservoir, the Vdp has been extensively employed to predict waterflood behaviour in a layer-cake reservoir with no crossflow between layers.

5.5 Facies Scale Heterogeneity

A master sedimentary log panel for the six logged wells is provided in Appendix E. These logged sections form the basis for describing and quantifying the heterogeneity within the East

Brae MSFA at the facies- and element-scales. Facie-scale heterogeneity are discussed initially, followed by element-scale heterogeneity in section 5.6.

5.5.1 Facies and Bed Character

Clean, Massive Sands (SM). Clean, SM1 and SM2 facies (*sensu* Stow and Johansson, 2000) constitute the majority (e.g. ~ 80%) of the cored interval within most wells in the East Brae Field (Figure 5-6A and Figure 5-14). The facies forms part of sandstone beds that are compositionally mature quartz arenite, characterised by well sorted, medium to lower coarse-grained sands and dispersed mm-scale carbonaceous and mudstone flecks. Facies thicknesses range from 0.1 m to over 1 m, and typically form continuous sequences up to 40 m thick. Amalgamation surfaces are common and are most often identified by grain size breaks (sand on sand; fine sand overlain by coarse sand) and/or localised concentration of carbonaceous fragments. Grading for the most part is absent, but where present, is restricted to the base and top of the bed and consists of coarse-tail and distribution grading respectively. However, a crude normal to inverse grading is locally visible in the accessory carbonaceous component. SM3 patchy texture facies is rarely observed in the East Brae MSFA, but where present occurs as thin intervals (< 20 cm) surround by SM1 and/or SM2 facies. A crude stratification resembling SL2 are locally picked out by the carbonaceous component, and indicates deposition from thin near-bed layers that are fed and driven by an overlying high-concentration flow (Cartigny et al., 2013; Talling et al. 2012; Sumner et al. 2008). Irregular and discontinuous clay 'streaks' are also visible throughout beds. However, these are interpreted as dewatering and consolidation features, rather than primary sedimentary structures. Very rarely, the clay streaks transition vertically into sub-vertical pipe structures. Outsized clasts are rare and usually < 1 cm in diameter, and present as dispersed graded (B4), ordered stratified (B5) or clustered floating (A3) types (*sensu* Stow and Johansson, 2000).

Heterogeneity in the SM facies is subdued, with frequent amalgamation of clean sand layers, as well as scarcity of well-defined sedimentary structures and clean nature of the sands. The amalgamated natures could imply scouring of finer grained background sediments. This translates into a relatively uniform distribution in porosity and permeability measurement from core plugs, with small variations associated with textural changes, such as graded tops to massive sands. The discontinuous nature of the clay streaks, and the dispersed carbonaceous and mud flecks, are also unlikely to impose significant heterogeneity. Thus, porosity and permeability measurements through these intervals only show minor variations. However, it is possible that the tool resolution may not be able to capture these features due to the size of the data support (volume over which the measurement is made). In rare cases, core plugs do capture these heterogeneities and disclose zones with only marginal porosity and permeability (e.g. Appendix E.1 Well 16/03a-E1, 13060-13064 ft, ϕ = 9.2 – 11% and Kh = 2.9 – 38 mD). These

will act as baffles to flow, since the lateral extent of these features is inferred to be limited to tens of metres due to the extensive scouring by successive beds. Outsized clasts are also likely to form minor baffles.

Clean, Structured Sands (SL and SR). Structured facies, consisting of thick to thin stratified sands (SL2 and SL3), parallel laminated sands (SL1) and ripple laminated sands (SR), are a subordinate facies, representing approximately 10% of the cored interval (Figure 5-6H). They best resemble incomplete Bouma and Lowe sequences (e.g. T_{BCE}, T_{ABC} or S3-T_{BC}) and typically constitute well sorted, medium grained, thin to thick (0.1 to 0.6 m) caps to the massive sands that form sequences up to 40 m thick (see above). The thicker structured caps characteristically occur towards the top of the massive sand sequences, while thinner intervals occur below amalgamation surfaces. The thickness variation is most likely a reflection of the degree of scouring by successive flows. Discrete structured beds are also common and are found interbedded with fine grained background sediments. These typically range from 0.1 to 1 m and are likely to record back-stepping of the sand system or deposition in fringe locations. Within these beds, the contacts are sharp, planar to undulating at the base, reflecting scouring and/or differential loading by the sand. Top boundaries are typically gradational to sharp. Normal distribution grading is common, with the facies characteristically grading from medium to very fine sand and silt. A gradual transition to mudstone is, however, rarely observed due to scouring and amalgamation of sand units. Even in discrete structured beds, the transition to the overlying mudstone is marked by grain size breaks, which represents bypass of the silt fraction possibly via fluid mud layers (Stevenson et al. 2014). Similar to the massive sands, cm-scale outsized clasts are common and are usually ordered stratified (B5) or dispersed graded (B4) types. In exceptional cases, stratified rip-up clasts are observed at the top of the facies, and occasionally continue into the overlying mudstone layer.

Where structured facies cap the massive sands, geological heterogeneities are subdued. Comparison of core porosity and permeability values show little variation between the two facies. However, it is likely that the heterogeneity induced by the sedimentary structures is averaged at measurements taken at the plug-scale. Therefore, the primary heterogeneity in the structured facies is associated with the discrete beds, which are interbedded with thin mudstone layers. However, at the core scale, it is impossible to determine the lateral extent of these mudstone layers and thus whether they form barriers or baffles. The presence of outsize mudclasts in the structured sands suggests updip erosion of the intervening mud layers. It is therefore likely that discrete beds are laterally connected to each other, potentially creating tortuous pathways for fluid flow. Features such as scour, flame and load structures may also improve vertical connectivity, but again these are difficult to determine at the core scale.

Mudstone (M). Following the massive sand facies, the mudstone facies (MM and ML) is the second most abundant facies encountered in the cored intervals (Figure 5-6B). These are black to dark grey in colour and laminated to massive in character. They can form sequences up to ~30 m thick (e.g. Well 16/03a-E1), but are more commonly between 5 cm and 1m thick. They are likely to represent background settling of sediments derived from biogenic and terrestrial sources, and abandonment of the East Brae fan system. Mudstone partings are characteristically flaggy to slabby, and contain abundant carbonaceous fragments, implying a strong terrestrial input into the basin. Bioturbation for the most part is absent but, locally, subvertical *Rhizocorallium* can be identified in thicker mudstone sequences. Rare pyrite and calcite nodules, a few cm in diameters, are also observed in these intervals.

The mudstone facies represent a strong geological heterogeneity in the system, particularly in cases where bed thicknesses exceed 1 m. It is likely that these thicker units extend for several hundred metres to form major baffles to flow. Indeed, the thick mudstone interval identified in Well 16/03a-E1 represents a field-wide abandonment of the sand system that compartmentalises the reservoir into an upper and lower unit (Branter, 2003). In terms of the more typical thinner mudstone beds, these are likely to impart significant permeability anisotropy characterised by low Kv/Kh ratios. However, this is dependent on the continuity of the mudstone facies, with increased erosion and greater connectivity likely to be present proximal to the sand fairway, where the magnitude and frequency of the turbidity current are likely to be greatest (Stephen et al., 2001).

Chaotic Facies (DC). This facies comprises disorganised and slumped intervals (Figure 5-6D), and discordant sand injections (Figure 5-6G). The former consists of thin to thick sand and mud layers (HM) that have been subjected to post-depositional remobilisation, possibly due to an above grade slope, and include 1) concordant slumped intervals with internally preserved bedding; and 2) discordant to chaotically slumped intervals with no internal coherency of strata. The difference in the two styles of deformation can be attributed to the ductility and competency of the material prior to remobilisation; the latter sub-facies clearly being less consolidated and prone to significant break-up during transport. In both cases, deformation occurred along a thin basal shear zone that is typically located above a mudstone layer, and which most likely facilitated movement. In concordant slumped intervals, the beds are deformed into asymmetrical to monoclinal folds, while discordant intervals are characterised by non-parallel, irregular to nodular remnant bedding geometries. Thicknesses of the deformed intervals vary between a few centimetres to 2 m.

Discordant sand injections are observable in most examined cores, particularly in mud-dominated and slumped intervals. They tend to be thin (few mm to 2 cm) and relatively short (<15cm), and consist of silt to very fine grained sands. They are closely associated with underlying clean sandstone units, which is likely the source of the injected sand. The upward flexure of the intruded lithology and sedimentary structures (i.e. lamination) lends further support to emplacement from below. Due to subsequent compaction of the host lithology, the injections are also often contorted. Due to the close association with the clean sand, they are interpreted to form by fluidisation of the clean sand, possibly due to excess pore-pressure induced by the overburden of the sedimentary load during burial. This in turn causes seal failure and remobilisation of the sand (Hurst, 2011). However, the exact trigger for this remobilisation is still poorly understood (*ibid*.).

In terms of disorganised and slumped intervals, bed scale heterogeneity is likely to be strong, particularly in thicker intervals which could extend for a few hundred metres. The internal architecture of the facies is complex, with local sand amalgamation due to folding and scouring of the mudstone during remobilisation. This is likely to create tortuous paths for fluid flow. However, based on core-scale features, there appears to be insufficient connectivity between the sand layers due to the patchy distribution of the amalgamation contacts. Sampling bias during conventional core analysis also prevents quantitative assessment of heterogeneity at the bed scale for this sub-facies. In contrast, discordant sand injections are likely to improve vertical connectivity between sands intervals. However, this is dependent on thickness and volume of the sand injections. In the East Brae, the short, infrequent and isolated nature of the injections suggests that they are unlikely to enable connectivity over production timescales.

5.5.2 Markov Chain

Markov Process at Proximal, Medial and Distal Locations. The transition counts (Fij), upward transition probability (Pij),) and the normalised difference (Zij) matrices for the three grouped locations (proximal, medial and distal) are given in Table 5-4. For each transition pair, the row facies code represents the lower facies and the column facies code, the upper facies. The chi-squared statistics for each grouping at 55 (proximal and medial) and 41 (distal) degrees of freedom, and a 99.5% confidence level, indicate a strong inclination towards an ordered sequence. Figure 5-9 to 5-11 shows the Markov transition diagrams based on the normalised difference matrix (Zij) for the strongest transition paths (value exceeding 2.0) in the three grouped localities. It is important to note at this stage that the normalised difference matrices provide a framework of identifying large difference between the observed and expected transitions, and thus the transitions that contributed most towards the chi-squared value. However, by considering both the normalised difference matrix and the observed transition

matrix, a more accurate description of the internal heterogeneity within the East Brae MSFA can be derived.

Table 5-4: The transition count, upward transition, upward expected probability and the normalised difference matrices for the proximal, medial and distal Wells of the East Brae Fields. Values in bold in the normalised difference matrix are used to construct the Markov chain diagram, supplemented by data from the transition count matrix.

Proximal Wells

Transition Count Matrix (Fij)

i,j	Sr	SI1	SI2	G/S	SM1	SM2	SM3	MM/ML	DC	Total
Sr	-	0	0	1	0	1	0	8	1	**11.00**
SI1	4	-	2	6	6	4	0	25	1	**48.00**
SI2	7	4	-	18	16	8	0	40	0	**93.00**
G/S	0	2	1	-	37	14	0	0	1	**55.00**
SM1	2	24	43	22	-	43	1	50	8	**193.00**
SM2	0	13	27	8	47	-	0	26	2	**123.00**
SM3	0	0	0	0	1	1	-	0	0	**2.00**
MM/ML	0	7	17	0	80	47	1	-	3	**155.00**
DC	0	1	0	0	7	2	0	8	-	**18.00**
Total	**13.00**	**51.00**	**90.00**	**55.00**	**194.00**	**120.00**	**2.00**	**157.00**	**16.00**	**698.00**

Upward Expected Probability Matrix ($\hat{P}ij$)

i,j	Sr	SI1	SI2	G/S	SM1	SM2	SM3	MM/ML	DC
Sr	-	0.06	0.12	0.07	0.33	0.17	0.00	0.23	0.02
SI1	0.02	-	0.12	0.07	0.35	0.17	0.00	0.25	0.02
SI2	0.02	0.07	-	0.08	0.37	0.18	0.00	0.26	0.02
G/S	0.02	0.07	0.12	-	0.35	0.18	0.00	0.25	0.02
SM1	0.02	0.09	0.17	0.10	-	0.24	0.00	0.34	0.03
SM2	0.02	0.07	0.14	0.08	0.39	-	0.00	0.28	0.02
SM3	0.01	0.06	0.12	0.07	0.33	0.16	-	0.23	0.02
MM	0.02	0.08	0.15	0.09	0.42	0.21	0.00	-	0.02
DC	0.02	0.06	0.12	0.07	0.33	0.17	0.00	0.24	-

Upward Transition Probability Matrix ($\hat{P}ij$)

i,j	Sr	SI1	SI2	G/S	SM1	SM2	SM3	MM/ML	DC
Sr	-	0.00	0.00	0.09	0.00	0.09	0.00	0.73	0.09
SI1	0.08	-	0.04	0.13	0.13	0.08	0.00	0.52	0.02
SI2	0.08	0.04	-	0.19	0.17	0.09	0.00	0.43	0.00
G/S	0.00	0.04	0.02	-	0.67	0.25	0.00	0.00	0.02
SM1	0.01	0.12	0.22	0.11	-	0.22	0.01	0.26	0.04
SM2	0.00	0.11	0.22	0.07	0.38	-	0.00	0.21	0.02
SM3	0.00	0.00	0.00	0.00	0.50	0.50	-	0.00	0.00
MM	0.00	0.05	0.11	0.00	0.52	0.30	0.01	-	0.02
DC	0.00	0.06	0.00	0.00	0.39	0.11	0.00	0.44	-

Normalised Difference Matrix ($Zij=Fij-Eij/VEij$)

i,j	Sr	SI1	SI2	G/S	SM1	SM2	SM3	MM/ML	DC
Sr	-	-0.83	-1.14	**0.29**	-1.91	-0.61	-0.16	**3.38**	**1.74**
SI1	**3.70**	-	-1.61	**1.40**	-2.61	-1.51	-0.34	**3.84**	0.05
SI2	**4.33**	-0.97	-	**4.14**	-3.12	-2.22	-0.49	**3.19**	-1.40
G/S	-0.94	-0.85	-2.23	-	**4.06**	**1.41**	-0.37	-3.69	-0.09
SM1	-1.10	**1.53**	**1.70**	**0.65**	-	-0.55	**0.43**	-1.98	**1.17**
SM2	-1.48	**1.32**	**2.41**	-0.58	-0.13	-	-0.58	-1.36	-0.44
SM3	-0.17	-0.35	-0.48	-0.37	**0.43**	**1.18**	-	-0.68	-0.19
MM	-1.73	-1.53	-1.32	-3.67	**1.77**	**2.45**	**0.80**	-	-0.38
DC	-0.52	-0.12	-1.46	-1.11	**0.43**	-0.57	-0.20	**1.84**	-

Medial Wells

Transition Count Matrix (Fij)

i,j	Sr	SI1	SI2	G/S	SM1	SM2	SM3	MM	DC	Total
Sr	-	1.00	0.00	8.00	0.00	0.00	0.00	11.00	1.00	**21.00**
SI1	16.00	-	3.00	32.00	10.00	2.00	0.00	39.00	0.00	**102.00**
SI2	0.00	29.00	-	13.00	32.00	10.00	0.00	13.00	0.00	**97.00**
G/S	0.00	1.00	6.00	-	45.00	33.00	0.00	0.00	0.00	**85.00**
SM1	1.00	35.00	46.00	14.00	-	61.00	1.00	57.00	2.00	**217.00**
SM2	4.00	34.00	29.00	18.00	29.00	-	0.00	51.00	0.00	**165.00**
SM3	0.00	0.00	2.00	0.00	0.00	0.00	-	0.00	0.00	**2.00**
MM	0.00	9.00	13.00	0.00	94.00	58.00	1.00	-	3.00	**178.00**
DC	0.00	1.00	1.00	0.00	1.00	2.00	0.00	1.00	-	**6.00**
Total	**21.00**	**110.00**	**100.00**	**85.00**	**211.00**	**166.00**	**2.00**	**172.00**	**6.00**	**873.00**

Upward Expected Probability Matrix ($\hat{P}ij$)

i,j	Sr	SI1	SI2	G/S	SM1	SM2	SM3	MM	DC
Sr	-	0.12	0.11	0.09	0.28	0.20	0.00	0.21	0.01
SI1	0.02	-	0.12	0.10	0.31	0.22	0.00	0.23	0.01
SI2	0.02	0.13	-	0.10	0.30	0.21	0.00	0.23	0.01
G/S	0.02	0.13	0.11	-	0.30	0.21	0.00	0.22	0.01
SM1	0.03	0.16	0.14	0.12	-	0.26	0.00	0.28	0.01
SM2	0.02	0.14	0.13	0.11	0.34	-	0.00	0.25	0.01
SM3	0.02	0.12	0.10	0.09	0.27	0.19	-	0.20	0.01
MM	0.03	0.14	0.13	0.11	0.34	0.24	0.00	-	0.01
DC	0.02	0.12	0.10	0.09	0.27	0.19	0.00	0.20	-

Upward Transition Probability Matrix ($\hat{P}ij$)

i,j	Sr	SI1	SI2	G/S	SM1	SM2	SM3	MM	DC
Sr	-	0.05	0.00	0.38	0.00	0.00	0.00	0.52	0.05
SI1	0.16	-	0.03	0.31	0.10	0.02	0.00	0.38	0.00
SI2	0.00	0.30	-	0.13	0.33	0.10	0.00	0.13	0.00
G/S	0.00	0.01	0.07	-	0.53	0.39	0.00	0.00	0.00
SM1	0.00	0.16	0.21	0.06	-	0.28	0.00	0.26	0.01
SM2	0.02	0.21	0.18	0.11	0.18	-	0.00	0.31	0.00
SM3	0.00	0.00	1.00	0.00	0.00	0.00	-	0.00	0.00
MM	0.00	0.05	0.07	0.00	0.53	0.33	0.01	-	0.02
DC	0.00	0.17	0.17	0.00	0.17	0.33	0.00	0.17	-

Normalised Difference Matrix ($Zij=Fij-Eij/VEij$)

i,j	Sr	SI1	SI2	G/S	SM1	SM2	SM3	MM	DC
Sr	0.00	-0.93	-1.49	**4.50**	-2.42	-2.02	-0.20	**3.19**	**2.53**
SI1	**9.02**	0.00	-2.59	**6.95**	-3.82	-4.27	-0.46	**3.24**	-0.81
SI2	-1.47	**4.69**	0.00	**1.17**	**0.45**	-2.35	-0.45	-1.91	-0.78
G/S	-1.36	-2.97	-1.18	0.00	**3.89**	**3.60**	-0.42	-4.34	-0.72
SM1	-2.03	**0.12**	**2.70**	-2.34	0.00	**0.52**	0.59	-0.45	**0.25**
SM2	-0.04	**2.18**	**1.70**	0.07	-3.57	0.00	-0.62	**1.50**	-1.07
SM3	-0.20	-0.48	**3.93**	-0.42	-0.74	-0.62	0.00	-0.64	-0.11
MM	-2.11	-3.29	-2.11	-4.40	**4.24**	**2.34**	0.90	0.00	**1.55**
DC	-0.35	0.35	0.46	-0.73	-0.52	0.77	-0.11	-0.22	0.00

Distal Wells

Transition Count Matrix (Fij)

i,j	Sr	SI1	SI2	G/S	SM1	SM2	MM	DC	Total
Sr	-	0	0	0	0	0	1	0	**1.00**
SI1	1	-	1	10	3	4	17	1	**37.00**
SI2	0	8	-	12	21	3	27	0	**71.00**
G/S	0	0	5	-	30	14	0	0	**49.00**
SM1	1	19	37	15	-	56	56	1	**185.00**
SM2	0	2	17	13	38	-	34	0	**104.00**
MM	0	4	12	0	89	31	-	1	**137.00**
DC	0	0	0	0	0	0	3	-	**3.00**
Total	**2.00**	**33.00**	**72.00**	**50.00**	**181.00**	**108.00**	**138.00**	**3.00**	**587.00**

Upward Expected Probability Matrix ($\hat{P}ij$)

i,j	Sr	SI1	SI2	G/S	SM1	SM2	MM	DC
Sr	-	0.04	0.10	0.07	0.38	0.17	0.23	0.00
SI1	0.00	-	0.11	0.07	0.40	0.17	0.24	0.00
SI2	0.00	0.05	-	0.08	0.42	0.19	0.26	0.00
G/S	0.00	0.05	0.11	-	0.41	0.18	0.25	0.00
SM1	0.00	0.07	0.17	0.11	-	0.27	0.37	0.01
SM2	0.00	0.05	0.12	0.08	0.45	-	0.28	0.00
MM	0.00	0.06	0.13	0.09	0.49	0.22	-	0.01
DC	0.00	0.04	0.10	0.07	0.38	0.17	0.23	-

Upward Transition Probability Matrix ($\hat{P}ij$)

i,j	Sr	SI1	SI2	G/S	SM1	SM2	MM	DC
Sr	-	0.00	0.00	0.00	0.00	0.00	1.00	0.00
SI1	0.03	-	0.03	0.27	0.08	0.11	0.46	0.03
SI2	0.00	0.11	-	0.17	0.30	0.04	0.38	0.00
SI3	0.00	0.00	0.00	0.00	0.00	0.00	0.00	0.00
G/S	0.00	0.00	0.10	-	0.61	0.29	0.00	0.00
SM1	0.01	0.10	0.20	0.08	-	0.30	0.30	0.01
SM2	0.00	0.02	0.16	0.13	0.37	-	0.33	0.00
MM	0.00	0.03	0.09	0.00	0.65	0.23	-	0.01
DC	0.00	0.00	0.00	0.00	0.00	0.00	1.00	-

Normalised Difference Matrix ($Zij=Fij-Eij/VEij$)

i,j	Sr	SI1	SI2	G/S	SM1	SM2	MM	DC
Sr	-	-0.21	-0.32	-0.26	-0.62	-0.41	**1.60**	-0.06
SI1	**2.85**	-	-1.50	**4.47**	-3.05	-0.96	**2.69**	2.19
SI2	-0.45	**2.36**	-	**2.79**	-1.65	-2.80	**2.03**	-0.55
SI3	0.00	0.00	0.00	0.00	0.00	0.00	0.00	0.00
G/S	-0.37	-1.54	-0.19	-	**2.25**	1.78	-3.49	-0.45
SM1	0.26	1.55	**1.11**	-1.24	-	0.93	-1.55	-0.15
SM2	-0.57	-1.52	**1.14**	**1.49**	-1.35	-	**0.97**	-0.70
MM	-0.68	-1.41	-1.50	-3.51	**2.61**	**0.26**	-	0.37
DC	-0.09	-0.37	-0.56	-0.46	-1.07	-0.71	2.76	-

General Trends. Prior to a discussion on the preferred transitions for individual groupings, traits common to all three are initially highlighted. All three groups show two common sequences: isolated sand beds and amalgamated sand packages up to 40 metres thick. Within the isolated sand beds, the transition consists of mudstones (MM/ML) overlain by massive

sands (SM1 or SM2), which are in turn overlain by either structured facies (SL1 or SL2) or mudstones (MM/ML). Observations from cores indicate that the latter transitions are more common, such that isolated sands represent DWMS *sensu stricto* (Stow and Johansson, 2000). In contrast, the amalgamated packages show more complex transitions. Amalgamation surfaces and grain size breaks are common, and typically truncate cycles. These surfaces are more common at the base and middle of the packages and separate massive or structured sands from similar facies. Towards the top, amalgamation surfaces become less common and transitions to thin mudstone layers is more likely. Also common at the top are cyclic transitions involving graded and ungraded massive sands (SM), and thin stratified sands (SL2).

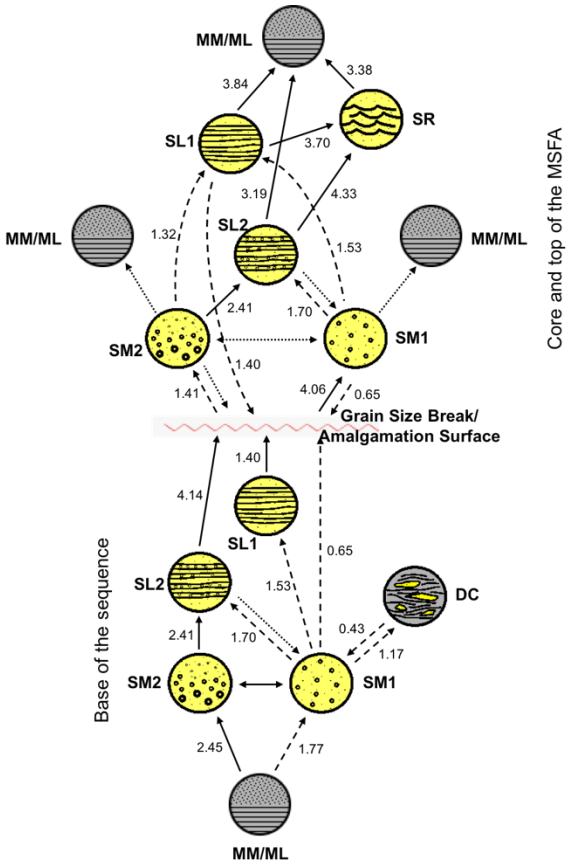

Figure 5-9: Markov transition diagram showing the most preferred upward transitions between facies states in proximal wells in the East Brae Field. Z_{ij} value of +2.0 (solid lines) is chosen to identify preferred transitions since they contribute most to the X^2 values. Dashed lines indicate transitions with Z_{ij} values of less than +2.0, while dotted lines are based on the observed transition count matrix.

Proximal. Figure 5-9 shows the Markov transition diagram for the proximal wells. Within the MSFA, the dominant statistical transition involves graded massive sands (SM2) at the base transitioning to stratified sands prior to an amalgamation surface marked by a subtle grain size break. Above the grain size break, a cyclic trend is likely involving massive and structured sands prior to a transition to rippled sands and/or mudstone facies. However, it should be noted

that the most common *observed* transition at the base involves ungraded massive sands to thin stratified sands prior to the cycle being truncated by an amalgamation surface.

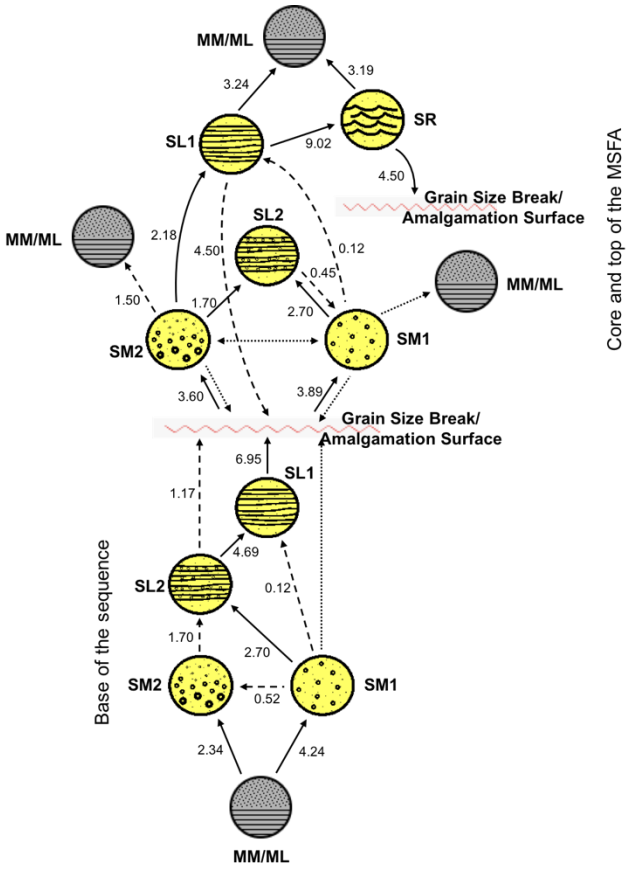

Figure 5-10: Markov transition diagram showing the most preferred upward transitions between facies states in medial wells in the East Brae Field. See Figure 5-9 for detailed description of the transition lines.

Medial. Figure 5-10 shows the transition diagram for medial wells. The preferred transitions within the MSFA are not too dissimilar to the proximal wells and show mudstones overlain by massive sands, followed by thin stratified sands and parallel laminated sands before the cycle is truncated by an amalgamation surface. The core of the MSFA is defined by cyclic trends involving ungraded and graded massive sands and structured sands that are again truncated by amalgamation surfaces. Locally towards the top of individual beds parallel laminated sands transition to rippled sands before being truncated by an amalgamation surface. These transition are primarily seen towards the top of the MSFA.

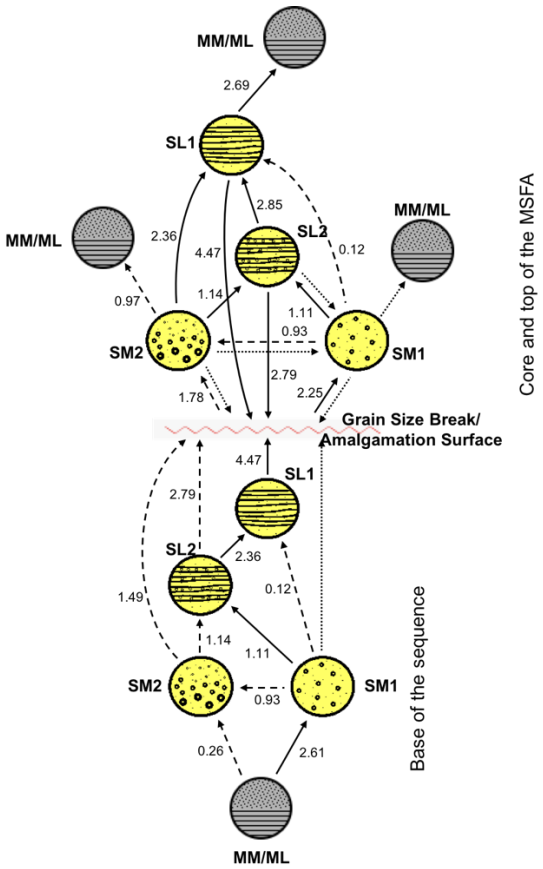

Figure 5-11: Markov transition diagram showing the most preferred upward transitions between facies states in Distal wells in the East Brae Field. See Figure 5-9 for detailed description of the transition lines.

Distal. Figure 5-11 shows the transition diagram for distal wells. Again, similarities can be seen to the proximal and medial wells both at the base and core/top of the MSFA. Individual beds show massive sands at the base followed by the structured sands. Amalgamation surfaces are common and truncate cycles consisting of ungraded and graded massive sands and thin stratified sands. However, distal localities show a preference for ungraded massive sands at the base of beds and above amalgamation surface. Towards the top of MSFA packages, thin mudstones (ML/MM) become more common and show a transition from parallel laminated sands, or directly from massive sands according to the transition count matrix. It is also worth noting that there is a distinct lack of rippled laminated sands at the top of beds, unlike proximal and medial localities.

5.5.3 Entropy Analysis

The computed entropy E(Post) and E(Pre), and the respective normalised entropy R(Post) and R(Pre) for each facies state are shown in Table 5-5 and Figure 5-12. E(Post) and E(Pre) relationship show that the influence of each facies on the preceding or succeeding facies is non-random, but is also non-cyclic i.e. asymmetrical, with proximal wells showing subtle evidence of upper truncated facies states e.g. Sr and Sl1. For most of the facies in the three groupings, the entropies are subequal and $E(Pre) = E(Post) \neq 0$, which indicates a level of dependency of one facies on the other. However, most of the facies states show relatively high entropy values,

indicating a rather disorderly sequence. This can be explained by the frequent amalgamation horizons (G/S) within the MSFA that disrupt cycles. For proximal Wells, the amalgamation surface truncate upper facies states as deduced from the entropy distribution diagram (Figure 5-12A). For the remaining two groupings, entropy distributions show A4 asymmetric cycles *sensu stricto* Hattori (1974). The normalised entropy values for state G/S shows similar values, indicating G/S overlies and is overlain by more than one facies state. Only facies SM3 comes close to approaching E(Post) = E(Pre) = 0, however, the low occurrence of this facies, precludes a statistically valid interpretation. No other systematic trend can be deduced from the entropy sets as we move from proximal to distal wells.

Table 5-5: Table show the entropy sets for the three well grouping. E(Pre) is entropy before deposition, while E(Post) is entropy after deposition. Together they serve as an indicaton of the variety of lithological transitions immediately after and before the occurrence of state i, respectively. State G/S are amalgamation surfaces identified by the presence of subtle grain size breaks in the MSFA.

Proximal Wells

E(Pre)	R(Pre)	i,j	E(Post)	R(Post)	Relationship
0.63	0.20	**SR**	1.28	0.40	E(Post)>E(Pre)
2.05	0.65	**SL1**	2.15	0.68	E(Post)>E(Pre)
2.36	0.74	**SL2**	2.20	0.69	E(Pre)>E(Post)
1.36	0.43	**G/S**	1.27	0.40	E(Pre)>E(Post)
3.72	1.17	**SM1**	2.50	0.79	E(Pre)>E(Post)
2.69	0.85	**SM2**	2.18	0.69	E(Pre)>E(Post)
0.10	0.03	**SM3**	1.00	0.32	E(Post)>E(Pre)
2.93	0.92	**MM/ML**	1.72	0.54	E(Pre)>E(Post)
0.60	0.19	**DC**	1.63	0.52	E(Post)>E(Pre)

Medial Wells

E(Pre)	R(Pre)	i,j	E(Post)	R(Post)	Relationship
1.07	0.41	**SR**	1.44	0.56	E(Post)>E(Pre)
1.74	0.67	**SL1**	2.06	0.80	E(Post)>E(Pre)
1.86	0.72	**SL2**	2.16	0.84	E(Post)>E(Pre)
1.23	0.48	**G/S**	1.36	0.53	E(Post)>E(Pre)
3.78	1.46	**SM1**	2.31	0.89	E(Pre)>E(Post)
2.87	1.11	**SM2**	2.35	0.91	E(Pre)>E(Post)
0.11	0.04	**SM3**	0.00	0.00	E(Pre)>E(Post)
2.71	1.05	**MM/ML**	1.65	0.64	E(Pre)>E(Post)
0.28	0.11	**DC**	2.25	0.87	E(Post)>E(Pre)

Distal Wells

E(Pre)	R(Pre)	i,j	E(Post)	R(Post)	Relationship
0.05	0.02	**SR**	0.00	0.00	E(Pre)>E(post)
2.29	0.72	**SL1**	2.09	0.66	E(Pre)>E(post)
1.95	0.62	**SL2**	2.03	0.64	E(Post)>E(Pre)
1.22	0.39	**G/S**	1.29	0.41	E(post)>E(Pre)
2.84	0.90	**SM1**	2.22	0.70	E(Pre)>E(Post)
2.21	0.70	**SM2**	1.97	0.62	E(Pre)>E(Post)
2.45	0.77	**MM/ML**	1.40	0.44	E(Pre)>E(Post)
0.12	0.04	**DC**	0.00	0.00	E(Pre)>E(Post)

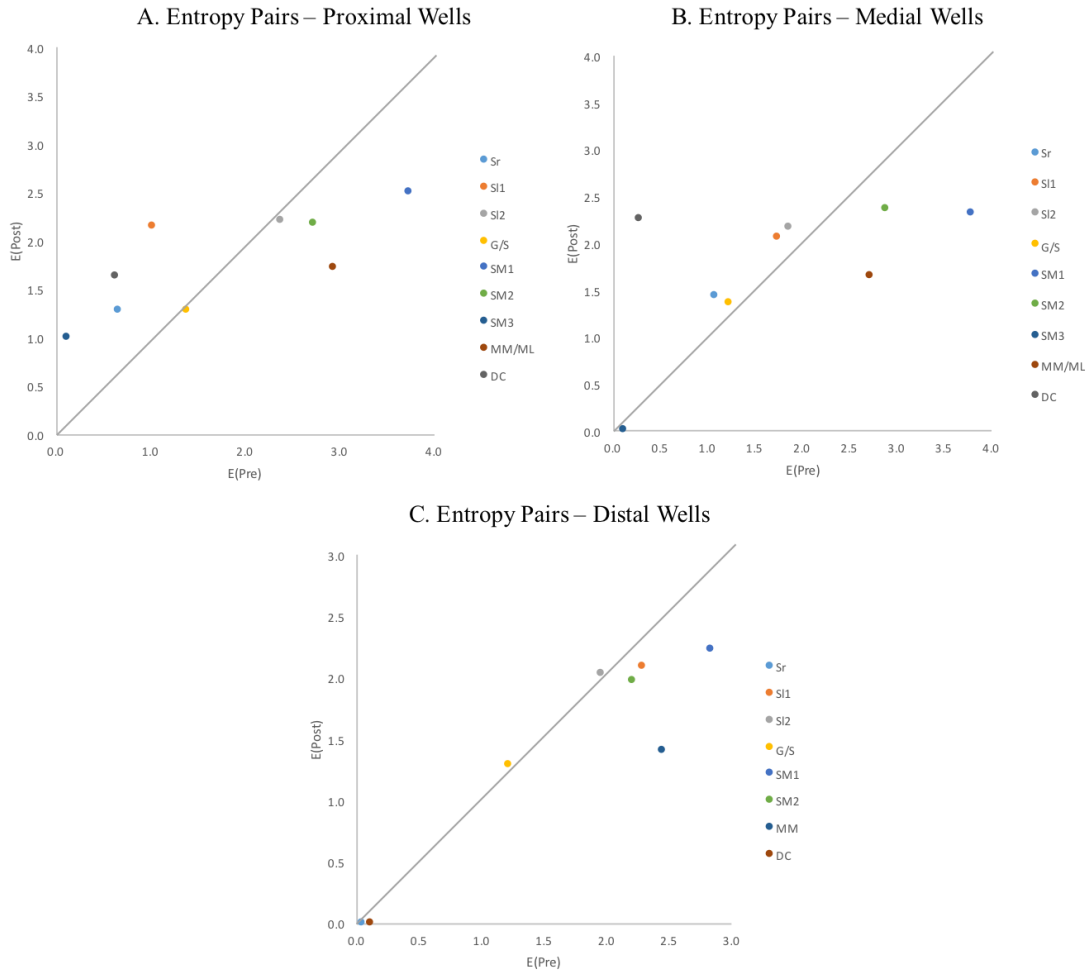

Figure 5-12: Distribution of entropy sets with respect to individual states for the three Well groupings: A. Proximal; B. Medial; and C. Distal. The entropy distributions show non-cyclic asymmetrical sedimentation with a degree of disorder and upper truncated states.

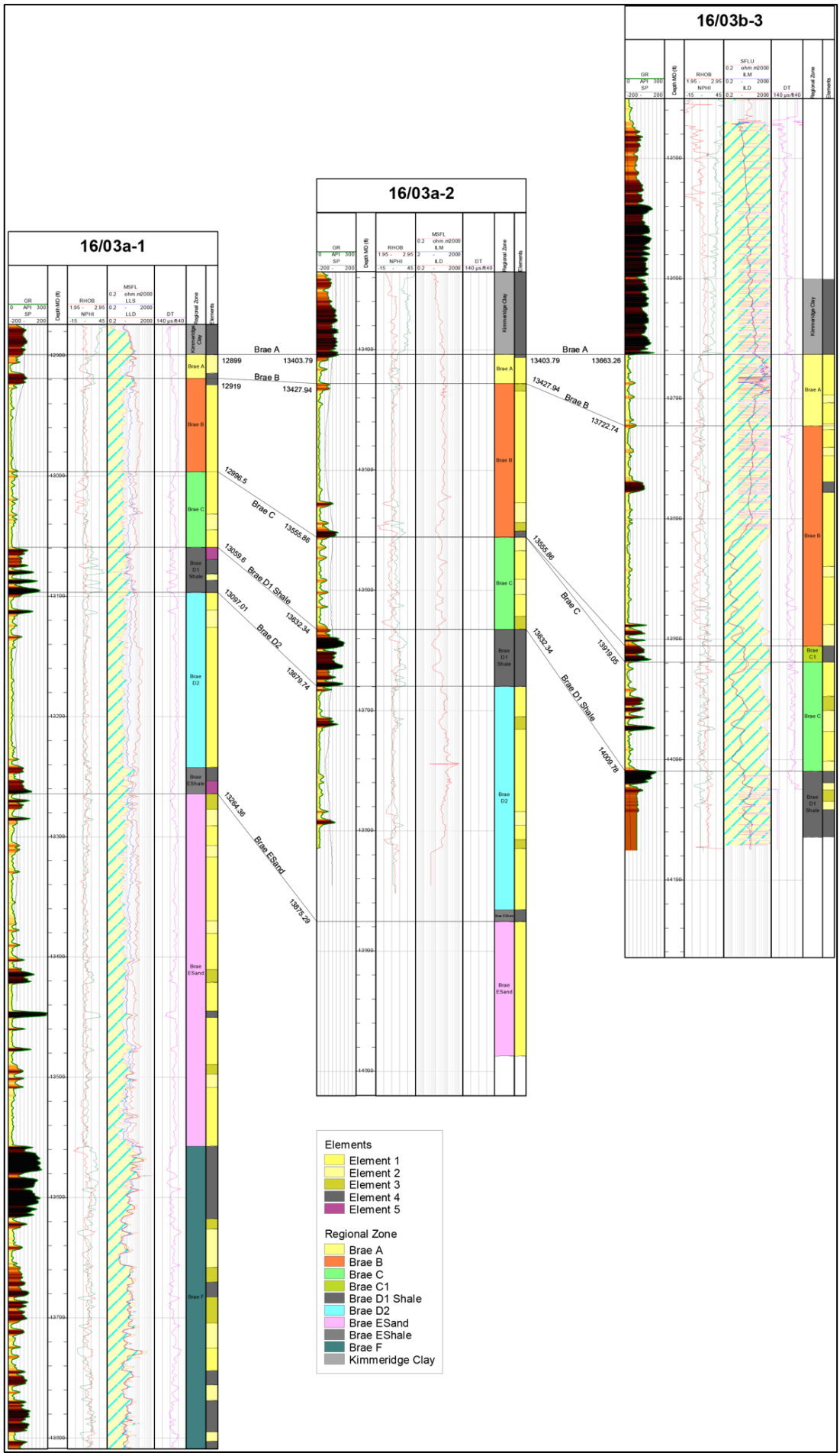
16/03a-1
16/03a-2
16/03b-3
Brae A
12899
13403.79
Brae B
12919
13427.94
12986.5
Brae C
13555.86
13058.6
Brae D1 Shale
13632.34
13097.01
Brae D2
13678.74
13204.36
Brae ESand
13875.29
Brae A
13403.79
13663.26
13427.94
Brae B
13722.74
13525.86
Brae C
13918.05
13632.34
Brae D1 Shale
14009.78
Elements
Element 1
Element 2
Element 3
Element 4
Element 5
Regional Zone
Brae A
Brae B
Brae C
Brae C1
Brae D1 Shale
Brae D2
Brae ESand
Brae EShale
Brae F
Kimmeridge Clay

Figure 5-13: (Above) Well logs from three cored wells showing the log character in the constituent parts of the MSFA. The log character is correlated to uncored wells to identify MSFA depositional elements. Location of the wells can be found in Figure 5-1 and a brief description of the wireline character for each depositional element is given in Appendix E.2.

5.6 Depositional Element Scale Heterogeneity.

It has been previously noted that the Brae area comprises point-source fan systems that have well-developed channel complexes containing conglomeratic and sandstone facies in the proximal areas (Brehm, 2003; Gupta et al. 2000; Turner et al. 1987). In the East Brae area, no such channel complexes have been identified in seismic data, although this could be partly due to the poor seismic resolution. Furthermore, core data show a lack of deep erosion at the bases of sand packages, as well as no pre-channel mass-transport complexes (Mayall et al., 2006; Pickering and Corregidor, 2005). However, the fining-upward motif observed in the well logs could be attributed to channel fill and abandonment facies. Based on this evidence, it is tentatively suggested that the East Brae lithofacies accumulated downstream of the main channel complex, in what could very well represent the channel-lobe transition zone (CLTZ). Recent studies of modern and ancient CLTZ indicate that they contain numerous distributary channels that have high aspect ratios (width-thickness). Both outcrop and subsurface data reveal frequent avulsion and amalgamation of these channels, resulting in sandstones that can be mistaken for laterally continuous depositional units resembling sheet-like architectural elements (Clark, 1998; Drinkwater and Pickering 2001; Kenyon et al., 2002; Posamentier and Walker, 2006). Areas of high amalgamation ratios are likely to be proximal to the principle sediment conduit at a given time where flows are likely to be erosive, while finer-grained and thinner beds are likely to represent off-axis or distal depositional settings (Pickering and Hiscott, 2015). A similar depositional model for East Brae has also been proposed by Branter (2003), Brehm (2003) Turner and Allen (1991) and Turner and Connell (1991). Within this broad depositional environment, the different depositional elements are defined and described based on stacking patterns and scale of observations, which is related to the position of the principal sediment supply route. For uncored wells, depositional elements are inferred using wireline log character (described in Appendix E.2). For each depositional element, the heterogeneity in terms of sedimentary architecture is described based on observations made at the core scale. This is then correlated to the uncored wells using the wireline character for each defined element (Figure 5-13). Quantification of the variability in porosity and permeability is undertaken using the coefficients described in section 5.4.4, log-derived property values and the 20ft curves.

Element One. Element one is the dominant depositional element in the East Brae MSFA, and consists dominantly of amalgamated massive sands, with minor structured sandstones and minor intercalations of mudstones and chaotic facies (Figure 5-14A). The element can form sequences up to 40 metres thick with a sand:shale ratio of >0.85. Mudstone and chaotic facies, where present, are typically centimetre to decimetre-thick, and the amalgamation ratio (>70%)

demonstrates that these are likely to be laterally restricted (10's of metres) due to extensive erosion and scouring. The abundance of cm-scale mudclasts attests to updip erosion of intervening non-reservoir facies. Therefore, at the field-scale, there are no significant barriers to flow, negligible sediment heterogeneity and laterally continuous sandbody geometry in this element. The transition to and from element one is gradational to sharp, often underlain and overlain by element two and three. These elements likely represent progressive off-axis sedimentation. Well log data demonstrates lateral continuity along depositional strike and dip for between 3 and 5 km, after which element one passes into element two or three. These elements are, therefore, likely to cap element one. Rarely, element four (e.g. D1 Shale and E Shale) occurs above and below element one, implying rapid onset and abandonment of the sand-rich system.

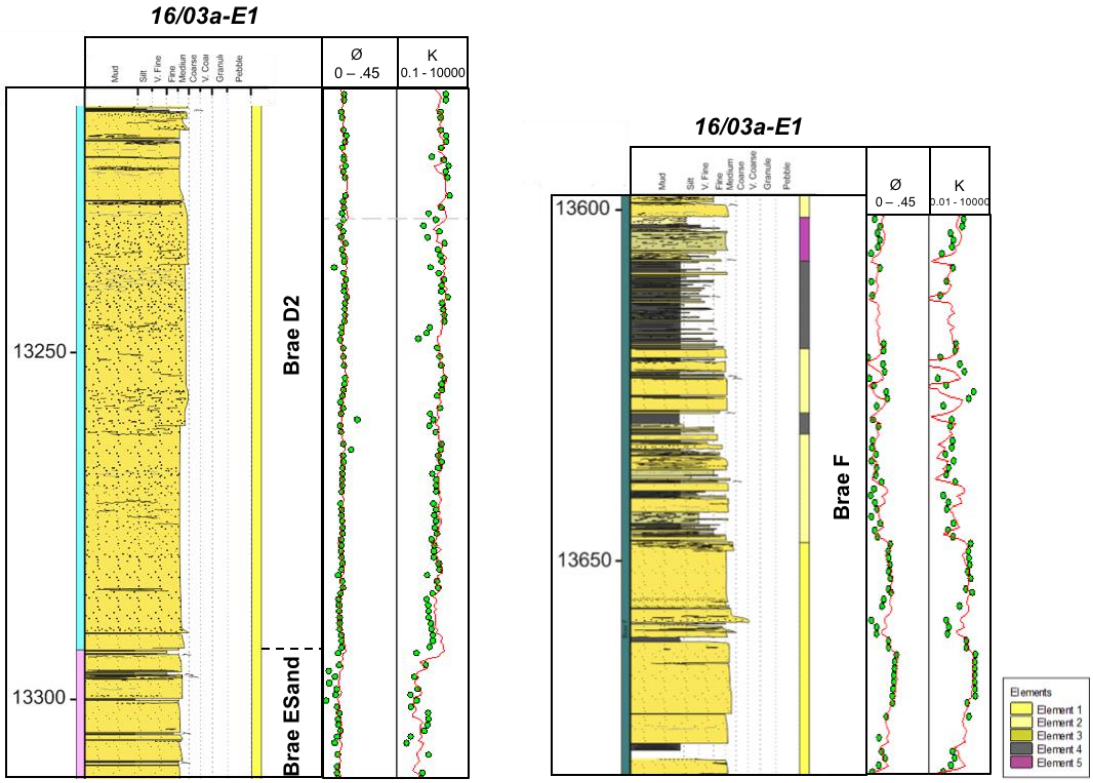

Figure 5-14: Lithofacies association of depositional elements one (left) and two (right). Element colour key is also provided.

While it is difficult to quantify the degree of erosion, the overall character of the element suggests deposition in channels located in an axial lobe setting or channel-lobe transition zone. In both modern and ancient turbidite systems, large scale incision that remove fan abandonment facies is observed in proximal settings (Bourget et al., 2010; Gervais et al., 2006). This is also the case for the South Brae and North Brae system, which is considered to be the proximal equivalent of East Brae. No such lobe-on-lobe scouring has been observed in East Brae. In contrast, channel-fill that are located in the lobe or channel-lobe transition zone are generally

only a few metres thick, a few hundreds of metres across, and inferred to be highly mobile due to a lack of levées and ephemeral in nature (Pickering and Hiscott, 2015; Prélat et al., 2009). The localised scouring results in high sand on sand amalgamation, creating depositional units that may be mistakenly interpreted as laterally extensive sheets in core data, which is likely the case for element one in the East Brae. Similar features have also been observed in the Precambrian Kongsfjord Formation in Arctic Norway, which has in part been interpreted as a channel-lobe transition zone characterised by amalgamated sandstone beds, small scale erosive scours and minor non-reservoir facies (Pickering 1981; 1985). Based on this evidence, an axial lobe or channel-lobe transition zone is the preferred interpretation for element one.

The negligible sedimentary heterogeneity is reflected in the core porosity and permeability of element one (Figure 5-14). Transects through this element reveal uniform distribution with a mean porosity of 13% and permeability of 89 mD, and a SD of ± 5% and 10 mD, respectively. Minor variation are associated with textural changes and presence of mudclasts and carbonaceous debris. This is also reflected in the static heterogeneity coefficients measured in the cored and uncored intervals of this element. The mean porosity CV is 0.2 (σ 0.12), while the LC show low to moderate heterogeneity values of 0.277 (σ 0.12). The Vdp is also comparatively low with a mean value of 0.12 (σ 0.16) across the field. However, the CV values for permeability appear to be more heterogeneous with a value of 0.75 (σ 0.45). This may be related to the influence the measurement scale of the original data has on the magnitude of the variability, as well as the simplicity of calculating the CV.

Element Two. Element two is similar in character to element one, but has a lower sand: shale ratio (between 0.5 and 0.85). It comprises amalgamated and isolated, massive and structured sands ($T_{B\text{-}2,3}$) interbedded with centimetre to decimetre-thick mudstones, chaotic facies and heterolithics (HM_2 and HM_3) lithofacies (Figure 5-14). Sand bed thickness are up to 1m, but locally occur as composite sequences between 3 and 5 m thick with thin discontinuous intervals of mudstone rip-up clasts lining amalgamation horizons, similar to in element one. Permeability transects through the sand sequences show subtle variations associated with laminated (clay and organic material) bed tops. The increased abundance of non-reservoir facies in this element also implies that scouring and erosion by subsequent flows is less effective, and that the associated heterogeneities are likely to be more extensive than element one. This could be attributed to the nature of the turbidity currents in terms of their magnitude and frequency, and is likely to represent increasingly off-axis sedimentation or a change from confined to unconfined deposition in a lobe or channel-lobe transition. In the latter case, loss of confinement would lead to flows becoming dominantly depositional and promoting preservation of non-reservoir facies. However, similar to element one, the high amalgamation ratio (> 50%), the relatively thin nature of non-reservoir facies and abundance of mudstone clasts indicate locally increased

vertical connectivity between sand beds. The amalgamation ratio in particular is a useful predictor of the permeability anisotropy ratio. Based on observation of discontinuous shale lengths from multiple turbidite succession, Stephen et al. (2001) identified a log-linear relationship between the two parameters, which could be used to infer the degree of erosion and thus their lengths. Hence, the remnant non-reservoir facies in this element are more likely to form baffles rather than barriers.

Element two is genetically related to element one and commonly overlies it (Figure 5-14 and 5-16). These transitions typically occur over thicknesses of 5 to 10 m. Very rarely, element two underlies element one, but is thinner due to scouring and erosion by element one depositing flows. Well correlations also shows lateral transitions to element one over a distance of ~0.5 km, indicating lateral connectivity to high-quality laterally extensive sandstones sequences. Less commonly, element two transitions vertically and laterally into elements three and four, indicating progressive shift and/or eventual abandonment of the sand fairway.

The higher degree of geological heterogeneity in element two compared to element one is also reflected in the mean porosity and permeability CV values, which are 0.25 (σ 0.12) and 0.97 (σ 0.44) respectively. Similarly, LC and Vdp are also higher at 0.35 (σ of 0.12) and 0.25 (σ of 0.2), respectively. These higher values are to be expected given the lower sand: shale ratio in element 2, as well as the structured nature of the sands which could impart pore scale heterogeneity to porosity and permeability measurements. Furthermore, since the deposits of element two are peripheral to the axis of the sand fairway, they are likely to be deposited by less energetic flows. As a consequence, the competence of the flows is reduced, which is likely to have a detrimental impact on the permeability. This could therefore explain the significant increase in permeability heterogeneity observed in the CV and Vdp.

Element Three. Comprising predominantly medium to very thin-bedded structured sands separated by centimetre to decimetre-thick background deposits (sand: shale ratio of < 0.5), element three represents deposition peripheral to the active sand-rich system, most likely as distal and lateral-marginal equivalents (Figure 5-15). Thick-bedded massive sands (subordinate facies) are still locally developed, but are now separated by decimetre-thick mudstones, deformed units or intervals of thinly-interbedded sandstone and mudstones (HM_1). The increased proportion of structured sands, particularly parallel-laminated (T_{B-1}) and cross laminated sands, attests to lower density flows with subdued erosion and scouring at the base. As such, mud-prone intervals have a greater preservation potential and may extend for 100s of metres laterally, forming significant baffles and/or barriers to vertical flow. The preservation potential of mudstone, as well as the structured nature of sand layers, is likely to impart

significant permeability anisotropy characterised by low Kv/Kh ratios. However, the genetic relationship of the sand beds to element one and two implies that these will be laterally connected to better quality elements (one and two) along strike and up-dip. Furthermore, the occurrence of thicker isolated massive sands, suggest more energetic flows were sporadically capable of traversing these fringe settings, although it is unlikely that these sand beds provide sufficient vertical connectivity due to a lack of erosion and amalgamation.

Element three is typically sandwiched between element one and/or two (Figure 5-15), indicating rapid shifting of the axis of sedimentation. These transitions are sharp, occurring over less than a metre. Rarely, a gradual off-axis sedimentation is recorded whereby element two and four occur above or below element three. As with element two, the mean values for CV (i.e. porosity and permeability) and LC, as measured across the East Brae field, is marginally higher at 0.28 (σ 0.11), 0.38 (σ 0.13) and 0.28 (σ 0.11) respectively. However, the Vdp has a lower value of 0.23 (σ 0.15). A possible reason for this could be the weight placed on the central portion of the data rather than the extreme values of permeability. As highlight by Rashid et al. (2010), this tend to suppress heterogeneity values. In this instance, the extreme values could be the interbedded mudstone layers. An alternative explanation could be found in the thickness of element three. Since the heterogeneity coefficients are calculated using a 41 sample interval (i.e. 20ft), and due to the fact that many element three intervals are smaller than 20ft, the Vdp values may be suppressed by sampling of less heterogeneous intervals above and below the element (i.e. element one and two). This overlap of the support size (20 ft) into the adjacent elements will smooth the heterogeneity curve and is discussed in more detail in section 5.7. However, it should be noted that the other heterogeneity coefficients are not affected in the same way.

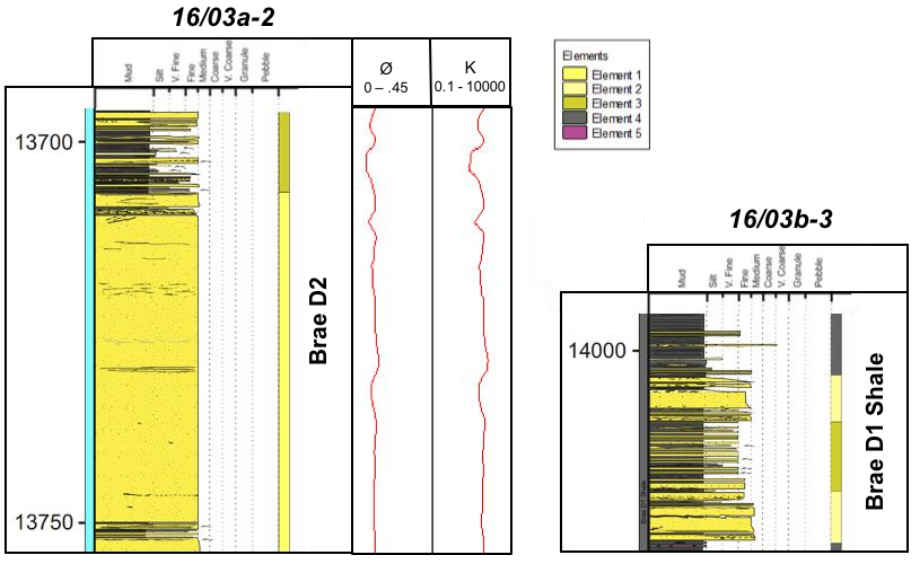

Figure 5-15: Lithofacies association of depositional elements one, two, three and four. A porosity and permeability curve for Well 16/03b-3 was not created due to a lack of wireline data at this depth.

Element Four. Element four is a mud-dominated interval, consisting predominantly of massive to silt-laminated mudstones, and subordinate interbedded very fine to fine grained sand-mud couplets (HM1) and mud-rich chaotic facies (Figure 5-16). Interval thicknesses range from a few metres up to 60 metres (e.g. Well 16/03a-1) and the sand: shale ratio is less than 0.25. Lateral distribution of this element is irregular, with thinner intervals likely extending a few hundred metres from the well (e.g. C1) to form significant barriers. These intervals are interpreted to represent localised cut-off of the sediment supply due to migration of the axis of sedimentation or allogenic factors such as base-level rise. In contrast, the thicker intervals (e.g. D1 Shale) are more extensive and mantle the fan system. These intervals represent complete switch off of the sediment supply into the basin as a result of allogenic controls. The extension of these shale-rich intervals into adjacent fields (e.g. South Brae, North Brae) lend support to this interpretation (Turner et al., 1987). Sneider et al.(1995) noted that major regressive and transgressive cycles are the primary controls on the distribution of sediment facies and reservoir in the South Viking Graben. Thus flooding of the local sediment source (northwest of the Fladen Ground Spur according to Turner and Connell, 1991), may account for the abrupt abandonment of the fan. An example of such a unit is the D1 Shale, which pressure profiles show to be a field-wide barrier that stratigraphically compartmentalises the reservoir (Branter, 2003). Transition to and from the element is characteristically sharp, directly overlying and underlying the amalgamated sands of element one. On rare occasions, there is a progressive transition to and from element four, with element two or three sandwiched between elements four and one (Figure 5-14 and 5-16). Again, internal (e.g. avulsion) and external (tectonics, sea-level change) factors are the likely causes of these abrupt onset or abandonment of the fan system.

Since element four has no reservoir potential, results of the heterogeneity coefficients are only presented for brevity. CV for porosity and permeability is 0.29 (σ 0.11) and 1.17 (σ 0.55), respectively, while, LC and Vdp are 0.39 (σ 0.12) and 0.31 (σ 0.22), respectively. With the exception of Vdp, the heterogeneity coefficients are similar to element three. Even though a non-reservoir element, the heterogeneity coefficients for element four indicate moderate heterogeneity due to the fact that static coefficients measure only the variation of a property, and not its impact on reservoir performance.

Element Five. Element five consists of concordant and discordant deformed intervals such as slumps, slides and moderately to highly cohesive debris flows (i.e. chaotic facies - DC), locally interbedded with thick mudstone layers (Figure 5-16). Interval thickness ranges up to 5 m and the sand: shale ratio is < 0.3. They are predominantly associated with thick-mud rich intervals such as element four, within which distinct glide planes are visible and define the bounding surfaces of the deformed layers. It is difficult to determine from core data whether these layers

represent laterally extensive heterogeneity, but thicker intervals are inferred to be continuous over a few hundred metres. Deformation was probably triggered gravitationally by an above grade slope, or cyclic or single shock events (e.g. seismic). Since element five is found associated with element four, and due to its mud-rich nature, the overall log responses are similar to element four. However, in more sand-rich intervals GR values are suppressed, resulting in a serrated gamma response (e.g. Well 16/03a-E1, depth 13535ft to 13551ft md). Due to these similarities in the log character, the element is difficult to determine in uncored wells. The heterogeneity values were therefore only calculated for the cored wells. The mean CV values for porosity and permeability are 0.33 (σ 0.13) and 1.55 (σ 0.58), respectively. The LC is 0.50 (σ 0.11) and the Vdp value is 0.44 (σ 0.22).

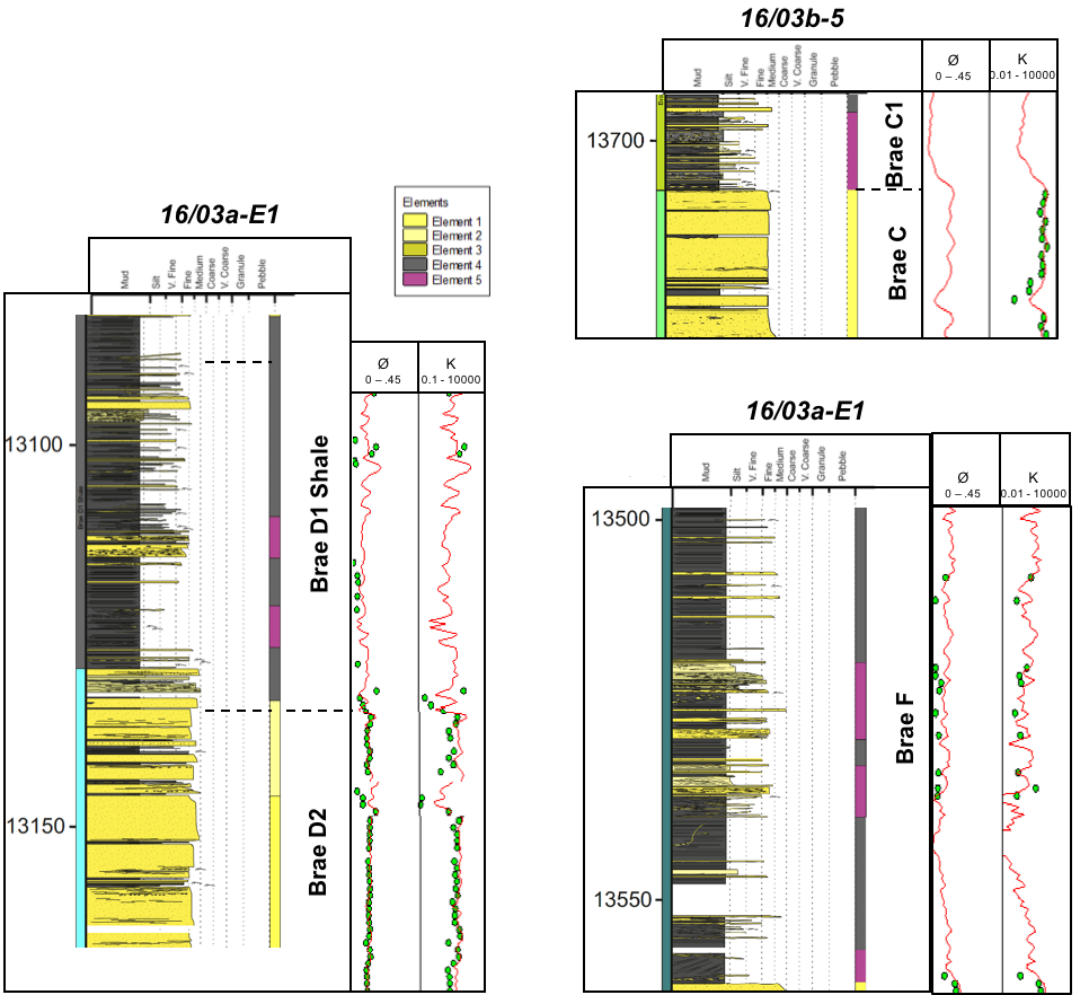

Figure 5-16:Lithofacies association of depositional elements four and five.

Summary of Element-Scale Heterogeneity. Core description of the East Brae Formation at the bed- and element-scale reveals that sedimentological heterogeneity exists at various scales. This has had a primary control on the porosity and permeability variability, which is corroborated by the static heterogeneity coefficients, and reveals low to moderate heterogeneity

for element one to five. Although heterogeneity is generally low, a trend is observed: element one is the least heterogeneous, with subsequent elements becoming increasingly heterogeneous (Figure 5-17). However, the standard deviation reveals significant dispersion about the mean, especially in terms of permeability when assessed using the CV. This dispersion in the permeability may be partly accounted for by the logarithmic scale used for permeability measurements, partly by diagenetic alteration, and partly by depositional processes. In the following sections, the variability in the porosity and permeability is assessed to define layers in the East Brae reservoir section that could be linked to particular reservoir behaviour.

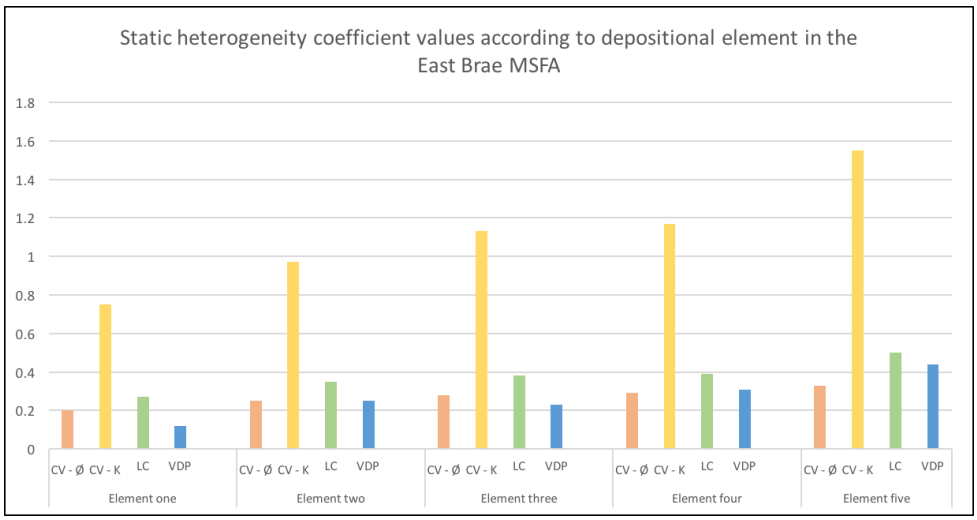

Figure 5-17: Graph showing the systematic increase in most heterogeneity values between depositional element one to five. The increase in the values is a ultimately a reflection of the sedimentological processes responsible for the deposition of the elements.

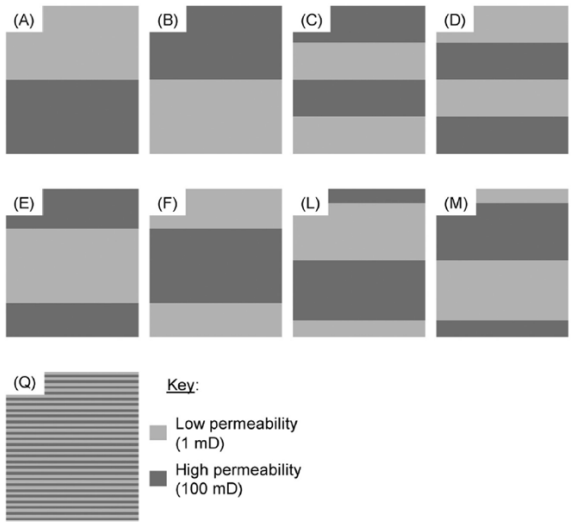

Figure 5-18: Simple box models illustrating the non-uniqueness of static heterogeneity coefficients in terms of temporal arrangement of contrasting layers. Each model has the same heterogeneity value regardless of the internal arrangement. After Fitch et al (2015).

5.7 Heterogeneity Zones within the MSFA.

Using numerical techniques, as well as facies analysis, it is shown that heterogeneity exists at various scales in the East Brae MSFA. In the following section, subtle variations in the heterogeneity coefficients are assessed to identify zones in the MSFA, which could correspond to baffles, seals/barriers, speed and/or thief zones. However, the standard method of calculating the static heterogeneity coefficients are inadequate for such an analysis due to the non-uniqueness of the heterogeneity value. Fitch et al. (2015) provided a simple demonstration of this issue by using a simple box model consisting of 100 layers; 50 layers were assigned a value of 1 and the remaining 50 layers were assigned a value of 100 (Figure 5-18). These two values could represent any reservoir property (e.g. porosity, saturation), but in this case are permeability values. The authors developed nine realisations by varying the temporal organisation of the 'high' and 'low' value layers, and calculated the heterogeneity of each model. Regardless of the temporal arrangement, each model generated the same heterogeneity value. However, under dynamic simulation, each model would behave differently in terms of sweep-efficiency, production and water breakthrough (*ibid.*). To address this issue, the present study uses a moving window to generate heterogeneity curves to identify potential layering. It is initially speculated that the smaller the window size, the higher the curve resolution, which in turn provides more accurate information on the temporal arrangement of layers. However, it should be noted that a smaller window size will result in compressed heterogeneity values for LC and VDP (Fitch et al. 2015; Jensen and Lake, 1988). Therefore, initially the 20ft curve is used to identify zones in the MSFA of the East Brae, as this curve meets the minimum number of sample points (40) recommended by Jensen and Lake (1988). For succinctness, only the results from wells 16/03a-1, 03b-7 and 3a-E20 are presented. The results from the remaining wells are provided in Appendix E.3. The MLP for these wells are then employed to validate the zones in terms of reservoir performance (e.g. Attia and Shuaibu, 2015; Gunter et al., 1997; Mahjour et al., 2016).

Since four heterogeneity curves were calculated (i.e. LC, Vdp, CVϕ and CVk) for each well, a choice has to be made on which curve to employ to identify the zones. The CV is the simplest technique for generating heterogeneity values. However, Lake and Jensen (1991) judged that the CV is negatively biased and is smaller than the true value of the population. The Vdp, in contrast, is a mathematically complex but statistically more robust technique. However, Jensen and Currie (1990) and Rashid et al. (2012) argued that outliers or influential points may greatly influence the regression line used to estimate the 50^{th} and 84^{th} percentile, thus affecting the heterogeneity value. Furthermore, the permeability data in each of the moving window needs to be log-normally distributed (Hirasaki 1984; Pintos et al., 2011). In the present study, this does not hold for all the wells. As such, the VDP values on occasion falls outside the bounds for some wells (16/03b-9, 3b-7, 3a-E1, 3a-E7, 3a-E14 and 3a-E15; Figure 5-19 and Appendix E.3;

Patrick Corbett Pers. Comm. 2017), rendering the heterogeneity curve ineffective as a tool to identifying layering. Lastly, based on detailed analysis of the LC value using a series of synthetic linear and exponential data populations, Fitch et al. (2013) adjudged the LC values to more accurately reflect the heterogeneity within a formation. Moreover, since the LC value is bounded between 0 and 1, it can effortlessly be compared between wells, as well as between stratigraphic members. However, it should be noted that the LC suffers from the same negative bias as the CV if small sample numbers are used (Jensen and Lake, 1988). After taking into consideration these factors, it was determined that the LC curve is the most appropriate to utilise for identifying layering in the MSFA.

Figure 5-19 shows the zoning for the three wells: 16/03a-1, 16/03b-7 and 16/3a-E20. The boundaries are based on thresholded values using the ranges provided by Fitch et al. (2015): (1) < 0.16 – low heterogeneity, (2) 0.16 to 0.25 – moderate linear heterogeneity, and (3) between 0.25 and 0.86 – high level exponential heterogeneity. These ranges provide an appropriate starting point to define the zones, rather than arbitrarily assigning class boundaries, and show strong correlation between all the heterogeneity curves (Figure 5-19; Brae ESand). The defined boundaries also show a weak correlation to changes in the gamma ray, especially where there is a significant change in sedimentary patterns e.g. element one to element three/four/five, with increasing heterogeneity values corresponding to increasing API values. However, the thresholded values provide limited correlation to the porosity/permeability curve, especially between the heterogeneity range 0.25 and 0.86. This could principally be a consequence of the wide range of values that fall within this class. Although it should be noted that peaks and troughs in these properties do not always correspond to changes in the heterogeneity values within this class range (Figure 5-19; Well 16/03a-E20 between 14541 – 14650 ft MD). An alternative explanation for the discrepancy could be due to the overlap of the support size of heterogeneity coefficients. Since the heterogeneity values for each HC corresponds to the mid-point of the moving window, abrupt changes in porosity and permeability do not translate to abrupt changes in heterogeneity values. This is due to the sample window moving down one point at a time, resulting in a smooth transition. In these cases, the trough or peak in the heterogeneity value may be located 10ft (half the window size) above or below the corresponding change in porosity/permeability trend.

There is also a weak correlation between the heterogeneity curves and the element boundaries that were defined based on sediment facies association and wireline log character (Figure 5-19). However, due to the subjective nature of grouping facies and defining bed thickness trends (Chen and Hiscott, 1999a; Hiscott, 1981; Mutti and Ricci Lucchi, 1972), these correlations are not as strong as the porosity/permeability properties or the gamma ray curve. As mentioned above, any discrepancies can be related to the window size and the method of calculating the

heterogeneity curve, as well as the threshold values used for the zoning. Notwithstanding, the location of the present layer boundaries can potentially be used as a guide to refine element boundaries, thus providing a more statistically valid criterion for defining depositional elements. This is particularly applicable for the East Brae Formation where the porosity and permeability is primarily controlled by the sediment texture (Branter, 2003; Leishman, 1994; Maast et al., 2011), which is in turn controlled by the transport and depositional processes.

Transects down the various heterogeneity curves within individual elements also reveal that heterogeneity values are not uniform, but vary considerable. For example, in Well 16/03a-1, the Brae D2 interval consists of ~150ft of massive sands belonging to depositional element one (Figure 5-14). From core observations, heterogeneity is clearly suppressed in this interval. However, the present thresholded LC values reveal that that this sequence can be subdivided into a number of discrete zones (e.g. at ~ 13172ft, 13205ft, 13210ft dd etc.) based on the heterogeneity in porosity and permeability. Similar trends are also observed in thick element one deposits in the Brae ESand, C and B of wells 16/03a-E20 and 3b-7 (Figure 5-19), as well as wells 03a-E1, 3b-5 and 3b-3 (Appendix E.3). The potential significance of this ‘layering’ is discussed in terms of flow performance using the MLP below.

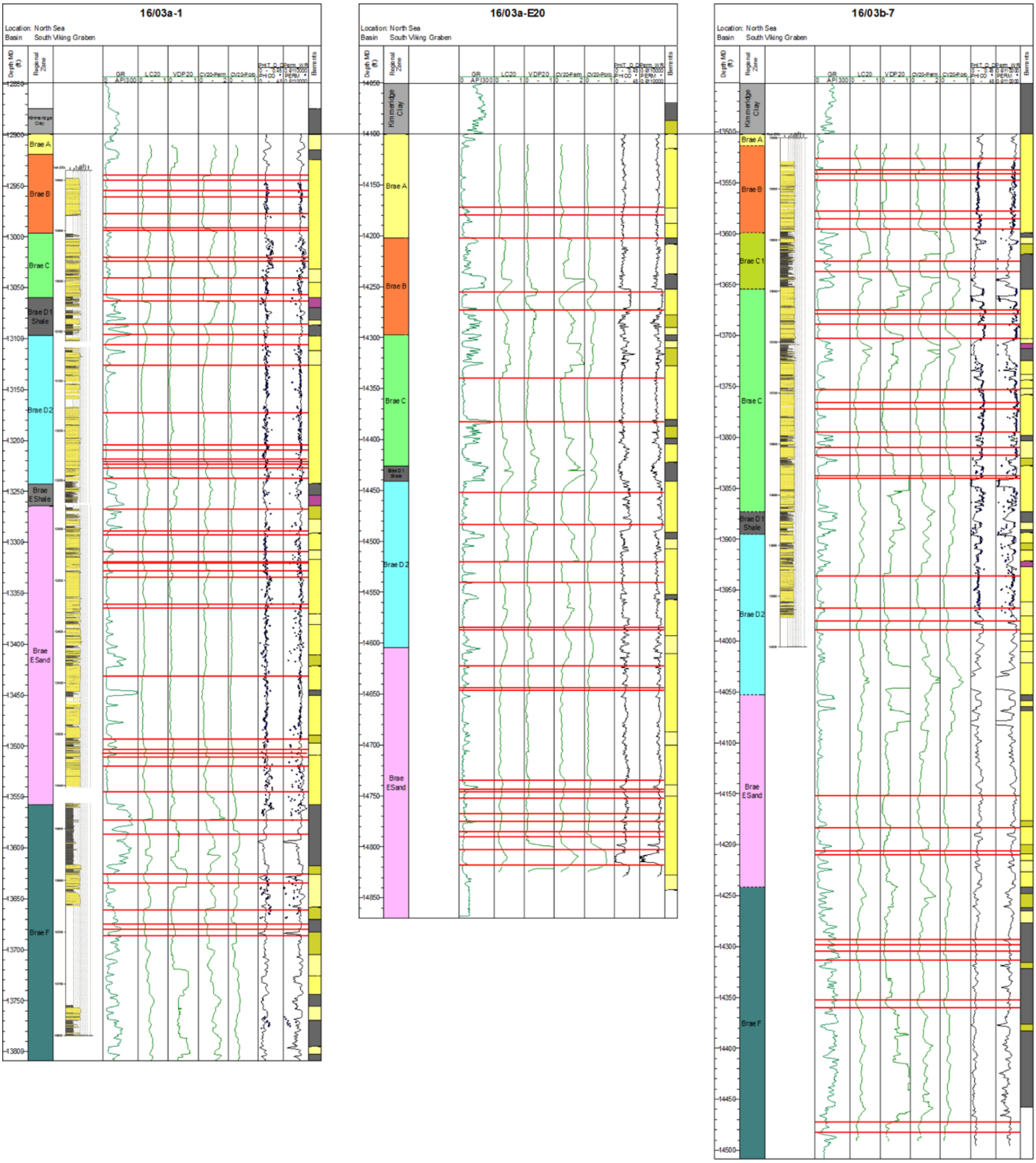

Figure 5-19: Identification of layering using the LC curve. Thresholded values are 0.16, 0.25 and 0.86 (after Ftich et al. (2015). A strong correlation can be observed between the heterogeneity curves, as well as the gamma ray and porosity/permeability curves although on a weaker level. A much weaker correlation can also be observed to the depositional element boundaries. However, since depositional elements are defined based on trends in sedimentary characteristics that are considered subjective, the heterogeneity curves in this instance can be used to adjust depositional element boundaries.

5.7.1 Correlating Heterogeneity Coefficients to the MLP.

Figures 5-20 to 5-22 show the modified Lorenz plots for the three wells. The zone boundaries from the heterogeneity curves have been transferred across to the appropriate depths along the line of cumulative flow-storage capacity. Zone boundaries that occur at significant inflection points on the MLP are also indicated with an arrow. What is important to note is that not all the zone boundaries coincide with inflection points. However, those that do, correspond to the 0.25 thresholded value on the heterogeneity curves. As noted by Fitch et al (2013; 2015), this LC value separates two reservoir classes: a change from linear to exponential increase in property values within the data set. What is indeterminate at this stage is whether this marks a change in reservoir behaviour i.e. storage capacity vs flow capacity. Analysis of the remaining inflection points also reveal a similar correlation at 0.35 ± 0.01, albeit not as strongly as the 0.25 threshold (Figure 5-20 to 5-22). Using the 0.25 threshold, no distinct trends are recognised. A value above and below 0.25 correspond to both high and low flow/storage capacity. Even within individual Brae members, these two opposing trends can be recognised (e.g. Brae B and C Figure 5-20 to 5-22).

One possible explanation for the lack of correlation between the LC heterogeneity values and the MLP could be the non-uniqueness of the LC value. As noted by Fitch et al. (2015) a variety of porosity and permeability distributions can generate the same heterogeneity value. In a real reservoir, the pore distribution can have a significant impact on fluid flow in terms of storativity and transmissivity. Thus, although an attempt was made to deal with the non-uniqueness of the Lorenz Coefficient by considering a moving window, the technique ultimately fails to identify speed/thief zones, and baffles and barriers in the manner of the MLP. An additional reason why the heterogeneity curves failed to predict reservoir behaviour is due to the reliance only on porosity and permeability variation. It has been shown through material balance that flow unit speed is dependent the k/Φ ratio, as well as the phase mobility and the pressure gradient. As such, it may not wholly be possible to predict flow performance from the heterogeneity coefficient generated from a moving window, at least for the East Brae MSFA.

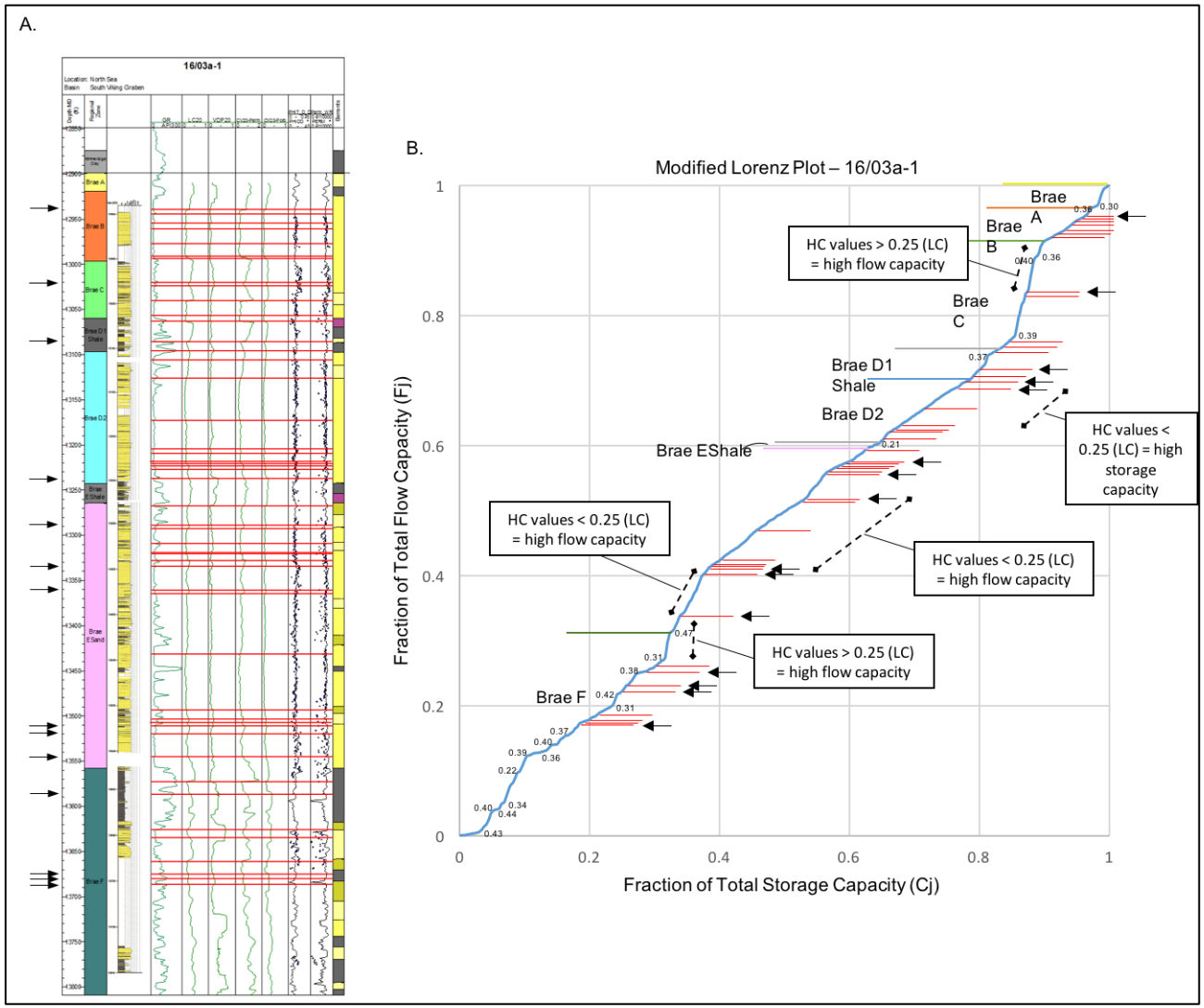

Figure 5-20: Modified Lorenz Plot (MLP) for Well 16/03a-1 showing the location of the threshold boundaries (after Fitch et al. 2013) from the LC 20ft curve. Arrows indicate location of the 0.25 threshold boundary, which commonly shows a small inflection in the MLP. The transition corresponds to a change from linear to exponential data set. However, no consistent trends are identified in terms of reservoir behaviour. Values along the line of cumulative flow and storage are the heterogeneity coefficient values at the inflection points not picked up by the thresholded ranges.

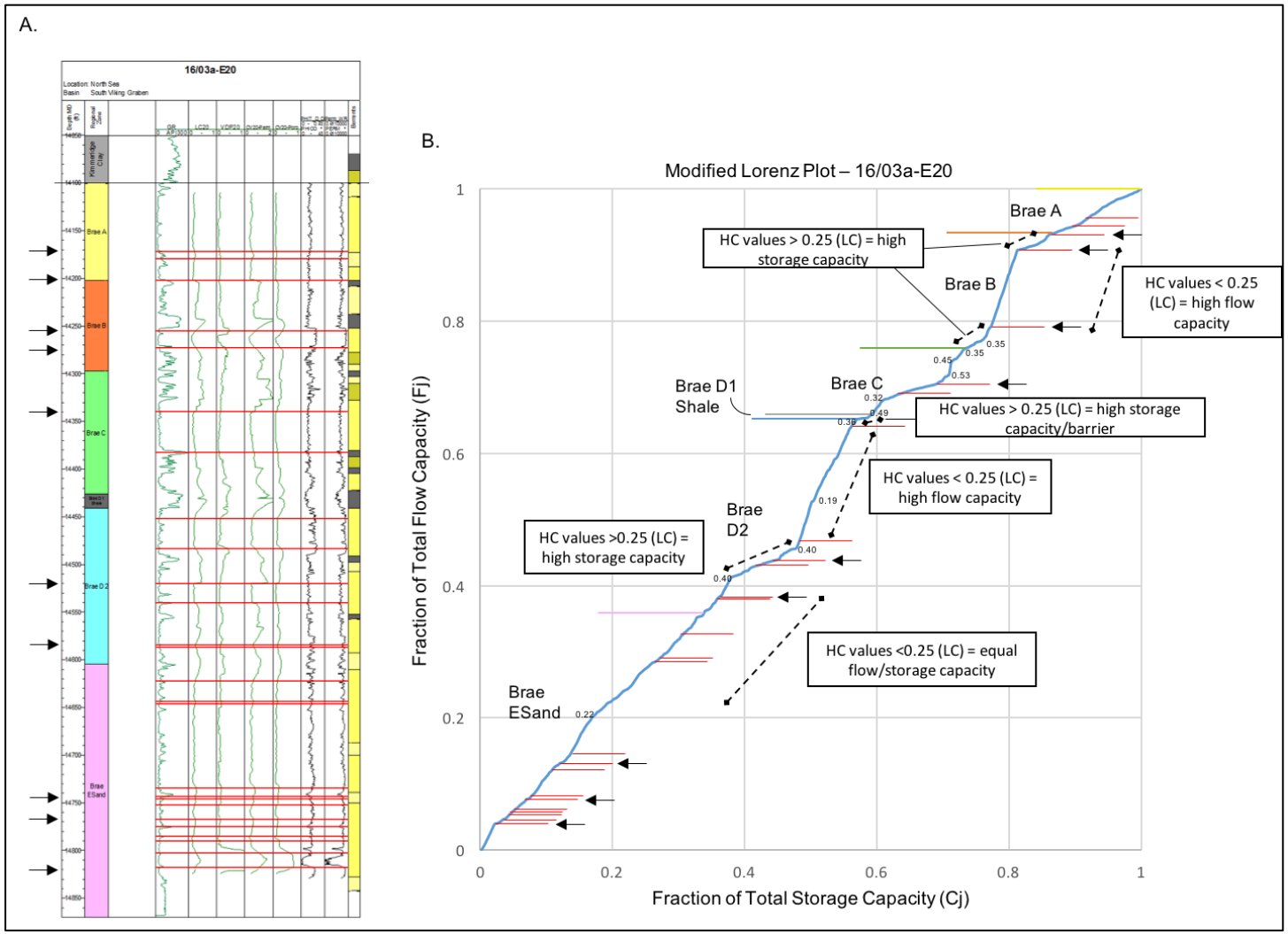

Figure 5-21: Modified Lorenz Plot (MLP) for Well 16/03a-E20 showing the location of the threshold boundaries (after Fitch et al. 2013) from the LC 20ft curve. Arrows indicate location of the 0.25 threshold boundary, which commonly shows a small inflection in the MLP. The transition corresponds to a change from linear to exponential data set. However, no consistent trends are identified in terms of reservoir behaviour. Values along the line of cumulative flow and storage are the heterogeneity coefficient values at the inflection points not picked up by the thresholded ranges.

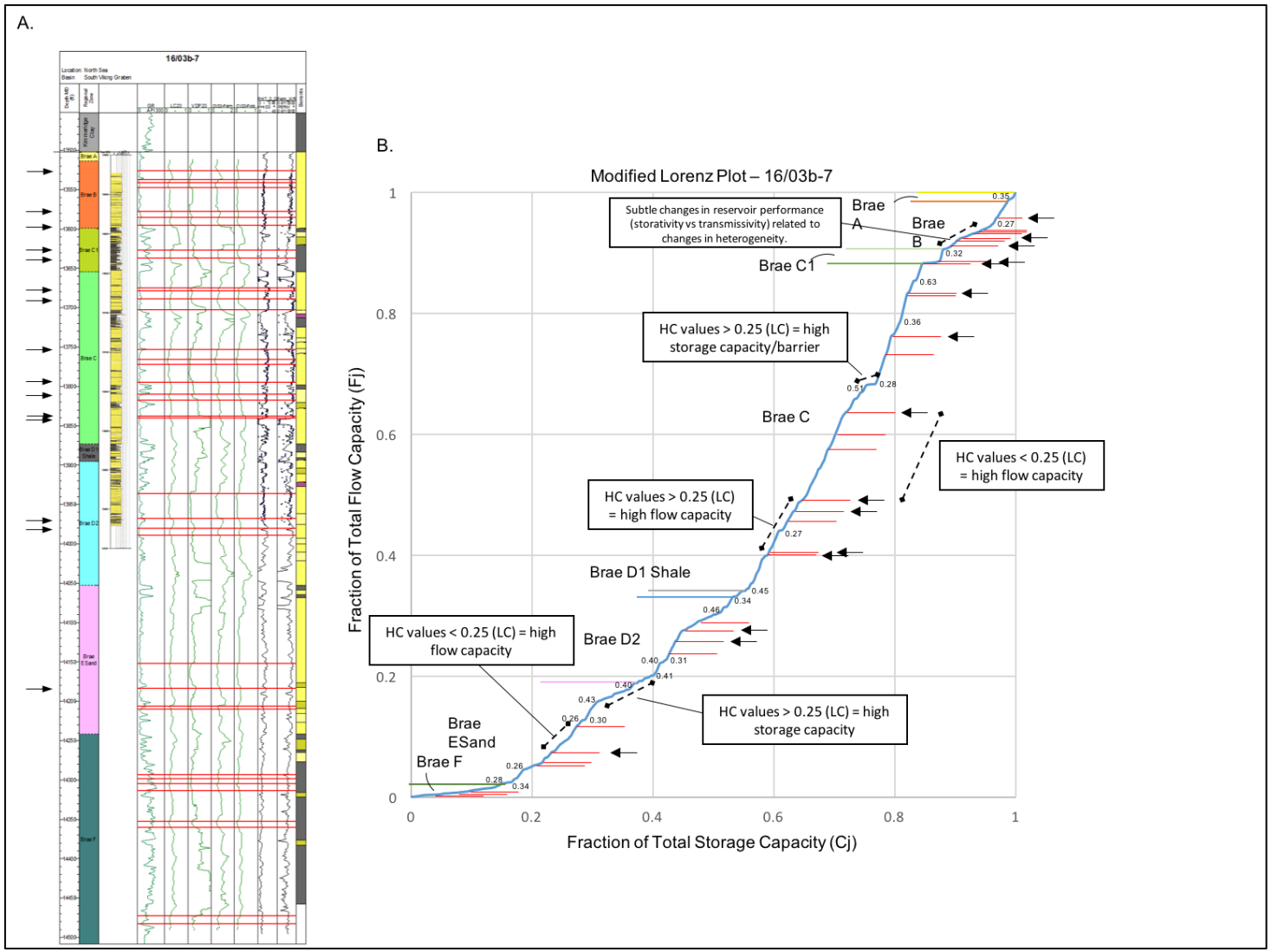

Figure 5-22: Modified Lorenz Plot (MLP) for Well 16/03b-7 showing the location of the threshold boundaries (after Fitch et al. 2013) from the LC 20ft curve. Arrows indicate location of the 0.25 threshold boundary, which commonly shows a small inflection in the MLP. The transition corresponds to a change from linear to exponential data set. However, no consistent trends are identified in terms of reservoir behaviour. Values along the line of cumulative flow and storage are the heterogeneity coefficient values at the inflection points not picked up by the thresholded ranges.

5.7.2 Modified Lorenz Plots (MLP) and MSFA Heterogeneity.

Despite the heterogeneity curves being unsuccessful at accurately predicting reservoir behaviour in terms of location of baffles, barriers, speed and thief zones, the MLP have been employed in the following section to infer changes in reservoir flow characteristics within MSFA. These plots are ideal to detect vertical stratification which, when all things considered, has the greatest impact on the performance of a fluid injection project and the fraction of mobile hydrocarbon recovered. Figures 5-23 to 5-25 shows the MLP for wells 16/03a-1, 16/03a-E1 and 16/03b-7, along with select cored intervals (MLP for other wells can be found in Appendix E.4. and exhibit similar relationships). Subtle changes in MSFA reservoir behaviour are detected along the line of cumulative flow-storage capacity, with decreased sand-shale ratio translating to increased storage capacity (potential barriers or baffles; slope angle is less than 45°) and thicker amalgamated units (e.g. element one) corresponding to zones with similar flow and storage capacity (45° slope angle) or increased flow capacity (slope angle is greater than 45°). Examples of the former are seen in Well 16/03b-7 – Brae C (Figure 5-25), where increased bed-scale heterogeneity (i.e. lower sand-shale ratio, thinner beds, subtle grain size changes, sedimentary structures) leads to reduced vertical connectivity and permeability in element one and two at 13672, 13686 ft md and 13751 ft mD. These intervals are likely to have been deposited by low-concentration flows, peripheral to the sand fairway axis. An increase in storage capacity (or a decrease in flow) is also seen at 13660ft mD. However, in this instance, it is unrelated to significant visible bed-scale heterogeneity. Diagenetic alteration (i.e. patchy calcite/quartz cementation) could explain a change in reservoir behaviour, although no variations were observed in the gamma ray, porosity, density or acoustic logs. It is nonetheless plausible that any diagenetic cements were below the log resolution, but still influenced the pore-throat distribution. Alternatively, textural changes related to depositional flow process (i.e. low competence flows or low density flows) may account for the change in reservoir behaviour. Core data indicated subtle normal grading within the massive sand at ~13660ft md (associated with the carbonaceous debris component). It has long been established that permeability decreases and porosity increases with decreasing grain size diameter (Masch and Denny, 1966). The small inflections towards increased storage capacity within massive sands at the bed-scale could be caused by subtle decreases in grain size.

Examples of zones with high flow capacity or equal storage and flow capacity are seen in Well 16/03b-7 (Brae B – 13578-13599ft md and Brae C – 13751-13798 ft md), 16/03a-1 (Brae B – 12942.5-12996.5 ft md, Brae C – 12996.5-13032 ft md, and Brae E) and 16/03a-E1 (Brae B – 12888-13004 ft md, Brae C and D2). Such intervals commonly consist of element one and are characterised by a high amalgamation ratio (> ~80%) as well as thicker beds and reduced bed-scale heterogeneity (sedimentary structures and grain size variation). The amalgamation ratio is

primarily controlled by the depositional environment and the magnitude and frequency of sediment flows. It therefore seems plausible to assume that deposits proximal to the axis of the sand fairway are likely to represent high flow capacity. The exception to this trend is the ESand interval in Well 16/03a-E1 (Figure 5-24), which accounts for ~ 13% of the storage capacity but only 1.2% of the flow capacity (between 13458.5 ft and 13306 ft md). This interval could form a significant baffle or barrier to flow performance if laterally extensive. However, the same interval correlated to the nearby Well 16/03a-1 shows high flow capacity. This clearly demonstrates the variable character of the same massive sands in terms of reservoir behaviour. An inaccurate log-derived porosity and permeability curves for one of the wells could explain this discrepancy, although a qualitative and quantitative comparison to the core porosity and permeability show a good match (Table 5-3). Alternatively, the baffle could be a result of patchy diagenetic cements and/or mechanical compaction (Leishman, 1994).

Thin, high permeable zones with negligible storage capacity (i.e. thief zones) are also recognised from the MLP. Such beds occur at the top and bases to element one sequences (Figure 5-20 – 13913 ft md), and very rarely as isolated massive sands encased in mudstone layers (Figure 5-19 – 12888 – 12898 ft md and Appendix E.1 and E – Well 16/03a-2). The effectiveness of these beds/intervals as thief zones will be dependent on the permeability contrast with the adjacent layers, as well as their thickness, continuity and position within the depositional element (Amy et al. 2013). In terms of their position, high-permeable zones that are located towards the top of an element, in conjunction with low permeability layers that act as barriers, will encourage more efficient lateral migration of fluids. This is predominantly related to vertical permeability trends and effects of viscous and gravity forces on hydrocarbon displacement (Dake, 2001).

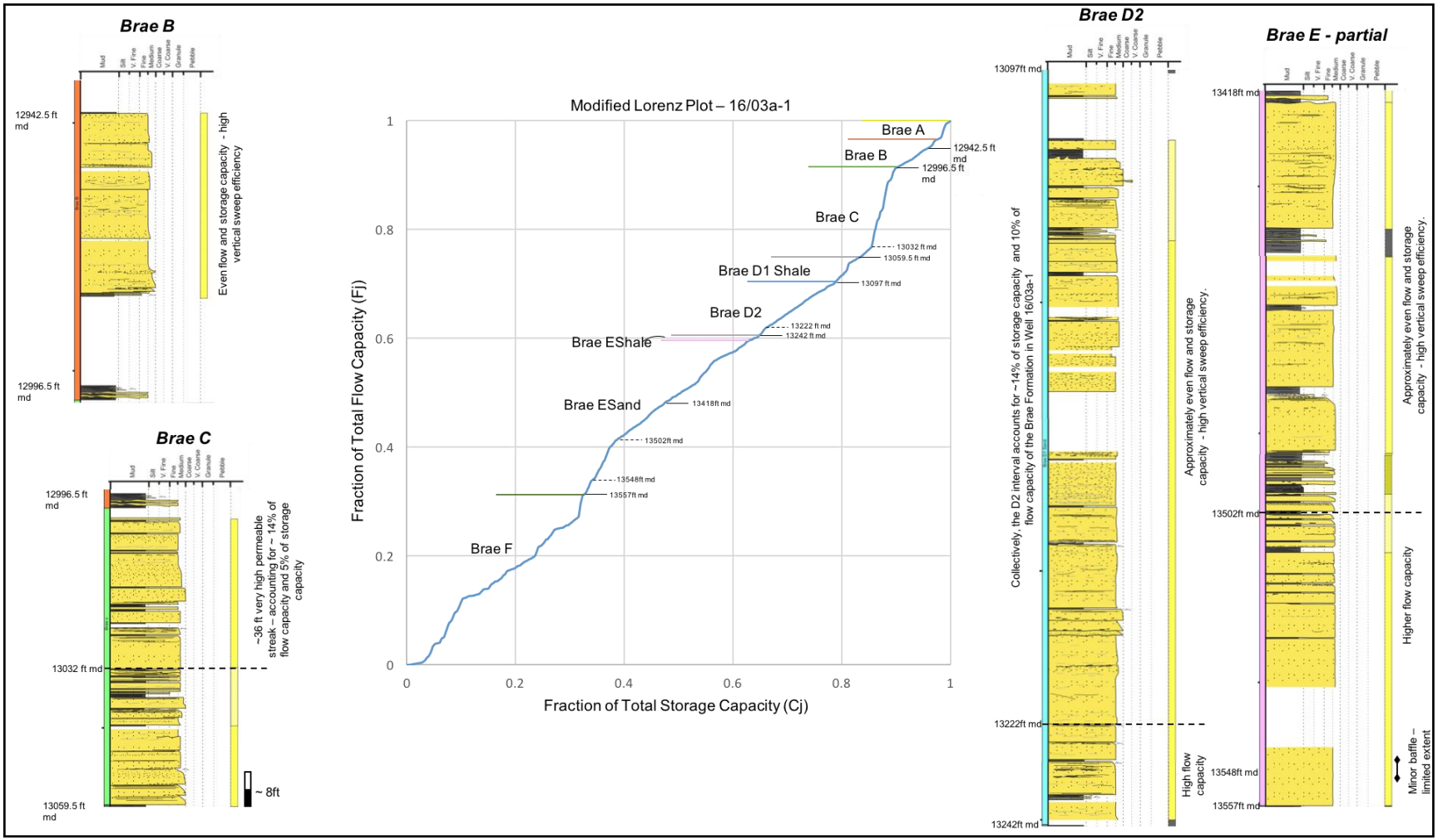

Figure 5-23: MLP for Well 16/03a-1 and inserts of cored intervals, showing locations of barriers, baffles, thief and storage zones and their sedimentological characteristics.

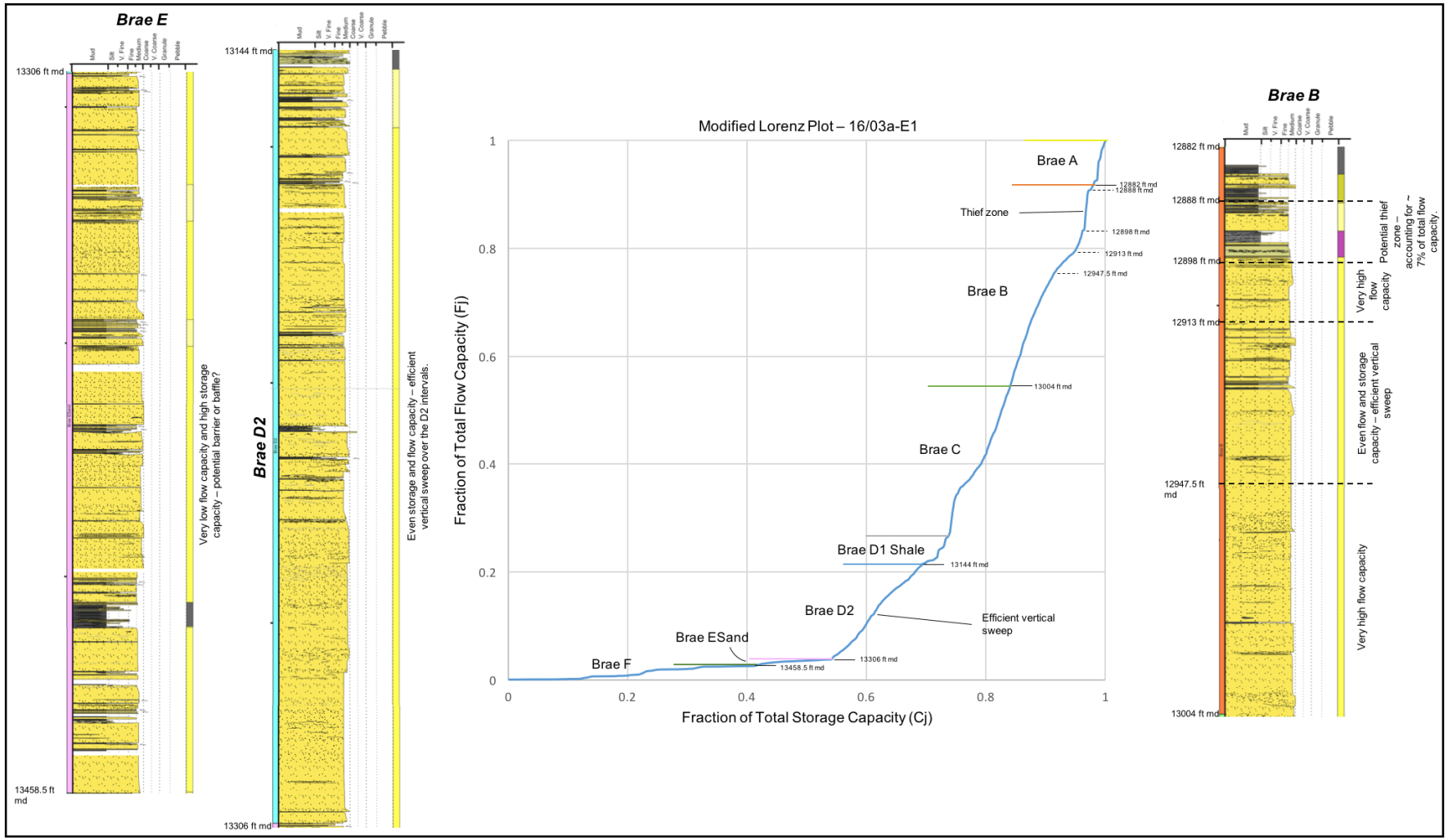

Figure 5-24: MLP for Well 16/03a- E1 and inserts of cored intervals, showing locations of barriers, baffles, thief and storage zones and their sedimentological characteristics.

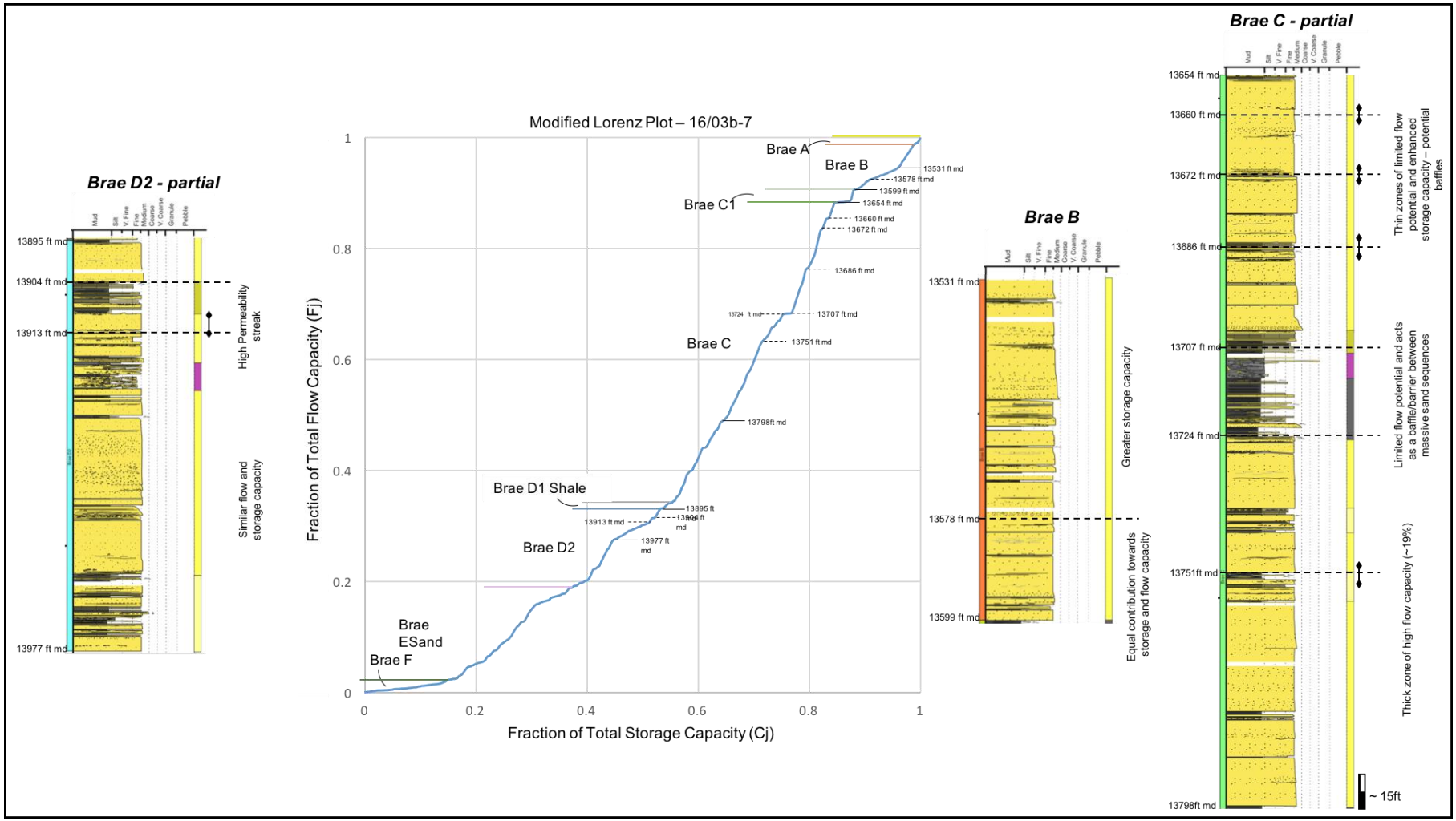

Figure 5-25: MLP for Well 16/03a-1 and inserts of cored intervals, showing locations of barriers, baffles, thief and storage zones and their sedimentological characteristics.

5.8 Discussion.

Massive sands and MSFAs form prolific oil and gas reservoirs in many hydrocarbons fields around the world. Due to their visually suppressed vertical (and areal) heterogeneity, it can be assumed that production from these reservoirs is expected to derive a high recovery efficiency (Tyler and Finley, 1992). However, the results presented in the foregoing sections suggest that massive sands and MSFA are vertically and areally heterogeneous, at least in the case of the East Brae Field. In this section, the vertical and areal heterogeneity are discussed in terms of the implications of developing and producing from massive sands and MSFAs.

5.8.1 Implication of Areal and Vertical Heterogeneity in Massive Sands and the MSFA.

Areal Heterogeneity. The East Brae sedimentology is interpreted to be a dissipative system, within which areal heterogeneity is relatively low. This is based on interpretation of the core and wireline data, which indicate that: (i) massive sand sequences are continuous between wells, (ii) interbedded mudstones are thin and discontinuous having been eroded by subsequent sediment-flows, (iii) lower NTG sequences are connected laterally to better quality reservoirs, and (iv) a lack of diagenetic cements (Leishman, 1994; Maast, 2011). This is not to say that areal heterogeneity is completely absent in the East Brae MSFA. A simple correlation using the MLP for wells 16/03a-1 and 16/03a-E1 shows how massive sand packages (e.g. ESand) behave differently in terms of storativity and transmissivity. In this instance the differences can be attributed to the degree of mechanical compaction (see Leishman, 1994), since they share similar sedimentary characteristics and lack diagenetic cementation. Furthermore, a crude proximality trend is also seen in terms of NTG and grain size towards Well 16/03b-9, as well as a E-W confinement of the sand fairway for the Brae A, B and C intervals (Figure 5-2). Barring these two trends, and based on a cursory review of the data, no significant proximality trends in terms of the grain size, sedimentary structures, NTG or bed thickness, is discernible in the East Brae field. This conclusion is also supported by Leishman (1994), who undertook a detailed sedimentological analysis of the field. As such, advanced secondary recovery techniques for example horizontal drilling, may be of limited use in MSFA similar to the East Brae, not least due to the discontinuous shale layers. However, the use of horizontal wells could help constrain the MSFA architecture, in particular thickness trends, connectivity, and extent of internal shale layers (see below for details on shale distribution).

Vertical Heterogeneity. Unlike areal heterogeneity, vertical heterogeneity was relatively easy to detect using the core data, statistical analysis, wireline logs and heterogeneity coefficient data. Collectively, they indicate that subtle but significant vertical heterogeneity is present within the massive sands and the MSFA of the East Brae Formation. Sedimentologically, these

heterogeneities take the form of sedimentary structures, textural changes, accessory features (carbonaceous fragments, mudclasts etc), thin mudstone beds, thin to thick heterolithic intervals, and chaotic/deformed units at the bed scale. Capillary pressure effects are likely to increase at these intervals, leading to bypassed oil. At the element scale, they can be field-wide mudstone layers which compartmentalise the reservoir (e.g. D1 Shale; Banter, 2003). Depending on their lateral extent, these are likely to form baffles and barriers, respectively, due to their negative impact on porosity and permeability. Petrophysical heterogeneity takes the form of variable permeability (thief zones) and porosity (barriers/baffles) distributions within massive sands and the MSFA, as indicated by the heterogeneity curves (Figure 5-19) and the MLP (Figure 5-23 to 5-25). In the East Brae Field, the distribution of these two properties is primarily controlled by the sedimentary environment and depositional processes, with minor modification by mechanical and chemical diagenesis (Leishman, 1994; Maast, 2011). These internal heterogeneities are likely to increase the volume of hydrocarbon by-passed.

Permeability heterogeneity, in particular, has a fundamental control on the displacement mechanics of hydrocarbons (Zhao et al., 2016). This can be illustrated by considering the permeability distribution vertically within a continuous reservoir section. In a water flooding project, high permeability intervals located at the base of massive sands are likely to act as channels, leading to premature breakthrough of the displacing fluid (water) and low mobile oil recovery. In contrast, high permeability intervals located at the top of massive sand are likely to enhances recovery through the development of a sharp, even displacement front (Dake, 2001). These trends are directly related to the interaction of the vertical permeability distribution, and the effects of gravity slumping and viscous forces (Amy et al., 2013; Dake, 2001). An intermediate situation can arise if the permeable interval is located in the middle, in which case an even displacement front forms across the lower section, with slow recovery from the top. The opposite trends are observed if the displacing fluid is gas due its low density and increased buoyancy. In the East Brae Field, the heterogeneity curves demonstrate that vertical variability in the permeability exist at the element scale, both between and within elements (Figure 5-19). From the MLP, thin high permeability layers have been recognised towards the top and base of element one sequences (Figure 5-23 to 5-25 and Appendix E). As mentioned previously, this distribution is largely controlled by depositional processes and the sedimentary environment. In conventional turbidites (e.g. Bouma sequence), permeability decreases vertically within a bed due to the influence of decreasing grain size and presence of sedimentary structures which impart pore-scale heterogeneity (Shepard, 1989; Van den Berg et al., 2003). Within the massive sands studied here, normal distribution grading over the thickness of a bed is absent in the framework component, although subtle variations in textural trends cannot be disregarded without further textural analysis. Nonetheless, crude normal and inverse grading is recognised in the carbonaceous debris/mud flecks present within most beds, implying partial turbulence

(Shanmugam, 2016; Talling et al., 2012), and kinetic sieving and grain to grain interaction (Legros, 2002; Savage and Lum, 1988), respectively, characterised the depositing flows. The effects of these flow processes on near-bed sedimentation is likely to result in 'subtle' variations in textural characteristics and ultimately the permeability (and porosity) distribution, and thus the location of thief zones. This 'subtle' variation could be reflected in, for example, improved sorting and/or grading in the fine-tail, as identified by Sylvester and Lowe (2004) in their analysis of Carpathian turbidites, as well as in Chapter 4 of this thesis (textural study of the Grès de Peïra Cava and Numidian Flysch formations).

The distribution of carbonaceous debris and/or mud flecks vertically within element one and two sequences also has the potential to influence the permeability distribution, and thus the presence of high flow capacity and/or thief zones in massive sands. Due to the ductility of the clasts, they are likely to occlude both pore throats and intergranular pore spaces. While it is difficult to detect this using log-derived properties, rare core plugs taken from such intervals shows marginal porosity and permeability from these intervals (e.g. Appendix E.1; Well 16/03a-E1, 13060-13064ft, ϕ = 9.2 – 11% and Kh = 2.9 – 38 mD). The low density of this material implies that buoyant lift is a viable clast support mechanism within the transporting flow (Hampton, 1979; Lowe, 1979). Consequently, the carbonaceous debris and/or mud flecks are likely to be transported in the turbulent top and tail of the flow. The distribution of these accessory components within the deposit will thus be controlled by the longitudinal flow structure and its evolution spatially and temporally (Kneller and McCaffrey, 2003).

The detailed core logging, development of the depositional model and the MLP has also revealed an association between the depositional environment and permeability distribution. The high flow capacity units at the base of a massive sand succession, through which early water breakthrough can occur, are located primarily in element one deposits. These units correspond to the axis of the sand fairway, a region that is likely to be dominated by high magnitude flows with increased competence. This is confirmed by visual grain size comparison, which demonstrates that grain size is predominantly between 300 to 500 μm. With progressive off-axis sedimentation, grain size decreases to between 150 to 500 μm within the massive and structured sands. Based on this simple relationship, a development decision could be made to avoid these high permeability streaks by drilling in off-axis positions to avoid early water breakthrough. However, in a system consisting of shallow, rapidly avulsing channels, this may not be feasible.

An additional factor affecting the vertical permeability distribution (and the *Kv/Kh*) is the shale layer continuity and distribution. Although it is impossible to determine the shale layer length

from core data, their vertical distribution and the degree of sand on sand contact (the amalgamation ratio) can be estimated. In this instance, these two parameters are a reflection of the degree of erosion of the shale layers, and inferences can be made on their lengths based on the knowledge of the depositional environments. Element one and two represent the two most sand-rich elements with a NTG and amalgamation ratio of >0.5. These two elements constitute the channel-lobe transition (axial and off-axis to the sand fairway, respectively), within which, based on outcrop analogues, shale lengths are typically less than 10 m (Clarke, 1998; Drinkwater and Pickering, 2001). With progressive distance from the sand fairway, the amalgamation ratio and the NTG decreases (i.e. Element three), and shale lengths are likely to increase. Analysis of the effects of shale length and the amalgamation ratio in two-dimensional reservoir simulations show that both parameters can be used as a predictor for displacement efficiency. In the simulations of Stephen et al. (2001), these two parameter show a linear relationship with displacement efficiency; higher the proportion of shale removed/amalgamation ratio, the greater the displacement efficiency. Their models show that the balance of gravity, capillary and viscous forces is dependent on the proportion of shale removed, as well as the distribution of the sand on sand contacts. With increasing shale removed, local barriers to fluid flow are removed and gravitational effects dominate over capillary forces. Vertical sweep efficiency improves, as well as the fraction of mobile oil recovered. Similar results were also reported by Jackson and Muggeridge (2000). However, for viscous dominated flows, with endpoint mobility ratio greater than 1, Jackson and Muggeridge (2000) showed that the presence of shale layers has negligible effect on the displacement. These conclusions were drawn from horizontal shale layers. However, if the shale layers are inclined and continuous over large distance areally, which was not analysed in this study, then displacement efficiency is significantly affected regardless of flow parameters (i.e. mobility ratio and gravity, viscous or capillary forces; Jackson and Muggeridge, 2000; Muggeridge et al., 2005).

5.8.2 Application of the Heterogeneity Curves in Optimising Layering in Static Reservoir Models.

Despite the non-uniqueness of the heterogeneity values in terms of predicting reservoir behaviour, the values themselves can be employed to optimise the number of layers to be used in a static reservoir model. Such an approach can be useful in honouring the foot by foot scale vertical heterogeneity of the reservoir, as well as transmissibility upscaling. Figure 5-26 illustrates how employing the heterogeneity coefficients can lead to an optimal layering system. The simplest approach would involve thresholding the curves by ranges depending on reservoir behaviour, for example in the manner of Fitch et al. (2015). Different heterogeneity curves (e.g. VDP or CV permeability) and threshold ranges will impact not only the number of layers but also the location of layer boundaries. The window size will also impact the number and location

of layers, with smaller window sizes displaying greater detail compared to larger windows. However, it is recommended that a minimum window size of 20 ft is employed to compensate for the negative bias encountered when using fewer (< 40) samples. It is also further recommended that the LC curve is employed due to its simplicity, statistical robustness and utility of single and dual-properties (i.e. porosity and permeability).

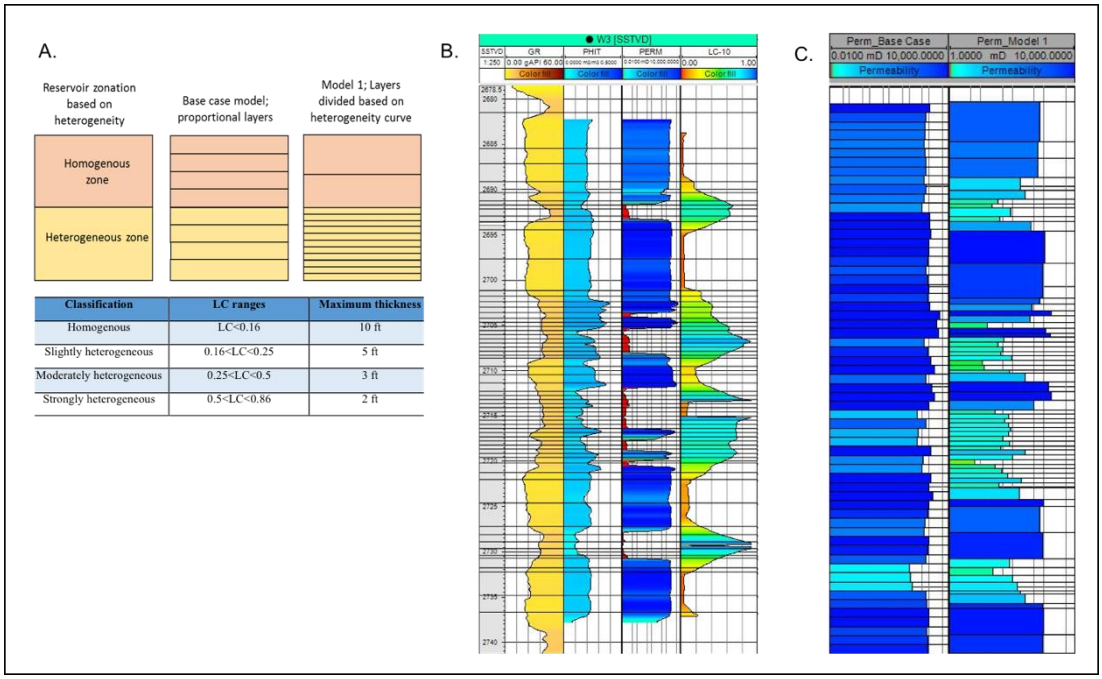

Classification	LC ranges	Maximum thickness
Homogenous	LC<0.16	10 ft
Slightly heterogeneous	0.16<LC<0.25	5 ft
Moderately heterogeneous	0.25<LC<0.5	3 ft
Strongly heterogeneous	0.5<LC<0.86	2 ft

Figure 5-26: A) Schematic block diagram illustrating heterogeneous zones represented by thinner layers in the reservoir model and the maximum thickness ranges for a given range of heterogeneity. B) Well W3 from the Maureen Field showing the gamma curve, and the log-derived porosity and permeability curves used to generate the LC curve using a 10ft moving window. Black horizontal lines represent the layering scheme to be used for this well. Thinner layers correspond to higher heterogeneity, which can be interfered from the serrated gamma curve and are likely to represent interbedded mud and sandstone layers. C) Upscaled permeability model for Well W3 for both the base case and heterogeneity curve derived (Perm_Model 1) layering scheme. Note that in the latter, the upscaled permeability better represents the vertical permeability distribution for Well W3. Please refer to Appendix G for a detailed description of the work flow and results.

For each heterogeneity range, a maximum thickness is assigned to layers that will constitute the heterogeneity interval according to the aims and objectives of the static model. This results in heterogeneous zones having thinner layers in the static model compared to homogeneous zones (Figure 5-26), within which petrophysical properties are upscaled. A case study is provided in Appendix G, in which two static reservoir models were developed for the Maureen Field in the North Sea; one of these using the heterogeneity curves to define the layering scheme. The Maureen Field shares many sedimentological similarities to the East Brae Field: high NTG, laterally extensive massive sands, persistent mudstone facies, and little or no diagenetic impact on reservoir quality, and thus provided an ideal analogue. Since this case study was an initial step in assessing the heterogeneity curves and its use to guide layering within reservoir models, a number of issues were not clearly addressed. One such issue is layer thickness inconsistency across the model for a given heterogeneity value. This was primarily due to a desire to keep the

same number of layers within each well; a situation that may not necessarily be appropriate in more detailed reservoir models. An additional issue was the choice of layer thickness for a given heterogeneity range. In the case study, the thicknesses were arbitrarily chosen, with thinner layers corresponding to higher heterogeneity ranges. Ultimately, this issue may not be resolved since heterogeneity coefficients are non-unique and no clear and consistent range has been provided (see Jensen and Currie, 1990; Jensen and Lake, 1988; Fitch et al., 2013). Furthermore, the subjective nature of assigning layer thickness for a given heterogeneity range may be desirable, as this provides an opportunity to assign layer thicknesses according to the aims and objectives of the study (e.g. off the cuff model with limited data vs mature field model with large amounts of data). No production data was available for the Maureen Field; thus history matching was not performed. Despite this, qualitative assessment of the case study suggests the improved layering strategy is able to capture the heterogeneity reliably, leading to a more accurate reservoir model.

5.9 Summary.

Studies detailing the degree and scale of internal heterogeneity of massive sands and massive sand facies associations (MSFA) are very scarse and limited to descriptions of sediment facies variability. This study presents results from the East Brae Field in the South Viking Graben, North Sea, in which geological and petrophysical heterogeneity has been described and quantified at the facies and depositional element (i.e. facies association) scale from a MSFA. The field provides a unique opportunity to study the vertical variability in massive sands due to the extensive core coverage, the abundance of massive sands, and the limited diagenetic alteration of the initial pore distribution. With regards to the latter point, the lack of or minor diagenetic alteration allows any variability in petrophysical properties to be directly related to the textural parameters, and thus the depositional processes.

Approximately 80% of the facies in the East Brae Field consists of thick bedded graded and ungraded massive sands forming sequences ranging in thickness from 0.1 to 40 metres. They are formed of compositionally and texturally mature sands, and emplaced incrementally by high-concentration near bed layers at the base of concentrated turbulent flows. Bed-scale geological heterogeneities are subdued, reflecting a scarcity of sedimentary structures and frequent amalgamation surfaces indicative of scouring of fine grained material. This has translated into a uniform distribution in porosity and permeability at the facies scale as measured from core plug data, with any local changes attributed to textural variations, minor clay streaks and limited diagenetic alteration. Statistical analysis of facies reveals an element of non-randomness, but non-cyclicity to the deposition of facies, and level of dependency of one facies sate on the other. Cycles are generally interrupted by amalgamation of beds, which truncate upper facies states and impart a degree of disorder to the sequences of MSFA.

The massive sands are interbedded with thin to thick sequences of structured sands, mudstones, heterolithics and minor concordant chaotic facies. These facies can be grouped into 5 depositional elements based on the abundance and thickness of massive sands, stacking patterns and scale of observations. From core and log scale observations, the elements have been interpreted as part of a channel-lobe transition zone, downstream of a channel complex that is located to the southwest in the vicinity of the North Brae Field. The internal sedimentological variability in the elements is probably related to the proximity to the axis of the sand fairway. Progressive off-axis sedimentation is characterised by reduced massive sand abundance and amalgamation, increased structured sands and lower sand: shale ratio. Thick field wide mudstones represent cut-off of the coarse clastic material into the system, most probably related to relative sea-level changes.

The variability in log-derived porosity and permeability for each depositional element of the MSFA has been quantified using static heterogeneity coefficients. An unconventional approach utilising a moving window (10, 20 and 50ft) is used to generate a continuous curve of heterogeneity values. It was expected that such an approach would reduce the issues related to the spatial reorganisation of the properties, and provide a medium to visualise vertical changes in heterogeneity (i.e. layering) between and within elements (inputs for static and dynamic models). The low sedimentological heterogeneity has had a fundamental control on the petrophysical properties. All of the elements are characterised by low to moderate averaged petrophysical heterogeneity, with element one possessing the lowest heterogeneity values and element five the highest. More significantly, the curves reveal internal variations that define layers based on different heterogeneity values within the massive sands. The layering is strongly correlated between the different static coefficients, but shows a weak correlation to the gamma, porosity-permeability curves, and depositional element boundaries. The weak correlation to these properties is due to the support size overlap, an unavoidable flaw of the moving window which incorporates values from adjacent intervals as the window moves downwards. Furthermore, the heterogeneity curves also show a weak correlation to locations of baffles, barriers, speed and thief zones identified on the modified Lorenz plot.

Despite a weak correlation, a threshold value of 0.25 on the heterogeneity curves correspond to an inflection on the MLP, which signals a change in reservoir behaviour. In terms of heterogeneity, this threshold value indicates a change from a linear to exponential increase in property values within the dataset. However, the consequence of this change in terms of increased storativity or transmissivity remains unclear. One possible reason for this could be due to the inherent non-uniqueness of the Lorenz coefficient value. But also because flow unit speed is not only dependent on k/Φ ratio, but phase mobility and the pressure gradient as well. Additional internal layers within thick massive sand packages and the MSFA were identified on

the modified Lorenz curve based on flow performance, and can be related to the degree of sedimentological heterogeneity. In general, higher flow capacity is located in areas proximal to the axis of the sand fairway, where sedimentological heterogeneity is low. Minor deviation from this trend can be related to localised modification by diagenetic processes. The distribution of these heterogeneities, in particular in terms of permeability, can have a fundamental control on the displacement mechanics of hydrocarbons in massive sands.

Chapter 6 – Synthesis

6.1 Aims.

The aims of this thesis were: 1) to elucidate the internal character of DWMS and identify the processes responsible for their formation, and 2) to assess how the internal character introduces heterogeneity in terms of reservoir properties, and the effects this may have on the development and production strategies of hydrocarbons hosted in massive sands. After an initial review of massive sands and depositional models, a hierarchical approach was adopted that worked towards fulfilling these aims, specifically by:

1. Documenting the vertical trends in the grain size and grain fabric in the framework and zircon components from graded and ungraded massive sands.
2. Documenting the macroscopic internal bed character, vertical and lateral facies transitions and external bed geometry of massive sands in laterally extensive beds.
3. Describing and quantifying sedimentological and petrophysical heterogeneity in a MSFA.

Chapters 3 to 5 worked towards fulfilling these objectives, and within each chapter a substantive discussion is provided that reviews the findings in the context of the existing knowledge of DWMS at the various hierarchical scales. Therefore, this chapter synthesises the key finds to highlight the internal character of massive sands, present a new model for DWMS, and to explore the impact that the internal and external character has on hydrocarbon exploration.

6.2 What Internal Heterogeneities Are Recognised in Massive Sands?

6.2.1 Types of Massive Sands.

Field work in the Grès de Peïra Cava, the Tunisian Numidian Flysch Formation, and the East Brae MSFA reveal *three* varieties of massive sands: ungraded massive sands (DWMS *sensu stricto*), graded massive sands, and massive sands with ‘patchy’ texture. While the first two have been well documented, the latter has only recently been identified in the Miocene Marnoso-Arenacea Formation in the northern Italian Apennines (e.g. Talling et al. 2013). It is characterised by the juxtaposition of irregular ‘patches’ of fine and coarser grains and no

primary sedimentary structures. This facies was not part of the original definition of DWMS nor formed part of the MSFA by Stow and Johansson (2000). However, due to its massive character, it has been incorporated into the MSFA *sensu stricto* Stow and Johansson (2000).

6.2.2 Vertical Trends in Grain Size and Grain Fabric.

The mean grain size ranges over the sand-size faction for massive sands. At the macroscopic scale, ungraded massive sands appear to be texturally homogenous. However, grading may be present in the accessory components i.e. carbonaceous and mudclast fragments. In comparison, graded massive sands may exhibit coarse-tail or distribution grading, while an irregular grading is observed in massive sands with 'patchy' texture.

At the microscopic scale, textural analysis of seven ungraded and graded massive sands from the Numidian Flysch and the Grès de Peïra Cava reveal that massive sands are characterised by a variety of grain-size trends, including: non-grading, normal-grading, inverse grading and an anomalous 'jagged' trend. These trends do not define the entire grain size distribution, but rather different percentiles at different heights within the bed. Thus at the grain-scale, it can be concluded that massive sands are not homogeneous, as they appear to be are at the bed-scale (Kneller and Branny, 1995; Stow and Johansson, 2000). While no universal trend characterises all the beds, three (Grès de Peïra Cava) out of the seven beds show a consistent divergent to convergent trends in the fine- and coarse-tail component. Vertically converging trends have been identified previously (e.g. Sylvester and Lowe, 2004), however, the divergent trend at the base is unique to this study. This implies that different grain support and settling processes influenced different percentiles of the grain size distribution during deposition. Only two (Numidian Flysch) of the seven beds show no vertical changes in grain size vertically. Due to the similarity in grain fabric between these and the other beds, they are interpreted to be deposited by the same processes. The reason for their ungraded character could lie in the sediment concentrations, with higher sediment concentrations suppressing grain segregation processes (Cartigny et al. 2013). The remaining two beds show an anomalous 'jagged' trend consisting of alternating fining and coarsening profiles in the different percentiles. This is difficult to reconcile has been interpreted as short-term fluctuation in sediment concentration and/or velocity, or sampling error. While the latter cannot be discounted, the similar grain size trends between the heavy mineral and framework component implies that the trend could be primary in origin.

Grain fabric analysis in the massive intervals and beds shows a consistent flow-oblique trend (47°±26°) in the bedding-parallel sections and high imbrication angles (80°±55°) in the bedding perpendicular sections. This is consistent with previous fabric studies e.g. Baas et al. (1999),

Baas et al. (2007), Hiscott and Middleton (1980), and Rees (1983). Such a fabric is speculated to form in high concentration near bed layers, where the frequent grain interaction inhibits a flow parallel fabric, but are not so frequent as to prevent orbiting mechanisms dominating the production of a preferred orientation (Hughes, 1995; Rees, 1987). The statistically similar grain fabric between the ungraded and graded massive sands suggests that both facies were deposited by similar processes, a conclusion also reached by Baas et al. (1999) and Baas et al. (2007). Uniform fabric was also identified in certain beds, however, this coincided with the presence of large mudclasts and a patchy grain size texture (i.e. massive sand with patchy texture). The change in grain fabric with a change in facies is used to infer different depositional processes produced the 'patchy' texture. Such uniform fabric has been observed in debris flows (Baas 2007; Naruse and Masuda, 2006; Talling et al. 2013).

6.2.3 Internal Character, Vertical and Lateral Facies Transition, and Bed and Facies Geometry in Laterally Extensive Beds.

Internal Character. Macroscopically, ungraded and graded massive sands are similar in character. With the exception of grading, they lack any primary sedimentary structures that may otherwise aid in their interpretation. The presence of grading on the other hand implies grain segregation processes may have been active within the depositing flow. Thus ungraded massive sands represent DWMS *sensu stricto* (Stow and Johansson, 2000). Massive sands with patchy texture are characterised by patches of coarse and fine material. This structure is likely to be created by dissipation of pore pressure during or after deposition of the sediments.

All three massive sands contain mudclasts which can be used to infer flow processes, as highlighted by Stow and Johansson (2000). Graded and ungraded massive sands contain mm to cm long clasts that are order-stratified or clustered floating, or to isolated. These are primarily located in the middle or top of the massive sand interval or bed. There crudely stratified nature of indicates deposition from the base upwards by near bed layers, with the vertical position corresponding to the static bed at that point in time (Pickering and Hiscott, 2015; Postma et al. 1988). Massive sands with patchy texture contain on average larger mudclasts, which are present as nested discontinuous zones sub-parallel to bedding or as dispersed graded clasts. Similar to the ungraded and graded massive sand, they also occur in the middle or top of beds, and are likely to be deposited *en-masse* with the flow. Any size segregation depends on the relative densities of the clast and matrix, and the matrix strength (Baas et al. 2011; Sumner et al. 2009).

De-watering structures are common in the East Brae Field and typically consist of shallow dishes, pipes and contorted laminations. Sequences of these structures can be used to indicate

amalgamation of DWMS. De-watering structures are less common in the Grès de Peïra Cava and the Numidian Flysch, due in part to weathering effects. However, the high imbrication angles seen in the textural analysis suggests that de-watering may have been active in these beds as well (Baas et al. 2007).

Grain sizes breaks are a common feature of massive sands in the Grès de Peïra Cava. Four varieties were identified across the outlier. These grain size breaks demonstrate that massive sand depositing flows were not single surge-type waning flows (i.e. Type II and III; Kneller and McCaffrey, 2003; Stevenson et al. 2014) with uniform sediment concentrations (i.e. Type I and IV; Talling et al. 2012; Stevenson et al. 2014). Instead, the flows were highly stratified and surging at its source, which produced a highly variable bed character in the proximal and medial sections. In proximal and medial locations, the grain size breaks separate massive intervals from the surrounding structured facies. Moving downslope, the variability and abundance of the grain size breaks declines, indicating that flows organised themselves into simple surge structures (Ho et al. 2018; Kneller and Branney, 2003). The resulting deposit character is typically massive sands overlying mudstones. Thus, within the Grès de Peïra Cava, isolated massive sand beds are located in distal locations of the basin.

In the East Brae Formation, grain size breaks appear to be less common. This can be attributed to the high textural maturity which makes it difficult to identify changes in grain size changes in the MSFA. However, isolated massive sands show sharp transition to overlying mudstones (i.e. Type IV grain size breaks), again mirroring the trends seen in the Grès de Peïra Cava.

Vertical and Lateral Facies Transition. In the Grès de Peïra Cava, three downslope facies tract were recognised. All three contain massive sands that form the 'core' of the bed in *proximal* and *medial* locations. In *distal* locations they constitute the entirety of the bed, with or without a thin structured cap. Similarities to this general trend is also noted in the East Brae Field, which represents the distal equivalent of the North Brae Fan system. Within the East Brae, 80% of the facies comprise ungraded to graded massive sands, with little lateral sedimentological variations. Thus, it is suggested that massive sand beds are located in *distal* parts of basins. Parallels can also be drawn to other fan systems, most notably the South Brae-Miller Fan System, which is characterised by an abundance of massive sand facies in distal part of the system.

In the Grès de Peïra Cava, the facies tracts are differentiated in the distal locations by the internal character of the massive sands. Facies Tract I contain the ungraded massive sands, Facies Tract II contains massive sands with 'patchy' texture, and Facies Tract III contains

repetitive occurrences of ungraded and graded massive sands. While such a differentiation was not possible in the East Brae Field, due in part to the lack of detailed bed correlation framework, all of the MSFA packages did exhibit repetitive occurrence of ungraded and graded massive sands. It is likely that such internal bed character is typical of massive sand beds and packages. The presence of DWMS and MSFA in distal part of a basin indicates that certain processes may have operated to maintain the flow's concentration as it travelled downslope, or the flow underwent a transformation to 're-concentrate' it.

Markov analysis in the Grès de Peïra Cava demonstrates that the dominant vertical transition along the basin profile is the Tb-Tc, which forms a down-slope thinning cap to the massive sand beneath it. In *proximal* and *medial* locations, conglomeratic and thick stratified sands underlie the massive sands, thus the vertical sequence resembles the models of Lowe (1982), Mutti, (1991) and Kneller and McCaffrey (2003). However, it deviates from these established models in that it contains multiple grain size breaks and there is a repetitive occurrence of certain facies i.e. massive and thick stratified sands. All three massive sands form the dominant facies in the *distal* locations, thus they deviate from most models. These are locally capped by a thin structured unit with or without an intervening grain size break. Where a structured cap exists at the top of massive sands with patchy texture, this is always separated by a grain size break. Entropy analysis indicates that the graded massive sands and massive sands with patchy texture have a strong influence on the successor state in proximal and medial locations, while the ungraded massive sands are deposited under specific hydrodynamic conditions that is dependent on the preceding facies. This is reversed as the flow moves downslope to distal localities. The entropy analysis intimates the origin of the massive sand can be extrapolated from analysis of the underlying and overlying facies due to their dependency on each other (Hattori, 1974).

Due to the frequent amalgamation of beds in the East Brae MSFA, trends are more difficult to discern with any certainty. Generally, trends are similar to those observed in the Grès de Peïra Cava, but are truncated at the top due to amalgamation leading a more disorderly sequence consisting of repeating massive sands, structured sands and amalgamation surfaces. No systematic changes in the internal organisation was identified downdip, Entropy analysis likewise indicates a degree of dependence of the massive sands on the preceding and succeeding facies. However, the high entropy values, partly a due to the truncated facies trends, suggest a more disorderly sequences.

External Bed and Facies Geometry. The Grès de Peira Cava is a topographically confined basin with a relatively flat seafloor at the time of deposition of the eight beds studied in this thesis. Despite the simple basin configuration, two distinct down-slope bed geometries were

captured by the facies tracts. Beds belonging to Facies Tract I and II thin distally with a linear to sigmoidal profile. This trend is consistent with deposition from a depletive flow. However, unlike previous studies that indicate such depletive flows are characterised by reducing sediment concentrations and sedimentation rates away from the source. The laterally extensive occurrence of the massive sand facies indicates flows maintained their high concentrations either due to erosion and re-entrainment of sediments and/or interaction with basin topography (Cantero et al. 2012a; Patacci et al. 2015; Talling et al. 2007a). This result is important because it indicates massive sands can form in *distal parts* of the basin, contrary to most genetic facies models which place them closer to the source.

Beds belonging to Facies Tract III maintain or increase in thickness as the you move down-slope. It is likely that these beds were deposited by larger-volume flows that interacted with the confining topography to produce a thicker deposit at the base of the slope (Lamb et al. 2004). However, the poorly sorted nature of the sediment is also likely to increase the efficiency and corresponding run-out distance of the flow, and thus the potential for flow interaction with the confining topography (Salaheldin et al. 2000). The repetitive occurrence of ungraded and graded massive sands, and thin stratified sands in the *distal* reaches of Facies Tract III is used to postulate this interaction (Haughton, 1994; Patacci et al. 2015).

6.2.4 Sedimentological and Petrophysical Heterogeneity in a MSFA.

Approximately 80% of the East Brae is composed of graded and ungraded massive sands. These are associated with structured sandstones, mudstones and chaotic units (injectites, slumps etc.) that define 5 elements in the East Brae MSFA. Element one and two contains the majority of the massive sand facies, within which the sands form amalgamated units between 5 to 40 m thick. Sedimentological heterogeneity in theses sequences is visually suppressed. The main source of heterogeneity is from shale units, the continuity of which is inferred to be dependent on the proximity to the sand fairway. Other sources of heterogeneity arise from thin structured caps to the amalgamated sequences and the presence of woody and mudclast flecks. Elements three and four of the East Brae MSFA are more heterogeneous, reflecting the increased distance from the sand fairway. Massive sands within these elements are of the isolated variety. Internally, they share the same characteristics as element one and two massive sands.

The visually suppressed sedimentological heterogeneity is reflected in the petrophysical (i.e. porosity and permeability) heterogeneity, with all elements characterised by low to moderate heterogeneity derived from the static heterogeneity curves. More significant, however, is the systematic variation in the heterogeneity within the elements, as defined by the heterogeneity curves and modified Lorenz plots. These curves and plots show that within a visually

homogenous package of massive sand (MSFA *sensu stricto*), petrophysical heterogeneity varies such that subtle layering, not seen at the bed-scale, can be identified. These layers can be correlated between wells, and show a weak correlation to the gamma curve, porosity and permeability curves, and interpreted element boundaries. Such a layering scheme has its uses when defining a correlation framework for static models, and defining baffles, barriers, speed and thief zones when log blocking after upscaling.

6.3 How are the Three Massive Sand Facies Formed?

The origin of massive sands has been a hotly debated topic for the last 40 odd years. Kneller and Branny (1995) described massive sands as deposits of quasi-steady turbidity current that aggrade progressively. In contrast, Shanmugam (1996) envisions them as a product of *en-masse* freezing from a fast-moving, semi-rigid sandy mass flow. Other mechanisms have also been proposed (e.g. Baas, 2004; Gladstone and Pritchard, 2010; Postma et al. 2009; Stevenson and Peakall, 2010; Talling et al. 2013), which has exacerbated rather than solved the problem of their origin. Collectively, the results from the textural analysis (Chapter 4), and documenting the internal character and vertical and lateral transition in facies (Chapter 3) provide evidence on the origin of massive sands.

Ungraded and graded massive sands are formed by incremental deposition from high-concentration near bed layers (Cartigny et al. 2013; Sumner et al. 2008; Vrolijk and Southard, 1997). The similarities in the textural trends suggests that they share a genetically linked depositional process. Within these layers', turbulence is dampened and grain to grain interaction, kinetic sieving and frictional interlocking dominate, and act to prevent tractional reworking of sediments. The high sediment fallout rates initially prevent elutriation of fine material from the base of the flow, trapping the material. The influence of kinetic sieving and lack of elutriation contributes towards the fine-tail normal grading and coarse-tail inverse grading trends seen in massive sands. The shearing of these dispersion, which initially prevents deposition, partially rolls the grains along the static bed to produce the oblique-fabric and high-imbrication angles (Hughes, 1995; Rees, 1983). Since the sediments are rapidly dumped, dewatering may further enhance the imbrication angles (Baas et al. 2007). With decreasing sediment-fall out rates, the influence of grain segregation processes increases to the extent that elutriation of fines and suspension settling of coarser grains produces fine-tail inverse grading and coarse-tail normal grading. The reduced grain interaction also allows grains to be rotated to develop a flow-parallel fabric (Allen, 1984). Under higher sediment concentrations (> 45-50% Amy et al., 2006b; Cartigny et al., 2013), such grain segregation processes would not operate due to the constant grain interaction, resulting in an ungraded and massive deposit.

In contrast, the massive sands with 'patchy' texture is unlikely to form from the above processes. Instead, the uniform grain fabric, the elevated mud content and the presence of nested mudclast horizons, indicate deposition from debris flows (Talling et al. 2013; Shanmugum, 1996). Debris flows are known to develop transient excess pore pressure by gravitational loading which supports sediments during transport (Breien et al., 2010; Ilstadet al. 2004; Major, 2000; Major and Iverson, 1999). It is the dissipation of this excess pore pressure through transit and deposition that creates the 'patchy' texture via slow convention and elutriation (Talling et al. 2013). However, no experimental work has been able to reproduce this textural characteristic. Thus, the exact depositional process of massive sand with 'patchy' texture remains speculative.

Slow convection and elutriation of fines in response to the dissipation of pore pressure remobilised the sediments to create a 'patchy' texture. The presence of this facies in distal locations in a basin can be related to body transformation of an initially turbulent flow into a laminar flow without significant loss of interstitial fluid. This is based on the upslope transition to ungraded or graded massive sands, elevated mud content, and sub-parallel zones of mud clasts. The erosion of a muddy substrate or disintegration of mud clasts may provide the clay material necessary to facilitate this transformation. *En-masse* deposition ensues when shears stresses are no longer able to compete with the shear strength of the deforming material. Coupled with low hydraulic diffusivity, hydraulic pore pressures are maintained as the sediments come to rest.

6.3.1 Does the Palaeotopography Influence the Formation of Massive Sands?

It is common for sediment-gravity flows to travel down slopes with considerable topography (Kneller and McCaffrey, 1999). Typical responses will include switching between erosional and depositional behaviour, modification of the flow's internal characteristics, changes in slope stability, deflection or reflection of the flow, partial or complete ponding of the flows, and relocation of the depositional area (Haughton, 2000; Amy, 2000). In terms of the flow's internal characteristics, the topography will influence the flow thickness, duration, acceleration, grain-size distribution of the transported sediment, vertical movement due to turbulence and density stratification (Albertão et al. 2011). This will in turn influence the internal character of the resulting sediment facies.

It was difficult to characterise the influence of the palaeotopography (if any) within the Numidian Flysch and the East Brae basins had on the internal character of the deposit. No palaeoslope was recognised within either of these basin, and although a palaeoflow interpretation is possible in the East Brae system based on a regional well study, the current

well correlation is not refined enough to characterise the dimensions of the slope. On the other hand, the palaeotopography of the Grès de Peira Cava sub-basin has been well studied such that the geometry and orientation of the palaeoslopes are relatively well defined (Amy, 2000; Pickering and Hiscott, 1998)

Based on analysis of the internal character and bed geometry of the Grès de Peira Cava beds, it is suggested that the palaeotopography controlled the deposition of massive sands, as well as their distribution within the basin. Within all Facies Tracts, massive sands constitute the entirety of the bed in distal locations. This is contrary to previously established models (Kneller and McCaffrey, 2003; Lowe, 1988; Mutti, 1992). Flow deceleration and cessation induced by interaction with the distal slope is thought to have instigated transformation of the flow as turbulence was suppressed in all or parts of the flow. In Facie Tract I, the deceleration up the distal slope suppressed turbulence in the near bed region, allowing hindered settling and grain interaction to dominate to produce the massive character in beds in distal locations. In contrast, in Facies Tract II, the elevated mud content suggests that an initially concentrated turbulent flow transformed to a liquefied debris flow as it decelerated up the slope. Such a transformation ensured pore pressures remained elevated to produce the 'patchy' texture in massive sands.

An anomalous repetitive sequence of graded and ungraded massive sands is also recorded in distal locations of the Grès de Peira Cava sub-basin. This trend belongs to Facies Tract III, within which bed thickness increases distally. Previous repetitive sequences near confining slope have been detected by Felletti, (2002), Haughton (1994) and Remacha et al. (2005). In the current study, repetitive sequences are accredited to flow interaction with the confining topography, but as a result of the passage of internal waves created by the flow reflection and deflection. This conclusion was based on the recent experimental work by Lamb et al. (2006) and Patacci et al. (2015), who observed the development of internal waves and an upstream migrating sediment bore that induced short-term non-steady effects in flow concentration and velocity. The passage of these internals waves, as well as the increased sediment concentrations resulting from the inflating sediment bore upon flow reflection or deflection against the distal confining slope, is interpreted to be the cause of the alternating ungraded and graded massive sands in distal locations. Such a process is envisioned to operate when particularly large or highly efficient flows have long run out to interact with the distal topography (Mutti, 1992; Salaheldin et al. 2000; Talling et al. 2007a).

6.4 What are the Implications for the Hydrocarbon Industry?

As mentioned in the introduction, DWMS are prolific hydrocarbon reservoirs in many deep-water systems. Yet, despite their economic importance, the internal character and emplacement

mechanisms remain enigmatic. This can have a profound impact on hydrocarbon recovery, since the internal character and depositional processes control reservoir architecture, fluid pathways, and connectivity, which in turn will have impact on development strategy and recovery factor. Based on the results obtained in Chapters 3 to 5, the following findings are considered important for future exploration and development.

Grain- and Bed-Scale. Grain- and bed-scale impact on hydrocarbon exploration was investigated using the results from the Numidian Flysch and Grès de Peira Cava massive sands. Geometric properties of grains in reservoirs has long been known to fundamentally influence reservoir quality (i.e. porosity and permeability). While these properties may be modified during diagenesis, especially for carbonate rocks, it can be negligible in sandstone reservoirs. An example of such a reservoir is the East Brae Formation of the North Sea (see Chapter 5). Theoretically, porosity is independent of grain size. However, a dependency may arise due to separate, but connected parameters such as sorting. In this case, porosity generally decreases with reduced sorting, since small grains have a propensity to infiltrate and occlude pore spaces between larger grains. This also correlates to low permeability, since the occlusion of the pore spaces increases the tortuosity (a measure of geometric complexity that is inversely proportional to permeability) of the pore system. No consistent grain size trends were observed across the studied massive beds. This makes any inference on porosity-permeability trends in such sands difficult. However, a general trend involving diverging and converging fine- and coarse-tail components at the base and top, respectively, is seen in some beds (in both the framework and zircon components). Similar trends were also observed by Sylvester and Lowe (2004) and a case could be made that such trends are common in massive sands. When associated with grain sorting, these trends define pore and bed scale heterogeneity in reservoir quality. In the massive beds and intervals that display these trends, porosity and permeability is likely to be lowest in the middle of the bed, where the variability in grain size is greatest. This trend is different from trends in conventional turbidites (e.g. Bouma Sequence) in which permeability and porosity is highest at the base and middle of the beds (Shepard, 1989; Van den Berg et al. 2003). Furthermore, if the 'jagged' trends seen in bed 1 are primary in origin and are caused by short-scale non-steady effects in velocity and concentration, this could also induce intrabed cm- to dm-scale heterogeneity in porosity and permeability.

In addition to the grain size (and sorting), the grain fabric also has an appreciable influence on the permeability (if not the porosity) if grains are elongated with respect to their C-axis. Ordinarily, permeability is highest in the bedding parallel direction. However, even within the bedding parallel direction permeability is heterogeneous, with the highest values in the direction of the palaeoflow due to the flow-parallel alignment of the grains (Hailwood et al. 1999). A consistent trend in the majority of the samples from the massive intervals of bed is the flow-

oblique fabric, which indicates that maximum permeability direction and the palaeoflow are not aligned. Furthermore, a histogram of this variability displays an approximately uniform distribution, implying that flow in the X-Y plane may not have a preferential direction. In the bedding perpendicular plane (z), Griffiths (1949) noted maximum permeability is parallel to the angle of imbrication. Given that most samples have high imbrications angles (average of 80° ± 55.96°), this would contribute to a small difference in Kh-Kv ratio. This has some important consequences in terms of fluid flow. For example, fluid displacement techniques commonly used in industry (e.g. waterflood) will be more effective in the sub-vertical direction.

Taken collectively, the results imply that grain size and sorting are the most likely parameters controlling porosity and permeability in massive sands. The variability in these parameters was investigated in Chapter 5, which also discusses a framework for upscaling the effects of such variability to field scale grids for modelling.

Bed-scale. Since most subaqueous sediment flows deposit beds with initially high porosity and permeability, the sheet-like architecture that is common in many confined and unconfined turbidite systems (e.g. Garden Banks 191, Miller, Captain fields) gives rise to excellent reservoirs. However, as proven by this and numerous other studies, the internal character and geometry of such beds is not homogeneous. In the present study, the behaviour of the depositing flows has systematically imparted sedimentary structures and other sedimentological heterogeneities (i.e. grain size breaks, mudstone clasts, changes in geometry etc.) in the sands. These will control permeability anisotropy and directionality in fluid flow, and may form local thief or speed zones, or baffles and barriers. In all correlatable beds in the Grès de Peira Cava sub-basin, a proximality trend in terms of bed-scale heterogeneity can be defined; heterogeneity is visually suppressed in distal locations as the proportion of massive sand facies increases. However, the grain size (and bed thickness in most beds) also decreases distally, which will have a detrimental impact on permeability and porosity trends. Regardless, the vertical bed-scale permeability and porosity profile is likely to be uniform. In terms of permeability, the lack of, or reduced abundance of structured intervals (i.e Facies Tract I to III) in distal localities is likely to translate into high kv/kv ratio. While the thickening structured cap, as well as increased abundance of thin and thick stratified facies, in proximal location can induce local permeability anisotropy. This can be particularly significant for the flow of immiscible fluids, since capillary forces are sensitive to the pore throat distribution (Jensen et al., 1996).

Equally important at the bed-scale is the presence of grain size breaks, which in the Grès de Peira Cava sub-basin, can be traced downslope for 3 km. Sharp changes in vertical grain size profile will undoubtedly affect the vertical sweep efficiency. In proximal and medial locations,

Type I grain size breaks are associated with conglomeratic facies below and massive sands facies above the break. If the conglomeratic facies translate into thief zones during waterflooding, gravity slumping of the flood front occurs and reduces sweep efficiency in the massive sands. In contrast, the reduced abundance of grain size breaks in distal areas will produce a more even flood front and greater sweep efficiency. A similar conclusion was reached by Amy et al. (2013), who simulated the effects of basin position, distribution of permeability heterogeneity and sediment facies in the Grès de Peira Cava sub-basin. Proximal and medial locations are also associated with Type II and III grain size break, and depending on the distribution of facies above and below, can significantly affect flow at these locations.

All three types of massive sand facies contain mudclasts in varying abundance and characteristics. The results from core-scale simulation demonstrate that the mudclast fraction has a dominant impact on effective permeabilities, while orientation and aspect ratio are secondary effects (Cuthiell et al., 1991). Mudclasts in graded and ungraded massive facies occur as thin ordered stratified or clustered floating intervals. At the outcrop scale, they are discontinuous and traced for approximately 20 m where outcrop length allows. These mudclasts are unlikely to act as significant baffles to flows. In the massive sand with 'patchy' texture, the clasts are typically larger and occur as nested zones subparallel to the bedding. While the mudclast fraction in this facies is higher compared to graded and ungraded massive sands, they are also unlikely to act as significant baffles due to their discontinuous character.

Element-scale. Element-scale heterogeneity and its impact on hydrocarbon exploration and development was studies in the East Brae MSFA. Here, the sedimentological heterogeneity is controlled by the proximity to the sand fairway, where erosion of intervening shales produces amalgamated massive sands up to 40 m thick. Porosity and permeability transects through these packages are relatively uniform. However, the MLP reveal multiple thief or speed zones, and baffles and barriers within these packages. The location of these zones can have significant impact on vertical efficiency. Thief zones are located primarily at the base of amalgamated units, where grain size is generally coarser. A development decision could be made to avoid these high permeability zones by drilling in an off-axis position. However, in a system consisting of rapidly convulsing channels, such as the East Brae, this may not be feasible as multiple high permeability streaks may be present in a single massive sand package.

Static heterogeneity coefficient curves developed as part of this study also reveal internal layering within massive sands. While these curves do not correspond to specific reservoir behaviour, they can be used to optimise layering in static models. An initial case study indicates that such an approach of layering within a MSFA better accounts for the permeability variability in the reservoir model, and thus fluid flow in the reservoir.

6.5 Limitations and Future Work.

During the course of this study, several limitations were identified. Firstly, concerning the textural analysis of the massive sands, the use of thin sections and a representative element volume has truncated the coarse-tail component. This implies that the coarse-tail may not have been fully represented in the samples analysed, and any subsequent analysis was biased. Furthermore, samples were collected using the conventional sampling programme, that is to say, at regular intervals. Again this may have introduced bias, such as not sampling subtle grain size variations. This in turn leads to over-interpretation and often incorrect interpretation of textural trends. Secondly, in terms of the lateral and vertical facies transition, cross-flow documentation of facies was not possible, at least in the proximal and medial locations. Thus the field measurements can be considered as 2-D cross-sections. The accuracy of the correlation framework also has to be questioned. Although it was judged to be highly reliable and accurate, question marks still remain since lateral walkout was only possible in proximal locations and no biostratigraphic timelines were established. And lastly, the effect of diagenetic alteration of the pore distribution in the East Brae Field has to be considered. While various petrological studies indicate that grain texture is the primary control on reservoir properties in the field, localised diagenetic cements may have significantly influenced the porosity and permeability.

This study has also identified several areas for future work that would advance our understanding of massive sands and related deposits.

1. Microstructures – while massive sands may be macroscopically structureless, they may contain microstructures. Such structures could further shed light on the mechanics of the near bed layers that produce massive sands. Initial studies have used flume studies (e.g. Naruse and Masuda, 2006) and digital image analysis to identify shear-like glide structures and linked them to laminar flow behaviour. Any future studies could analyse outcrop or subsurface data to identify similar structures in massive sands using for example digital image analysis, SCOPIX X-ray radiography, and full core CT scans. The presence of any microscopic structures could be used to refine the model proposed here. However, prior to this analysis, significant improvements need to be made in the field of grain segmentation to separate touching grains.

2. Near bed layers –Cartigny et al. (2013) and Postma et al. (2014) observed short-timescale fluctuations in velocity and sediment concentrations in near-bed high-concentrations. A tentative link between this process and the ‘jagged’ grain size trend in bed 1 is proposed in this study. A more detailed analysis of the textural changes

associated with these subtle fluctuation is necessary to fully understand the small-scale sedimentary heterogeneity, and its impact on reservoir properties.

3. Gravity transformation – Physical and numerical experiments has shed light on turbulence dampening in flows (e.g. Baas et al. 2011; Cantero et a., 2012). There is now a need to document this in natural flows and link it to the deposit character. Important strides have been made in this regard with recently collected data from the Monterey Canyon (e.g. Xu et a., 2014). Yet the deposit character remains poorly defined.

4. Subsurface data – outcrop analysis of massive sands is at a mature stage. However, image analysis data calibrated to core or behind-outcrop wells can be used to provide a wealth of information on sediment facies, geometries and petrophysical properties of potential reservoir intervals. An interpretative framework for massive sands and associated facies can be constructed from such an analysis, which integrates image characteristics and sediment facies, and could be used to aid understanding of reservoir properties.

Chapter 7– Appendices.

7.1 Appendix A. Facies Scheme, Processes and Deposit Character.

Below is a review of the features seen in deep-water successions analysed as part of this study (i.e. Numidian Flysch, Grès de Peïra Cava and Brae Formation) and the near-bed sedimentation processes responsible for their formation. The review broadly follows the deposit-based classification scheme proposed by Talling et al. (2012), which provides a rationale for the sub-division of subaqueous sediment flows based on deposit character. Processes and deposits related to slides, slumps and injection structures were not considered by these authors, but are given a cursory review since they form minor deposits in the East Brae Field.

7.1.1 Slides, Slumps and Injectites.

Slides and Slumps (DC_1). Slides and slumps involve the movement of coherent masses of sediments bounded on all sides by distinct failure planes (Mulder and Cochonat, 1996). They range in size and volume from a few m^3 to several hundred to thousands of km^3, with a potential runout distance in excess of 200 km. Differentiation between slides and slumps is based on the Skempton ratio *h/l*, where *h* is the depth to the slip surface and *l* is the length of failure: slides are translational, characterised by flat, slope-parallel failure surface and a Skempton ratio of <0.15, whereas slumps are rotational and deep rooted with a ratio of 0.15 to 0.33 (Skempton and Hutchinson, 1969). The failure surface is normally predetermined and corresponds to a discrete layer with low shear resistance such as permeable sand layers or clay and sand interbeds (e.g. hemipelagic, pelagic and contouritic deposits; Mulder, 2010). In slides, internal deformation of layers is minimal and is localised along the basal failure surface. In contrast, the internal structure of slumps is relatively chaotic and deformed, with the degree and style of deformation varying with position of the moving layer and the strength and heterogeneity of the material (Stow et al. 1996). Slope instability is the primary cause of these sediment deformation processes, which in turn is influenced by; (1) quantity, type and rate of sediments delivered to the deep-water system, (2) sediment thickness and angle of repose, (3) changes in seafloor pressure and temperature, which can affect hydrate stability and generation of free gas, and (4) variations in seismicity. Deposition or cessation of sediment movement occurs on decreasing slope angles when the downward component of gravity cannot exceed or balance basal and internal frictional forces (Lee, 2009; Pickering et al., 2015; Tappin, 2010).

In the present study, slides and slumps (Figure 7-1) constitute minor facies observed in the East Brae Formation, and comprise cm to dm thick intervals of folded and contorted layers. Discrete internal glide and shear surfaces are visible, defining the lower surface of the deposit. These are

characteristically restricted to mudstone layers and typically are smooth. Internal structure and layer thickness are highly variable, with beds displaying asymmetrical and monoclinal folding to irregular and nodular remnant bedding geometries. Thicknesses of these constituent beds range between a few millimetres to less than 20 cm, while the deformed unit as a whole has a thickness of less than 2 m.

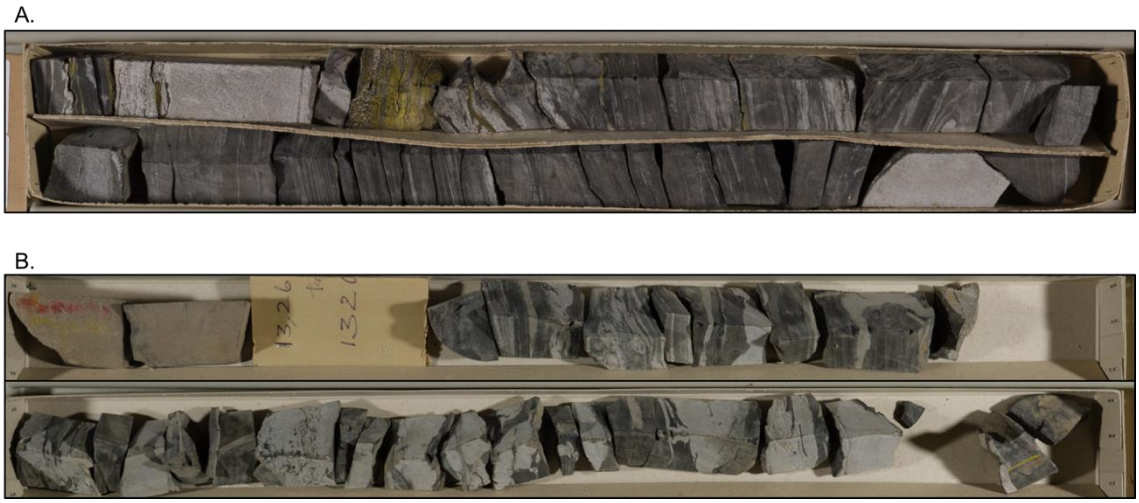

Figure 7-1: Slide and slump facies constitute a minor portion of the deposits in the present study. They are only observed in the cored intervals of the East Brae Formation, thus their lateral extent have to be inferred from our understanding of the depositional system.

Injectites (DC_2). Sand injection structures are a common feature of many deep-water systems. In rare instances, they can host hydrocarbons as in the case of the Upper Miocene deep-marine Santa Cruz Mudstone (Thompson et al., 2007). More commonly, however, sand injections facilitate vertical connectivity between sand intervals depending on injectite intensity, thickness and textural properties. Hurst et al. (2011) recognised four architectural elements of injectite structures: parent units, dykes, sills and 'extrudites'. In the present study, only dykes (discordant, cross-cutting the host layers) and sills (concordant, approximately parallel to the host bedding) were observed. Both occur as thin (few mm to < 2 cm) and relatively short (<15 cm) sand bodies, consisting of very fine grained sands. They are closely associated with the underlying clean sandstone unit, which is likely to be the parent unit of the dykes and sills. The upward flexure of the intruded lithology and sedimentary structure (i.e. lamination) lends further support to emplacement from below. In many cases, the structures have been contorted, indicating post-emplacement compaction of the host succession. The exact cause of injection structures remain ambiguous, although Hurst et al. (2011) identified a number of trigger mechanisms including; migration of fluids into the parent body, seismicity, and overpressuring caused by rapid loading. Regardless of the trigger mechanism, the hydrofracture of an overlying seal-quality lithology promotes the upward injection of sand into an open fracture network when the sand becomes fluidised (*ibid.*). This is caused by the high pore-pressure in the parent

unit opposing the principle stresses, causing the differential stress to intersect the host strata's failure envelope to create extensional fractures (Hurst et al. 2011 and references therein).

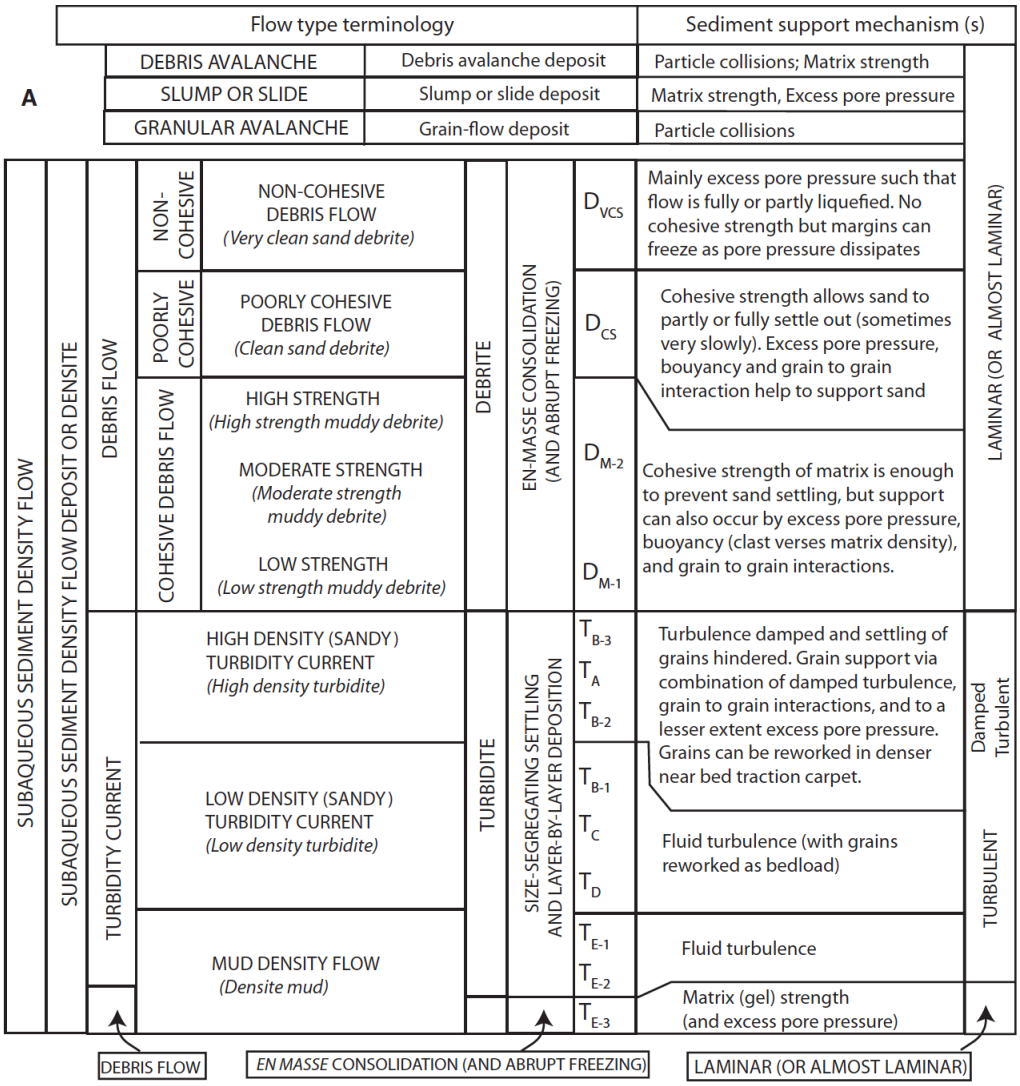

Figure 7-2: Terminology used to describe subaqueous sediment flows according to Talling et al. (2012).

7.1.2 Subaqueous Sediment Flows

Talling et al. (2012) preferred the term *'subaqueous sediment density flows'* to describe a single flow event and the different types of flows that may occur within the single event as it moves downslope. Figure 7-2 shows the terminology proposed by Talling et al. (2012) to sub-divide sediment flows based on the features seen in the deposits. Flows are initially subdivided according to the style of deposition; incremental (progressively) or *en masse* consolidation. Flows that deposit their sediment load incrementally from a turbulent suspension are termed *turbidity currents* and their deposits *turbidites*, while flows that deposit en masse are termed *debris flow* and their deposits as *debrites* (Figure 7-2). The differences in these two styles are explored further below. Turbidites are further subdivided based on the features observed in the

deposit (Figure 7-2), which may indicate whether turbulence was dampened, hindered or unhindered, and thus provide clues to near bed sediment concentration and bed aggradation rates (Talling et al., 2012). Debris flows, in contrast are subdivided based on their matrix mud content and presence of outsized clasts. These criteria for subdividing subaqueous sediment flows were chosen by Talling et al. (2012) for the following reasons: 1) the deposit character is a direct reflection of the settling behaviours of the flow, 2) as mud concentration in the flow decreases, abrupt changes in settling behaviour from en masse consolidation to layer-by-layer deposition exhibiting size segregation has been noted in a number of flume experiments (Baas et al. 2009; Baas et al. 2011; Sumner et al. 2009), and (3) the type of deposit appears to correlate with whether a flow is laminar or turbulent at the time of deposition. This last factor is related to the amount of mud needed to damp turbulence and the amount needed to support particles (Sumner et al., 2009).

Turbidity Currents and Incremental Deposition. The term turbidity current was originally coined to denote a turbid flow. However, the widely accepted definition of a turbidity current describes them as sediment flows in which grains are suspended by fluid turbulence, and from which grains settle out progressively, such that the deposit aggrades incrementally in a layer-by-layer fashion. Since the deposit is produced incrementally, the vertical organisation of a deposit at a specific location is a reflection of the evolving flow conditions at that location through time (Kneller, 1995; Kneller and Branney, 1995. Furthermore, by documenting the lateral changes in the vertical organisation in extensive turbidite beds, spatial changes in the turbidity current can also be investigated (Amy et al. 2006; Ricci Lucci, 1978; Talling et al. 2007b). Due to size segregation and incremental deposition, turbidites are commonly graded, unless flow velocity is constant or only a single grain size is available (Kneller and Branney, 1995; Sylvester and Lowe, 2004). Deposition of any outsized clast occurs along discrete horizons in the deposit and is related to their location in the flow; the clast being carried in the body of the flow and emplaced on top of existing sediments deposited by the frontal parts of the flow (Kneller and Branney, 1995; Sumner et al., 2012).

Vertical gradient in sediment concentration in a turbidity current leads to development of a thin (cm-scale) highly concentrated bed-load zone, variously termed traction carpet (Dzulynski and Sanders, 1962), laminar sheared layer (Vrolijk and Southard, 1997) or laminar layer (Kuenen, 1966; Sumner et al. 2008). These laminar layers are fed from the overlying flow and are plastic in behaviour, freezing from the base up due to interlocking of grains. Shanmugam (1996) argued that these layers should be recognised as a sandy debris flow (sensu stricto), irrespective of whether the plastic behaviour represents only the basal part of the flow or the entire flow. However, since the overall deposit is produced incrementally in a layer-by-layer fashion, the process that created the deposit is classified as a turbidity current (Kneller and McCaffrey,

2003; Talling et al., 2012). These laminar layers are genetically linked to the overriding turbulent flow (Vrolijk and Southard, 1997), in contrast to debris flows which are driven by the downslope component of gravity. Due to incremental deposition, the thickness of a turbidite is more closely linked to the aggradation rate and the duration of the flow, rather than the flow thickness.

Debris Flows and En-Masse Deposition. The term debris flow describes a subaqueous sediment flow that is laminar in character and plastic in behaviour, and in which sediment is supported chiefly by processes other than fluid turbulence (i.e. matrix support, excess pore fluid pressure, grain interaction and buoyancy; Dasgupta, 2003; Pierson and Costa, 1987; Talling et al., 2012). The flow keeps on moving until the shear stresses are unable to overcome the internal shear strength and the sediments are deposited *en-masse*, after which consolidation of the deposit continues. Field observations and experimental data show that debris flow deposits may also accumulate incrementally, whereby individual surges of debris flows freeze *en-masse* and aggrade vertically (Davies, 1986; Iverson, 1997). However, since the dominant depositional mechanism is *en-masse*, regardless of the incremental nature of aggradation, the deposit is considered a debrite. Furthermore, since the shear stress and internal shear strength vary across the flow (or surges), *en masse* settling of the failed mass is not instantaneous, but rather progressive with material at the lateral edges and upper parts of the flow 'freezing' first. Due to this *en-masse* freezing of the entire flow, deposit thickness of debris flows is more closely related to flow thickness.

Due to the *en-masse* deposition of sediments, differential settling of grains does not occur. However, experiments of Baas et al. (2011) and Sumner et al. (2009) has shown settling and grain size segregation does occur after the flow if the weight of the grains exceed the shear strength of the matrix. This process produces a basal clean sand that can be graded or ungraded, while any coarser sediment remaining in the debrite consolidates to produce an ungraded deposit (Sumner et al., 2009). Inverse grading has also been typically used as a recognition criterion for debris flow deposition. Such intervals were considered to be a product of intergranular collision which created dispersive pressure that acted on larger grains. It has, however, been indicated that dispersive pressure gradients in flows are inherently hydrostatic, and only grains lighter than the bulk density of the flow are pushed up (Legros, 2002). Thus in order to explain inverse grading, an alternative mechanism was put forth by Savage and Lum (1988), and validated experimentally most recently by Sumner et al. (2008), whereby smaller grains percolate between the larger grains. This process is termed kinetic sieving. In addition, outsized clasts, if present, may also undergo size segregation upwards or downwards depending on the relative densities of the clast and matrix, and the matrix strength. Hence, grading of clasts may be present in debrites, even though the matrix may have undergone no size segregation.

7.1.3 Deposit Character and Depositional Processes.

The deposits of subaqueous sediment flows and the flow processes responsible for their emplacement are now reviewed. It is beyond the scope of this study to review all the deposit characteristics observed in the deep-water environment. Therefore, only those deposit characteristics observed in the deep-water succession of the of the Numidian Flysch (Tunisia), Grès de Peïra Cava (France) and the Brae Formation (Viking Graben, UKCS), which have been analysed as part of this study, are reviewed using the terminology and classification scheme developed by Talling et al. (2012). As will be noted in subsequent chapters, the deposit character or facies (i.e. a body of sedimentary rock with specific physical, chemical and biological characteristics deposited under specific hydrodynamic conditions) scheme is hierarchical, dividing the deposits based on lithology and then on the basis of characteristics observed within the deposit. Therefore, individual layers of sedimentary rock may consist of a number of facies arranged vertically and laterally as the flow evolves temporally and spatially.

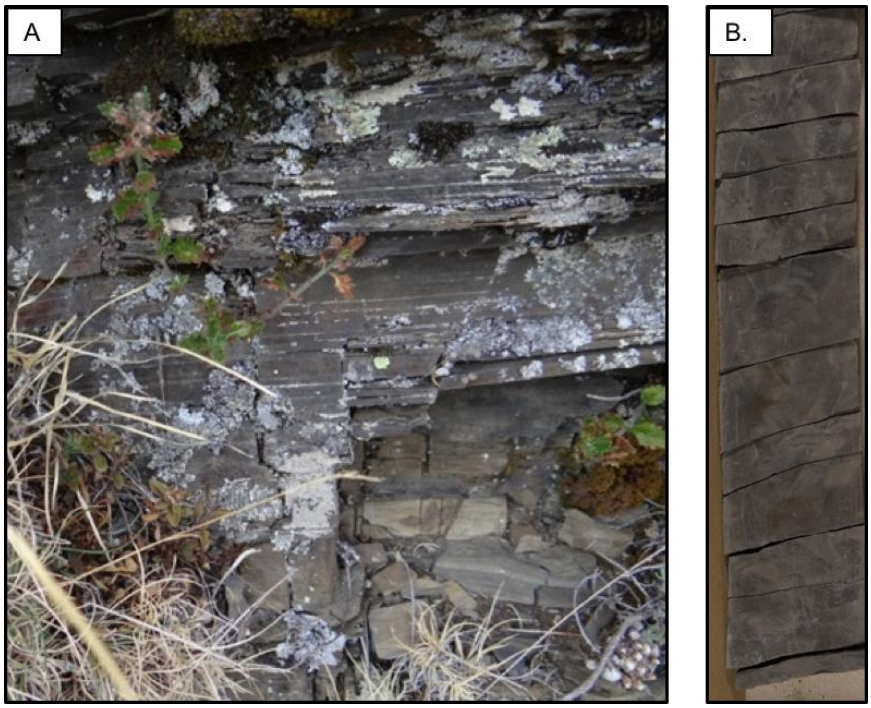

Figure 7-3: Outcrop and core photograph of mudstone facies. A) Laminated mudstone (ML: Grés de Peïra Cava) and B) massive mudstone (MM; East Brae Formation).

Mudstone (M): Mudstone facies in the present study consists of laminated (ML) and massive mudstones (MM; Figure 7-3). The cohesive properties of mud has a profound effect on settling behaviour, flow rheology (viscosity and turbulence) and velocity, and thus flow deposits. It arises from the surface electrical charges (Van der Waals forces), body forces as well as biological processes such as polymetric binding (slimes and mucus produced by bacteria and micro-benthos), and is important in particle aggregation (McAnally et al., 2007; Stow and Bowen, 1980; Talling et al., 2012). Settling and aggregation of mud particles can initiate from

mud concentrations as low as 0.01%, with larger floc sizes (>100 μm) settling at the same rate as coarser silt and sand particles (0.01 to 1 cm s^{-1}; *ibid)*. Observations from shallow marine environments and flume experiments have shown floc deposition may occur at flow speeds up to 25 cm s^{-1} (Baas and Best, 2002; Baas et al., 2016; McAnally et al., 2007). With increasing mud concentrations (> 0.5% by volume), turbulence is damped and the mud flocs may form a continuous network of bonds or gels which imparts strengths to the muddy flow (Stevenson et al., 2014; Talling et al., 2012). This allows larger particles (> 1mm) to be supported in the mud matrix during transport, but can settle once the flow has stopped moving to produce a clean sand layer at the base of the mudstone (Amy et al., 2006; Baas et al., 2016; Baas et al., 2011; Sumner et al., 2009).

Laminated mudstone facies in the present study are up to 50 cm thick. Individual laminae are 0.1 to < 4 mm thick, typically planar and continuous, and are considered to form part of the same flow rather than separate events due to a gradational contact with the underlying deposits and lack of erosive features. A number of mechanisms have been proposed to explain their formation, but have not been successfully reproduced experimentally. The presence of laminae indicates deposition from dilute flows with grain-by-grain or aggregate settling. Stow and Bowen (1980) proposed a model whereby lamination results from break-up of flocs containing mud and silt in an expanded, highly turbulent, dilute flow. Silt and fine sands are deposited during floc break up, followed by gradual mud deposition, which damps turbulences and further enhances mud deposition. A similar model was also proposed by McCave and Jones (1988), however, these authors envisioned deposition from a denser, laminae fluid mud layer or laminar plug. In this latter model, the vertical structure of the deposits resembles the vertical structure of the flow. As such, the former model of Stow and Bowen (1980) is adopted in this study.

The massive mudstone (MM) in this study are primarily ungraded, with minor graded massive mudstones present at the transition from sand layers. Graded mudstones can be up to 50 cm thick, while the ungraded massive mudstones can form intervals several metres in thickness. Unlike laminated mudstones, these facies must form from particle settling or *en*-masse deposition from a gel or mud fluid layer without particle reworking. For grading to be present, the mud concentration should be sufficient to allow differential settling of larger mud flocs, silts and sand grains either during or after deposition (Baas et al., 2009; Sumner et al., 2009).

Siltstone (Z): Laminated (ZL) and massive (ZM) siltstones are a minor facies in the present study. They occur as relatively thin, graded or ungraded intervals up to 10 cm thick. The origin of this facies has proven difficult to reconcile, partly due to the difficulty in recognising it in most outcrops, and partly due to our inability to reproduce it satisfactorily in experiments.

Flume experiments have shown a narrow stability field in which lower plane beds can occur, but this is in the presence of coarser particles (> 800 μm; Southard, 1991). Lowe (1988) suggested that silt laminated beds can form under waning condition from dilute flows, especially when the duration for bedload reworking is too short to produce ripples. However, this mechanism has not been reproduced in flume experiments. Extrapolation of hydrodynamic processes from the Tc division of the Bouma sequence suggest grain-by-grain deposition from suspension, followed by traction transport along the bottom to produce lamination (Pickering and Hiscott, 2015). Massive silt (ZM) are, in contrast, likely to form from rapid mass deposition from a concentrated flow, due to a combination of increased intergranular friction and cohesion (*ibid.*)

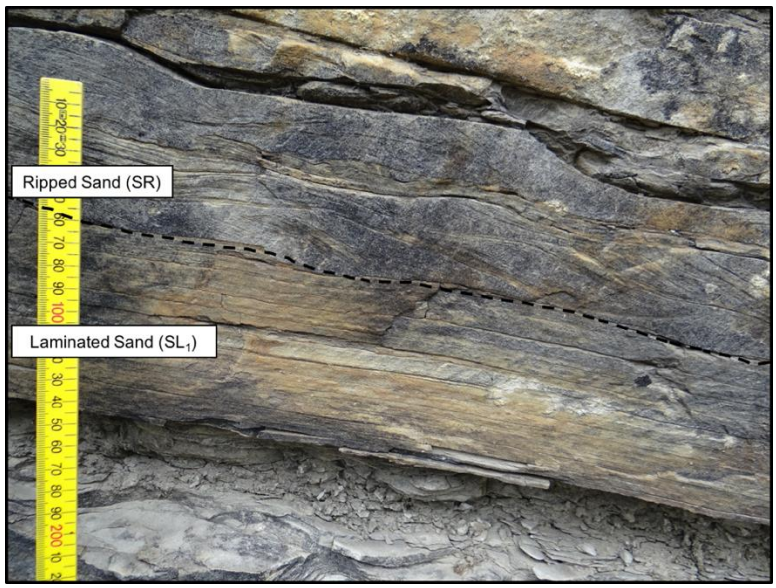

Figure 7-4: Outcrop photograph of ripple lamination (SR) and parallel lamination (SL_1). Both of these facies are deposited by low-density turbidity currents where particles are reworked as bedload.

Sandstone, rippled (SR). This facies is equivalent to the Bouma T_C division and is common in the deep-water sedimentary successions documented as part of this study (Figure 7-4). The ripple intervals typically consist of sand grains ranging in size between 50 μm to 800 μm, wavelength of < 20 cm and amplitude of < 6 cm. Bouma (1962) also reported convoluted ripples, most likely a result of dewatering from the underlying sand facies or rapid deposition. There is a strong agreement from flume experiments and numerical simulations that ripples record deposition from a relatively dilute and turbulent flow, with low sediment fall out rates and where the particles are reworked as bedload. They are not present in laminar flows or flow in which turbulence is damped by high concentrations or cohesive muds (Baas, 2000). Various experiments have also shown that the residence time need to be several minutes for ripples to form (Baas, 1994; 1999; 2000). For finer grained sediments, this residence time is longer

(Sumner et al., 2008), especially in unsteady flows. Using numerical simulation, Jobe et al. (2012) calculated a sediment fallout rate of between 0.15 mm s^{-1} and 0.26 mm^{-1} under which ripples are likely to form. At higher sedimentation rates, ripples are suppressed and massive sandstones are likely to form (Arnott and Hand, 1989; Sumner et al., 2008; Cartigny et al., 2013).

Sandstone, laminated (SL). Three different types of planar laminated sands (SL; Figure 7-4 and 7-5) have been identified in the present study; parallel laminated sands (SL_1; equivalent to Bouma T_B), thin-spaced stratification (SL_2) and thick-spaced stratification (SL_3). They have been well document in field and experimental studies (e.g. Cartigny et al., 2013; Hiscott, 1994b; Hiscott and Middleton, 1980; Lowe, 1982; Mutti, 1992; Postma and Cartigny, 2014; Sohn, 1997; Sumner et al., 2012) and have been incorporated into most 'classical' facies sequences (e.g. Lowe sequence, Bouma Sequences, Mutti's genetic facies tract).

The parallel laminated (SL_1) facies consist of stratified sands with individual laminae typically less than 3 mm thick. Laminae can be traced for several metres laterally and show little or no grain size variation between laminae. This type of stratification has previously been attributed to deposition from dilute turbidity currents in the upper stage plane bed regime. The experiments of Best and Bridge (1992) demonstrated individual laminae forming by migration and burial of low amplitude bedwaves under low sediment fall-out rates (0.014 mm s^{-1}). Sediment sorting on the lee side of the bedwaves and kinetic sieving of finer particles into the substrate led to the development of planar and wavy laminae. Preservation of the laminae was highly dependent on sediment fall-out rates and the sequence of bedwaves of different height crossing any point (ibid).

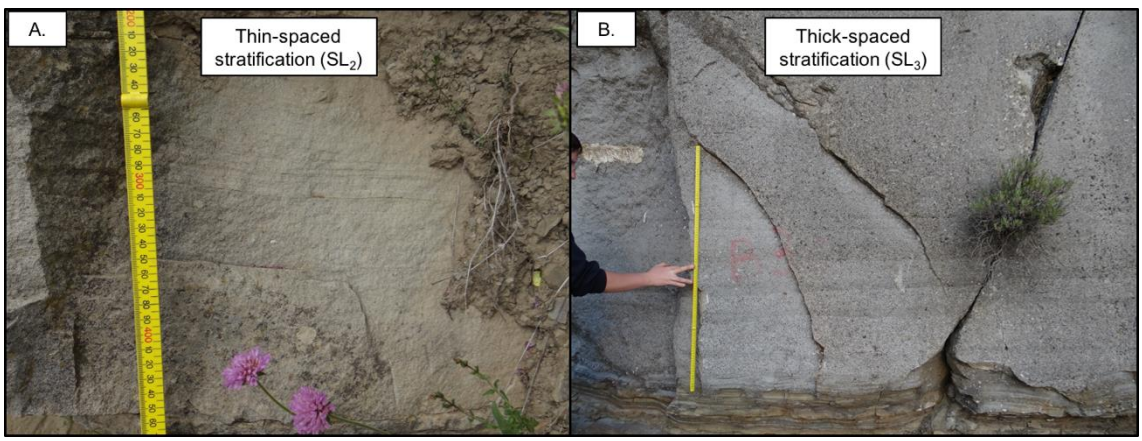

Figure 7-5: Outcrop photo showing (A) thin-spaced stratification (SL_2) and (B) thick-spaced stratification (SL_3). Flume experiments have shown such stratification forming from collapsing high-concentration laminar layers beneath high-density turbidity currents.

The experiments of Vrolijk and Southard (1997) demonstrated that stratification can also form under high aggradation rates and higher sediment concentration (> 10 % by volume). This stratification has been previously termed traction carpets (Figure 7-5B; Dzulynski and Sanders, 1962), but have been renamed as spaced stratification by Hiscott (1994b) based on hydrodynamic considerations. They differ from lamination produced by bedwaves in that deposition occurs via collapsing high-concentration laminar layers at the base of the flow. In the present study, two types of spaced stratification have been identified; thin-spaced stratification (SL_2) and thick-spaced stratification (SL_3; Figure 7-5B). Thin-spaced laminations are between 3 to 10 mm thick, show crude normal or inverse grading, have sharp to diffuse contacts and can be traced for less than a metre laterally. The thickness of individual laminae typically varies laterally due to erosion by the overlying laminae. They typically form part of crudely normal graded interval. Flume experiments have shown thin-stratification forming via deposition from mm-thick high-concentration (10 to 35%) near bed layers that are characterised by hindered settling, grain-to-grain interaction and damped turbulence (Cartigny et al., 2013; Hiscott, 1994b; Postma and Cartigny, 2014; Postma et al., 2014; Sumner et al., 2008; Vrolijk and Southard, 1997). Deposition is initiated by frictional interlocking of grains from the base up. Since the layers are fed and driven by the overlying flow, the grains are laterally sheared and partially eroded to form crude stratification (Sumner et al., 2008).

In contrast, thick-spaced laminations are > 1 cm to < 15 cm thick and are equivalent to the S_2 division of Lowe (1982) and F4 division of Mutti (1992). Individual 'laminae' are associated with coarser grain size (545 μm – 4 mm), and are typically ungraded. However, normal and inverse grading can also occur over a restricted range (1 – 2 cm) at the base of the laminae. Overall, the deposit shows a stepped grain size and thickness profile, with subsequent laminae consisting of finer grain sizes and thinner interval size. Stratification of this type has also attributed to collapsing laminar shear layer, similar to those that produce thin-spaced stratification (Cartigny et al., 2013; Hiscott, 1994b; Sumner et al., 2008). However, theoretical consideration suggest that laminar flows at the base of flows are at most a few centimetres thick (i.e. 10 grains; Hiscott, 1994b; Sohn, 1997) and therefore unlikely to produce the thicker spaced-stratification. Recent experimental evidence, nonetheless, indicates that the characteristics of the near bed layer varies depending on the concentrations of the layer, which is in turn dependent on the sediment fallout-rate from the overlying turbulent suspension (Cartigny et al. 2013). It is likely that higher shear velocities could lead to thicker intervals of sediment being sheared into laminar layer. Fluctuations in either of these characteristics could therefore also lead to inverse or normal grading, while a high sediment concentration (> 20% by volume; Cartigny et al., 2013; Cartigny and Postma, 2014) and constant sediment fallout-rate could produce ungraded laminae.

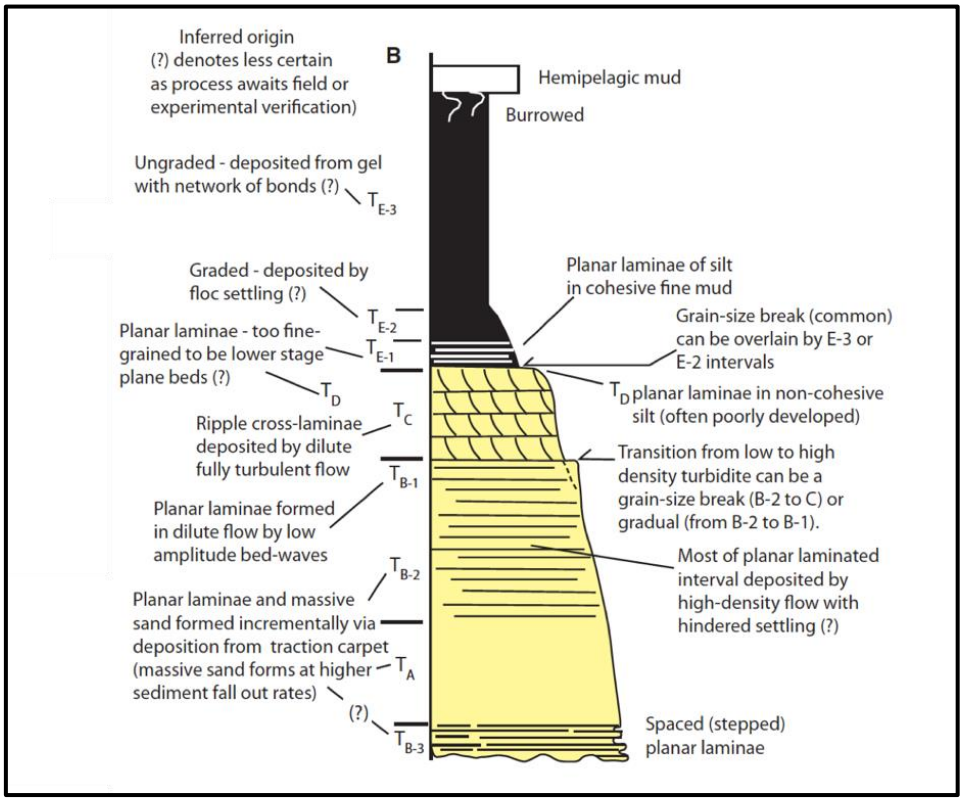

Figure 7-6: A modified Bouma (1962) sequence of commonly found facies within turbidites and their inferred depositional processes after Talling et al. (2012. Based on numerous field studies, the position of the thick-spaced stratification (T_{B-3}) and thin-spaced stratification (T_{B-2}) have been placed below and above the massive interval respectively. Due to the depositional processes responsible for their formation, as well parallel lamination, Talling et al. (2012) placed the boundary between high- and low-density turbidity current between the parallel laminated and thin-spaced stratification.

Shanmugam (1996), (1997) and (2000) argued that no clear definition exists for high-density turbidity currents in terms of their flow density and sediment concentrations. It is universally accepted that turbidity currents have a continuum of sediment concentrations. However, Talling et al. (2012) argued convincingly that a distinction between low and high-density turbidity currents can be justified in a deposit-based classification. Both planar and ripple-laminated sands have been shown to form from fully turbulent flows. Such flows allow tractional reworking of sediments and are characterised by unhindered settling. With higher sediment concentrations, sediment fallout-rates increase and turbulence is dampened in a near-bed layer characterised by hindered settling and grain-to-grain interaction. Under these conditions, thin-spaced stratification is deposited via collapse of near bed layers. The boundary between deposits of low and high-density turbidity current could therefore lie within planar stratified sands, possibly the transition between parallel (SL_1) and thin-spaced (SL_2) stratification (Figure 7-6; Talling et al., 2012). As will be discussed in Chapter 3, this transition is also locally marked by a grain size break which is likely to indicate a change in settling regime from capacity to competence driven deposition (Kneller and McCaffrey 2003; Stevenson et al., 2014; Talling et al., 2012b).

Sandstone, massive (SM). An in-depth review of massive sandstone facies, the processes proposed of their formation, as well as vertical and lateral facies transitions to and from massive sands, and facies geometry is provided in Chapter 2.

Conglomerate (C). Conglomeratic facies in this group can be supported by sand- and gravel-matrix (CM1), clast contacts (CM2) and mud-matrix (CM3; Figure 7-7). Bed thickness and lateral continuity varies, although they tend to be > 1m and laterally continuous for < 0.5 km. The CM1 facies, in general, consists of a mixture of cobble and pebble sized clasts floating in a poorly graded and sorted matrix of coarse sand to granules, and predominantly lacks any form of stratification (Figure 7-7A). Clast (composed of mudstone and sandstone) size range from cm to > 1m, but is dependent upon the composition with sand clasts typically larger than mud. These clasts are commonly disorganised and chaotically distributed, but can occasionally show inverse/normal grading and/or crude imbrication defined stratification. In comparison, the CM2 facies is clast-supported (granules to cobbles), predominantly massive with rare occurrence of crude stratification and coarse-tail grading towards the top of beds (Figure 2-7B). Imbrication is less developed in most occurrences of this facies. Outsize mud- and sand clasts vary in size from cm to > 1m, and are chaotically distributed throughout the bed or display a crude ordered stratification (B5; Johansson and Stow (1995)). Lastly, the CM3 facies consists of cm to > 1m floating clasts in a 10-50% muddy matrix (Figure 7-7C). Clasts consist of mudstone and sandstone fragments that commonly display a chaotic fabric and dispersion. Bed shape at outcrop scale may appear tabular, but the facies shows abrupt pinch out over a short distance.

Figure 7-7: Outcrop photographs of the common conglomeratic facies found in the present study: (A) poorly sorted sand and gravel-supported conglomerates, (B) clast-supported conglomerate, and (C) mud-matrix conglomerate.

According to the classification scheme of Talling et al. (2012), all three conglomeratic facies can be described as deposits of debris flows, with the mud-matrix content determining whether they are cohesive, poorly cohesive or non-cohesive debrites. The amount of mud content in a flow has a fundamental control on its behaviour since it can affect yield strength, viscosity, hydraulic diffusivity, rate of ambient fluid entrainment, size of clasts supported and dampen turbulence (Baas et al., 2016; Iverson, 1997; Iverson 2010). Cohesive debrites are defined as

having > 20% cohesive mud, while non- and poorly cohesive debrites have less than 20% mud by volume. This sub-division is based on the inherent bimodality of mud concentrations observed in many well studied ancient deep-water successions (e.g. Marnoso Arenacea, Grès d'Annot, Jackford Group, East Carpathian Flysch; Amy et al., 2006; Golob, 2003; Talling et al., 2012; Sylvester and Lowe, 2004). Based on this, the CM1 and CM2 facies can be described as a poorly- or non-cohesive debris flow, while CM3 as cohesive debris flows. Iverson (1997) and Marr et al. (2001) noted that there is a continuum of cohesive debris flows depending on the yield strength of the material. However, in a deposit-based classification, it is almost impossible to determine the yield-strength of the material. Experimental data using kaolin mud has nonetheless shown a positive correlation between yield strength and clast size (Hampton, 1975; Talling et al., 2002; Talling et al., 2012). Therefore, a subdivision based on the presence of clasts and their size was proposed by Talling et al. (2012) to categories cohesive debris flow deposits into high-, moderate and low-strength cohesive debrites. Utilising this subdivision, the CM3 facies can be classified as a deposit of a moderate-strength debris flow. Such flows are characterised by laminar behaviour, en-masse deposition due to the high mud content, fluid entrainment along their upper boundary to produce an overlying turbidity current, and laterally limited in extent (Amy et al., 2006; Haughton et al., 2003; Talling et al., 2004). Due to the moderate yield strength, grading of outsize clasts, as well as coarser sand grains, may occur after deposition of the sediments (Amy, 2006; Baas et al., 2009; Sumner et al., 2009).

CM1 and CM2 facies, in contrast, are deposits of non-cohesive debris flows. These flows have excess pore pressure and grain-to-grain interaction as the dominant clast support mechanism. Lowe (1982) and Mulder and Alexander (2001) argue that such flows may have limited lateral extent since the pore-pressure dissipates rapidly, especially on low angle slopes. However, the incorporation of small amounts of clays can reduce the hydraulic diffusivity and settling rates, thus allowing greater run out distance (Iverson, 1997; Iverson and Major, 2010; Kaitna et al., 2016). A high hydraulic diffusivity and well connected pores will, on the other hand, lead to flow transformation to a high-density turbidity current as the initial debris flow moves downslope (Mulder and Alexander, 2001; Mutti, 1992; Pickering and Hiscott, 2015). Such a transformation could be marked by normal coarse-tail or distribution grading (Sanders, 1962; Middleton and Hampton, 1973; Sanders, 1965; Shanmugam, 1996). Deposition begins due to frictional interlocking of grains and the sediments come to rest *en-masse*.

7.2 Appendix B. Image Segmentation Algorithm

During the post processing phase, images were binarised to separate grains from matrix. However, a visual inspection of the image after binarisation revealed 'touching' grains. As such, a watershed-like grain identification and quantification algorithm was created with the aid of Dr Zeyun Jiang at Heriot-Watt University. The brief description of the algorithm was written by Dr Zeyun Jiang follows.

Basic Concept. Figure 7-8 shows the algorithm procedures for identifying and quantifying grains from a 2D or 3D rock images, including initialization, local maxima search, region growing and merging, and grain quantification. The initialization is carried out prior to any operations in relevance to the watershed algorithm, which mainly consists of image enhancement and binarization, reducing noise (in particular here, removing all tiny grains) and computation of grain distance map to quantify the position of each grain pixel/voxel in relation to the pore space. The search of local maxima is a key step for all watershed-like algorithm, and then using all local maxima as seeds to conduct region growing and accomplish the region segmentation after all growing regions meeting each other to form dams. The major problem with the watershed algorithm is overestimation – two or more individual grains have been mistakenly merged into a single grain, so a final step – region merging is performed to overcome this limitation. Based on the identified grains form an image, many commonly-used characteristics can be measured or calculated.

Watershed Algorithm. This is one of image segmentations, i.e., partitioning an image into disjoint regions, such that each region is homogeneous (e.g., either pores or grains) with respect to some property, such as grey value or texture. The intuitive idea underlying watershed algorithm (Serra, 1982; Vincent and Soille, 1991) comes from geography: it is that of a landscape or topographic relief which is flooded by water, watersheds being the divide lines of the domains of attraction of rain falling over the region. An alternative approach is to imagine the landscape being immersed in a lake, with holes pierced in local minima (or maxima). Basins (catchments) will fill up with water starting at these local minima (Figure 7-9A), and, at points where water coming from different basins would meet (Fig. 7-9B), dams are built. When the water level has reached the highest peak in the landscape, the process is stopped (Fig. 7-9C). As a result, the landscape is partitioned into regions or basins separated by dams, called watershed lines or simply watersheds.

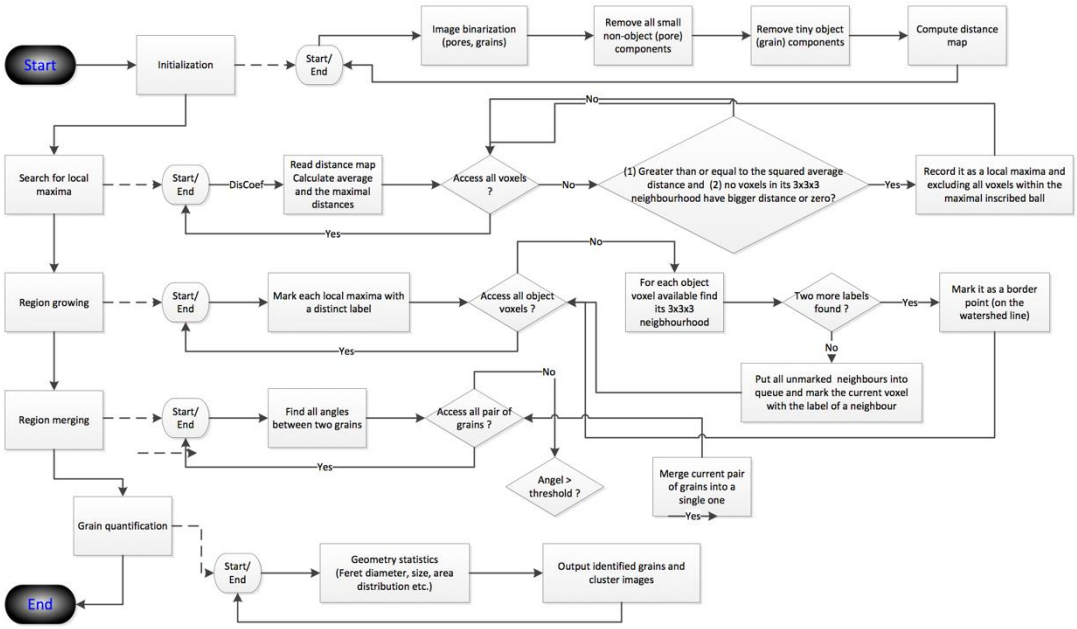

Figure 7-8: The algorithm procedures for grain identification and quantification based on 2D or 3D rock images.

Digital Image Analysis. A digital image can be considered as a function that is defined on a bounded subset (i.e., the defining domain) of the discrete space, and has integer values, obtained by scanning a sample with an imaging device/method such as Scanning Electron Microscope (SEM) or X-ray Computed Tomography (CT). The defining domain is also called as image nesting domain, Ω, and each dimension of the domain is a sub-set of the discrete space $Z^+ = \{0, 1, 2, \ldots\}$, commonly $\Omega = \{0, 1, \ldots, M-1\}$ for a 2D image and $\Omega = [0, 1, \ldots, M-1] \times [0, 1, \ldots, N-1]$ for a 3D image. The image value at each point (i.e. pixel in 2D or voxel in 3D) is an integer, and the image is referred as a binary image (see Figure 7-10) if only two possible integers (e.g. 0 and 1) as image values to distinguish object (e.g. pore) and non-object (e.g. solid/grain) points in the nesting image, where normally 1s for object points and 0s for non-object points. To convert a grey-level image into a binary image, there is a lot of approaches, which is proved be the critical step of the whole process of the watershed algorithm.

Distance Map. For any binary image, $f(p)$ $p \in \Omega$, we can define a distance map (see Figure 7-11). For each object voxel on the image nesting domain there is a positive integer assigned to represent the squared Euclidean distance (SED) to its nearest non-object voxel, and for each non-object voxel 0 is simply assigned. Therefore, a distance map $\Gamma(p)$ is a function defined the same nesting domain of the corresponding binary image $f()$, i.e. $p \in \Omega$; and the value at each point p is equal to the squared radius of the maximal inscribed ball centred at p. For the details of a 3D efficient algorithm, you are referred to the paper by Jiang et al. (2007).

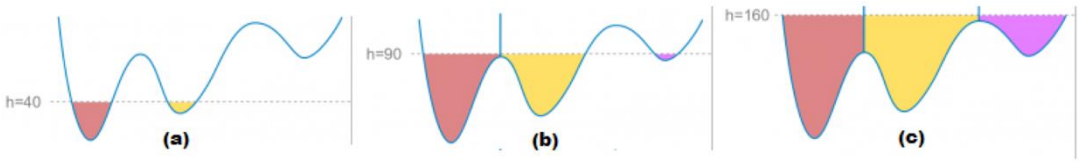

Figure 7-9: Schematic overview of watershed flooding in 1D.

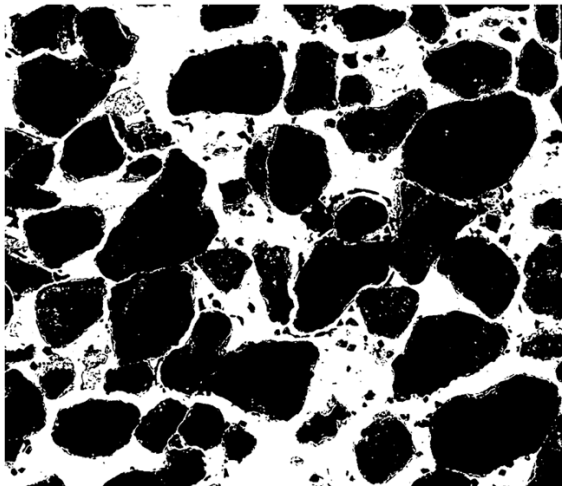

Figure 7-10: A 2D binary image (grains in black and pores in white).

Local Maxima/Minima. From the distance map of a binary image, it is clear that the centres of grains are most likely the local maxima, i.e., the point (pixel/voxel) of the maximal distance value locally. To avoid the over-estimation of local maxima with regard to the specific feature of grains, we introduce a new definition for local maxima. Let , $I(.)$ on Ω, be a binary image composed either grains or pores, and $D(.)$ on Ω be its distance map. A point $p \in \Omega$ in grain region is a local maxima (see Figure 7-12) if the following two conditions are satisfied:

1. There is no point q in its neighborhood $N(\mathrm{p})$ that has a bigger SED value, i.e., $D(q) < D(p)$ for each $\mathrm{q} \in N(p)$.
2. The maximal inscribed circle/ball $\mathrm{B}(p)$does not overlap with any $\mathrm{B}(q)$ of other local maxima q;

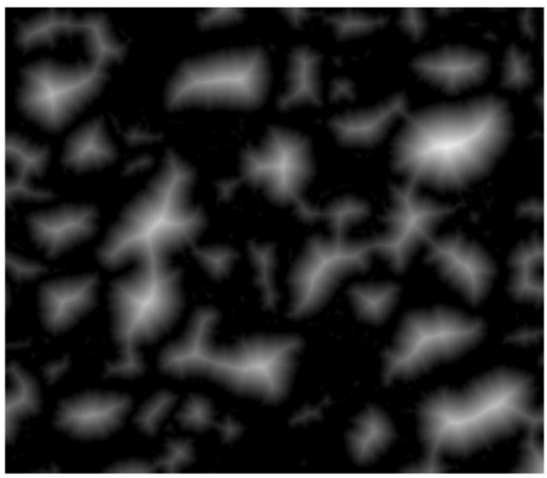

Figure 7-11: The distance map of the binary image shown in Figure 7-10 representing by the grey level (0 – 255: 0 in black, 255 in white) the corresponding squared Euclidean distance

The neighbourhood of a pixel in 2D images is the set of all 8-neighoburs, i.e., $N(p) = \{(q_x,q_y) \mid \max(|q_x-p_x|, |q_y-p_y|) \leq 1\}$, and in 3D $N(p) = \{(q_x,q_y,q_z) \mid \max(|q_x-p_x|, |q_y-p_y|, |q_z-p_z|) \leq 1\}$. The first condition makes sure that the local maxima is in central of a grain as much as possible, however duet to image noise there could exist a lot of fake local maxima. And the second conditions ensure that there is any two pairs of maximal inscribed balls overlapping each other, where the maximal inscribed ball $B(p)$ of a point p of SED value d is defined by $B(p) = \{(q_x,q_y,q_z) \mid (q_x-p_x)^2 + (q_y-p_y)^2 + (q_z-p_z)^2 \leq d\}$ in 3D. In the implementation of the above two conditions, after the first condition has been through we simply check if there is any marked voxel in B(p) to check the second condition. This is equivalent to the definition if whenever a point is identified as a local maxima all points in its maximal inscribed ball are marked.

Region Growing. Considering all identified local maxima as seeds (i.e., region centres), the regions are then grown from these seeds to adjacent points depending on a region membership criterion. The criterion could be, for example, pixel intensity, grayscale texture, or colour. Our criterion is the distance layer in the distance map. In other words, the algorithm starts at the seeds of the largest SED value and grow the corresponding sees or regions into neighbour points; and then search for all seeds or region border points of the second largest SED value; Doing the same with the third largest SED value and continue until all object remains accessed.

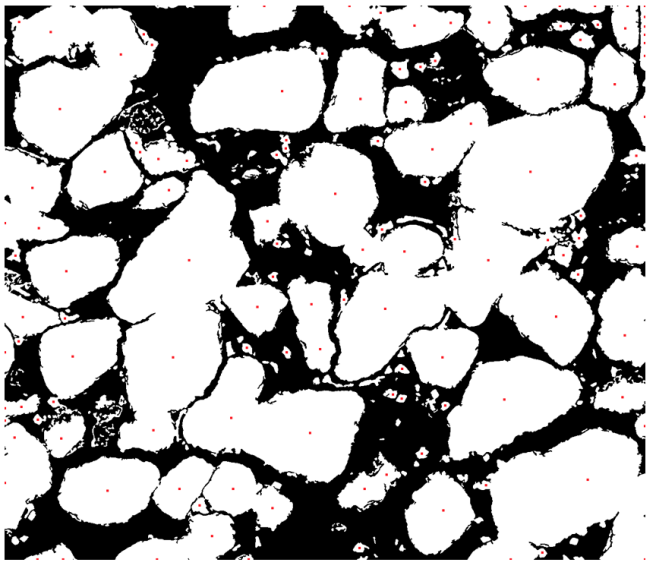

Figure 7-12: Identification of local maxima (in red) from the distance map shown in Figure 7-11

Region Merging. It is very often the over-segmentation happening for many watershed-like algorithms, as you can see that from Figure 7-12 some two grains or even three grains should be single grains. The key is which feature of two or more grains should be defined to consider

merging, from our investigation on grain morphological properties the contact angles are highlighted.

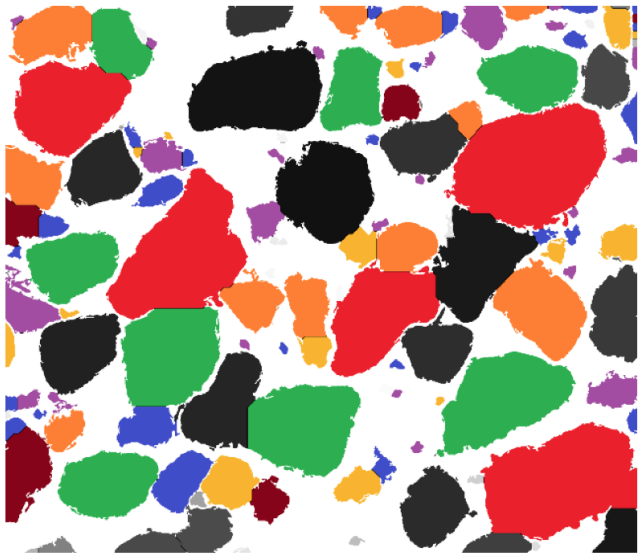

Figure 7-13: Illustration of region growing based on the local maxima identification shown in Figure 7-12

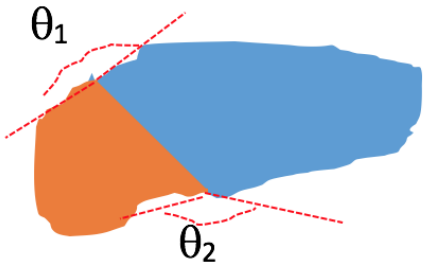

Figure 7-14: The contact angle between two grains in 2D.

Figure 7-14 shows two contact angle for the two grains in 2D. Obviously the bigger the contact angle is, the more likely the two grains should be merged. In 3D simply we can define such contact angle in the three orthogonal planes. To be more robust, we use the average contact angle with a pre-defined threshold to determine whether two grains should be merged. After merging two grains (Figure 7-15) into a single grain, and this grain will be further checked with any other neighbouring grains to decide if merging needs to be carried out.

Grain Quantification.

***Major axes*:** For each grain we can define two or three major axes. In 2D, the longest segment in a grain is defined as the primary axis, and the orthogonal segment to the primary axis is defined as a secondary axis. In 3D, the longest segment of a grain in XY, XZ or YZ planes is referred as the primary axis and the plane is called primary plane, and the longest segment on the orthogonal planes to the primary plane is defined as the second axis, and similarly we have

the third axis. Figure 7-16 shows an example of the primary axes of all identified grains. With major axes, it is handy to measure grain orientation or sorting patterns.

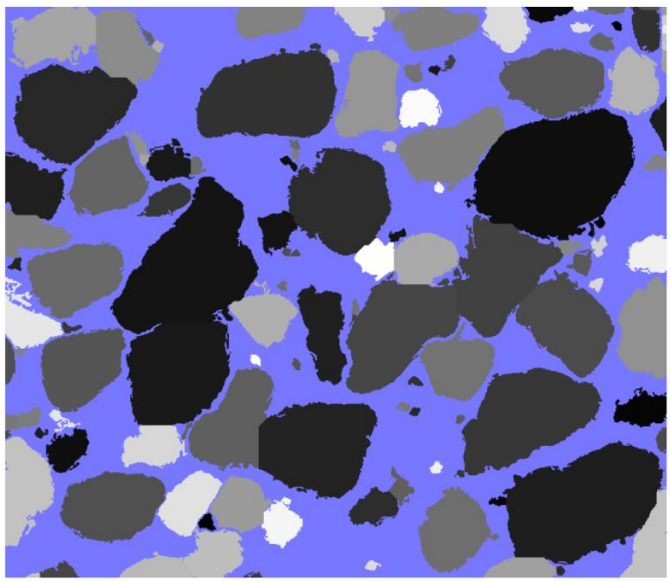

Figure 7-15: Merged grains with pre-defined threshold 180^0.

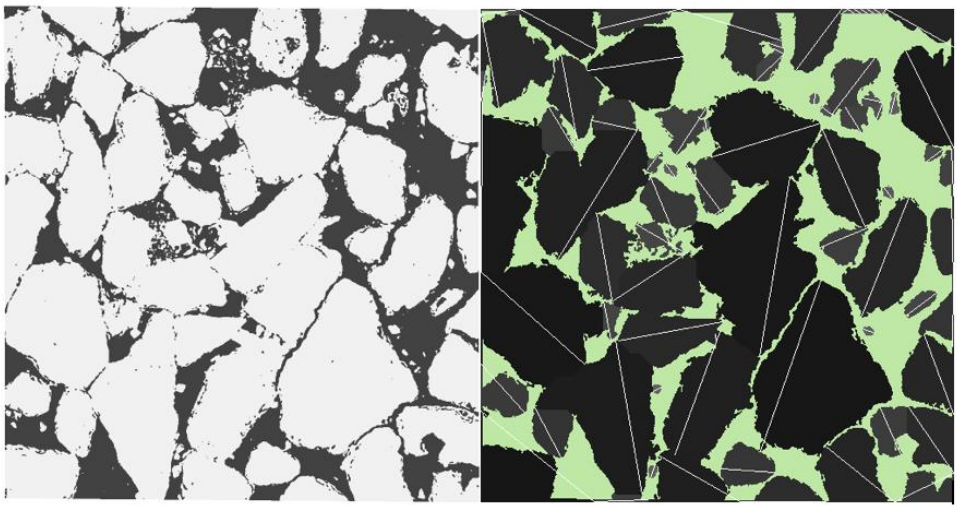

Figure 7-16: Primary axis of grains.

Grain size: For each grain, the original seed or the seed of the biggest SED values among all merged grain seeds can be defined as its centre. The corresponding SED values on grain centres can then be defined as its inscribed radii, further we have the size distribution (Figure 7-17).

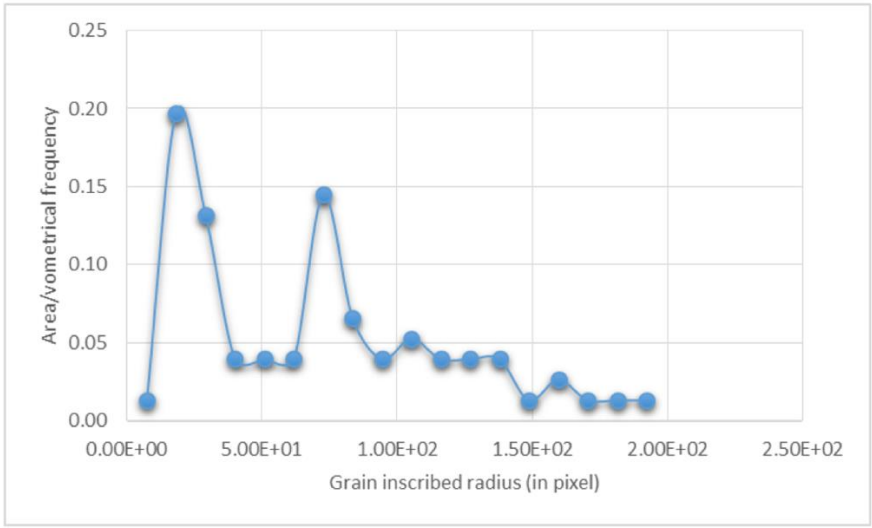

Figure 7-17: Grain size distribution

***Convexity*:** The convexity, S, of an object (grain) is defined as the ratio of the object volume to the volume of the convex hull of the object. The convex hull of an object can be formed by a method called Jarvis's March (Parker J.R.).

Shape: Let Q be the boundary pixels of the object. The shape feature, U, is defined as

$$U = \frac{|Q|^3}{64\pi V^2}$$

Where |·| denotes the number of elements in a set.

***Circularity*:** Let p denote the centre of an object, then the distance between an object voxel and the centre can be described as d. The circularity, C, is defined as

C = mean (d) / stddev(d)

References.

Jiang, Z., Wu, K., Couples, G., van Dijk, M. I. J., Sorbie, K. S., Ma, J., 2007, Efficient extraction of networks from three-dimensional porous media: Water Resources Research, v. 43, no 12, p. W12S03

Serra, J., 1982, Image Analysis and Mathematical Morphology: Academic Press, New York

7.3 Appendix C. Grès de Peïra Cava Master Correlaton

Due to its outsized dimensions, the master correlation panel (Grès de Peïra Cava) of the beds studied to analysis lateral and vertical facies changes in massive sand depositing flow is provided in a CD affixed to this volume.

7.4 Appendix D. REV Table For Image Analysis

Table 7-1: Image dimensions, input parameters for the REV calculation according the van den Berg et al. (2003), and the final image size. Values in red indicate maximum length of possible for that image due to limited rock sample size. Dash (-) in the REV column indicates that no REV was calculated and the whole image was taken for analysis.

	Image Size				REV Calculation after van Den Berg et al. (2003)						Final Image Size (Pixel)	
Sample	x (pixel)	y (pixel)	x (cm)	y (cm)	REA Glass	Mean Dig. Glass	Mean Dig. Sample	Res Glass	Res Sample	REV (pixel)	x	y
1a	14621.5	24438.5	20.1	33.6	1300^2	350	125	5.38	0.6870	6080	7585	5211
1.1aa	39339	53173	26.63	35.78	1300^2	350	725	5.38	0.6769	14870	14921	14902
2a	18994	23655	26.16	32.67	1300^2	350	125	5.38	1.3770	3034	7875	5150
2.2a	30841	41637	21.03	28.32	1300^2	350	725	5.38	0.6819	14762	15085	14905
3a	17038	23698	23.36	32.36	1300^2	350	125	5.38	1.3710	3048	7500	5009
4a	37461	48171	25.69	32.98	1300^2	350	500	5.38	0.6858	12189	12465	12527
5a	36643	55127	25.23	37.64	1300^2	350	500	5.38	0.6885	12140	12506	12514
6a	36406	56409	24.76	38.88	1300^2	350	500	5.38	0.6801	12291	12513	12522
7a	37101	48499	25.23	33.29	1300^2	350	500	5.38	0.6800	12292	12695	12640
8a	36408	47247	24.76	32.05	1300^2	350	500	5.38	0.6800	12292	12519	12524
9a	35239	54634	23.83	36.71	1300^2	350	420	5.38	0.6762	11329	11404	11408
10a	21946	54774	14.97	37.02	1300^2	350	420	5.38	0.6821	11231	11362	11395
11a	38780	49338	26.16	33.29	1300^2	350	545	5.38	0.6745	12937	13060	13036
12a	38458	45301	26.16	31.11	1300^2	350	545	5.38	0.6802	12830	13504	13074
13a	37284	45903	26.69	31.43	1300^2	350	707	5.38	0.7158	13885	14005	14004
14a	34626	51290	23.83	35.15	1300^2	350	707	5.38	0.6882	14443	14526	14533
15a	48183	27323	32.5	18.43	1300^2	350	707	5.38	0.6745	14737	15577	1550
16a	28841	54129	18.95	35.43	1300^2	350	545	5.38	0.6570	13282	15017	15091
17a	28053	49865	19.17	33.91	1300^2	350	545	5.38	0.6833	12771	15017	15032
18a	32165	50654	21.96	34.22	1300^2	350	545	5.38	0.6827	12783	15125	15042
19a	33968	43213	23.36	29.56	1300^2	350	1000	5.38	0.6877	17190	26630	30040
20a	28129	45115	19.17	30.49	1300^2	350	1000	5.38	0.6815	17346	18042	18011
21a	22984	48095	15.44	32.05	1300^2	350	840	5.38	0.6718	16129	16541	16527
22a	34941	51896	23.83	35.15	1300^2	350	840	5.38	0.6820	15887	17037	17106
23a	33909	51188	23.36	34.84	1300^2	350	707	5.38	0.6889	14429	17388	17259
24a	28000	47170	19.17	32.05	1300^2	350	500	5.38	0.6846	12209	15061	15064
25a	30764	49618	21.03	33.6	1300^2	350	1500	5.38	0.6835	21180	21272	21227
26a	30342	46672	20.56	31.11	1300^2	350	1500	5.38	0.6776	21367	25038	25057
27a	27249	37805	27.08	37.4	1300^2	350	1500	5.38	0.9937	14569	17037	17011
28a	30445	41944	26.39	35.92	1300^2	350	1500	5.38	0.8668	16703	19560	19508
29a	32423	48910	21.96	32.98	1300^2	350	1000	5.38	0.6772	17454	21518	21502
30a	36320	52401	24.76	35.37	1300^2	350	707	5.38	0.6817	14581	15006	15010
31a	29292	48226	20.1	32.67	1300^2	350	354	5.38	0.6861	10250	14660	14663
32a	27865	49093	19.17	33.6	1300^2	350	354	5.38	0.6879	10224	15004	15046
33a	28796	12843	37.9	16.86	1300^2	350	354	5.38	1.3161	-	27316	11085
34a	31987	45710	21.96	31.11	1300^2	350	1410	5.38	0.6865	20447	21063	25985
35a	25188	50050	17.3	34.22	1300^2	350	1410	5.38	0.6868	20438	20572	20577
36a	26481	50626	18.23	34.22	1300^2	350	1000	5.38	0.6884	17172	17099	17178
37a	36506	49054	24.76	33.29	1300^2	350	840	5.38	0.6782	15975	15559	15567
1b	40184	54780	27.090	36.7100	1300^2	350	125	5.38	0.6741	12398	18389	18317
1.1b	48839	34701	32.94	23.41	1300^2	350	125	5.38	0.6745	12396	18339	18280
2b	36899	44393	25.23	30.18	1300^2	350	125	5.38	0.6837	12224	15136	15123
3b	37042	52358	25.23	35.47	1300^2	350	125	5.38	0.6811	12272	18181	18053
4b	33101	55776	22.43	37.64	1300^2	350	500	5.38	0.6776	12336	16067	16008
5b	32378	54571	21.96	36.71	1300^2	350	500	5.38	0.6782	12325	17550	16812
6b	35980	61932	24.29	41.37	1300^2	350	500	5.38	0.6751	12382	16532	16591
7b	27381	33832	18.7	23.34	1300^2	350	500	5.38	0.683	12240	16217	16289
8b	36244	47370	24.76	32.36	1300^2	350	500	5.38	0.683	12236	16777	16757
9b	29532	61046	20.1	41.37	1300^2	350	420	5.38	0.6806	11256	16546	16220
10b	26253	67705	18.23	45.72	1300^2	350	420	5.38	0.6943	11033	16651	16569
11b	34443	53151	23.36	35.78	1300^2	350	545	5.38	0.6872	12868	16776	16428
12b	39825	49397	27.09	33.6	1300^2	350	545	5.38	0.6802	12830	16622	16557
13b	31180	46461	21.03	31.43	1300^2	350	1000	5.38	0.6744	17527	18109	18047
14b	39474	43544	39474	43544	1300^2	350	800	5.38	0.6746	15673	16381	16392
15b	48183	27323	32.5	18.43	1300^2	350	707	5.38	0.6745	14737	18585	18085
16b	37517	42255	25.3	28.5	1300^2	350	545	5.38	0.6743	12941	15128	15172
17b	33654	49622	22.7	33.47	1300^2	350	545	5.38	0.6745	12939	15113	15119
18a	47851	33832	32.27	22.82	1300^2	350	545	5.38	0.6743	7621	7666	8516
19b	51499	21884	34.74	14.76	1300^2	350	1000	5.38	0.6745	17525	18385	27659
20b	49785	34584	33.58	23.33	1300^2	350	1000	5.38	0.6745	17527	18098	18099
21b	24604	54479	16.59	36.74	1300^2	350	840	5.38	0.6742	16068	16519	16763
22b	14403	54557	9.71	36.8	1300^2	350	840	5.38	0.6741	16071	**11807**	23559
23b	36416	43599	24.56	29.41	1300^2	350	707	5.38	0.6744	14738	17026	17021
24b	33739	28568	22.76	19.27	1300^2	350	707	5.38	0.6746	14735	15571	15550
25b	28828	37553	19.44	25.33	1300^2	350	1500	5.38	0.6743	21471	20312	27259
26b	28828	37553	19.44	25.33	1300^2	350	1500	5.38	0.6743	21471	**21359**	22588
27b	42045	31226	28.36	21.06	1300^2	350	1500	5.38	0.6745	21465	**18376**	**19277**
28b	37525	33761	25.31	22.77	1300^2	350	1500	5.38	0.6744	21466	**19512**	**19532**
29b	26165	32053	17.65	21.62	1300^2	350	1000	5.38	0.6745	17525	18068	20538
30b	43369	36250	29.25	24.45	1300^2	350	707	5.38	14738	14738	15176	15007
31b	30638	45935	20.66	30.98	1300^2	350	354	5.38	0.6743	10430	19512	19532
32b	50204	27850	33.86	18.78	1300^2	350	354	5.38	0.6744	10429	13529	13424
33b	34407	49880	23.21	33.64	1300^2	350	354	5.38	0.6745	10427	25120	35048
34b	36202	45142	24.42	30.45	1300^2	350	354	5.38	0.6745	10427	21165	24530
35b	35257	48461	23.78	32.69	1300^2	350	1410	5.38	20812	20812	21696	21240
36b	38845	52892	26.2	35.67	1300^2	350	1000	5.38	0.6744	17527	18107	18566
37b	34332	33269	23.16	22.44	1300^2	350	350	5.38	0.6746	10367	13175	13809

7.5 Appendices E. East Brae

7.5.1 Appendix E.1. East Brae Master Sedimentary Log Panel

Due to its outsized dimensions, the master sedimentary log of all the cores logged in the East Brae is provided in a CD affixed to this CD.

7.5.2 Appendix E.2. Description of the Wireline Character

A brief summary description of the wireline character for each depositional element is given below. The motif was used in the interpretation of the depositional environment of the East Brae Field.

Depositional Element One. Wireline character for element one displays a predominantly blocky shape for the GR log, but become serrated in areas where mudstones and chaotic facies thickness is above log resolution (Figure 7-18). GR API values are suppressed (mean API of 37) across the field, allowing easy identification of this element in uncored intervals. Density and neutron logs also display a blocky character in most wells and show a close proximity to each other. This is due to the presence of gas in the reservoir, which suppresses the density values (mean 2.3 g/cm^3) and locally causes the neutron curve to crossover. Locally, the two curves become serrated where there are minor intercalations of mudstones, chaotic facies and in some cases abundant mudstone clasts (e.g. Well 16/03b-03, depth 13700 – 13750 md) and carbonate cemented layers. Similar patterns are also repeated in the sonic log, where the transit time values are the lowest compared to other depositional element. The resistivity curves in contrast do not show a consistent trend across the field. However, in the element one intervals of wells 16/03a-E1 and 16/03b-7, resistivity curve character is blocky with generally high values. Where each curve displays a blocky character, the base and top transition is sharp.

Depositional Element Two. Wireline character is similar to element one (Figure 7-18), but the GR curve displays a uniform blocky character on a smaller scale. The lower sand: shale ratio in this element is reflected by an increasingly serrated GR curve with high API values (Figure 7-18). Similar distinguishing trends to element one are also observed in the density and neutron curves for element two. However, due to the increased mud content, the sonic values are higher compared to element one.

Depositional Element Three. Element three is typically sandwiched between element one, indicating rapid shifting of the axis of sedimentation. These transitions are sharp, occurring over less than a metre. Rarely, a gradual off-axis sedimentation is recorded whereby element two and four occur above or below element three. These transitions are reflected in the GR and

resistivity curve character, such that element three displays a predictable symmetrical hour glass shape when alternating with element one, and a funnel or bell shape when transitioning to element two or four, respectively (Figure 7-18). Crudely similar trends are also observed in the density curve, where it is not greatly affected by the gas, as well as the sonic curve. More commonly, however, a shift to higher density values is observed compared to element one and two, most likely due to the increased mud content which is less likely to be affected by the presence of gas.

Depositional Element Four. Wireline log response for element four is characterised by prominent high-gamma intervals in all wells (mean API of 154 with SD of 45; Figure 7-18). Along intervals of thin interbedded sand and mud layers, the response becomes serrated depending on the thickness of the sand layers, with layers below the tool resolution resulting in averaging of the GR values. The bulk density (2.05 and 2.71 g/cm^3, with a mean density of 2.47 g/cm^3) and neutron (0.07 and 0.26 pu.) tools display a clear separation; density readings are on average higher in element four due to the presence of gas in the thick sand layers that constitute elements one and two. Sonic velocity values are also correspondingly higher, indicative of uniform mudstone layers, while resistivity readings are on average lower than the surrounding sand-rich intervals.

Depositional Element Five. Since element five is found associated with element four, and due to its mud-rich nature, the overall log responses are similar to element four. However, in more sand-rich intervals GR values are suppressed, resulting in a serrated gamma response (e.g. Well 16/03a-E1, depth 13535ft to 13551ft md). In uncored wells, it is very difficult to determine the presence of element five.

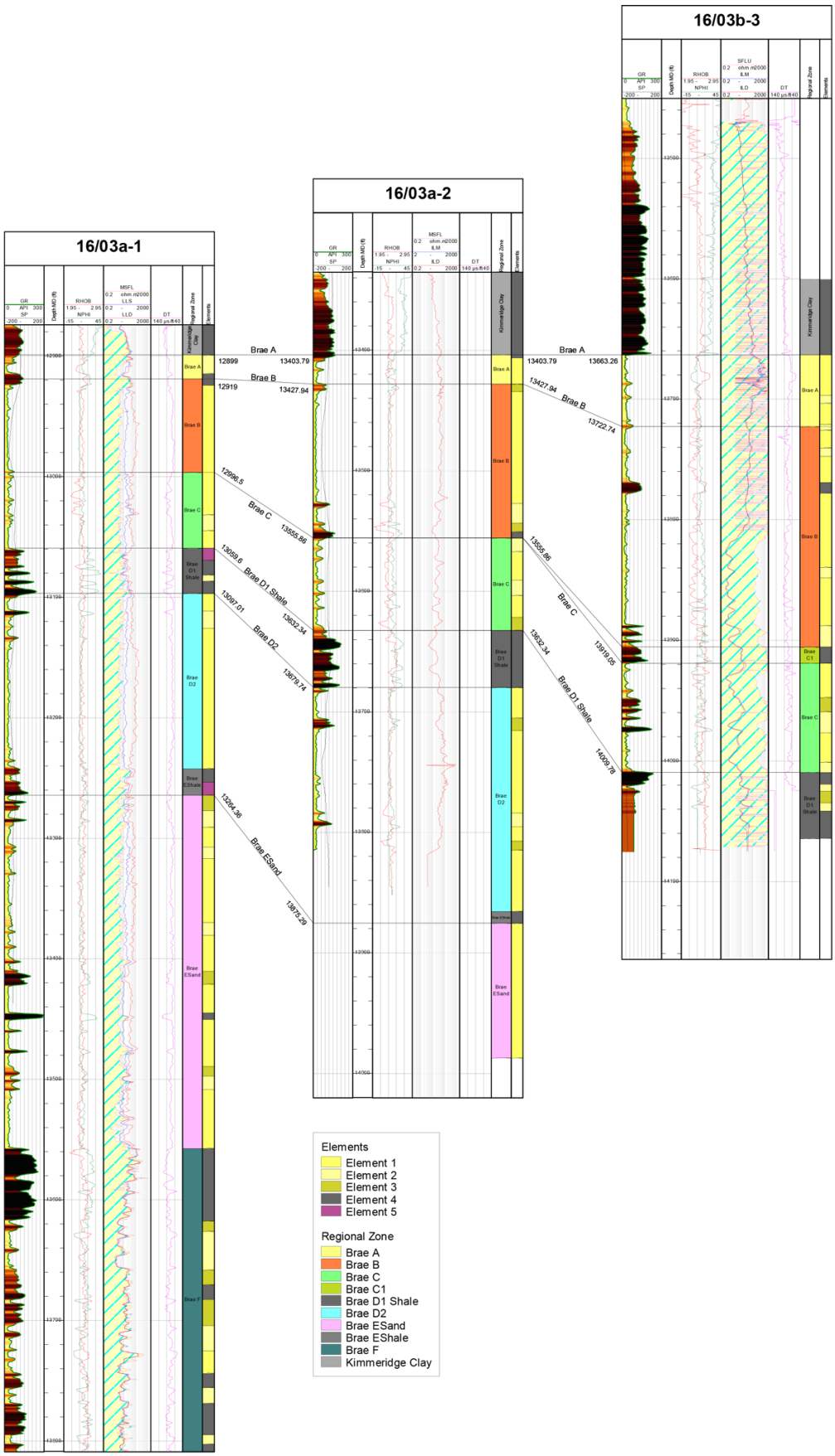

Figure 7-18: Well logs from three cored wells showing the log character in the constituent parts of the MSFA. The log character is correlated to uncored wells to infer spatial variability in sediment facies and depositional environment.

7.5.3 Appendix E.3. Heterogeneity Curves for all East Brae Wells

For succinctness, only the heterogeneity curves from wells 16/07a-1, 03b-7 and 3a-E20 were presented in the main text. The results from the remaining wells are provided in a CD affixed to the thesis. The curves are presented according to individual window sizes (10ft, 20ft and 50ft) as well as summary panels at 1:1000 and 1:2500 scale.

7.5.4 Appendix E.4. Modified Lorenz Plots

Modified Lorenz Plots of remaining wells not discussed in the main text.

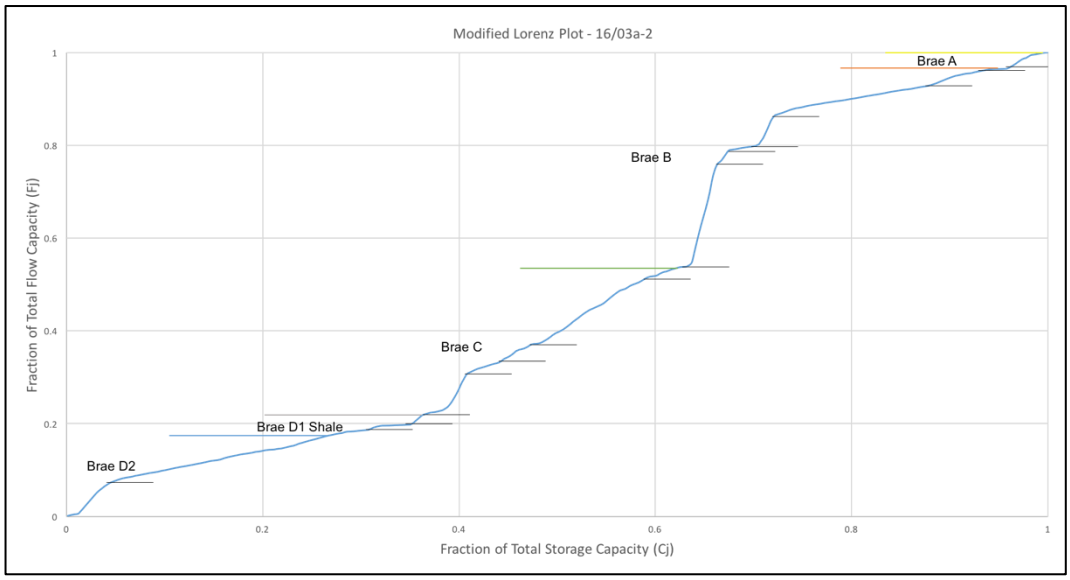

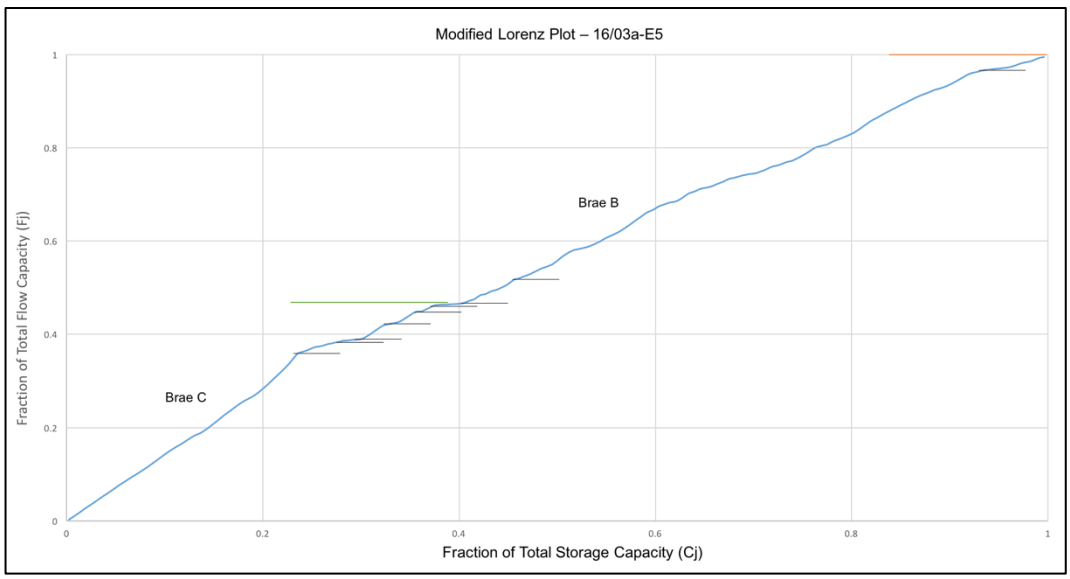

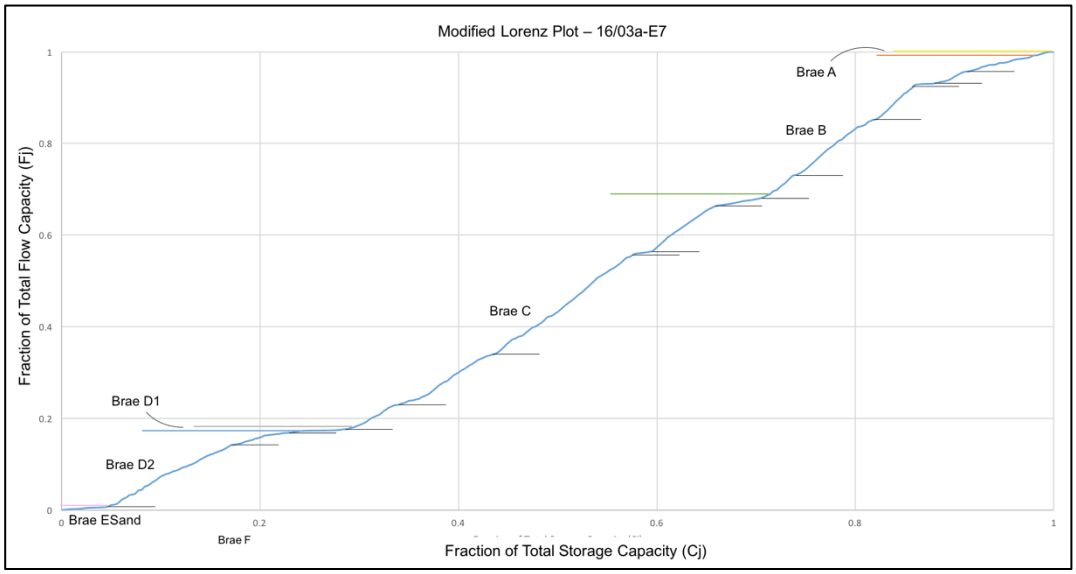
Modified Lorenz Plot – 16/03a-E7
Fraction of Total Flow Capacity (Fj)
Fraction of Total Storage Capacity (Cj)
Brae A
Brae B
Brae C
Brae D1
Brae D2
Brae ESand
Brae F

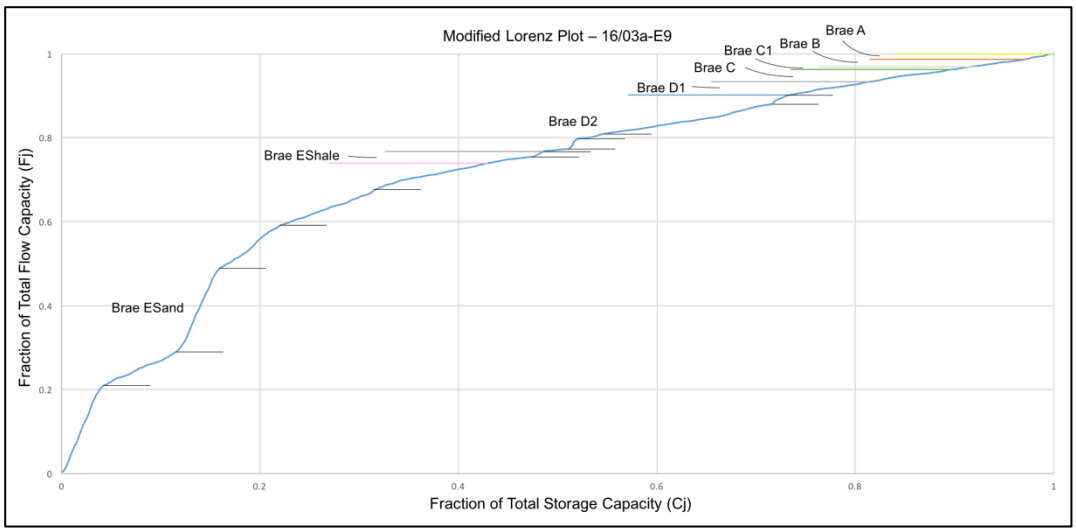
Modified Lorenz Plot – 16/03a-E9
Fraction of Total Flow Capacity (Fj)
Fraction of Total Storage Capacity (Cj)
Brae A
Brae B
Brae C1
Brae C
Brae D1
Brae D2
Brae EShale
Brae ESand

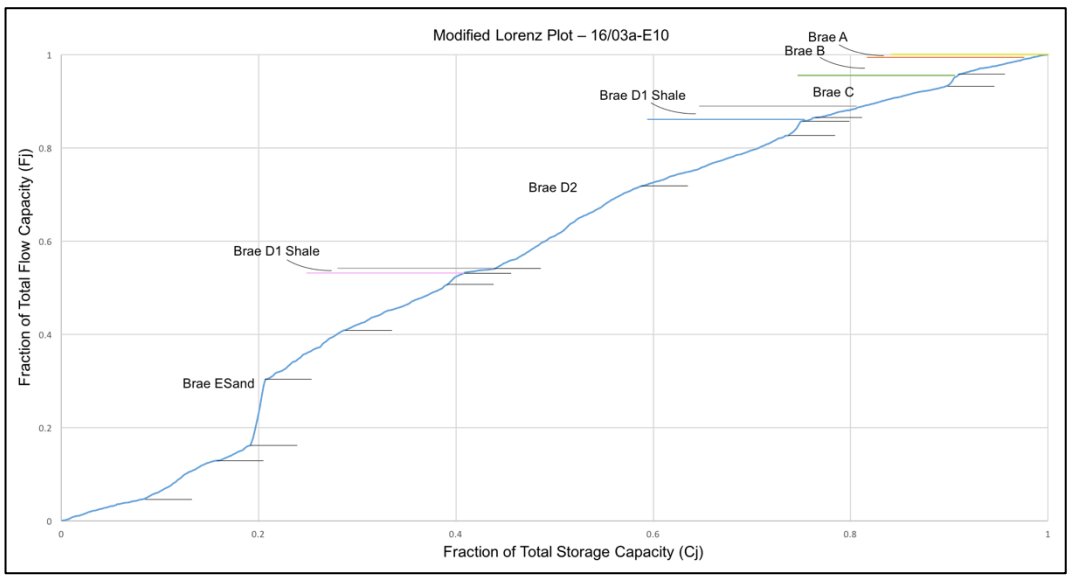
Modified Lorenz Plot – 16/03a-E10
Fraction of Total Flow Capacity (Fj)
Fraction of Total Storage Capacity (Cj)
Brae A
Brae B
Brae C
Brae D1 Shale
Brae D2
Brae D1 Shale
Brae ESand

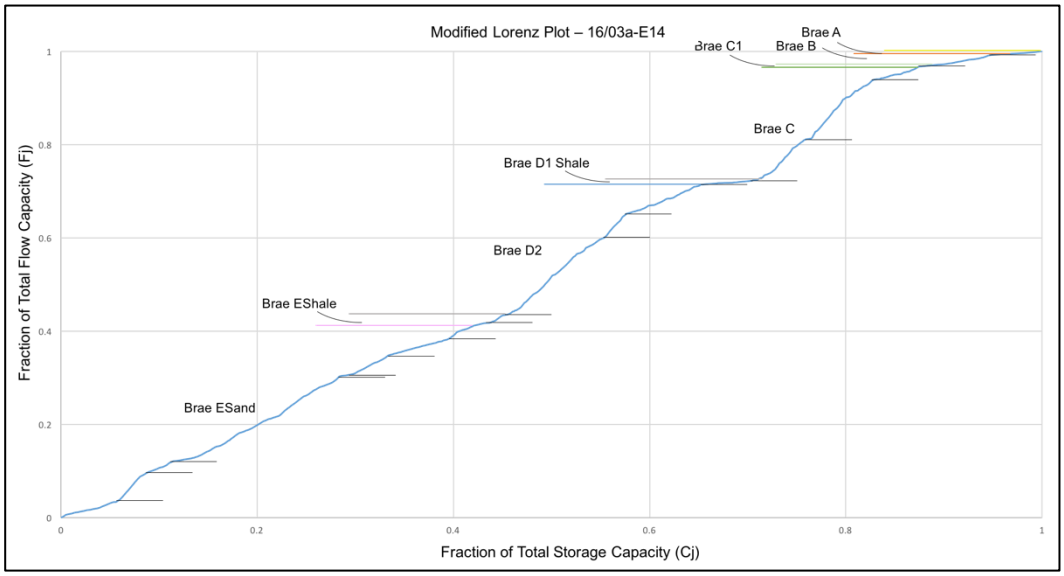
Modified Lorenz Plot – 16/03a-E14
Brae A
Brae C1
Brae B
Brae C
Brae D1 Shale
Brae D2
Brae EShale
Brae ESand
Fraction of Total Flow Capacity (Fj)
Fraction of Total Storage Capacity (Cj)
0
0.2
0.4
0.6
0.8
1

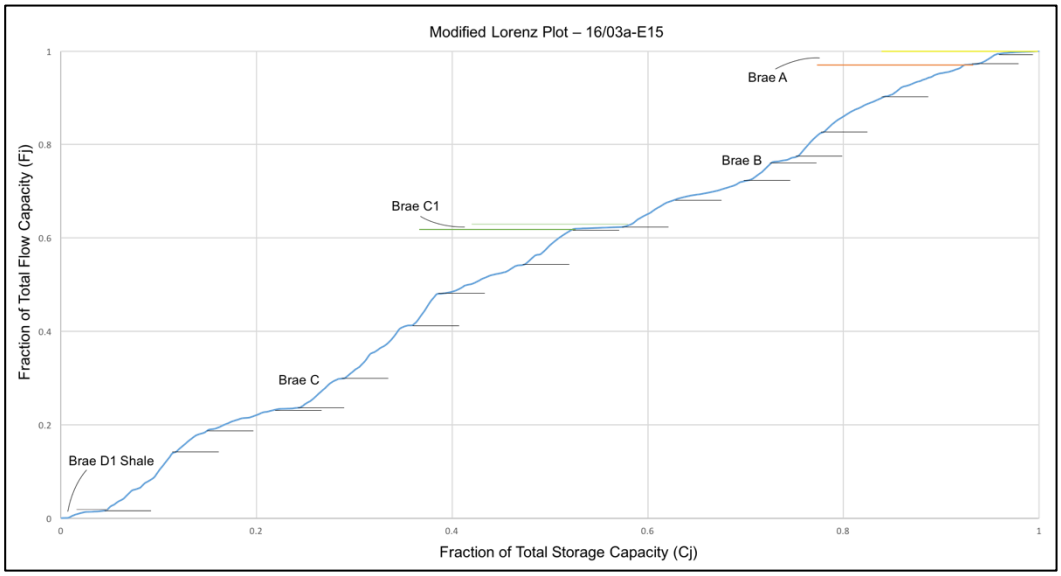
Modified Lorenz Plot – 16/03a-E15
Brae A
Brae B
Brae C1
Brae C
Brae D1 Shale
Fraction of Total Flow Capacity (Fj)
Fraction of Total Storage Capacity (Cj)
0
0.2
0.4
0.6
0.8
1

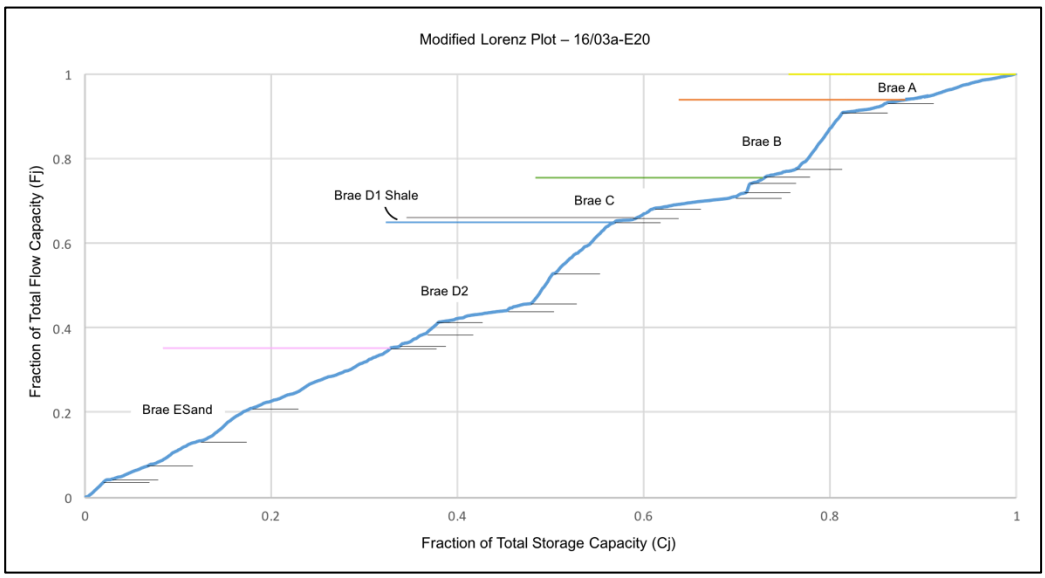
Modified Lorenz Plot – 16/03a-E20
Brae A
Brae B
Brae D1 Shale
Brae C
Brae D2
Brae ESand
Fraction of Total Flow Capacity (Fj)
Fraction of Total Storage Capacity (Cj)
0
0.2
0.4
0.6
0.8
1

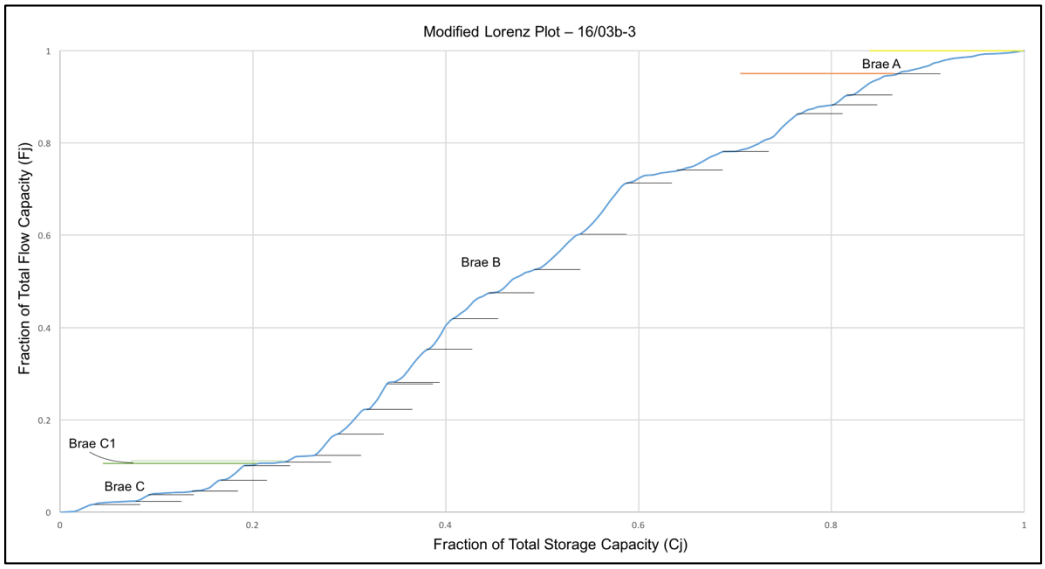
Modified Lorenz Plot – 16/03b-3
Fraction of Total Flow Capacity (Fj)
Fraction of Total Storage Capacity (Cj)
Brae A
Brae B
Brae C1
Brae C
0
0.2
0.4
0.6
0.8
1

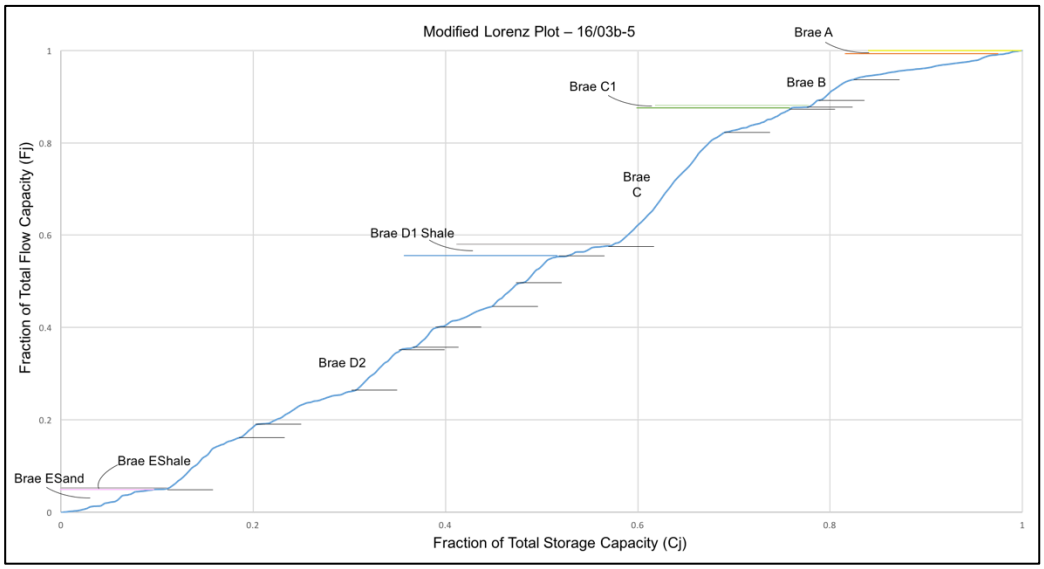
Modified Lorenz Plot – 16/03b-5
Fraction of Total Flow Capacity (Fj)
Fraction of Total Storage Capacity (Cj)
Brae A
Brae C1
Brae B
Brae C
Brae D1 Shale
Brae D2
Brae EShale
Brae ESand
0
0.2
0.4
0.6
0.8
1

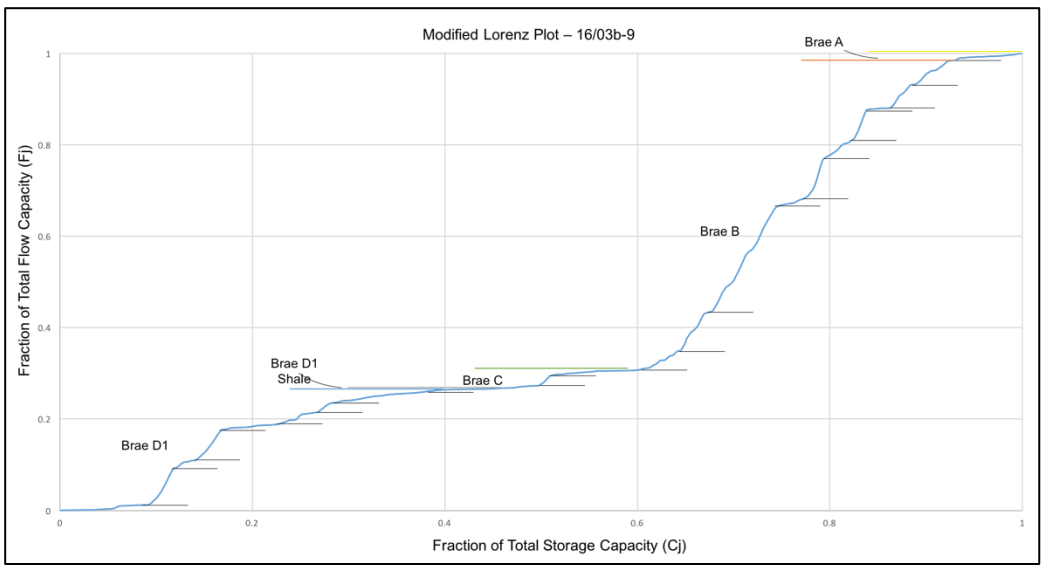
Modified Lorenz Plot – 16/03b-9
Fraction of Total Flow Capacity (Fj)
Fraction of Total Storage Capacity (Cj)
Brae A
Brae B
Brae D1 Shale
Brae C
Brae D1
0
0.2
0.4
0.6
0.8
1

7.6 Appendix F. MatLab Code For Heterogeneity Curves

To generate the heterogeneity curves, a moving window was used, in which the window was moved one sample point at a time as the calculations are performed. The heterogeneity value for a given interval is plotted at the mid-point of the interval. All computations are performed in Matlab. While the code was generated as part of this study, the first author gave permission to Nur Yusrina Yakub to use it for a case study to determine optimum layering scheme for reservoir modelling and upscaling. Full reference is: Yakub, N. Y., 2017, Optimal layering scheme in a reservoir by quantifying the heterogeneity coefficient [MSc Independent Project]: Heriot-Watt University, 52 p.

```
%% Program to calculate Lorez coefficient from the LOG data
% Load the log data
clc
clear all
load ('16-3b-9.mat')
%% Create Variables and get input data
disp ('This program calculate the moving window log for Heterogeneity Cofeeicients')
disp('Minimum Points = 20')
disp('Minimun Interval = 10Ft.')
Interval = input('Interval Length \n');
minpoint =20;
points = length(Log1);
i=1;j=1;loop =1;
if Interval >= 10
 while  j<=points

  %% Define the points for which calculation has to be done
  currentpoint =i; endpoint =j;
  startdepth = Log1(i,1); enddepth = Log1(j,1); valid=0;
  while (enddepth-startdepth)<=Interval && j <= points-1
     if(Log1(j,2)~= -9999)
        valid = valid+1;
     end
     j=j+1;
     enddepth = Log1(j,1);
  end
  j= j-1;
   if (j == (points-1))
      j = points;
   end
    enddepth = Log1(j,1);
%  i , j, valid ,(enddepth - startdepth)
    if (valid >= minpoint)
       DepthAvg(loop,1) = (Log1(i,1)+Log1(j,1))/2;
```

```
        kh = zeros(valid-1,1);
        storativity = zeros(valid-1,1);
        count=1;
         for p = i:j-1
            if(Log1(p,2)~= -9999)
              % Find the next valid point
                q=p+1;
                while (Log1(q,2)== -9999 && q<= j)
                   q=q+1;
                end
             kh(count)= Log1(p,2)* (Log1(q,1) -Log1(p,1));
             storativity(count) = Log1(p,3)* (Log1(q,1) -Log1(p,1));
             count = count+1;
            end
         end

%% Calculate Lorenz Coefficient
    kh = sort(kh);
    storativity = sort(storativity);
    sumkh = sum(kh);
    sumstorage= sum(storativity);
    kh = kh./sumkh;
    storativity = storativity./sumstorage;
    khtotal = zeros(count,1);stortotal = zeros (count,1);
    khtotal(2:count,1)= kh(1:count-1,1);
    stortotal(2:count,1)= storativity(1:count-1,1);

   for k = 2:count
       khtotal(k)= khtotal(k) +khtotal(k-1);
       stortotal(k)= stortotal(k)+stortotal(k-1);
   end



%% Calculate area under the curve
   area = zeros(count,1);
   for l = 1:count-1
       area(l) = area(l)+0.5*(stortotal(l+1)+stortotal(l))*(khtotal(l+1)-khtotal(l));
   end
  LorenzCoeff(loop,1) = (sum(area)-0.5)*2;

% i , j , valid, DepthAvg
%          khtotal
%          stortotal
%          count
%          loop
%   pause
```

```
  %% Calculate CV and DParsons Coeff
% Make an array of valid poro and perm
poro = zeros(valid,1);perm = zeros(valid,1);
counter =1;
 for qq = i:j
  if (Log1(qq,2)~= -9999 && Log1(qq,3)~= -9999)
        perm(counter) = Log1(qq,2); poro(counter)=Log1(qq,3);
        counter = counter +1;
  end
 end
%CV @permeability

  stdev= std(perm);
  Avg = mean(perm);
  CVperm(loop,1)= stdev/Avg;

%CV @POROSITY
  stdev= std(poro);
  Avg = mean(poro);
  CVporo(loop,1)= stdev/Avg;

%   Dykstra -Parsons Coefficient
   k = log(perm);
   k = sort(k);
   Med= median(k);
   Per = prctile(k,15.9);
   DParsons(loop,1) = (Med-Per)/Med;

   clear poro perm
   loop = loop+1;
    end
   i=i+1; j=i;


%%save ('Well-16-3a-2-Win-25ft');

 end
 figure(2);subplot(1,4,1); plot(LorenzCoeff,DepthAvg); title('LorenzCoeff');
 subplot(1,4,2); plot(DParsons,DepthAvg); title('Dykstra-Parsons');
 subplot(1,4,3); plot(CVperm,DepthAvg); title('Coeff of Variation-PERM');
 subplot(1,4,4); plot(CVporo,DepthAvg); title('Coeff of Variation-PORO');

else
 disp('Input interval is less than the minm')
end
```

7.7 Appendix G. Application of Heterogeneity Curves in Modelling

A SPE style paper was written by Nur Yurina Yakub (under the supervision of Urval Satish Patel and Ankesh Anupam) which highlighted the use of the heterogeneity curves in optimising layering in static reservoir models. This paper was based on the MSc thesis submitted by Nur Yusrina Yakub as partial fulfilment of a degree in MSc Petroleum Engineering (Yakub, N. Y., 2017, Optimal layering scheme in a reservoir by quantifying the heterogeneity coefficient [MSc Independent Project]: Heriot-Watt University, 52 p.). A copy of the SPE style paper is provided in the attached CD.

Bibliography

Aas, T. E., Howell, J. A., Janocko, M., And Midtkandal, I., 2010, Re-Created Early Oligocene Seabed Bathymetry And Process-Based Simulations Of The Peïra Cava Turbidite System: Journal Of The Geological Society, V. 167, No. 5, P. 857-875.

Adams, S. J., 2005a, Core-To-Log Comparison-What's A Good Match?, SPE Annual Technical Conference And Exhibition: Dallas. Texas, Society Of Petroleum Engineers, P. 1 - 7.

-, 2005b, Quantifying Petrophysical Uncertainties, SPE Asia Pacific Oil And Gas Conference And Exhibition: Jakarta, Indonesia, Society Of Petroleum Engineers, P. 1 - 6.

Albertão, G. A., Mulder, Thierry, M., And Eschard, R., 2011, Impact Of Salt-Related Palaeotopography On The Distribution Of Turbidite Reservoirs: Evidence From Well-Seismic Analysis And Structural Restorations In Brazalian Offshore: Marine And Petroleum Geology, V28, P. 1023-1046.

Al Ja'Aidi, O. S., Mccaffrey, W. D., And Kneller, B. C., 2004, Factors Influencing The Deposit Geometry Of Experimental Turbidity Currents: Implications For Sand-Body Architecture In Confined Basins: Geological Society, London, Special Publications, V. 222, No. 1, P. 45 - 58.

Alcalá, F. J., Guerrera, F., Martín-Martín, M., Raffaelli, G., And Serrano, F., 2013, Geodynamic Implications Derived From Numidian-Like Distal Turbidites Deposited Along The Internal–External Domain Boundary Of The Betic Cordillera (S Spain): Terra Nova, V. 25, No. 2, P. 119-129.

Alharbi, A. M., 2013, Experimental Evaluation Of The Effect Of Carbonate Heterogeneity On Oil Recovery To Water And Gas Injections [Doctor Of Philosophy: University Of Calgary.

Allen, J. R. L., 1964, Primary Current Lineation In The Lower Old Red Sandstone (Devonian), Anglo-Welsh Basin: Sedimentology, V. 3, No. 2, P. 89-108.

-, 1982, Sedimentary Structures: Their Character And Physical Basis, Elsevier Scientific Publishing Company, Development In Sedimentology, 593/663 P.:

-, 1991, The Bouma Division A And The Possible Duration Of Turbidity Currents: Journal Of Sedimentary Research, V. 61, No. 2, P. 291-295.

Allen, P. A., And Allen, J. R., 2004, Basin Analysis: Principles And Application, Blackwell Publishing, 560 P.:

Alpay, O. A., 1972, A Practical Approach To Defining Reservoir Heterogeneity: Journal Of Petroleum Technology, P. 841 - 848.

Amaefule, J. O., Altunbay, M., Tiab, D., Kersey, D. G., And Keelan, D. K., 1993, Enhanced Reservoir Description: Using Core And Log Data To Identify Hydraulic (Flow) Units And Predict Permeability In Uncored Intervals/Wells, 68th Annual Technical Conference And Exhibition Of The Society Of Petroleum Engineers: Houston, Texas, Society Of Petroleum Engineers, P. 205 - 220.

Amour, F., Mutti, M., Christ, N., Immenhauser, A., Agar, S. M., Benson, G. S., Tomás, S., Alway, R., And Kabiri, L., 2012, Capturing And Modelling Metre-Scale Spatial Facies Heterogeneity In A Jurassic Ramp Setting (Central High Atlas, Morocco): Sedimentology, V. 59, No. 4, P. 1158-1189.

Amy, L., Kneller, B., And Mccaffrey, W. D., 2000, Evaluating The Links Between Turbidite Characteristics And Gross System Architecture: Upscaling Insights From The Turbidite Sheet System Of Peira Cava, SE France: Deep-Water Reservoirs Of The World: Houston, SEPM, Gulf Coast Section, P. 1-15.

Amy, L. A., 2000, Architectural Analysis Of A Sand-Rich Confined Turbidite Basin: The Grass De Peira Cava, South-East France [Doctor Of Philosophy: University Of Leeds, 233 P.

Amy, L. A., Hogg, A. J., Peakall, J., And Talling, P. J., 2005a, Abrupt Transitions In Gravity Currents: Journal Of Geophysical Research: Earth Surface, V. 110, No. F3, P. 1 - 19.

Amy, L. A., Kneller, B. C., And Mccaffrey, W. D., 2007, Facies Architecture Of The Gres De Peira Cava, SE France: Landward Stacking Patterns In Ponded Turbiditic Basins: Journal Of The Geological Society, V. 164, No. 1, P. 143-162.

Amy, L. A., Mccaffrey, W. D., And Kneller, B. C., 2004, The Influence Of A Lateral Basin-Slope On The Depositional Patterns Of Natural And Experimental Turbidity Currents: Geological Society, London, Special Publications, V. 221, No. 1, P. 311-330.

Amy, L. A., Mccaffrey, W. D., And Talling, P. J., 2009, Special Issue Introduction: Sediment Gravity Flows – Recent Insights Into Their Dynamic And Stratified/Composite Nature: Marine And Petroleum Geology, V. 26, No. 10, P. 1897-1899.

Amy, L. A., Peachey, S. A., Gardiner, A. R., Pickup, G. E., Mackay, E., And Stephen, K. D., 2013, Recovery Efficiency From A Turbidite Sheet System: Numerical Simulation Of Waterflooding Using Outcrop-Based Geological Models: Petroleum Geoscience, V. 19, No. 2, P. 123 - 137.

Amy, L. A., Peakall, J., And Talling, P. J., 2005b, Density- And Viscosity-Stratified Gravity Currents: Insight From Laboratory Experiments And Implications For Submarine Flow Deposits: Sedimentary Geology, V. 179, No. 1, P. 5-29.

Amy, L. A., And Talling, P. J., 2006, Anatomy Of Turbidites And Linked Debrites Based On Long Distance (120× 30 Km) Bed Correlation, Marnoso Arenacea Formation, Northern Apennines, Italy: Sedimentology, V. 53, No. 1, P. 161-212.

Amy, L. A., Talling, P. J., Edmonds, V. O., Sumner, E. J., And Lesueur, A., 2006, An Experimental Investigation Of Sand–Mud Suspension Settling Behaviour: Implications For Bimodal Mud Contents Of Submarine Flow Deposits: Sedimentology, V. 53, No. 6, P. 1411-1434.

Amy, L. A., Talling, P. J., Peakall, J., Wynn, R. B., And Arzola Thynne, R. G., 2005c, Bed Geometry Used To Test Recognition Criteria Of Turbidites And (Sandy) Debrites: Sedimentary Geology, V. 179, No. 1, P. 163-174.

Apps, G., Peel, F., And Elliott, T., 2004, The Structural Setting And Palaeogeographical Evolution Of The Grès d'Annot Basin: Geological Society, London, Special Publications, V. 221, No. 1, P. 65.

Apps, G. M., 1987, The Evolution Of The Gres d'Annot Basin, S.W. Alps. [Ph.D: University Of Liverpool, 432 P.

Arnott, R. W. C., And Hand, B. M., 1989, Bedforms, Primary Structures And Grain Fabric In The Presence Of Suspended Sediment Rain: Journal Of Sedimentary Research, V. 59, No. 6, P. 1062 1069.

Arora, K., 2011, Geodesy, Figure Of The Earth, *In* Gupta, H., Ed., Encyclopedia Of Solid Earth Geophysics: Netherlands, Springer, P. 313 - 568.

Attia, A. M., And Shuaibu, H., 2015, Identification Of Barriers And Productive Zones Using Reservoir Characterization: International Advanced Research Journal In Science, Engineering And Technology, V. 2, No. 12, P. 8 - 23.

Baas, J. H., 2000, EZ-ROSE: A Computer Program For Equal-Area Circular Histograms And Statistical Analysis Of Two-Dimensional Vectorial Data: Computers & Geosciences, V. 26, No. 2, P. 153-166.

-, 2004, Conditions For Formation Of Massive Turbiditic Sandstones By Primary Depositional Processes: Sedimentary Geology, V. 166, No. 3, P. 293-310.

Baas, J. H., And Best, J. L., 2002, Turbulence Modulation In Clay-Rich Sediment-Laden Flows And Some Implications For Sediment Deposition: Journal Of Sedimentary Research, V. 72, No. 3, P. 336-340.

Baas, J. H., Best, J. L., And Peakall, J., 2011, Depositional Processes, Bedform Development And Hybrid Bed Formation In Rapidly Decelerated Cohesive (Mud–Sand) Sediment Flows: Sedimentology, V. 58, No. 7, P. 1953-1987.

Baas, J. H., Best, J. L., Peakall, J., And Wang, M., 2009, A Phase Diagram For Turbulent, Transitional, And Laminar Clay Suspension Flows: Journal Of Sedimentary Research, V. 79, No. 4, P. 162-183.

Baas, J. H., Hailwood, E. A., Mccaffrey, W. D., Kay, M., And Jones, R., 2007, Directional Petrological Characterisation Of Deep-Marine Sandstones Using Grain Fabric And Permeability Anisotropy: Methodologies, Theory, Application And Suggestions For Integration: Earth-Science Reviews, V. 82, No. 1, P. 101-142.

Baas, J. H., Manica, R., Puhl, E., And De Oliveira Borges, A. L., 2016, Thresholds Of Intrabed Flow And Other Interactions Of Turbidity Currents With Soft Muddy Substrates: Sedimentology, V. 63, No. 7, P. 2002-2036.

Baas, J. H., Manica, R., Puhl, E., Verhagen, I., And Borges, A. L. D. O., 2014, Processes And Products Of Turbidity Currents Entering Soft Muddy Substrates: Geology, V. 42, No. 5, P. 371-374.

Baas, J. H., Mccaffrey, W. D., Haughton, P. D. W., And Choux, C., 2005, Coupling Between Suspended Sediment Distribution And Turbulence Structure In A Laboratory Turbidity Current: Journal Of Geophysical Research: Oceans, V. 110, No. C11, P. 1 - 20.

Baas, J. H., Van Dam, R. L., And Storms, J. E. A., 2000, Duration Of Deposition From Decelerating High-Density Turbidity Currents: Sedimentary Geology, V. 136, No. 1, P. 71-88.

Baas, J. H., Van Kesteren, W., And Postma, G., 2004, Deposits Of Depletive High-Density Turbidity Currents: A Flume Analogue Of Bed Geometry, Structure And Texture: Sedimentology, V. 51, No. 5, P. 1053-1088.

Bagnold, R. A ., 1954, Experiments On A Gravity-Free Dispersion Of Large Solid Spheres In A Newtonian Fluid Under Shear: Proceedings Of The Royal Society Of London. Series A. Mathematical And Physical Sciences, V. 225, No. 1160, P. 49 - 63.

Bagnold, R. A,., 1962, Auto-Suspension Of Transported Sediment; Turbidity Currents: Proceedings Of The Royal Society Of London. Series A. Mathematical And Physical Sciences, V. 265, No. 1322, P. 315 - 319.

Barnes, H. A., 1999, The Yield Stress—A Review Or ‘Παντα Ρει’—Everything Flows?: Journal Of Non-Newtonian Fluid Mechanics, V. 81, No. 1, P. 133-178.

Barraud, J., 2006, The Use Of Watershed Segmentation And GIS Software For Textural Analysis Of Thin Sections: Journal Of Volcanology And Geothermal Research, V. 154, No. 1–2, P. 17-33.

Bates, C. C., 1953, Rational theory of delta formation: American Association of Petroleum Geologist: Bulletins, V. 37, N. 9, P. 2119-2162.

Batok Embanglian, E., 2013, An Investigation Of The Relationship Between Reservoir Quality And Heterogeneity In A North Sea, Clastic Reservoir: The Effect Of Measurement Resolution [Master Of Science In Petroleum Engineering: Imperial College London, 1 - 34 P.

Bear, D. C., And Weyl, P. K., 1973, Influence Of Texture On Porosity And Permeability Of Unconsolidated Sands: American Association Of Petroleum Geologists Bulletin, V. 57, No. 2, P. 349-369.

Biggin, A., Suttie, N., And Shaw, J., 2011, Paleomagnetic Field Intensity, *In* Gupta, H., Ed., Encyclopedia Of Solid Earth Geophysics: Netherlands, Springer, P. 919 - 1012.

Bjørlykke, K., 2010, Petroleum Geoscience: From Sedimentary Environments To Rock Physics., Chap. Introduction To Petroleum Geology, Berlin, Springer, 507 P.:

Blanchette, F., Strauss, M., Meiburg, E., Kneller, B., And Glinsky, M. E., 2005, High-Resolution Numerical Simulations Of Resuspending Gravity Currents: Conditions For Self-Sustainment: Journal Of Geophysical Research: Oceans, V. 110, No. C12, P. N/A-N/A.

Blatt, H. G., Middleton, G. V., And Murray, R. C., 1980, Origin Of Sedimentary Rocks, 2nd Eds, Engleswood Cliffs, New Jersey: Prentice-Hall.

Blott, S. J., And Pye, K., 2001, GRADISTAT: A Grain Size Distribution And Statistics Package For The Analysis Of Unconsolidated Sediments: Earth Surface Processes And Landforms, V. 26, No. 11, P. 1237-1248.

-, 2008, Particle Shape: A Review And New Methods Of Characterization And Classification: Sedimentology, V. 55, No. 1, P. 31-63.

Bonham-Carter, G., And Qiuming, C., 2008, Progress In Geomathematics, Berlin, Springer, 550 P.:

Bonnecaze, R. T., Huppert, H. E., And Lister, J. R., 1996, Patterns Of Sedimentation From Polydispersed Turbidity Currents: Proceedings: Mathematical, Physical And Engineering Sciences, V. 452, No. 1953, P. 2247-2261.

Borka, S., 2016, Markov Chains And Entropy Tests In Genetic-Based Lithofacies Analysis Of Deep-Water Clastic Depositional Systems: Open Geosciences, V. 8, No. 1, P. 45 - 51.

Bornemann, E., Doveton, J. H., And Clair, P. N. S., 1982, Lithofacies Analysis Of The Viola Limestone In South-Central Kansas, Kansas Geological Survey, V. 3.

Bouma, A. H., 1962, Sedimentology Of Some Flysch Deposits: A Graphic Approach To Facies Interpretation, Amsterdam, Elsevie.
-, 1990, Clastic Depositional Styles And Reservoir Potential Of Mediterranean Basins: AAPG Bulletin, V. 74, No. 5, P. 532-546.
-, 2004, Key Controls On The Characteristics Of Turbidite Systems: Geological Society, London, Special Publications, V. 222, No. 1, P. 9 - 22.
Bouma, A. H., And Coleman, J. M., 1984, Peira-Cava Turbidite Systems, France, *In* Bouma, A. H., Normark, W. R., And Barnes, N. E., Eds., Submarine Fans And Related Turbidite Systems, P. 217-222.
Bouma, A. H., And Pluenneke, J. L., 1975, Structural And Textural Characteristics Of Debrites From The Philippine Sea: IODP.
Bourget, J., Zaragosi, S., Mulder, T., Schneider, J. L., Garlan, T., Van Toer, A., Mas, V., And Ellouz-Zimmermann, N., 2010, Hyperpycnal-Fed Turbidite Lobe Architecture And Recent Sedimentary Processes: A Case From The Al'Batha Turbidite System, Oman Margin: Sedimentary Geology, V. 229, P. 144-159.
Bowman, A., 2016, Outcrop Analogues For Hydrocarbon Reservoirs In The Columbus Basin, Offshore East Trinidad: Geological Society, London, Special Publications, V. 436, P. 1 - 42.
Brackenridge, R., Stow, D. V., And Hernández-Molina, F. J., 2011, Contourites Within A Deep-Water Sequence Stratigraphic Framework: Geo-Marine Letters, V. 31, No. 5-6, P. 343-360.
Brackenridge, R. E., 2014, Contourite Sands In The Gulf Of Cadiz: Characterisation, Controls And Wider Implications For Hydrocarbon Exploration [Doctor Of Philosophy In Petroleum Geoscience: Heriot-Watt University, 257 P.
Bramlette, N. M., And Bradley, W. H., 1940, Geology And Biology Of North Atlantic Deepsea Cores, Part I: US Geological Survey Professional Paper, V. 196A, P. 1-34.
Branter, S. R. F., 2003, The East Brae Field, Blocks 16/03a, 16/03b, UK North Sea: Geological Society, London, Memoirs, V. 20, No. 1, P. 191 - 197.
Brehm, J. A., 2003, The North Brae And Beinn Fields, Block 16/7a, UK North Sea: Geological Society, London, Memoirs, V. 20, No. 1, P. 199 - 209.
Breien, H., De Blasio, F. V., Elverhøi, A., Nystuen, J. P., And Harbitz, C. B., 2010, Transport Mechanisms Of Sand In Deep-Marine Environments—Insights Based On Laboratory Experiments: Journal Of Sedimentary Research, V. 80, No. 11, P. 975-990.
Bridge, J. S., 1981, Hydraulic Interpretation Of Grain-Size Distributions Using A Physical Model For Bedload Transport: Journal Of Sedimentary Research, V. 51, No. 4, P. 1109 - 1124.
Bryn, P., Berg, K., Forsberg, C. F., Solhiem, A., and Kvalstad, T (2005) Explaining The Storegga Slide: Marine and Petroleum Geology, V 22, No 1-2, P. 11-19.
Buchter, B., Hinz, C., And Flühler, H., 1994, Sample Size For Determination Of Coarse Fragment Content In A Stony Soil: Geoderma, V. 63, No. 3, P. 265-275.
Buckman, J., 2014, Use Of Automated Image Acquisition And Stitching In Scanning Electron Microscopy: Imaging Of Large Scale Areas Of Materials At High Resolution: Microscopy Analysis, V. 28, No. 1, P. 13-15.
Buller, A. T., And Mcmanus, J., 1972, Modes Of Turbidite Deposition Deduced From Grain-Size Analyses: Geological Magazine, V. 109, No. 6, P. 491-500.
Bursik, M. I., And Woods, A. W., 2000, The Effects Of Topography On Sedimentation From Particle-Laden Turbulent Density Currents: Journal Of Sedimentary Research, V. 70, No. 1, P. 53 - 62.
Buscombe, D., 2008, Estimation Of Grain-Size Distributions And Associated Parameters From Digital Images Of Sediment: Sedimentary Geology, V. 210, No. 1–2, P. 1-10.
-, 2013, Transferable Wavelet Method For Grain-Size Distribution From Images Of Sediment Surfaces And Thin Sections, And Other Natural Granular Patterns: Sedimentology, V. 60, No. 7, P. 1709-1732.
Cantero, M. I., Balachandar, S., Cantelli, A., Pirmez, C., And Parker, G., 2009, Turbidity Current With A Roof: Direct Numerical Simulation Of Self-Stratified Turbulent Channel Flow Driven By Suspended Sediment: Journal Of Geophysical Research: Oceans, V. 114, No. C3, P. 1 - 20.

Cantero, M. I., Cantelli, A., Pirmez, C., Balachandar, S., Mohrig, D., Hickson, T. A., Yeh, T.-H., Naruse, H., And Parker, G., 2012, Emplacement Of Massive Turbidites Linked To Extinction Of Turbulence In Turbidity Currents: Nature Geoscience, V. 5, No. 1, P. 42-45.

Carey, S. N., Sigurdsson, H., And Sparks, R. S. J., 1988, Experimental Studies Of Particles-Laden Plumes: Journal of Geophysical Research, V. 93, No. B12, P. 15314-15328.

Carle, S. F., And Fogg, G. E., 1997, Modeling Spatial Variability With One And Multidimensional Continuous-Lag Markov Chains: Mathematical Geology, V. 29, No. 7, P. 891-918.

Carlson, J., 1998, Analytical And Statistical Approaches Toward Understanding Sedimentation In Siliciclastic Depositional Systems [Doctor Of Philosophy: Massachusetts Institute Of Technology, 964 P.

Carlson, J., And Grotzinger, J. P., 2001, Submarine Fan Environment Inferred From Turbidite Thickness Distributions: Sedimentology, V. 48, No. 6, P. 1331-1351.

Carter, R. M., 1975, A Discussion And Classification Of Subaqueous Mass-Transport With Particular Application To Grain-Flow, Slurry-Flow, And Fluxoturbidites: Earth-Science Reviews, V. 11, No. 2, P. 145-177.

Cartigny, M. J. B., Eggenhuisen, J. T., Hansen, E. W. M., And Postma, G., 2013, Concentration-Dependent Flow Stratification In Experimental High-Density Turbidity Currents And Their Relevance To Turbidite Facies Modelsconcentration-Dependent Stratification In High-Density Turbidity Currents: Journal Of Sedimentary Research, V. 83, No. 12, P. 1047-1065.

Cascalho, J., And Fradique, C., 2007, The Sources And Hydraulic Sorting Of Heavy Minerals On The Northern Portuguese Continental Margin, *In* Mange, M. A., And Wright, D. T., Eds., Heavy Minerals In Use, Volume 58, Elsevier, P. 75-110.

Cassar, C., Nicolas, M., And Pouliquen, O., 2005, Submarine Granular Flows Down Inclined Planes: Physics Of Fluids, V. 17, No. 10, P. 1 - 11.

Chandler, D. M., And Hubbard, B., 2008, Quantifying Sample Bias In Clast Fabric Measurements: Sedimentology, V. 55, No. 4, P. 925-938.

Chen, C., And Hiscott, R. N., 1999a, Statistical Analysis Of Facies Clustering In Submarine-Fan Turbidite Successions: Journal Of Sedimentary Research, V. 69, No. 2, P. 505 - 517.

-, 1999b, Statistical Analysis Of Turbidite Cycles In Submarine Fan Successions: Tests For Short-Term Persistence: Journal Of Sedimentary Research, V. 69, No. 2, P. 486 - 504.

Choi, K., Jackson, M. D., Hampson, G. J., Jones, A. D. W., And Reynolds, A. D., 2011, Predicting The Impact Of Sedimentological Heterogeneity On Gas–Oil And Water–Oil Displacements: Fluvio-Deltaic Pereriv Suite Reservoir, Azeri–Chirag–Gunashli Oilfield, South Caspian Basin: Petroleum Geoscience, V. 17, No. 2, P. 143 - 164.

Cifelli, F., Mattei, M., Chadima, M., Lenser, S., And Hirt, A. M., 2009, The Magnetic Fabric In "Undeformed Clays": AMS And Neutron Texture Analyses From The Rif Chain (Morocco): Tectonophysics, V. 466, No. 1, P. 79-88.

CLARE, M. A., 2004, Late Quaternary Sedimentation In The North Cretan Trough, Variation Between Its Basins And The Potential Emplacement Of Two Megaturbidites: Fugro Geoconsulting Limited.

Clark, J. D., 1998, Scales Of Heterogeneity Within The Ross Formation Turbidite System, Country Clare, West Ireland: Department Of Petroleum Engineering.

Clark, J. D., And Andy, G., 1999, Quantitative Characterisation Of Deep - Water Genetic Units In The Grès d'Annot Formation, South-East France: Department Of Petroleum Engineering.

Clark, J. D., And Stanbrook, D. A., 2001, Formation Of Large-Scale Shear Structures During Deposition From High-Density Turbidity Currents, Grès d'Annot Formation, South-East France, Particulate Gravity Currents, Blackwell Publishing Ltd., P. 217-232.

Cockings, J. H., Kessler, L. G., Mazza, T. A., And Riley, L. A., 1992, Bathonian to mid-Oxfordian sequence stratigraphy of the South Vikig Graben, North Sea. *In*: Hardman, R. F. P (ed.) Exploration Britian: Geological insights for the next decade: The Geological Society, London, Special Publications, V. 67, P. 65-105.

Colburn, I. P., 1968, Grain Fabrics In Turbidite Sandstone Beds And Their Relationship To Sole Mark Trends On The Same Beds: Journal Of Sedimentary Research, V. 38, No. 1, P. 146 - 158.

Collinson, J. D., Mountney, N. P., And Thompson, D., 2006, Sedimentary Structures, Terra Publishing.

Corbett, P. W. M., 2012, The Role Of Geoengineering In Field Development, *In* Gomes, J. S., Ed., New Technologies In The Oil And Gas Industry: Rijeka, Intech, P. 181 - 198.

Coward, M., 1996, Forward Modelling Of The East Brae Structure, Marathon Uk Internal Report.

Cuthiell, D. L., Bachu, S., Kramers, J. W., And Yuan, L.-P., 1991, Characterizing Shale Clast Heterogeneities And Their Effect On Fluid Flow A2 - Lake, Larry W, *In* Carroll, H. B., And Wesson, T. C., Eds., Reservoir Characterization Ii, Academic Press, P. 226-250.

Dade, W. B., And Huppert, H. E., 1995, A Box Model For Non-Entraining, Suspension-Driven Gravity Surges On Horizontal Surfaces: Sedimentology, V. 42, No. 3, P. 453-470.

Dade, W. B., Lister, J. R., And Huppert, H. E., 1994, Fine-Sediment Deposition From Gravity Surges On Uniform Slopes: Journal Of Sedimentary Research, V. 64, No. 3, P. 423 - 432.

Dake, L. P., 2001, The Practice Of Reservoir Engineering, Elsevier, Developments In Petroleum Geoscience, 572 P.:

Dakin, N. C., 2016, Geometry, Architecture And The Erosive Nature Of Mass-Transport Deposits In Deep-Marine Environments: Ainsa Basin (Pyrenees) And Buzzard Field (North Sea) [Doctor Of Philosophy: University College London, 427 P.

Dall'olio, E., Felletti, F., And Muttoni, G., 2013, Magnetic-Fabric Analysis As A Tool To Constrain Mechanisms Of Deep-Water Mudstone Deposition In The Marnoso Arenacea Formation (Miocene, Italy): Journal Of Sedimentary Research, V. 83, No. 2, P. 170-182.

Daly, R. A., 1936, Origin Of Submarine Canyons: American Journal Of Science, V. Series 5 Vol. 31, No. 186, P. 401-420.

Dasgupta, P., 2003, Sediment Gravity Flow—The Conceptual Problems: Earth-Science Reviews, V. 62, No. 3, P. 265-281.

Dasgupta, P., And Manna, P., 2011, Geometrical Mechanism Of Inverse Grading In Grain-Flow Deposits: An Experimental Revelation: Earth-Science Reviews, V. 104, No. 1, P. 186-198.

Davies, I. C., And Walker, R. G., 1974, Transport And Deposition Of Resedimented Conglomerates; The Cap Enrage Formation, Cambro-Ordovician, Gaspe, Quebec: Journal Of Sedimentary Research, V. 44, No. 4, P. 1200-1216.

Davis, C., Haughton, P., Mccaffrey, W., Scott, E., Hogg, N., And Kitching, D., 2009, Character And Distribution Of Hybrid Sediment Gravity Flow Deposits From The Outer Forties Fan, Palaeocene Central North Sea, UKCS: Marine And Petroleum Geology, V. 26, No. 10, P. 1919-1939.

De Blasio, F. V., Engvik, L., Harbitz, C. B., And Elverhøi, A., 2004, Hydroplaning And Submarine Debris Flows: Journal Of Geophysical Research: Oceans, V. 109, No. C1, P. 1 - 15.

De Rooij, F., And Dalziel, S. B., 2001, Time- And Space-Resolved Measurements Of Deposition Under Turbidity Currents, Particulate Gravity Currents, Blackwell Publishing Ltd., P. 207-215.

Deghirmandjian, O., 2001, Identification And Characterization Of Hydraulic Flow Units In The San Juan Formation, Orocual Field, Venezuela [Master Of Science In Petroleum Engineering: Texas A&M University, 277 P.

Delannay, R., Valance, A., Mangeney, A., Roche, O., And Richard, P., 2017, Granular And Particle-Laden Flows: From Laboratory Experiments To Field Observations: Journal Of Physics D: Applied Physics, V. 50, No. 5, P. 1 - 41.

Desouky, S. E. D. M., 2005, Predicting Permeability In Un-Cored Intervals/Wells Using Hydraulic Flow Unit Approach, V. 44, No. 7, P. 1 - 4.

Dewey, J. F., Helman, M. L., Knott, S. D., Turco, E., And Hutton, D. H. W., 1989, Kinematics Of The Western Mediterranean: Geological Society, London, Special Publications, V. 45, No. 1, P. 265-283.

Dindarloo, S. R., Bagherieh, A., Hower, J. C., Calder, J. H., And Wagner, N. J., 2015, Coal Modeling Using Markov Chain And Monte Carlo Simulation: Analysis Of Microlithotype And Lithotype Succession: Sedimentary Geology, V. 329, No. Supplement C, P. 1-11.

Dorrell, R. M., Hogg, A. J., And Pritchard, D., 2013, Polydisperse Suspensions: Erosion, Deposition, And Flow Capacity: Journal Of Geophysical Research: Earth Surface, V. 118, No. 3, P. 1939-1955.

Dorrell, R. M., Hogg, A. J., Sumner, E. J., And Talling, P. J., 2011, The Structure Of The Deposit Produced By Sedimentation Of Polydisperse Suspensions: Journal Of Geophysical Research: Earth Surface, V. 116, No. F1, P. 1 - 12.

Dott Jr, R. H., 1963, Dynamics Of Subaqueous Gravity Depositional Processes: AAPG Bulletin, V. 47, No. 1, P. 104-128.

Drinkwater, N. J., And Pickering, K. T., 2001, Architectural Elements In A High-Continuity Sand-Prone Turbidite System, Late Precambrian Kongsfjord Formation, Northern Norway: Application To Hydrocarbon Reservoir Characterisation: American Association Of Petroleum Geologists Bulletin, V. 85, No. 10, P. 1731-1751.

Duller, R. A., Mountney, N. P., And Russell, A. J., 2010, Particle Fabric And Sedimentation Of Structureless Sand, Southern Iceland: Journal Of Sedimentary Research, V. 80, No. 6, P. 562-577.

Dunster, J. N., 1997, The Lady Loretta Formation: Sedimentology And Stratiform Sediment-Hosted Base Metal Mineralisation [Doctor Of Philosophy: University Of Tasmania, 421 P.

Duranti, D., And Hurst, A., 2004, Fluidization And Injection In The Deep-Water Sandstones Of The Eocene Alba Formation (UK North Sea): Sedimentology, V. 51, No. 3, P. 503-529.

Dutta, S., Pantano-Rubino, C., Cantaero, M. I., Garcia, M. H., And Parker, G., 2012, Effects Of Self-Stratification On Turbidity Currents: A Large Eddy Simulation Approach, XIX International Conference On Water Resources: University Of Illinois At Urbana-Champaign, P. 1-10.

Edwards, D. A., Leeder, M. R., Best, J. L., And Pantin, H. M., 1994, On Experimental Reflected Density Currents And The Interpretation Of Certain Turbidites: Sedimentology, V. 41, No. 3, P. 437-461.

Eggenhuisen, J. T., Cartigny, M. J. B., And De Leeuw, J., 2017, Physical Theory For Near-Bed Turbulent Particle Suspension Capacity: Earth Surface Dynamics, V. 5, No. 2, P. 269 - 282.

Eggenhuisen, J. T., And Mccaffrey, W. D., 2012a, Dynamic Deviation Of Fluid Pressure From Hydrostatic Pressure In Turbidity Currents: Geology, V. 40, No. 4, P. 295-298.

-, 2012b, The Vertical Turbulence Structure Of Experimental Turbidity Currents Encountering Basal Obstructions: Implications For Vertical Suspended Sediment Distribution In Non-Equilibrium Currents: Sedimentology, V. 59, No. 3, P. 1101-1120.

Ehlig-Economides, C. A., Laine, R. E., Oguntaee, B., And Serpen, E., 2004, Effect Of Areal Heterogeneity On Waterflood Performance Between Parallel Horizontal Wells, 2004 SPE International Petroleum Conference: Puebia, Mexico, Society Of Petroleum Engineers, P. 1 - 7.

El Euchi, H., Saidi, M., Fourati, L., And El Maherssi, C., 2004, Northern Tunisia Thrust Belt: Deformation Models And Hydrocarbon System: AAPG Hedberg Series, V. 1, P. 370–390.

El Maherssi, C., Saidi, M., And Fourati, L., The Turbiditic Systems Of The Oligo- Miocene Numidian Flysch – A New Exploration Target In Northern Tunisia *In* Proceedings EAGE 63rd Conference And Technical Exhibition,, Amsterdam, 2001.

Elliott, T., Apps, G., Davies, H., Evans, M., Ghibaudo, G., And Graham, R. H., 1985a, Field Excursion B: A Structural And Sedimentological Traverse Through The Tertiary Foreland Basin Of The External Alps Of South-East France, International Association Of Sedimentologist, Field Excursion Guide Book.

-, 1985b, Field Excursion B: A Structural And Sedimentological Traverse Through The Tertiary Foreland Basin Of The External Alps Of South-East France, International Association Of Sedimentologist, Field Excursion Guide Book, 39-73 P.:

Faber, V., 1994, Clustering And The Continuous K-Means Algorithm: Los Alamos Science, V. 22, P. 138 - 144.

Faugères, J.-C., And Mulder, T., 2011, Contour Currents And Contourite Drifts, *In* Heiko, H., And Thierry, M., Eds., Developments In Sedimentology, Volume Volume 63, Elsevier, P. 149-214.

Faugères, J.-C., Stow, D. A. V., Imbert, P., And Viana, A., 1999, Seismic Features Diagnostic Of Contourite Drifts: Marine Geology, V. 162, No. 1, P. 1-38.

Fazulah, F., 2016, Hydraulic Flow Unit Characterisation Of Homogeneous Deep-Water Massive Sandstones:Brae Formation, Viking Graben, North Sea [Master In Science Petroleum Engineering: Heriot-Watt University, 47 P.

Felix, M., 2002, Flow Structure Of Turbidity Currents: Sedimentology, V. 49, No. 3, P. 397-419.

Felix, M., Leszczyński, S., Ślączka, A., Uchman, A., Amy, L., And Peakall, J., 2009, Field Expressions Of The Transformation Of Debris Flows Into Turbidity Currents, With Examples From The Polish Carpathians And The French Maritime Alps: Marine And Petroleum Geology, V. 26, No. 10, P. 2011-2020.

Felix, M., And Peakall, J., 2006, Transformation Of Debris Flows Into Turbidity Currents: Mechanisms Inferred From Laboratory Experiments: Sedimentology, V. 53, No. 1, P. 107-123.

Felletti, F., 2002, Complex Bedding Geometries And Facies Associations Of The Turbiditic Fill Of A Confined Basin In A Transpressive Setting (Castagnola Fm., Tertiary Piedmont Basin, NW Italy): Sedimentology, V. 49, No. 4, P. 645-667.

-, 2004, Spatial Variability Of Hurst Statistics In The Castagnola Formation, Tertiary Piedmont Basin, NW Italy: Discrimination Of Sub-Environments In A Confined Turbidite System: Geological Society, London, Special Publications, V. 222, No. 1, P. 285 - 305.

Felletti, F., Dall'Olio, E., And Muttoni, G., 2016, Determining Flow Directions In Turbidites: An Integrated Sedimentological And Magnetic Fabric Study Of The Miocene Marnoso Arenacea Formation (Northern Apennines, Italy): Sedimentary Geology, V. 335, No. Supplement C, P. 197-215.

Felsenthal, M., And Gangle, F. J., 1975, A Case Study Of Thief Zones In A California Waterflood, V. 27, No. 11, P. 1385 - 1391.

Fernandes, J. S., Appoloni, C. R., And Fernandes, C. P., 2012, Determination Of The Representative Elementary Volume For The Study Of Sandstones And Siltstones By X-Ray Microtomography: Materials Research, V. 15, P. 662-670.

Fildes, C., Stow, D., Riahi, S., Soussi, M., Patel, U., Milton, A., And Marsh, S., 2010, European Provenance Of The Numidian Flysch In Northern Tunisia: Terra Nova, V. 22, No. 2, P. 94-102.

Fisher, R. V., 1983, Flow Transformations In Sediment Gravity Flows: Geology, V. 11, No. 5, P. 273-274.

Fitch, P., Davies, S., Lovell, M., And Pritchard, T., 2013, Reservoir Quality And Reservoir Heterogeneity: Petrophysical Application Of The Lorenz Coefficient: Petrophysics, V. 54, No. 5, P. 465-474.

Fitch, P. J. R., 2011, Heterogeneity In The Petrophysical Properties Of Carbonate Reservoirs [Doctor Of Philosophy: University Of Leicester, 265 P.

Fitch, P. J. R., Lovell, M. A., Davies, S. J., Pritchard, T., And Harvey, P. K., 2015, An Integrated And Quantitative Approach To Petrophysical Heterogeneity: Marine And Petroleum Geology, V. 63, No. Supplement C, P. 82-96.

Folk, R. L., And Ward, W. C., 1957, Brazos River Bar: A Study In The Significance Of Grain Size Parameters: Journal Of Sedimentary Research, V. 27, No. 1, P. 3-26.

Fonnesu, M., Haughton, P., Felletti, F., And Mccaffrey, W., 2015, Short Length-Scale Variability Of Hybrid Event Beds And Its Applied Significance: Marine And Petroleum Geology, V. 67, No. Supplement C, P. 583-603.

Fonnesu, M., Patacci, M., Haughton, P. D. W., Felletti, F., And Mccaffrey, W. D., 2016, Hybrid Event Beds Generated By Local Substrate Delamination On A Confined-Basin Floor: Journal Of Sedimentary Research, V. 86, No. 8, P. 929-943.

Fortey, N. J., 1995, Image Analysis In Mineralogy And Petrology, Mineralogical Magazine, Volume 59, P. 177 - 178.

Francus, P., 1998, An Image-Analysis Technique To Measure Grain-Size Variation In Thin Sections Of Soft Clastic Sediments: Sedimentary Geology, V. 121, No. 3, P. 289-298.
Francus, P., Bradley, R., And Thurow, J., 2004, An Introduction To Image Analysis, Sediments And Paleoenvironments, Image Analysis, Sediments And Paleoenvironments, Volume 7, Springer Netherlands, P. 1-7.
Frihy, O. E., 2007, The Nile Delta: Processes Of Heavy Mineral Sorting And Depositional Patterns, *In* Mange, M. A., And Wright, D. T., Eds., Heavy Minerals In Use, Volume 58, Elsevier, P. 49-74.
Furuya, M., 2011, SAR INTERFEROMETRY, *In* Gupta, H., Ed., Encyclopedia Of Solid Earth Geophysics: Netherlands, Springer, P. 1041 - 1420.
Gaile, G. L., And Burt, J. E., 1980, Directional Statistics, Norwich, Geo Abstracts, University Of East Anglia, 39 P.:
Galy, V., Beyssac, O., France-Lanord, C., And Eglinton, T., 2008, Recycling Of Graphite During Himalayan Erosion: A Geological Stabilization Of Carbon In The Crust: Science, V. 322, No. 5903, P. 943 - 945.
Galy, V., France-Lanord, C., Beyssac, O., Faure, P., Kudrass, H., And Palhol, F., 2007, Efficient Organic Carbon Burial In The Bengal Fan Sustained By The Himalayan Erosional System: Nature, V. 450, P. 407 - 411.
Gani, M. R., 2004, From Turbid To Lucid: A Straightforward Approach To Sediment Gravity Flows And Their Deposits: The Sedimentary Record, V. 2, No. 3, P. 4-8.
Garcia, D., Joseph, P., Maréchal, B., And Moutte, J., 2004a, Patterns Of Geochemical Variability In Relation To Turbidite Facies In The Grès d'Annot Formation: Geological Society, London, Special Publications, V. 221, No. 1, P. 349-365.
-, 2004b, Patterns Of Geochemical Variability In Relation To Turbidite Facies In The Grès d'Annot Formation: Geological Society, London, Special Publications, V. 221, No. 1, P. 349.
Garcia, M., And Parker, G., 1989, Experiments On Hydraulic Jumps In Turbidity Currents Near A Canyon-Fan Transition: Science, V. 245, No. 4916, P. 393.
Garcia, M. H., 1990, Depositing And Eroding Sediment-Driven Flows: Turbidity Currents [Doctor Of Philosophy: University Of Minnesota, 212 P.
García, M. H., 1993, Hydraulic Jumps In Sediment-Driven Bottom Currents: Journal Of Hydraulic Engineering, V. 119, No. 10, P. 1094-1117.
Gardiner, A. R., 2006, The Variability Of Turbidite Sandbody Pinchout And Its Impact On Hydrocarbon Recovery In Stratigraphically Trapped Fields: Geological Society, London, Special Publications, V. 254, No. 1, P. 267 - 287.
Garland, C. R., Haughton, P., King, R. F., And Moulds, T. P., 1999, Capturing Reservoir Heterogeneity In A Sand-Rich Submarine Fan, Miller Field: Geological Society, London, Petroleum Geology Conference Series, V. 5, No. 1, P. 1199.
Garton, M., And Mcilroy, D., 2006, Large Thin Slicing: A New Method For The Study Of Fabrics In Lithified Sediments: Journal Of Sedimentary Research, V. 76, No. 11, P. 1252-1256.
Gaudette, H. E., Hurley, P. M., And Lajmi, T., 1975, Source Area Of The Numidian Flych Of Tunisia As Suggested By Detrital Zircon Ages, The Geological Society Of America Annual Meetings Boulder Colorado, P. 1083–1084.
Gee, M. J. R., Masson, D. G., Watts, A. B., And Allen, P. A., 1999, The Saharan Debris Flow: An Insight Into The Mechanics Of Long Runout Submarine Debris Flows: Sedimentology, V. 46, No. 2, P. 317-335.
Gervais, A., Savoye, B., Mulder, T., And Gonthier, E., 2006, Sandy Modern Turbidite Lobes: A New Insight From High Resolution Seismic Data: Marine And Petroleum Geology, V. 23, P. 485-502.
Ghedan, S. G., Boloushi, Y. A., And Saleh, M. B. F., 2010, Thief Zones And Effectiveness Of Water-Shut-Off Treatments Under Variable Levels Of Gravity And Reservoir Heterogeneity In Carbonate Reservoirs, SPE EUROPEC/EAGE Annual Conference And Exhibition: Barcelona, Spain, Society Of Petroleum Engineers, P. 1 - 11.
Ghibaudo, G., 1992, Subaqueous Sediment Gravity Flow Deposits: Practical Criteria For Their Field Description And Classification: Sedimentology, V. 39, No. 3, P. 423-454.

Ghosh, J. K., Mazumder, B. S., Saha, M. R., And Sengupta, S., 1986, Deposition Of Sand By Suspension Currents: Experimental And Theoretical Studies: Journal Of Sedimentary Research, V. 56, No. 1, P. 57 - 66.

Gilbert, G. K., 1890, Lake Bonneville, 1.

Gillemot, K. A., Somfai, E., And Börzsönyi, T., 2017, Shear-Driven Segregation Of Dry Granular Materials With Different Friction Coefficients: Soft Matter, V. 13, No. 2, P. 415-420.

Gingerich, P. D., 1969, Markov Analysis Of Cyclic Alluvial Sediments: Notes: Journal Of Sedimentary Research, V. 39, No. 1, P. 330-332.

Gitman, I. M., Askes, H., And Sluys, L. J., 2007, Representative Volume: Existence And Size Determination: Engineering Fracture Mechanics, V. 74, No. 16, P. 2518-2534.

Gladstone, C., Phillips, J. C., And Sparks, R. S. J., 1998, Experiments On Bidisperse, Constant-Volume Gravity Currents: Propagation And Sediment Deposition: Sedimentology, V. 45, No. 5, P. 833-843.

Gladstone, C., And Pritchard, D., 2010, Patterns Of Deposition From Experimental Turbidity Currents With Reversing Buoyancy: Sedimentology, V. 57, No. 1, P. 53-84.

Gladstone, C., And Sparks, R. S. J., 2002, The Significance Of Grain-Size Breaks In Turbidites And Pyroclastic Density Current Deposits: Journal Of Sedimentary Research, V. 72, No. 1, P. 182-191.

Gluyas, J., And Swarbrick, R., 2013, Petroleum Geoscience, John Wiley & Sons, 376 P.:

Golob, D. J., 2003, Correlation Of Core Characteristics To Outcrop Upper Jackfork Group Turbidites, Degray Lake, Arkansas [Master Of Science (MS): Louisiana State University And Agricultural And Mechanical College Follow, 99 P.

Gonthier, E., Faugeres, J.-C., And Stow, D., 1984, Contourite Facies Of The Faro Drift, Gulf Of Cadiz, *In* Stow, D. A. V., And Piper, D. J. W., Eds., Fine-Grained Sediments: Deep-Water Processes And Facies, Volume 15: London, Geological Society, Special Publication, P. 275-292.

Gonzalez-Bonorino, G., And Middleton, G. V., 1976, A Devonian Submarine Fan In Western Argentina: Journal Of Sedimentary Research, V. 46, No. 1, P. 56 - 69.

Goodman, L. A., 1968, The Analysis Of Cross-Classified Data: Independence, Quasi-Independence, And Interactions In Contingency Tables With Or Without Missing Entries: Journal Of The American Statistical Association, V. 63, No. 324, P. 1091-1131.

Graham, J. G. U., 1986, Approximate Confidence Intervals For The Mean Direction Of A Von Mises Distribution: Biometrika, V. 73, No. 2, P. 525-527.

Gray, T. E., Alexander, J. A. N., And Leeder, M. R., 2005, Quantifying Velocity And Turbulence Structure In Depositing Sustained Turbidity Currents Across Breaks In Slope: Sedimentology, V. 52, No. 3, P. 467-488.

Grieve, R. A. F., And Osinski, G. R., 2011, Impact Craters On Earth, *In* Gupta, H., Ed., Encyclopedia Of Solid Earth Geophysics: Netherlands, Springer, P. 593 - 668.

Griffiths, J. C., 1949, Directional Permeability And Dimensional Orientation In Bradford Sand: Pennsylvania State College Mineral Industries Experiment Station Bulletin, V. 54, P. 138-163.

Groenenberg, R., 2007, Process-Based Modelling Of Turbidity-Current Hydrodynamics And Sedimentation [Doctor Of Philosophy: Delft University Of Technology, 214 P.

Guerrera, F., Martin-Algarra, A., And Perrone, V., 1993, Late Oligocene-Miocene Syn-/-Late-Orogenic Successions In Western And Central Mediterranean Chains From The Betic Cordillera To The Southern Apennines*: Terra Nova, V. 5, No. 6, P. 525-544.

Guerrera, F., Martín-Algarra, A., And Martín-Martín, M., 2012, Tectono-Sedimentary Evolution Of The 'Numidian Formation' And Lateral Facies (Southern Branch Of The Western Tethys): Constraints For Central-Western Mediterranean Geodynamics: Terra Nova, V. 24, No. 1, P. 34-41.

Guerrera, F., Martín-Martín, M., Perrone, V., And Tramontana, M., 2005, Tectono-Sedimentary Evolution Of The Southern Branch Of The Western Tethys (Maghrebian Flysch Basin And Lucanian Ocean): Consequences For Western Mediterranean Geodynamics: Terra Nova, V. 17, No. 4, P. 358-367.

Guillén, J., Acosta, J., Chiocci, F. L., And Palanques, A., 2017, Atlas Of Bedforms In The Western Mediterranean, Switzerland, Springer, 307 P.:
Gunter, G. W., Finneran, J. M., Hartmann, D. J., And Miller, J. D., 1997a, Early Determination Of Reservoir Flow Units Using An Integrated Petrophysical Method, SPE Annual Technical Conference And Exhibition: San Antonio, Texas, Society Of Petroleum Engineers, P. 1 - 8.
Gunter, G. W., Pinch, J. J., Finneran, J. M., And Bryant, W. T., 1997b, Overview Of An Integrated Process Model To Develop Petrophysical Based Reservoir Descriptions, SPE Annual Technical Conference And Exhibition: San Antonio, Texas, Society Of Petroleum Engineers, P. 475 - 479.
Hailwood, E. A., Bowen, D., Ding, F., Corbett, P. W. M., And Whattler, P., 1999, Characterising Pore Fabrics In Sediments By Anisotropy Of Magnetic Susceptibility Analysis, *In* Tarlin, D. H., And Tuner, P., Eds., Palaeomagnetism And Diagenesis In Sediments, Volume 151: London, Geological Society, P. 125-126.
Hammer, Ø., 2017, Past - Paleontological Statistcs. Reference Manual: University Of Oslo.
Hampton, M. A., 1972, The Role Of Subaqueous Debris Flow In Generating Turbidity Currents: Journal Of Sedimentary Research, V. 42, No. 4, P. 775 - 793.
-, 1975, Competence Of Fine-Grained Debris Flows: Journal Of Sedimentary Research, V. 45, No. 4, P. 834 - 844.
-, 1979, Buoyancy In Debris Flows: Journal Of Sedimentary Research, V. 49, No. 3, P. 753 - 758.
Hand, B. M., 1997, Inverse Grading Resulting From Coarse-Sediment Transport Lag: Journal Of Sedimentary Research, V. 67, No. 1, P. 124-129.
Hatampour, A., Schaffie, M., And Jafari, S., 2015, Hydraulic Flow Units, Depositional Facies And Pore Type Of Kangan And Dalan Formations, South Pars Gas Field, Iran: Journal Of Natural Gas Science And Engineering, V. 23, No. Supplement C, P. 171-183.
Hatcher, R. D., 1990, Structural Geology: Principles, Concepts, And Problems, London, Merrill Publishing.
Hattori, I., 1976, Entropy In Markov Chains And Discrimination Of Cyclic Patterns In Lithologic Successions: Journal Of The International Association For Mathematical Geology, V. 8, No. 4, P. 477-497.
Haughton, P., Davis, C., Mccaffrey, W., And Barker, S., 2009, Hybrid Sediment Gravity Flow Deposits – Classification, Origin And Significance: Marine And Petroleum Geology, V. 26, No. 10, P. 1900-1918.
Haughton, P. D. W., 1994, Deposits Of Deflected And Ponded Turbidityents, Currents, Sorbas Basin, Southeast Spain: Journal Of Sedimentary Research, V. 64, No. 2, P. 233 - 246.
-, 2000, Evolving Turbidite Systems On A Deforming Basin Floor, Tabernas, SE Spain: Sedimentology, V. 47, No. 3, P. 497-518.
Haughton, P. D. W., Barker, S. P., And Mccaffrey, W. D., 2003, 'Linked' Debrites In Sand-Rich Turbidite Systems – Origin And Significance: Sedimentology, V. 50, No. 3, P. 459-482.
Heezen, B., Hollister, C., And Ruddiman, W., 1966, Shaping The Continental Rise By Deep Geostrophic Contour Currents: Science, V. 152, P. 502-508.
Heezen, B. C., And Ewing, W. M., 1952, Turbidity Currents And Submarine Slumps, And The 1929 Grand Banks [Newfoundland] Earthquake: American Journal Of Science, V. 250, No. 12, P. 849-873.
Heilbronner, R., And Barrett, S., 2013, Image Analysis In Earth Sciences: Microstructures And Textures Of Earth Materials, Springer Science & Business Media, 520 P.:
Heimsund, S., 2007, Numerical Simulation Of Turbidity Currents: A New Perspective For Small-And Large-Scale Sedimentological Experiments [Candidatus Scientiarum Degree In Sedimentology/Petroleum Geology The University Of Bergen, 140 P.
Hesse, R., And Khodabakhsh, S., 2006, Significance Of Fine-Grained Sediment Lofting From Melt-Water Generated Turbidity Currents For The Timing Of Glaciomarine Sediment Transport Into The Deep Sea: Sedimentary Geology, V. 186, No. 1, P. 1-11.
Hesse, R., Rashid, H., And Khodabakhsh, S., 2004, Fine-Grained Sediment Lofting From Meltwater-Generated Turbidity Currents During Heinrich Events: Geology, V. 32, No. 5, P. 449-452.

Hildebrandt, C., And Egenhoff, S., 2007, Shallow-Marine Massive Sandstone Sheets As Indicators Of Palaeoseismic Liquefaction — An Example From The Ordovician Shelf Of Central Bolivia: Sedimentary Geology, V. 202, No. 4, P. 581-595.

Hirasaki, G. J., 1984, Properties Of Log-Normal Permeability Distribution For Stratified Reservoirs, Society Of Petroleum Engineers, P. 1 - 18.

Hirayama, J., And Nakajima, T., 1977, Analytical Study Of Turbidites, Otadai Formation, Boso Peninsula, Japan: Sedimentology, V. 24, No. 6, P. 747-779.

Hiscott, N. R., 1977, Sedimentology And Regional Implications Of Deep-Water Sandstones Of The Tourelle Formation, Ordovician, Quebec [Doctor Of Philosophy: Mcmaster University, 704 P.

Hiscott, R. N., 1981, Deep-Sea Fan Deposits In The Macigno Formation (Middle-Upper Oligocene) Of The Gordana Valley, Northern Apennines, Italy–Discussion: Journal Of Sedimentary Petrology, V. 51, P. 1015-1021.

-, 1994a, Loss Of Capacity, Not Competence, As The Fundamental Process Governing Deposition From Turbidity Currents: Journal Of Sedimentary Research, V. 64, No. 2, P. 209 - 214.

-, 1994b, Traction-Carpet Stratification In Turbidites-Fact Or Fiction?: Journal Of Sedimentary Research, V. 64, No. 2, P. 204 - 208.

-, 1994c, Traction-Carpet Stratification In Turbidites-Fact Or Fiction?: Journal Of Sedimentary Research, V. 64, No. 2, P. 703 - 704.

Hiscott, R. N., Hall, F. R., And Pirmez, C., 1997, Turbidity-Current Overspill From The Amazon Channel: Texture Of The Silt/Sand Load, Paleoflow From Anisotropy Of Magnetic Susceptibility, And Implications For Flow Processes, National Science Foundation, P. 53-78.

Hiscott, R. N., And Middleton, G. V., 1979, Depositional Mechanics Of Thick-Bedded Sandstones At The Base Of A Submarine Slope, Tourelle Formation (Lower Ordovcian), Quebec, Canada, *In* Doyle, L. J., And Pilkey, O. H., Eds., Geology Of Continental Slopes, Volume 27, Society Of Economist, Paleontologists And Mineralogists Special Publication, P. 307-326.

-, 1980, Fabric Of Coarse Deep-Water Sandstones Tourelle Formation, Quebec, Canada: Journal Of Sedimentary Research, V. 50, No. 3, P. 703 - 722.

Hodgson, D. M., 2009, Distribution And Origin Of Hybrid Beds In Sand-Rich Submarine Fans Of The Tanqua Depocentre, Karoo Basin, South Africa: Marine And Petroleum Geology, V. 26, No. 10, P. 1940-1956.

Hodson, J. M., And Alexander, J., 2010, The Effects Of Grain-Density Variation On Turbidity Currents And Some Implications For The Deposition Of Carbonate Turbidites: Journal Of Sedimentary Research, V. 80, No. 6, P. 515-528.

Hogg, A. J., Hupper, H. W., Hallworth, M. A., 1999, Reversing Bouyancy Of Particle-Driven Gravity Currents: Physics Of Fluids, V. 11, No. 11, P. 2891-2900.

Hollister, C. D., 1967, Sediment Distribution And Deep Circulation In The Western North Atlantic [Ph.D.: Columbia University, 467 P.

Hongling, Z., Zenglin, W., And Jing, W., 2011, Watering Crest Along A Horizontal Well In A Heterogeneous Reservoir With Bottom Water: Petroleum Science And Technology, V. 29, No. 23, P. 2471-2479.

Hota, R. N., Adhikari, P. C., Mohanty, A., And Maejima, W., 2012, Cyclic Sedimentation Of The Barakar Formation, Singrauli Coalfield, India: Statistical Assessment From Borehole Logs: Open Journal Of Geology, V. 2, No. 1, P. 1 - 13.

Hovadik, J. M., And Larue, D. K., 2007, Static Characterizations Of Reservoirs: Refining The Concepts Of Connectivity And Continuity: Petroleum Geoscience, V. 13, No. 3, P. 195 - 211.

Hubbard, S. M., Covault, J. A., Fildani, A., And Romans, B. W., 2014, Sediment Transfer And Deposition In Slope Channels: Deciphering The Record Of Enigmatic Deep-Sea Processes From Outcrop: Geological Society Of America Bulletin, V. 126, No. 5-6, P. 857-871.

Hughes, S. R., Alexander, J., And Druitt, T. H., 1995, Anisotropic Grain Fabric: Volcanic And Laboratory Analogues For Turbidites: Geological Society, London, Special Publications, V. 94, No. 1, P. 51.

Hurst, A., And Cronin, B. T., 2001, The Origin Of Consolidation Laminae And Dish Structures In Some Deep-Water Sandstones: Journal Of Sedimentary Research, V. 71, No. 1, P. 136-143.

Hurst, A., Scott, A., And Vigorito, M., 2011, Physical Characteristics Of Sand Injectites: Earth-Science Reviews, V. 106, No. 3, P. 215-246.

Hussain, A., 2012, Diagenesis And Reservoir Quality Of Upper Jurassic Sandstones In The South Viking Graben [Master In Petroleum Geology And Petroleum Geophysics: University Of Oslo, 142 P.

Hürzeler, B. E., Imberger, J., And Ivey, G. N., 1996, Dynamics Of Turbidity Current With Reversing Buoyancy: Journal Of Hydraulic Engineering, V. 122, No. 5, P. 230-236.

Ilstad, T., Marr, J. G., Elverhøi, A., And Harbitz, C. B., 2004, Laboratory Studies Of Subaqueous Debris Flows By Measurements Of Pore-Fluid Pressure And Total Stress: Marine Geology, V. 213, No. 1, P. 403-414.

Isyaku, A. A., Rust, D., Teeuw, R., And Whitworth, M., 2016, Integrated Well Log And 2-D Seismic Data Interpretation To Image The Subsurface Stratigraphy And Structure In North-Eastern Bornu (Chad) Basin: Journal Of African Earth Sciences, V. 121, No. Supplement C, P. 1-15.

Ito, M., 2008, Downfan Transformation From Turbidity Currents To Debris Flows At A Channel-To-Lobe Transitional Zone: The Lower Pleistocene Otadai Formation, Boso Peninsula, Japan: Journal Of Sedimentary Research, V. 78, No. 10, P. 668-682.

Ivaldi, J. P., 1974, Origines Des Material Detritique Des Series Grès D' Annot D'apres Leas Donnees De La Thermoluminescence: Geol. Alpine, V. 50, P. 75-98.

Iverson, R. M., 1997, The Physics Of Debris Flows: Reviews Of Geophysics, V. 35, No. 3, P. 245-296.

-, 2003, The Debris-Flow Rheology Myth, 3rd International Conference On Debris-Flow Hazards Mitigation: Mechanics, Prediction, And Assessment, Volume 1: Davos, USGS Publications Warehouse, P. 303-314.

Iverson, R. M., Logan, M., Lahusen, R. G., And Berti, M., 2010, The Perfect Debris Flow? Aggregated Results From 28 Large-Scale Experiments: Journal Of Geophysical Research: Earth Surface, V. 115, No. F3, P. 1 - 29.

Iverson, R. M., And Vallance, J. W., 2001, New Views Of Granular Mass Flows: Geology, V. 29, No. 2, P. 115-118.

Izadi, M., And Ghalambor, A., 2012, A New Approach In Permeability And Hydraulic Flow Unit Determination, SPE International Symposium And Exhibition On Formation Damage Control: Louisiana, USA, Society Of Petroleum Engineers, P. 1 - 9.

J. Van Der Lingen, G., 1969, The Turbidite Problem, New Zealand, Taylor & Francis, New Zealand Journal Of Geology And Geophysics,, 7-50 P.:

Jackson, C. A. L., Larsen, E., Hanslien, S., And Tjemsland, A.-E., 2011, Controls On Synrift Turbidite Deposition On The Hanging Wall Of The South Viking Graben, North Sea Rift System, Offshore Norway: AAPG Bulletin, V. 95, No. 9, P. 1557-1587.

Jackson, M. D., And Muggeridge, A. H., 2000, Effect Of Discontinuous Shales On Reservoir Performance During Horizontal Waterflooding, SPE Reservoir Simulation Symposium, Volume 5: Houston, Society Of Petroleum Engineers, P. 446 - 455.

Jacoby, W., And Smilde, P. L., 2009, Gravity Interpretation: Fundamentals And Application Of Gravity Inversion And Geological Interpretation, Springer Science & Business Media, 412 P.:

Janocko, M., 2008, Pinchout Geometry Of Sheet-Like Sandstone Beds: A New Statistical Approach To The Problem Of Lateral Bed Thinning Based On Outcrop Measurements [Master Of Science In Geology/ Sedimentology: Universitetet I Tromsø, 143 P.

Jean, S., 1985, Les Grès d'Annot Au NW Du Massif De l'Argentera-Mercantour - Sèdimentologie, Palèogèographie [Ph.D: Université De Grenoble, 243 P.

Jensen, J. J., Lake, L. W., Corbett, P. W. M., And Goggin, D. J., 2000, Statistics For Petroleum Engineering And Geoscientists, Handbook Of Petroleum Exploration And Production, 362 P.:

Jensen, J. L., Corbett, P. W. M., Pickup, G. E., And Ringrose, P. S., 1996, Permeability Semivariograms, Geological Structure, And Flow Performance: Mathematical Geology, V. 28, No. 4, P. 419-435.

Jensen, J. L., And Currie, I. D., 1990, A New Method For Estimating The Dykstra-Parsons Coefficient To Characterize Reservoir Heterogeneity: SPE Reservoir Engineering V. 5, No. 3, P. 369 - 374.

Jensen, J. L., And Lake, L. W., 1988, The Influence Of Sample Size And Permeability Distribution On Heterogeneity Measures: SPE Reservoir Engineering V. 3, No. 2, P. 629 - 637.

Jeong, S. W., Locat, J., Leroueil, S., And Malet, J.-P., 2010, Rheological Properties Of Fine-Grained Sediment: The Roles Of Texture And Mineralogy: Canadian Geotechnical Journal, V. 47, No. 10, P. 1085-1100.

Jobe, Z., Sylvester, Z., Pittaluga, M. B., Frascati, A., Pirmez, C., Minisini, D., Howes, N., And Cantelli, A., 2017, Facies Architecture Of Submarine Channel Deposits On The Western Niger Delta Slope: Implications For Grain-Size And Density Stratification In Turbidity Currents: Journal Of Geophysical Research: Earth Surface, V. 122, No. 2, P. 473-491.

Jobe, Z. R., Lowe, D. R., And Morris, W. R., 2012, Climbing-Ripple Successions In Turbidite Systems: Depositional Environments, Sedimentation Rates And Accumulation Times: Sedimentology, V. 59, No. 3, P. 867-898.

Johansson, M., Braakenburg, N. E., Stow, D. A. V., And Faugères, J.-C., 1998a, Deep-Water Massive Sands: Facies, Processes And Channel Geometry In The Numidian Flysch, Sicily: Sedimentary Geology, V. 115, No. 1–4, P. 233-265.

-, 1998b, Deep-Water Massive Sands: Facies, Processes And Channel Geometry In The Numidian Flysch, Sicily: Sedimentary Geology, V. 115, No. 1, P. 233-265.

Johansson, M., And Stow, D. A. V., 1995, A Classification Scheme For Shale Clasts In Deep Water Sandstones: Geological Society, London, Special Publications, V. 94, No. 1, P. 221.

Johnson, C. G., Kokelaar, B. P., Iverson, R. M., Logan, M., Lahusen, R. G., And Gray, J. M. N. T., 2012, Grain-Size Segregation And Levee Formation In Geophysical Mass Flows: Journal Of Geophysical Research: Earth Surface, V. 117, No. F1, P. N/A-N/A.

Johnson, M. R., 1994, Thin Section Grain Size Analysis Revisited: Sedimentology, V. 41, No. 5, P. 985-999.

Jones, L. S., Garrett, S. W., Macleod, M., Guy, M., Condon, P. J., And Notman, L., 1999, Britannia Field, UK Central North Sea: Modelling Heterogeneity In Unusual Deep-Water Deposits: Geological Society, London, Petroleum Geology Conference 				Series, V. 5, No. 1, P. 1115 - 1124.

Joseph, L. H., Rea, D. K., And Van Der Pluijm, B. A., 1998, Use Of Grain Size And Magnetic Fabric Analyses To Distinguish Among Depositional Environments: Paleoceanography, V. 13, No. 5, P. 491-501.

Joseph, P., And Lomas, S. A., 2004, Deep-Water Sedimentation In The Alpine Foreland Basin Of SE France: New Perspectives On The Grès d'Annot And Related Systems—An Introduction: Geological Society, London, Special Publications, V. 221, No. 1, P. 1.

Julien, P., Lan, Y., And Berthault, G., 1993, Experiments On Stratification Of Heterogeneous Sand Mixtures: Bulletin-Societe Geologique De France, V. 164, No. 5, P. 649-660.

Kaitna, R., Palucis, M. C., Yohannes, B., Hill, K. M., And Dietrich, W. E., 2016, Effects Of Coarse Grain Size Distribution And Fine Particle Content On Pore Fluid Pressure And Shear Behavior In Experimental Debris Flows: Journal Of Geophysical Research: Earth Surface, V. 121, No. 2, P. 415-441.

Kane, I. A., Kneller, B. C., Dykstra, M., Kassem, A., And Mccaffrey, W. D., 2007, Anatomy Of A Submarine Channel–Levee: An Example From Upper Cretaceous Slope Sediments, Rosario Formation, Baja California, Mexico: Marine And Petroleum Geology, V. 24, No. 6, P. 540-563.

Kane, I. A., And Pontén, A. S. M., 2012, Submarine Transitional Flow Deposits In The Paleogene Gulf Of Mexico: Geology, V. 40, No. 12, P. 1119-1122.

Kanit, T., Forest, S., Galliet, I., Mounoury, V., And Jeulin, D., 2003, Determination Of The Size Of The Representative Volume Element For Random Composites: Statistical And Numerical Approach: International Journal Of Solids And Structures, V. 40, No. 13–14, P. 3647-3679.

Kazerouni, A. M., Friis, H., Svendsen, J. B., And Weibel, R., 2011, Heavy Mineral Sorting In Downwards Injected Palaeocene Sandstone, Siri Canyon, Danish North Sea: Sedimentary Geology, V. 236, No. 3, P. 279-285.

Kenyon, N. H., Klauckle, I., Millington, J., And Ivanov, M. K., 2002, Sandy Submarine Canyon-Mouth Lobes On The Western Margin Of Corsica And Sardinia, Mediterranean Sea: Marine Geology, V. 184, P. 69-84.

Khan, Z. A., 1996, Quasi-Independence And Entropy Analysis Of A Late Orogenic Middle Siwalik Molasse Sequence In Kuluchaur Area, Pauri Garhwal, India: Geoinformatics, V. 7, No. 1-2, P. 135-145.

Klein, G. D., 1966, Dispersal And Petrology Of Sandstones Of Stanley-Jackfork Boundary, Ouachita Fold Belt, Arkansaa And Oklahoma.: AAPG Bulletin, V. 50, No. 2, P. 308-326.

Kneller, B., 1995, Beyond The Turbidite Paradigm: Physical Models For Deposition Of Turbidites And Their Implications For Reservoir Prediction: Geological Society, London, Special Publications, V. 94, No. 1, P. 31 - 49.

Kneller, B., And Buckee, C., 2000, The Structure And Fluid Mechanics Of Turbidity Currents: A Review Of Some Recent Studies And Their Geological Implications: Sedimentology, V. 47, P. 62-94.

Kneller, B., Edwards, D., Mccaffrey, W., And Moore, R., 1991, Oblique Reflection Of Turbidity Currents: Geology, V. 19, No. 3, P. 250-252.

Kneller, B., And Mccaffrey, W., 1999, Depositional Effects Of Flow Nonuniformity And Stratification Within Turbidity Currents Approaching A Bounding Slope; Deflection, Reflection, And Facies Variation: Journal Of Sedimentary Research, V. 69, No. 5, P. 980-991.

Kneller, B. C., Bennett, S. J., And Mccaffrey, W. D., 1999, Velocity Structure, Turbulence And Fluid Stresses In Experimental Gravity Currents: Journal Of Geophysical Research: Oceans, V. 104, No. C3, P. 5381-5391.

Kneller, B. C., And Branney, M. J., 1995, Sustained High-Density Turbidity Currents And The Deposition Of Thick Massive Sands: Sedimentology, V. 42, No. 4, P. 607-616.

Kneller, B. C., And Mccaffrey, W. D., 1998, Topographic Effects On Turbidite Systems: The Grès d'Annot, Alpes Maritimes And Hautes Provence, SE France. Field Excursion Handbook, Conference On Sediment Transport And Deposition By Particulate Gravity Currents: Leeds.

-, 2003, The Interpretation Of Vertical Sequences In Turbidite Beds: The Influence Of Longitudinal Flow Structure: Journal Of Sedimentary Research, V. 73, No. 5, P. 706-713.

Komar, P. D., 1985, The Hydraulic Interpretation Of Turbidites From Their Grain Sizes And Sedimentary Structures: Sedimentology, V. 32, No. 3, P. 395-407.

-, 2007, The Entrainment, Transport And Sorting Of Heavy Minerals By Waves And Currents, *In* Maria, A. M., And Wright, D. T., Eds., Heavy Minerals In Use, Volume 58, Elsevier, P. 3-48.

Kostic, S., And Parker, G., 2006, The Response Of Turbidity Currents To A Canyon–Fan Transition: Internal Hydraulic Jumps And Depositional Signatures: Journal Of Hydraulic Research, V. 44, No. 5, P. 631-653.

Kranck, K., 1984, Grain-Size Characteristics Of Turbidites: Geological Society, London, Special Publications, V. 15, No. 1, P. 83.

Kubo, Y. S., 2004, Experimental And Numerical Study Of Topographic Effects On Deposition From Two-Dimensional, Particle-Driven Density Currents: Sedimentary Geology, V. 164, No. 3, P. 311-326.

Kuenen, P. H., 1937, Experiments In Connection With Daly's Hypothesis On The Formation Of Submarine Canyons: Leidsche Geologishe Mededeelingen, V. 8, P. 327-335.

-, 1957, Sole Markings Of Graded Graywacke Beds: The Journal Of Geology, V. 65, No. 3, P. 231-258.

Kuenen, P. H., 1966, Experimental Turbidite Lamination in a Circular Flume: Geology, V. 74, No. 5, P. 523-545.

Kuenen, P. H., And Migliorini, C. I., 1950, Turbidity Currents As A Cause Of Graded Bedding: Journal Of Geology, V. 58, No. 2, P. 91-127.

Laberg, J. S., And Vorren, T. O., 1995, Late Weichselian Submarine Debris Flow Deposits On The Bear Island Trough Mouth Fan: Marine Geology, V. 127, No. 1, P. 45-72.
Labourdette, R., Crumeyrolle, P., And Remacha, E., 2008, Characterisation Of Dynamic Flow Patterns In Turbidite Reservoirs Using 3D Outcrop Analogues: Example Of The Eocene Morillo Turbidite System (South-Central Pyrenees, Spain): Marine And Petroleum Geology, V. 25, No. 3, P. 255-270.
Lamb, M. P., Hickson, T., Marr, J. G., Sheets, B., Paola, C., And Parker, G., 2004, Surging Versus Continuous Turbidity Currents: Flow Dynamics And Deposits In An Experimental Intraslope Minibasin: Journal Of Sedimentary Research, V. 74, No. 1, P. 148-155.
Lamb, M. P., Toniolo, H., And Parker, G., 2006, Trapping Of Sustained Turbidity Currents By Intraslope Minibasins: Sedimentology, V. 53, No. 1, P. 147-160.
Lanza, R., And Meloni, A., 2006, The Earth's Magnetism: An Introduction For Geologists, Berlin, Springer, 286 P.:
Laval, A., Cremer, M., Beghin, P., And Ravenne, C., 1988, Density Surges: Two-Dimensional Experiments: Sedimentology, V. 35, No. 1, P. 73-84.
Leclair, S. F., And Arnott, R. W. C., 2003, Coarse-Tail Graded, Structureless Strata: Indicators Of An Internal Hydraulic Jump, *In* Roberts, H. H., Rosen, N. C., Fillon, R. H., And Anderson, J. B., Eds., Shelf Margin Deltas And Linked Down Slope Petroleum Systems–Global Significance And Future Exploration Potential, SEPM Society For Sedimentary Geology.
-, 2005, Parallel Lamination Formed By High-Density Turbidity Currents: Journal Of Sedimentary Research, V. 75, No. 1, P. 1-5.
Lee, H. J., 2009, Timing Of Occurrence Of Large Submarine Landslides On The Atlantic Ocean Margin: Marine Geology, V. 264, P. 53-64.
Lee, S. E., Amy, L. A., And Talling, P. J., 2004, The Character And Origin Of Thick Base-Of-Slope Sandstone Units Of The Peïra Cava Outlier, SE France: Geological Society, London, Special Publications, V. 221, No. 1, P. 331-347.
Lee, S. E., Talling, P. J., Ernst, G. G. J., And Hogg, A. J., 2002, Occurrence And Origin Of Submarine Plunge Pools At The Base Of The US Continental Slope: Marine Geology, V. 185, No. 3, P. 363-377.
Lee, S. H., Jung, W.-Y., Bahk, J. J., Gardner, J. M., Kim, J. K., And Lee, S. H., 2013, Depositional Features Of Co-Genetic Turbidite–Debrite Beds And Possible Mechanisms For Their Formation In Distal Lobated Bodies Beyond The Base-Of-Slope, Ulleung Basin, East Sea (Japan Sea): Marine Geology, V. 346, No. Supplement C, P. 124-140.
Legros, F., 2002, Can Dispersive Pressure Cause Inverse Grading In Grain Flows?: Journal Of Sedimentary Research, V. 72, No. 1, P. 166-170.
Leishman, P. M., Sedimentology, Reservoir Geometry And Reservoir Quality Of The East Brae Field, UK North Sea [Doctor Of Philosophy: University Of Aberdeen, 407 P.
Lewis, T., Francus, P., Bradley, R. S., And Kanamaru, K., 2010, An Automated System For The Statistical Analysis Of Sediment Texture And Structure At The Micro Scale: Computers & Geosciences, V. 36, No. 10, P. 1374-1383.
Li, Y., Cai, H., And Cheng, C., 2015, Reservoir Classification And Evaluation Methods Based On R35 Pore Throat Radius, 2015 AASRI International Conference On Industrial Electronics And Applications (IEA 2015), Atlantis Press, P. 175 - 179.
Lien, T., Walker, R. G., And Martinsen, O. J., 2003, Turbidites In The Upper Carboniferous Ross Formation, Western Ireland: Reconstruction Of A Channel And Spillover System: Sedimentology, V. 50, No. 1, P. 113-148.
Locat, J., And Lee, H. J., 2005, Subaqueous Debris Flows, Debris-Flow Hazards And Related Phenomena: Berlin, Springer, P. 203-245.
Lowe, D. R., 1975, Water Escape Structures In Coarse-Grained Sediments: Sedimentology, V. 22, No. 2, P. 157-204.
-, 1976a, Grain Flow And Grain Flow Deposits: Journal Of Sedimentary Research, V. 46, No. 1, P. 188 - 199.
-, 1976b, Subaqueous Liquefied And Fluidized Sediment Flows And Their Deposits: Sedimentology, V. 23, No. 3, P. 285-308.

-, 1979, Sediment Gravity Flows: Their Classification And Some Problems Of Application To Natural Flows And Deposits, V. 27, P. 75 - 82.
-, 1982, Sediment Gravity Flows: II Depositional Models With Special Reference To The Deposits Of High-Density Turbidity Currents: Journal Of Sedimentary Research, V. 52, No. 1, P. 279 - 297.
-, 1988, Suspended-Load Fallout Rate As An Independent Variable In The Analysis Of Current Structures: Sedimentology, V. 35, No. 5, P. 765-776.
Lowe, D. R., And Guy, M., 2000, Slurry-Flow Deposits In The Britannia Formation (Lower Cretaceous), North Sea: A New Perspective On The Turbidity Current And Debris Flow Problem: Sedimentology, V. 47, No. 1, P. 31-70.
Lowe, D. R., And Lopiccolo, R. D., 1974, The Characteristics And Origins Of Dish And Pillar Structures: Journal Of Sedimentary Research, V. 44, No. 2, P. 484 - 501.
Lüthi, S., 1981, Some New Aspects Of Two-Dimensional Turbidity Currents*: Sedimentology, V. 28, No. 1, P. 97-105.
Maast, T. E., Jahren, J., And Bjorlykke, K., 2011, Diagenetic Controls On Reservoir Quality In Middle To Upper Jurassic Sandstones In The South Viking Graben, North Sea: AAPG Bulletin, V. 95, No. 11, P. 1937-1958.
Macauley, R. V., And Hubbard, S. M., 2013, Slope Channel Sedimentary Processes And Stratigraphic Stacking, Cretaceous Tres Pasos Formation Slope System, Chilean Patagonia: Marine And Petroleum Geology, V. 41, No. Supplement C, P. 146-162.
Macdonald, D. I. M., 1986, Proximal To Distal Sedimentological Variation In A Linear Turbidite Trough: Implications For The Fan Model: Sedimentology, V. 33, No. 2, P. 243-259.
Macdonald, R. G., Alexander, J. A. N., Bacon, J. C., And Cooker, M. J., 2009, Flow Patterns, Sedimentation And Deposit Architecture Under A Hydraulic Jump On A Non-Eroding Bed: Defining Hydraulic-Jump Unit Bars: Sedimentology, V. 56, No. 5, P. 1346-1367.
Mahjour, S. K., Al-Askari, M. K. G., And Masihi, M., 2016, Flow-Units Verification, Using Statistical Zonation And Application Of Stratigraphic Modified Lorenz Plot In Tabnak Gas Field: Egyptian Journal Of Petroleum, V. 25, No. 2, P. 215-220.
Major, J. J., 1998, Pebble Orientation On Large, Experimental Debris-Flow Deposits: Sedimentary Geology, V. 117, No. 3, P. 151-164.
-, 2000, Gravity-Driven Consolidation Of Granular Slurries--Implications For Debris-Flow Deposition And Deposit Characteristics: Journal Of Sedimentary Research, V. 70, No. 1, P. 64-83.
Major, J. J., And Iverson, R. M., 1999, Debris-Flow Deposition: Effects Of Pore-Fluid Pressure And Friction Concentrated At Flow Margins: Geological Society Of America Bulletin, V. 111, No. 10, P. 1424-1434.
Malgesini, G., 2012, Evolution Of Submarine Sediment Density Flows Deduced From Long Distance Bed Correlations [Doctor Of Philosophy: University Of Southampton, 226 P.
Malgesini, G., Talling, P. J., Hogg, A. J., Armitage, D., Goater, A., And Felletti, F., 2015, Quantitative Analysis Of Submarine-Flow Deposit Shape In The Marnoso-Arenacea Formation: What Is The Signature Of Hindered Settling From Dense Near-Bed Layers?: Journal Of Sedimentary Research, V. 85, No. 2, P. 170-191.
Malureanu, II, And Batistatu, V. M., 2010, The Analysis Of Reservoir Heterogeneity From Well Log DATA: Scientific Annals, V. 99, P. 149-154.
Mange, M. A., And Morton, A. C., 2007, Geochemistry Of Heavy Minerals, *In* Maria, A. M., And Wright, D. T., Eds., Heavy Minerals In Use, Volume 58, Elsevier, P. 345-391.
Mange, M. A., And Wright, D. T., 2007, High-Resolution Heavy Mineral Analysis (HRHMA): A Brief Summary, *In* Maria, A. M., And Wright, D. T., Eds., Heavy Minerals In Use, Volume 58, Elsevier, P. 433-436.
Manica, R., 2012, Sediment Gravity Flows: Study Based On Experimental Simulations, *In* Schulz, H., Ed., Hydrodynamics-Natural Water Bodies: Europe, Intech, P. 263 - 286.
Manica, R., Baas, J. H., Maestri, R., Peakall, J., And Borges, A. L., 2010, A First Experimentally Derived Classification Of Submarine Sediment Gravity Flows, AAPG Annual Convention And Exhibition: New Orleans, USA, American Association Of Petroleum Geologist.

Marchand, A. M. E., Smalley, P. C., Haszeldine, R. S., And Fallick, A. E., 2002, Note On The Importance Of Hydrocarbon Fill For Reservoir Quality Prediction In Sandstones: AAPG Bulletin, V. 86, No. 9, P. 1561-1572.

Maria, A. M., And Wright, D. T., 2007, Introduction And Overview, *In* Maria, A. M., And Wright, D. T., Eds., Heavy Minerals In Use, Volume 58, Elsevier, P. Xxvii - Xliv.

Marini, M., Felletti, F., Milli, S., And Patacci, M., 2016a, The Thick-Bedded Tail Of Turbidite Thickness Distribution As A Proxy For Flow Confinement: Examples From Tertiary Basins Of Central And Northern Apennines (Italy): Sedimentary Geology, V. 341, No. Supplement C, P. 96-118.

Marini, M., Patacci, M., Felletti, F., And Mccaffrey, W. D., 2016b, Fill To Spill Stratigraphic Evolution Of A Confined Turbidite Mini-Basin Succession, And Its Likely Well Bore Expression: The Castagnola Fm, NW Italy: Marine And Petroleum Geology, V. 69, No. Supplement C, P. 94-111.

Marr, J. G., Harff, P. A., Shanmugam, G., And Parker, G., 2001, Experiments On Subaqueous Sandy Gravity Flows: The Role Of Clay And Water Content In Flow Dynamics And Depositional Structures: Geological Society Of America Bulletin, V. 113, No. 11, P. 1377-1386.

Masch, F. D., And Denny, K. J., 1966, Grain Size Distribution And Its Effect On The Permeability Of Unconsolidated Sands: Water Resources Research, V. 2, No. 4, P. 665-677.

Masson, D. G., Harbitz, C. B., Wynn, R. B., Pederson, G., And Løvholt, F., 2006, Submarine Landslides: Processes, Triggers And Hazard Prediction: Philosphical Transactions Of The Royal Society, V. 364, P. 2009 - 2039.

Masson, D. G., Huvenne, V. A. I., De Stigter, H. C., Wolff, G. A., Kiriakoulakis, K., Arzola, R. G., And Blackbird, S., 2010, Efficient Burial Of Carbon In A Submarine Canyon: Geology, V. 38, No. 9, P. 831-834.

Mayall, M., Jones, E., And Casey, M., 2006, Turbidite Channel Reservoirs - Key Elements In Facies Prediction And Effective Development: Marine And Petroleum Geology, V. 23, P. 821-841.

Mcanally William, H., Friedrichs, C., Hamilton, D., Hayter, E., Shrestha, P., Rodriguez, H., Sheremet, A., Teeter, A., And Null, N., 2007, Management Of Fluid Mud In Estuaries, Bays, And Lakes. I: Present State Of Understanding On Character And Behavior: Journal Of Hydraulic Engineering, V. 133, No. 1, P. 9-22.

Mcardell, B. W., Bartelt, P., And Kowalski, J., 2007, Field Observations Of Basal Forces And Fluid Pore Pressure In A Debris Flow: Geophysical Research Letters, V. 34, No. 7, P. 1 - 4.

Mccaffrey, W., And Kneller, B., 2001, Process Controls On The Development Of Stratigraphic Trap Potential On The Margins Of Confined Turbidite Systems And Aids To Reservoir Evaluation: AAPG Bulletin, V. 85, No. 6, P. 971-988.

Mccaffrey, W. D., Choux, C. M., Baas, J. H., And Haughton, P. D. W., 2003, Spatio-Temporal Evolution Of Velocity Structure, Concentration And Grain-Size Stratification Within Experimental Particulate Gravity Currents: Marine And Petroleum Geology, V. 20, No. 6, P. 851-860.

Mccaffrey, W. D., And Kneller, B. C., 2004, Scale Effects Of Non-Uniformity On Deposition From Turbidity Currents With Reference To The Grès d'Annot Of SE France: Geological Society, London, Special Publications, V. 221, No. 1, P. 301-310.

Mccave, I. N., And Jones, K. P. N., 1988, Deposition Of Ungraded Muds From High-Density Non-Turbulent Turbidity Currents: Nature, V. 333, P. 250.

Mcintosh, C. K., 2007, The Controls On Sedimentation And Implication For Facies Prediction In The Buzzard Feld, UK North Sea [Ph.D: Heriot-Watt University.

Mckinley, J. M., Atkinson, P. M., Lloyd, C. D., Ruffell, A. H., And Worden, R. H., 2011, How Porosity And Permeability Vary Spatially With Grain Size, Sorting, Cement Volume, And Mineral Dissolution In Fluvial Triassic Sandstones: The Value Of Geostatistics And Local Regression: Journal Of Sedimentary Research, V. 81, No. 12, P. 844-858.

Mckinnon, M., 2013, Depositional Character Of" Syn-Rift" Deep-Water Deposits: A Case Study From The Upper Jurassic Buzzard Turbidite System [Doctor Of Philosophy: University Of Aberdeen, 351 P.

Meiburg, E., And Kneller, B., 2009, Turbidity Currents And Their Deposits: Annual Review Of Fluid Mechanics, V. 42, No. 1, P. 135-156.
Mesri, G., Terzaghi, K., And Peck, R. B., 1996, Soil Mechanics In Engineering Practice, New York, Wiley.
Meyer, R., And Krause, F. F., 2006, Permeability Anisotropy And Heterogeneity Of A Sandstone Reservoir Analogue: An Estuarine To Shore Face Deposition System In The Vergelle Member, Milk River Formation, Writing-On-Stone Provincial Park, Southern Alberta: Bulletin Of Canadian Geology, V. 54, No. 4, P. 301-318.
Miall, A. D., 1973, Markov Chain Analysis Applied To An Ancient Alluvial Plain Succession: Sedimentology, V. 20, No. 3, P. 347-364.
Middleton, G. V., 1962, Size And Sphericity Of Quartz Grains In Two Turbidite Formations: Journal Of Sedimentary Research, V. 32, No. 4, P. 725-742.
-, 1970, Experimental Studies Related To Problems Of Flysch Sedimentation, The Geological Association Of Canada, 253-272 P.:
Middleton, G. V., And Hampton, M. A., 1973, Sediment Gravity Flows: Mechanics Of Flow And Deposition, Turbidites And Deep Water Sedimentation, Pacific Section SEPM, P. 1 - 38.
Migliorini, C. I., 1943, Sul Modo Di Formazione Dei Complessi Tipo Macigno: Boll. Soc. Geol. Ital, V. 62, P. 48–49.
-, 1946, L'eta Del Macigno Dell'appennino Sulla Sinistra Del Serchia E Considerazione Sul Rimaneggiamento Del Macroforaminifera.: Boll. Soc. Geol. Ital, V. 63, P. 75-90.
Milne, J., 1897, Sub-Oceanic Changes (Continued): The Geographical Journal, V. 10, No. 3, P. 259-285.
Mohrig, D., And Marr, J. G., 2003, Constraining The Efficiency Of Turbidity Current Generation From Submarine Debris Flows And Slides Using Laboratory Experiments: Marine And Petroleum Geology, V. 20, No. 6, P. 883-899.
Motanated, K., 2014, Mechanisms Of Sedimentation Inferred From Quantitative Characteristics Of Heavy And Light Minerals Sorting And Abundance [Doctor Of Philosophy: Texas A&M University, 77 P.
Motanated, K., And Tice, M. M., 2016, Hydraulic Evolution Of High-Density Turbidity Currents From The Brushy Canyon Formation, Eddy County, New Mexico Inferred By Comparison To Settling And Sorting Experiments: Sedimentary Geology, V. 337, P. 69-80.
Mueller, P., Patacci, M., And Di Giulio, A., 2017, Hybrid Event Beds In The Proximal To Distal Extensive Lobe Domain Of The Coarse-Grained And Sand-Rich Bordighera Turbidite System (NW Italy): Marine And Petroleum Geology, V. 86, No. Supplement C, P. 908-931.
Muggeridge, A. H., Jackson, M. D., Agbehi, O. R., Al-Shuraiqi, H., And Grattoni, C. A., 2005, Quantifying Bypassed Oil In The Vicinity Of Discontinuous Shales During Gravity Dominated Flow, SPE Europec/EAGE Annual Conference: Madrid, Spain, Society Of Petroleum Engineers, P. 1 - 11.
Mulder, T., 2011a, Gravity Processes And Deposits On Continental Slope, Rise And Abyssal Plains, *In* Hüneke, H., And Mulder, T., Eds., Developments In Sedimentology, Volume 63, Elsevier, P. 25-148.
-, 2011b, Gravity Processes And Deposits On Continental Slope, Rise And Abyssal Plains, *In* Hüneke, H., And Mulder, T., Eds., Deep-Sea Sediments, Volume 63: France, Elsevier, P. 25-148.
Mulder, T., And Alexander, J., 2001a, Abrupt Change In Slope Causes Variation In The Deposit Thickness Of Concentrated Particle-Driven Density Currents: Marine Geology, V. 175, No. 1, P. 221-235.
-, 2001b, The Physical Character Of Subaqueous Sedimentary Density Flows And Their Deposits: Sedimentology, V. 48, No. 2, P. 269-299.
Mulder, T., Callec, Y., Parize, O., Joseph, P., Schneider, J.-L., Robin, C., Dujoncquoy, E., Salles, T., Allard, J., Bonnel, C., Ducassou, E., Etienne, S., Ferger, B., Gaudin, M., Hanquiez, V., Linares, F., Marchès, E., Toucanne, S., And Zaragosi, S., 2010, High-Resolution Analysis Of Submarine Lobes Deposits: Seismic-Scale Outcrops Of The Lauzanier Area (SE Alps, France): Sedimentary Geology, V. 229, No. 3, P. 160-191.

Mulder, T., Migeon, S., Savoye, B., And Faugères, J. C., 2001, Inversely Graded Turbidite Sequences In The Deep Mediterranean: A Record Of Deposits From Flood-Generated Turbidity Currents?: Geo-Marine Letters, V. 21, No. 2, P. 86-93.

Mulder, T., Savoye, B., And Syvitski, J. P. M., 1997, Numerical Modelling Of A Mid-Sized Gravity Flow: The 1979 Nice Turbidity Current (Dynamics, Processes, Sediment Budget And Seafloor Impact): Sedimentology, V. 44, No. 2, P. 305-326.

Mulder, T., And Syvitski, J. P. M., 1995, Turbidity Currents Generated At River Mouths During Exceptional Discharges To The World Oceans: The Journal Of Geology, V. 103, No. 3, P. 285-299.

Mulder, T., Syvitski, J. P. M., Migeon, S., Faugères, J.-C., And Savoye, B., 2003, Marine Hyperpycnal Flows: Initiation, Behavior And Related Deposits. A Review: Marine And Petroleum Geology, V. 20, No. 6, P. 861-882.

Murray, C. J., Lowe, D. R., Graham, S. A., Martinez, P. A., Zeng, J., Carroll, A. R., Cox, R., Hendrix, M., Heubeck, C., And Miller, D., 1996, Statistical Analysis Of Bed-Thickness Patterns In A Turbidite Section From The Great Valley Sequence, Cache Creek, Northern California: Journal Of Sedimentary Research, V. 66, No. 5, P. 900 - 908.

Mutti, E., 1992, Turbidite Sandstones, Agip, Istituto Di Geologia, Università Di Parma, 275 P.:

Mutti, E., Bernoulli, D., Lucchi, F. R., And Tinterri, R., 2009, Turbidites And Turbidity Currents From Alpine 'Flysch' To The Exploration Of Continental Margins: Sedimentology, V. 56, No. 1, P. 267-318.

Mutti, E., And Normark, W. R., 1987, Comparing Examples Of Modern And Ancient Turbidite Systems: Problems And Concepts, *In* Leggett, J. K., And Zuffa, G. G., Eds., Marine Clastic Sedimentology: Concepts And Case Studies: Dordrecht, Springer Netherlands, P. 1-38.

Mutti, E., And Ricci Lucchi, F., 1972, Le Torbiditi Dell'appennino Settentrionale: Introduzione All'analisi Di Facies: Mem.Soc.Geol.It, V. 11, No. 2, P. 161-199.

-, 1978, Turbidites Of The Northern Apennines: Introduction To Facies Analysis: International Geology Review, V. 20, No. 2, P. 125-166.

Mutti, E., Tinterri, R., Benevelli, G., Biase, D. D., And Cavanna, G., 2003, Deltaic, Mixed And Turbidite Sedimentation Of Ancient Foreland Basins: Marine And Petroleum Geology, V. 20, No. 6, P. 733-755.

Nakajima, T., 2006, Hyperpycnites Deposited 700 Km Away From River Mouths In The Central Japan Sea: Journal Of Sedimentary Research, V. 76, No. 1, P. 60-73.

Nardin, T. R., Hein, F. J., Gorsline, D. S., And Edwards, B. D., 1979, A Review Of Mass Movement Processes Sediment And Acoustic Characteristics, And Contrasts In Slope And Base-Of-Slope Systems Versus Canyon-Fan-Basin Floor Systems, V. 27, P. 61 - 73.

Naruse, H., And Masuda, F., 2006, Visualization Of The Internal Structure Of The Massive Division In Experimental Sediment-Gravity-Flow Deposits By Mapping Of Grain Fabric: Journal Of Sedimentary Research, V. 76, No. 5, P. 854-865.

Nazeer, A., Abbasi, S. A., And Solangi, S. H., 2016, Sedimentary Facies Interpretation Of Gamma Ray (GR) Log As Basic Well Logs In Central And Lower Indus Basin Of Pakistan: Geodesy And Geodynamics, V. 7, No. 6, P. 432-443.

Nederbragt , A. J., Francus, P., Bollmann, J., And Soreghan, M., 2004, Image Calibration, Filtering And Processing, Dordrecht, The Netherlands, Kluwer Academic, Image Analysis, Sediments And Paleoenvironments, 24 P.:

Neethling, J. M., 2009, Stratigraphic Evolution And Characteristics Of Lobes: A High-Resolution Study Of Fan 3, Tanqua Karoo, South Africa [Master Of Science: University Of Stellenbosch, 136 P.

Nichols, R. J., 1995, The Liquification And Remobilization Of Sandy Sediments: Geological Society, London, Special Publications, V. 94, No. 1, P. 63-76.

Norema, H., Locatb, J., And Schieldropc, B., 1990, An Approach To The Physics And The Modeling Of Submarine Flowslides: Marine Geotechnology, V. 9, No. 2, P. 93-111.

Nurmi, R., Charara, M., Waterhouse, M., And Park, R., 1990, Heterogeneities In Carbonate Reservoirs: Detection And Analysis Using Borehole Electrical Imagery: Geological Society, London, Special Publications, V. 48, No. 1, P. 95 - 111.

Obi, S., Mode, A., Ekwe, A., Nnebedum, O., Ede, And Ogechi, E., 2013, Paleocurrent Analysis As Tool For Reservoir Property Estimation: A Case Study Of Eocene Outcrops In Southeastern Nigeria: American Journal Of Scientific And Industrial Research, V. 4, No. 1, P. 137-152.

Omoboriowo, A. O., Chiadikobi, K. C., And Chiaghanam, O. I., 2012, Depositional Environment And Petrophysical Characteristics Of" LEPA" Reservoir, Amma Field, Eastern Niger Delta, Nigeria: International Journal Of Pure & Applied Sciences & Technology, V. 10, No. 2, P. 38 - 61.

Onyeagoro, K., Naruk, S., Van Der Vlugt, F., Barton, M., Pirmez, C., And O'Byrne, C., 2007, Impact Of Structural And Stratigraphic Heterogeneities In Deep Water Development, Nigeria Annual International Conference And Exhibition: Abuja, Nigeria, Society Of Petroleum Engineers, P. 1 - 6.

Oyanyan, R. O., And Oti, M. N., 2016, Heterogeneities And Intra Sand-Body Compartmentalization In Late Oligocene Delta-Front Deposit, Niger Delta, Nigeria: American Journal Of Geoscience, V. 6, No. 1, P. 47-64.

Pantin, H. M., And Leeder, M. R., 1987, Reverse Flow In Turbidity Currents: The Role Of Internal Solitons: Sedimentology, V. 34, No. 6, P. 1143-1155.

Paola, C., Wiele, S. M., And Reinhart, M. A., 1989, Upper-Regime Parallel Lamination As The Result Of Turbulent Sediment Transport And Low-Amplitude Bed Forms: Sedimentology, V. 36, No. 1, P. 47-59.

Parkash, B., And Middleton, G. V., 1970, Downcurrent Textural Changes In Ordovician Turbidite Greywackes: Sedimentology, V. 14, No. 3-4, P. 259-293.

Parsons, J. D., Whipple, K. X., And Simoni, A., 2001, Experimental Study Of The Grain-Flow, Fluid- Mud Transition In Debris Flows: The Journal Of Geology, V. 109, No. 4, P. 427-447.

Partington, M. A., Mitchener, B. C., Milton, N. J., And Fraser, A. J., 1993, Genetic Sequence Stratigraphy For The North Sea Late Jurassic And Early Cretaceous: Distribution And Prediction Of Kimmeridgian–Late Ryazanian Reservoirs In The North Sea And Adjacent Areas: Geological Society, London, Petroleum Geology Conference Series, V. 4, No. 1, P. 347.

Parés, J. M., Hassold, N. J. C., Rea, D. K., And Van Der Pluijm, B. A., 2007, Paleocurrent Directions From Paleomagnetic Reorientation Of Magnetic Fabrics In Deep-Sea Sediments At The Antarctic Peninsula Pacific Margin (ODP Sites 1095, 1101): Marine Geology, V. 242, No. 4, P. 261-269.

Patacci, M., Haughton, P. D. W., And Mccaffrey, W. D., 2014, Rheological Complexity In Sediment Gravity Flows Forced To Decelerate Against A Confining Slope, Braux, SE Francecurrent RIPPLES: Journal Of Sedimentary Research, V. 84, No. 4, P. 270-277.

-, 2015, Flow Behavior Of Ponded Turbidity Currents: Journal Of Sedimentary Research, V. 85, No. 8, P. 885-902.

Patacci, P., Mccaffrey, W. D., And Haughton, P. D., Role Of Internal Waves Within Ponded Turbidity Currents: Experimental Data And Deposit Implications, *In* Proceedings AAPG Annual Convention And Exhibition, New Orleans, Louisiana, U.S.A, 2010.

Pettijohn, F. J., Potter, P. E., And Siever, R., 1987, Sand And Sandstone, New York, Springer-Verlag.

Pettingill, H. S., Turbidite Giants: Lessons From The World's 40 Largest Turbidite Discoveries, *In* Proceedings EAGE/AAPG Third Research Symposium, Almeria, Spain, 1998, Volume AO27.

Pewsey, A., Neuhauser, M., And Ruxton, G. D., 2013, Circular Statistics In R, Oxford, Oxford University Press, 183 P.:

Pickering, K. T., 1981, Two Types Of Outer Fan Lobe Sequence From The Late Precambrian Kongsford Formation Submarine Fan, Finnmark, North Norway: Journal Of Sedimentary Petrology, V. 51, P. 1277-1286.

-, 1985, Kongsfjorf Turbidite System, Norway, *In* Bouma, A. H., Normark, W. R., And Barnes, N. E., Eds., Submarine Fans And Related Turbidite Systems: New York, Springer, P. 267-273.

Pickering, K. T., And Corregidor, J., 2005, Mass-Transport Complexes (MTC) And Tectonic Control On Basin-Floor Submarine Fans, Middle Eocene, South Spanish Pyrenees: Journal Of Sedimentary Research, V. 75, P. 761-783.

Pickering, K. T., And Hilton, V. C., 1998, Turbidite Systems Of Southeast France: Application To Hydrocarbon Prospectively, London, Vallis Press.

Pickering, K. T., And Hiscott, R. N., 2015, Deep Marine Systems: Processes, Deposits, Environments, Tectonics And Sedimentation, John Wiley & Sons Ltd, 658 P.:

Pickering, K. T., Hoscott, H. N., And Hien, F. J., 1989, Deep Marine Environments: Clastic Sedimentation And Tectonics, London, Unwin Hyman, 416 P.:

Pierce, J. W., And Graus, R. R., 1981, Use And Misuses Of The Phi -Scale; Discussion: Journal Of Sedimentary Research, P. 1348 - 1350.

Pierson, T. C., And Costa, J. E., 1987, Arheologic Classification Of Suberial Sediment-Water Flows, *In* Costa, J. E., And Wieczorek, G. F., Eds., Debris Flows/Avalanches, Processes, Recognitionm And Mitigation Vol. VII: Boulder, CO, Geological Society of America Reviews in Engineering Geology, P 1-12.

Pintos, S., Bohorquez, C., And Queipo, N. V., 2011, Asymptotic Dykstra–Parsons Distribution, Estimates And Confidence Intervals: Mathematical Geosciences, V. 43, No. 3, P. 329-343.

Piper, D. J. W., 1978, Turbidite Muds And Silts On Deepsea Fans And Abyssal Plains, *In* Stanley, D. J., And Kelling, G., Eds., Sedimentation In Submarine Canyons, Fans And Trenches: Stroudsburg, Pennsylvanian, Dowden, Hutchinson And Ross, P. 163-176.

Piper, D. J. W., Cochonat, P., And Morrison, M. L., 1999, The Sequence Of Events Around The Epicentre Of The 1929 Grand Banks Earthquake: Initiation Of Debris Flows And Turbidity Current Inferred From Sidescan Sonar: Sedimentology, V. 46, No. 1, P. 79-97.

Piper, J. D. A., Elliot, M. T., And Kneller, B. C., 1996, Anisotropy Of Magnetic Susceptibility In A Palaeozoic Flysch Basin: The Windermere Supergroup, Northern England: Sedimentary Geology, V. 106, No. 3, P. 235-258.

Piper, J. D., Shor, A. N., And Clarke, J. E. H., 1988, The 1929 “Grand Banks” earthqauke, slump, and turbidity current, *In* Clifton, H. E., Ed., Sedimentologic Consequences of Convulsive Geologic Events: Geological Society of America, P. 77-92.

Plink-Björklund, P., And Steel, R. J., 2004, Initiation Of Turbidity Currents: Outcrop Evidence For Eocene Hyperpycnal Flow Turbidites: Sedimentary Geology, V. 165, No. 1, P. 29-52.

Pochat, S., And Van Den Driessche, J., 2007, Impact Of Synsedimentary Metre-Scale Normal Fault Scarps On Sediment Gravity Flow Dynamics: An Example From The Grès d’Annot Formation, SE France: Sedimentary Geology, V. 202, No. 4, P. 796-820.

Posamentier, H. W., And Walker, R. G., 2006, Deep-Water Turbidites And Submarine Fans, Facies Models Revisited: London, Society Of Economic Paleonologists And Mineralogists, P. 397-520.

Postma, G., 1986, Classification For Sediment Gravity-Flow Deposits Based On Flow Conditions During Sedimentation: Geology, V. 14, No. 4, P. 291-294.

Postma, G., Cartigny, M., And Kleverlaan, K., 2009, Structureless, Coarse-Tail Graded Bouma Ta Formed By Internal Hydraulic Jump Of The Turbidity Current?: Sedimentary Geology, V. 219, No. 1, P. 1-6.

Postma, G., And Cartigny, M. J. B., 2014, Supercritical And Subcritical Turbidity Currents And Their Deposits—A Synthesis: Geology, V. 42, No. 11, P. 987-990.

Postma, G., Kleverlaan, K., And Cartigny, M. J. B., 2014, Recognition Of Cyclic Steps In Sandy And Gravelly Turbidite Sequences, And Consequences For The Bouma Facies Model: Sedimentology, V. 61, No. 7, P. 2268-2290.

Postma, G., Nemec, W., And Kleinspehn, K. L., 1988, Large Floating Clasts In Turbidites: A Mechanism For Their Emplacement: Sedimentary Geology, V. 58, No. 1, P. 47-61.

Potter, P. E., And Blakely, R. F., 1968, Random Processes And Lithologic Transitions: The Journal Of Geology, V. 76, No. 2, P. 154-170.

Poulsen, M. L. K., Friis, H., Svendsen, J. B., Jensen, C. B., And Bruhn, R., 2007, The Application Of Bulk Rock Geochemistry To Reveal Heavy Mineral Sorting And Flow Units In Thick, Massive Gravity Flow Deposits, Siri Canyon Palaeocene Sandstones,

Danish North Sea, *In* Mange, M. A., And Wright, D. T., Eds., Developments In Sedimentology, Volume 58, Elsevier, P. 1099-1121.

Powers, D. W., And Easterling, R. G., 1982, Improved Methodology For Using Embedded Markov Chains To Describe Cyclical Sediments: Journal Of Sedimentary Research, V. 52, No. 3, P. 913 - 923.

Prelat, A., Hodgson, D. M., And Flint, S. S., 2009, Evolution, Architecture And Hierarchy Of Distribution Deep-Water Deposit: A High-Resolution Outcrop Investigation From The Permian Karoo Basin, South Africa: Sedimentology, V. 56.

Pritchard, D., And Gladstone, C., 2009, Reversing Buoyancy In Turbidity Currents: Developing A Hypothesis For Flow Transformation And For Deposit Facies And Architecture: Marine And Petroleum Geology, V. 26, No. 10, P. 1997-2010.

Prosser, D. J., Mckeever, M. E., Hogg, A. J. C., And Hurst, A., 1995, Permeability Heterogeneity Within Massive Jurassic Submarine Fan Sandstones From The Miller Field, Northern North Sea, UK: Geological Society, London, Special Publications, V. 94, No. 1, P. 201 - 219.

Purkis, S., Vlaswinkel, B., And Gracias, N., 2012, Vertical-To-Lateral Transitions Among Cretaceous Carbonate Facies—A Means To 3-D Framework Construction Via Markov Analysis: Journal Of Sedimentary Research, V. 82, No. 4, P. 232-243.

Purvis, K., Kao, J., Flanagan, K., Henderson, J., And Duranti, D., 2002, Complex Reservoir Geometries In A Deep Water Clastic Sequence, Gryphon Field, UKCS: Injection Structures, Geological Modelling And Reservoir Simulation: Marine And Petroleum Geology, V. 19, No. 2, P. 161-179.

Pyrcz, M. J., And Deutsch, C. V., 2003, The Whole Story On The Hole Effect: Geostatistical Association Of Australasia, Newsletter, V. 18, P. 1 - 16.

Rahimpour-Bonab, H., Mehrabi, H., Navidtalab, A., And Izadi-Mazidi, E., 2012, Flow Unit Distribution And Reservoir Modelling In Cretaceous Carbonates Of The Sarvak Formation, Abteymour Oilfield, Dezful Embayment, Sw Iran: Journal Of Petroleum Geology, V. 35, No. 3, P. 213-236.

Rashid, B., Muggeridge, A., Bal, A., And Williams, G. J. J., 2012, Quantifying The Impact Of Permeability Heterogeneity On Secondary-Recovery Performance, V. 17, No. 2, P. 455-468.

Rawson, P. F., And Riley, L. A., 1982, Latest Jurassic - Early Cretaceous Events And The "Late Cimmerian Unconformity" In The North Sea Area: Bulletin Of The American Association Of Petroleum Geologists, V. 66, P. 2628-2648.

Raychaudhuri, A., And Dutta, J., 2012, Image Binarization Using Multi-Layer Perceptron: A Semi-Supervised Approach: IJEIR, V. 1, No. 2, P. 134-139.

Reading, H. G., And Richards, M., 1994, Turbidite Systems In Deep-Water Basin Margins Classified By Grain Size And Feeder System: AAPG Bulletin, V. 78, No. 5, P. 792-822.

Rebesco, M., Hernández-Molina, F. J., Van Rooij, D., And Wåhlin, A., 2014, Contourites And Associated Sediments Controlled By Deep-Water Circulation Processes: State-Of-The-Art And Future Considerations: Marine Geology, V. 352, P. 111-154.

Reeder, M. S., 2000, Megaturbidites And The Late Quaternary Regional Sedimentology Of The Eastern And Central Mediterranean Sea [Doctor Of Philosophy: University Of Southampton, 382 P.

Rees, A. I., 1979, The Orientation Of Grains In A Sheared Dispersion: Tectonophysics, V. 55, No. 3, P. 275-287.

-, 1983, Experiments On The Production Of Transverse Grain Alignment In A Sheared Dispersion: Sedimentology, V. 30, No. 3, P. 437-448.

Rees, A. I., Von Rad, U., And Shepard, F. P., 1968, Magnetic Fabric Of Sediments From The La Jolla Submarine Canyon And Fan, California: Marine Geology, V. 6, No. 2, P. 145-178.

Remacha, E., And Fernández, L. P., 2003, High-Resolution Correlation Patterns In The Turbidite Systems Of The Hecho Group (South-Central Pyrenees, Spain): Marine And Petroleum Geology, V. 20, No. 6, P. 711-726.

Riahi, S., 2011, Sedimentology, Stratigraphy, Provenance And Reservoir Potential Of The Oligo-Miocene Numidian Flysch, Northern Tunisia [Ph.D: Université De Tunis, 423 P.

Riahi, S., Soussi, M., Kamel, B., Kmar, B. I. L., Stow, D., Sami, K., And Mourad, B., 2010, Stratigraphy, Sedimentology And Structure Of The Numidian Flysch Thrust Belt In Northern Tunisia: Journal Of African Earth Sciences, V. 57, No. 1–2, P. 109-126.

Ricci Lucci, F., And Valmori, E., 1980, Basin-Wide Turbidites In A Miocene, Over-Supplied Deep-Sea Plain: A Geometrical Analysis: Sedimentology, V. 27, P. 241-270.

Riley, L. A., Roberts, M. J., And Connell, E. R., 1989, The Application Of Palynology In The Interpretation Of Brae Formation Stratigraphy And Reservoir Geology., Correlation In Hydrocarbon Exploration: London, Graham And Trotman, P. 339-356.

Rodine, J. D., And Johnson, A. M., 1976, The Ability Of Debris, Heavily Freighted With Coarse Clastic Materials, To Flow On Gentle Slopes: Sedimentology, V. 23, No. 2, P. 213-234.

Rooksby, S. K., 1991, The Miller Field, Blocks 16/7B, 16/8B, UK North Sea: Geological Society, London, Memoirs, V. 14, No. 1, P. 159 - 164.

Rothman, D. H., Grotzinger, J. P., And Flemings, P., 1994, Scaling In Turbidite Deposition: Journal Of Sedimentary Research, V. 64, No. 1, P. 59 - 67.

Rouvier, H., 1977, Géologie De l'Extrême Nord Tunisien: Tectoniques Et Paléogéographies Superposées À L'extrémité Orientale De La Chaîne Nord Maghrébine: Uni. P. & M. Curie., 703 P.

Rusnak, G. A., 1957, The Orientation Of Sand Grains Under Conditions Of "Unidirectional" Fluid Flow: 1. Theory And Experiment: The Journal Of Geology, V. 65, No. 4, P. 384-409.

Russ, J. C., 2011, The Image Processing Handbook, Sixth Edition, CRC Press, Inc., 885 P.:

Sadler, P. M., 1982, Bed-Thickness And Grain Size Of Turbidites: Sedimentology, V. 29, No. 1, P. 37-51.

Sagnotti, L., 2011, Magnetic Anisotropy, *In* Gupta, H., Ed., Encyclopedia Of Solid Earth Geophysics: Netherlands, Springer, P. 715 - 876.

Sahni, A., Dehghani, K., And Prieditis, J., 2005, Benchmarking Heterogeneity Of Simulation Models, SPE Annual Technical Conference And Exhibition, Volume SPE Paper 96838: Dallas, Texas, Society Of Petroleum Engineers.

Sakai, T., Yokokawa, M., Kubo, Y. S., Endo, N., And Masuda, F., 2002, Grain Fabric Of Experimental Gravity Flow Deposits: Sedimentary Geology, V. 154, No. 1, P. 1-10.

Salaheldin, T. M., Imran, J., Chaudhry, M. H., And Reed, C., 2000, Role Of Fine-Grained Sediment In Turbidity Current Flow Dynamics And Resulting Deposits: Marine Geology, V. 171, No. 1, P. 21-38.

Sallenger, A. H., 1979, Inverse Grading And Hydraulic Equivalence In Grain-Flow Deposits: Journal Of Sedimentary Petrology, V. 49, No. 2, P. 553-562.

Sanders, J. E., 1960, Primary Sedimentary Structures Formed By Turbidity Currents And Related Resedimentation Mechanisms, P. 192 - 219.

-, 1965, Primary Sedimentary Structures Formed By Turbidity Currents And Related Resedimentation Mechanisms, *In* Middleton, G. V., Ed., Primary Sedimentary Structures And Their Hydrodynamic Interpretation, Volume 12, Society Of Economic Paleontologists And Mineralogists Special Publication, P. 192-219.

Sarmah, R. K., 2013, Study Of Cyclic Pattern And Lithofacies Variability By Application Of Markov Chains And Entropy Analysis To Tikak Parbat Formation, Makum Coal Basin, North Eastern India: European International Journal Of Science And Technology, V. 2, No. 6, P. 41-55.

Savage, S. B., And Lun, C. K. K., 1988, Particle Size Segregation In Inclined Chute Flow Of Dry Cohesionless Granular Solids: Journal Of Fluid Mechanics, V. 189, P. 311-335.

Scheidegger, A. E., And Potter, P. E., 1965, Textural Studies Of Graded Bedding. Observation And Theory: Sedimentology, V. 5, No. 4, P. 289-304.

Schmalz , J. P., And Rahme, H. S., 1950, T He Variations In Water Flood Performance With Variation In Permeability Profile: Production Monthly, V. 15, No. 9.

Schwarzacher, W., 1963, Orientation Of Crinoids By Current Action: Journal Of Sedimentary Research, V. 33, No. 3, P. 580-586.

Scott, K. M., 1967, Intra-Bed Palaeocurrent Variations In A Silurian Flysch Sequence, Kirkcudbrightshire, Southern Uplands Of Scotland: Scottish Journal Of Geology, V. 3, No. 2, P. 268 - 281.

Seelos, K., And Sirocko, F., 2005, RADIUS – Rapid Particle Analysis Of Digital Images By Ultra-High-Resolution Scanning Of Thin Sections: Sedimentology, V. 52, No. 3, P. 669-681.

Selmaoui, N., Repetti, B., Laporte-Magoni, C., And Allenbach, M., 2004, Coupled Strata And Granulometry Detection On Indurated Cores By Gray-Level Image Analysis: Geo-Marine Letters, V. 24, No. 4, P. 241-251.

Sequeiros, O. E., Cantelli, A., Viparelli, E., White, J. D. L., García, M. H., And Parker, G., 2009, Modeling Turbidity Currents With Nonuniform Sediment And Reverse Buoyancy: Water Resources Research, V. 45, No. 6, P. 1 - 28.

Sestini, G., And Pranzini, G., 1965, Correlation Of Sedimentary Fabric And Sole Marks As Current Indicators In Turbidites: Journal Of Sedimentary Research, V. 35, No. 1, P. 100-108.

Shanmugam, G., 1996, High-Density Turbidity Currents: Are They Sandy Debris Flows?: PERSPECTIVES: Journal Of Sedimentary Research, V. 66, No. 1, P. 2 - 10.

-, 1997, The Bouma Sequence And The Turbidite Mind Set: Earth-Science Reviews, V. 42, No. 4, P. 201-229.

-, 2000, 50 Years Of The Turbidite Paradigm (1950s—1990s): Deep-Water Processes And Facies Models—A Critical Perspective: Marine And Petroleum Geology, V. 17, No. 2, P. 285-342.

-, 2002, Ten Turbidite Myths: Earth-Science Reviews, V. 58, No. 3, P. 311-341.

-, 2006, Deep-Water Processes And Facies Models: Implications For Sandstone Petroleum Reservoirs, Elsevier, 500 P.:

-, 2012, New Perspectives On Deep-Water Sandstones : Origin, Recognition, Initiation, And Reservoir Quality, Kidlington, Oxford, UK, Elsevier, Handbook Of Petroleum Exploration And Productio.

-, 2016, Submarine Fans: A Critical Retrospective (1950–2015): Journal Of Palaeogeography, V. 5, No. 2, P. 110-184.

Shanmugam, G., And Benedict, G. L., 1978, Fine-Grained Carbonate Debris Flow, Ordovician Basin Margin, Southern Appalachians: Journal Of Sedimentary Research, V. 48, No. 4, P. 1233-1239.

Shanmugam, G., And Moiola, R. J., 1995, Reinterpretation Of Depositional Processes In A Classic Flesh Sequence (Pennsylvanian Jackford Group), Ouachita Mountains, Arkansas And Oklahoma: AAPG Bulletin, V. 79, No. 5, P. 672-695.

Shanmugam, G., And Wang, Y., 2014, Review Of Research In Internal-Wave And Internal-Tide Deposits Of China: Discussion: Journal Of Palaeogeography, V. 3, No. 4, P. 332-350.

Shanmugam, G. S. T., 2010, Sandy-Mass-Transport Deposits (SMTD) In Deep-Water Environments: Recognition, Geometry, And Reservoir Quality, AAPG Annual Convention And Exhibition: Louisiana, USA, P. 234.

Sharma, M., Sharma, S., Khan, Z. A., Singh, I. B., And Srivastrava, P., 1999, Partial Independence And Entropy Analysis Of Middle Siwalik Succession, Jammu Area, India: Geoinformatics, V. 10, No. 3, P. 169-185.

Shepherd, R. G., 1989, Correlations Of Permeability And Grain Size: Ground Water, V. 27, No. 5, P. 633-638.

Shipp, R. C., Weimer, P., And Posamentier, H. W., 2011, Mass-Transport Deposits In Deepwater Settings, SEPM Soc For Sed Geology, 532 P.:

Shipra, S., S, D., And Sahoo, S. R., 2015, Application Of Markov Chain And Entropy Function For Cyclicity Analysis Of A Lithostratigraphic Sequence - A Case History From The Kolhan Basin,Jharkhand, Eastern India: Journal Of Geology & Geophysics, V. 4, No. 5, P. 1 - 7.

Shringarpure, M. S., Cantero, M. I., And Balachandar, S., 2014, Mechanisms Of Complete Turbulence Suppression In Turbidity Currents Driven By Mono-Disperse And Bi-Disperse Suspensions Of Sediment: The Journal Of Computational Multiphase Flows, V. 6, No. 3, P. 221-245.

Shukla, U. K., Khan, Z. A., And Singh, I. B., 1996, Markov Chain Analysis Of The Shallow Marine Bhuj Sandstone Of Early Cretaceous Age, Kachchh Basin, India: Geological Society Of India, V. 48, No. 5, P. 567-578.

Signorini, R., 1936, Determinazione Del Senso Di Sedimentazionedegli Strati Nelle Formazioni Arenacee Nell'appenninosettentrionale: Boll. Soc. Geol. It, V. 55, P. 259-265.
Sinclair, H. D., 1994, The Influence Of Lateral Basinal Slopes On Turbidite Sedimentation In The Annot Sandstones Of SE France: Journal Of Sedimentary Research, V. 64, No. 1, P. 42 - 54.
-, 1997, Tectonostratigraphic Model For Underfilled Peripheral Foreland Basins: An Alpine Perspective: Geological Society Of American Bulletin, V. 109, No. 3, P. 324-346.
Sinclair, H. D., And Cowie, P. A., 2003, Basin- Floor Topography And The Scaling Of Turbidites: The Journal Of Geology, V. 111, No. 3, P. 277-299.
Skempton, A. W., And Hutchinson, J. N., 1969, Stability Of Natural Slopes And Embankment Foundations. State-Of-The-Art Report, Internation Conference On Soil Mechanics And Foundation Engineering, Volume 7th: Mexico City, P. 291-335.
Smith, D. E., Shi, S., Cullingford, R. A., Dawson, A. G., Dawson, S., Firth, C. R., Foster, I. D. L., Fretwell, P. T., Haggart, B. A., Holloway, L. K., And Long, D., 2004, The Holocene Storegga Slide Tsunami In The United Kingdom: Quaternary Science Reviews, V. 23, No. 23-24, P. 2291-2321.
Smith, J. T., And Cobb, W. M., 1997, Waterflooding, Evansville, Midwest Office Of The Petroleum Technology Transfer Council, 584 P.:
Snabre, P., Pouligny, B., Metayer, C., And Nadal, F., 2009, Size Segregation And Particle Velocity Fluctuations In Settling Concentrated Suspensions: Rheologica Acta, V. 48, No. 8, P. 855-870.
Sohn, Y. K., 1997, On Traction-Carpet Sedimentation: Journal Of Sedimentary Research, V. 67, No. 3, P. 502 - 509.
Soliman, O. M., And Balilah, A. Y., 2015, Deep-Marine To Shelf-Margin Deltaic Sedimentation, Silurian Succession, Saudi Arabia, AAPG Annual Convention & Exhibition: Denver, Colorado.
Southard, J. B., 1991, Experimental Determination of Bed-Form Stability: Annual Reviews in Earth Planet Science, V. 19, P. 423-455.
Southern, S. J., Patacci, M., Felletti, F., And Mccaffrey, W. D., 2015, Influence Of Flow Containment And Substrate Entrainment Upon Sandy Hybrid Event Beds Containing A Co-Genetic Mud-Clast-Rich Division: Sedimentary Geology, V. 321, No. Supplement C, P. 105-122.
Sparks, R. S. J., Bonnecaze, R. T., Huppert, H. E., Lister, J. R., Hallworth, M. A., Mader, H., And Phillips, J., 1993, Sediment-Laden Gravity Currents With Reversing Buoyancy: Earth And Planetary Science Letters, V. 114, No. 2, P. 243-257.
Spence, S., And Kreutz, H., 2003, The Kingfisher Field, Block 16/8a, UK North Sea: Geological Society, London, Memoirs, V. 20, No. 1, P. 305 - 314.
Spinewine, B., Rensonnet, D., Clare, M., Capart, H., De Thier, T., And Dan-Unterseh, G., 2013, Numerical Modelling Of Runout And Velocity For Slide-Induced Submarine Density Flows: A Building Block Of An Integrated Geohazards Assessment For Deepwater Developments, Offshore Technology Conference: Houston, P. 1 - 18.
Spychala, Y. T., Hodgson, D. M., Stevenson, C. J., And Flint, S. S., 2017, Aggradational Lobe Fringes: The Influence Of Subtle Intrabasinal Seabed Topography On Sediment Gravity Flow Processes And Lobe Stacking Patterns: Sedimentology, V. 64, No. 2, P. 582-608.
Stanley, D. J., 1961, Etudes Sedimentologique Des Gres D' Annot Et De Leurs Equivelents Lateraux [Ph.D: Université De Grenoble, 158 P.
-, 1963, Vertical Petrographic Variability In The Annot Sandstones: Some Preliminary Observations And Generalisations: Journal Of Sedimentary Petrology, V. 33, No. 3, P. 783-788.
Stanley, D. J., And Bouma, A. H., 1964, Methodology And Paleogeographic Interpretation Of Flysch Formations: A Summary Of Studies In The Maritime Alps, Developments In Sedimentology, Volume Volume 3, Elsevier, P. 34-64.
Stanley, D. J., Palmer, H. D., And Dill, R. F., 1978, Coarse Sediment Transport By Mass Flow And Turbidity Current Processes And Downslope Transformations In Annoy Sandstone Canyon-Fan Valley Systems, *In* Stanley, D. J., And Kelling, G., Eds., Sedimentation N Submarine Canyons, Fan, And Trenches: Stroudsburg, PA, Dowden, Hutchinson And Ross, P. 85 - 113.

Starek, D., Soták, J., Jablonský, J., And Marschalko, R., 2013, Large-Volume Gravity Flow Deposits In The Central Carpathian Paleogene Basin (Orava Region, Slovakia): Evidence For Hyperpycnal River Discharge In Deep-Sea Fans: Geologica Carpathica, V. 64, No. 4, P. 305-326.

Staňová, S., And Soták, J., 2004, Turbidite Bed Thickness Distributions Applied In Interpretation Of Submarine-Fan Depositional Environments Of The Kyčera Beds (Rača Unit, Magura Group): Geolines, V. 17, P. 82-84.

Staňová, S., Soták, J., And Hudec, N., 2009, Markov Chain Analysis Of Turbiditic Facies And Flow Dynamics (Magura Zone, Outer Western Carpathians, NW Slovakia): Geologica Carpathica, V. 60, No. 4, P. 295-305.

Steel, E., Buttles, J., Simms, A. R., Mohrig, D., And Meiburg, E., 2017, The Role Of Buoyancy Reversal In Turbidite Deposition And Submarine Fan Geometry: Geology, V. 45, No. 1, P. 35-38.

Stephen, K. D., Clark, J. D., And Gardiner, A. R., 2001, Outcrop-Based Stochastic Modelling Of Turbidite Amalgamation And Its Effects On Hydrocarbon Recovery: Petroleum Geoscience, V. 7, No. 2, P. 163 - 172.

Stevenson, C. J., Jackson, C. A. L., Hodgson, D. M., Hubbard, S. M., And Eggenhuisen, J. T., 2015, Deep-Water Sediment Bypass: Journal Of Sedimentary Research, V. 85, No. 9, P. 1058-1081.

Stevenson, C. J., And Peakall, J., 2010, Effects Of Topography On Lofting Gravity Flows: Implications For The Deposition Of Deep-Water Massive Sands: Marine And Petroleum Geology, V. 27, No. 7, P. 1366-1378.

Stevenson, C. J., Talling, P. J., Masson, D. G., Sumner, E. J., Frenz, M., And Wynn, R. B., 2014, The Spatial And Temporal Distribution Of Grain-Size Breaks In Turbidites: Sedimentology, V. 61, No. 4, P. 1120-1156.

Stevenson, C. J., Talling, P. J., Wynn, R. B., Masson, D. G., Hunt, J. E., Frenz, M., Akhmetzhanhov, A., And Cronin, B. T., 2013, The Flows That Left No Trace: Very Large-Volume Turbidity Currents That Bypassed Sediment Through Submarine Channels Without Eroding The Sea Floor: Marine And Petroleum Geology, V. 41, No. Supplement C, P. 186-205.

Stow, D., Hunter, S., Wilkinson, D., And Hernández-Molina, F., 2008, The Nature Of Contourite Deposition, *In* Rebesco, M., And Camerlenghi, A., Eds., Contourites, Volume 60, Developments In Sedimentology, P. 143-156.

Stow, D. A. V., 1984, Turbidite Facies, Associations, And Sequences In The Southeastern Angola Basin: Initial Reports Of The Deep Sea Drilling Project, V. 75, P. 785 - 799.

-, 1985, Deep-Sea Clastics: Where Are We And Where Are We Going?: Geological Society, London, Special Publications, V. 18, No. 1, P. 67.

-, 1986, Deep Clastic Seas, *In* Reading, H. G., Ed., Sedimentary Environments And Facies: Oxford, Blackwell, P. 399-444.

-, 2005, Sedimentary Rocks In The Field: A Colour Guide, UK, Academic Press.

Stow, D. A. V., And Bowen, A. J., 1980, A Physical Model For The Transport And Sorting Of Fine-Grained Sediment By Turbidity Currents: Sedimentology, V. 27, No. 1, P. 31-46.

Stow, D. A. V., Brackenridge, R., Patel, U., And Toulmin, S., 2012, Geohazards And Ocean Hazards In Deepwater: Overview And Methods Of Assessment, Offshore Technology Conference: Houston, Texas, USA, Onepetro.

Stow, D. A. V., Hernández-Molina, F. J., Llave, E., Sayago-Gil, M., Del Río, V. D., And Branson, A., 2009, Bedform-Velocity Matrix: The Estimation Of Bottom Current Velocity From Bedform Observations: Geology, V. 37, No. 4, P. 327-330.

Stow, D. A. V., And Johansson, M., 2000, Deep-Water Massive Sands: Nature, Origin And Hydrocarbon Implications: Marine And Petroleum Geology, V. 17, No. 2, P. 145-174.

Stow, D. A. V., And Mayall, M., 2000, Deep-Water Sedimentary Systems: New Models For The 21st Century: Marine And Petroleum Geology, V. 17, No. 2, P. 125-135.

Stow, D. A. V., And Piper, D. J. W., 1984, Deep-Water Fine-Grained Sediments: Facies Models: Geological Society, London, Special Publications, V. 15, No. 1, P. 611 - 646.

Strachan, L. J., 2008, Flow Transformations In Slumps: A Case Study From The Waitemata Basin, New Zealand: Sedimentology, V. 55, No. 5, P. 1311-1332.

Straub, K. M., And Pyles, D. R., 2012, Quantifying The Hierarchical Organization Of Compensation In Submarine Fans Using Surface Statistics: Journal Of Sedimentary Research, V. 82, No. 11, P. 889-898.

Sumner, E. J., Amy, L. A., And Talling, P. J., 2008, Deposit Structure And Processes Of Sand Deposition From Decelerating Sediment Suspensions: Journal Of Sedimentary Research, V. 78, No. 8, P. 529-547.

Sumner, E. J., Peakall, J., Parsons, D. R., Wynn, R. B., Darby, S. E., Dorrell, R. M., Mcphail, S. D., Perrett, J., Webb, A., And White, D., 2013, First Direct Measurements Of Hydraulic Jumps In An Active Submarine Density Current: Geophysical Research Letters, V. 40, No. 22, P. 5904-5908.

Sumner, E. J., Talling, P. J., And Amy, L. A., 2009, Deposits Of Flows Transitional Between Turbidity Current And Debris Flow: Geology, V. 37, No. 11, P. 991-994.

Sumner, E. J., Talling, P. J., Amy, L. A., Wynn, R. B., Stevenson, C. J., And Frenz, M., 2012, Facies Architecture Of Individual Basin-Plain Turbidites: Comparison With Existing Models And Implications For Flow Processes: Sedimentology, V. 59, No. 6, P. 1850-1887.

Svendsen, J. B., And Hartley, N. R., 2002, Synthetic Heavy Mineral Stratigraphy: Applications And Limitations: Marine And Petroleum Geology, V. 19, No. 4, P. 389-405.

Svirsky, D., Ryazanov, A., Pankov, M., Corbett, P. W. M., And Posysoev, A., 2004, Hydraulic Flow Units Resolve Reservoir Description Challenges In A Siberian Oil Field, SPE Asia Pacific Conference On Integrated Modelling For Asset Management: Kuala Lumpur, Malaysia, Society Of Petroleum Engineers, P. 1 - 15.

Sylvester, Z., And Lowe, D. R., 2002, Textural Trends In Deposits Of Collapsing Turbidity Currents: Sedimentology Of Turbidites And Slurry Beds From The Oligocene Flysch Of The East Carpathians, Romania, AAPG Annual Meeting: Houston, Texas, Citeseer, P. 1 - 6.

-, 2004, Textural Trends In Turbidites And Slurry Beds From The Oligocene Flysch Of The East Carpathians, Romania: Sedimentology, V. 51, No. 5, P. 945-972.

Synolakis, C. E., And Kong, L., 2006, Runup Measurements Of The December 2004 Indian Ocean Tsunami: Earthquake Spectra, V. 22, No. S3, P. 67-91.

Sébastien, P. M. Z., 2001, Les Systemes Turbiditiques Profonds De La Marge Celtiquearmoricaine (Golfe De Gascogne) : Physiographie Et Evolution Au Cours Des Derniers 30 000 Ans [Docteur: L'universite Bordeaux I, 295 P.

Taira, A., And Scholle, P. A., 1979, Deposition Of Resedimented Sandstone Beds In The Pico Formation, Ventura Basin, California, As Interpreted From Magnetic Fabric Measurements: Geological Society Of America Bulletin, V. 90, No. 10, P. 952-962.

Talling, P. J., 2001, On The Frequency Distribution Of Turbidite Thickness: Sedimentology, V. 48, No. 6, P. 1297-1329.

Talling, P. J., Allin, J., Armitage, D. A., Arnott, R. W. C., Cartigny, M. J. B., Clare, M. A., Felletti, F., Covault, J. A., Girardclos, S., And Hansen, E., 2015, Key Future Directions For Research On Turbidity Currents And Their Depositskey Future Directions For Research On Turbidity Currents And Their Deposits: Journal Of Sedimentary Research, V. 85, No. 2, P. 153-169.

Talling, P. J., Amy, L. A., And Wynn, R. B., 2007a, New Insight Into The Evolution Of Large-Volume Turbidity Currents: Comparison Of Turbidite Shape And Previous Modelling Results: Sedimentology, V. 54, No. 4, P. 737-769.

Talling, P. J., Amy, L. A., Wynn, R. B., Blackbourn, G., And Gibson, O., 2007b, Evolution Of Turbidity Currents Deduced From Extensive Thin Turbidites: Marnoso Arenacea Formation (Miocene), Italian Apennines: Journal Of Sedimentary Research, V. 77, No. 3, P. 172-196.

Talling, P. J., Amy, L. A., Wynn, R. B., Peakall, J., And Robinson, M., 2004, Beds Comprising Debrite Sandwiched Within Co-Genetic Turbidite: Origin And Widespread Occurrence In Distal Depositional Environments: Sedimentology, V. 51, No. 1, P. 163-194.

Talling, P. J., Malgesini, G., And Felletti, F., 2013a, Can Liquefied Debris Flows Deposit Clean Sand Over Large Areas Of Sea Floor? Field Evidence From The Marnoso-Arenacea Formation, Italian Apennines: Sedimentology, V. 60, No. 3, P. 720-762.

Talling, P. J., Masson, D. G., Sumner, E. J., And Malgesini, G., 2012, Subaqueous Sediment Density Flows: Depositional Processes And Deposit Types: Sedimentology, V. 59, No. 7, P. 1937-2003.

Talling, P. J., Paull, C. K., And Piper, D. J. W., 2013b, How Are Subaqueous Sediment Density Flows Triggered, What Is Their Internal Structure And How Does It Evolve? Direct Observations From Monitoring Of Active Flows: Earth-Science Reviews, V. 125, No. Supplement C, P. 244-287.

Talling, P. J., Wynn, R. B., Masson, D. G., Frenz, M., Cronin, B. T., Schiebel, R., Akhmetzhanov, A. M., Dallmeier-Tiessen, S., Benetti, S., Weaver, P. P. E., Georgiopoulou, A., Zühlsdorff, C., And Amy, L. A., 2007c, Onset Of Submarine Debris Flow Deposition Far From Original Giant Landslide: Nature, V. 450, P. 541 - 544.

Talling, P. J., Wynn, R. B., Schmmidt, D. N., Rixon, R., Sumner, E., And Amy, L., 2010, How Did Thin Submarine Debris Flows Carry Boulder-Sized Intraclasts For Remarkable Distances Across Low Gradients To The Far Reaches Of The Mississippi Fan?: Journal Of Sedimentary Research, V. 80, No. 10, P. 829-851.

Tappin, D. R., 2010, Mass Transport Events And Their Tsunami Hazard, *In* Mosher, D. C., Shipp, C., Moscardelli, L., Chaytor, J., Baxter, C., Lee, H., And Urgeles, R., Eds., Submarine Mass Movement And Their Consequences, Volume 28: London, Springer Science, P. 667-684.

Teh, W., Willhite, G. P., And Doveton, J. H., 2012, Improved Reservoir Characterization In The Ogallah Field Using Petrophysical Classifiers Within Electrofacies, SPE Improved Oil Recovery Symposium: Tulsa, Oklahoma, Society Of Petroleum Engineers, P. 15 - 33.

Terklay, V., And Arnott, R. W. C., 2014, Matrix-rich And Associated Matrix-poor Sandstones: Avulsion Splays In Slope And Basin-floor Strata: Sedimentology, V. 61, No. 5, P. 1175-1197.

Tewari, R. C., Singh, D. P., And Khan, Z. A., 2009, Application Of Markov Chain And Entropy Analysis To Lithologic Succession — An Example From The Early Permian Barakar Formation, Bellampalli Coalfield, Andhra Pradesh, India: Journal Of Earth System Science, V. 118, No. 5, P. 583 - 596.

Thomas, A. R. A., 2007, An Integrated Grain-Size And Heavy Mineral Analysis Of The Palaeocene Strata Of The London Basin, *In* Maria, A. M., And Wright, D. T., Eds., Heavy Minerals In Use, Volume 58, Elsevier, P. 307-322.

Thomas, M. F. H., 2011, Sedimentology And Basin Context Of The Numidian Flysch Formation, Sicily And Tunisia [Doctor Of Philosophy: University Of Manchester, 278 P.

Thomas, M. F. H., Bodin, S., Redfern, J., And Irving, D. H. B., 2010, A Constrained African Craton Source For The Cenozoic Numidian Flysch: Implications For The Palaeogeography Of The Western Mediterranean Basin: Earth-Science Reviews, V. 101, No. 1–2, P. 1-23.

Thompson, B. J., Garrison, R. E., And Moore, C. J., 2007, A Reservoir-Scale Miocene Injectite Near Santa Cruz, California, *In* Hurst, A., And Cartwright, J., Eds., Sand Injectites: Implications For Hydrocarbon Exploration And Production, Volume 87: Tulsa, Oklahoma, American Association Of Petroleum Geologists Memoir, P. 151-162.

Thomson, J., 2016, An Integrated Approach To Quantifying Petrophysical Heterogeneity In The Deep-Marine East Brae Formation, Viking Graben,North Sea [Master Of Science In Petroleum Engineering: Heriot - Watt University, 49 P.

Tilston, M., Arnott, R. W. C., Rennie, C. D., And Long, B., 2015, The Influence Of Grain Size On The Velocity And Sediment Concentration Profiles And Depositional Record Of Turbidity Currents: Geology, V. 43, No. 9, P. 839-842.

Tinterri, R., Drago, M., Consonni, A., Davoli, G., And Mutti, E., 2003, Modelling Subaqueous Bipartite Sediment Gravity Flows On The Basis Of Outcrop Constraints: First Results: Marine And Petroleum Geology, V. 20, No. 6–8, P. 911-933.

Tita, D. E., And Djomeni, A. L., 2016, Application Of Markov Chain And Entropy Analysis To Lithologic Succession-An Example From The Post-Rift Cretaceous And Tertiary

Formations, Kombe-Nsepe Area, Douala Subbasin, Cameroon: International Journal Of Scientific And Research Publications, V. 6, No. 5, P. 692 - 709.
Toniolo, H., Lamb, M., And Parker, G., 2006, Depositional Turbidity Currents In Diapiric Minibasins On The Continental Slope: Formulation And Theory: Journal Of Sedimentary Research, V. 76, No. 5, P. 783-797.
Torricelli, S., And Biffi, U., 2001, Palynostratigraphy Of The Numidian Flysch Of Northern Tunisia (Oligocene–Early Miocene) Palynology, V. 25, P. 29–55.
Totten, M. W., And Hanan, M. A., 2007, Heavy Minerals In Shales, *In* Mange, M. A., And Wright, D. T., Eds., Heavy Minerals In Use, Volume 58, Elsevier, P. 323-341.
Trofimovs, J., Amy, L., Boudon, G., Deplus, C., H Doyle, E., Fournier, N., Hart, M., Komorowski, J.-C., Le Friant, A., Lock, E. J., Pudsey, C., Ryan, G., R J Sparks, S., And Talling, P. J., 2006, Submarine Pyroclastic Deposits Formed At The Soufrière Hills Volcano, Montserrat (1995--2003): What Happens When Pyroclastic Flows Enter The Ocean?, Geology, 4 P.:
Tucker, M. E., 2003, Sedimentary Rocks In The Field, John Wiley & Sons, 249 P.:
Turner, C. C., And Allen, P. J., 1991, The Central Brae Field, Block 16/7a, UK North Sea: Geological Society, London, Memoirs, V. 14, No. 1, P. 49 - 54.
Turner, C. C., Cohen, J. M., Connell, E. R., And Cooper, D. M., 1987, A Depositional Model For The South Brae Oilfield: Petroleum Geology Of Northwest Europe. Graham & Trotman, London, P. 853-864.
Turner, C. C., And Connell, E. R., 1991, Stratigraphic Relationships Between Upper Jurassic Submarine Fan Sequences In The Brae Area, U.K. North Sea: The Implications For Reservoir Distribution, 23rd Annual Offshore Technology Conference: Houston, Texas, Offshore Technology Conference, P. 83 - 91.
Tyler, N., And Finley, R. J., 1992, Architectural Controls On The Recovery Of Hydrocarbons From Sandstone Reservoirs, P. 1.
Underhill, J. R., 2003, The Tectonic And Stratigraphic Framework Of The United Kingdom's Oil And Gas Fields: Geological Society, London, Memoirs, V. 20, No. 1, P. 17 59.
Van Den Berg, E. H., Bense, V. F., And Schlager, W., 2003, Assessing Textural Variation In Laminated Sands Using Digital Image Analysis Of Thin Sections: Journal Of Sedimentary Research, V. 73, No. 1, P. 133-143.
Van Den Berg, E. H., Meesters, A. G. C. A., Kenter, J. A. M., And Schlager, W., 2002, Automated Separation Of Touching Grains In Digital Images Of Thin Sections: Computers & Geosciences, V. 28, No. 2, P. 179-190.
Varnes, D. J., 1978, Slope Movement Types And Processes: Special Report, V. 176, P. 11-33.
Vrolijk, P. J., And Southard, J. B., 1997, Experiments On Rapid Deposition Of Sand From High-Velocity Flows: Geoscience Canada, V. 24, No. 1, P. 45 - 54.
Walker, R. G., 1975, Generalized Facies Models For Resedimented Conglomerates Of Turbidite Association: Geological Society Of America Bulletin, V. 86, No. 6, P. 737-748.
-, 1978, Deep-Water Pebbly Sandstones And Conglomerates - Facies And Reservoir Characteristics, Offshore Technology Conference: Houston, Offshore Technology Conference, P. 581 - 584.
Ward, S. N., 2001, Landslide Tsunami: Journal Of Geophysical Research: Solid Earth, V. 106, No. B6, P. 11201-11215.
Weirich, F., 1988, Field Evidence For Hydraulic Jumps In Subaqeous Sediment Gravity Flows, USA, 626-629 P.:
Wezel, F. C., 1970, Numidian Flysch: An Oligocene - Early Miocene Continental Rise Deposit Off The African Platform: Nature, V. 228, No. 5268, P. 275-276.
Wust, G., 1936, Schichtung Und Zirkulation Atlantik Ozean. Das Bodenwasser Und Die Stratosphere.: Wissenschaftliche Ergebnisse Der Deutschen Atlantischen Expedition "Meteor" 1925–1927, V. 6, P. 1-288.
Xu, H., And Maccarthy, I. A. J., 1998, Markov Chain Analysis Of Vertical Facies Sequences Using A Computer Software Package (SAVFS): Courtmacsherry Formation (Tournaisian), Southern Ireland: Computers & Geosciences, V. 24, No. 2, P. 131-139.
Xu, J., Noble, M., And K. Rosenfeld, L., 2004, In-Situ Measurements Of Velocity Structure Within Turbidity Currents, 9311 P.:

Xu, J. P., Sequeiros, O. E., And Noble, M. A., 2014, Sediment Concentrations, Flow Conditions, And Downstream Evolution Of Two Turbidity Currents, Monterey Canyon, USA: Deep Sea Research Part I: Oceanographic Research Papers, V. 89, No. Supplement C, P. 11-34.

Xu, Q., Shi, W., Xie, X., Manger, W., Mcguire, P., Zhang, X., Wang, R., And Xu, Z., 2016, Deep-Lacustrine Sandy Debrites And Turbidites In The Lower Triassic Yanchang Formation, Southeast Ordos Basin, Central China: Facies Distribution And Reservoir Quality: Marine And Petroleum Geology, V. 77, No. Supplement C, P. 1095-1107.

Yagishita, K., Ashi, J., Ninomiya, S., And Taira, A., 2004, Two Types Of Plane Beds Under Upper-Flow-Regime In Flume Experiments: Evidence From Grain Fabric: Sedimentary Geology, V. 163, No. 3, P. 229-236.

Yaich, C., 1997, Dynamique Sédimentaire, Eustatisme Et Tectonique Durant l'Oligo-Miocène En Tunisie Centro-Septentrionale. Formations Fortuna, Messiouta Et Grijima; Numidien Et Gréso-Micacé: Tunis, P. 479.

Yakub, N. Y., 2017, Optimal Layering Scheme In A Reservoir By Quantifying The Heterogeneity Coefficient [Msc Independent Project]: Heriot-Watt University, 52 P.

Young, I. T., Gerbrands, J. J., And Van Vliet, L. J., 1998, Fundamentals Of Image Processing, Delft University Of Technology Delft.

Zavala, C., And Arcuri, M., 2016, Intrabasinal And Extrabasinal Turbidites: Origin And Distinctive Characteristics: Sedimentary Geology, V. 337, No. Supplement C, P. 36-54.

Zavala, C., Arcuri, M., Gamero, H., Contreras, C., And Di Meglio, M., 2011, A Genetic Facies Tract For The Analysis Of Sustained Hyperpycnal Flow Deposits, 31-51 P.:

Zhao, L., Li, L., Wu, Z., And Zhang, C., 2016, Analytical Model Of Waterflood Sweep Efficiency In Vertical Heterogeneous Reservoirs Under Constant Pressure: Mathematical Problems In Engineering, V. 2016, P. 1 - 10.

Zheng, S.-Y., Corbett, P. W. M., Ryseth, A., And Stewart, G., 2000, Uncertainty In Well Test And Core Permeability Analysis: A Case Study In Fluvial Channel Reservoirs, Northern North Sea, Norway: AAPG Bulletin, V. 84, No. 12, P. 1929-1954.

Zhou, H., Wu, J., And Zhang, J., 2010a, Digital Image Processing: Part I, Ventus Publishing Aps, 72 P.:

-, 2010b, Digital Image Processing: Part II, Ventus Publishing Aps, 91 P.:

Zou, C., Wang, L., Li, Y., Tao, S., And Hou, L., 2012, Deep-Lacustrine Transformation Of Sandy Debrites Into Turbidites, Upper Triassic, Central China: Sedimentary Geology, V. 265-266, No. Supplement C, P. 143-155.